In-situ opvolgen van het vervormingsgedrag van voor de lucht- en ruimtevaart gekwalificeerde composieten met behulp van verbeterde draw-tower-Braggsensoren

In-situ Deformation Monitoring of Aerospace Qualified Composites with Embedded Improved Draw Tower Fibre Bragg Gratings

Eli Voet

Promotoren: prof. dr. ir. J. Degrieck, dr. ir. G. Luyckx
Proefschrift ingediend tot het behalen van de graad van
Doctor in de Ingenieurswetenschappen

Vakgroep Toegepaste Materiaalwetenschappen
Voorzitter: prof. dr. ir. J. Degrieck
Faculteit Ingenieurswetenschappen en Architectuur
Academiejaar 2010 - 2011

UNIVERSITEIT
GENT

ISBN 978-90-8578-422-7
NUR 971, 968
Wettelijk depot: D/2011/10.500/26

DANKWOORD – DANKSAGUNG - ACKNOWLEDGEMENTS

Het begon allemaal een vijftal jaar geleden. Ik als mecanicien, volledig in ornaat met overall, veiligheidsschoenen met stalen tip en tot in de ellebogen in de olie, te werken aan vliegtuigzuigermotoren, met de visie om mij via die weg op te werken naar gecertificeerde mecanicien in de vliegtuigindustrie. Ik moet toch even kwijt dat ik bij nader inzien zeer blij ben dat men mij bij FOS&S, met name de CTO Johan Vlekken en mijn vader Marc Voet, destijds gevraagd heeft om binnen een toch wel ambitieus federaal onderzoeksproject mee aan de slag te gaan. Aangezien FOS&S een zeer goede samenwerking had met de Universiteit Gent binnen een ander Europees project; het welbefaamde (voor sommigen onder ons) MASSFOS project voor de ESA, zou, indien ik akkoord ging natuurlijk, dit nieuwe project me tevens de mogelijkheid kunnen bieden om op termijn een doctoraat te behalen. Ik moest toen even goed slikken om dit alles te vatten en uiteraard heb ik dan ook even de tijd genomen om het nodige uit te pluizen en op een rijtje te zetten, samen met mijn toen nog pas afgestudeerde 'medegezel', Tine. Omdat ik toen nog een Industrieel Ingenieur Elektromechanica was, en dus niet mocht doctoreren zonder een predoctorale opleiding te volgen aan de universiteit, heb ik op dat moment besloten om dit binnen een Erasmus-Socrates uitwisselingsprogramma te doen tussen de Universiteit Gent en de Fachhochschule-Jena in Duitsland. De link tussen België en Duitsland is het Institut für Photonische Technologie in Jena (IPHT-Jena), waar FOS&S toen al een goede samenwerking mee had en waar ik mij in de instituutsreine en magnifieke labo's ten volle kon voorbereiden, zoals dat hoort binnen een postgraduaat - predoctorale opleiding, met een onderzoeksvoorbereidend project. Voilà, dit is zowat het voortraject dat ik gelukkig met succes heb kunnen afleggen om zo eindelijk met mijn doctoraat te mogen starten! Op zich al een zeer verrijkende ervaring en voorbode op de carrière die zou volgen.

Het doorstaan van een doctoraat kan je eigenlijk zien als het rijpen van een onderzoeker, zoals een goede wijn op eiken vaten, en het vergaren van een hele boel kennis, inzicht en ervaring. Dit kan pas als de wetenschapper effectief een aantal jaar (zelfstandig) onderzoek mag doen, weliswaar met vallen en opstaan en met de hulp van anderen. Het traject dat je doorloopt vóór het worden van een doctor is niet makkelijk samen te vatten, en al bij al kan ik enkel zeggen: wat een fantastische levenservaring! Én uiteraard is dit zeker niet de verdienste van mezelf alleen. Daarom eerst en vooral een woordje van dank, om te beginnen aan Herrn Prof. Hartmut Bartelt van het IPHT-Jena; Danke Sehr Professor Bartelt, dass Sie mir Damals als Gast empfangen haben in dass Institut und dass ich die darauf folgende Jahren ohne weitere Bedingungen meine Doktorarbeit ausführen könnte.

Nu ik dan toch begonnen ben met het uiteindelijke dankwoord zal ik trachten dit in een soort van chronologische volgorde te vervolledigen; Danke Eric Lindner! Einfach dafür dass ich (und später Tine) dich kennen gelernt habe, erst zusammen an einen Schreibtisch am IPHT mit der „Tiense Suiker" (dein Erste Wörter Flämisch), und darnach in Peter sein Garten neben der Grill mit der Echte Thüringer Bratwurst, ein Becks in die Hand, zusammen mit super tolle Deutsche Freunde!! Danke Peter, Suzi, Seb, Alec, Sonja, Olf, Sabrine und Olli für ihre Gastfreundschaft und herrliche Zeit in Jena. Sicher nicht zu vergessen, Danke Christoph! für deine Einführung in der Draw Tower Technologie, für deine mithilfe! Ohne deine Kenntnis, Leidenschaft und Unterstutzung werde ich nie die 80 µm Faser und Gitter erzogen haben. Dass gleiche gilt auch für Jens, danke um meine Faser wörtlich mit die hand

zu ziehen! Danke Martin und Christiane, für die immer gute Stimmung und ihre Hilfe im Labor. Manfred, auch dir sollte ich danken, für die herrliche Diskussionen über Faser Bragg Gitter und vieles anderes, aber auch für dass segelfliegen, dass ich Jena und die Schöne „Bergen“ und Umgebung mall erlebt habe in alle Ruhe von Weit da oben. Danke an alle anderen am IPHT die ich vergesse habe, aber die mindestens ebenso wichtig gewesen sein für meine Arbeit. Uiteraard kan ik nu niet anders dan het hele rijtje te overlopen. Een bedankje aan iedereen is misschien wel wat moeilijk, omdat ik altijd wel iemand zal vergeten, maar toch ga ik een poging ondernemen.

In eerste instantie natuurlijk bedankt aan mijn ouders, familieleden en vrienden, gewoonweg omdat jullie de belangrijkste personen zijn in mijn leven en omdat zonder jullie er nog zelfs geen sprake zou zijn van te zijn wie ik nu ben. Dit is natuurlijk de allereerste vereiste, waarvoor echt wel merci Mamtje, Pa om me aan te moedigen om te doen wat ik doe en te zijn wie ik nu ben en vooral om te leren om nooit op te geven! Bedankt aan heel de familie, om het in Kobe zijn woorden te zeggen ‘dadu’ Tati, Moeke, Vake, Pake Jos, Pake Gerard, Opi Leo, Meetje Evi en Nonkel Jorn voor jullie steun in de voorbije jaren en natuurlijk niet te vergeten Tine mijn fantastisch vrouwtje die me verdraagt in de soms moeilijke en hectische situaties en toch telkens weer steunt in wat ik doe, en Kobe mijn kleine deugniet! want bij jullie voel ik me Eli en dat is wie ik werkelijk ben.

Ik wil mijn hoofdpromotor Prof. Joris Degrieck bedanken, een fantastische Professor en briljante wetenschapper. Joris, bedankt simpelweg omdat je zo een buitengewone mens bent, om me met open armen te ontvangen op je vakgroep, eerst als predoctorale student en dan als doctorandus. Ik hoop ten zeerste dat mijn boekje iets heeft bijgedragen aan de (je) wetenschap. Geert, ‘me mate’, ondertussen post-doc en tevens een geweldige co-promotor, bedankt voor alles! Samen zijn we één uniform Bragg rooster dat gewoonweg multi-axiaal gaat (inderdaad fibre optic rules!). I owe You (en de familie) big time! Een bedankje aan Luc, jij bent de techneut, de eerste bouwsteen en ondersteuning van vele onderzoeken, ook die van mij! Dank je Ives, voor het mee in gang zetten van het onderzoeksprogramma, ik heb onze composietplaten goed kunnen gebruiken! Dank aan Prof. Wim VP voor je inzichten in de complexe wereld van de woven-fabrics, thanks Reddy for the Meso-scale modelling, we have gained much more insight now, the FBGs are grateful!! en dank aan Prof. Wim DW voor je initiatie in het samenbrengen en verder opvolgen van het huwelijk tussen de Bragg sensoren en de composieten. Dank je Martine voor de koffie, hotelboekingen en aanzet tot feestjes, spijtig dat ik niet meer daar kon zijn. Stefan, jij en ik weten welke de ‘farthest’ crack was in Budapest, naar mijn weten een legendarisch ECCM congres. Bedankt aan het hele FOS&S team, dat zeer dynamisch is moet ik wel zeggen, allen bedankt voor jullie steun en geduld de voorbije jaren. Toch in het bijzonder dank aan Jo, voor onze zeer aangename discussies en vooral om me de voorbije jaren wegwijs te maken in de wondere wereld van de FBGs. Hierbij aansluitend toch ook wel een extra bedankje aan Jan VR, die tevens gebeten is door dit Bragg virus, Jan ik hoop van harte dat wij samen nog veel watertjes mogen doorzwemmen!! Dank aan TenCate en Stork Fokker Aerospace voor het mogen gebruiken van jullie faciliteiten en vooral voor het lekker taaie composiet!! LAST BUT NOT LEAST; dank je Pa voor de kans die ik gekregen heb, ik heb er trachten het beste van te maken!! Ik hoop dat ik je fier heb gemaakt…

PUBLICATION LIST

Publications in international journa1 of the Science Citation Index (a1):

De Baere, I., **E. Voet**, W. Van Paepegem, J. Vlekken, V. Cnudde, B. Masschaele, and J. Degrieck, Strain monitoring in thermoplastic composites with optical fiber sensors: Embedding process, visualization with micro-tomography, and fatigue results. Journal of Thermoplastic Composite Materials, 2007. 20(5): p. 453-472.

De Baere, I., G. Luyckx, **E. Voet**, W. Van Paepegem, and J. Degrieck, On the feasibility of optical fibre sensors for strain monitoring in thermoplastic composites under fatigue loading conditions. Optics and Lasers in Engineering, 2009. 47(3-4): p. 403-411.

Geernaert, T., Luyckx, G., **Voet, E**., Nasilowski, T., Chah, K., Becker, M., Bartelt, H., Urbanczyk, W., Wojcik, J., De Waele, W., Degrieck, J., Terryn, H., Berghmans, F., and Thienpont, H.. Transversal Load Sensing With Fiber Bragg Gratings in Microstructured Optical Fibers. Ieee Photonics Technology Letters, 2009. 21(1-4): p. 6-8.

Luyckx, G., **E. Voet**, T. Geernaert, K. Chah, T. Nasilowski, W. De Waele, W. Van Paepegem, M. Becker, H. Bartelt, W. Urbanczyk, J. Wojcik, J. Degrieck, F. Berghmans, and H. Thienpont, Response of FBGs in Microstructured and Bow Tie Fibers Embedded in Laminated Composite. Ieee Photonics Technology Letters, 2009. 21(18): p. 1290-1292.

Geernaert, T., G. Luyckx, **E. Voet**, T. Nasilowski, K. Chah, M. Becker, H. Bartelt, W. Urbanczyk, J. Wojcik, W. De Waele, J. Dearieck, H. Terryn, F. Berghmans, and H. Thienpont, Transversal Load Sensing With Fiber Bragg Gratings in Microstructured Optical Fibers. Ieee Photonics Technology Letters, 2009. 21(1-4): p. 6-8.

Luyckx, G., **E. Voet**, W. De Waele, and J. Degrieck, et al., Multi-axial strain transfer from laminated CFRP composites to embedded Bragg sensor: I. Parametric study. Smart Materials & Structures, 2010. 19(10).

Voet, E., G. Luyckx, W. De Waele, and J. Degrieck, Multi-axial strain transfer from laminated CFRP composites to embedded Bragg sensor: II. Experimental validation. Smart Materials & Structures, 2010. 19(10).

Luyckx, G., **Voet, E.**, Lammens, N., and Degrieck, J., *Strain Measurements of Composite Laminates with Embedded Fibre Bragg Gratings: Criticism and Opportunities for Research.* Sensors, 2010. **11**(1): p. 384-408.

Sonnenfeld, C., S. Sulejmani, T. Geernaert, S. Eve, N. Lammens, G. Luyckx, **E. Voet**, J. Degrieck, W. Urbanczyk, P. Mergo, M. Becker, H. Bartelt, F. Berghmans, and H. Thienpont, Micro-structured optical fiber sensors embedded in laminate

composite for smart material applications. Sensors, 2011(Advanced Embedded Sensors)_in review.

Daggumati, S., **E. Voet**, W. Van Paepegem, J. Degrieck, T. Praet, B. Verhegghe, J. Xu, D.S. Ivanov, S.V. Lomov, and I. Verpoest, LOCAL STRAIN IN A 5 - HARNESS SATIN WEAVE COMPOSITE UNDER STATIC TENSION: PART II – Meso-FE analysis. Composites Science and Technology, 2010_in review.

Daggumati, S., **E. Voet**, W. Van Paepegem, J. Degrieck, J. Xu, S.V. Lomov, and I. Verpoest, LOCAL STRAIN IN A 5 - HARNESS SATIN WEAVE COMPOSITE UNDER STATIC TENSION: PART I – Experimental Analysis. Composites Science and Technology, 2010_in review.

Voet E., Luyckx G., Lammens N., De Waele W. and Degrieck J., Multi-axial strain monitoring of cross-ply laminated CFRP composites using residual strain induced birefringent FBGs. Composites Part A, 2011_in review

Publications in ISI proceedings (p1):

Voet, E., Luyckx G., De Baere I., Degrieck J., Hartmut B., Vlekken J., Jacobs E., High Strain monitoring during Fatigue Loading of Thermoplastic Composites using imbedded Draw Tower Fibre Bragg Grating Sensors, in Emboding Intelligence in Structures and Integrated Systems, P. Vincenzini and F. Casciati, Editors. 2009. p. 441-446.

Luyckx, G., **E. Voet**, W. De Waele, W. Van Paepegem, J. Degrieck, and J. Vlekken, et al., Strain monitoring of FRP elements using an embedded fibre optic sensor, in Emboding Intelligence in Structures and Integrated Systems, P. Vincenzini and F. Casciati, Editors. 2009. p. 435-440.

De Baere, I., G. Luyckx, W. Van Paepegem, J. Degrieck, **E. Voet**, and J. Vlekken, The use of optical fibers for fatigue testing of fiber-reinforced thermoplastics, in Emerging Technologies in Non-Destructive Testing, G. Busse, et al., Editors. 2008. p. 65-70.

Publications in conference proceedings (c1):

Parlevliet, P.P., **E. Voet**, H. Bersee, and A. Beukers. *Process monitoring with FBG sensors during vacuum infusion of thick composite laminates*. in *ICCM 16*. 2007. Kyoto, Japan.

De Baere, I., Luyckx, G., Van Paepegem, W., Degrieck, J., **Voet, E.**, and Vlekken, J. The use of optical fibers for fatigue testing of fiber-reinforced thermoplastics. in 4th International Conference on Emerging Technologies in Non-Destructive Testing. 2007. Stuttgart, GERMANY.

Voet, E., Luyckx G., De Baere I., Degrieck J., Hartmut B., Vlekken J., Jacobs E., High strain measurements during fatigue cycling in fibre reinforced thermoplastic composites using imbedded draw tower fibre Bragg grating sensors. in ECCM 13. 2008. Stockholm, Sweden.

De Baere, I., Van Paepegem, W., **Voet, E.**, and Degrieck, J. Fatigue testing of carbon fabric thermoplastics: different testing and instrumentation strategies. in SAMPE EUROPE 28th International Conference (SEICO 08), Composites Forever, Affortable, Durable, Sustainable and Creatable. 2008.

Van Roosbroeck, J., J. Vlekken, **E. Voet**, and M. Voet, A New Methodology for Fiber Optic Strain Gage Measurements and its Characterization. in SENSOR+TEST Conference Opto. 2009. Nürnberg, Germany.

Voet, E., Luyckx, G., Degrieck, J.. Response of embedded fibre Bragg gratings: strain transfer effects. In the Proceedings of OFS20. 2009. Edinburgh, UK.

Geernaert, T., Luyckx, G., **Voet, E**., Nasilowski, T. A., Chah, K., Becker, M., Bartelt, H., Urbanczyk, W., Wójcik, J., De Waele, W., Degrieck J., Berghmans, F., Thienpont, H., "Fiber Bragg gratings in microstructured optical fibers for stress Monitoring", In proceedings of the SPIE conference on optics and opto-electronics. 2009. Praag, CZECH REPUBLIC.

Geernaert, T., Luyckx, G., **Voet, E**., Nasilowski, T. A., Chah, K., Becker, M., Bartelt, H., Urbanczyk, W., Wójcik, J., De Waele, W., Degrieck, J., Berghmans, F., Thienpont, H., "Fiber Bragg gratings in microstructured optical fibers for stress Monitoring", In Proceeding of Sensor + Test. 2009. Nurnburg, GERMANY.

Luyckx, G., **Voet, E**., Geernaert, T., Nasilowski, T., Chah, K., Becker, M., Bartelt, H., Urbanczyk, W., Wojcik, J., De Waele, W., Degrieck, J., Terryn, H., Berghmans, F., and Thienpont, H., Benchmarking the response of Bragg gratings written in micro-structured and bow-tie fiber embedded in composites. In the Proceedings of OFS20. 2009. Edinburgh, UK.

Geernaert, T., Berghmans, F., Nasilowski, T., Thienpont, H., Luyckx, G., **Voet, E**., Degrieck, J., Urbanczyk, W., Wojcik, J., Becker, M., Bartelt, H., "Analyse de contraintes dans les matériaux composites à l'aide de réseaux de Bragg dans des fibres micro-structurées." In the Proceedings of Mesures et techniques Optiques pour l'Industrie. 2009. Reims, FRANCE.

Geernaert, T., Luyckx, G., **Voet, E**., Nasilowski, T. A., Becker, M., Bartelt, H., Urbanczyk, W., Wójcik, J., De Waele, W., Degrieck J., Berghmans, F., Thienpont, H., "Fiber Bragg gratings in microstructured optical fibers for stress Monitoring in composite laminates", Abstract submission to ESA Workshop on Fibre Optic Sensors for Space Applications, 2009, Noordwijk, THE NETHERLANDS.

Luyckx, G., **Voet, E**., Degrieck, J., De Waele, W., Vlekken, J., Vermeiren, J., "Multi-Axial Stress and Strain sensing of thermo hardened composite elements

using Fibre Optic Sensors", Abstract submission to ESA Workshop on Fibre Optic Sensors for Space Applications, 2009, Noordwijk, THE NETHERLANDS.

Voet, E., S. Daggumati, G. Luyckx, I. De Baere, W. Van Paepegem, and J. Degrieck, Evaluation of local strain distribution in a satin weave composite using fibre Bragg gratings. in ECCM14. 2010. Budapest, Hungary.

Daggumati, S., **Voet, E.**, Van Paepegem, W., Degrieck, J., Praet, T., Verhegghe, B., Xu, J., Lomov, S.V., and Verpoest, I. Evaluation of local strain profiles in a satin weave composite : experimental vs meso-Fe modelling. in Composite Materials, 14th European conference, Proceedings. 2010: European Society of Composite Materials (ESCM).

Daggumati, S., **Voet, E.**, Van Paepegem, W., Degrieck, J., Praet, T., Verhegghe, B., Xu, J., Lomov, S.V., and Verpoest, I. Influence of the internal yarn nesting (shifting) on the local structural response of a satin weave composite : an experimental and numerical overview. in Textile Composites, 10th International conference, Proceedings. 2010.

C. Sonnenfeld, S. Sulejmani, T. Geernaert, F. Berghmans, H. Thienpont, S. Eve, G. Luyck, N. Lammens, **E. Voet**, J. Degrieck, P. Dubruel, K. Adesanya, W. Urbanczyk, P. Mergo, M. Becker, H. Bartelt , "Capteurs à fibre optique pour matériaux composites", Proc. 11ème Colloque International Francophone du Club CMOI/SFO,Méthodes et Techniques Optiques pour l'Industrie - CMOI 2010, Toulouse-Labège, France, 15-19 November 2010

Voet E., Luyckx G., Degrieck J., Van Paepegem W., Evaluation of the transversal strain state in a satin weave composite using fibre Bragg gratings, OFS 21, 2011, Ottawa, Canada_conference proceedings accepted for oral presentation.

Luyckx G., **Voet E.,** Lammens N., De Waele W., Degrieck J., Experimental validation of a numerically determined multi-axial strain transfer from CFRP-laminates to embedded Bragg sensors, OFS 21, 2011, Ottawa, Canada_conference proceedings accepted for oral presentation.

Aan mijn allerliefste vrouw

Tine

en
onze fantastische zoon

Kobe

TABLE OF CONTENTS

LIST OF SYMBOLS

A	Rayleigh scattering coefficient
$\alpha_{IR}(\lambda)$	Transmission loss due to infrared absorption
$\alpha_R(\lambda)$	Rayleigh scattering
$\alpha_t(\lambda)$	Total fibre transmission loss
$\alpha_{UV}(\lambda)$	Transmission loss due to ultra violet absorption
Δ	Relative refractive index change
E	Stiffness, Young Modulus of the material
ε	Strain, elongation
G	Shear stiffness of the material
λ	Optical wavelength
λ_0	Nominal Bragg wavelength
λ_B	Bragg wavelength
λ_D	Design wavelength
$\Lambda(z)$	Period (or pitch) of a fibre Bragg grating
I_{FBG}	FBG Reflectivity (Intensity)
$n(z)$	Refractive index
n_0	Refractive index of air
n_1	Refractive index of the fibre core
n_2	Refractive index of the fibre cladding
$\overline{n}$	Effective refractive index
$\Delta n_d(z)$	Homogeneous mode index modulation
$\Delta n_g(z)$	Modulation depth of refractive index
ν	Poisson's ratio
$\Phi(z)$	Phase
p_{11}, p_{12}	Pockels' Coefficients (strain optic coefficients)
R	FBG Reflectivity (dB)
$R_\perp$	Reflection coefficient (perpendicular polarization)
$R_\parallel$	Reflection coefficient (parallel polarization)
R_{Fres}	Fresnel reflection
σ	Stress
S_ε	Strain gauge factor
S_F	Load sensitivity
S_σ	Stress sensitivity
S_{T1}, S_{T2}	Linear and quadratic temperature coefficient
T_g	Glass transition temperature
V	Normalized frequency (V-parameter)

LIST OF ABBREVIATIONS

ASE	Amplified Spontaneous Emission
CMT	Coupled Mode Theory
CFBG	Chirped Fibre Bragg Gratings
CFRP	Carbon Fibre Reinforced Plastic
dB(m)	Decibel(milli)
DT	Draw Tower (fibre)
DTG®	Draw Tower Grating
ESI	Equivalent Step-Index
FBG	Fibre Bragg Grating
FC / APC	Fibre Connector / Angled Physical Contact
FEM	Finite Element Modelling
FWHM	Full Width at Half Maxima
FRP	Fibre Reinforced Plastic
GODC	Germanium Oxygen-Deficient Centres
GFRP	Glass Fibre Reinforced Plastic
HiBi	Hi-Birefringent
MCVD	Modified Chemical Vapor Deposition
MOF	Microstructured Optical Fibre
NA	Numerical Aperture
NDT	Non-Destructive Testing
nm	Nanometer (10^{-9}m)
ORMOCER®	ORganic MOdified CERamic
OSA	Optical Spectrum Analyser
OVD	Outside Vapor Deposition
PMCVD	Plasma Enhanced CVD
pm	Picometer (10^{-12}m)
PPS	PolyPhenylene Sulfide
SMF	Single Mode Fibre
UD	Uni-Directional
VAD	Vapor-phase Axial Deposition

NEDERLANDSTALIGE SAMENVATTING

De afgelopen 10 - 20 jaar, is er steeds meer vraag naar het ontwikkelen en uitwerken van Structural Health Monitoring (SHM) systemen of "structuurbewakings-systemen" in verschillende toepassingsgebieden zoals de lucht- en ruimtevaart, de civiele techniek en mechanische constructies in het algemeen. Deze behoefte wordt ondermeer gedreven door de enorme economische en levensreddende voordelen die SHM technologieën te bieden hebben. Het gebruik van optische Bragg sensoren (FBG's) in SHM is wereldwijd verspreid en heeft betrekking op alle van de bovengenoemde toepassingsgebieden. Bovendien toont de composietgemeenschap veel interesse in het inbedden van FBG's in composietstructuren, voornamelijk met betrekking tot de lucht- en ruimtevaart.
Composieten, gekwalificeerd voor de lucht- en ruimtevaart, zijn extreem presterende constructiematerialen, die vandaag de dag steeds meer toegepast worden in primaire structuren van het vliegtuig zoals bv. de romp, de vleugels en het staartvlak. De nieuwe generatie vliegtuigen zoals de Boeing 787, de Airbus 350, en de Bombardier C-series zullen alle worden vervaardigd uit 50 % geavanceerde composieten (Carbon versterkte laminaten, koolstofversterkte sandwichpanelen, glasvezel versterkt kunststof, en andere vormen van composieten). Dit is meer dan het dubbele in vergelijking met de huidige generatie vliegtuigen zoals de A380, met maar 20 % composiet materiaal.

Een interessant aspect op technologisch vlak van sensoren, is dat vliegtuig-fabrikanten zoals Airbus en Boeiing op zoek zijn naar de opname van SHM systemen en technologie (zoals glasvezelsensoren, met name Bragg sensoren) in hun vliegtuigen. Zo zal het vliegtuig in staat haar eigen structuurgedrag op te volgen en naargelang de werkelijke belasting, zelf onderhoudsintervallen te bepalen. Echter, men moet beseffen dat het mechanisch gedrag van anisotrope vezelversterkte kunststoffen (VVK's) significant verschilt met conventionele isotrope bouwmaterialen. In tegenstelling tot staal, aluminium (magnesium) en titanium legeringen, bestaan er geen gedetailleerde histogrammen van de talrijke composietmaterialen die vandaag op de markt zijn of die, nog belangrijker, op dit eigenste moment worden ontwikkeld. Ter verbetering van de kennis over het structureel gedrag van VVK's op lange termijn, moeten we de feedback van de aangelegde belastingen, vervormingen en temperaturen van (en met name binnen) de bestaande composietconstructies in reële omstandigheden registreren. De geïntegreerde SHM technologie en meetsystemen kunnen tevens gebruikt worden tijdens de validatie-programma's, wat zal leiden tot zeer waardevolle informatie die tijdens de ontwerpfase in rekening gebracht kan worden en waarmee men de levensduurvoorspelling van het composiet kan verbeteren. Bovendien zal het opvolgen van de geïnduceerde rekken in reële composietstructuren tijdens gebruik, meer inzicht en vertrouwen verschaffen in het lange termijn gedrag van hoogwaardige composietstructuren.

Het belang van Airbus (en Boeing) in Bragg sensoren rechtvaardigt het hier uitgevoerde onderzoek. In dit proefschrift zal de auteur zich richten op het toezicht op de rek, en dus op de vervorming (en permanente rek) tijdens de volledige levensduur van koolstof versterkte kunststof laminaten met ingebedde Bragg sensoren.

Het onderzoek is opgebouwd uit twee delen:

1. Deel I: De verbeterde 'draw tower' Bragg sensor: Vervaardiging en karakterisering,
2. Deel II: DTG®'s ingebed in thermohardende- en thermoplastische composieten.

Het doel van het eerste deel van dit onderzoek is om de bestaande 'draw tower' technologie te gebruiken om zo een verbeterde (dunnere) versie van de bestaande hoog kwalitatieve, 'draw tower' Bragg sensor (DTG®) te vervaardigen. Met het oog op het behalen van nauwkeurigere metingen en het behouden van structurele integriteit, heeft het onderzoek zich gericht op het reduceren van de totale diameter van de optische vezel, waardoor zo de verstoring van het composiet vermindert en de integratie in de versterkingsvezels verbetert. Het doel is om een 80 µm DTG® te ontwikkelen met gelijkaardige of zelfs betere eigenschappen dan de standaard 125 µm versie.
Na de productie van de nieuwe sensoren, zal de auteur zich richten op het karakteriseren van de eigenschappen van de nieuwe 80 µm DTG®'s. De opto-mechanische en thermo-optische eigenschappen zullen onder de loep worden genomen. De kalibratiemethoden en de verschillende gebruikte opstellingen zullen door de auteur uitvoerig worden besproken. De (axiale) rekgevoeligheid ('Gauge factor') zal worden bepaald en een speciaal ontworpen compressie opstelling wordt toegepast om de elasto-optische coëfficiënten van de optische vezel te bepalen.
Met behulp van een tweede orde polynomische fit, zullen de lineaire en kwadratische temperatuurscoëfficiënten worden bepaald voor een groot temperatuurbereik (-22.5 °C tot 135 °C), die nadien voornamelijk gebruikt zullen worden voor temperatuur compensatie technieken.
Omdat de DTG®'s ingebed worden in thermohardende en thermo-plastische vezelversterkte composieten (deel II), is het noodzakelijk om de karakteristieken van de Bragg sensor bij verhoogde temperaturen te onderzoeken. De maximale temperatuur bij fabricage voor een typische uithardingcyclus van koolstof-epoxy laminaten is 180 ° C, en voor de koolstof-PPS (polyfenyleen-sulfide) laminaten kan de temperatuur oplopen tot zelfs meer dan 300 ° C gedurende meer dan een uur. Zodanig is het noodzakelijk om de thermische stabiliteit van de Bragg roosters verder te onderzoeken.

In deel II van het onderzoek gaat de auteur de DTG®'s in specifieke soorten van thermohardende en thermoplastische koolstofversterkte laminaten inbedden (Figuur 0-1). In beide gevallen zullen de sensoren worden gebruikt om het rekveld op te meten in het composiet.

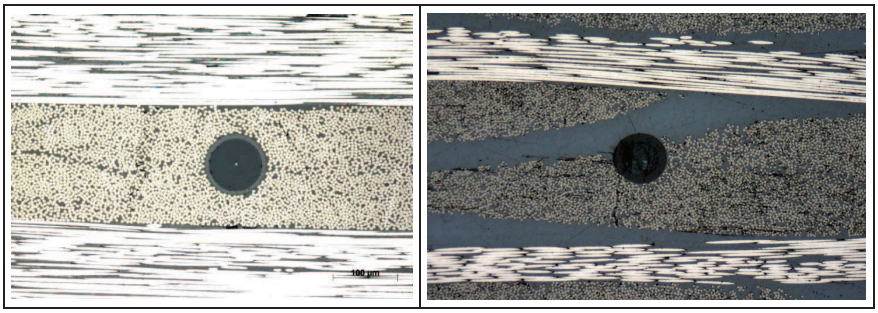

Figuur 0-1: Optische vezel ingebed in een thermohardend koolstof-epoxy laminaat (links), en thermoplastisch koolstofweefsel versterkt PPS (rechts).

De relatie tussen de rek van een ingebedde sensor en die van het omringende materiaal is eenvoudig, wanneer de elastische eigenschappen van beide materialen dezelfde zijn. Echter, in werkelijkheid, bestaat er een verschil tussen de eigenschappen (e.g. de elasticiteitsmodulus, Poisson's ratio) van het omringende materiaal en de geïntegreerde sensor, dus zal er een verschil in rek optreden in beide materialen. Met betrekking tot het meten van de rek in composiet materialen met behulp van een ingebedde Bragg sensor, zal de auteur tijdens dit werk de exacte rekoverdracht van het composietlaminaat op de ingebedde sensor definiëren.

De aanpak is echter niet zo eenvoudig dan dat men denkt. Composiet laminaten vertonen grote (niet-uniforme) residuële rekken (transversaal, alsmede ook longitudinaal), die vaak worden gezien als een struikelblok, omdat neveneffecten kunnen optreden in het gereflecteerde Bragg spectrum (e.g. dubbelbrekend effect). In plaats van het verwaarlozen van deze bijwerkingen, zal de auteur precies het tegenovergestelde doen en juist die neveneffecten opmeten; de geïnduceerde dubbelbreking zal worden geëxploiteerd om dwarsrek te meten en om de verschillende rekken in en uit het vlak van elkaar te scheiden, dus kunnen we stellen dat de functionaliteit van de ingebedde Bragg sensor meervoudig is. De auteur zal de ingebedde DTG®'s gebruiken in meerdere stadia van de levenscyclus van het composietmateriaal. Het gebruik van de sensor begint bij het opvolgen van het composiet productieproces en het eindigt met vermoeiingsproeven tot het falen van de composietlaminaten.
Tijdens de verschillende experimenten, zullen de sensoren worden blootgesteld aan hoge temperaturen, hoge druk, extreme longitudinale- en transversale rekken, en tegelijkertijd zal de sensor dienen om zeer nauwkeurig (multi-axiale) microrekken ($\sim 10^{-6}$) op te meten in het composiet.

In dit werk zal worden aangetoond dat de ingebedde (geoptimaliseerde) DTG® een waardevol en multifunctioneel instrument is om interne mechanische en thermisch geïnduceerde rekvelden op te meten in vezelversterkte kunststoffen.

ENGLISH SUMMARY

The last 10 – 20 years, there have been increasing demands to develop and deploy structural health monitoring (SHM) systems on various aerospace, civil and mechanical structures. These demands are driven by the tremendous economical and life-safety benefits that SHM technologies can provide. The usage of FBGs as a sensor in SHM is widespread and covers all of the formerly listed application fields. Moreover, the process of embedding FBGs in fibre reinforced plastic structures has gained lots of interest in the composite community mainly with regard to aerospace applications.
Aerospace certified fibre reinforced plastics (FRPs) are extreme performing construction materials, which today are increasingly applied in primary structures of the aircraft, such as the fuselage, the wings and the fin. The new generation aircrafts such as the Boeing 787, the Airbus 350, and the Bombardier C-Series will contain all approximately 50 % of advanced composites (Carbon reinforced laminates, carbon reinforced sandwich panels, glass fibre reinforced plastics, and other types of composites). This is more than double compared to the currently flying aircrafts such as the A380 with approximately 20 % of composite material.
An interesting aspect on the technological point of view of sensing is that airplane manufacturers such as Airbus and Boeiing are looking at incorporating health-monitoring systems (such as optical fibre sensors, especially fibre Bragg gratings) that will allow the (composite) airplane to self-monitor and report maintenance requirements to ground-based computer systems.
However, one has to realize that the mechanical behaviour of anisotropic FRPs is significantly different compared to conventional isotropic construction materials. Unlike steel, aluminium (magnesium) alloys and titanium, no detailed histograms exist of the numerous composite materials which are on the market today or even more important, which are being developed at the mean time. To improve the knowledge on the (long term) structural response of composite materials, we need to record the feedback from applied loads, deformations and temperatures of (and especially inside) existing composite structures in real conditions. Incorporated monitoring systems can actually already be of added value during the validation programs and can be utilized to characterize the material and structure under test, which will lead to highly valuable information for design criteria and composite lifetime predictions. Furthermore, the monitoring of an in-service structure should greatly enhance the insight and confidence in the (long-term) behaviour of high performance composite structures.

The interest by Airbus and Boeing in fibre Bragg gratings justifies the research performed here. In this dissertation, the author focuses on monitoring the strain and (permanent) deformation in carbon reinforced plastic laminates with embedded fibre Bragg gratings. The research is divided in two main parts:

1. Part I: An improved draw tower fibre Bragg grating: manufacturing and characterization
2. Part II: DTG®s embedded in thermoset and thermoplastic composites

In the first part of this research, we utilize the existing fibre draw tower technology, to manufacture an improved version of the existing in-line high quality, draw tower

fibre Bragg gratings (DTG®s). With respect to accurate measurements and structural integrity, the research focuses on reducing the total diameter of the optical fibre, so the distortion in the composite is reduced and the incorporation in the reinforcement fibres is enhanced.
An 80 µm DTG®s is manufactured with equivalent and even, in some cases, better properties as the standard 125 µm version. After manufacturing of the new sensor, the author focuses more in detail on the characterization of the sensor' properties of the new 80 µm DTG®s. The author elaborates in detail the methods of calibration and the different setups which are applied. The (axial) strain gauge factor is determined and moreover the strain-optic coefficients are determined with an especially designed transverse compression testing setup. With the help of a second order polynomial fitting, the linear and quadratic temperature sensitivities are quantified for a large temperature range (-22.5 °C till 135 °C). These temperature coefficients are important for later use in temperature compensation techniques. In addition, we defined the DTG®'s characteristics at elevated temperatures because during curing the temperature typically increases up to 180 °C for carbon-epoxy laminates and exceeds 300 °C for carbon-PPS (Polyphenylene Sulfide) laminates. Therefore, the thermal stability of the Bragg gratings is studied.

In part II, the author embeds the DTG®s in specific types of thermoset and thermoplastic carbon reinforced plastic laminates (Figure 0-1. In both cases the sensors are utilised to measure the strain field inside the composite material.

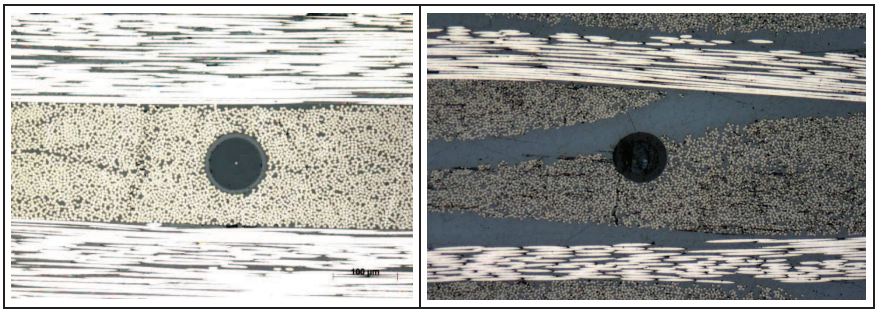

Figure 0-1: Optical fibre embedded in a thermoset carbon-epoxy laminate (left), and thermoplastic carbon-PPS woven-fabric laminate (right).

The strain relationship of an integrated sensor and the host material is simple when the elastic properties of both materials are the same. However, in reality, a difference in properties (e.g. Young's Modulus, Poisson's ratio) exists between the host material and the embedded sensor, hence, a different strain state in both materials exists. With regard to measuring strains of composite materials using an embedded fibre Bragg grating, the author defines the exact strain transfer from the composite laminate to the embedded sensor.

The approach, however, is not as straightforward as one might think. Composite laminates exhibit large (non-uniform) residual strains (transverse as well as longitudinal), which are often seen as a stumbling-stone because side-effects can appear in the Bragg spectrum (e.g. birefringence effect). Instead of neglecting these effects, the author does exactly the opposite; the induced birefringence is 'exploited'

to measure transverse strains and to discriminate in-plane and out-of-plane strains, hence, the functionality of the embedded fibre Bragg grating is multiple. The author applies the embedded DTG®s in several stages of the composite lifetime. Starting with the monitoring of the composite manufacturing process and ending with fatigue testing until failure of the composite laminates. During the different experiments, the sensors are subjected to high temperatures, high pressures, extreme longitudinal strains and transverse strains and in the mean time, they are employed to very accurately measure (multi-axial) strains inside composites at microstrain level ($\sim 10^{-6}$).

In this work will be shown that the embedded (improved) DTG® is a valuable and multifunctional tool to study the internal mechanical and thermal strain states in fibre reinforced plastics.

Chapter 1 GENERAL INTRODUCTION

1. 1. FUTURE AEROSPACE COMPOSITES WILL FLY WITH INCORPORATED NERVOUS SYSTEMS_PROBLEM STATEMENT

Aerospace certified fibre reinforced plastics (FRPs) are extreme performing construction materials, which today are increasingly applied in primary structures of the aircraft. The new generation aircrafts such as the Boeing 787, the Airbus 350, and the Bombardier C-Series will contain all approximately 50 % of advanced composites (Carbon reinforced laminates, carbon reinforced sandwich panels, glass fibre reinforced plastics, and other types of composites). This is more than double compared to the current flying aircrafts such as the A380 with approximately 20 % of composite material. Airbus even claims that an aircraft's innovative all-new carbon fibre reinforced plastic (CFRP) fuselage would result in lower fuel consumption, i.e. a 25 % step-change fuel efficiency compared to its current long-range competitor, as well as in easier maintenance [1]. Recently (October 2010), Bombardier has announced that the first phase of the new Bombardier wing manufacturing and assembly facility in Belfast is complete. Bombardier's Belfast operation has developed an innovative Resin Transfer Infusion (RTI) technology to manufacture the large one-piece wing skins and structural spars for the wing torque box.
These examples of the new generation aircrafts and manufacturing technology illustrate well the evolution towards the future of composite materials in commercial aviation. As an example, an overview of the material distribution for the Bombardier C-Series and A350 XWB is given in Figure 1-1.
Both next generation planes use the double of FRPs compared to the classical aluminium and aluminium/lithium material for their structural components. In contrary to the Airbus A350, the fuselage of the C-Series is still manufactured mainly out of Alumium Lithium alloy, where the fuselage of the A350 is composed out of Aluminium frames combined with carbon laminated skins.

Aerospace certified composites: extreme performing materials

The load type and magnitude which is experienced during the repeated ground-to-air-to-ground cycle of an aircraft in-service is different in every step of the cycle and is depend on the component of the structure. A nice overview of typical stresses applied on the complete structure is given in Figure 1-2. Note, that the fuselage typical experiences hoop stresses and longitudinal and compression stresses and that the wings are mainly loaded in compression (top skin) and tension (lower skin).

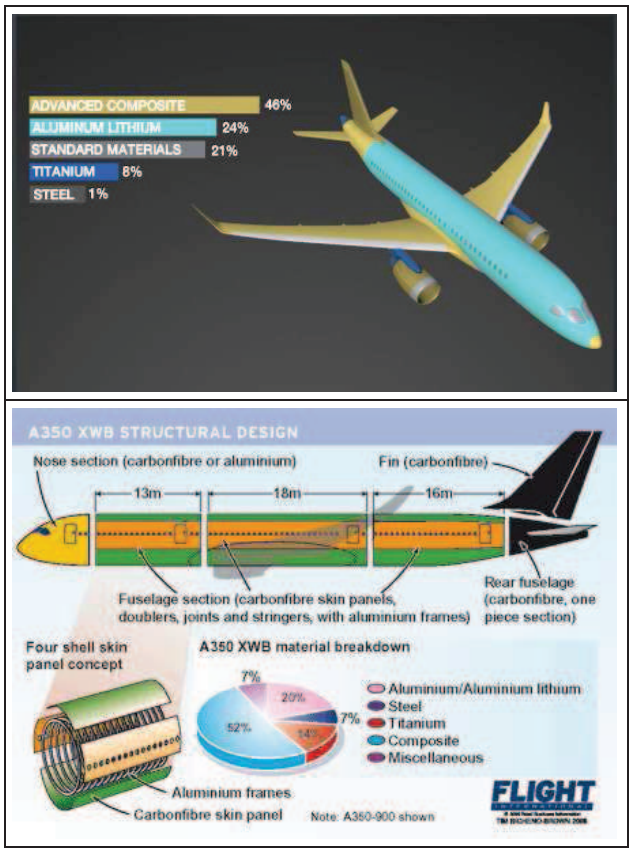

Figure 1-1: Material overview of the Bombardier (top, courtesy of Bombardier Aerospace), and A350 lay-out (bottom, Courtesy of Airbus).

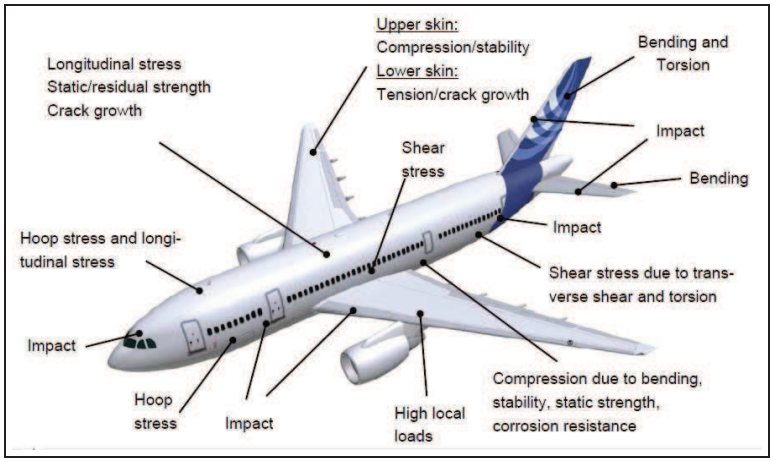

Figure 1-2: Structural and external loads on the aircraft (Courtesy of Airbus)

A striking example of the extreme tension and compression of the composite wings of a new generation aircraft has already been illustrated during the first flight-test of the new Boeing 787 Dreamliner, mid December 2009, see Figure 1-4.

Figure 1-3: First landing of the new Boeing 787 Dreamliner.

The picture of the landing illustrates well the 'extreme' flexible and aerodynamic composite wings. It is clear that the use of composite materials opens new opportunities on the level of structural performances, but also puts high demands on the level of monitoring the structures (deformation monitoring, impact, fatigue damage, ...). Namely, extreme performing materials exhibit complex material properties which are difficult to measure and to interpret. Besides flight-tests, extended static and fatigue test-programs are carried out by the manufacturer prior to flight, to validate their analytical models and to mimic the ground-to-air-to-ground cycle. Exciting to know is that during static testing the wings are flexed upward by approximately 7.6 meters (Figure 1-4) and that the fuselage is pressurized to 150 % of the most extreme forces the airplane is ever expected to experience while in service. Video records of various load tests and famous wing break tests are widely spread around the world and can be viewed on YouTube [2].

Figure 1-4: Static load test on the composite wing box (courtesy of Boeing).

An interesting aspect on the technological point of view of sensing, is that airplane manufacturers such as Airbus and Boeiing are looking at incorporating health-monitoring systems, that will allow the airplane to self-monitor and report maintenance requirements to ground-based computer systems. Incorporated monitoring systems could actually be used during the validation programs too. In

2007 (at the start of this doctoral thesis), Airbus and Boeing joined an international aerospace group (SHM-AISC) to promote industry-wide co-operation on the development of structural health monitoring (SHM) technology. To quote the chairman of the SHM-AISC, Stanford University professor of aeronautics and astronautics Fu-Kuo Chang [3]:

" We're talking about building a nervous system for aircraft. SHM technologies can give maintenance professionals information about what is going on in an aircraft's structure whenever it is needed".

Incorporating sensors in composites to monitor the internal strain and deformation of the structure, is indeed the best way to proceed and to better study the long term behaviour and strength throughout the lifetime of composite structures . However, to do this, we need to have technologies which fit the composite requirements.
Five promising SHM technologies are under investigations at Airbus [4]:

- Acousto Ultrasonic patches
- Comparative Vacuum Method
- Optical fibres, especially Fibre Bragg Gratings
- Acoustic emission
- Embedded eddy current sensors

The interest by Airbus (and Boeing) in fibre Bragg gratings justifies the research performed here. In this dissertation, the author will focus on monitoring the strain, and thus on the deformation (and permanent strains) during the complete lifetime of carbon reinforced plastic laminates with improved, smaller diameter, high elongation, fibre Bragg gratings.

Fibre Bragg gratings as potential SHM technology

Over the last 10 years, several new conferences have been developed that focus directly on structural health monitoring (EWSHM, IWSHM, ETNDT, OFS, SMART,…). Already at a very early stage in these conferences, the use of embedded fibre Bragg gratings, mostly for SHM in aeronautics, has been presented. The FBGs have a number of well-known advantages over electrical sensors including their insensitivity to electromagnetic interference, their small dimensions (diameter ~40 µm – 250 µm) and light weight, their multiplexing capabilities (i.e. multiple sensors in one fibre) and their resistance to corrosion which can be used for the benefit of integrating them into a composite structure.
In parallel to the SHM conferences, we see that in the composite community (ECCM, ICCM, SAMPE, etc…) and the optical fibre sensors (OFS) community, the FBG has proven to be a remarkable effective and versatile sensing component which can measure all kinds of physical parameters, but most commonly it is used as a highly accurate (embedded) strain sensor.
The fact that there is worldwide research on the level of incorporating fibre Bragg gratings in FRP materials to measure strain and material deformations [5] proves that, together with the growing interest of usage of FRPs in commercial airplanes, an enormous potential SHM market for the fibre Bragg grating sensing technology exists.

However, despite the numerous literature on embedded FBGs in composites, see Chapter 5 for an extended literature overview, there is still a lack of understanding the local internal (complex) composite strain fields which act on the incorporated Bragg grating. This interaction is studied in detail in this dissertation. It will be shown that multi-axial strains are acting on the embedded sensor already during manufacturing (residual strains) and that by combining FE-analysis together with experimental validation and using a dual FBG sensor configuration, multi-axial strain transfer effects can be determined and thus the 3D strain state (i.e. in-plane and out of plane strains) can be measured using embedded FBGs. The results, shown in this work, are the first multi-axial strain measurements performed in carbon-epoxy laminates with embedded uni-axial FBGs. The key to do this, is to use the residual strain induced birefringence effects after manufacturing of the composite, which allows to measure transverse strains. Full elaboration on this matter is found in Chapter 7.
If the embedded FBGs will serve as a SHM technology to measure strain and deformation over the lifetime of high grade and extreme performing composite material, the sensor should outlive the material of interest. Hence we are obliged to use high quality gratings or preferable, coated (non-fragile) FBGs. In this work the author will perform fatigue testing on high performing thermoplastic woven fabrics (i.e. Cetex® [6]) with ORMOCER® coated FBGs embedded. The sensors are used to measure the long term deformations of the material (i.e. stiffness degradation and permanent strains). To do that, the author has used a repetitive progressive (quasi-static) load sequence, alternated with fatigue cycling, which allows to study the sensor response at specific intervals during the lifetime of the composite.
The results for the sensors developed in this work are very promising with regard to SHM technology, moreover; the permanent deformation is measured until failure of the composite.
Before switching to the justification of this dissertation, the reader is first briefly introduced to some basic knowledge on composite materials and fibre Bragg grating sensors.

1. 2. INTRODUCTION TO THERMOSET & THERMOPLASTIC FIBRE REINFORCED PLASTICS

Unlike metals or ceramics, composite materials are composed of two are more constituents. Typical stiff reinforcement fibres are combined with a though matrix (binder) to form a fibre reinforced composite. There are many types of composites, depending on the composite constituents. Various kinds of reinforcement fibres; i.e. carbon-, glass-, organic-, metal- and ceramic fibres are combined with matrix materials such as metals, ceramics and polymers. Because of a large variety in the format of reinforcement fibres (e.g. continuous, chopped, nano, etc., Figure 1-5, top) and the fibre morphology (e.g. uni-directional, woven fabric, stitched or 3D preform, Figure 1-5, bottom), and a large variety of composite fabrications techniques, (autoclave, hot moulding, filament winding, automatic tape layering, RTM, RTI, etc…), composite material properties can be engineered and tuned to meet specific stiffness, strength and manufacturing requirements.
Because of the enormous availability of new composite materials, it is not possible to give a complete overview of the existing fibre reinforced composites. With regard to the high grade aerospace certified materials used in this work (i.e. uni-directional

carbon-epoxy and woven-fabric carbon-PPS), only a selection of common used *FRPs* or *polymer matrix composites* is considered.
Plastic resins or polymers used as matrix materials for FRPs are classified as *thermosetting plastic* (thermoset) and *thermoplastic*. Thermosetting polymers (e.g. polyester, epoxy, vinyl ester and phenolic) are materials that irreversible cure and form due to the polymer cross-linking. This implies that once thermoset polymers are cured they are non-recyclable, except as filler material. This is in contrast to thermoplastics polymers (e.g. PP, PA, PEI, PPS, PEEK and PEKK) which are materials that can be softened and (re-)shaped or melted and moulded again. Hence, thermoplastic FRPs are classified as 'recyclable'. The most important qualities of both polymer types are summarized in Table 1-1.

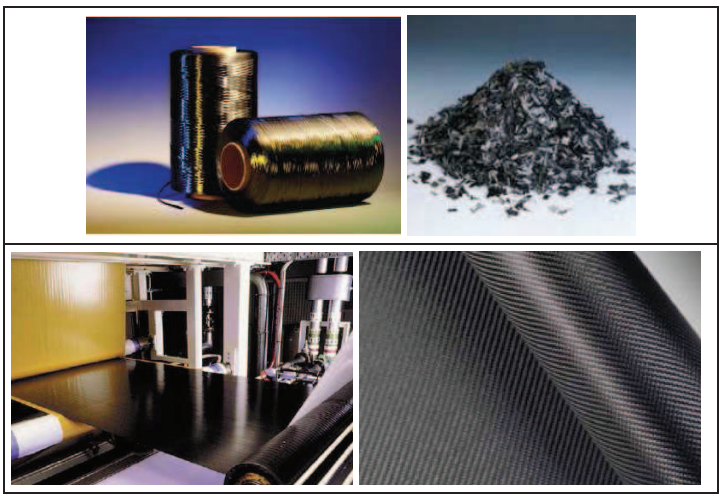

Figure 1-5: Continuous and chopped fibre (top), uni-directional pre-preg and woven fabric (bottom) [7].

Table 1-1: Thermoset versus thermoplastic qualities

Thermoset	***Thermoplastic***
• Interlinked (cross-linked) polymer molecules • Permanently rigid after heating and cooling • Non-reversible Process, material *cannot be recycled!*	• Linear molecular chains • Can be softened above glass-transition temperature (T_g) and viscosity of plastic decreases as the temperature rises • Reversible Process, material *can be recycled!*
• Chemical Changes • Lower Initial Material Cost • High Heat/Creep Resistance • Lower Coefficient of Thermal Expansion • Higher Arc Resistance	• Physical Changes • Lower Total Part Cost • Higher Impact Strength • Higher Flexural Strength • Higher Tensile Strength • Reduced Scrap

If the polymers are in liquid phase (i.e. uncured thermoset and molten thermoplastics), they can be used to impregnate and bond stiff reinforcement fibres (e.g. carbon, glass, aramid, hemp and flax), hence, a high strength composite material can be fabricated, which renders superior strength properties than those of the base (cured) matrix material. As an example, in Figure 1-6 the linear stress-strain relation for different fibre reinforcing materials are plotted against a "soft" epoxy-resin.

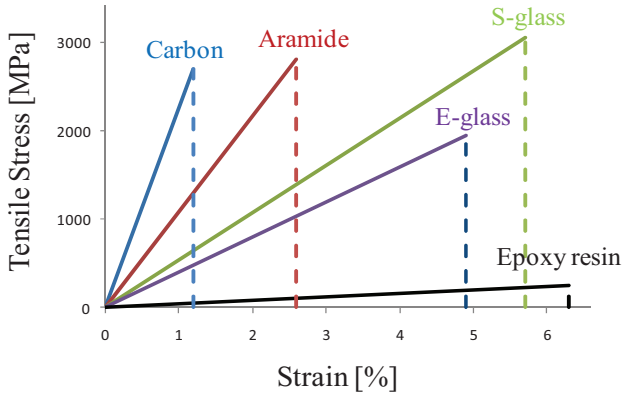

Figure 1-6: Stress-strain relation of common reinforcement fibre types and standard epoxy resin.

The role of the tough, but soft, matrix is to support the fibres and to bond them together. The matrix is responsible for transferring any applied loads to the fibres and additionally, it gives the composite environmental resistance. The fibre reinforcements provide composites an excellent stiffness and strength, while offering significant weight savings over metals. Typically for the materials used in this dissertation, the stiffness of the high modulus uni-directional carbon-epoxy reinforced plastic (CFRP) is approximately 300 GPa and for the woven carbon fabric with PPS matrix (Cetex®) this is approximately 60 GPa.
To compare composites and other construction materials, it is common to use the specific stiffness (or specific modulus), which is the Young-modulus per unit density, also calculated from the well-known Ashby diagrams. This is illustrated in the diagram below:

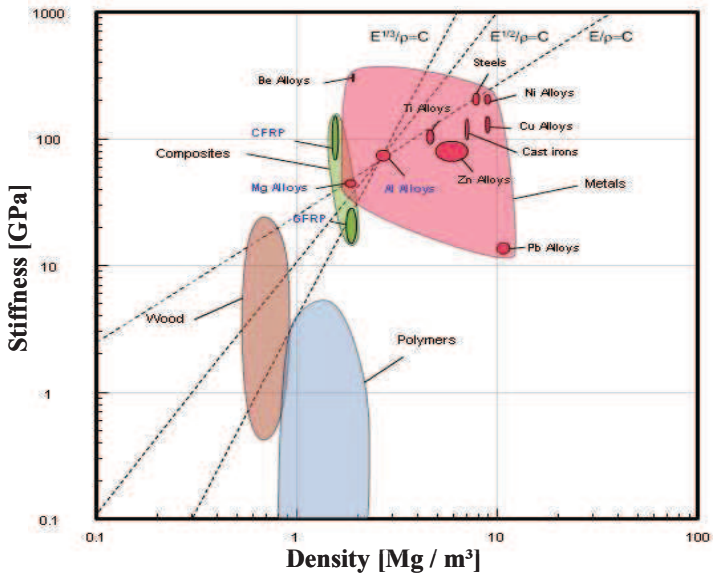

Figure 1-7: Example of an Ashby diagram with the Young modulus plotted against the Density of the material [8].

Although the value of the stiffness of for example metals and FRPs is in the same order of magnitude, the density of metals is much higher compared to the reinforced plastics. Hence, the specific modulus is much higher for the carbon fibre reinforced plastics (CFRP), than for most of the metals. Therefore, there is a high interest in for instance the aeronautical industry to use more composite materials in civil airplanes to save weight.

Because of the ability to tune the fibre reinforced composite characteristics, the usage of FRPs covers an extremely broad spectrum, ranging from *small* electronic prints, tennis-rackets until *medium sized* car body panels, helicopter blades, pressure vessels, *large* wind turbine blades, boat hulls, airplane components such as floor panels, tails, skins or even *complete fuselages*, satellites, telescopes, high pressure pipelines, and many more.

As an example, two applications of the materials used in this work are shown in Figure 1-8: a fuselage of an advanced composite cargo aircraft made of high grade thermoset CFRP laminates (left) and a rudder of the tail-section of the Gulfstream G650 business jet, made of thermoplastic carbon-PPS woven fabrics (right). Note that the latter example has won the prestigious JEC innovation award (April 2010) in the category Aeronautics, for the first welded thermoplastic composite rudder and elevator of the all new Gulfstream G650 tail section. No bolts, rivets, or inserts are used to connect the stiffeners and panels of the rudder, instead an innovative inductive welding techniques based on thermoplastic powders are used, which allows to work much faster without deterioration of the rudders' mechanical properties.

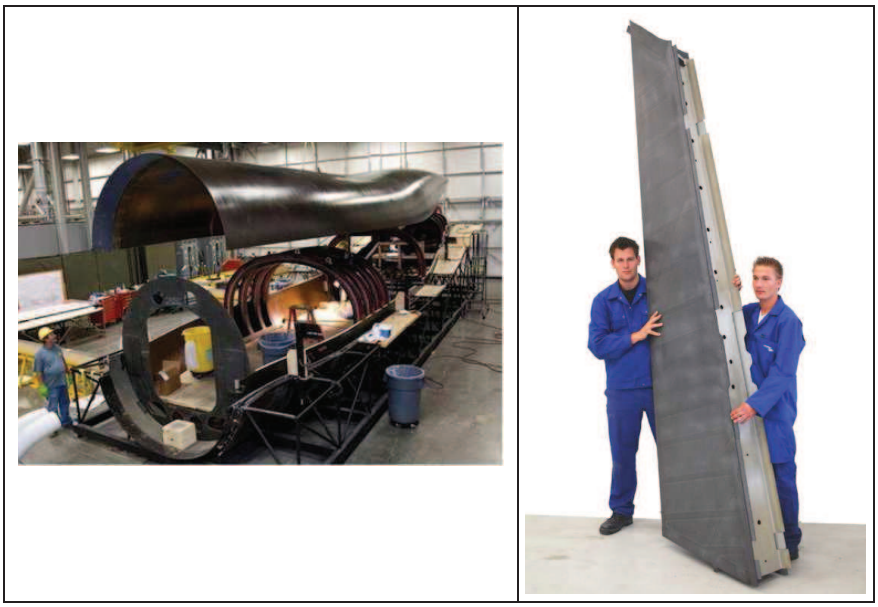

Figure 1-8: Examples of FRP structures: Fuselage with large CFRP hulls of an Advanced Composite Cargo Aircraft (left, Courtesy of U.S. Air Force Research Laboratory's), G650 rudder with welded components made of carbon-PPS woven fabrics [9] (right).

1. 3. FIBRE BRAGG GRATINGS_STRAIN SENSING PRINCIPLE

Fibre Bragg grating technology is not a novelty and exists already more than three decades. In 1978, founder K.O. Hill had discovered how to write a grating in an optical fibre by using the interference of the injected light with the 4% Fressnel back reflection of the fibre's end face [10]. In his experiment, an internal wave interferes with the back-reflected light from the end of the fibre, to create a standing wave in the fibre, the Bragg grating, which realizes the Bragg condition precisely for the wavelength coupled in the fibre. More than 10 years later, G. Meltz founded the holographic sidelong inscription of Bragg gratings [11]. This technique was really pioneering, because it allowed writing fibre gratings with arbitrary wavelengths using a different inscription wavelength than the one which was reflected by the Bragg grating. It allowed writing FBGs in the wavelength windows of 0.8µm, 1.3µm and 1.5µm, which is of interest for the telecommunication industry because of low attenuation and dispersion characteristics of the optical fibre in that wavelength window. Later, the phase-mask technique based on a diffraction grating, was developed by K.O. Hill in 1993 [12], which is nowadays a well adapted technique for the commercial manufacturing of FBGs. Since then, fibre Bragg gratings have had an enormous impact on optical communication systems, fibre lasers and optical fibre sensors. FBGs are commonly being used as reflective filters for dispersion compensation for high bit-rate data communication using optical fibres and discrete fibre optic sensors, mostly for (point) measuring of strain and temperature. In this work, the Bragg gratings are written in highly Germanium-doped optical fibres during the drawing of the optical fibre in a fibre draw tower, see

Chapter 2. A holographic method based on an interferometer is applied to write uniform Type I uni-axial FBGs. In the next sub-section, the basic sensing principle of an FBG is explained. This principle is further elaborated in detail in Chapter 4 of this dissertation.

1. 3. 1. Basic FBG measurement principle

The FBG is a passive and discrete optical component at a specific spot in an optical fibre. An optical fibre consists of a fibre core and a fibre cladding. The Bragg grating is an area in the fibre core with a pre-defined length, L_g and an alternating periodic refractive index change, i.e. n_1 ,n_2 (Figure 1-9). An FBG acts as an optical filter or reflection filter and provides a frequency dependent reflection spectrum or stop band to the incident signal over a specific bandwidth. The stop band is centred at the *Bragg wavelength*, λ_B, and is given by the well-known Bragg condition $\lambda_B = 2\overline{n}\Lambda_{FBG}$, where Λ_{FBG} is the *grating period* and $\overline{n}$ is the *mode index* or *effective refractive index* of the fibre.

The very basic principle of strain sensing of a non-embedded fibre Bragg grating is shown in Figure 1-10. When the fibre, having a nominal length, L_0, is being elongated to a certain length L, the grating period will be strained and the refractive index of the fibre will change as well. As a consequence, a positive Bragg peak shift is induced. In fact, an FBG forms the optical equivalent for a resistive strain gage (RSG). The basic principle of both types of sensor is the same: only one parameter will change when being strained. For an RSG, it is the resistance of the wire which changes as a function of strain and for the optical counterpart, it is the Bragg wavelength which shifts.

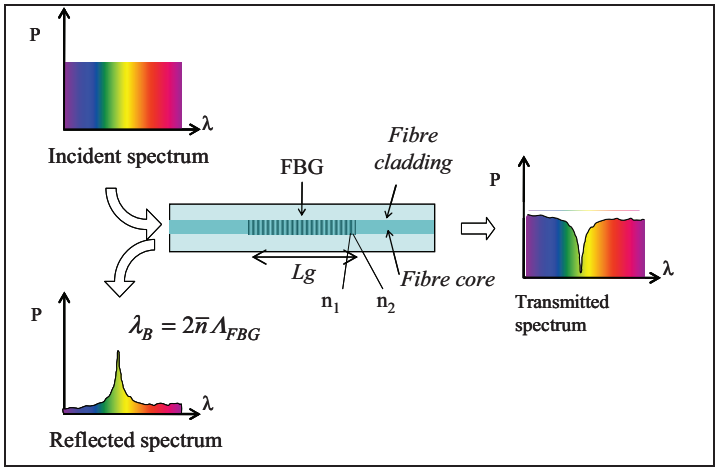

Figure 1-9 Basic fibre Bragg grating principle, (Reprinted with permission of FOS&S bvba)

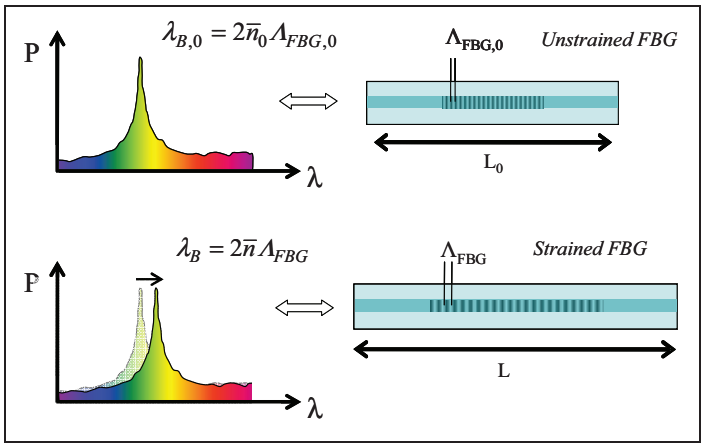

Figure 1-10 Basic fibre Bragg grating strain sensing principle, (Reprinted with permission of FOS&S bvba)

For an FBG the dependency on strain and/or temperature is understood by the basic linear approximation

$$\frac{\Delta\lambda}{\lambda_{B,0}} = S_\varepsilon.\Delta\varepsilon_{mech,f} + g\left(\Delta T\right) \qquad 1\text{-}1$$

with $\Delta\lambda = \lambda_B - \lambda_{B,0}$, the *wavelength shift* at a specific moment, $\lambda_{B,0}$, the *nominal wavelength* or *reference wavelength*, S_ε, the *strain gauge parameter*, $\Delta\varepsilon_{mech,f}$, the mechanically induced strain relative to the start of the measurement and $g(\Delta T)$, the *intrinsic temperature sensitivity function* of the FBG. For a detailed derivation of Equation 1-1 the reader is referred to Chapter 4 or Apendix B.
As an example, an isothermal state is assumed (i.e. $\Delta T=0$), hence, the term for intrinsic temperature sensitivity can be omitted. A typical value for the value of S_ε for the FBGs being tested in this research is 0.777. Equation 1-1 can then be written as

$$\Delta\varepsilon_{mech,f} = \frac{1}{0.777}\frac{\Delta\lambda}{\lambda_{B,0}}. \qquad 1\text{-}2$$

Equation 1-2 represents the basic linear approximation to calculate the longitudinal strain for a *non-embedded FBG*. Only a simple representation of the strain sensing principle is given here. For a more detailed explanation on the dependency on strain and temperature of FBGs and embedded FBGs, the reader is referred to Chapter 4 and Chapter 7, respectively.

1. 3. 2. Strain response for the embedded fibre Bragg grating

With respect to the scope of the work, the author would already like to add some small remarks about strain sensing using embedded FBGs in composites, as a precursor on the effects discussed further in this work.

First of all, the given formulation for calculating the longitudinal (see Equation 1-2) strain present in the optical fibre is based on the assumption that strain transfer from host material to the sensor is 100%. In principle, one can assume that the embedded optical fibre follows the elongation of the composite layers, only if the fibre sensor is well consolidated, see Figure 1-11b.
Second of all, Equation 1-2 is only valid in the case when no extrinsic (extra) transverse effects are present which could cause errors in the Bragg wavelength shift determination, hence, faulty strain calculations. If large transverse stress is acting on the grating, birefringence effects will occur, hence, the Bragg peak will be affected and splits in two distinct Bragg peaks (Figure 1-11c). The wavelength shift occurring due to these effects should be taken into account as well. The method of doing so is further explained in Chapter 7.
Finally, an FBG will sense non-uniform strains. If we embed an FBG for instance in woven fabrics, in which the optical fibre is surrounded by a pattern of (random) yarns and matrix material, the sensor will be subjected to a more complex strain field. Such non-uniform strain distribution will disturb the reflected Bragg spectrum and again (large) errors could occur in the Bragg peak determination and strain calculation in general (Figure 1-11d). Details on these effects and concerning strain conversions are given in Chapter 8.
The examples shown in Figure 1-11 indicate, that the spectral response of an embedded FBG differs from that of a non-embedded FBG. To calculate strains inside composites, we need to take into account all effects acting on the Bragg grating. These effects will be elaborated in detail further in this work.

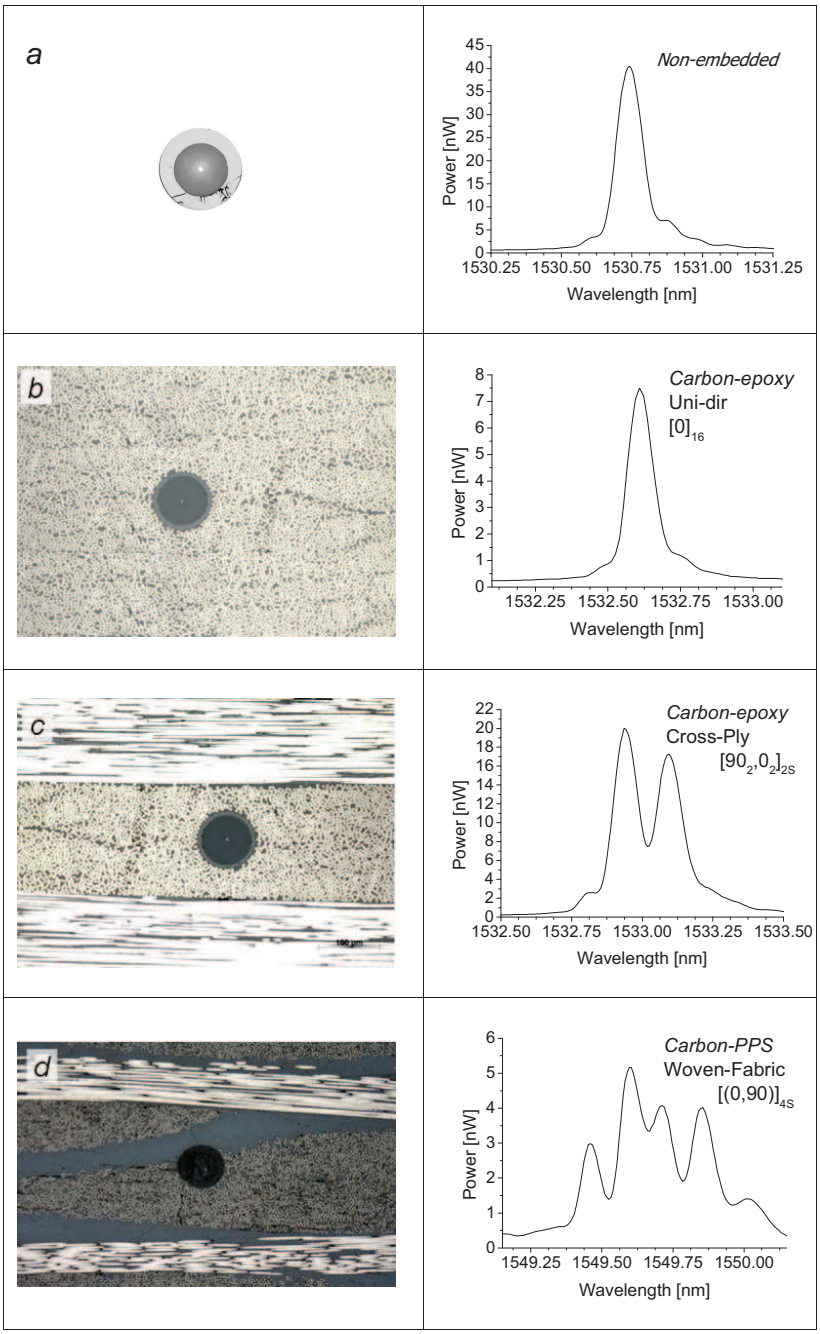

Figure 1-11 Bragg peak response of non-embedded FBG (a), embedded in a UD composite (b), embedded in a cross-ply (c), and embedded in a woven fabric (d).

1. 4. JUSTIFICATION - SCOPE OF THE RESEARCH

Over the last 10 – 20 years, there have been increasing demands to develop and deploy SHM systems on various aerospace, civil and mechanical structures [13]. These demands are driven by the tremendous economical and life-safety benefits that SHM technologies can provide. The usage of FBGs as a sensor in SHM is widespread and covers all of the former listed application fields [14]. Moreover, the process of embedding FBGs in composite structures has gained lots of interest in the composite community mainly with regard to aerospace applications. Numerous researchers have already proven the feasibility of embedding FBGs in fibre reinforced plastics for multiple purposes, such as measuring (residual) strain, temperature, delaminations and damage at impact [5]. In the same time composite materials are increasingly being used in aircraft primary structures (Section 1. 1.) because of their superior strength properties over metallic materials (Section 1. 2.).

FRPs exhibit, however, anisotropic material properties and different phases of materials. The fact that they are complex materials results in different internal strain states and non-uniform strain distributions. Determination of the internal strain fields, material deformation and the remaining strength and life of the material, is thus a challenging task. In close collaboration between the company FOS&S bvba (Fibre Optic Sensors & Sensing systems, Geel), the IPHT-Jena (Institute of Photonic Technology, Jena, Germany) and the Ghent University, Department of Materials Science and Engineering, a research project has been started to deal with this task.

The main questions which arises are: How can we integrate sensors into the structure and how can we gather accurate and efficient information on the structural health of the composite material during its lifetime? The answer of this question will be dealt with in this work by the usage of improved embedded fibre Bragg gratings in two different types of aerospace qualified composites.

The main research goal is to develop smaller diameter high quality fibre Bragg gratings which are suited to be embedded in extreme performing aerospace composites to accurately monitor the in-situ strains and material deformation.

Extreme performing materials need high quality sensors (Part I)

In this dissertation, the author will first of all demonstrate the manufacturing of high quality 80 µm draw tower fibre Bragg gratings. This part of the research is carried out at the IPHT-Jena in Germany during several trials. These sensors should feature the same sensing properties as the standard 125 µm version and should be beneficial with regard to embedding them into fibre reinforced composites. Before employing them as strain sensor, they should be accurately calibrated. To increase the accuracy of the sensor, the author has gone into the fundamentals of the well-known Bragg equation and has derived a new logarithmic approach for its strain sensitivity. This approach, instead of the commonly used linear approximation, is needed to accurately measure extreme strains (~1 %) over large temperature ranges (-60 °C up to 300 °C). The methods of characterization developed and applied in this work are not restricted to the uniform FBGs used in this work, but are applicable as well for other conventional FBGs or even for future generation FBGs (e.g. in microstructured optical fibres 'MOFs').

Complex materials need reliable sensors and methods to measure accurate strains (Part II)

In the second part, the author will focus on two aerospace certified carbon fibre reinforced plastics, i.e. thermoset carbon-epoxy (uni-directional pre-pregs) and thermoplastic carbon-PPS (woven-fabric semi-pregs), each with its own characteristics and complexity. The goal is to embed the FBGs to accurately measure strains in both type of materials. The approach, however, is not that straightforward as one might think. Composite laminates exhibit large (non-uniform) residual strains (transverse as well as longitudinal), which are often seen as a stumbling-stone because side-effects can appear in the Bragg spectrum. Instead of neglecting these effects, the author will do exactly the opposite; the induced birefringence will be 'exploited' to measure transverse strains and to discriminate in-plane and out-of-plane strains. Based on the logarithmic approach of Part I, a temperature compensating formalism is derived to deal with the cross-sensitivity of strain and temperature of the FBG. This allows to measure thermal strains in composites and even to define the CTE of the material. The ultimate goal of this dissertation is to overcome the difficulties encountered when embedding the fibre Bragg gratings and to find methods to gather the necessary information from the embedded sensor to perform materials research. This will allow to use the embedded FBGs as reliable SHM technology.

1. 5. OUTLINE OF THE DISSERTATION

This dissertation is divided into two main parts: in the first part the author will elaborate the development and complete characterization of the new 80 µm DTG®, and in the second part the author will embed and use the newly developed DTG®s together with the reference DTG®s to measure strains inside composite materials. Chapter 2, 3 and 4 are devoted to the optical fibre part (Part I) with Chapter 2 serving as an introduction to the fibre optics and fibre Bragg grating principles, and Chapter 5,6, 7 and 8 are devoted to the embedding of the optical fibre and the measurements with the sensors (Part II), with Chapter 5 serving as an introduction to strain measurements in composite materials using embedded FBGs.

PART I: The improved draw tower fibre Bragg grating: Manufacturing and characterization

The smaller diameter sensor will be developed, manufactured, fully characterized and compared with the standard 125 µm version.

1. 5. 1. Chapter 2: Draw tower fibre Bragg grating technology

This chapter will serve as an introduction to the reader on fibre Bragg grating manufacturing technology. It will give an overview on the differences between (fragile) conventional FBGs and the high quality (in-line) draw tower fibre Bragg gratings used in this work. Further in this section, the fundamentals of optical fibres are explained and the difference between standard single mode fibre and the highly

doped DTG®-fibre is discussed. Details are given on the manufacturing of the new highly purified fibre preform (i.e. the fibre material for the 80 µm DTG®s). The fibre Bragg grating writing methods are discussed with some additional details on the in-line writing method applied in this work. Finally, the author will highlight the coating applicator (i.e. DTG®-nozzle) to apply the ORMOCER® fibre coating. This device is optimized during the research to obtain a thinner and well concentric coating layer on the smaller diameter fibre.

1. 5. 2. Chapter 3: Developing & Manufacturing the newly 80µm draw tower grating

In this chapter the author presents the development and manufacturing of the new 80µm draw tower grating (DTG®). Two dedicated fibre preforms were developed: one suited for the 80 µm fibre and one to produce an 125 µm fibre, which will serve as reference fibre throughout this work. The preforms are characterized and the core radii and the effective refractive index of the highly Germanium doped fibre is determined. To minimize the overall coating diameter of the smaller diameter fibre and to enhance the coating concentricity, new coating nozzles are developed and applied. The tensile strength of the resulting fibres is tested and Weibull plots are plotted. At the end of this chapter a few notes are given on the handling and splicing of the newly 80 µm fibre.

1. 5. 3. Chapter 4: DTG® characteristics_80µm versus 125µm

Here the author will focus on the characterization of the optical properties, the opto-mechanical and thermo-optic properties. These properties are being compared with the reference 125 µm DTG®s. The (axial) strain gauge factor will be determined analytically and validated experimentally using different calibration setups. The strain-optic coefficients of the DTG®s will be determined by using an especially designed transverse compression setup. The temperature sensitivity is determined using a logarithmic approach and a second order polynomial fitting. The thermal stability of the DTG®s at 350 °C is studied to imitate the embedding conditions Additional to that, the temperature dependency of the strain gauge factor and stress sensitivity will be investigated for a large temperature range (-60 °C – 140 °C), and finally a method using two Bragg gratings, to estimate the stiffness (Young' modulus) of the ORMOCER® coating will be demonstrated.

PART II: DTG®s embedded in Thermo-set and Thermoplastic composites

The fully characterized sensor is ready to be embedded in the composite and will be used to establish accurate strain measurements inside carbon fibre reinforced laminates.

1. 5. 4. Chapter 5: Measuring strain with embedded Fibre Bragg Gratings_an introduction

The emphasis of this Chapter is to provide a general overview on strain measurements in fibre reinforced plastics by the usage of embedded fibre Bragg gratings. The reader will first be introduced to some technical issues which needs to

be considered when embedding FBGs in carbon fibre reinforced plastic (CFRP) laminates. Different topics are addressed, such as: the need to monitor residual strains during the manufacturing process, the existence of a strain transfer mechanism between the host material and the embedded optical fibre, the spectral response of the reflected Bragg peak to different types of composite materials and laminate stacking. The author will show in this chapter the principles to determine the peak wavelength of (distorted) Bragg spectra and a method is given to distinguish between transverse and longitudinal strain effects. Inevitable, an FBG exhibits a cross-sensitivity of strain and temperature. At the end of this chapter the basic principle of temperature compensating methods are given.

1. 5. 5. Chapter 6: Cure and consolidation cycle effects

First a literature overview is given on the research of residual strain monitoring with fibre Bragg gratings with some points of attention from the author with regard to the research which is presented. In this chapter, the manufacturing of the thermoset and thermoplastic test-coupons is discussed with the focus on monitoring of the residual strains with the embedded DTG®s. Different methods and approaches are used to calculate the transverse residual strain difference from the birefringence effects in the Bragg gratings and the longitudinal strain is measured by using encapsulated DTG®s. An attempt is made to disconnect the transverse and longitudinal strain and a method with polarization controlled testing is used to determine the birefringence in severely distorted spectra.

1. 5. 6. Chapter 7: Mechanical testing of thermoset CFRPs

This chapter focuses on the usage of the newly developed 80 µm DTG®s to measure multi-axial strains inside thermoset CFRP cross-ply laminates. This chapter is a continuation of the validation process of the multi-axial strain transfer matrix (i.e. TC-mattrix) which has been used in the framework of the research of Luyckx G. [15]. There the transfer matrix has been validated only for an out-of-plane loading case. In this dissertation first a matrix formalism is developed, based on the method applied by Luyckx G., to relate the sensor response (i.e. wavelength shifts) of a specific FBG-configuration with the strains in the core of the optical fibre by using the fibre's intrinsic strain-optic coefficients determined in Chapter 3. This matrix formalism is also referred to as the *K-matrix*. Then in the *strain transfer step* a relation has to be found between the measured strain in the optical fibre and the one in the composite material. The mechanism of the strain transfer from host material to sensor will be analysed in detail using finite element simulations.
In this work, the author will go a step further than the work performed by Luyckx G. and the strain transfer matrix is experimentally validated by loading CFRP laminates with embedded DTG®s along three independent loading directions. Both non-coated and coated 80 µm DTG®s are tested. In the continuation of Luyckx' research, a parametrical study is performed by varying the coating material properties, to investigate the interaction of a coated optical fibre with the composite laminate. The response of the embedded coated DTG® is validated for a transverse out-of-plane loading condition, for a number of varied TC-matrices.

1. 5. 7. Chapter 8: Mechanical and thermal testing of thermoplastic CFRPs

The purpose is to investigate the local longitudinal (in-situ) strain distribution, and to study the (permanent) deformation of the thermoplastic carbon-PPS woven fabrics by using embedded DTG®s during tension-tension fatigue testing at strain levels up to 0.5 % and tensile testing up to failure (approximately 1 % strain). The local internal composite strain field is evaluated from examinations of the spectral response of the embedded DTG®s and compared with digital image correlation (DIC), and meso-FE simulations.
The mechanical loading methodology used in this chapter is the key to gather the necessary sensor output from the embedded DTG®. It consists of repetitive progressive (quasi-static) loading cycles, alternated with fatigue loading cycles, and allows to perform measurements at specific intervals, and at specific load levels. Additionally, tests are performed to determine the birefringence effects and thus the transverse strain difference. It is found that the method applied here is well suited to characterize the long term behaviour of composite CFRP laminates in lab conditions. Additional to the mechanical testing, a detailed temperature test is performed to investigate the residual strain release and annealing effects during thermal cycling Moreover, the CTE of the laminates is determined using surface mounted and embedded DTG®s.

1. 5. 8. Chapter 9: Conclusions and future perspectives

In this concluding chapter the main achievements and conclusions in the work on the level of embedding FBGs in fibre reinforced plastics and monitoring of the strain and deformation of composite laminates are recapitulated. Finally, the author will give his recommendations with regard to future work and he will put forward which realisations of this work are relevant with regard to the industrial application. The author will close his work with an abstract of a new European research project which has started in September 2010, where a continuation of his work on the further improvement on smaller diameter Bragg sensors specially, is assured.

1. 6. REFERENCES

1. Airbus. Available from: http://www.airbus.com/aircraftfamilies/passengeraircraft/a350xwbfamily/.
2. YouTube. Available from: http://www.youtube.com/.
3. Coppinger, R. *Airbus and Boeing back structural monitoring*. 2007; Available from: http://www.flightglobal.com/articles/2007/02/20/212184/airbus-and-boeing-back-structural-monitoring.html.
4. Assler, H. *Design of aircraft structures under special consideration of NDT*. 2006; Available from: http://www.scribd.com/doc/36796525/4/Example-6-SHM-Potential-SHM-Applications.

5. Luyckx, G., Voet, E., Lammens, N., and Degrieck, J., *Strain Measurements of Composite Laminates with Embedded Fibre Bragg Gratings: Criticism and Opportunities for Research.* Sensors. **11**(1): p. 384-408.
6. Ten Cate. Available from: http://www.tencate.com/smartsite.dws?id=9483.
7. Hexcel. 2007; Available from: http://www.hexcel.com/.
8. Ashby. Available from: http://www.excelcalcs.com/images/repository/Material%20Selection%20in%20Mechanical%20Design.png.
9. Ticona. *Innovation waward for breaktrhough technology of G650 rudder and elevator*. 2010; Available from: http://www.ticona.com/home/news-details?id=15410.
10. Hill, K.O., Fujii, Y., Johnson, D.C., and Kawasaki, B.S., *Photosensitivity in optical fiber waveguides- application to reflection filter fabrication.* Applied Physics Letters, 1978. **32**(10): p. 647-649.
11. Meltz, G., Morey, W.W., and Glenn, W.H., *Formation of Bragg gratings in optical fibers by a transverse holographic method.* Optics Letters, 1989. **14**(15): p. 823-825.
12. Hill, K.O., Malo, B., Bilodeau, F., Johnson, D.C., and Albert, J., *Bragg gratings fabricated in monomode photosensitive optical-fiber by UV exposure through a phase mask.* Applied Physics Letters, 1993. **63**(3): p. 424-424.
13. *Philosophical transactions of the royal society*. Structural health monitoring. Vol. 365. 2007.
14. *Structural health monitoring*. in *Third European Workshop*. 2006. Granada,Spain.
15. Luyckx, G., *Multi-axial strain monitoring of fibre reinforced thermosetting plastics using embedded highly birefringent optical fibre Bragg sensors*, in *Department of Materials Science & Engineering*. 2010, Ghent University.

PART I

The improved draw tower fibre Bragg grating: Manufacturing and characterization

In Part I of the dissertation a smaller diameter draw tower fibre Bragg grating will be manufactured. The cladding diameter of the fibre will be reduced from 125 µm to 80 µm, to enhance the incorporation of the optical fibre in fibre reinforced plastics. To be able to reduce the cladding diameter without changing the mode field diameter of the (single mode) optical fibre we first need to produce a new highly photosensitive fibre preform rod with adapted dimensions.

The next step is to use this preform to draw the 80 µm optical fibre. Unlike classical FBG-writing, typically performed at an optical table setup, the FBGs in this work are written during the drawing process and immediately coated after the FBG inscription. This is the main principle of draw tower fibre Bragg gratings or DTG®s. Several manufacturing cycles will be performed in order to optimize the sensor' properties. Optimizing of the sensors focuses mainly on the level of the FBG reflectivity and the coating concentricity and reduction of the coating outer diameter.

After manufacturing, the optical fibre and DTG®s are fully characterized. First the optical fibre properties such as the effective step index (ESI), the (effective) refractive index, the fibre attenuation as well as the mechanical properties, such as the tensile strength and Weibull parameters will be determined.

Then with regard to the DTG®s' sensing properties the opto-mechanical properties (i.e. strain sensitivity parameters), thermo-optic properties (i.e. temperature sensitivity parameters), and the thermal stability with regard to reflectivity decay- and Bragg wavelength shift at high temperatures are studied.

When all parameters are known and validated the improved sensor will be embedded and used to measure strains and deformation in Part II of the dissertation.

Chapter 2 DRAW TOWER FIBRE BRAGG GRATING TECHNOLOGY

2. 1. INTRODUCTION

The basic requirements or 'ingredients' for sensors used in structural health monitoring (SHM) is that they should be reliable, reproducible, accurate and stable in time. However, not all FBGs have the same quality. Optical as well as mechanical properties of Bragg gratings can vary depending on the technology which is applied to produce them. The most common known type is the stripped FBG, which is written in a hydrogenated standard Single Mode (SM) fibre (e.g. Corning SMF 128), with the coating locally removed primary inscription. Although these FBGs are very accurate, reproducible, and relatively easy to produce they are not very reliable on the long term, because they are prone breaking and tensile stress can be poor compared to pristine fibres. Obviously, when thinking about using FBGs as strain sensors this disadvantage makes them less suitable, certainly if one wants to employ the strain sensors at high strain levels or lower stain levels on a long term. To overcome this problem it is maybe better to choose an (in-line) FBG manufacturing process where coating-removal is not necessary and thus the strain sensing element is more robust.

This chapter starts with an overview on the difference between conventional FBGs and the high quality in-line FBGs (Section 2. 2.). Next, the principles of the draw tower fibre Bragg grating (DTG® [1]) production process and its features will be elaborated (Section 2. 3.). This in-line FBG manufacturing technology will be applied in this work to produce the newly developed smaller diameter (80 µm) FBGs sensors. Further in this section the fundamentals of optical fibres are explained and the difference between standard single mode fibre and the highly doped DTG®-fibre is discussed (Section 2. 4.). Details are given on the highly purified fibre preform (i.e. the fibre material) manufacturing process (Section 2. 5. and the basic principles of the fibre Bragg grating writing method are discussed with some additional details on the writing method applied in this work (Section 2. 6. .). Finally the author will highlight a crucial topic in the manufacturing process and development of the smaller diameter fibre. At a certain point in the draw tower process a polymer coating will be applied on top of the drawn optical fibre and FBG (Section 2. 7.). The coating will protect the optical fibre and should serve as a good transfer medium to transfer the strain onto the optical fibre. This topic needs special attention with regard to the coating on the new 80 µm fibre, which is discussed in detail in Chapter 3, but also concerning the annealing and bleaching of the FBG, which has positive as well as some negative effects, respectively.

2. 2. FROM CONVENTIAL FBGS TO HIGH QUALITY DTG®S

Optical fibres are made of synthetic fused silica with an extreme high degree of purity (Section 2. 5.). Fused silica fibre is a linear elastic material with a high failure stress (approximately 5000 MPa) [2-3] and a failure strain of more than 6 %, which is much higher than the in-service strain levels for most of the composites, or materials commonly used for structural components, see also Chapter 3 on the tensile strength of the fibres used in this work. This (elastic) property of optical fibres should be exploited when considering health monitoring of composite structures. The sensor technology should outlive the material of interest, i.e. failure of the host material should first occur before the sensor gets damaged. However to maintain such high failure strains the presence of flaws in the silica surface should be avoided. Flaws in optical fibres has been studied for many years since the nineties [4-5]. The failure strength of optical fibres is strongly related to presence of flaws in the cladding surface. To prevent the fibre abrasion by external influences the optical fibre is therefore directly protected with a polymer coating during the fibre drawing process. In [6] recommendations are given to minimize early failures for both fibre processing and fibre handling. It is stated there are in general internal and external flaw types in optical fibres. Stripping, recoating and handling (e.g. cabling) have an abrasive effect on the fibre coating or silica/coating interface. It is demonstrated in [7] that the toughness and fatigue properties of the interface is key in determining the fibre lifetime. With respect to the afore mentioned properties of optical fibres, it is discussed in the following subsections, the quality of commercially available fibre Bragg gratings, fabricated using conventional FBG writing methods and the state-of-the art in-line FBG writing technologies, such as the draw tower process used in this work.

2. 2. 1. Quality of fibre Bragg gratings

The impression is very often that optical fibre sensors are brittle and fragile. This is certainly true for c*onventional FBG sensors*. Typically standard FBGs are fabricated by first stripping the coating of standard telecom fibre at a specific point along the fibre (e.g. Corning SMF 28) and then writing the gratings in the fibre on an optical table setup using a UV laser. Stripping the fibre coating by means of mechanical tools or laser etching strongly affects the mechanical strength and fibre tensile strength[2-3, 8]. When the coating is removed using chemical acids however, the tensile strength can in principle be kept the same as for the pristine fibre with coating [9]. However, stripping of the FBG area stays labour intensive and risk of fibre breakage when the fibre is being handled is high. In both methods discussed, the stripped area can then be recoated with the same polymer as the original one.

Examples of a stripped FBG, recoated FBG and ORMOCER® coated FBG are shown in Figure 2-1.

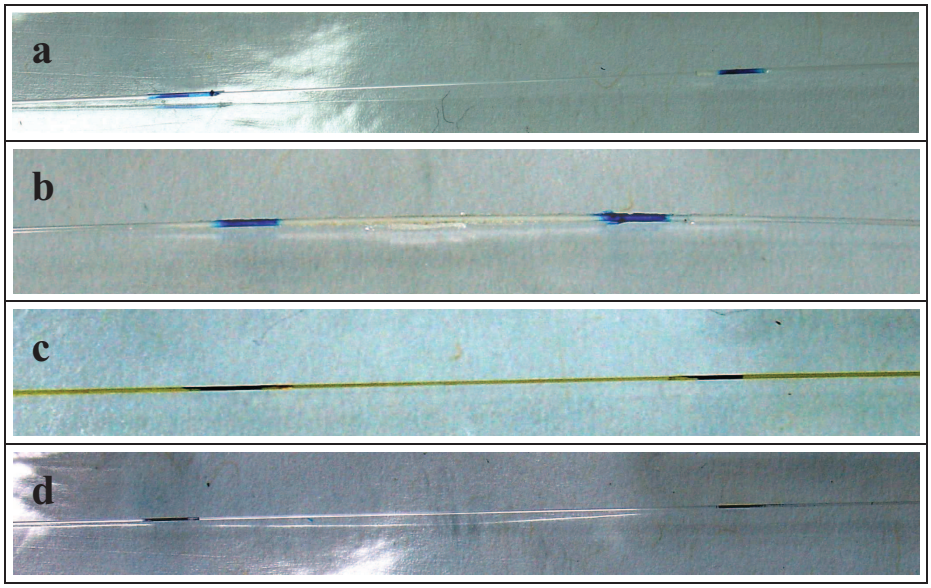

Figure 2-1: Acrylate Stripped (a), Acrylate recoated (b), Polyimide recoated (c) and ORMOCER® coated (d) FBGs

In Figure 2-1b, the acrylate recoated FBG shows clearly discontinuities in the recoating area. In the centre area we notice the coating has flown during curing, hence, a small portion of the coating has got a burr, which is slightly flattened. In Figure 2-1c the polyimide recoating area has much better quality, however, the coating is slightly thinner in the recoated zone than the pristine polyimide coating. Although the quality of this recoating is much better than in the case of the acrylate material, applying a recoating on the stripped fibre area does not match the original primary coating. The last is highly relevant if the FBG should serve as accurate strain (or temperature) sensor.

The procedure of recoating is different from the in-line coating process during the (continuous) fibre drawing process. Local recoating is typically applied “manually” using a desktop recoater consisting of a little mould surrounding the FBG area and a curing system, UV or thermal. An example of a commercial fibre recoater is shown in Figure 2-2:

Figure 2-2: Compact fibre recoater

Although the disadvantageous properties of conventional FBG writing, this technique is still commonly used. The conventional method is widely used to write uniform (rectangular) FBGs or used to write more complex type of gratings such as chirped and apodized FBGs, see Section 2. 6. 1. , Figure 2-16. It is often applied in research to write FBGs in other types of fibre, such as smaller diameter fibres, highly birefringent fibre (e.g. Bow-tie), Photonic Crystal Fibre (PCF) or in Plastic Optical Fibres (POF). Describing all these different research fields is beyond the scope of this research, therefore only two relevant researches with respect to smaller diameter optical fibres, used in composites, are briefly mentioned.

Geert Luyckx et al. [10] used 80 µm FBGs, written in commercially available highly birefringent Bow-tie fibres, to measure multi-axial strain inside CFRP laminates. In the research of Satori et al. [11], together with Hitachi Cable Ltd, a smaller diameter fibre of 40 µm has been developed for damage detection in composite laminates. The fibre is coated with a polyimide coating and has a total outer diameter of 52 µm. They also used the conventional FBG writing process and etched away the polyimide coating primary to writing the FBGs. Satori et al. showed the feasibility of embedding 40 µm FBGs in one fibre reinforced composite ply. They evaluated the FBG sensors for practical applications to detect damage evolution inside the composite laminates. Since the year 2000, several other Japanese research groups [12-15] used the same 40 µm fibre and FBGs. They reported strain and temperature measurements and damage detection using high speed interrogation systems in composite laminates. However, all research is performed using stripped and/or recoated (fragile) FBGs. No reporting of other smaller diameter fibre developments for usage in composites is found in literature thus far, nor the use of 80 µm coated FBGs, which is the aim in this research..

Recently a fully automated reel to reel system, like the proprietary LxSix in-line grating manufacturing [16], exists to fabricate high quality recoated FBGs. The technology makes use of a laser system to locally remove the coating, the fibre is stopped and the FBG is written in the stripped fibre area. Afterwards the FBG is recoated and the coating is cured. In principle this procedure is likewise the

"conventional" FBG writing, but it is carried out by a completely computer controlled system in a clean atmosphere, hence, it is possible to assure higher recoating quality and mechanical and thermal reliability. Such FBGs are especially developed for (high) temperature sensing applications such as down hole SAGD (Steam Assisted Gravity Drainage). However the strain range of these type of gratings stays limited up to maximum 0.34% of strain [16] hence they are not suited for long term strain sensing at elevated strain levels.
Lately other (automated) FBG inscription techniques are commercially available without stripping and recoating the fibre. This overcomes the problems stated above and hence keeping the pristine fibre strength. In general two writing processes are suitable for writing of gratings in-line and simultaneously retaining the high ultimate strain of the pristine fibre(coating). Both methods are discussed in the next paragraph.

2. 2. 2. In-line FBG writing_state of the art

The so called "cold writing" of FBGs [17] through the coating and writing FBGs during fibre drawing [18-23] use the state of the art methods to obtain high quality coated FBGs. Sabeus Inc has developed in recent years a fully automated cold writing process by using near-UV light (300 nm) to write sensors directly through the coating. In principle a multiple layered coating is used, starting with a thin primary UV transparent coating (to write the FBG). The method of writing is similar to the reel to reel system from LxSix where the fibre is stopped to write the gratings. It is then followed by a secondary protective layer (or multiple layers) to enhance mechanical properties. This process has many advantages over conventional FBG writing, such as its high reliability, the possibility to maintain the original strength of the fibre, the possibility of making spliceless FBG arrays, its flexibility in design wavelength and spacing. However, an important drawback is the freedom of choice of (UV transparent) primary coating materials. Degradation of coating properties or effect on the FBG quality have to be avoided. Research regarding the cold writing and the search for suitable coatings is ongoing [17]. It shows great potential in the telecom industry as well as in the optical sensing.
For optical sensors this primary coating is of major importance regarding the strain transfer from composite structure to the optical fibre sensor. If the coating material is to soft there is no optimal transfer from the host (or substrate) to the stiff silica [24]. If adhesion between the coating and fibre surface (interface) is poor, debonding of the coating could occur at higher strain levels or after a certain period of time. As such care should be taken to choose coatings with appropriate stiffness (and toughness) and adhesive properties with regard to the silica fibre.

Another technique, presented in the early nineties by Naval Research Laboratory, allows producing optical fibre Bragg grating arrays in-line on a fibre draw tower during the fibre drawing process by using an automated computer controlled interferometer [18]. This technique exhibits the same advantages of the cold writing process, though it has a freedom of use regarding the coating material as the FBG is written right before putting the polymer layer. However, writing gratings during the drawing process is possible only on condition that, the fibre is highly photosensitive, and that fibre drawing speed is slow. Typical speed of the fibre during a DTG® production run is approximately 10 m/min, which is very slow compared to the typical speed of 10 m/sec used in telecommunication industry. Although the 10 m/min to produce draw tower gratings is slow, still a few kilometres of fibre or sensor arrays with hundreds or thousands of sensors, can be produced within one day.

Two other research groups, Institute of Photonics Technologies –Jena (IPHT-Jena, Germany) and Southampton University (UK) further explored the draw tower capabilities. The research was mainly focussed on writing single pulse TypeI and TypeII (i.e. high temperature stable) gratings during fibre drawing. The IPHT uses a Talbot-Interferometer (Section 2. 6. 3.) to produce single pulse FBGs with specific coatings suitable for high strain and high temperature sensing [20-23].

Since 2005 a spin off company named FBGS-technologies, was created out of the IPHT for commercial exploitation of Draw Tower Gratings (DTG®s [1]). As will be further discussed in Section 2. 3. , the coated DTG® area and pristine fibre coating are equal, because no stripping and recoating is involved in this process. This type of FBG keeps its pristine fibre strength and coating quality maintains high. Besides, the ORMOCER® coating can resist high temperatures with an excellent adhesion to the silica fibre because of its inorganic-organic hybrid polymer structure [25]. DTG®s are well suited for accurate strain sensing in a wide range of applications and extreme conditions as will be shown in part II in this work. The tensile strength of standard 125µm DTG®s exceeds more than 5000MPa (see Chapter 3). It is this production facility which has been adapted during this dissertation to develop the 80 µm draw tower grating. The working principle of the draw tower setup is discussed in the next section.

2. 3. DRAW TOWER SETUP

A standard fibre draw tower setup, as employed in industry to manufacture telecom optical fibres, consists of a number of raw materials and accessories, see Figure 2-3 :

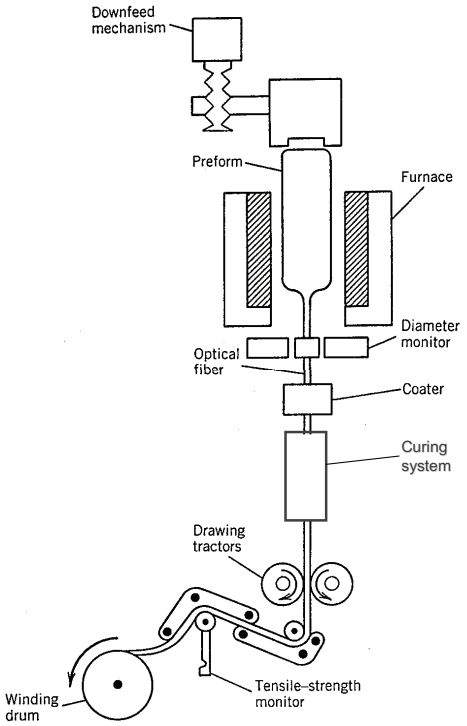

Figure 2-3: Standard fibre drawing setup used in industry [26].

From top to bottom we see a preform *downfeed mechanism*, a silica *preform* rod (Section 2. 5.), which is heated by a high temperature (2000C°) preform *furnace*, a *diameter monitor* to measure the drawn *optical fibre* cladding diameter, a coating applicator (Section 2. 7.) to apply is *coating material*, a UV or thermal coating *curing system* (Section 2. 7.), a *drawing tractor* (capstan) to pull the fibre, a *tensile strength measurement devices* and a *fibre winding drum*. Everything is automated and using a computer and dedicated controlling software with feedback loop.

By adding the following items to the standard drawing setup a dedicated FBG manufacturing draw tower setup is created (see Figure 2-4):

- a UV laser and laser interferometer system (Section 2. 6. 3.),
- special coating(s)
- an FBG marking system

The concept of the complete draw tower setup is depicted schematically in Figure 2-4. It shows the production process with all its components necessary to manufacture draw tower fibre Bragg gratings (i.e. DTG®s [1]). Throughout the

work the acronym DTG® is used when we speak about coated FBGs which are manufactured at the draw tower setup.

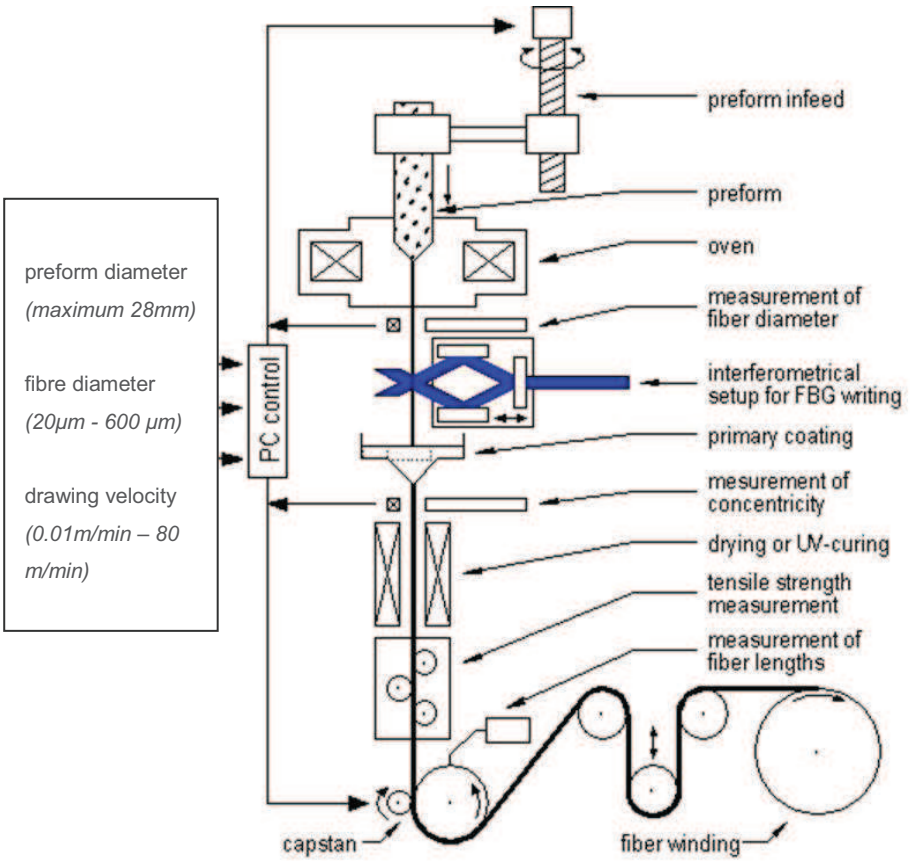

Figure 2-4: Production process setup for making Draw Tower Gratings (© FBGS-Technologies; Reprinted with permission).

It is a fully computer controlled process with a number of adjustable parameters, such as: the laser pulse frequency, the fibre preform in-feed speed, the fibre drawing speed, the fibre tension, the grating wavelength, the inter-grating distance, and the coating material. By proper software control with information on the fibre drawing speed (i.e. capstan speed), the laser pulse frequency is set and the Talbot interferometer (Section 2. 6. 3.) is controlled to write gratings with a specific wavelength and inter-grating distance. Because the draw tower technology allows modifying the afore mentioned process parameters it is possible to create variable FBG arrays, to use different coating materials and/or coating diameters, and by using the appropriate fibre preform (Section 2. 5.) to create optical fibres with other diameters (i.e. 80 µm, see Chapter3). Standard preform- and fibre-diameter are

23mm and 125µm, respectively with a fibre drawing speed of approximately 8 to 10m/min.

One very important strength of the draw tower technology is that no stripping of the coating is involved when manufacturing the DTG®s. These types of FBGs are coated immediately after the FBG inscription (Figure 2-4), hence, the quality of the coating at the position of a DTG® is identical to the coated fibre without a grating. Figure 2-5 shows the result of a "standard" ORMOCER® (ORganic MOdified Ceramic, [27] coated 125 µm fibre produced at the draw tower of FBGS-technologies.

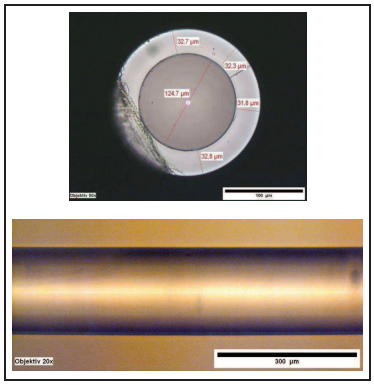

Figure 2-5: Cross sectional view and side view of an ORMOCER® coated 125µm fibre.

From the fibre cross section depicted in Figure 2-5, we see that the coating is concentric with the silica fibre and that is has a uniform thickness and a smooth surface along the length of the fibre, hence, the coating provides an excellent mechanical protection to the fibre and DTG®s.

As mentioned before, the fibre speed in this setup is kept low (10 m/min). In order to write gratings in the continuously moving fibre a *UV laser pulse* of approximately 9 ns and an *interferometrical setup* is used, see Figure 2-4 and Section 2. 6. 3. . The linear stages of the interferometer are controlled with Labview-software and permits writing grating arrays with a spectral distance up to 2 nm/cm. Physically this means that we are able to write successive DTG®s with a spatial separation of minimal one centimetre and a wavelength difference (peak to peak) of maximal 2 nm. If the spatial distance is increased to for instance one meter the wavelength difference can then be increased to maximal 200 nm, which shows variability of the system. Hence, the setup allows writing single DTG®s or (dense) sensor arrays with gratings at specific (short) distances. Additionally, it allows creating more complex or variable FBG array configurations. This is explained in the following example. In Figure 2-6 is shown a reflection spectrum with an array of 8 DTG®s with each sensor separated approximately by 1.2 m.

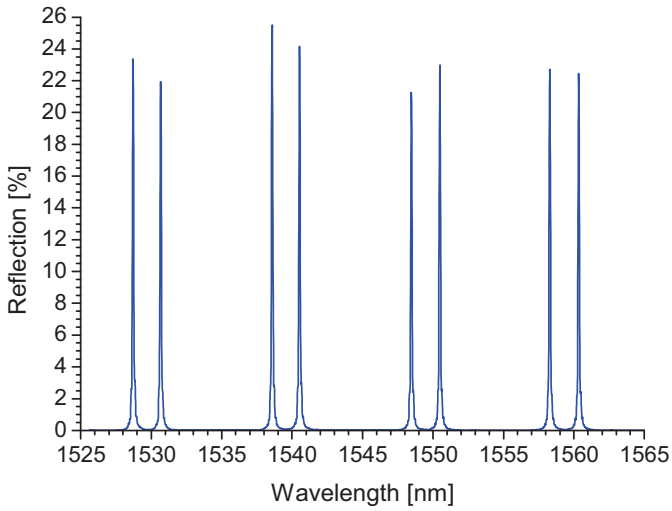

Figure 2-6: Reflection spectrum for a DTG® array with reflectivity ~22% for single pulse (Type I) gratings obtained with pulse energy of 0.7J/cm² .

The array consists of 4 grating pairs with a reflectivity of approximately 22 %, with each pair having a spectral distance of approximately 2 nm (e.g. the first pair in Figure 2-6 at 1528.5 nm and 1530.5 nm). The successive grating pairs, however, are shifted by about 5 nm. As such, the parameters controlling the interferometer have to be changed continuously during the drawing process to retain the right timing of writing the grating. The separation of 1.2 m is fixed, however the rate at which the wavelength change should occur is varied, i.e. 1.667 nm/m between the single gratings in each pair and 4.1667 nm/m between the first and the last grating of the successive pairs. This example clearly illustrates the flexibility of the draw tower setup. More detailed information regarding the interferometer is given in Section 2. 6. 3. .

At the end of the process the fibre is wound on a drum. To find back the gratings (i.e. holograms) after inscription, the position of the DTG® is marked with two small black dots on the coating surface, just before fibre winding. One marking is put before the grating, and one marking is put after the grating. Typical 3 cm of spacing is taken in between the dots, with the DTG® positioned in the middle, see Section 2. 2. 1. , Figure 2-1, d.

2. 4. BASIC FIBRE OPTICAL PROPERTIES

In the next paragraphs some fundamentals on optical fibres are given. This section contains qualitative information on the properties of fused silica fibre in general, but

more specific information on the properties of the draw tower fibres which are used in this work. It deals with the total internal reflection principle, the refractive index of doped silica and how a refractive index profile is achieved. This is followed by a small comparison between the bending loss in standard step index fibre and draw tower fibre.

2. 4. 1. Propagation of light in an optical fibre

2. 4. 1. a. Refractive index profile

To achieve total internal reflection, an optical fibre consists of a radial refractive index profile with a core having a higher index of refraction (n_1) than the surrounding cladding (n_2). As such the injected ray of light is reflected at the boundary of core and cladding (Figure 2-7) and transmitted towards the fibre end.
To achieve such a radial refractive index profile a special vapour deposition method (Section 2. 5.) is used to manufacture highly purified and doped fibre preforms (i.e. glass rod with typical diameter of 20-30mm) with a core and a cladding. The ratio core/cladding is fixed by the preform manufacturing. So, when the thin optical fibre is drawn, the refractive index profile is exactly the same as present in the preform. There exists many different refractive index profiles suited for optical fibres. The most common ones, used as waveguides for datatransmission in telecommunication systems, are (Figure 2-7): Step Index Multi Mode, Graded Index Multi Mode and Step Index Single Mode. The most common one used fibre for optical fibre sensors, and thus FBG sensors, is the SM fibre, with or without a highly doped fibre core.

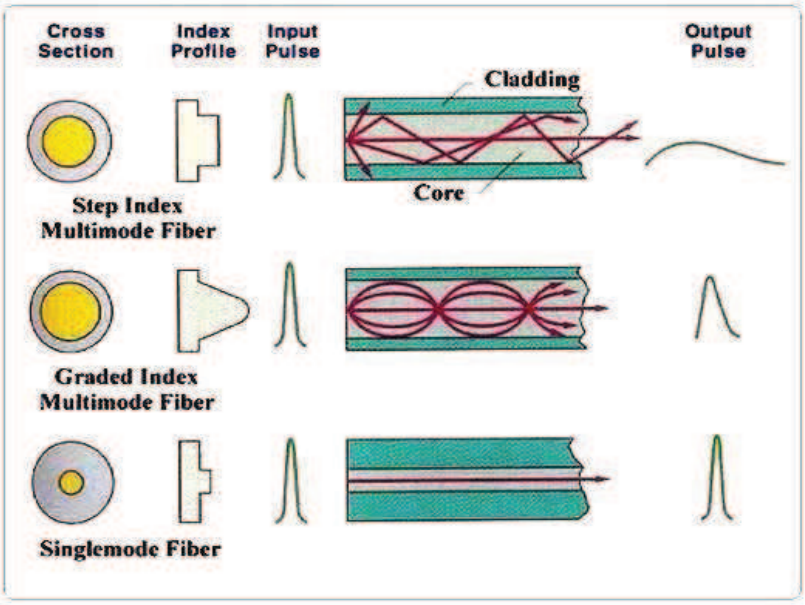

Figure 2-7: Some examples of the most common commercial optical fibres.

The radial refractive index profile of a fibre is given by:

$$n^2(r) = n_1^2 \cdot \left[1 - 2 \cdot \Delta \cdot (\frac{r}{a})^{\alpha}\right] \qquad \text{for } 0 \le r \le a \text{ (core)}$$
$$n^2(r) = n_2^2 = \text{constant} \qquad \text{for } r > a \text{ (cladding)} \qquad 2\text{-}1$$

where n_1 and n_2 are the refractive index of the core and cladding, respectively, r is the radius, a is the core radius and α is the profile coefficient of refractive index.
The parameter Δ is the relative (or fractional) refractive index change and is given by:

$$\Delta = \frac{n_1 - n_2}{n_1}. \qquad 2\text{-}2$$

In Equation 2-1 a triangular, parabolic (graded index), or step index profile can be obtained by setting α = 1, 2, or ∞, respectively, see Figure 2-9. Modification of the profile is possible by changing the relative refractive index parameter, Δ, and depends on the kind of dopant and dopant-concentrations used for each sintered layer of silica during the preform manufacturing (Section 2. 5.). More exotic refractive index distributions exist if a depressed or multiple cladding is used to achieve minimum fibre attenuation at specific wavelength windows or dispersion controlled fibres [26]. These special types of profiles are not within the scope of the research and will further not be discussed. The single mode fibres further discussed in this work are step index fibres.

2. 4. 1. b. Ray propagation model

The basic working principle of such fibres is understood by the basic ray propagation model shown in Figure 2-8. Here a ray is incident at the core centre, making an angle θ_i with the fibre axis. The ray is refracted in the fibre core with index, n_1 and bends towards the normal with an angle of refraction, θ_r, because of $n_0 < n_1$ (Snell's law). The angle θ_r is given by:

$$n_0 \sin\theta_i = n_1 \sin\theta_r . \qquad 2\text{-}3$$

The ray propagates in the fibre core is then refracted again at the core-cladding interface. However, refraction in only possible for an angle of incidence Φ such that $\sin\Phi < n_2 / n_1$ with n_2 the index of refraction of the fibre cladding. For angles larger than a critical angle Φ_C defined by

$$\sin\Phi_C = n_2 / n_1 , \qquad 2\text{-}4$$

the ray will experience total internal reflection at the core-cladding interface, hence the ray remains confined in the fibre core.

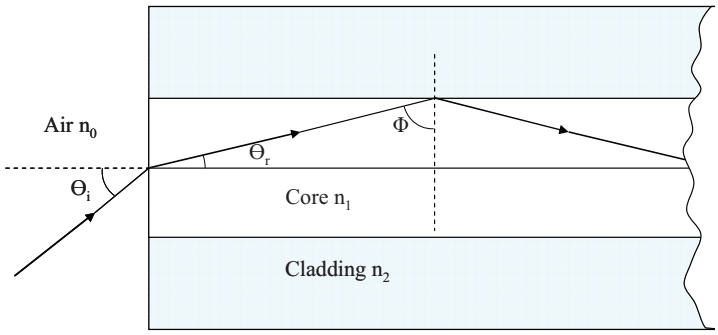

Figure 2-8: Light propagation through total internal reflection in a step index fibre.

Noting by using simple goniometrical relations that $\theta_r = \pi/2 - \theta_C$ in Figure 2-8 and substituting in Equation 2-4 we can write

$$n_0 \sin\theta_i = n_1 \cos\Phi_c = \sqrt{n_1^2 - n_2^2} = NA \qquad 2\text{-}5$$

The term $n_0 \sin\theta_i$ is known as the numerical aperture, NA, which represents the light gathering capacity of the optical fibre and can be calculated from Equation 2-5 using the refractive indices of the fibre core and cladding.

The relation between the relative index change, Δ and the NA of a fibre is approximated by [26]:

$$\Delta \approx \frac{NA^2}{2n_1^2} \qquad 2\text{-}6$$

This relation indicates that Δ should be made as large as possible in order to couple maximum light into the fibre. However, such fibres are normally not useful for the purpose of optical communications because of an optical phenomenon known as modal dispersion which is understood by the ray model where different rays travel along paths of different lengths. Although for single mode fibres this modal dispersion is absent, as there is only one mode propagating in the fibre, there still exists fibre dispersion which has two contributions, material dispersion and waveguide dispersion. The relative index, Δ, is interrelated with those two contributions. By tailoring the radial refractive index profile (Equation 2-1) and thus the relative index, Δ, it is possible to make dispersion shifted and dispersion flattened fibres for specific wavelength regions. However, this is not subject of the research and for specialized literature the reader is referred to [26]. The fibres used in this dissertation are single mode step index fibres with a fibre core highly doped with GeO_2. As such these fibres have a high NA which is useful for sensing purposes.

2. 4. 1. c. Dopants, fibre refractive index and optical wavelength

Optical glass fibre is made of fused noncrystalline silica (SiO_2) which has low optical loss, hence, light can be transported over long distances. Standard (telecom) low-loss single mode optical fibres consist essentially of fused silica (SiO_2) mixed with a small amount of other materials, called the "dopants", such as GeO_2 (or P_2O_5), to increase the refractive index of the fibre core, or with F (or B_2O_3), to reduce the refractive index of the fibre cladding (Figure 2-9).

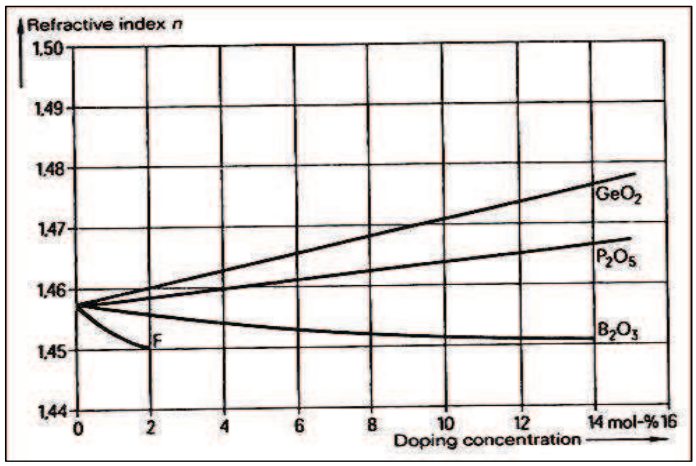

Figure 2-9: Refractive index as function of dopant concentrations for silica (measured for λ approx. 0,6µm) [28].

As seen in Figure 2-9, one is able to tune the refractive index of the silica fibres by adding different dopants and dopant concentrations (indicated in mol%). In the same time the refractive index of any optical material varies with optical wavelength. The value of this refractive index as function of wavelength is well approximated by Sellmeier's dispersion equation [29]:

$$n^2(\lambda)-1=\sum_i \frac{S_i\cdot\lambda^2}{\lambda^2-\lambda_i^2}\cong\frac{a_1\lambda^2}{\lambda^2-b_1}+\frac{a_2\lambda^2}{\lambda^2-b_2}+\frac{a_3\lambda^2}{\lambda^2-b_3}\quad , \qquad 2\text{-}7$$

with S_j the oscillator strength, λ_j the resonance wavelength and a_i and b_i with i=1-3 the empirically obtained parameters found by fitting the measured dispersion curves in to Equation 2-7. They depend on the amount of dopants and have been tabulated for several doped silica fibres in [29]. For example for pure silica the parameters are found to be $a_1 = 0.6961663$, $a_2 = 0.4079426$, $a_3 = 0.8974994$, $b_1 = 0.004679148$, $b_2 = 0.01351206$ and $b_3 = 97.934002$. Examples of the variation of the refractive index with wavelength using Equation 2-7 are plotted in Figure 2-10. The refractive index for pure silica is found to be $n = 1.444$ at a wavelength of 1550nm and is indicated by the dotted line. Throughout the work this value for n will be used as refractive index for the fibre cladding (i.e. n_2). As seen in the curves for the GeO_2 dopant, the total refractive index shift towards higher values compared to curve for the pure fused silica, see difference between the dotted lines at 1550nm. This is in accordance with the plots shown in Figure 2-9. It is also noted that the origin of these plots lies at a refractive index of $n = 1.458$ which is exactly the corresponding refractive index of pure fused silica at a wavelength of 0.6µm in the dispersion curve of Figure 2-10, see the dashed-dotted line at 0.6µm.

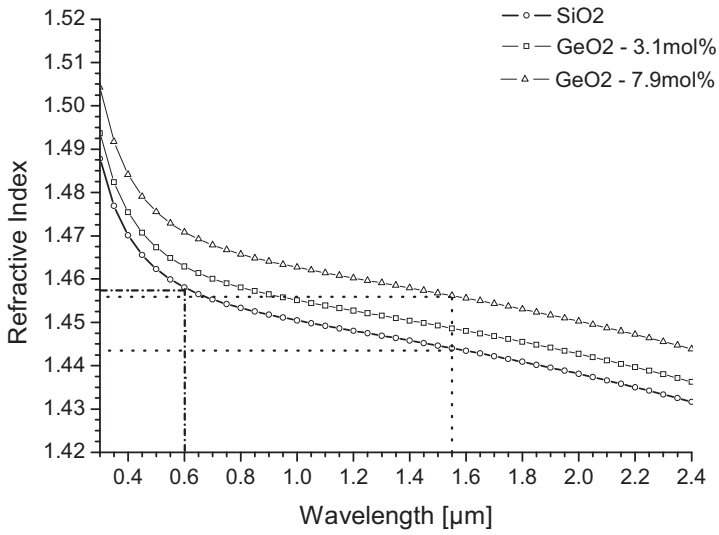

Figure 2-10: Refractive index of pure fused silica and GeO_2 doped silica according Sellmeier's dispersion equation.

2. 4. 2. Standard single mode fibre versus Draw tower fibre

The standard single mode fibre (SMF) and the highly $Ge0_2$ doped draw tower fibre (DT fibre) are single mode step index fibres. However, it should be noted that quite some difference exists in optical properties between both types. This section briefly describes a few of them.

2. 4. 2. a. Standard SMF

Standard SM step index telecom fibres have relatively low GeO_2 dopant concentrations, typically in the order of a few mol percentages. They have a relative refractive index ranging from $\Delta = 1$ to $5 \cdot 10^{-3}$. Substituting this in Equation 2-1 and taking $n_1 = 1.45$ the NA for these fibres ranges from 0.065 till 0.145. As an example we focus on the Corning® SMF-28® [30]. It has a cladding with a diameter of 125 µm and a core of 8.2 µm. The fibre core is doped with approximately 3mol% of GeO_2 with a refractive index of $n_{core} = 1.4476$ (at $\lambda = 1.55 \mu m$). Using Equation 2-1 it shows that the numerical aperture is equal to $NA = 0.10$ for this specific fibre, which falls within the range of the former quoted limits. The fibre is designed to be single mode for $\lambda > 1.2$ µm, (i.e. cutoff wavelength, see Equation A-6, Appendix A), with a low attenuation, which is approximately 0.2 dB/km at 1.55 µm. However, bending loss in this standard SM fibre is relatively high, certainly considering small curvatures. In the datasheet of the Corning® SMF-28® is stated that the bending loss

is smaller than 0.5dB for one loop around a 32 mm mandrel. In a small scale bending loss experiment shown in Section 2. 4. 2. c. , performed on an identical type of standard SMF fibre from Alcatel, it is shown that bending losses exceed 5 dB for mandrels with diameters smaller than 15 mm. Bending loss should be avoided in telecom networks and therefore these fibres are usually coated with a soft acrylate coating with a diameter of 250 µm and in addition jacketed (buffered) so curving of the fibre is limited and thus micro/macro-bending loss is kept low. Lately advances in tuning of the index profiles (in accordance with Equation 2-1) of single mode fibres has lead to special fibre types (e.g. Corning® SMF-28e®XB) with improved macrobend performances [30]. The bending loss for this specific fibre is smaller than 0.5dB for one loop around a 10 mm mandrel, which is still high compared to the values reported for the DT fibre macrobending loss, see Section 2. 4. 2. c. .It should be noted that the acrylate coated fibres are not really suited for accurate strain sensing and embedding in composites. Standard acrylate coatings tend to have a bad strain transfer effect from host material to the fibre sensor because of low Young – modulus [24]. Moreover the high bending loss is harmful for the sensing signals as it could lead to signal drop-outs or inaccurate measurements when composite structures are being loaded.

2. 4. 2. b. DTG®-fibre

The optical fibres used in this work have a refractive index of the core of $n_1 = 1.4593$ (see calculations in Section 3.2.3) and a relative refractive index of $\Delta = 10.48 \cdot 10^{-3}$ (using Equation 2-2). Substituting this in Equation 2-6 the numerical aperture of the DTG®-fibre corresponds to $NA_{DTGF} \approx 0.209$, which is more than twice as high compared to standard telecom SMF. A high numerical aperture means that the fibre will have a high capacity of guiding the light. So at first sight a higher NA is more favourable, however, due to very high GeO_2 concentration in the DTG®s-fibre core attenuation is high as well. Fibre loss measured in the DTG®-fibre developed in this research is as high as 11dB/km (at 1550nm) for the 125µm version and it is even higher, nearly 18dB/km (at 1550nm), for the 80µm fibre, which is extremely high. The origin of this attenuation found in the high GeO_2 dopant concentration, i.e. approximately 19mol%, and is described in detail in Section 3.2.2. This high GeO_2 mol% is necessary to inscribe single pulse fibre Bragg gratings (Section 2. 6.) since it increases the photosensitivity of the core. This type of fibre is clearly not suited as transmission medium for long distance telecommunication systems. Moreover, it is neither suited to serve for long distance optical sensing lines (i.e. kilometres). Too high power loss could eventually lead to inaccuracies of your measurement. However, if we for instance focus on health monitoring of composite structures like wings, fuselages, hulls, etc…, it is

noted that for these sensing networks the actual sensing lines are usually of shorter distances, i.e. in the range of tens of meters or maximum a few 100m. The (longer) connection lines between the sensing lines and the FBG interrogator could then be exchanged by standard SMF with low optical loss, stipulated that connection losses are kept as low as possible. Lately commercial available FBG interrogators use "high" power broadband light sources (i.e. in the mW range) and although high attenuation is present the optical power in the sensing network is usually sufficient if the connection losses are kept within the limits (typical <0.5dB per splice). In large sensing networks with a large number of multiplexed sensors and optical component (i.e. optical switches, circulators, 3dB couplers and fusion splices) attention should be paid to the total available optical power budget.
Because of the high NA, however, the DTG®-fibre is very insensitive to bending loss. This feature is an advantage compared to standard single mode fibre, certainly with regard to embedding in woven fabrics, which is the subject of this thesis. With regard to the bending loss, a small scale macrobending experiment has been performed to estimate the difference in bending sensitivity between the SMF and the DT fibre. Moreover, to confirm that the DTG®-fibre has extreme low loss due to macrobending. The results presented below clearly illustrate that there exists a large difference between the two fibre types.

2. 4. 2. c. Bending loss in SMF and DTG®-fibre

A few simple transmission measurements were performed to estimate and compare the bending loss in 125 µm SMF and in two different 125 µm DTG®-fibres by looping them around small cylinders (spools). In a first test, a cylinder with diameter 40 mm is used (Figure 2-11). All three, the SMF, a DTG®-fibre for the 830 nm range and one for the 1550 nm range, were looped 40 times around the Teflon Cylinder in order to estimate the attenuation as function of the number of loops. No large difference has been found in this test; results show that the SMF has a small attenuation of 0.35 dB/40loops, while the DTG fibres have about zero loss.

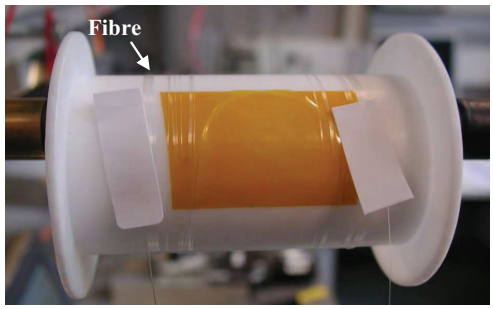

Figure 2-11: Attenuation test mandrel of 40mm for winding up the fibres.

However, if the diameter of the cylinder is decreased to 15 mm, 10 mm or 5 mm, the loss difference becomes much higher, see Figure 2-12. When the fibre is looped around the 5 mm cylinder, the loss in the SMF is as high as 40 dB against 0.025 dB for the DTG®-fibre for the 1550 nm range.

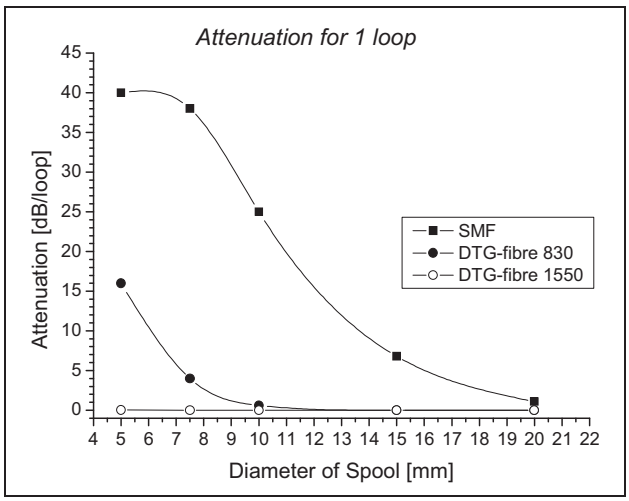

Figure 2-12: Attenuation curve for 1 loop versus different diameter sizes of test cylinder (bottom).

Figure 2-13, shows two measurements performed using the 5mm diameter mandrel. Each plot shows the reference curve (left y-axis) of the fibre without macro-bending and the measurement curve (right y-axis), with the SMF fibre showing large scattering (top-left figure). In contrary, the DTG®-fibre for the 1550nm range hardly shows any scatter (top-right figure) with the loss curve being very flat and just below zero.

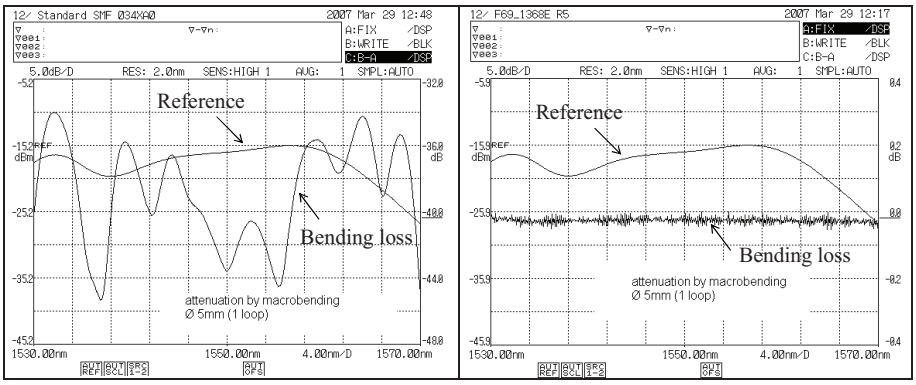

Figure 2-13: Plots of the transmission measurements on a mandrel of 5mm, SMF (left) and DTG®-fibre (right), with the attenuation plotted on the right y-axis.

It should be noted that the measurements shown are a rough estimate of the bending losses in the optical fibres and that they should not be taken as exact values, though they clearly illustrate the difference in fibre bending loss for the three types of fibre. The bending loss of the 1550 nm DTG®-fibre is extremely low which is favourable when embedding them in composites.

2. 5. FUSED SILICA PREFORM RODS

Fibre production in a fibre draw tower process starts by making a glass preform rod (bar) which will then serve as fibre material. This section discusses how highly doped preforms are fabricated and how an optical fibre is then manufactured.

2. 5. 1. Preform manufacturing

The most important factor in fibre preforms is the purity of the silica glass to have high transparency and low-loss. A second important point is the doping concentration of the silica, which should be well controlled, in order to fabricate the required refractive index (profiles). Impurities like transition metals (e.g., Cu, Fe, and Co) and OH^- ion, were found to be the main cause for the high loss in optical fibres. It was learned that the content of transition metals must be held below 0.1 ppb(10^{-10}) and that of the OH^--ion below 10 ppb [26]. To achieve such low impurity-concentrations special processes based on chemical vapour deposition were developed. Only the most common ones are mentioned here. They are roughly classified as follows:

1. MCVD (Modified Chemical Vapor Deposition)
2. PMCVD (Plasma Enhanced CVD)
3. OVD (Outside Vapor Deposition)
4. VAD (Vapor-phase axial deposition)

All methods listed here are based on oxidation reactions of material vapours at high temperatures to homogeneously produce fine particles of (doped) glass which are called “soot”. Afterwards the soot is vitrified and high purity glass deposits mostly inside a rotating hollow silica tube or on top of a rotating thin mandrel (i.e. OVD process). PMCVD and MCVD is based on the same principle except that plasma flames are used in place of oxyhydrogen flames. The OVD method uses the same apparatus as used for the CVD, but this method generally uses a rotating ceramic starting mandrel to deposit the glass layers. The glass rod is then removed from the mandrel, dehydrated and vitrified in a heating furnace to form a preform rod. The size of the preform rods using the afore mentioned methods is limited by the size of the silica tube. Therefore the length of the fibre from such preforms is generally maximal 20 to 40km. Unlike the methods previously mentioned the VAD method permits producing endless fibre material. Here porous soot of (doped) silica is continuously made on a rotating silica boule and the rotating soot rod is pulled up, dehydrated and then consolidated in a furnace. As such fibre material is renewed and hence fibre drawing can continuously run.
The method of interest for fabrication of the preforms in this work is the MCVD (Modified Chemical Vapour Deposition) process, as shown in Figure 2-14.

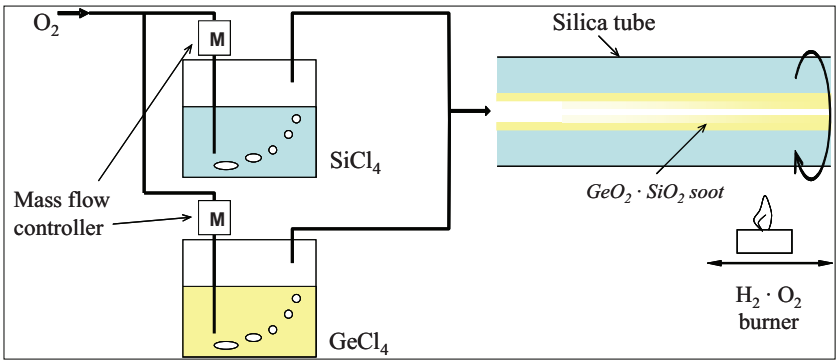

Figure 2-14: Principle of Modified Chemical Vapour Deposition (MCVD) process for the fabrication of GeO_2 doped silica preform rods

In the MCVD-process above, $SiCl_4$ and $GeCl_4$ is made to flow with a carrier gas O_2 into a rotating silica tube and the mixed vapours are heated till temperatures higher than 1800 °C using a oxy-hydrogen torch outside the tube. An oxidizing reaction takes place in the tube and deposit (or soot) of SiO_2 and $GeO2 \cdot SiO2$ vitrifies on the inner wall of the tube:

$$SiCl_4 + O_2 \rightarrow SiO_2 + 2Cl_2$$
$$GeCl_4 + O_2 \rightarrow GeO_2 + 2Cl_2 \qquad \text{2-8}$$

With the MCVD-process a cladding and core layer is created inside the rotating thin silica tube with the help of mass-flow controllers which tune very precisely the concentration of dopant material in the deposited silica glass layers. The schematic MCVD-process in Figure 2-14 shows the example of $GeCl_4$ dopant for creating GeO_2. Usually an industrial MCVD-process consists of more than one additive dopant and by employing different metal halide vapours or Fluor, it is possible to create exotic fibre perform profiles according Equation 2-1. At a specific time the tube is almost filled completely with vitrified or doped silica, and only a very thin hole is remaining. The tube is then further heated with the torch and collapsed into a rod with a round, solid cross section and is called a fibre preform rod.
As learned from Figure 2-9, the dopant in the fibre affects the value of its refractive index depending on the kind of dopant and its concentration (in mol%). Adding a small mol% of GeO_2 (e.g. 8mol%) rationally increases the refractive index ($\Delta n \approx 10^{-2}$, respectively). As mentioned before the fibre used within this research has a maximal GeO_2 concentration of approx. 19mol% which is extremely high to enhance the photosensitivity needed to produce single pulse FBGs, see Section 2. 6. 3.

2. 5. 2. From preform rod to optical fibre

To make fibre out of the solid preform bar, it is heated in a graphite resistance furnace (1600 °C - 2000 °C), see Figure 2-15, and consequently drawn into a thin fibre with the desired diameter.

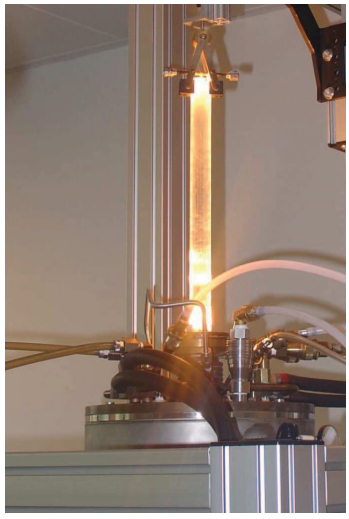

Figure 2-15: Glowing fibre preform in a furnace on top of the draw tower.

Unlike metal (or plastic) wire drawing, where the size of the wire is decreased by pulling material through (several) decreasing dies, optical fibre drawing starts from a glowing glass preform serving as fibre material. Primarily the preform tip is (pre)-shaped in a cone with a small glass bar spliced to the tip. At the start of the drawing process the melted glass cone needs to be pulled manually (i.e. by gently pulling the spliced glass bar by hand). At first we get a fibre with a (large) discontinuous fibre diameter, and the expenditure of the glass is high. The fibre is then pulled further by the draw tower capstan motor (see Figure 2-4) where the pulling speed is at first manually controlled and tuned until the fibre has reached a diameter close to the desired cladding diameter. This preliminary handling is really critical and needs to be executed very carefully by a skilled technician. It is noted in this stage that the coating nozzle to apply the protective polymer coating (Section 2. 7.) is not applied yet. Therefore the optical fibre being drawn is still bare glass fibre and extremely fragile. The coating material is only added when the fibre has reached the appropriate (constant) diameter.
A typical preform for standard optical fibre has an *outer diameter D*, of 28 mm and a *length L*, of approx. 80 cm. As an example, assuming volumetric equality we can manufacture about 40 km of fibre with a cladding *diameter* of 125 μm.

In the next section is explained which common methods are used to write fibre Bragg gratings in single mode fibres and how they can be written in-line during the fibre drawing process to fabricate DTG®s.

2. 6. FIBRE BRAGG GRATINGS WRITING METHOD

As mentioned before, the refractive index of a silica fibre is controllable by using different dopants and dopant concentrations. As shown in Chapter 2. 1. it is possible to increase and decrease the index of refraction, and hence changing the radial refractive index profile of the fibre. The GeO_2 dopant in the core of the fibre increases the refractive index but additionally it exhibits photosensitive properties which is most convenient for FBG writing. By illuminating a photosensitive core with UV-light or more precise with a UV interference pattern, it is possible to create a holographic grating pattern. Typical SM fibre without high GeO_2 doping is not readily suited for writing FBGs using UV light (e.g. UV Excimer Laser). Low GeO_2 doped fibres are usually hydrogenated on beforehand to enhance photosensitivity. However, such SM fibres are not suited to write in-line FBGs on a draw tower. The next subsection introduces the most common FBG refractive index patterns followed by an overview of the basic principles on how to write such grating pattern inside an optical fibre.

2. 6. 1. Common FBG refractive index patterns

Bragg gratings are classified according to their refractive index pattern. Without taking into account the radial index profile of the fibre (Equation 2-1), the refractive index modulation along the length of the fibre Bragg grating varies as

$$n(z) = n_1 + \Delta n_d(z) + \Delta n_g(z)\cos\left(\frac{2\pi}{\Lambda(z)}z + \Phi(z)\right), \qquad 2\text{-}9$$

where n_1 is the refractive index of the fibre core, Δn_d is the average or homogeneous mode index modulation induced by exposure to UV light, Δn_g is the modulation depth which is always a positive value (typical $\sim 10^{-4}$), $\Lambda(z)$ is the period of the grating and $\Phi(z)$ is the phase of the grating. All variables in Equations 2-9 are z-dependent and by tuning the FBG writing conditions the profile of the index modulation is changed. Fibre gratings are classified into different types according to their refractive index profiles in axial direction (see Figure 2-16):

a) **Uniform FBG:** For a uniform or rectangle grating no z-dependence of the variables in Equation 2-9 exists and its reflection spectrum is approximated by Equation 2-10, see further in this section.
b) **Chirped FBG:** In chirped gratings the period of the grating, $\Lambda(z)$, is z-dependent and thus the optical period, $n\Lambda$ in a chirped grating changes over its length. With $\lambda_B = 2\bar{n}\Lambda$, the Bragg wavelength also varies along the grating length, and because an optical pulse has a number of frequency components, each corresponding wavelength will be reflected at other distances in the grating. A chirp can also be achieved by applying local UV exposure and changing of the averaged index, $\Delta n_d(z)$, along the grating length. As a result the *Chirped FBG spectrum* is broader than that of a uniform grating.
c) **Apodized FBG:** Gratings with position dependent index Δn_d, and modulation depth Δn_g, are called *apodized gratings*. In practice such non-uniform index change occurs naturally when an ultraviolet Gaussian beam is used to write the grating. In general such apodized gratings smoothens the spectrum.
d) **Tapered FBG:** If only the modulation depth n_g is made non-uniformly along the grating length, the side-modes of the reflected spectrum are suppressed and as a consequence the coupling coefficient along the grating length are tapered. Such effect is desired in the telecommunication for dispersion compensation in uniform gratings.

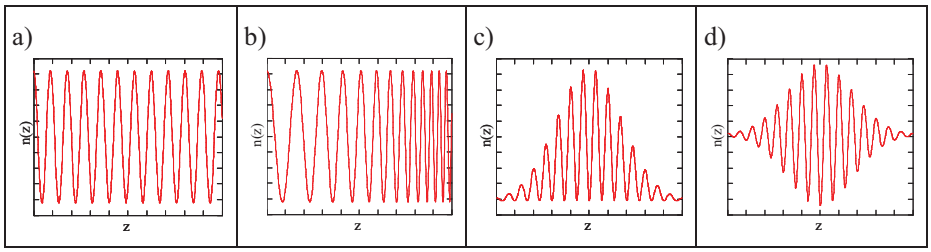

Figure 2-16: Grating types after the form of the index profile according Equation 2-9 (a) Uniform FBG, (b) Chirped FBG, (c) Apodized FBG and (d) Tapered FBG.

It is noted for a grating chirp the effect of a z-dependent change of the phase, $\phi(z)$, can be expressed the same as a z-dependent grating period, Λ(z), by using $\phi(z) = \int_0^z \frac{2\pi}{\Lambda(z)} dz$. As such it is not possible to distinguish both effects. Typical in field distribution calculations inside fibre Bragg gratings, used for filtering purposes, the shape of the periodic perturbation is calculated by using only the phase as given in the latter relation [31].

The FBGs discussed in this work have a uniform or rectangular shaped grating (Figure 2-16a). They are classified as low reflection TypeI gratings [32]. The reflectivity spectrum for such type of FBGs with a length, *L,* is approximated by (Equation A-21, Appendix A):

$$R(\Delta\beta) = (\kappa L)^2 \,\mathrm{sinc}^2(\Delta\beta L), \qquad 2\text{-}10$$

with κ the coupling coefficient and $\Delta\beta$ the detuning from the Bragg wavelength (AppendixA). The maximum reflectivity is then given by (Equation A-22, Appendix A):

$$R_{\max} = (\kappa L)^2 = \left(\frac{\pi \Delta n_g \Gamma L}{\lambda_D} \right)^2, \qquad 2\text{-}11$$

with λ_D the design-wavelength, which is well approximated by $\lambda_D = \lambda_B$ if $\Delta n_d \approx 0$. Equation 2-11 shows the maximum reflectivity is depending on the square of the modulation depth, Δn_g of the grating. From Equation 2-11 it is clear that the limitations of the reflection of draw tower gratings lies strongly in the modulation of the refractive index, which is on its turn directly proportional to the photosensitivity of the fibre core and the pulse energy used to write the grating. As an example a measured spectrum is fitted against a numerical modelled spectrum using Equation 2-10, see Figure 2-17. The length of the grating is 8mm and the modulation depth is

taken $\Delta n_g = 4.3 \cdot 10^{-5}$. Although the resemblance is good on the level of peak shape, peak width and maximum reflectivity, a slight difference in noticed in the side lobes of the FBG. The wavelengths of the side lobes correspond well, however, the lobes are a little higher in the case of the measured spectrum and the symmetry is slightly disturbed. It is believed the writing conditions during drawing such as lateral fluctuation of the fibre and the fact the fibre moves vertically during grating inscription, have an impact on the contrast spectral shape. However, the side lobe suppression of the DTG®s manufactured in this work is more than 10dB and enough to perform accurate Bragg peak measurements. Detailed analysis of the FBG profile is not subject of the research.

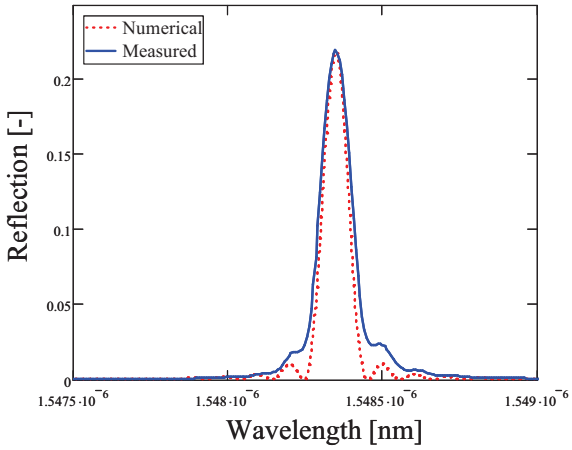

Figure 2-17: Measured (solid line) and numerical spectrum (dotted line) for a 8mm uniform grating.

2. 6. 2. Common FBG writing methods

There are only a few techniques suited to write Bragg gratings in optical fibres. The most common used methods are listed below followed by a brief explanation of their working principle:

1) Interference (or holographic) method,
2) phase mask exposure technique,
3) point-to-point lighting using high power femto-second (fs) lasers.

An interference pattern (or holographic induced index modulation) is created by splitting a laser beam into two separate beams and then reuniting them to form an interference pattern at the point of recombination. The beam is split in two by using a diffraction grating (i.e. phase mask) and reunited at an angle of $2\vartheta_{FBG}$ using two

mirrors. In Figure 2-20 is shown an example of the Talbot interferometer principle which is used in this work.

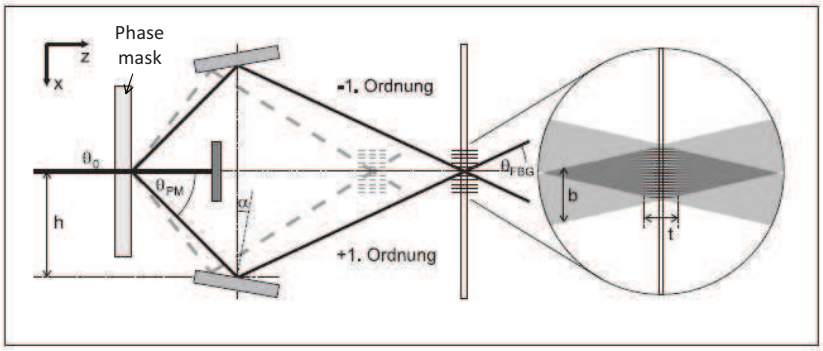

Figure 2-18: Sketch of the Talbot interferometer with phase mask [33-34].

The two beams interfere and perpendicular to the plane of incidence an interference-pattern arises in the doped (photosensitive) fibre-core with a grating period

$$\Lambda_{FBG} = \frac{\lambda_{UV}}{2\sin\theta_{FBG}}. \qquad 2\text{-}12$$

The interferometer is build so that the angle ϑ_{FBG} can be changed to write FBGs with a different grating period. To obtain equal interference-stripes this setup has high demands on laser-source, optical components and mechanical stability. This concept is used for the draw-tower, together with a phase mask as beam-splitter (i.e. diffraction element).. This technique allows only of writing non-chirped gratings. The focus of the interference pattern is maximal for one design wavelength (i.e. grating period) only. As such the contrast, i.e. modulation depth, of the interference pattern will be inferior and hence the chirped FBG spectrum will have lower reflectivity. The interferometer is further explained in detail in Section 2. 6. 3.
The second technique makes use of a phase mask (i.e. diffraction grating) put close to the optical fibre and UV-lighting to create a refractive index pattern in the photosensitive fibre-core (Figure 2-19). This technique was used for the first time around 1993 by K.O. Hill & Co [34]. Because of this phase mask a binary transmission phase-grating is achieved in the fibre core with two height-steps. They are depicted schematically as black and with stripes in Figure 2-19. It is important to reduce the zero-order transmission (destructive interference) which is achieved by choosing the *groove-depth* $t = \frac{\lambda_{UV}}{2(n_{SiO_2} - n_{air})} \approx \lambda_{UV}$ [[33].

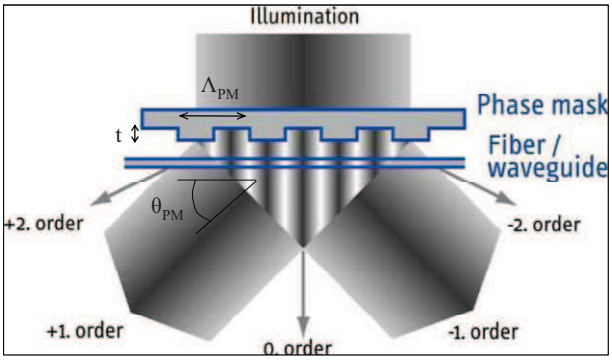

Figure 2-19: Phase mask [35].

For the m[th] order of diffraction, the *diffraction-angle* θ_{PM}, will be fixed for a defined *grating period of the phase-mask* Λ_{PM}. For the case of a perpendicular illumination this results in

$$\sin\theta_{PM} = m\frac{\lambda_{UV}}{\Lambda_{PM}}. \qquad 2\text{-}13$$

If the zero-diffraction order is successfully depressed, only the +1 and -1 diffraction orders will dominate. These two orders overlap right behind the phase-mask and interfere to create a interference-pattern. Using Equation 2-12and Equation 2-13 and with $\theta_{PM} = \theta_{FBG}$ we get

$$\Lambda_{FBG} = \frac{1}{2}\Lambda_{PM}, \qquad 2\text{-}14$$

which shows that the phase-mask period must be half the Bragg grating period. By using a linear grating period change or a variable groove-depth along the grating length, the phase-mask technique is adaptable to write chirped- and apodized-index patterns (Figure 2-16). For transferring the interference-pattern in the fibre it has to be fixed very close to the phase-mask. The laser-beam can be moved along the phase-mask (scanning). An important disadvantage, or problem of the phase-mask technique is that the Bragg wavelength or type of grating is fixed. To have other Bragg wavelengths another phase-mask or special techniques have to be used. Bending or stretching of the fibre during inscription are the most common methods to make this technique more flexible to write variable FBG wavelengths.

The point-to-point technique is a very time consuming and complex sequential writing technique because gratings typically have more than 10000 grating-periods. Moreover a fibre works like a cylindrical lens and hampers the sub-µm writing.

Inscribing gratings with the point-to-point writing method in combination with the phase-mask technique is found to be a completion of the flexibility of the phase-mask technique because of the possibility to write high uniformly, long and very complex grating structures. Lately the use of femto-second laser is a common technique to write point-to-point grating structures inside conventional (doped and non-doped) fibres. Because of the high laser intensity, the femto-second lasers are for instance used to write high temperature gratings.

In the next section a few points are highlighted with regard to the technique used to write Draw Tower Gratings (DTG®s), which is the same technique as being employed to write 80 µm gratings designed and fabricated in this work (Chapter 4).

2. 6. 3. DTG® inscription method

To understand the procedure of writing single gratings and grating arrays in-line using single laser pulses this section gives a short description on the working principle of the interferometric setup used in combination with a draw-tower system (Figure 2-4). To achieve fast and accurate variation in Bragg wavelength a Talbot-interferometer is used as depicted in Figure 2-20. The system is positioned in between the furnace, which heats the fibre preform, and the coating cup, see Figure 2-4.

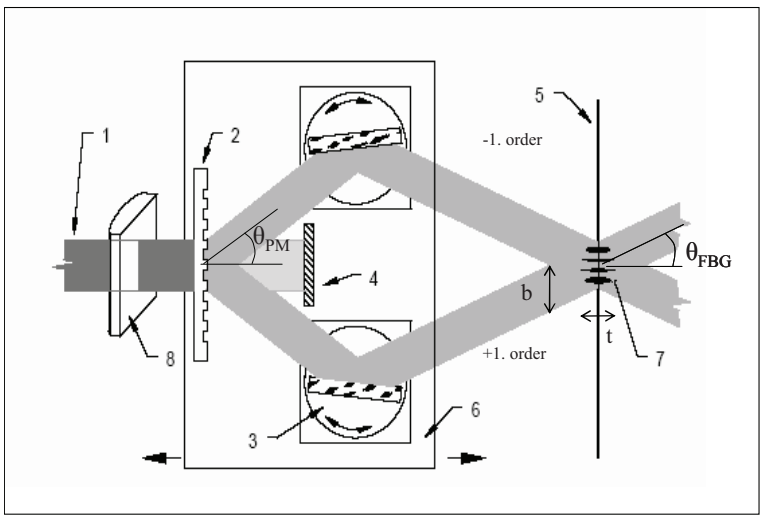

Figure 2-20: Talbot interferometer setup with UV Laser beam (1), a diffractive beam splitter (2), a dielectric mirror on a rotation element (3), a zeroth-order blocking component (4), the optical fibre (5), a mirror + beam-splitters on a linear-table (moveable) (6), an interference-pattern creating the FBG (7).

A *diffraction grating* (2) is placed as beam-splitter together with two *rotating mirrors* (3) to reunite the -1. order and +1. order of the beam and to change the period (i.e. Bragg wavelength) in the *interference pattern* (7). The zeroth order of the diffracted laser-beam is blocked (4) to have no disturbance on the *interference-pattern* (7). The angle of the *mirrors* (3) is adjustable by using two independent (but synchronized) linear rotation stages. By changing the mirror angle, the angle θ_{FBG} is changed and as a result, the period of the grating Λ_{FBG} is changed (Equation 2-12) to obtain the specified Bragg wavelength $\lambda_B = 2\bar{n}\Lambda_{FBG}$. This is the main principle of the interferometer function, and it is because of this feature that one is able to write in-line FBG arrays with different wavelengths (Figure 2-6). Of course the procedure is not that easy as it seems, namely by changing the mirror-angle the focus of the *interference pattern* (7) moves, hence the *linear-table* (6), at which the *mirrors* (3) and the *diffraction grating* (2) are all fixed on, has to move (lateral) towards or away from the fibre to keep the interference-pattern in focus (see sketched path in Figure 2-18). By changing the width of the laser *beam* (1), the width of the overlap of the two parts of the split beam can be tuned, and as a result the length of the grating can be adjusted. Grating lengths starting from 2 mm up to 20 mm are possible with this Talbot-interferometer. In this work typical grating lengths of 8 mm are being used.
A phase-mask (i.e. diffraction grating) is used to split the beam in a *-1. order* and a *+1. order*. It has the advantage over a dielectric beam-splitter that the wave front orientation in the interferometer doesn't change. In a dielectric beam-splitting plate one part of the two beams is rotated 180° and thus influences the spatial coherence, see Figure 2-21a:

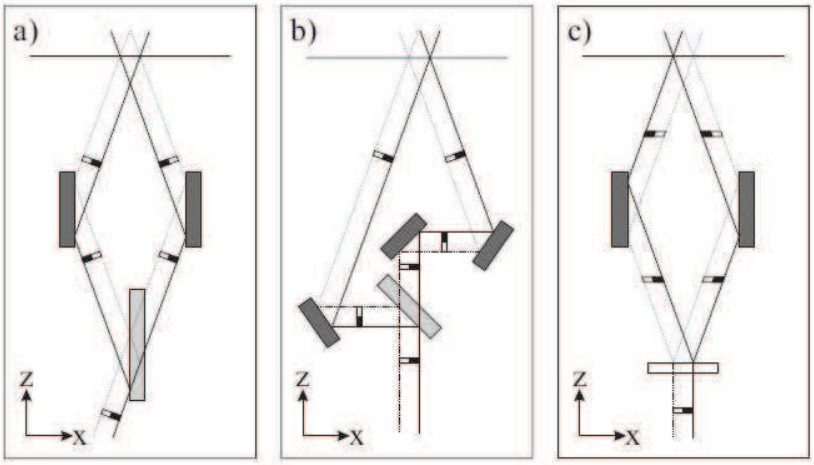

Figure 2-21: Comparison of interferometer principles to write gratings. A two-beam interferometer with a dielectric beam splitter (a), a three beam interferometer with dielectric beam splitter (b), and a Talbot interferometer with diffraction grating as beam splitter (c) [33].

As such the contrast of the interference-pattern at the sides of the grating is affected. To switch the orientation a third mirror can be used, see Figure 2-21b, however this creates an extra complexity in the setup: For a dielectric beam splitter the optical path length is identical for one point on the exposed fibre. Hence the difference in optical-path length between the diffracted beams influences the temporal coherence of the light and contrast of the interference pattern. The maximum grating-length is limited by the temporal coherence of the laser. For a diffraction grating (Figure 2-21c) the optical path for both beams is the same and the overlap of the two parts of the laser beam improves, without fading of the interference-contrast at the sides of the pattern. As a result the phase-mask is preferable placed in front of the interferometer to the dielectric beam splitter. One disadvantage in employing a phase-mask is the lower interference contrast because only 60-70% of the light is guided within the -1. –and +1 (zeroth order is blocked). This disadvantage can partly be compensated by focussing the laser-light with a *cylindrical lens* (8), as depicted in Figure 2-20).

The interference-pattern (see Figure 2-20) is largely responsible for the grating properties and has a *width b*, that is specified by the broadening of the laser-beam, and a *depth t*, that is specified by the coherence-properties of the laser. An Excimer laser (Compex 150T) displayed as a MOPA-system (Master Oscillator and Power Amplifier) from the company Lambda Physik is being used to write single pulse gratings. This MOPA-system improves the spatial and temporal coherence of the Excimer-laser without deterioration of the pulse-energy. The Compex 150T laser operates at a wavelength of 248 nm with a temporal coherence of $l_c^\tau = 20mm$ and a spatial coherence of $l_c^s = 650 \pm 20\mu m$. The pulse energy of the laser is approximately 200mJ at a beam size of approx. 8x22mm and can be tuned by using a *cylindrical lens*. For more detailed information about the laser coherence properties the reader is referred to [33].

2. 7. APPLYING ORMOCER® COATING

In general optical fibres are covered with a protective polymer coating. Standard 125 µm telecom SMF is usually covered with a double layer acrylate, consisting of a thin primarily layer of soft acrylate and a secondary thicker layer of hard acrylate, with a total outer diameter of 250 µm, or a tough single layer polyimide coating if higher temperatures are required with an outer diameter of about 150 µm. The FBGs in this work are coated with ORMOCER® (Organic Modified Ceramic) which is a UV-curable coating commonly used to produce commercial standard DTG®s. It is a tough material with a Young-Modulus of approximately 1 GPa (see Chapter 4 and Chapter 7) and can withstand long term to high temperatures (200 °C). From pull-out testing and fibre-coating stripping tests performed in the scope of the research of

Geert Luyckx [10] to define the fibre/matrix and coating/matrix properties from different coated fibres, it is found the ORMOCER® has a very strong bonding to the silica and additionally it is shown fibre failure occurred before complete pull-out. This shows there is a very good bonding of ORMOCER® to the epoxy material.
For a standard 125 µm fibre the outer coating diameter with ORMOCER® is typically 190 µm. For the newly developed 80 µm the outer coating diameter is approximately 115 µm – 140 µm depending on which coating nozzle has been applied (Chapter 3). This section briefly describes how the protective ORMOCER® coating is appropriately put on the draw tower fibre. For more details the reader is referred to Chapter 3, which is entirely devoted to the new developed 80 µm fibre using new coating applicators or nozzles. The draw tower setup uses an "open" gravitational coating system that operates at atmospheric pressure. Basically four things are needed to apply coating material onto the drawn fibre, see Figure 2-22:

1. Coating material (e.g. Acrylate, Polyimide, ORMOCER®),
2. a coating cup filled with liquid coating material,
3. a coating nozzle,
4. a curing system (thermal or UV).

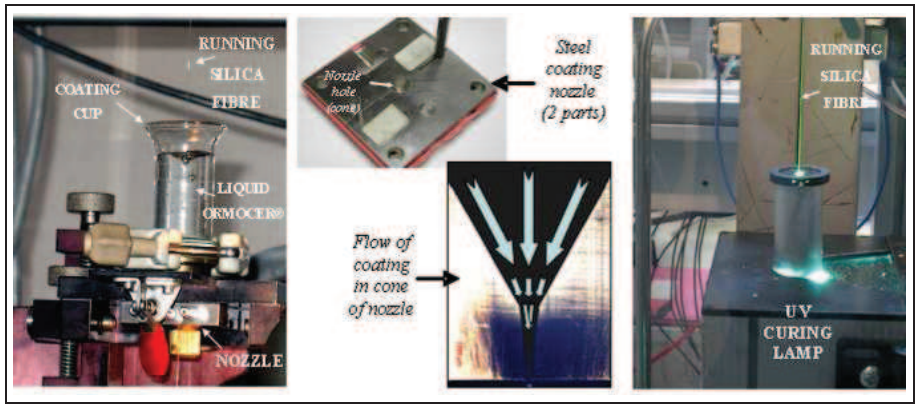

Figure 2-22: Polymer coating cup stage (left), nozzle and narrow nozzle cone (middle), UV curing lamp (right).

During the fibre drawing process, the fibre is conducted through a coating cup filled with liquid coating material, in this case a viscous transparent ORMOCER® (Figure 2-22, left). The coating nozzle is positioned directly underneath the cup so the fibre is firstly pulled through the liquid coating and then through the metal coating nozzle (Figure 2-22, middle). The cone of the nozzle is controlling the flow of the coating, towards the narrow end of the cone, hence centring the fibre. The end of the cone (i.e. bottom part) consists of a tiny hole (<200 µm) which defines the ultimate coating outer diameter. The nozzle is crucial to create a high quality fibre coating

with a good concentricity, hence producing reliable FBGs suitable for high elongation. Examples of fibre cross sections illustrating the coating concentricity are shown in Section 3.3.2.. As the fibre is continuously running, curing of the ORMOCER® should be done in a rapid way, since there is only a short time period available when the fibre is moving through the curing furnace. In the case of ORMOCER® a UV curing system is placed directly below the coating cup. The system is approximately 50 cm long and consists of a Hg UV lamp (i.e. tube) of approx. 15 cm length (Figure 2-22, right). There is an elliptically shaped mirror inside the lamp so that the focal distance matches the fibre position, as such UV light is well focussed on the fibre. The Hg lamp has a optical spectrum ranging from 200 nm to 310 nm (UVC – UVB) with single intensity peaks up to 600 nm, see Figure 2-23:

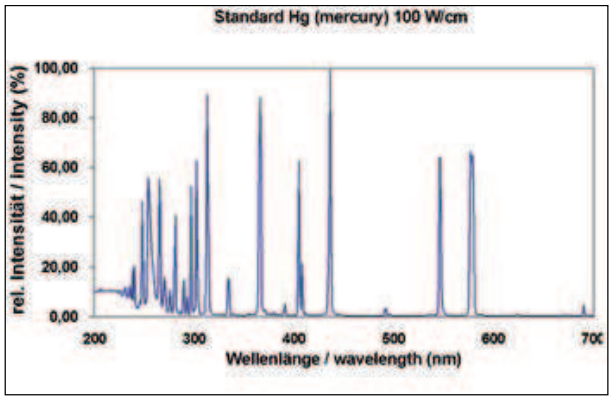

Figure 2-23: Example of the optical spectrum of the Hg tube [36].

It should be noted that the power of the UV light needs to be controlled well. The FBG inscription wavelength of the laser system (i.e. 248 nm) is close to the wavelengths emitted by the Hg-tube lamp, hence the reflectivity falls sharply if the FBG is exposed too long.

The effect of the UV-curing condition on the DTG®-reflectivity

A UV exposure test has been performed to study the reflectivity as function of temperature and UV radiation. Three different DTG® samples are used:

- DTG® 1: coating stripped
- DTG® 2: coated with standard ORMOCER®
- DTG® 3: black painted ORMOCER® coating (to block UV light)

The samples were put inside the UV- curing system and exposed for approximately 2 to 3 minutes. The wavelengths and reflected powers of all three samples were then

recorded during exposure. There are two effects which could influence the reflectivity to decrease, that is 1) the UV exposure itself and 2) the heat that is generated by the radiation. The results are shown in Figure 2-24. It is noticed that after 2 minutes the stripped DTG® has the largest drop in reflectivity, approximately 10 dB, and that the standard coated DTG® has a drop of approximately 3 dB. The same effect has been noticed by Hagemann [33], who performed measurements on the Bragg gratings during the inscription and drawing process. He reported that the FBG reflectivity drops approximately 50 % during the UV curing process (i.e. within approximately 2.4 seconds) of the ORMOCER® coating.
The black painted DTG® does not show any significant change in reflectivity, only 1.5 dB is lost. From this we can conclude that the UV-bleaching is the most important factor which causes the drop in reflectivity. However, it is noted the test has been performed on DTG®s, which are, obvious during the manufacturing, already being exposed short term to the UV curing process of the ORMOCER®. As such the gratings have already been annealed at the same UV and temperature condition. This explains that there is only a small extra loss of 1.5 dB when the black painted DTG® is exposed for approximately 2 - 3 minutes at the same temperature level. More details on the (thermal) annealing effect is found in Chapter 4.4.1. There the thermal stability of 80 µm and 125 µm DTG®s is discussed.

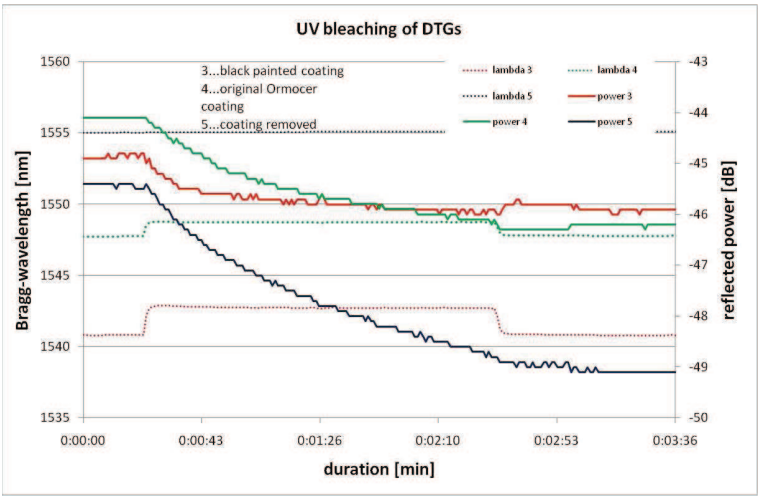

Figure 2-24: UV bleaching test of three DTG®s: stripped, standard ORMOCER® coated and black painted ORMOCER®.

The UV power should be high enough to cure the ORMOCER®, however it should be limited not to “bleach” (i.e. rubbing out) the FBG. Therefore the UV lamp is operated at approximately 30 % of the maximum power level of 240 W/cm.

2. 8. CONCLUSION

In this chapter the author has introduced the features of the state of the art draw tower grating technology and compared it with conventional FBG writing methods. It allows writing the FBGs in-line during the optical fibre drawing process and immediate application of a polymer coating after the grating inscription. As such it is possible to manufacture high quality coated draw tower fibre Bragg gratings (DTG®s), which are less fragile compared to conventional FBGs. Different steps of the process and its features are being highlighted throughout the chapter. The most important conclusions of each step of the process are given below.

Highly GeO_2-doped optical fibre

To write the DTG®s in one single laser shot and to have a descent FBG reflectivity (~22 %), the optical fibre needs to be highly photosensitive. To meet this requirement the fused silica preform core is highly doped with Germanium during the MCVD preform manufacturing process (~18mol% GeO_2). Because of the high dopant concentration, these fibres exhibit a high fibre attenuation compared to standard SMF, however, from bending tests using mandrels of different diameters, the author has found that the bending loss of the DTG®-fibre is extremely low. This result is a very interesting feature with regard to embedding the optical fibres and sensors later on in the woven-fabric laminates.

Interferometric holographic FBG inscription

To write the gratings during the fibre drawing process a Talbot interferometer is used. This holographic FBG inscription method allows changing the period of the interference pattern, hence it is possible to manufacture (dense) Bragg grating arrays (i.e. multiplexing) with different individual wavelengths and spatial distance. The Talbot interferometer used in this work allows only to produce the uniform type of FBG, as such the focus in this work is only on FBGs with a (uniform) periodic refractive index pattern.

Applying ORMOCER® coating

A liquid UV curable ORMOCER® coating is applied on the fibre using a coating cup operating at atmospheric pressure and a tapered coating nozzle with a very narrow nose. The coating applicator works fine to apply a (concentric) coating layer on the standard 125 µm fibre, however, when considering the manufacturing of the 80 µm DTG®, we need to optimize the nozzle design of the coating applicator to apply a thinner coating layer and to enhance the coating concentricity. Three new nozzles will be developed and tested throughout this work, results are shown in the next chapter. An important effect on the DTG®-reflectivity is noticed during the

UV-curing of the ORMOCER® coating. Tests are carried out to investigate the reflectivity drop as function of UV curing time. It is found that the reflectivity drop after exposure is as high as 50 %. Two effects are noticed: (i) UV bleaching (main contribution) and (ii) thermal annealing, due to the heat generation in the lamp. The thermal annealing effects will be further elaborated in Chapter 4 with regard to the thermal stability of the DTG®s manufactured in this work.

The next step is to use these features of the draw tower technology to manufacture smaller diameter optical fibres. This is subject of the next chapter.

2. 9. REFERENCES

1. FBGSTechnologies. Available from: http://www.fbgs-technologies.com/.
2. Tarpey, A.J., Kukureka, S.N., and Jurkschat, K., *The mechanical reliability of stripped and recoated polyimide fibres for optical fibre sensors*, in *Optical Fiber and Fiber Component Mechanical Reliability and Testing Ii*, M.J. Matthewson and C.R. Kurkjian, Editors. 2002. p. 141-151.
3. Pascal, M., *Reliability and lifetime of optical fibres and fibre Bragg gratings for metrology and telecommunications*, in *Département de Microtechnique*. 2001, École polytechnique fédérale de Lausanne (EPFL): Lausanne. p. 117.
4. Maurer, R., D., *Behaviour of flaws in fused silica fiber.* Strength of inorganic glass, 1985.
5. Holloway, D., G., *The fracture behaviour of glass.* glass tech, 1986. **27**(4): p. 120-133.
6. Glaesemann, G., Scott. *Advancements in mechanical strength and reliability of optical fibres*. in *Reliability of optical fibers and optical fiber systems*. 1999. Boston, Massachusetts: SPIE.
7. Wissuchek, D., J. *Effect of refractory particles on the strength of optical fibres*. in *Reliability of photonic materials and structures*. 1998. San Fransisco.
8. Volontinen, T., Zimnol, M., Tomoza, M., Lee, Y., K., and Raine, K. *Effect of mechanical stripping and arc-fusion on the strength and aging of a spliced recoated optical fiber*. in *Mat. Res.Soc.Symp.Proc.* 1998.
9. Matthewson, M.J., Kurkjian, C.R., and Hamblin, J.R., *Acid stripping of fused silica optical fibers without strength degradation.* Journal of Lightwave Technology, 1997. **15**(3): p. 490-497.
10. Luyckx, G., *Multi-axial strain monitoring of fibre reinforced thermosetting plastics using embedded highly birefringent optical fibre Bragg sensors*, in *Department of Materials Science & Engineering*. 2010, Ghent University.
11. Satori, K., Ikeda, Y., Kurosawa, Y., Hongo, A., and Takeda, N., *Development of small-diameter optical fiber sensors for damage detection in composite laminates*, in *Smart Structures and Materials 2000: Sensory*

Phenomena and Measurement Instrumentation for Smart Structures and Materials, R.O. Claus and W.B. Spillman, Editors. 2000. p. 104-111.
12. Kabashima, S., Ozaki, T., and Takeda, N., *Damage detection of satellite structures by optical fiber with small diameter*, in *Smart Structures and Material 2000: Smart Structures and Integrated Systems*, N.M. Werely, Editor. 2000. p. 343-351.
13. Okabe, Y., Tanaka, N., and Takeda, N., *Effect of fiber coating on crack detection in carbon fiber reinforced plastic composites using fiber Bragg grating sensors.* Smart Materials & Structures, 2002. **11**(6): p. 892-898.
14. Takeda, N., Okabe, Y., and Mizutani, T., *Damage detection in composites using optical fibre sensors.* Proceedings of the Institution of Mechanical Engineers Part G-Journal of Aerospace Engineering, 2007. **221**: p. 497-508.
15. Komatsuzaki, S., Kojima, S., Hongo, A., Takeda, N., and Sakurai, T., *Development of small-diameter optical fiber sensors and high-speed optical wavelength interrogator for damage detection in composite materials - art. no. 616703*, in *Smart Structures and Materials 2006: Smart Sensor Monitoring Systems and Applications*, D. Inaudi, et al., Editors. 2006. p. 16703-16703.
16. LxSix. Available from: http://www.lxdata.com/.
17. Sabeus. Available from: http://www.sabeus.com/public/fbgarray.php.
18. Askins, C.G., Putnam, M.A., Williams, G.M., and Friebele, E.J., *Stepped-wavelength optical-fiber Bragg grating arrays fabricated in-line on a draw tower.* Optics Letters, 1994. **19**(2): p. 147-149.
19. Friebele, E.J., Askins, C.G., Bosse, A.B., Kersey, A.D., Patrick, H.J., Pogue, W.R., Putnam, M.A., Simon, W.R., Tasker, F.A., Vincent, W.S., and Vohra, S.T., *Optical fiber sensors for spacecraft applications.* Smart Materials & Structures, 1999. **8**(6): p. 813-838.
20. Dong, L., Archambault, J.L., Reekie, L., Russell, P.S.J., and Payne, D.N., *SINGLE-PULSE BRAGG GRATINGS WRITTEN DURING FIBER DRAWING.* Electronics Letters, 1993. **29**(17): p. 1577-1578.
21. Chojetzki, C., Klaiberg, T., Ommer, J., Rothhardt, M., and Betz, D., *Fiber Bragg gratings for high temperature sensing applications.* Technisches Messen, 2004. **71**(10): p. 555-562.
22. Chojetzki, C., Rothhardt, M., Ommer, J., Unger, S., Schuster, K., and Mueller, H.R., *High-reflectivity draw-tower fiber Bragg gratings - arrays and single gratings of type II.* Optical Engineering, 2005. **44**(6).
23. Bartelt, H., Schuster, K., Unger, S., Chojetzki, C., Rothhardt, M., and Latka, I., *Single-pulse fiber Bragg gratings and specific coatings for use at elevated temperatures.* Applied Optics, 2007. **46**(17): p. 3417-3424.
24. Wan, K.T., Leung, C.K.Y., and Olson, N.G., *Investigation of the strain transfer for surface-attached optical fiber strain sensors.* Smart Materials & Structures, 2008. **17**(3).
25. Fraunhofer.
26. Agrawal, P., Govind., *Fiber-optic communication systems*. third ed. 2003: Wiley interscience.
27. Fraunhofer, i.; Available from: http://www.ormocer.de/EN/.

28. Mahlke, G. and Gössing, P., *Fiber Optic Cables: Fundamentals, Cable design, System Planning*. 2001, Erlangen and Munich: Publicis MCD Corporate Publishing.
29. Murata, H., *Handbook of optical fibres and cables*. second ed. 1996: Marcel Dekker, Inc.
30. Corning. Available from: http://www.corning.com/opticalfiber/products/SMF-28_ULL_fiber.aspx.
31. Muriel, M.A., Carballar, A., and Azana, J., *Field distributions inside fiber gratings.* Ieee Journal of Quantum Electronics, 1999. **35**(4): p. 548-558.
32. Chojetzki, C., Ommer, J., Grimm, S., and Bartelt, H., *Temperature dependence of type I-IA dual-fibre Bragg gratings.* Electronics Letters, 2004. **40**(25): p. 1576-1578.
33. Hagemann, V.J., *Untersuchungen zum dynamischen Einzelpuls-Einschreiben von Faser-Bragg-Gittern un zu deren Anwendung*. 2001, Friedrich-Schiller University: Jena.
34. Hill, K.O., Malo, B., Bilodeau, F., Johnson, D.C., and Albert, J., *Bragg gratings fabricated in monomode photosensitive optical-fiber by UV exposure through a phase mask.* Applied Physics Letters, 1993. **63**(3): p. 424-424.
35. Ibsen. Available from: http://www.ibsen.dk/phasemasks/fbgphasemasks.
36. Hoenle. Available from: http://www.hoenle.de/.

Chapter 3 MANUFACTURING THE 80µM DTG®

3. 1. INTRODUCTION

In this research the goal is to embed FBGs in CFRP laminates to measure the deformation during mechanical testing. With respect to accurate measurements and structural integrity, a first part of the research has focussed on reducing the total diameter of the optical fibre, so distortion in the composite is reduced and integration in the reinforcement fibres is enhanced. The purpose of this research is to use the draw tower technology (Chapter 2), to manufacture in-line high quality coated 80 µm FBGs or moreover the 80 µm DTG®s. It is chosen to decrease the cladding diameter of the fibre from 125 µm to 80 µm taking into account the following motives:

- feasibility of the available draw tower setup (Chapter 2) with respect to the stability of the fibre in combination with in-line FBG inscription,
- standard fibre diameters in telecom, with respect to handling of the fibre, i.e. (stripping), cleaving, splicing and connecterisation (FC / APC),
- optimization of the coating diameter with respect to new developments concerning the coating applicator (Section 3. 3.)

In this chapter the author presents the development and manufacturing of the 80µm draw tower grating (DTG®), starting with the development of two dedicated fibre preforms with the MCVD process (Section 3. 2.): one suited for 80 µm fibre and one preform to produce an 125 µm fibre, which will serve as reference fibre throughout this work. Likewise the 125 µm fibres, the 80 µm fibres are coated with ORMOCER® coating. To minimize the overall coating diameter of the newly developed 80 µm DTG®s, new coating nozzles were developed using advanced wire spark erosion technology (Section 3. 3.). Several draw tower runs are performed, in order to improve the coating concentricity and to reduce the outer diameter of the 80 µm DTG®s. The tensile strength of the resulting fibres is tested and compared with the 125 µm DTG®s (Section 3. 4.). At the end of this chapter a few notes are given on the handling and splicing of the newly 80 µm fibre to standard SMF, so the sensors can be easily connected to the FBG interrogator (Section 3. 5.).

3. 2. HIGHLY DOPED PREFORMS AND FIBRES

Two preform rods were developed at IPHT-Jena using the MCVD method, one for the newly 80 µm DTG®s and a second for the 125 µm reference DTG®s. Both preforms are shown in (Figure 3-1):

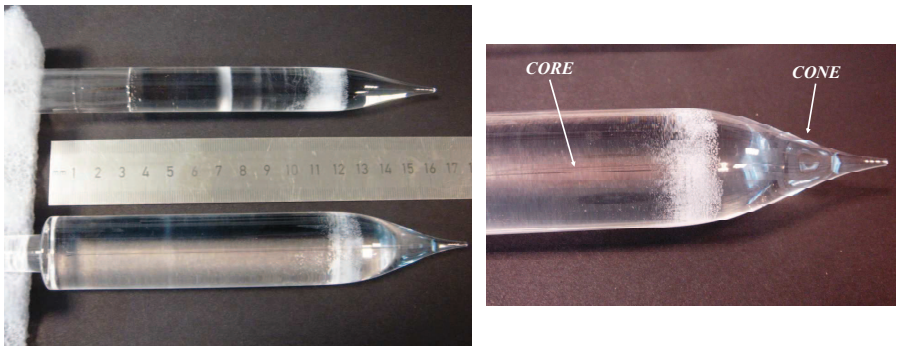

Figure 3-1 Silica fibre preform rods, used for the 80 µm (top left) and 125 µm (bottom left) fibre production, 125 µm preform cone with visible doped core (right).

To obtain the resulting preforms shown in Figure 3-1, left, first one "long" thin preform is processed with an original outer diameter of approximately 9mm. This rod possesses already the correct core / cladding ratio and radial refractive step index profile. In a second stage this "long" thin pre-fabricated rod has been cut into two separate pieces. The preform diameter of each piece is then increased to get the appropriate preform outer diameter. As such the core properties of both fibre preforms are kept identical, i.e. the photosensitivity because of the same GeO_2 dopant concentration and hence the *equivalent step index* (ESI), see Section 3. 2. 1. . Extra silica is then added to the cladding by "covering" the original preform piece with a second (highly purified) silica tube with an appropriate predetermined thickness. The tube is collapsed using an oxy-hydrogen torch (MCVD process, Section 3.4) and the procedure is repeated until the desired thickness is reached. The preform rod for the 80 µm fibre (*Preform_80*) is increased until 18.25 mm and the preform rod for the 125 µm (*Preform_125*) is increased until 28.16 mm. The two resulting preforms are shown in Figure 3-1, and in Table 3-1 are given the respective dimensions.

Table 3-1 Dimensions of the preforms for the 80 µm and 125 µm fibres.

	Preform_80	Preform_125
Nominal Length	180 mm	160 mm
Cladding diameter	18.25 mm	28.16 mm
Core diameter*	1.017 mm	1.017 mm
Fibre core diameter**	4.45 µm	4.51µm
Max. GeO_2 concentration	19mol%	19mol%

The core area in these preforms is highly doped with Germanium dioxide (i.e. maximum 19mol% GeO_2) during the MCVD process, which enhances the refractive index difference largely between the core and the pure silica cladding. The amount of doped core layers determines the core diameter. The core / cladding ratio is

* Determined from the ESI measurements (Section 3. 2. 1.)
** Calculated from the preform cladding/core ratio

designed using the normalized frequency, or V-parameter (Appendix A), which is determined by the cut-off wavelength of the fibre. Above this wavelength only the fundamental mode is transmitted and the optical fibre becomes single mode. The fibres in this work are designed to reach cut-off at approximately 1.2 µm, which is a typical value used for SMF.

As mentioned before, both preforms in principle have identical core properties, because both Preform_80 and Preform_125 are produced from the same original preform. However, a small difference in GeO_2 concentration could occur along the length of the long original rod. Due to the excessive heating during the preform collapsing process (Chapter 2), GeO_2 re-evaporates into GeO [1]. This vapour shifts along the hollow tube and will oxidize and vitrify once again. Collapsing, using the ox-hydrogen torch, is usually started at one side of the preform rod and slowly moves towards the other end of the preform until the rod is completely closed. As such, slight portions of dopant oxides are transferred from one side of the preform to the other, and small changes of GeO_2 concentrations between the two sides of the preform could occur during collapsing. This explains there could be a small difference in mol% GeO_2 between the Preform_80 and the Preform_125, although they are fabricated from the same original rod.

In the following sections the author will describe some more details on the optical and physical properties of the preforms and resulting optical fibres. It is discussed that the step index profile measurement of the preform (Section 3. 2. 1.), the transmission losses of the fibres (Section 3. 2. 2.), the resulting fibre core radius using the V-parameter (Section 3. 2. 3.), and the effective refractive index of the fibres (Section 3. 2. 4.).

3. 2. 1. Equivalent Step Index (ESI) profile

The Equivalent Step Index (ESI) profile has been measured at the IPHT-Jena using the original preform. The recorded index profile is shown in Figure 3-2. The difference in refractive index, Δn, is plotted on the ordinate and the path along the diameter of the preform (i.e. core and cladding area) on the abscissa. The step index, between core and cladding is found to be $\Delta n = 15.3 \cdot 10^{-3}$ (Figure 3-2), which is the mean refractive index difference calculated for the whole preform core area. It is indicated in Figure 3-2 by the rectangular area. This value does not correspond to the maximal GeO_2 doping concentration of 19mol% which has been mentioned before (Table 3-1). The maximal step index of the two peaks in Figure 3-2 is found to be approximately $\Delta n_{max} = 26 \cdot 10^{-3}$. From Figure 2-9 (Section 2.4.1.c), we indeed see that for dopant concentrations > 14mol% the index difference becomes $\Delta n > 20 \cdot 10^{-3}$. As such we expect that the maximal step index value is corresponding to the 19mol% GeO_2 concentration. Using Figure 3.3, we can estimate the real mean GeO_2 dopant concentration which corresponds to the ESI of $15.3 \cdot 10^{-3}$. The mean dopant concentration is then found to be approximately 11mol%. Note, however, that the curves plotted in Figure 2-9 are found from calculations in the 0.6 µm wavelength range.

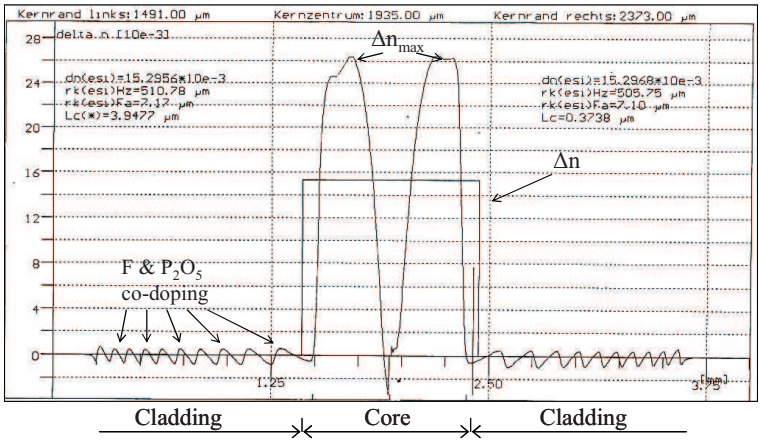

Figure 3-2 Equivalent Step Index profile measurement for the core / cladding in a 19mol% GeO_2 doped preform.

Noted that the measurement of the index profile is performed at only one location, i.e. near the end of the original preform, the real index value can slightly differ because of the afore mentioned effect of re-evaporation of GeO_2. However, using this refractive index measurement the mean core diameter of the preform is found to be 1.017mm. Taking the core / cladding ratio from the preforms (see Table 3-1) we can estimate that the fibre core diameter for the 80 µm and 125 µm fibre is approximately 4.45 µm and 4.51 µm, respectively. As will be shown in Section 3. 2. 3. , these values differ very little from the core diameters estimated using the cut-off wavelengths measured in Section 3. 2. 2. d. .

Typically in highly doped preforms manufactured using the MCVD process there exists a central index depression in the preform (Figure 3-2). It arises in the final stage, when the tube is being collapsed. This phenomena is caused mainly due to the vaporization and diffusion of the GeO_2 out of the inner and final doped layers of the core [1]. A special treatment using a fluorine compound in the preliminary collapse step can be used to reduce such a dip [1]. However, in order to enhance photosensitivity the collapsing of the preform used in this work is performed using a reducing helium atmosphere to substitute for oxygen [2] which does not reduce the depression and increases slightly the OH^- transmission loss. Additionally the germanium oxygen-deficient centres (GODC), due to the high GeO_2 doping, have a negative influence on the transmission properties of the silica core [3-4]. The total transmission loss inside the used fibres in this work will be further discussed in Section 3. 2. 2. c. .

Besides the central index depression we also notice the saw tooth like line on both sides of the core in Figure 3-2. These originate from the added co-doped cladding layers (ten in total) with a small amount of F and P_2O_5 (i.e. less than 1mol%). According to the chemists at the IPHT-Jena the co-doped cladding layers act as an isolating barrier, and can reduce the maximum temperature in the core of the preform by approximately 200°C. This reduction of ultimate temperature is necessary to prevent pre-collapsing of the tube, which could lead to inclusions (i.e. material imperfections) in the core area of the preform.

3. 2. 2. Transmission losses

In an optical fibre light is guided from one end of the fibre to the other end with a certain transmission loss (or attenuation) expressed in decibel per kilometre (dB/km). The attenuation is roughly divided into absorption losses and scattering losses. The main losses are summed up in Table 3-2.

Table 3-2 Main causes of loss in an optical fibre [5-6].

Loss	**Intrinsic**	**Extrinsic**
Scattering	*Rayleigh* (Brillouin, Raman)	Waveguide imperfections (Mie)
Absorption	Ultraviolet Infrared	Metal ions *OH ion* H_2

Fibre losses depend on the wavelength of the transmitted light. The total loss in a fibre is given by :

$$\alpha_t(\lambda) = \frac{A}{\lambda^4} + B + C(\lambda) + \alpha_{IR}(\lambda) + \alpha_{UV}(\lambda) \quad \text{(dB/km)} \qquad 3\text{-}1$$

where

A = coefficient of Rayleigh scattering loss

B = loss due to waveguide imperfection

$C(\lambda)$ = loss caused by impurities

$\alpha_{IR}(\lambda)$ = loss due to infrared absorption

$\alpha_{UV}(\lambda)$ = loss due to ultraviolet absorption

$\alpha_t(\lambda)$ = total loss of fibre

An example of the total transmission losses in a standard single mode silica fibre with wavelength is shown in Figure 3-3. The fibre losses in the 0.8 µm - 1.6 µm wavelength window are dominated mostly by material absorption due to water vapours (i.e. OH ion) and Rayleigh scattering, arising from microscopic fluctuations in density. In the next Sections the author will discuss in more detail the material absorption in silica fibres and the Rayleigh scattering and in Section 3. 2. 2. c. is discussed the measured total transmission losses on the 80 µm and 125 µm fibres.

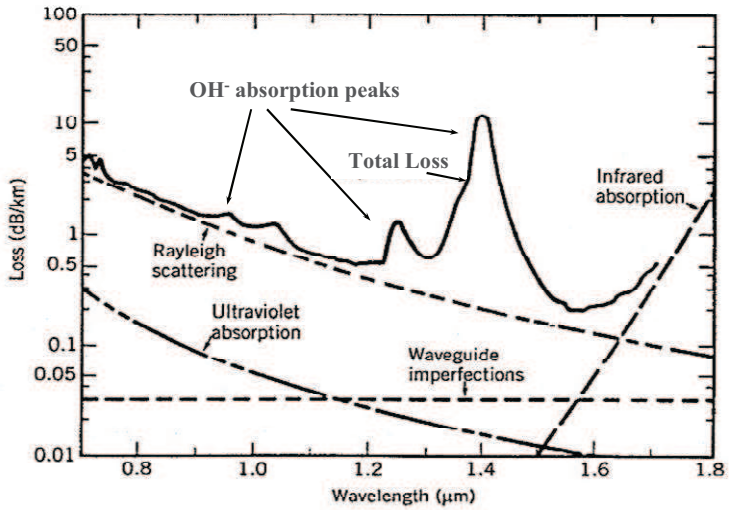

Figure 3-3 Transmission losses of an optical fibre (from [6]).

3. 2. 2. a. Material absorption

Any material intrinsically absorbs light at certain wavelengths corresponding to the electronic and vibrational resonances associated with specific molecules [6]. For silica fibres electronic resonances occur in the UV region ($\lambda < 0.4$ µm), i.e. UV absorption, whereas molecular vibrational resonances occur in the infrared region (λ>7 µm), i.e. IR absorption ($\alpha_{IR}(\lambda)$) . However, due to the amorphous nature of fused Silica the IR absorption bands significantly shows overtones extended into the near infrared region, starting from about 1.85µm [5] (Figure 3-3). In the case of the DTG® fibre the GeO_2 concentration in the core is high which causes the UV absorption curve ($\alpha_{UV}(\lambda)$) to move upwards. Its contribution to the total loss will increase and is further explained in Section 3. 2. 2. c. .

The main source of extrinsic absorption in optical fibres is due to the presence of the SiOH bonding (or GeOH bonds, e.g. in the case of higly GeO_2 doped preforms as used in this work). This bonding is owing to the diffusion of OH^- ion during the deposition and preform collapsing process in the MCVD process [5]. As seen in Figure 3-3, three dominating spectral peaks exist due to the OH^- vibrational resonance overtones near the 1.39-, 1.24-, and 0.95-µm wavelengths. Concentrations as low as 1 part per billion (ppb) of OH^- can cause a loss of about 50dB/km at 1.39 µm. Additionally, absorption peaks arise due to the presence of metal ion impurities like e.g. Fe, Cu, Co, Ni, Mn, and Cr. For modern available preform fabrication techniques such as MCVD and others (see Section 3.4) these impurities are typically kept smaller than 0.1ppb. From the enumerated metal impurities the Fe ion has the largest impact on fibre loss with an absorption peak arising at 1.1 µm, as seen in Figure 3-3. The OH^- concentrations in the preforms used in this work are higher compared to low loss preforms produced in telecom industry. The OH^- value is approximately 1.1 ppb and 1.04 ppb for the 80 µm- and 125 µm fibre, respectively (see Section 3. 2. 2. c.).

3. 2. 2. b. Rayleigh scattering

Another fundamental loss mechanism is the Rayleigh scattering which arises from local fluctuations in density. These density fluctuations lead to random fluctuations of the refractive index on a scale smaller than the optical wavelength [6]. Rayleigh scatter is far more greater (i.e. > 100 times) then scattering caused by waveguide imperfections, also referred to as Mie scattering (Table 3-2), occurring because of local density fluctuations on a scale longer than the optical wavelength. Therefore, only loss due to Rayleigh scattering is further discussed. The Rayleigh scattering is expressed by $\alpha_R = A/\lambda^4 (dB/km)$, with A the coefficient of Rayleigh scattering. The value of A is related to the constituents of the fibre core i.e. 1) the kind of dopant and 2) the relative index, Δ, which depends on the dopant concentrations (Section 2.4.1.c, Figure 2-9).
As previously mentioned in Section 2.4.2.b., a fibre with a high Δ exhibits a high fibre attenuation, hence, we expect that the highly doped fibre used for the 80 µm and 125 µm reference DTG®s, will have a large Rayleigh scattering coefficient. The Rayleigh scattering coefficients of the fibres used in this work are determined in the next section.

3. 2. 2. c. Measured total transmission loss

The total loss distribution in the highly doped draw tower fibre is measured for a 100m long section of both the 80 µm- and the 125 µm fibre. These sections are taken from the first manufacturing trial. The transmission losses are plotted in Figure 3-4. The plots clearly show the existing OH^- absorption increase of 41.7 dB/km (at 1.386 µm) for the 125 µm fibre and an increase of 43.3 dB/km (at 1.386 µm) for the 80 µm (the OH^- concentration is 1.04 ppb and 1.1 ppb, respectively). A smaller OH^- absorption peak is observed at 1.24 µm. From the loss distribution curve in Figure 3-4 (bottom) we notice that the 80 µm fibre contains an absorption peak at approximately 1.15 µm, in addition to the prominent OH^- absorption peaks at 1.39- ,and 1.24 µm caused by Si-OH and Ge-OH vibrations. Such peak can occur due to H_2 vibration. Murata [5] reported there exist H_2 combinational vibrations with a contribution at 1.17 µm, which is very close to the peak visible in the 80 µm fibre. Although its origin is not really clear it is believed the diffusion of Hydrogen in the thinner silica preform rod during the MCVD process (Section 2.5) occurs faster, hence, more H_2 could get trapped in the network of SiO_2.

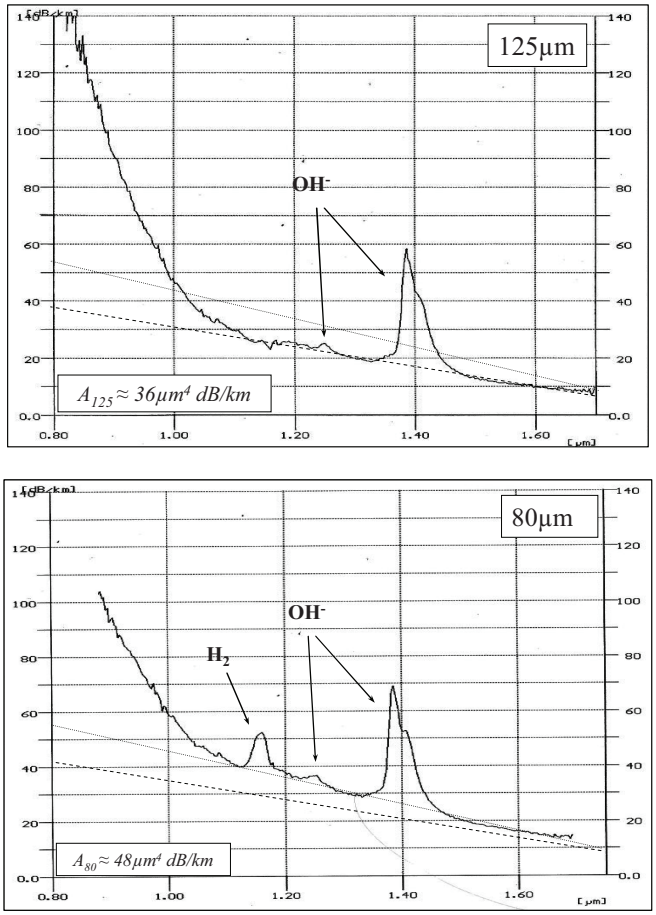

Figure 3-4 Total fibre attenuation (dB/km) measured for the 125 µm (top) and 80 µm (bottom) 100 m long fibre.

The total fibre loss at 1.55 µm is measured to be 11.3 dB/km for the 125 µm fibre and 17.6 dB/km for the 80 µm fibre. As stated in Section 3. 2. 2. b. , the main cause of this very high attenuation is the contribution of the Rayleigh scattering coefficient, *A*, which is directly proportional to the high GeO_2 concentration in the core. The slopes of the attenuation curves for both fibres, are indicated in each graph to compare results. The slope for the 80 µm fibre (dotted) is steeper than the slope for the 125 µm fibre (dashed), which indicates the value of *A* for the 80 µm fibre will be greater than the value of *A* for the 125 µm fibre. To calculate the Rayleigh coefficient, the measured attenuation is calculated over $1/\lambda^4$ (μm^{-4}). Values for the Rayleigh coefficient (in μm^4db/km) are indicated in the graphs. They are about 36- and 48 μm^4db/km for the 125 µm and 80 µm fibre, respectively. These values of *A* correspond approximately to a Rayleigh scattering of $\alpha_{R,125} = 6.28 dB/km$ and $\alpha_{R,80} = 8.33 dB/km$ at $\lambda = 1.55 \mu m$ for the 125 µm and 80 µm, respectively. The Rayleigh scattering contribution is about half of the total fibre loss. These contributions are extremely high compared to low loss SM fibre where *A* is typically

in the range of 0.7-0.9 µm^{4}dB/km, corresponding to $\alpha_R = 0.12 - 0.16 dB/km$ at $\lambda = 1.55 \mu m$.

Conventional analysis of the total attenuation in high Ge doped optical fibres has shown that the main optical loss is determined by the Rayleigh scattering and material absorption [5]. These loss components depend on drawing conditions like temperature, tension and speed, which differ when producing other fibres with different diameter, hence using other fibre preforms. This explains why the Rayleigh contribution is higher in the 80 µm fibre.

Excess losses are presumably caused by imperfections of the core-cladding boundary, due to a large viscosity mismatch of the core and cladding glass and to strong stresses that can create defects near the boundary [7]. Considerable additional absorption loss is caused by extra linear growth of the UV component ($\alpha_{UV}(\lambda)$) with GeO_2 content which originates from the GODC [3-4]. According to Dianov et al. the additional loss can be caused by inhomogeneities in distribution of GeO_2 and diffusion phenomena during the drawing process, which create additional GODC. It is believed that all afore mentioned induced effects are indeed the cause of the extreme high loss in the highly GeO_2 doped fibres produced in this work.

3. 2. 2. d. Cut-off wavelength

From the same piece of fibre as being used to measure the total loss distribution curve a small piece of fibre of approximately 2 m is used to estimate the cutoff wavelengths. An extra transmission measurement is performed using first a straight piece of fibre. Then the same fibre is curved in a circular groove of approximately 3 cm diameter so all other fibre modes are attenuated and only the fundamental mode is transmitted. By taking the difference between both transmission measurements the cut-off wavelength can be determined with an accuracy of a few picometer. Using this method, the cut-off wavelength is found to be $\lambda_{CRe,125} = 1.214 \mu m$ for the 125 µm fibre and $\lambda_{CRe,80} = 1.225 \mu m$ for the 80 µm fibre. From these estimations the core radii is determined in the next Section.

3. 2. 3. Core radii

As discussed in Section 2.4.1.c the refractive index of pure SiO_2 is calculated using the Sellmeier dispersion equation at a wavelength of 1.55 µm and is found to be $n = n_2 = 1.444$. By using the afore determined mean ESI of $\Delta n = n_1 - n_2 = 15.3 \cdot 10^{-3}$, (Section 3. 2. 1.) the refractive index of the core equals $n_1 = 1.4593$. The fibre core radii of the 80 µm and 125 µm fibres can then be determined using the normalized frequency, or simply V-parameter, given by (Appendix A):

$$V = \frac{2\pi}{\lambda} a \sqrt{\left(n_1^2 - n_2^2\right)} \qquad 3\text{-}2$$

The transmission measurements performed in Section 3. 2. 2. c. provide us the real cut-off wavelengths of both fibres, $\lambda_{CRe,125} = 1.214 \mu m$ and $\lambda_{CRe,80} = 1.225 \mu m$. The fibres are designed such that $V < 2.405$, so they supports only the fundamental mode. By substituting the measured cut-off wavelengths for each fibre in Equation

3-2, and by using the calculated refractive index for the core (n_1) and the cladding (n_2), we find for $V = 2.405$ that $d_{125} = 2a_{125} = 4.45\mu m$ and $d_{80} = 2a_{80} = 4.49\mu m$. We notice the real core radii calculated from the measured preform core / cladding ratio given in Table 3-1 match very well with the values determined from the V-parameter. These calculations confirm that the preforms are indeed designed to manufacture 80 µm and 125 µm single mode fibres with a cut-off at approximately 1.2 µm.

3. 2. 4. Effective refractive index

The effective refractive index, $\overline{n}$, of the fibre is useful to determine as this parameter is implemented in the basic Bragg condition. It can be calculated from [6]:

$$\overline{n} = n_2 + b\Delta n , \qquad 3\text{-}3$$

with b, the normalized propagation constant approximated by:

$$b(V) \approx (1.1428 - 0.9960/V)^2 . \qquad 3\text{-}4$$

In Equation 3-4 we see that the normalized propagation constant is related to the V-parameter. Using Equation 3-2 we can calculate the V-parameter at $\lambda = 1.55\mu m$. By taking the fibre core radius determined in Section 3. 2. 3. and by filling in the respective values for n_2 and Δn given above, it is found that V_{125}=1.901 and V_{80}=1.918 for the 125 µm and 80 µm fibre, respectively. From Equation 3-4 the normalized propagation constant becomes $b_{125} \approx 0.383$ and $b_{80} \approx 0.389$. By using Equation 3-3 the mode index is then found to be $\overline{n}_{125} \approx \overline{n}_{80} = \overline{n} = 1.4459$. This value for the effective refractive index of each fibre will be applied for all calculations further in this work.

3. 3. COATING APPLICATOR_THE DTG® NOZZLE

The coating nozzle has already been introduced in Section 2.7. (Figure 2-22), and is used to apply a concentric polymer coating on the optical fibre. It exists of a cup, containing the liquid coating material, together with a coating nozzle (or die), right beneath. Typically the nozzle consists of two identical parts, each having half of a circular conical shape (Figure 3-5a), which can be closed very tightly forming a cone with a tiny exit hole.

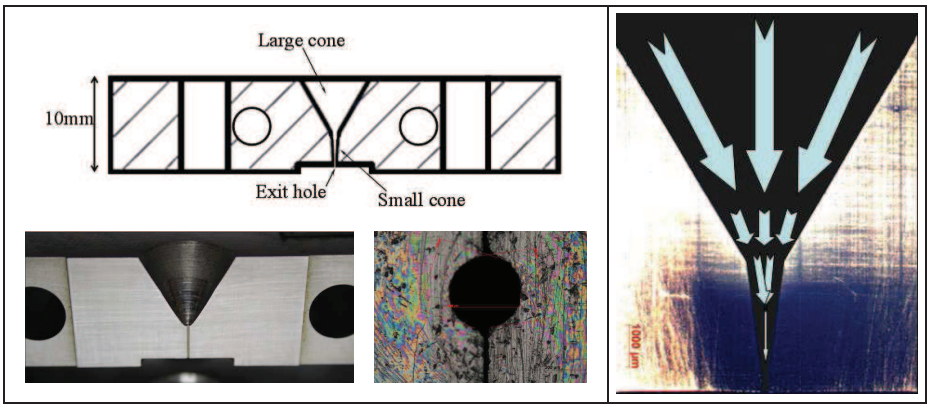

Figure 3-5 Example of a cross sectional drawing and pictures of one side of a coating nozzle and the closed exit hole (left), flow front of the coating material through the nozzle (right).

The basic working principle of a coating nozzle, as depicted in Figure 3-5, is based on the vertical flow from top to bottom of a viscous coating material (e.g. ORMOCER®), which sticks to the fibre while drawing. The flow of the coating fluid is defined not only by gravitational flow, but merely by the moving fibre, which generates a circulation of the fluid in the coating cup on top of the nozzle and a flow of the fluid in the cones. The flow front of the fluid starts in the larger cone area and propagates in the narrow cone towards the exit hole (Figure 3-5, right) . Because of the conical shape of the nozzle the pressure in the coating (i.e. surrounding the fibre) is increasing towards the end of the nozzle. Hence, the fibre is being centred towards the exit hole at the bottom of the nozzle.

The coating concentricity basically depends on two things: 1) the fibre alignment in the draw tower with regard to the position of the nozzle (Figure 2-4, Section 2.3) and 2) the shape and surface quality of the cones, and the circularity of the small hole at the bottom of the nozzle. *The thickness* of the (wet) coating is regulated by the flow of the coating, which on its turn is defined by the speed of the running fibre, and the dimension of the cones and exit hole. For commercial DTG®s (125 µm fibre) the fibre speed is approximately 10m/min and with a hole of 250 µm, the outer diameter of the cured ORMOCER® coating becomes approximately 190 µm. This same (standard) nozzle has also been applied to produce the 125 µm reference gratings. In addition the ultimate coating thickness depends on the duration of UV curing and intensity of the UV lamp too. However, in this work, the UV curing condition (i.e. curing time during drawing) has not been further investigated.

For the 80 µm fibre new coating nozzles had to be developed since several preliminary trials have shown that by using the available standard coating nozzle, the coating was relatively thick and that a good coating concentricity was hard to reproduce. For one of the trials the non-concentricity of the coating reached over 22 µm, which is harmful to the (bending) strength of the fibre and sensor performance when applied for measuring strain. The reason of this bad result is more fold: *first of all,* a thinner fibre is more difficult to centre if the exit hole, and thus the coating thickness, is taken to large. *Secondly,* the shape and dimension tolerances of the nozzle needs to be higher for a fibre which is approximately 1.5 times thinner, as

each small error in shape and possible misalignment of the two nozzle parts will have a larger impact on the resulting coating concentricity and uniformity than for the standard DTG® fibre.

In the following section the developments on the new coating nozzle with its technological challenge to achieve smaller but identical conical parts and cones with improved tolerance is discussed.

3. 3. 1. Coating nozzle build up

The nozzle as shown in Figure 3-6, left, consists of 2 separate metal parts (A & B) with in the centre of the two pieces the cone and small exit hole (1) of the nozzle. The complete nozzle should fit on a mechanical translation stage (Figure 3-6, right) It is fixed with a bolt (2) and it is roughly aligned onto the stage with metal pins which fit in the four holes (3). Part (A) is fixed and part (B) can slide, to open or close the nozzle. Each piece of the nozzle consists of two holes along the normal axis of the plane of the cones (Figure 3-5a) in which two metal sliding bars (6) are fit in to close and open the nozzle, i.e. part (B) can slide towards and away from the fixed part (A) using a hinge mechanism that is anchored in (5). In addition to the sliding bars the two parts fit well together using a self aligning mechanism consisting of precise fittings (4). The tolerance on the circularity of these fittings is only in the order of a few µm which helps to close the nozzle very precisely (Figure 3-6, left).

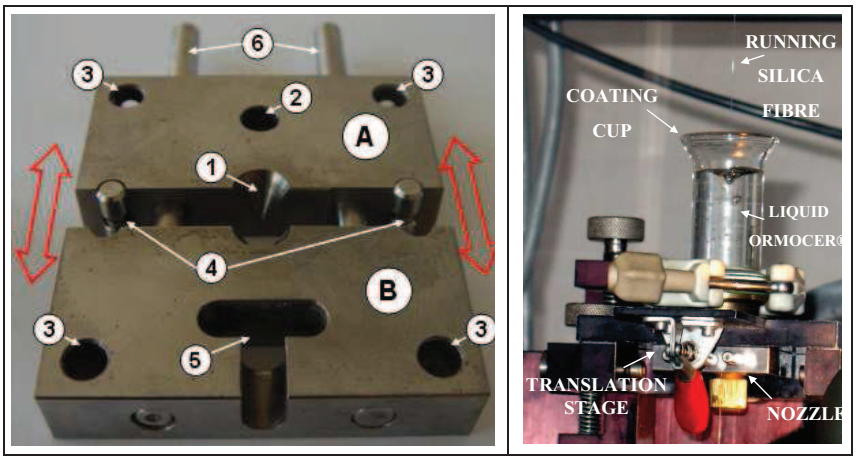

Figure 3-6 Metal coating nozzle with two identical parts well aligned and which fit exact together (left), complete coating applicator with cup, nozzle and mechanical translation stage (right).

The technological challenge is, to manufacture a nozzle out of two pieces with a exit hole smaller than 200 µm. The two parts should close well and should form a nice and smooth cone with a tiny exit hole with good circularity (Figure 3-5a) and a very fine surface roughness. The nozzles were conducted in two steps.
At first, conventional mechanical tooling was used to mill the large cone (1), to drill the four holes (3) to cut it in two parts (A) and (B) and to mill the T-shaped incision (5). Then for the precise tooling of the exit hole in the cone (1) and the fittings (4),

another technology was chosen. At first laser drilling technology was chosen to manufacture the tiny exit hole. A hole of 200 µm in the centre of the cone (1) with the two pieces held together was aimed for. Laser drilling is in principle very well suited to drill such small holes in thin metal specimens with high tolerances. However, in this case the pieces of work had a thickness of 2-3mm (i.e. area below the cone) and as a result the quality of the laser drilling was poor and the dimensions of the hole were not satisfying at all (see the cross-section in Figure 3-7). The reason of failure was due to the fact the laser drilling started at the side of the cone. This allowed centring the exit hole according to the cone. However, when the laser beam entered the metal a zone with melted metal was left at both parts. When the beam moved further in the pieces the result was better, however, some melt is still visible at the side and the dimensions are not constant over the length of the hole. Although the hole was aimed to be around 200 µm, from the measurements performed using a microscope the minimal and maximal diameter were 182 µm and 320 µm, respectively.

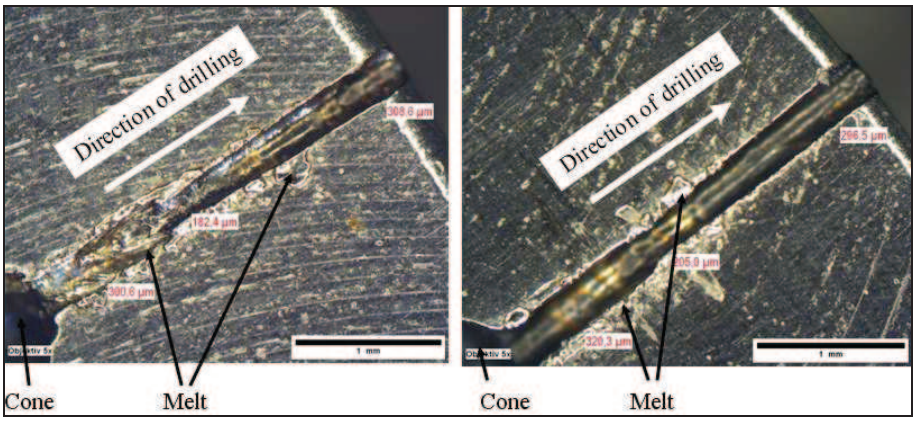

Figure 3-7 Bad result of laser drilling: cross-section taken with a microscope (object-glass of 50x) of the small exit hole.

The laser drilling was found not suited for this type of application. Other techniques of tooling were searched for and eventually a wire spark erosion technology is chosen. Three different coating nozzles are finalized using this technology. For each trial a draw tower production run is executed. The resulting quality and fibre coating dimensions of each separate trial will be showed in the following sections.

3. 3. 2. Nozzle finalizations and resulting coating quality

Wire spark erosion is also referred to as electric discharge machining (EDM) which is a manufacturing process in which material is removed by current discharges (sparks) between an electrode (i.e. wire) and the piece of work. In wire spark erosion the electrode is wound off from a spool, as such the electrode tool is continuously refreshed and it pristine dimensions are kept. A liquid dielectric is used to carry away the particles which are eroded from the workpiece. The piece of work is positioned on a table which can move in X, Y and Z direction. The eroding wire is held between upper and lower diamond guides, which can move in the X-Y plane,

The upper guide can independently be moved along two additional axes. As such tapered as well as transitioning shapes can be cut out of any (hard) metal with a very high accuracy.
All three nozzles, discussed in the following subsections are finalized using the wire spark erosion technology. Nozzle 1 was finalized using a wire of 100 µm diameter, achieving an exit hole of 240 µm. Nozzle 2 & 3 were finalized using a wire of 70 µm to achieve a tapered shape and smaller diameter of the exit hole. The diameter of the exit hole is 180 µm and 148 µm in Nozzle 2 and Nozzle 3, respectively.
The concentricity of coating and optical fibre is very important. It defines how well the optical fibre is centred within the coating layer, or how homogeneous the coating material is surrounding the optical fibre. The coating non-concentricity parameter, (t_{NC}) is defined as the maximal shift of the position of the centre of the fibre with respect to the centre of the coating, both assumed to be circular, see Figure 3-8, Equation 3-5.

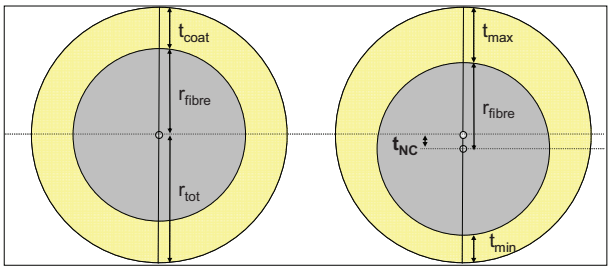

Figure 3-8 Maximum coating non-concentricity.

$$t_{NC} = (r_{fibre} + t_{max}) - r_{tot} = \frac{t_{max} - t_{min}}{2}$$
$$\text{with} \quad t_{coat} = (t_{max} + t_{min})/2 \qquad 3\text{-}5$$
$$\text{and} \quad r_{tot} = r_{fibre} + t_{coat}$$

The values of the non-concentricity is given in each section of the described nozzle. All the non-concentricity values are summarized in Table 3-3, given in Section 3. 3. 2. d. .

3. 3. 2. a. DTG®-NOZZLE1

For the first nozzle an exit hole of approximately 240 µm diameter was achieved using standard machining algorithms. The obtained result is shown in Figure 3-9, left. The hole is starting at the end of the large cone with an abrupt change in diameter. The finishing surface roughness was very good, see Figure 3-9, left, which is an advantageous property of the wire spark erosion technology. Although the abrupt transition zone, a first successful trial was executed with this nozzle to coat the 80 µm fibre. The resulting coating thickness and concentricity was measured from different samples cut at the beginning and end of the production run using a microscope with camera and appurtenance software (Figure 3-9, right). In order to measure both the cladding and the coating, the fibre is cleaved with coating. The

consequence of cleaving a non-stripped fibre, is that a small part of the coating at one side of the fibre is being damaged (blurred edge in Figure 3-9, right). The total diameter was about 138 µm and a slight coating non-concentricity <3.6 µm (Equation 3-5) was found. More details are found in Table 3-3, Section 3. 3. 2. d. .

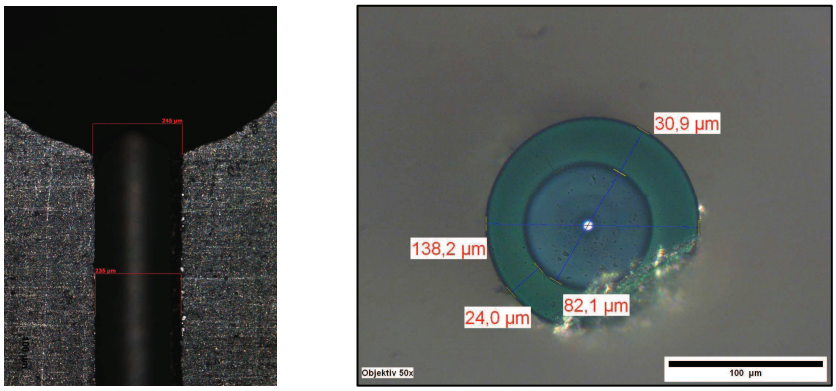

Figure 3-9: DTG®-nozzle1 with an exit hole diameter of 240 µm approximately (left), resulting fibre coating, diameter approx 138 µm (right).

3. 3. 2. b. DTG®-NOZZLE2

In order to improve the coating concentricity, a second nozzle was manufactured which is similar to the first one but with slight modifications concerning the transition of the large cone towards the exit hole. The large cone slightly passes into a smaller cone which leads to the exit hole. The result is shown in Figure 3-10 (left). Instead of 100 µm a 70 µm sparking wire was used. Therefore the diameter of the exit hole was decreased. Moreover, a special program has been used during manufacturing to create the (second) small conical part and cylindrical part in one motion without touching the larger cone and still keeping all this centralized with respect to the large cone. The exit hole diameter was approximately 180 µm. Even though a more complex shape has been formed in this nozzle it should be noted again that a very good surface roughness was achieved with the wire spark technology, which is an advantage for achieving a highly uniform and concentric coating layer.

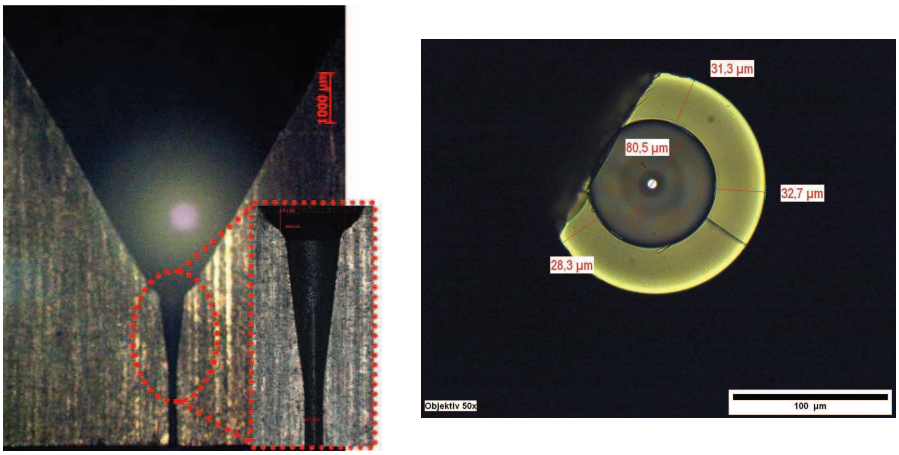

Figure 3-10: DTG®-nozzle2 with two conical parts and an exit hole of 180 µm (left) resulting fibre coating, diameter approx 142 µm (right).

This second nozzle delivered excellent results in terms of the coating concentricity, as shown by the cross-section in Figure 3-10, right. The non-concentricity is improved from <3.6 µm till only 2.2 µm (Table 3-3, Section 3. 3. 2. d.). The total outer diameter is approximately 142 µm. Even though the first nozzle has a larger exit hole compared to Nozzle2 (240 µm compared to 180 µm, the coating diameter is nearly the same for both Nozzle 1 and Nozzle 2 (138 µm and 142 µm respectively). Note that a little error occurred in the shape of the exit hole at one side of Nozzle 2, see Figure 3-11. During the wire erosion, the tapering was mirrored towards the exit hole only at one side of the nozzle and influenced the magnitude towards the end of the exit hole.

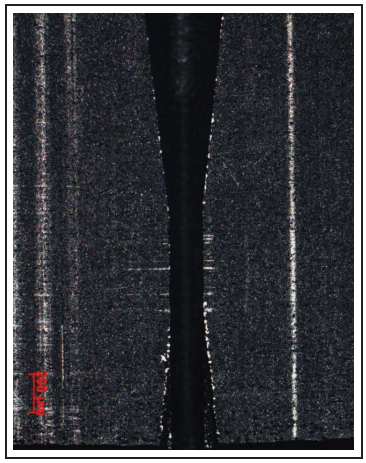

Figure 3-11: Erosion tapering error at one side of Nozzle2 causing a small deviation at the exit hole.

It could be that this faulty shape at one side of the hole has caused the outer diameter of the applied coating to be in the same range as the result we obtained with Nozzle 1. Hence in a third trial the small cone is made longer, to keep the cylindrical

part of the exit hole shorter and in the same time to aim for smaller dimensions of the exit hole.

3. 3. 2. c. DTG®-NOZZLE3

In order to further reduce the coating diameter, a third nozzle has been manufactured. In this trial we aimed for the minimal achievable diameter, possible to obtain with the available spark wire technology. A lot of effort is put in tuning the machining algorithm to obtain smaller dimensions using the minimal allowed sparking wire that fits the machine. This DTG®-nozzle has the same setup as the second version (i.e. two conical parts and a cylindrical part), but the exit hole diameter has been further reduced from 180 µm to approximately 148 µm. Microscopic pictures of the nozzle are shown in Figure 3-12. Slight modifications were made concerning the transition zone between the two cones and the length of each part. To avoid the mirrored tapering seen in Nozzle 2, the second small cone was elongated and as a consequence, the cylindrical part towards the exit hole was kept very short (approximately 550 µm). In this way, the tapering of the smaller cone was achieved without altering the exit hole. In the same time, the diameter of the exit hole could be reduced further without changing the smooth surface roughness. It should be noted that, taken into account the combination of the conical shaping with the small exit hole of 148 µm, the resulting nozzle is really the state of the art using spark wire erosion.

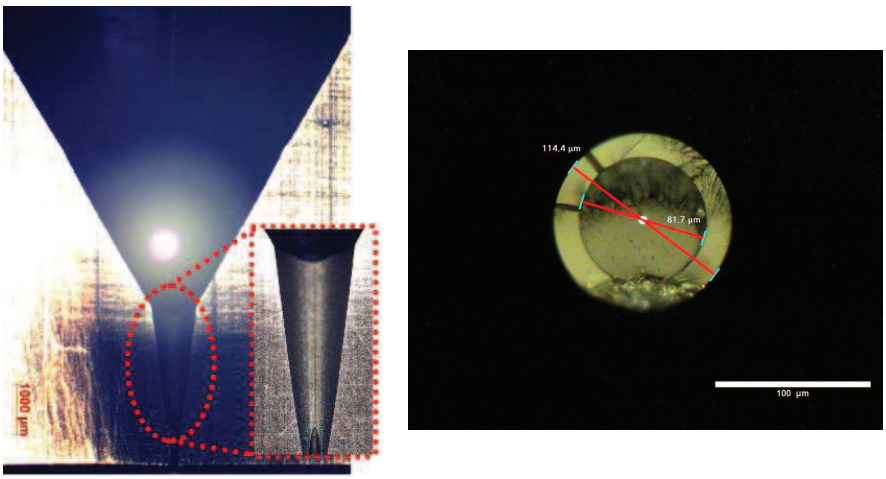

Figure 3-12: Third version of the DTG®-nozzle with an exit hole of 148 µm diameter, showing two conical parts (left) and the transition to the cylindrical part (right).

Again we succeeded in drawing 80 µm fibre with an excellent coating concentricity. In this case the non-concentricity has been reduced to <1 µm (Table 3-3, Section 3. 3. 2. d.). A slightly higher drawing speed, together with a smaller exit hole, resulted in an outer diameter of the ORMOCER® coated fibre of only 114 µm, see Table 3-3. As such, the coating thickness for the 80 µm coated fibre is reduced from approximately 30 µm to about 16 µm with enhanced coating concentricity. Note that

these dimensions are very close to the thickness of a typical composite reinforcement layer (~0.1 mm), hence the dimension of the new 80 µm coated DTG®s has improved significantly compared to the standard 190 µm outer diameter of the 125 µm DTG®.

3. 3. 2. d. Summary table of the 80 µm fibre / coating dimensions

In Table 3-3, the dimensions of the 80 µm coated fibres of all afore described trials are summarized. The features of the nozzles which are applied during each trial, are indicated as well. We can compare the fibre / coating dimensions of the manufactured 80 µm fibres in Table 3-3, to the standard 125 µm coated fibre which have a total outer diameter of 190 µm, corresponding to a coating thickness of 32.5 µm. If we compare for example the 82 µm / 114 µm DTG® fibre of Trial 3 with the standard 125 µm / 190 µm DTG®-fibre, we have reduced the cladding with approximately 34 % and the coating (i.e. total outer diameter) with 40 %.

Table 3-3: Summary results of all three trials and associated nozzles.

	Trial1 (nozzle1)[*] *PR2008_1*	*Trial2 (nozzle2)*[**] *PR2008_2*	*Trial3 (nozzle3)*[*] *PR2009_1*
Nozzle features	1 cone Exit hole = 240 µm	2 cones Exit hole = 180 µm[***]	2cones Exit hole =150 µm
ØCladding (µm)	82.5 ± 0.7	80.5 ± 0.1	81.8 ± 0.1
ØCoating (µm)	139.0 ± 0.7	142.6 ± 0.6	114.0 ± 0.4
Mean coating thickness (µm)	28.2	31.1	16.1
Non-concentricity, t_{NC}, (µm)	3.2 ± 0.3	2.2 ± 0.0	0.6 ± 0.3

In analogy to composite materials we can also compare the fibre / coating volume fraction of the two fibres. The volume fractions are proportional to the square of the ratio of the diameters (~$Ø_{clad}^2$/ $Ø_{tot}^2$). We define $v_f = V_{clad}/V_{tot} = d_{clad}^2/d_{tot}^2$, and $v_{coat} = 1 - v_f$, as the fibre –and coating volume fractions. In Table 3-4, the volume fractions are calculated for the 80 µm fibres of Table 3-3, and compared to the standard 125 µm reference fibre.

[*] deduced from 3 samples (begin, mid, end production run)
[**] deduced from 2 samples (begin, end production run)
[***] one side of the exit hole shows a small deviation of the original circular shape (see Section 3. 3. 2. b.)

Table 3-4: Comparison of the fibre-cladding and coating volume fraction for the 80 µm DTG®-fibres to a 125 µm DTG®-fibre.

	Trial1 (PR2008_1)	*Trial2 (PR2008_2)*	*Trial3 (PR2009_1)*	*125 µm / 190 µm*
v_f	0.352	0.319	0.515	0.433
$v_{coat} = 1 - v_f$	0.648	0.681	0.485	0.567

These values illustrate that proportionately, the thinner DTG®-fibres of Trial 1 & 2, have more coating material than the standard 125 µm DTG®-fibre, and that the thinner fibre of Trial 3 has less coating material.

3. 4. FIBRE TENSILE STRENGTH

When applying an optical fibre sensor to measure strain inside composite materials, it is of importance to know what is the mechanical strength of the sensing element itself. Ideally the sensor should outlive the construction material. Failure strains of more than 1 % strain are not exceptional in composites. Therefore, the mechanical performance of the newly developed 80 µm DTG®-fibre has been investigated using a dynamic proof-test. Dynamic, in the sense that the fibre is loaded (i.e. strained in axial direction) by ramping up a translation stage, at which the fibre is attached to, with a continuous speed. A mechanical test-frame (Zwick Z010) is used to investigate the tensile strength (Figure 3-13, left). The frame has a 200N-loadcell, and two adapted fibre-clamps with spools are used to attach the fibre ends. The spools have a diameter of approximately 120mm, and they are foreseen with thread, to wind up the fibre at each stage, see Figure 3-13.

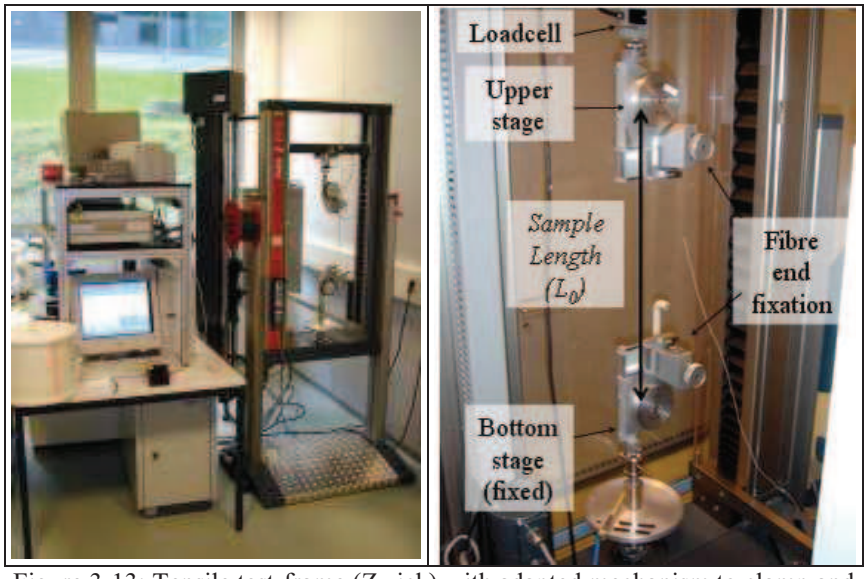

Figure 3-13: Tensile test-frame (Zwick) with adapted mechanism to clamp and fixate the fibre at both stages.

The "free" fibre-length between the stages is taken approximately 500mm. The cross-head speed of the upper displacement stage is set to 30 mm/min, which corresponds to a strain rate of approximately 0.001 %/sec. The applied force is recorded during the tensioning of the fibres until breakage, and the break force is noted for each specimen.
The newly developed 80 µm DTG®-fibre is compared to a 125 µm reference DTG®-fibre. In total fifteen pieces of a 82 µm fibre of Trial3 (Table 3-3) were tested, and five pieces of the 125 µm reference fibre were used as comparison.

3. 4. 1. Ultimate fibre strain and stress

No extensometer is used to measure the strain during these experiments, however, because silica fibre is a linear elastic material, we can use Hooke's Law ($\sigma = \varepsilon E$), to determine the strain in the fibres. The applied stress in the fibre is calculated from the relation between the applied force (measured from the load-cell) and the fibre cross-sectional surface. The calculated strain in the coated fibre is then given by:

$$\varepsilon_f = \frac{F}{E_{tot} A_{tot}}, \qquad 3\text{-}6$$

with A_{tot} the total cross-section surface of the fibre with coating and E_{tot}, the composite modulus of the coated fibre. By assuming perfect contact conditions between the fibre coating material and the silica surface, which is well approximated in the case of the ORMOCER® coating, the composite modulus of the coated fibre is given by:

$$E_{tot} = \frac{A_f}{A_{tot}} E_f + \frac{A_c}{A_{tot}} E_c, \qquad 3\text{-}7$$

where E_f, is the Young modulus of the silica fibre, E_c, is the Young modulus of the fibre coating and A_f and A_c are the cross-section surfaces of the optical fibre and coating, respectively. By substituting $E_f = 72.4\ GPa$ [8] and the Young modulus for ORMOCER®, $E_c = 1.8\ GPa$ (determined in Section 4.1.4) in Equation 3-7, and noting that the surface fractions equal the volume fractions given in Table 3-4, the composite modulus of the 82 µm / 114 µm (PR2009_1) and 125 µm / 190 µm fibres are $E_{tot,82/114} = 38.3$ GPa and $E_{tot,125/190} = 32.4$ GPa, respectively. With regard to the results of the determined Young's modulus of the ORMOCER® in Chapter 4 the author remarks that there is an uncertainty on the exact value of the stiffness of the coating. Results from Chapter 7 on FE-simulations to determine the optimal properties of the coating of the embedded optical fibres, showed an optimum stiffness of $E_{c,optimum} = 0.8\ GPa$. However, because the determination of the Young's modulus in Chapter 4 is done for a non-embedded optical fibre, here the value of $E_c = 1.8\ GPa$ is chosen to perform the calculations.

Using the composite moduli determined above, and substituting in Equation 3-6, the theoretical applied strain in each fibre can be calculated from the applied force. The course of the applied force against the theoretical strain is shown in Figure 3-14, for both fibres.

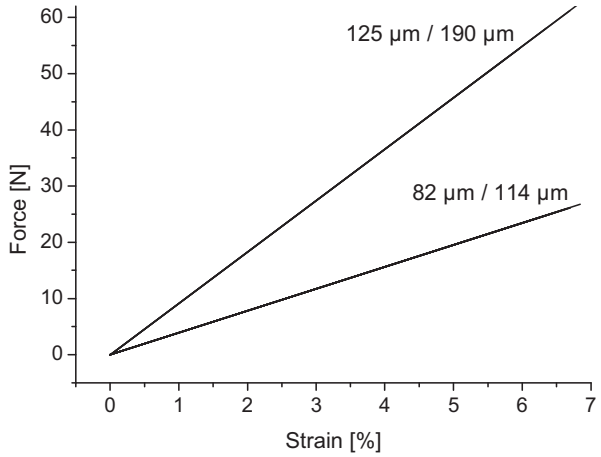

Figure 3-14: Fibre tensile test on 5 x 125 µm reference samples (PR2007_2) and 15 x 82 µm samples (PR2009_1), with the applied force plotted against the calculated strain using the composite modulus, E_{tot} (cross-head speed 30mm/min and probe lengths 500mm).

The maximum force at breakage is used to determine the tensile strain (ε_{ULT}). Using again Hooke's Law and the Young modulus of the silica fibre, the tensile strength ($\sigma_{f,ULT}$) of the silica fibres is determined. Additionally, using the composite moduli of both fibres, the (composite) tensile strength of the fibre with coating, is calculated ($\sigma_{comp,ULT}$). All values for the 82 µm and 125 µm fibres, are given in Table 3-5:

Table 3-5: Statistics on the maximal applied force, the calculated tensile strain and tensile strength of the 82 µm and 125 µm fibres.

Fibre	Fmax [N]	ε_{ULT} [%]	$\sigma_{f,ULT}$ [MPa] (mean)	$\sigma_{f,ULT}$ [MPa] (median)	$\sigma_{comp,ULT}$ [MPa]
82 / 114 µm (N=15)	25.3 ± 0.8	6.46 ± 0.21	4668 ± 150	4658	2478 ± 80
125 / 190 µm (N=5)	58.0 ± 4.6	6.33 ± 0.50	4567 ± 362	4573	2047 ± 162

As expected, the ultimate strain and stress of the thinner DTG®-fibre is similar to the standard 125 µm DTG®-fibre. It is noted that, when the coating of the optical fibre is neglected in the calculation of the tensile strength, the calculated tensile strength will be overestimated. For example, without taking into account the coating of the 125 µm and simply using calculating the stress from the maximal force (58 N) and the cross-section of the silica (i.e. $A_f = 0.01227 mm^2$), the (mean) tensile strength is then found, $\sigma_{f,ULT} = 58\ N / 0.01227\ mm^2 = 4727\ MPa$. Compared to the mean

value of 4567 MPa for the 125 µm given in Table 3-5, the value is approximately 3.5 % higher.

3. 4. 2. Weibull diagram

To investigate the mechanical strength of optical fibres it is common to use the density-distribution of local microcracks or flaws. The probability of rupture, $F(\sigma)$, at which a piece of fibre will snap at a certain tensile stress σ, is related to the density and the number of cracks. The statistical Weibull law provides a relationship between the probability $F(\sigma)$, and the applied stress, and is given by:

$$\ln\left[-\ln\left(1-F(\sigma)\right)\right] = m\left[\ln\left(\frac{\sigma}{\sigma_0}\right)\right]. \qquad 3\text{-}8$$

Where m is a size parameter of the fibre defects and σ_0 is a scale parameter or simply the Weibull parameter. The evolution of the double logarithmic equation $\ln\left[-\ln\left(1-F(\sigma)\right)\right]$ against $\ln(\sigma)$ is called the Weibull diagram, which enables to calculate m and σ_0 from the slope and curve intersection with the stress axis. To plot the Weibull diagram and to find the m and σ_0 parameter, the results of the 82 µm and 125 µm fibre pieces of Section 3. 4. 1. are used. The calculated stress values σ_i, with $i = 1...N$, are arranged in ascending order and for each tensile stress σ_i the cumulative probability $F_i(\sigma)$, is written as:

$$F_i(\sigma) = \frac{i-0.5}{N}, \qquad 3\text{-}9$$

with the amount of fibre pieces for the 82 µm fibre and 125 µm fibre is $N_{82\mu m}$=15 and $N_{125\mu m}$=5, respectively (Table 3-5). The resulting Weibull diagram is shown in Figure 3-15. The size parameter m is determined from the linear slope of the plotted curves. From linear fitting, we find that $m_{82\mu m} \approx 37$ and $m_{125\mu m} \approx 15$. The value of m of the 125 µm fibre is lower, indicating that the defects found at the fibre surface have varying sizes, which results in different values of the tensile stress [9] it is noted that the amount of samples in the case of the 125 µm fibre (i.e. N=5) is not optimal. According the CEI-IEC 793-1-3 [10] the amount of fibre test pieces should be at least N=15. Even though the number of samples for the 125 µm fibre N =5, we can clearly see from the Weibull diagram in Figure 3-15 that indeed the distribution of the tensile stress for the 125 µm fibre is broader than in the case of the 82 µm fibre.

By calculating the intersection with the stress axis (i.e. taking $F = 0.5$), Equation 3-8 transforms into:

$$\frac{\sigma(0.5)}{\sqrt[m]{\ln 2}} = \frac{\sigma_M}{\sqrt[m]{\ln 2}} = \sigma_0, \qquad 3\text{-}10$$

with the tensile stress $\sigma(0.5)$ at $F = 0.5$ representing the median tensile stress, hence $\sigma(0.5) = \sigma_M$. The values of the median tensile stress σ_M , are the same as the values as given in Table 3-5, i.e. $\sigma_{M,82\mu m} = 4658$ MPa and $\sigma_{M,125\mu m} = 4567$ MPa . Substituting the median tensile stresses and filling in the size parameter *m*, for the corresponding fibres, in Equation 3-10, we then find that $\sigma_{0,82\mu m} = 4704$ MPa and $\sigma_{0,125\mu m} = 4680$ MPa , which are slightly higher than median tensile stresses.

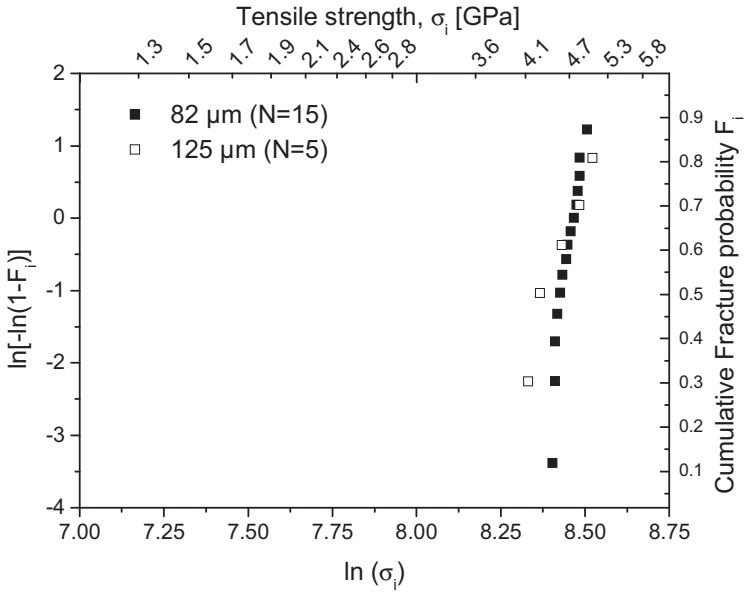

Figure 3-15: Weibull diagram: strength distribution of the 82 / 114 µm and 125 / 190 µm.

The median tensile strength values for the DTG®-fibres are in accordance with the strength values found in literature for silica fibres, which ranges from 4 - 7 GPa, depending on the strain rate during the experiment [5, 11-12]. The m-values depend largely on the fibre drawing conditions and coating application. For standard telecom fibres, the values are exceeding m>100, hence we can conclude that the drawing conditions to produce the DTG®-fibres are not matching those of industry. However, compared to mechanically stripped and recoated fibres with m-values of m = 4 – 5 [12-13], we can say that both the 82 µm (m = 37) and 125 µm (m = 15) DTG®-fibres have better averaged defects sizes on the fibre surface and thus a higher failure stress.

As stated in the beginning of this section, the mechanical performance of the sensing element should be equal or better than the mechanical properties of the structural element. The investigations on the tensile strength of both DTG®-fibres has shown that the performance on the level of both the ultimate strain and stress values is outstanding. In Table 3-6 the ultimate strain and stress values of some typical composite materials and standard construction materials are compared with the ones determined for the DTG®-fibres.

Table 3-6: Mechanical performance of the DTG®-fibre compared to other typical materials.

	Silica fibre (coated)*	CFRP (epoxy)	CFRP (PPS)	GFRP (nylon)	Al**	Steel**	Titanium**
ε_{ULT} [%]	6	1.1	1.3	2	30	40	18
σ_{ULT} [MPa]	4700	1800	760	180	620	500 - 700	1580

Hence, from the table above we can conclude that the mechanical performance of the optical fibre exceeds most of the mechanical performance of composites and other construction materials. Taking only into account the elastic regime, at which most applications of construction materials are limited to, the optical fibre is suitable to be used as strain sensing element for any of the above enumerated materials.

3. 5. 80 µM FIBRE HANDLING & SPLICING

In order to connect and use the 80 µm DTG®s, we have in principle two options:

1. direct connecterisation of a fibre ferrule and (FC /APC) to the fibre end
2. splicing to a standard SMF pigtail with a fibre connector (FC / APC)

The first option is possible and has been applied at the beginning of this dissertation, but it has to be noted, direct ferrule connecterisation has to be carried out by a specialised company (e.g. Diamond-fo [14]). As such, each time experiments have to be carried out, the ferrules need to be provided before testing, which is not practical when applying research, hence this option is not used throughout the work.
This section focuses on the second option, and it is described briefly how to prepare and handle the 80 µm DTG®-fibre and how to splice it (i.e. connect) to a standard 125 µm SMF. The main steps in preparation and handling are identical to the standard procedures used for standard telecom fibres.
At first, the preparation of the 80 µm fibre consists of removing the polymer coating (i.e. ORMOCER®) with a standard stripper tool (e.g. Miller). To remove the ORMOCER® material a slightly higher stripping force has to be exceeded in comparison to for instance standard soft poly-Acrylate coatings. To remove coatings of 80 µm optical fibres, a commercially (adapted) stripping tool is available, however, when using the standard Miller tool for 125 µm fibres (Figure 3-16, left) and holding it tilted, this works fine as well.
To cleave the fibre end, an adapted Fujikura fibre cleaver is used (Figure 3-16, left). Adaptation of the cleaver has been carried out manually by slightly moving the cutting blade upwards. As such, it is optimized for the thinner 80 µm cladding. Another cleaver, such as the "one-click" FBC006 cleaver from the company Corning without any adaptation, is suitable as well, and has been used varied

* taking into account the polymer coating material and 'composite' modulus
** Elongation at break (plastic regime)

throughout the work. Together with the 80 µm fibre a standard 125 µm pigtail with a fibre connector is prepared as well (Figure 3-17, right). Both fibres are then placed in a core aligner fusion splicer (Fitel splicer, Figure 3-16, right). It should be noted, in order to keep the splice losses low, a core aligner is preferred over a cladding-aligner splicer.

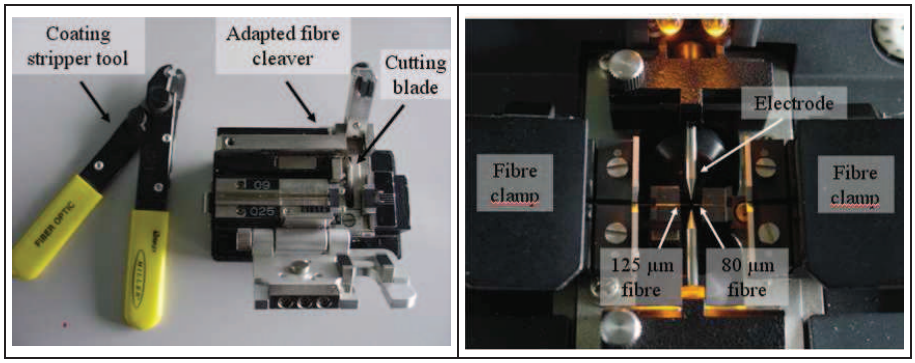

Figure 3-16: Fibre stripping and cleaving tools (left), splicing device (right).

An adapted fusing program is used to splice the fibres with different diameter. Mainly the arc-power, arc-time and gap between the fibre ends has been changed. After fusion splice a conical shape is visible and typically a splice loss of 0.78dB is present when splicing a standard 125 µm SMF to the 80 µm DTG®-fibre. The result is shown in Figure 3-17, left. It is noted that, the main cause of the splice loss is due to the fact that the mode field diameter, i.e. fibre core, of the highly doped 80 µm fibre is smaller than the 125 µm SMF. Note that because of the smaller core of the highly doped optical fibre, one should use a core-alignemnt splicer to avoid excessive losses

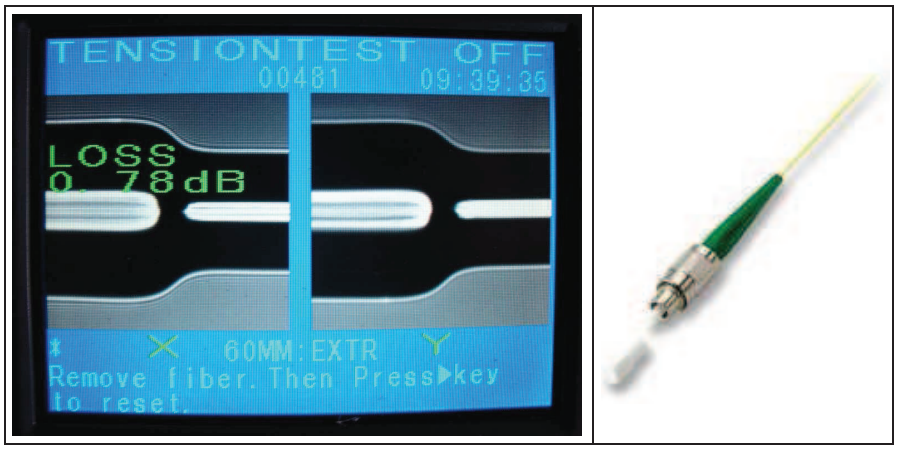

Figure 3-17: Splicing-result of a standard SMF 125 µm fibre with a 80 µm DTG® - fibre (left), standard 125 µm fibre connector and pigtail (right)

3. 6. CONCLUSIONS

In this chapter the author has elaborated in detail the manufacturing of the 80 µm DTG®s starting from the production of a highly GeO_2 - doped fibre, up to the application of the ORMOCER® coating using three newly developed DTG®-nozzles. In fact two preforms are manufactured from one original long preform: one for the new 80 µm fibre (Preform_80) and one for the 125 µm reference fibre (Preform_125).

The optical properties of both fibres

The Equivalent Step Index (ESI) of the single mode fibre is determined from the original preform with $\Delta n = 15.3 \cdot 10^{-3}$. A typical central index depression is seen in the centre of the highly doped preform core area which is caused by the vaporization and diffusion of the GeO_2 out of the inner layers of the core during the preform collapsing process. The total fibre loss for both fibres is high: 11.3 dB/km for the 125 µm fibre and 17.6 dB/km for the 80 µm fibre, measured at $\lambda = 1.55 \mu m$. The extreme high loss in the fibres originates from inhomogeneities in distribution of the GeO_2 and the germanium oxygen-deficient centres (GODC). The higher transmission losses of the 80 µm compared to the 125 µm fibre are most probably explained by the difference in drawing conditions, like temperature, tension and fibre speed during drawing, which differ when producing fibre with other diameters. The cut-off wavelength are measured from a piece of fibre (approximately 100 m), with $\lambda_{Cutoff} \approx 1.2 \mu m$ which is a typical design cut-off wavelength for single mode fibres. The core radii are determined from both the ESI and the V-parameter (with V =2.405). Good agreement is found between the measured values and the calculated ones which confirms that the preforms are indeed designed to manufacture 80 µm and 125 µm single mode fibres with a cut-off at approximately 1.2 µm. As expected the diameter of the core of both fibres is nearly identical with $d \approx 4.5 \mu m$, which is only half of the core diameter of standard single mode fibres. From the ESI (Δn), the V-parameter and the normalized propagation constant, the effective refractive index of the optical fibre is determined with $\overline{n} = 1.4459$. This value of the effective refractive index will be used in all further calculations in this work.

Application of ORMOCER® coating

All fibres manufactured in this work are coated with the ORMOCER® coating material used for the standard DTG®s. New coating-nozzles with smaller exit holes are developed using the state of the art wire spark erosion technology. An optimization procedure resulted in three different coating nozzles. The first two nozzles delivered a relative thick coating diameter of approximately 140 µm and the coating concentricity is satisfying. However, the final design delivered very good results with a total coating diameter of approximately 114 µm and an excellent coating concentricity (<1 µm). These dimensions are very close to the thickness of a typical composite reinforcement layer (~0.1 mm), hence the dimension of the new 80 µm coated DTG®s has improved significantly compared to the standard 190 µm outer diameter of the 125 µm DTG®.

The fibre tensile strength
The tensile strain of both the 80 µm and 125 µm fibres is higher than 6 %, and the median tensile strength $\sigma_{f,ULT} \approx 4600$ MPa, which proves that the mechanical properties of both the optical fibres are equivalent. Additional to these calculations the author has plotted a Weibull diagram for both fibre tests. The Weibull parameter (σ_0)of both fibres is found slightly higher $\sigma_0 \approx 4700 MPa$ than the median tensile strength ($\sigma_{f,ULT} \approx 4600$ MPa) found from simple statistical analysis. The Weibull size parameter (or m-value) however, is found lower for the 125 µm fibre, indicating that the defects at the fibre' surface have varying sizes. However, because the number of test samples (N=5) for the 125 µm are not optimal no conclusion are drawn. The size parameter of the 80 µm fibre with N=15, is found $m_{82\mu m} \approx 37$ which is a much higher value compared to stripped optical fibres with typically m-values of m = 4 – 5 .
The tensile strength (and strain) of both DTG®-fibres is outstanding. Compared to the mechanical performance of the aerospace qualified composites used in this dissertation, the optical fibre has an ultimate strain which is more than five times higher and an ultimate stress that is approximately three times higher. These results prove that from mechanical point of view the newly developed DTG®s are very well suited to be used for composite testing.

Splicing and connecting the 80 µm fibres
With regard to the splicing of the new 80 µm fibres to standard SMF one should remark that the core radius (and thus mode field diameter) of the highly doped optical fibre is half of the core of the (typically 9 – 10 µm). To avoid excessive splice losses, the author recommends to use a splicing device with core-alignment instead of a cladding-alignment.

The fibres and produced DTG®s during the production trials are now ready to be characterized. This will be performed in detail in the next chapter, and again both the 80 µm -and 125 µm DTG®s are evaluated and compared.

3. 7. REFERENCES

1. Liegois, M., Lavanant, G., Boniort, J.Y., and Lesergent, C., *MCVD preform central dip reduction by collapse under fluorinated atmosphere.* Journal of Non-Crystalline Solids, 1982. **47**(1-2): p. 247-249.
2. Dong, L., Pinkstone, J., Russell, P.S., and Payne, D.N., *Ultraviolet-absorption in modified chemical-vapor-deposition preforms.* Journal of the Optical Society of America B-Optical Physics, 1994. **11**(10): p. 2106-2111.
3. Mashinsky, V.M., Dianov, E.M., Neustruev, V.B., Lavrishchev, S.V., Guryanov, A.N., Khopin, V.F., Vechkanov, N.N., and Sazhin, O.D., *UV absorption and excess optical loss in preforms and fibers with high Germanium content*, in *Fiber Optic Materials and Components*, H.H. Yuce, D.K. Paul, and R.A. Greenwell, Editors. 1994. p. 105-112.

4. Dianov, E.M., Mashinsky, V.M., Neustruev, V.B., Sazhin, O.D., Guryanov, A.N., Khopin, V.F., Vechkanov, N.N., and Lavrishchev, S.V., *Origin of excess loss in single-mode optical fibers with high GeO2-doped silica core.* Optical Fiber Technology, 1997. **3**(1): p. 77-86.
5. Murata, H., *Handbook of optical fibres and cables*. second ed. 1996: Marcel Dekker, Inc.
6. Agrawal, P., Govind., *Fiber-optic communication systems*. third ed. 2003: Wiley interscience.
7. Masaharu, O., Kazuyuki, S., and Katsusuke, T., *Optical loss property of silica-based single-mode fibers.* Journal of Lightwave Technology, 1992. **10**(5).
8. Fukuhara, M., Wang, X.M., Inoue, A., and Yin, F.X., *Low temperature dependence of elastic moduli and internal friction for the glassy alloy Zr55Cu30Al10Ni5.* Physica Status Solidi-Rapid Research Letters, 2007. **1**(5): p. 220-222.
9. Zhao, F.M., Okabe, T., and Takeda, N., *The estimation of statistical fiber strength by fragmentation tests of single-fiber composites.* Composites Science and Technology, 2000. **60**(10): p. 1965-1974.
10. International electroechnical comission, G., Swiss, , *International standard IEC 793-1-3*. 1995.
11. Tarpey, A.J., Kukureka, S.N., and Jurkschat, K., *The mechanical reliability of stripped and recoated polyimide fibres for optical fibre sensors*, in *Optical Fiber and Fiber Component Mechanical Reliability and Testing Ii*, M.J. Matthewson and C.R. Kurkjian, Editors. 2002. p. 141-151.
12. Volontinen, T., Zimnol, M., Tomoza, M., Lee, Y., K., and Raine, K. *Effect of mechanical stripping and arc-fusion on the strength and aging of a spliced recoated optical fiber*. in *Mat. Res.Soc.Symp.Proc.* 1998.
13. Mauron, P., *Reliability and lifetime of optical fibres and fibre Bragg gratings for metrology and telecommunications*, in *Département de Microtechnique*. 2001, École polytechnique fédérale de Lausanne (EPFL): Lausanne. p. 117.
14. Diamond-fo. Available from: http:/www.diamond-fo.com.

Chapter 4 DTG® CHARACTERISTICS_80µM VERSUS 125µM

4. 1. INTRODUCTION

Typical in draw tower production runs, batch calibration is performed on a few DTG®s or specially produced (calibration) sensor arrays instead of calibrating each single sensor. The calibration coefficients of these DTG®s are then representative for the whole production batch of that specific run. The same approach of characterisation is being used here. For each draw tower production trial of the 80 µm, an extra dedicated array of 8 or more DTG®s in series is produced to be characterized. At first, for each run of the 80 µm we performed a 125 µm (reference) run as well, to compare the performance of the 80 µm DTG®s. This approach was stopped when the development of the 80 µm was finished. Hereafter, only 80 µm sensors where produced, mostly to try out the new coating nozzles as has been elaborated in (Chapter 3).

This chapter will focus on the characterization of the optical properties of the new 80 µm DTG®s, such as the reflectivity and the full width at half maximum (Section 4. 2.), but more important the DTG®s' opto-mechanical and thermo-optic characteristics are determined by means of calibration (Section 4. 4.). In this chapter the author will elaborate in detail the methods of calibration and the different setups which are being used. The (axial) strain gauge factor will be determined and an especially designed transverse compression testing setup is used to determine the strain-optic coefficients. The temperature sensitivity is determined by using highly accurate and stable dry-well calibrators. Because the DTG®s will be embedded in (thermoset and thermoplastic) fibre reinforced composites (PART II) we need to define its characteristics at elevated temperatures. The temperature level for a typical curing cycle of carbon-epoxy laminates is 180 °C, however, for the carbon-PPS (Polyphenylene Sulfide) laminates temperatures exceed 300 °C for more than one hour. As such the thermal stability of the gratings is studied (Section 4. 5.). Additional to that, the temperature dependency of the strain gauge factor and stress sensitivity will be investigated for a large temperature range, and finally a method using two Bragg gratings, to estimate the stiffness (Young' modulus) of the ORMOCER® coating will be demonstrated. All DTG®s-properties which are determined in this Chapter are then summarized at the end of this chapter in a specification table (Section 4. 6. .

To characterize (and test) the DTG®s, the author has used the same FBG-interrogating system throughout the entire work. A short section will be devoted to that first (Section 4. 2.).

4. 2. FBG INTERROGATION

An FBG reflects a portion of the injected light which is known as the Bragg spectrum with the maximum reflection occurring at the Bragg wavelength, λ_B. The amount of reflected light is depending on the grating strength, i.e. refractive index modulation, and length of the FBG (Appendix A). Using an amplified spontaneous emission (ASE) broadband light source (depolarized), and an optical spectrum analyser (OSA), or in this case a commercial Bragg interrogator like the FBG-

scanX08 system from FOS&S bvba [1] (Figure 4-1), the Bragg spectrum of every grating is measured (scanned) and saved in ASCII file format to perform post-calculations.
This section briefly describes some details on the optical performance of the interrogation system. The used FBG-scan system is a static system operating at scanning frequencies <1Hz. Its OSA is based on a Fabry-Perot filter which enables slow but precise scanning of the full optical C-band (i.e. 1527 nm till 1567 nm). It has an absolute wavelength accuracy of ± 10 pm and a wavelength read-out resolution of 2 pm [1]. It contains an optical switch (not shown in Figure 4-1) with 8 channels, enabling to connect multiple chains at once. All connected channels are scanned sequentially and data of all FBGs connected is stored within 1 or 2 minutes. Note that the specifications of this system (e.g. slow scanning speed) are not state of the art compared to the dynamic commercial Bragg interrogators which are on the market today. However, Chapter 5 & 6 will show that care should be taken when analysing the response of embedded fibre Braggs, as the spectral shape can get heavily distorted. Therefore, the author would like to state already at this stage that interpretation on the level of the spectral response of (embedded) FBGs is in some cases much better, than simply working with the "pre-calculated" Bragg wavelength, based on standard peak picking algorithms, such as the centroid peak algorithm or FWHM based algorithm [2]. The analysis of the spectral response of embedded FBGs should be done with care, hence, in this research we focus on the static analysis of the Bragg spectra, where the specifications of the used FBG-scan system (static), fits very well the requirements for the FBG characterisation and later on for the detailed distorted spectral analysis in Chapter 6, 7 and 8.

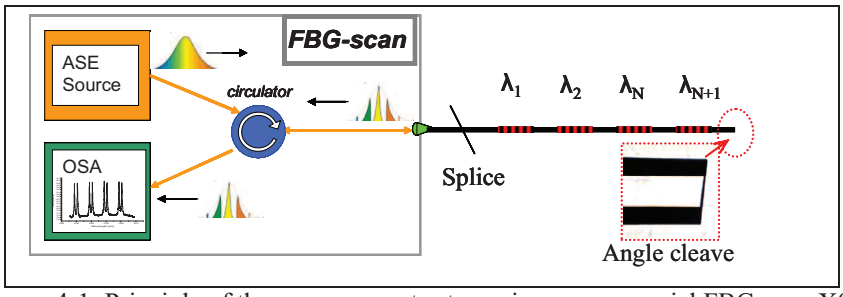

Figure 4-1: Principle of the measurement setup using a commercial FBG-scan X08 system from FOS&S, bvba, with light source, optical spectrum analyser and an optical fibre connected containing an FBG chain.

4. 3. CALCULATION OF THE FBG REFLECTIVITY

After saving the full spectrum, the maximum reflection of each peak is measured using commercially available statistical software. The measurements were performed at room temperature and 80 µm and 125 µm DTG® arrays (i.e. chains) are compared (Figure 4-3). The fibre in such research is typically a few meters long and contains 8 DTG®s in series with each DTG® having a length, L_{FBG}, of 8mm.

The used FBG reflectivity experimental approach, is based on a separate reflection measurement of each optical channel (i.e. fibre), and is conducted as following:

1. an FBG reflection measurement (Figure 4-3, left) is done using the setup as depicted in Figure 4-1 (the endface of the fibre treated to avoid Fresnel back reflections),
2. a reference reflection of the maximum Fresnel backreflection is measured (approx. 3.5%) of the fibre with splice, but without FBGs,
3. the calculation of the reflectivity is performed using the data of Step 1 & 2.

The procedure followed to determine the reflectivity is simple and straightforward, however, care should be taken that the back reflection at the fibre end face of the sensor chain is kept as low as possible. High back reflections increase the noise level, hence, they could interfere with the measurement signal in Step1, which eventually could lead to an inaccurate spectral response. For accurate spectral peaks, the noise level should be kept as low as possible, certainly when the spectral distance between two distinct peaks is small, see the example of 8 reflected Bragg peaks in Figure 4-3. Reducing the back reflection is typically done by cleaving the fibre end at a certain angle, typically 7° or 8° with regard to the normal axis of the fibre. The basic physics behind back reflection at angled facets is briefly explained in the following subsection.

4. 3. 1. Reducing back reflections by angled fibre facet

The theory behind the low total back reflection from an angled facet as shown in Figure 4-1 is explained by Figure 4-2. The incident ray is coming from inside the fibre along the fibre axis and is reflected at an angle of incidence, θ_i , at the fibre/air interface.

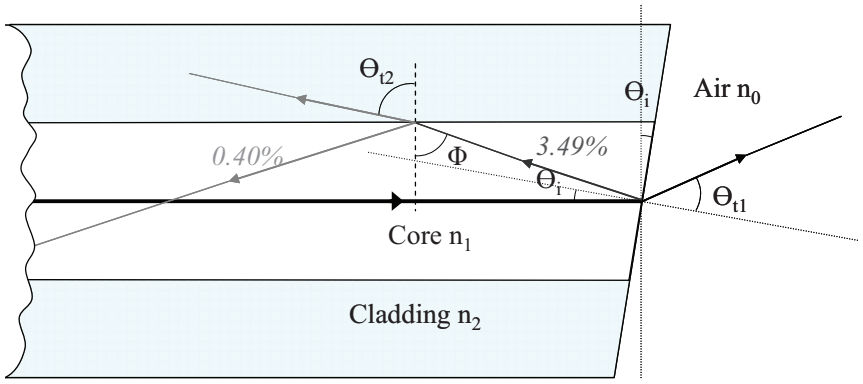

Figure 4-2: Backreflection occuring at an angled fibre end facet.

The intensity of the reflected light depends on the angle of incidence, which is dependent on the direction of polarization of the propagating light, i.e. perpendicular or parallel to the plane of incidence. The reflection coefficients can be calculated from [3]:

$$R_{\perp} = \frac{\sin^2(\theta_i - \theta_t)}{\sin^2(\theta_i + \theta_t)}, \qquad 4\text{-}1$$

and

$$R_{\parallel} = \frac{\tan^2(\theta_i - \theta_t)}{\tan^2(\theta_i + \theta_t)}, \qquad 4\text{-}2$$

with $R_{\perp}$ and $R_{\parallel}$ the coefficient of reflection for the field oscillation perpendicular and parallel to the plane of incidence, respectively. For unpolarized light the oscillations are assumed to be an equal mix of both and the reflection coefficient is then given by:

$$R_{unp} = \frac{R_{\perp} + R_{\parallel}}{2} \qquad 4\text{-}3$$

For an angle of incidence of $\theta_i = 7°$ and from $n_1 \sin\theta_i = n_0 \sin\theta_{t1}$, with $n_1 = 1.4593$ (Section 3.2.4) and $n_0 = 1$, the angle of transmission $\theta_{t1} = 10.24°$ and the reflection coefficients become $R_{1\perp} = 3.644\%$ and $R_{1\parallel} = 3.335\%$. For unpolarized light the reflection at the angled end facet is then $R_{1unp} = 3.490\%$

This small fraction of reflected light propagates backwards in the fibre and is refracted again at an angle of incidence ϕ, at the core-cladding interface along the length of the fibre, see Figure 4-2. Refraction occurs when $\phi < \phi_c$, from Equation 2-4 (Section 2.4.1) with $n_1 = 1.4593$ and $n_2 = 1.444$, the critical angle is $\phi_c = 81.7°$, for this type of highly GeO_2 doped fibre. Noting that $\phi = 180° - (90° + 2\theta_i) \approx 76°$ (Figure 4-2) $\phi < \phi_c$ is satisfied and thus the reflected light will be refracted at the core-cladding interface. By using $n_1 \sin\phi = n_2 \sin\theta_{t2}$ we find that $\theta_{t2} = 78.69°$. Again we can use Equations 4-1, 4-2 and 4-3 but replacing θ_i by ϕ, and θ_{t1} by θ_{t2} we obtain that the reflections coefficients at the core / cladding interface are $R_{2\perp} = 1.204\%$, $R_{2\parallel} = 0.986\%$ and $R_{2unp} = 1.095\%$.

The total backreflection for unpolarized light after being reflected at the endface and once being refracted along the fibre length is then found to be $R_{unp,total} = R_{1unp} \cdot R_{2unp} = 0.401\%$, which is very small compared to the initial reflection of 3.49%. Since such refraction occurs throughout the fibre length, the portion of light finally arriving at the detector will be negligible small. Hence, the back reflections can be highly reduced or even completely suppressed by using angle fibre facets. This is also the basic mechanism of an APC (Angled Physical Contact) low loss fibre connector.

It is noted that the same effect of low back reflection can be obtained by cutting the fibre end at random with a scissor until the backscatter level becomes minimal. In this work this procedure is used instead of the standard procedure using the angle cleaver. The reason because is that the angle cleaver is standard adjusted for 125 µm fibres. In the case of the 80 µm, angle cleaving was not optimal and the cleaving sometimes failed resulting in a high backscatter level. When using the angle cleaver, the coating should be stripped off before cleaving, which is in case of the 80 µm coated fibre, a little more difficult than for the standard 125 µm fibre, and takes some additional time. Therefore, in Step 1 it is preferred to manually cut the 80 µm fibres to minimize the backreflections.

4. 3. 2. The FBG reflectivity

In contrary to the first step, the measurement in the second step requires a maximum Fresnel back reflection to serve as reference level, see Figure 4-3, left. The reference level is plotted against the secondary y-axis of Figure 4-3, left. To achieve a high backreflection, the fibre end is cut straight using a standard fibre optic cleaver. The cut is performed after the splice (Figure 4-1), but before the first grating. As such the loss induced by the splice between connector pigtail and the draw tower fibre is taken into account when calculating the actual FBG reflectivity in Step3.

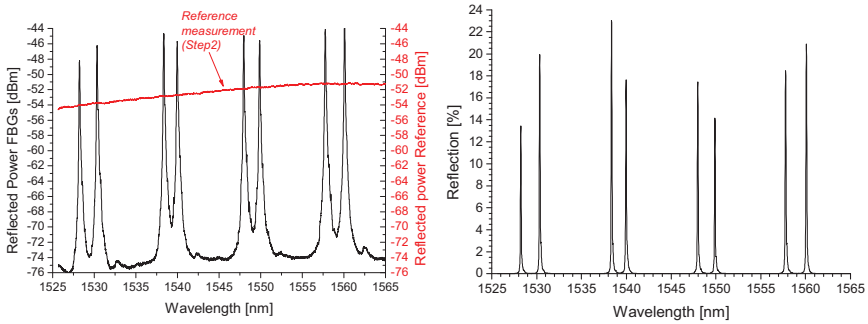

Figure 4-3: Example of the reflection of a 80µm DTG® chain and endface reference reflection in dBm (left), Calculated respective FBG reflectivity in % (right).

To determine the real reflectivity of each FBG, the total recorded spectrum is normalized to the Fresnel back reflected spectrum, to eliminate the spectral shape of the light source. The calculated reflectivity (intensity) is then given by:

$$I_{refl}(\lambda) = \frac{I_{FBG}(\lambda)}{I_{Fres}(\lambda)} \cdot R_{Fres} \cdot 100 \qquad 4\text{-}4$$

with

$$I_{FBG}(\lambda) = 10^{\frac{P_{FBG}(\lambda)}{10}}, \qquad 4\text{-}5$$

$$\mathrm{I}_{Fres}(\lambda) = 10^{\frac{P_{Fres}(\lambda)}{10}} \qquad 4\text{-}6$$

and

$$R_{Fres} = \left(\frac{n_0 - n_1}{n_0 + n_1} \right)^2 . \qquad 4\text{-}7$$

Where $P_{FBG}(\lambda)$ and $P_{Fres}(\lambda)$ are the measured spectra (in dBm) from Step1 and Step2 for the DTG® chain and Fresnel reflection, respectively (Figure 4-3, left). R_{Fres} is the Fresnel back reflection at the straight fibre end face, with n_0=1, the index of refraction of air and n_1=1.4593, the refractive index of the fibre core. This represents the actual fraction of the total incident power of the light source which is back reflected at the end face.
By filling in the values of the indices in Equation 4-7, $R_{Fres} = 3.488\%$. By substituting Equation 4-5 and 4-6 and by filling in R_{Fres} in Equation 4-4 the calculated reflectivity in percentage becomes:

$$I_{refl}(\lambda) = 10^{\frac{P_{FBG} - P_{Fres}}{10}} \cdot 3.488 \qquad 4\text{-}8$$

This equation is used in Step 3, to calculate the FBG reflectivity of all probes. The calculated values are summarized in Table 4-1:

Table 4-1: Summary table of all reflectivity values calculated from Equation 4-8.

Production Run	80µm	125µm
PR2007_1	20.99 ± 1.67 %	19.89 ± 1.55
PR2007_2	17.24 ± 3.28 %	15.72 ± 2.04
PR2008_1 (Nozzle1)*	18.12 ± 3.24 %	18.41 ± 1.82
PR2008_2 (Nozzle2)*	24.19 ± 0.90 %	/**
PR2009_1 (Nozzle3)*	4.31 ± 0.68 %	/**

As seen in Table 4-1, apart from the PR2009 trial, the reflectivity of the different chains ranges from 13 % till 25 % reflection. This is in good agreement with the standard reflectivity's of commercial DTG®s [4].The fluctuation in peak intensities (from Figure 4-3, right) is caused by power intensity fluctuations of the Excimer laser system during grating inscription and is visible in both 80 µm and 125 µm DTG®s chains. In all three validation runs (i.e. PR2007_1, PR2007_2 and PR2008_1), no significant difference in reflectivity between the 80 µm and 125 µm DTG®s is found. Hence, from the point of view of reflectivity, the same quality of single pulse FBGs (TypeI) is produced in a 80 µm and 125µm fibre. However, the 80 µm DTG®s of PR2007_2 and PR2008_1 showed some higher standard deviation. It is believed that the larger scattering is caused by the lower pulling force for the thinner fibre, this not to snap the fibre. Therefore, the fibre lateral movement can be slightly higher during drawing for a thinner fibre. The low reflection of approximately 4% for PR2009_1 is due to the low laser power, which was not

* The noted nozzles were used for the 80µm only.
** No more 125µm production runs executed (validation process was finished)

optimal at that time. Additionally, at this production run, Preform_80 was completely used, i.e. fibre material was gone. It is known that the amount of doping at the end of the preform is lower. Therefore the photosensitivity of the fibre is lower and the reflectivity of the single pulse gratings is lower as well.

4. 3. 3. The full width at half maxima (FWHM)

In analogy to signal processing to define the bandwidth of a signal at half of its power (i.e. at -3dB) the full width at half maxima (FWHM) is applied to define the spectral width of the Bragg peak at half the power of the peak. An example of the FWHM of a typical FBG spectrum is illustrated in Figure 4-4. The wavelength difference ($\Delta\lambda_{FWHM} = \lambda_{\max} - \lambda_{\min}$) is determined for all production runs of the 80 µm and 125 µm DTG®s shown in Table 4-1. The results are identical and it is found that $\Delta\lambda_{FWHM} = 110\,pm \pm 4.0\,pm$ for all DTG®s. Note that the length of the DTG®s is 8mm.

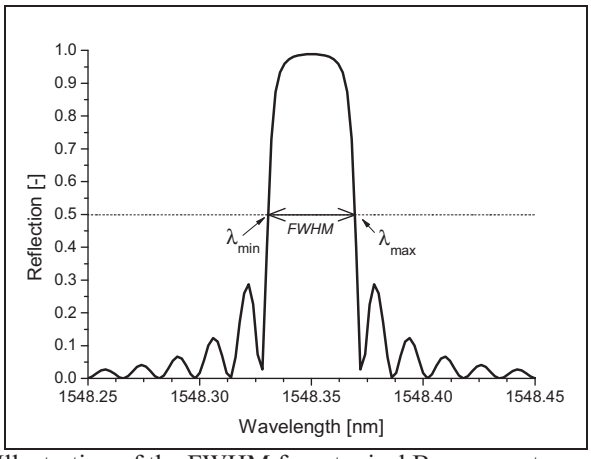

Figure 4-4: Illustration of the FWHM for a typical Bragg spectrum of a uniform FBG.

4. 4. CALIBRATION OF A NON-EMBEDDED DTG®

The Bragg-wavelength $\lambda_B(\varepsilon,T) = 2\bar{n}(\varepsilon,T)\Lambda(\varepsilon,T)$ of an FBG is specified by the effective refractive index of the fibre, $\bar{n}$, and the grating period, Λ. Both are dependent on strain and temperature and therefore, a mechanical as well as a thermal calibration is needed to define both sensitivities. The newly manufactured 80 µm- and the (classical) 125 µm reference DTG®s are calibrated for strain and temperature and the results are compared.

In Section 4. 4. 1. , several axial strain calibration methods to define the *strain gauge factor*, S_ε of the DTG, are discussed. In Section 4. 4. 2. , a transverse strain calibration method is applied. In this method, a diametrical compression setup is used to induce a *birefringence effect* in the core of the optical fibre. It allows to experimentally defining the *strain optic coefficients*, p_{11} and p_{12}. Further, the *temperature calibration* is discussed in Section 4. 4. 3. ; the *quadratic temperature coefficients*, S_{T1} and S_{T2} will be defined. The resulting strain and temperature sensitivities are consequently used as input for the experiments and calculations in

Chapter 6, 7 and 8, in which composite test-coupons with embedded DTG®s are loaded in a controllable manner.

4. 4. 1. Axial strain calibration

As has been mentioned before, an FBG is the optical equivalent of an electrical resistance strain gauge (RSG) or foil gauges, see Figure 4-5a. The strain gauge factor for RSGs (i.e. k-factor) is the proportionality factor between the relative change of the resistance and the strain being applied. In analogy with the RSG, an optical strain gauge factor, S_ε, which relates the Bragg wavelength shift to the strain present in the core of the optical fibre, is defined for the DTG®s.

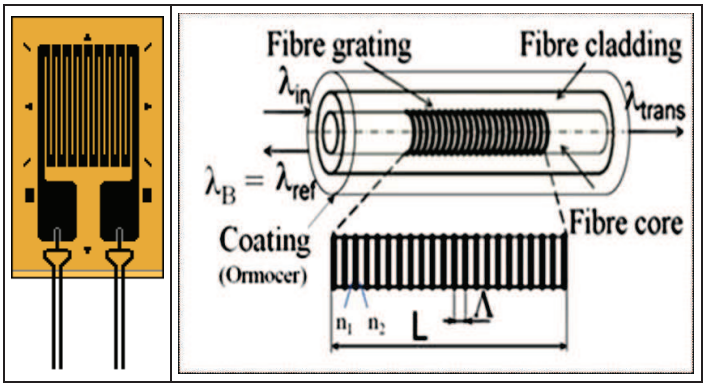

Figure 4-5: Electrical (foil) strain gauge (left), and coated fibre Bragg grating or optical strain gauge (right).

Common methods to calibrate electrical strain gauges make use of bonding the foil gauge with a suitable adhesive, such as cyanoacrylate, to a host beam with accurately known geometrical and material parameters. According to Window and Holister [5], a classical strain gauge is calibrated using the cantilever beam method. The same technique could be used to calibrate FBGs. However, there is a fundamental difference between a bonded flat thin foil gauge and a bonded circular fibre. In the case of a foil gauge, the bonding surface area is large and the adhesive layer between the strain gauge and the substrate is very thin. In the case of a bonded FBG, the fibre is completely surrounded with adhesive and only a small fraction of the adhesive layer is located between the fibre and the substrate. This is illustrated in Figure 4-6:

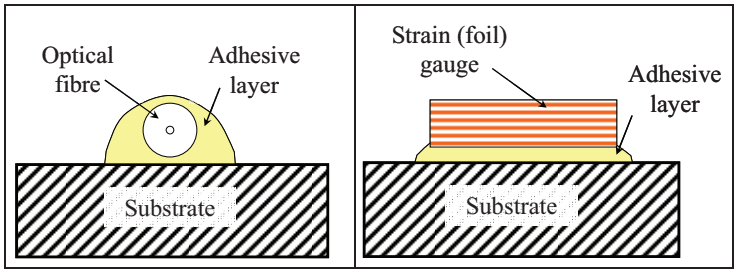

Figure 4-6: Illustration of the surface bonding of an optical fibre (left), and an electrical strain (foil) gauge (right).

It is clear that the strain transfer mechanism in both cases differs. Investigations on the axial strain transfer mechanism of bonded optical fibres with coating, have shown that a discrepancy exists between the strain of the substrate, its surface and the core of the optical fibre if the strain transfer is not optimal [6-7]. So, for accurate axial strain measurements, a number of parameters like the substrate stiffness, the kind of adhesive material, the adhesive thickness, the fibre coating type, the coating thickness, the bonding length, and last but not least the transverse strain effects because of a possible mismatch in Poisson's ratio between substrate and sensor need to be considered. In particular, the (multi-axial) strain transfer mechanism with respect to embedded optical fibres is discussed in Chapter 7.
Because of the uncertainties of the upper mentioned parameters with relation to a bonded FBG, calibration of a non-bonded FBG is preferred in this work. One of the non-bonded FBG calibration methods, is fixating an optical fibre piece at both ends of the fibre over a certain length, and applying force (or displacement) to strain it. Typically, the FBG is located in the middle of the fibre piece.

4. 4. 1. a. Theoretical background on the strain gauge factor

In all strain calibrations discussed in this work an isothermal condition (dT=0) is supposed, as such only the derivation of the Bragg equation shift as function of applied strain is considered. The *general Bragg wavelength* for a free fibre grating is given by (Appendix B, Equation B-5):

$$\lambda_B(d\varepsilon_i) = 2\overline{n}(d\varepsilon_i)\Lambda(d\varepsilon_i), \tag{4-9}$$

with both the *effective refractive index* $\overline{n}(\varepsilon)$ and the *grating period* $\Lambda(\varepsilon)$ being strain dependent. By deriving Equation 4-9 to strain and working out the linear relationship between the impermeability tensor and strain optic tensor for an isotropic medium and assuming pure axial strain the well known response of an FBG to an axial strain field is given by (Appendix B, Equation B-18):

$$\frac{d\lambda_B}{\lambda_B} = (1-P)d\varepsilon_{3'}, \tag{4-10}$$

with P the *strain-optic constant* defined by:

$$P = \frac{1}{2}\overline{n}^2\left(p_{12} - \upsilon_f\left(p_{11} + p_{12}\right)\right), \tag{4-11}$$

with p_{ij} the strain optic coefficients and ν_f the Poisson's ratio of the silica fibre.

Equation 4-10 can be integrated, see Appendix B, and by defining $(1-P)=S_\varepsilon$, the longitudinal *strain gauge factor*, or S_ε – *factor*, and using an arbitrary wavelength $\lambda_{B,0}$ at a corresponding axial strain $\varepsilon_{3',0}$ one gets (Appendix B, Equation B-22):

$$\ln\frac{\lambda_B}{\lambda_{B,0}} = S_\varepsilon \Delta\varepsilon_{3'} \qquad 4\text{-}12$$

with λ_B, the measured wavelength with regard to the initial Bragg wavelength, $\lambda_{B,0}$, and $\Delta\varepsilon_{3'}$, the strain in axial direction of the fibre (the indices ' are used to avoid confusion with the coordinate system of a single layer of a composite laminate).

Substitution of $p_{11}=0.113\pm0.005$, $p_{12}=0.252\pm0.005$ [8], $\nu_f=0.16$ for GeO_2 doped (quartz)glass-fibre [9] and $\bar{n}=1.4459$ (Chapter 3), in Equation 4-11, results in a strain-optic coefficient of $P=0.2024\pm0.0053$. Consequently, the theoretical strain gauge factor for the fibres in this work becomes $S_\varepsilon=0.7976\mp0.0053$.

Note that, if we would assume small wavelength and strain variations in Equation 4-10 such that $d\lambda_B=\Delta\lambda_B$ and $d\varepsilon_{3'}=\Delta\varepsilon_{3'}$, we would obtain the general 'linear' approximation which is often applied in literature to calculate the longitudinal strain from FBG readings. Obvious, from the integration elaborated above, the linear formula is the approximation of the mathematical correct logarithmic approach of Equation 4-12. If we would plot both equations against the applied strain during calibration, the results will thus not be equal, see Figure 4-7, left. A very small difference occurs, which is nearly invisible from Figure 4-7, left. However, if we calculate the difference of both curves (i.e. $(\Delta\lambda_B/\lambda_{B,0}-\ln\lambda_B/\lambda_{B,0})$ with respect to $\ln\lambda_B/\lambda_{B,0}$ we obtain the relative error which increases with applied strain, see Figure 4-7, right. The slope of the error curve is found approximately 0.004 / %strain. At low strain levels (e.g. <0.2 %) the linear equation is well approximated and errors stay below 0.1 %. However, if strains on the fibre are applied above 1.25 % the error exceeds 0.5 %, hence the calculated S_ε-factor from Equation 4-10 will be overestimated. This is an important notice with regard to the strain calibrations further applied in this Section, as the applied strain in the axial calibrations is ranging between 0.45 % and 2 %.

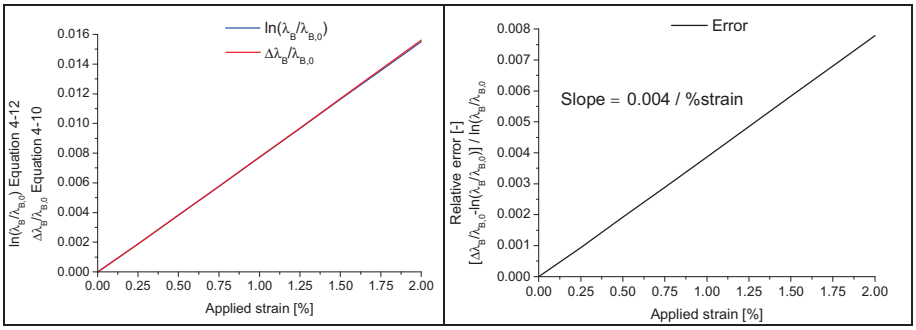

Figure 4-7: Difference between the linear and logarithmic approach (left), relative error with respect to the logarithmic approach (right).

Theoretical S_ε factor

The values found in literature for $\overline{n}$, ν_f and p_{11} and p_{12} show a relatively large scatter. Often the strain optic coefficients of Bertholds and Dandliker [8] are used, however, sometimes even the values of bulk silica are found in research. For the Poisson's ratio of silica very often $\nu_f = 0.16$ or $\nu_f = 0.17$ is found. For the effective refractive index of silica many times the value for pure silica is used (i.e. $\overline{n} = 1.458$), however, this is the refractive index at a wavelength of 0.6 µm, and thus does not count for wavelengths at 1.5 µm. Obvious if one uses different coefficients, the theoretical strain gauge factor can change considerably. As an example and to form an idea on the possible scatter of the theoretically determined S_ε factor, the author has calculated the S_ε factor (using Equation 4-12) for a few cases, by varying the values of the input parameters ($\overline{n}$, ν_f and p_{11} and p_{12}) often found in literature. Additionally, the author has used the strain optic coefficients which are experimentally determined in the scope of this work (Section 4. 4. 2. b.). The results are given in Table 4-2.

Table 4-2: Theoretical strain gauge factor for different cases.

Case	Optical parameters	Mean S_ε factor
Eli Voet (Theory)*	$\overline{n} = 1.4459$, $\nu_f = 0.16$ $p_{11} = 0.113 \pm 0.005$, $p_{12} = 0.252 \pm 0.005$	0.7976 ± 0.0053
Eli Voet (Experimental) (Section 4. 4. 2. b.)	$\overline{n} = 1.4459$, $\nu_f = 0.16$ $p_{11} = 0.112 \pm 0.008$, $p_{12} = 0.256 \pm 0.017$	0.7949 ± 0.0166
Abdi et al. [10]	$\overline{n} = 1.458$, $\nu_f = 0.17$ $p_{11} = 0.121$, $p_{12} = 0.270$	0.7837

From the scatter on the values in Table 4-2, we obtain a minimum and maximum theoretical value of $S_\varepsilon = 0.7924$ and $S_\varepsilon = 0.8029$. As such a variation of more than 0.7 % exist on the calculated strain compared to the mean theoretical value ($S_\varepsilon = 0.7976$). If we take a look at the mean S_ε factor found by Abdi et al. [10], the calculated strain is more than 1.7 % smaller compared to the mean theoretical value. By using the experimental obtained values determined in the scope of this work, the mean S_ε factor is found to be close to the theoretical value, using Bertholds' and Dandliker' strain optic coefficients. However, taking into account the large scatter on the experimental values, the calculation of the S_ε factor shows a large scatter as well. In this case a variation of more than 2 % is found. This exercise shows that the 'theoretical' S_ε factor varies significantly, and hence relative large errors are made

* using the values of Bertholds and Dandliker [8].

on the absolute strain calculation. Because of the possible errors we can make by using the theoretical strain gauge factor, the author emphasizes the importance of accurate axial calibrations of the FBG.
To calibrate the S_ε factor different axial calibration setups are used in this work. The setups and methods will be elaborated in the next paragraphs.

4. 4. 1. b. Calibration of the strain gauge factor

The calibrations in this work are performed on non-bonded coated DTG®s with a (gauge) length, L_{FBG}, of 8 mm. The calibrated 80 µm DTG®s originate from production run PR2008_1 and PR2008_2 (Chapter 3, Table 3-3), and have a coating diameter of approximately 140 µm. The 125 µm samples originate from production run PR2007_2 and PR2008_1, and have a coating diameter of approximately 190 µm. Preferable, a long piece of fibre (not always possible in the different calibration setups, see further) is clamped or fixed at two sides of the fibre with in the middle the DTG®. In this work, different approaches were applied to determine the strain gauge factor. All approaches were based on the use of two stages to which the fibre is fixed, however, different methods of fixating the fibre ends were examined. Automated- and manual setups were used to apply the axial strain on the fibre. All calibrations discussed in this section were performed at room temperature. In Section 4. 5. 2. a. the dependency of the strain gauge factor will be studied for a larger temperature range.

An automated and a manual calibration setup were used to perform the axial strain calibrations of the non-embedded fibres: The Automated calibration is executed on the same tensile test-frame (ZwickZ010), which has been used to test the tensile strength of the fibres (Section 3.4). As mentioned before, adapted fibre clamps with spools are used to hold the fibres and additional to the setup used during tensile testing, an optical extensometer with reflection points fixed to the fibre, is used to measure the applied strain (Figure 4-8). The manual calibration uses manually operated translation stages with different fibre clamping or fixation methods (Figure 4-11 and Figure 4-13)

Both calibration setups use the same interrogation equipment (i.e. FBG-scan X08 with depolarized light source) to read out the sensors. A second (stripped) DTG®, located next to the DTG®(s) under test, is used to compensate for intrinsic temperature effects. Additionally, during testing, the automated test setup is closed with Plexiglas sliding doors, and in the manual test setup the fibres are covered using a cardboard, to eliminate possible temperature fluctuations (Figure 4-13).

I. AUTOMATED CALIBRATION

The first setup consists of two stages to hold the fibre. The bottom stage is fixed to the frame (stationary) and the upper displacement stage is connected to a 200N loadcell, which is fixed to the cross-head which is automatically controlled (Figure 4-8, left). The fibre is wound up at both sides on two spools with thread, and fixed using the fibre clamps. By moving the (upper) displacement stage upwards, the fibre is stretched. A small reflector strip is stuck on two locations of the fibre, which

defines the nominal fibre length (i.e. gauge) (Figure 4-8, right). An optical extensometer system registers the distance between the reflection points and calculates the gauge length. Blocking the reflectors of rotation is important, to avoid measurement errors due to faulty reflections towards the optical system. Therefore, the fibre is positioned very close to a friction free backplane, see Figure 4-8, right, to freely move in the vertical (axial) direction without rotation. The relative movement between the reflection points related to the initial distance (i.e. gauge length) is here a measure for the applied strain.

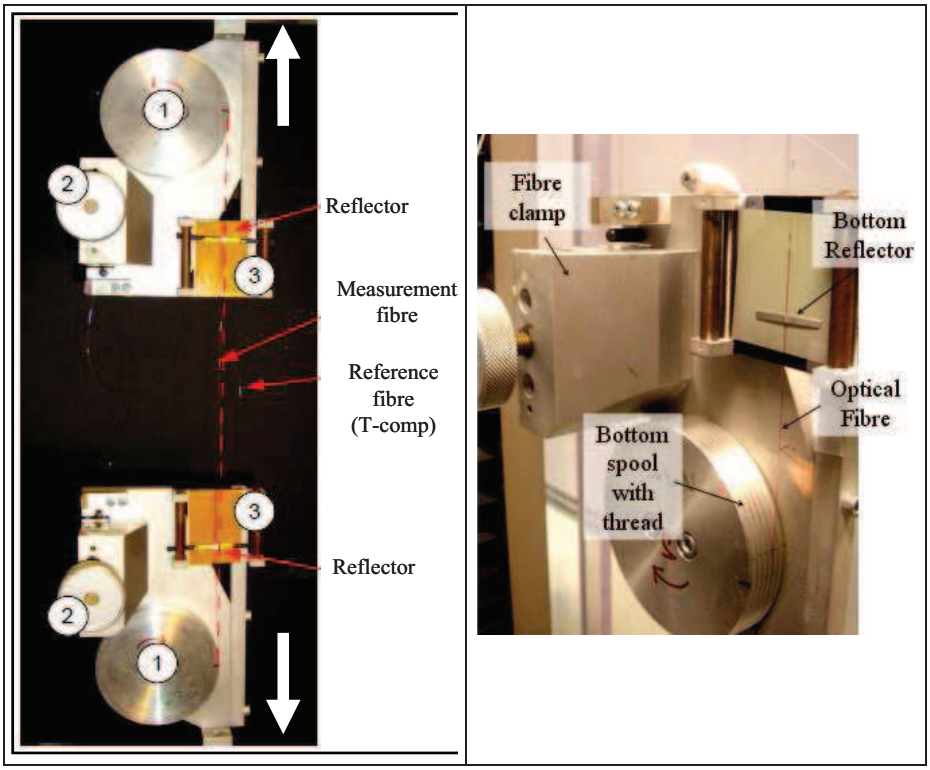

Figure 4-8: Automated calibration setup with the fibre tensioned between two stages mounted in the Zwick test-frame, with spools to wind up the fibre (1), fibre clamps to pretension the fibre on the spools (2), additional stages with high temperature polyimide film, to avoid fibre and reflectors from torsion (3) (LEFT), zoom of the bottom spool with thread to wound up and clamp the fibre (RIGHT).

Two different methods (Stepwise progressive loading and Ramped loading) are applied for the Automated setup: the Stepwise progressive loading and the Ramped loading. Firstly is discussed the Stepwise loading.

Stepwise progressive loading

The stepwise progressive loading method is performed using progressive steps of 0.3 % of strain up to maximum 1.2 %. The Zwick test-frame is set on strain control, and for each step the strain is held constant for approximately 80 seconds. The

gauge length between the reflection points is approximately 0.3 m. A small pretension is given at the start of the calibration to prestrain the fibre. This keeps the fibre windings better within the thread of the spool and thus measurement errors at the calibration start are avoided.
All test samples consist of an array of 2 DTG®s with a nominal wavelength of 1532 nm and 1548 nm, and a spatial separation of 250 mm, so, two sensors are calibrated at once. Both DTG®s are positioned in between the reflection points. In total, two 80 µm and three 125 µm samples are used and for each sample the calibration is repeated 5 times (Table 4-3). To calculate the S_ε-*factor*, the measured wavelength shift is logarithmically plotted against the measured strain perturbation according to Equation 4-12, see Figure 4-9:

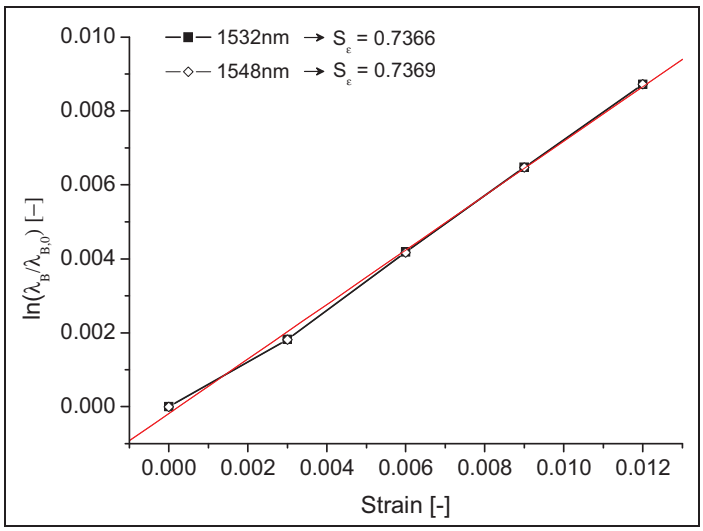

Figure 4-9: Example of a calibration curve for a 80µm DTG® pair using Setup I, stepwise loading.

The linear slopes of the curves in Figure 4-9 represent the S_ε-factor of the DTG®s. A non-linearity at 0.3 % applied strain in all the curves (80 µm and 125µm DTG®s) shows that the accuracy of the optical extensometer is not satisfying for strain levels below 0.5 %. According to the specifications of the optical extensometer, the accuracy on measuring the displacement is 5µm. However, afterwards in additional tests, drifts of more than 20 µm were registered without moving the stages. According to the manufacturer, the reason is found in the rather simple proportional control of the optical extensometer. As such, it is believed that the system is not reliable when using the stepwise approach. The calculated average of the S_ε-*factor*s and their standard deviations are given in Table 4-3:

Table 4-3 Overview of the axial calibration of 80µm and 125µm DTG®s using the automated test setup using a stepwise testing method

DTG® Sample	# samples	# tests / sample	S_ε-factor
80µm (PR2008_1)	2 (x2)	5	0.7318 ± 0.0103
125µm (PR2007_2)	3 (x2)	5	0.7466 ± 0.0211

Although these results are not very accurate, and the S_ε-*factor* of both sensors is far below the theoretical calculated value (i.e. 0.7976), we can already notice that the strain gauge factor for both the 80 µm- and 125 µm DTG®s are to be expected in the same range.

Ramped loading

Using once more the automated test setup, however, with the clamping stages closer together to make this fit in a climatic chamber (see Section 4. 5. 2.), *a ramped loading scheme* (0.017 N/sec) is used to calibrate the sensors. The strain is increased up to 1.5 %. Because of the limited space in the climate chamber, the distance between the reflectors is only 0.2 m (0.1 m smaller than for the step-wise loading). In total three 80 µm samples and three 125 µm samples are tested. The calibrations were repeated three times, however, some of the samples broke during testing, as such not all every calibration is repeated three times (see Table 4-4 for the exact number of tests). The Zwick test-frame is now used in load control with a fixed ramp to tension the fibre. Because no synchronization was available between the optical interrogator and the tensile bench, a slightly different approach is used to define the strain gauge parameter. The strain rate, ($d\varepsilon_{3'}/dt$), is monitored with the optical extensometer and simultaneously the wavelength shift in time, ($d\lambda/dt$) is monitored with the FBG interrogator. An example of such plots is shown in Figure 4-10:

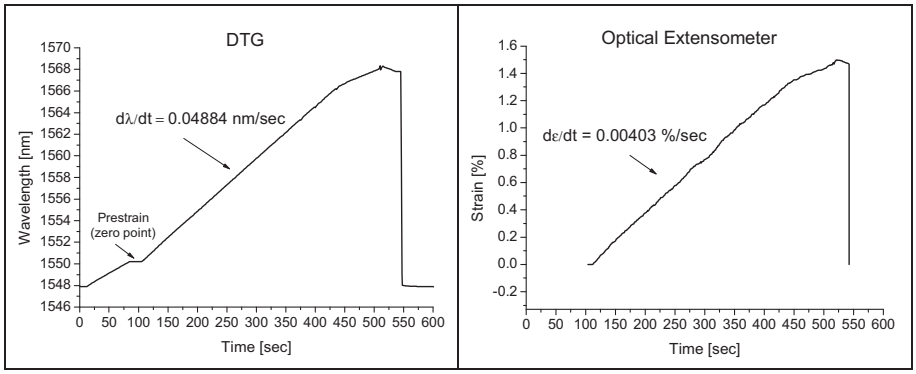

Figure 4-10: Plot of the wavelength versus time (left), plot of the applied strain versus time (right).

To determine the wavelength shift as function of the applied strain, ($d\lambda/d\varepsilon_{3'}$), the ratio of both slopes is taken which is given by:

$$\frac{d\lambda}{d\varepsilon} = \frac{\frac{d\lambda}{dt}}{\frac{d\varepsilon_{3'}}{dt}}. \qquad 4\text{-}13$$

The logarithmic formula of Equation 4-12 cannot be used here. Therefore, the S_ε-*factor* is found by using the relation between Bragg wavelength and strain given by Equation B-18 (Appendix B). The strain gauge factor is then given by:

$$S_\varepsilon = \frac{1}{\lambda_{B,0}} \frac{d\lambda_B}{d\varepsilon_{3'}}, \qquad 4\text{-}14$$

with $\lambda_{B,0}$, the initial nominal wavelength (zero point in Figure 4-10, left) of each calibration. The calculated averages of the S_ε-factor and their standard deviations are found in Table 4-4. Note that Equation 4-14 is similar to Equation 4-10. As mentioned, when using Equation 4-10 instead of using the logarithmic approach of Equation 4-12, errors in the order of -0.004 / % strain can occur in the calculated strain. For an applied strain of 1.5 % during calibrations, the *S_ε-factor* calculated using Equation 4-14, will then be approximately 0.6 % higher simply because of the error between the two approaches.

Table 4-4: Overview of the axial calibration of 80µm and 125µm DTG®s using the automated test setup using a ramped loading scheme

DTG® Sample	# samples	# tests (total)	S_ε-factor
80 µm (PR2008_1)	3	7	0.7866 ± 0.0153
125 µm (PR2008_1)	3	8	0.8004 ± 0.0211

Compared to the stepwise progressive calibration method, the nominal value of the *S_ε-factor* has increased (most probably due to the use of Equation 4-14), and approximates now the theoretical calculated value of 0.7976, though, the large scatter on the *S_ε-factor* remains the same. The experimental determined S_ε-factor remains in the same magnitude for both types of DTG®s (80 µm and 125 µm diameter). The accuracy of the strain measurements at lower strain levels is improved compared to the stepwise procedure, however, from Figure 4-10, right, after approximately 300 seconds we observe a fluctuation in the strain curve which is not clearly present in the wavelength plot, see Figure 4-10, left. At a certain strain level, exertion of the fibre in the thread on the spools occurs, which causes the fibre to relax (i.e. slip) a bit. Although the wavelength fluctuations due to the slippage are very small, and almost invisible (Figure 4-10, left), this his causes inaccurate strain measurements of the optical extensometer system. If we plot the force against time, we neither observe these kind of fluctuations. This behaviour has been noticed almost in all calibrations and is probably inherent to the optical extensometer system. Different procedures have been tried to optimize the measurements. However, no real improvements on the results is realised and no real explanation of the phenomena is found. Once more, it is believed that the large scatter in the *S_ε-factor* is solely owing to the inaccurate strain measurements of the optical extensometer system because of the rather simple proportional control, as explained for the Stepwise loading approach..

II. MANUAL CALIBRATION

In order to avoid a large scatter on the strain measurements another approach has been tried out. A manual calibration setup is used instead. The principle of straining the fibre is the same as the automated step-wise progressive loading: the fibre is stretched between two stages, with one end fixed to a stationary stage and one end to a displacement stage which can be moved by manually controlling a micrometer.

The strain on the fibre is calculated by dividing the relative movement of the displacement stage with the initial length of the fibre.

Two different methods of fixating the fibre ends are envisaged:clamping the fibre on small spools with thread (Figure 4-11) and fixating the fibre in steel capillaries (Figure 4-13).

Spools with thread to clamp fibre

This manual calibration test setup has been designed during a master thesis project and consists of two stages which fit on a rail (Figure 4-11, top). A fast and non-destructive calibration test setup was aimed for. The displacement stage can move by manually controlling a micrometer; the stationary stage is fixed on the rail using a screw. Small aluminium spools, provided with thread, are developed to wind up the fibre; a small nylon shell, provided by thread as well, is used to clamp the fibre without damaging its surface. The nylon shell thread fits exactly in the thread of the aluminium spools. A clamping ring is used to fix the two parts and thus grip the fibre (Figure 4-11, bottom).
By manually controlling a micrometer, with its head pushing the displacement stage (Figure 4-11, bottom), strain is applied on to the fibre. The maximum applied strain is 2%. Progressive steps of approximately 0.25% are used. For each step the strain is held constant for approximately 60 seconds. The nominal length of the fibre between the two fixation points is taken 0.8 m (at the prestrain level). Before the calibration test, the fibre is, first, put at the maximum strain (2%) for a short time to avoid slippage during the calibration test. Afterwards, at the start of the measurements, the fibres are pretensioned. This is called the zero-point for each calibration.

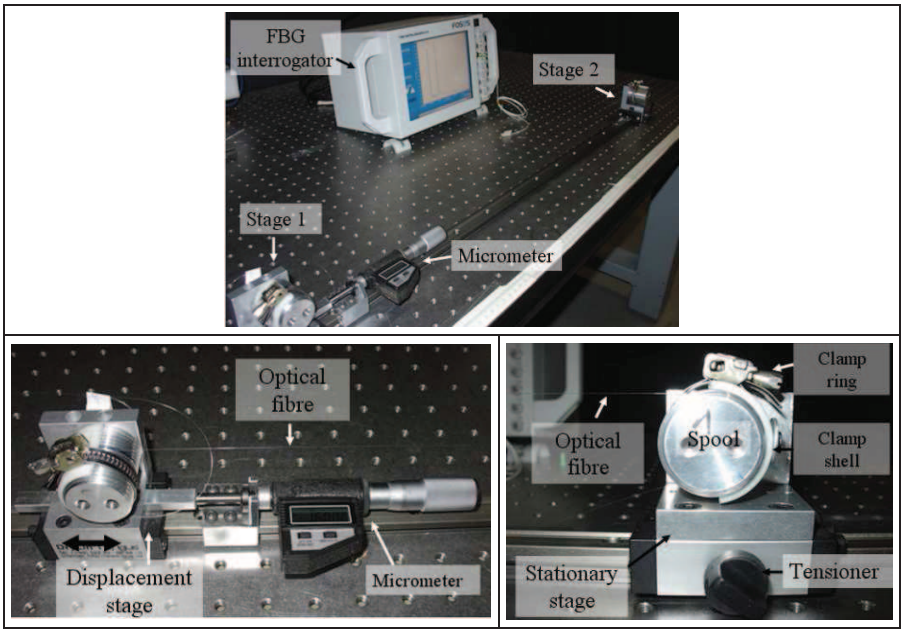

Figure 4-11: Manual calibration setup with the fibre tensioned between two stages (top), small threadwired spools to wound up and clamp the fibre (bottom).

All test-samples consist of an array of 2 DTG®s with a nominal wavelength of 1532 nm and 1548 nm, and a spatial separation of 250 mm. So, two sensors are calibrated at once. Only two 80 µm samples and one 125 µm sample were used to determine the S_ε-*factor*, because a large number of tests failed and a number of test-specimens got damaged during optimisation of this calibration setup. The calibration was repeated 2 times for the 80 µm DTG®s and three times for the 125 µm DTG®s (Table 4-5). To determine the S_ε-*factor*, the measured wavelength with respect to the initial wavelength, $\lambda_{B,0}$ is plotted logarithmic as function of the measured strain difference using Equation 4-12, and fitted linear (Figure 4-12). The slope of these curves represents then the S_ε-*factor*. The respective values of all calibrations are found in Table 4-6. The scattering on the S_ε-*factor* using this calibration setup is five to even ten times better than the one for the automated setup. Although not the same amount of sensor probes are calibrated and comparison is not really statistically justified, it is believed that the manual calibration is much more accurate. In Figure 4-12 an example of the manual calibration of the 80 µm and 125 µm DTG® pair using the spool setup is plotted. According to the plots, it seems that the 80 µm DTG®s have a smaller strain gauge factor than the 125µm DTG®s. However, if we examine the curves of the 80 µm DTG®s more in detail, we notice a non-linearity which is not visible for the 125µm DTG®s.

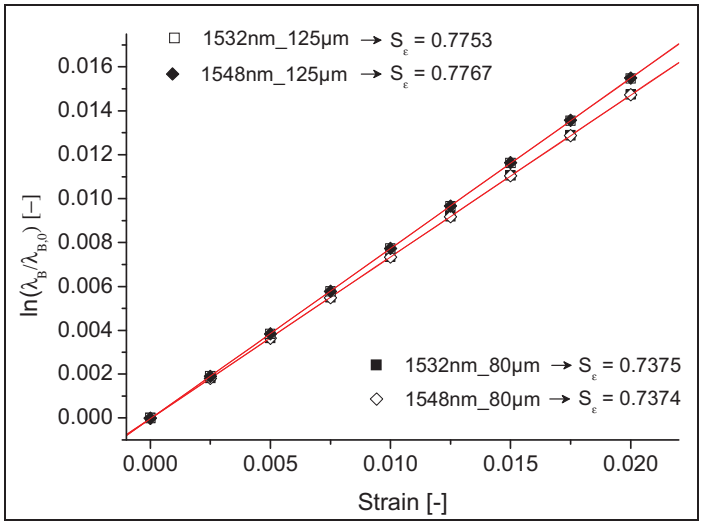

Figure 4-12: Example of a calibration curve for an 80 µm and 125 µm DTG® pair using the manually controlled setup with spool and thread to clamp the fibre,

It is believed that the origin of this effect lays in the ineffective clamping, especially at higher strain levels, of the thinner fibre in the aluminium spools. During optimization of the setup, this effect was fully eliminated for the 125 µm by using an extra clamp ring (Figure 4-11, bottom). However, for the 80 µm DTG®s, small slippage still occured. As a consequence, the applied displacement does not agree with the elongation of the fibre and the S_ε-*factor* of the 80 µm DTG®s is underestimated.

Table 4-5: Overview of the axial calibration of 80µm and 125µm DTG®s using the manually controlled setup with spool and thread to clamp the fibre.

DTG® Sample	# samples	# tests / sample	S_ε-factor
80µm (PR2008_1)	2 (x 2 DTGs)	2	0.7415 ± 0.0032
125µm (PR2007_2)	1 (x 2 DTGs)	3	0.7765 ± 0.0010

Fibre fixation via steel capillaries

Manual calibration of DTG®s using a spool to fixate the fibre is advantageous, because of the reusage of the fibres, however, slippage of the fibre and hence faulty strain calibrations can occur, certainly when considering an 80 µm optical fibre. In another attempt, the fibres are fixated in small steel capillaries. As for the setup with spool, a stationary stage and a displacement stage with micrometer is used to strain the fibre (Figure 4-13, left), however, now, the fibre is pulled through two steel capillaries with a length of 40 mm, an inner diameter of 0.9 mm and an outer diameter of 1.2 mm. They are fixed to the fibre using an epoxy glue. Afterwards, the capillaries are anchored in the two stages (Figure 4-13, right). The setup allows calibrating two separate optical fibre lines at once.

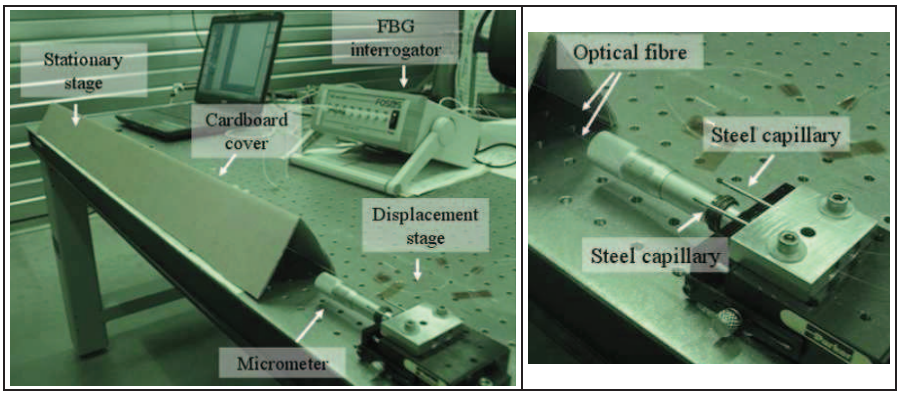

Figure 4-13: Manual calibration setup with the fibre tensioned between two stages (left), detail of the displacement stage with the anchored steel capillaries in which the fibre is embedded (right).

In total ten 125 µm single DTG®s and two 80 µm DTG® arrays consisting of eight sensors ranging from 1528 nm till 1548 nm, separated by 5 cm, are calibrated (Table 4-6). Because of the limited number of 80µm sensor lines, the calibration is repeated twice for the 80 µm DTG® arrays. The initial length of the fibre between the two fixation points is 0.8 m (at prestrain level).
The fibres are strained up to 0.45% using progressive steps of approximately 0.032%. For each step, the strain is kept constant for approximately 20 seconds. In Figure 4-14 a calibration curve of an 80 µm DTG® with minimum (1528 nm) and maximum (1548nm) initial wavelength is shown as an example.

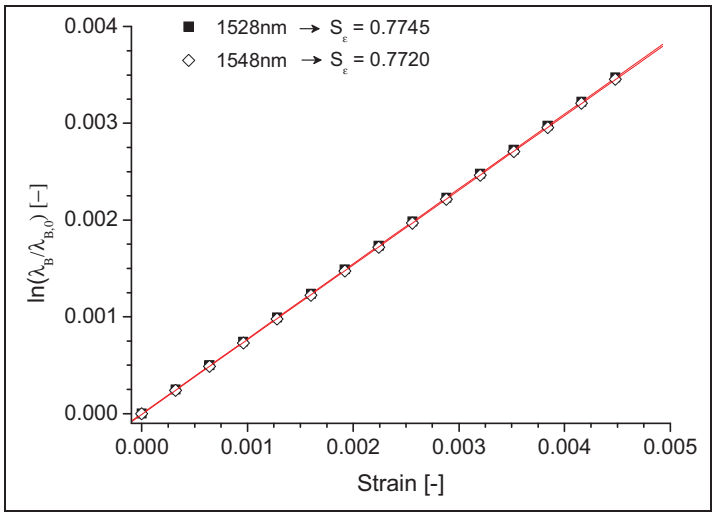

Figure 4-14: Calibration curve of two 80 µm DTG®s using a manually controlled setup in which the fibre is fixed to two anchored steel capillaries.

Again, the *S_ε-factor* is a little bit lower than the theoretical obtained value ($S_\varepsilon = 0.7976$), however, it is almost identical for the 80 µm and 125 µm DTG®s (Table 4-6). Moreover, the obtained value of the 125 µm sensors is quite similar to the one obtained by using the spools (Table 4-5). The scatter on the results is very low and is in the same order of magnitude as found for the spool setup. No difference is found between the 80 µm and 125 µm DTG®s.

Table 4-6: Overview of the axial calibration of 80µm and 125µm DTG®s using a manually controlled setup in which the fibre is fixed to two anchored steel capillaries.

DTG® Sample	# samples	# tests / sample	S_ε-factor
80µm (PR2008_2)	2 (x 8 DTG®s)	2	0.7764 ± 0.0021
125µm (PR2008_1)	10 (x 1 DTG®)	1	0.7773 ± 0.0020

Remark:
Instead of using anchored steel capillaries filled with epoxy to fix the fibre, the author has also experimented with fast-acting cyanoacrylate adhesive, to glue the fibre directly to the stages. The advantage of using such technique is that the steel capillaries become redundant by which you save time. Usually epoxy take some minutes (or hours) to cure depending on the curing temperature, in contrast with a fast-acting adhesive which only takes a few seconds. In addition, it is found that if the fibre is glued along approximately 3 cm at both ends, the calibration results do not differ.
However, care should be taken when fixating the optical fibre directly to the surface of the stages, certainly in the case of the 80 µm fibres. Uniform pressure (!) should be applied along the length of the glue-zone for a few seconds, If this is not the case, release of the fibre is possible during the calibration test.

4. 4. 1. c. Summary of the S_ε-factor

An overview of all the results (*S_ε-factor*) of the aforementioned setups and calibration methods is given in Figure 4-15:

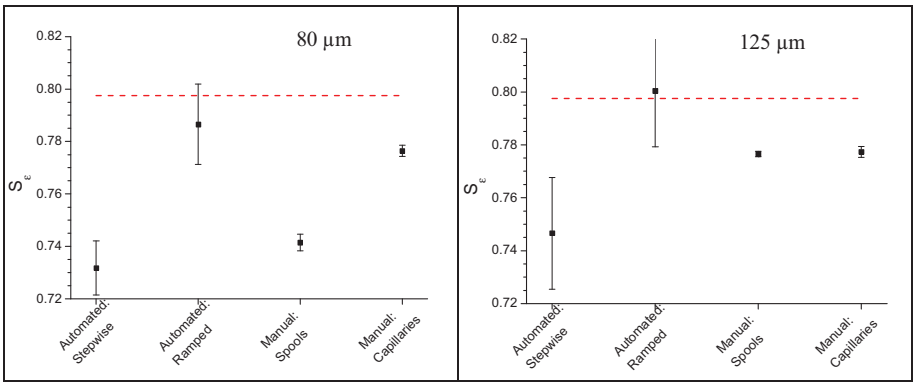

Figure 4-15: The mean S_ε-factors and resulting scatter for the different calibration setups. The theoretical value is indicated by a dashed line.

Remark that, a large scatter for the automated calibrations and a very small scatter for the manual calibrations has been found. Moreover, the absolute value for the automated setup significantly varies in how load is applied. For the 125µm DTG®s, the manually controlled setup with spools and thread to fix the fibre gives comparable results with the automatically controlled setup with ramped loading.. The results for the 80 µm DTG®s when using the manually controlled setup with spools are not satisfying. The manually controlled setup with anchored capillaries is the most accurate and repeatable calibration method, especially when considering 80 µm DTG®s. Nevertheless, the values obtained for the manually controlled calibrations (≈0.777) are still a little bit lower than the theoretical determined *S_ε-factor* of 0.7976 (dashed line in Figure 4-15, see also Table 4-2). The discrepancy is mainly caused by the uncertainty on the strain transfer of the steel capillary to the coated optical fibre which are bonded together with a thin adhesive layer.

In [6] the strain transfer mechanism of bonded optical fibres with coating has been investigated in detail. Wan et al. refer to the aforementioned effect as the shear lag characteristic of the bonded optical fibre. The shear lag coefficients represents the 'lagging' of the strain development in the optical fibre relative to the component and depends on the mechanical properties of the adhesive and that of the fibre coating, and on the bonding length. This is illustrated in Figure 4-16:

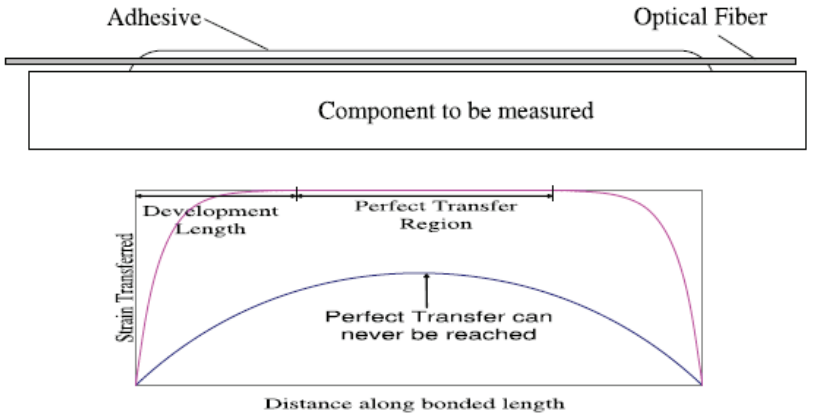

Figure 4-16: Illustration of the shear lag of a bonded optical fibre [6].

In the case of a small shear lag, for instance if a very soft coating is used, or if the bonding length is insufficient, a perfect strain transfer from the component to the fibre can never be reached. Wan et al. have used an empirical approach based on finite element results to modify the shear lag characteristic so that the analytical model of Li et al. [7] is valid for high shear lag characteristic. The shear lag coefficient can then be used to determine the strain transfer coefficient at any position along the bonded optical fibre, as depicted in Figure 4-16, bottom.

It is not the intention of the author to reproduce the investigations of Wan et al., however, based on the results presented in their paper, the author assumes that, the shear lag effect is the main cause of the differences between the theoretical and the experimentally determined S_ε*-factors*. The problem in this work, is the reverse case of what is studied by Wan et al.. Instead of straining the substrate on which the fibre is bonded, the fibre is strained by moving a rigid translation stage and thus the capillary in which the fibre is fixated with epoxy. The ratio between the theoretical S_ε*-factor* of 0.7976 and the experimentally determined S_ε*-factor* of 0.7769 (mean value from Table 4-6) represents the so-called strain transfer coefficient and equals to $0.7769 / 0.7976 = 0.974$.

The large difference in theoretically obtained gauge factors (Table 4-2) strongly affects the upper calculated strain transfer coefficient. The author emphasizes that no exact determination of the p_{11} and p_{12} parameters exists in literature for the highly GeO_2 – doped optical fibres used in this work. Therefore, the real theoretical value is difficult to predict and it is not possible to exactly define the strain transfer coefficient for this calibration setup. Therefore the experimental obtained value of $S_\varepsilon = 0.7769 \approx 0.777$ is taken for the calculations further used in this work.

In the next section the transverse calibration is discussed. Here a diametrical loading setup is used to define the p_{11} and p_{12} of the fibres experimentally.

4. 4. 2. Transverse strain calibration

4. 4. 2. a. Strain induced birefringence in DTG®s

We define, $d\varepsilon_{1'}$, $d\varepsilon_{2'}$, $d\varepsilon_{3'}$, as the three main strain perturbations along the fibre axes, see the coordinate system of the optical fibre in Figure 4-17, left. Shear will not be considered in this work because they have no effect on the refractive indices of the (isotropic) optical fibre and thus they do not affect the Bragg wavelength shifts [11-12]. When a *differential transverse strain* ($d\varepsilon_{1'} \neq d\varepsilon_{2'}$) is applied on the FBG, the core of the optical fibre will become birefringent. As a result, two orthogonal polarization axes will exist, and if the effect is high enough, the Bragg peak will split into two distinct ones, see Figure 4-17,right.

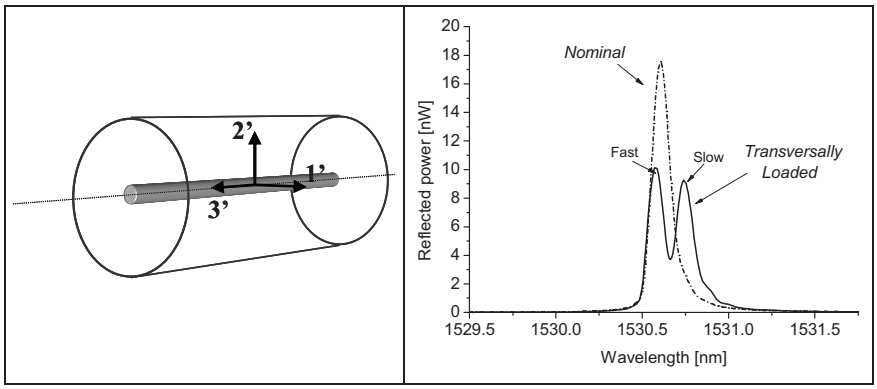

Figure 4-17: The used coordinate system of the optical fibre (left), spectral response of an FBG when a differential diametrical compressive load is applied(right).

The difference in transverse strain $\Delta\varepsilon_{trans}$, in the core of the optical fibre, can be calculated using the distance between the two distinct peaks of the spectrum, (Equation B-25, Appendix B):

$$\Delta\varepsilon_{1'} - \Delta\varepsilon_{2'} = \Delta\varepsilon_{trans} = \frac{2}{n_{eff}^2} \frac{\lambda_{B,1'} - \lambda_{B,2'}}{(\lambda_{B,0})(p_{12} - p_{11})}, \qquad 4\text{-}15$$

with $\lambda_{B,1'}$ and $\lambda_{B,2'}$ the wavelengths corresponding to the Bragg peaks polarized along the 1'- and 2'-axis, respectively and $\lambda_{B,0}$ the initial Bragg peak. Remark that since the focus is on SMF, the optical polarization axes are always equal to the mechanical loading axes. It is noted that in the following chapters (Chapter 6,7 and 8) Equation 4-15 will be used to estimate, the transverse strain difference induced in the fibre core, during the composite curing process and composite loading. Though, by using Equation 4-15, it is only possible to calculate the differential transverse strain and we are not able to distinguish whether the stress is applied along the 1'- or 2'- axis. Hence, it is neither possible to determine the individual strains, $\Delta\varepsilon_{1'}$ and $\Delta\varepsilon_{2'}$, from the split spectrum, Figure 4-17, right.

However, by applying a diametrical load we are able to produce a state of plane strain (i.e. $\varepsilon_{3'} = 0$) in the core of the optical fibre and we are able to investigate the strain induced birefringence effects. This makes it possible to experimentally determine the strain optic coefficients, p_{11} and p_{12} from the strain induced birefringence. This is further discussed in the forthcoming section.

4. 4. 2. b. Pure diametrical loading of a SM-fibre

Diametrical loading of the optical fibre has been investigated in detail by Luyckx G. to determine the strain optical coefficients of an axi-symmetric (or uni-axial) SM-fibre and a Bow-Tie fibre [13]. The procedure is based on applying load with a rigid body on a cylindrical optical fibre (Figure 4-18). As such, a plane strain state ($\varepsilon_{3'} = 0$) is created in the core of the optical fibre. A theory of contact is used to predict the shape of the contact region during loading [14]. Using this theory, the transverse strain components along the 1' –and 2'-axis can be calculated in the optical fibre in the vicinity of the contact region.

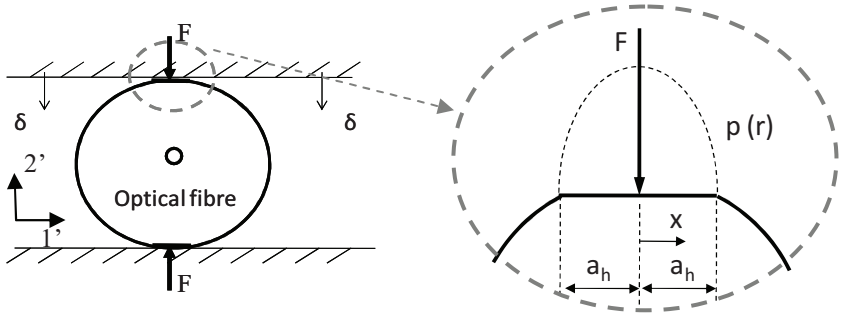

Figure 4-18: An optical fibre is loaded in compression (F) by a rigid body (left), a certain stress distribution p(r) is created at the contact interface (right) [13].

The compressive load per unit axial length (F) is induced by moving the upper body with a displacement δ (Figure 4-18), and gives rise to a Hertzian distribution of pressure which is given by:

$$p = \sqrt{\frac{2F}{\pi a_h}\left(1 - x^2 / a_h^2\right)}\,, \qquad 4\text{-}16$$

in which the semi-contact-width, a_h is defined as:

$$a_h = \sqrt{2FD_f / \pi E^*}\,. \qquad 4\text{-}17$$

Where E^* is the composite modulus of the optical fibre and the contacting body and D_f the diameter of the optical fibre. With this pressure distribution, the stress distribution in the centre of the optical fibre can be calculated [15]:

$$\Delta\sigma_{1'} = 2\frac{F}{\pi D_f} \qquad \Delta\sigma_{2'} = -6\frac{F}{\pi D_f}\,. \qquad 4\text{-}18$$

It comprises the superposition of the stress fields because of two concentrated forces F acting tangential on both sides of the optical fibre, i.e. action-reaction (Figure 4-18). Once the stress is known, the values of the strain state in the core of the fibre can be found from Hooke's law for plane strain and is given by [16]:

$$\begin{cases} \Delta\varepsilon_{1'} = \left(\frac{1-\upsilon_f^2}{E_f}\right)\left(\Delta\sigma_{1'} - \frac{\sigma_{2'}\upsilon_f}{1-\upsilon_f}\right) \\ \Delta\varepsilon_{2'} = \left(\frac{1-\upsilon_f^2}{E_f}\right)\left(\Delta\sigma_{2'} - \frac{\sigma_{1'}\upsilon_f}{1-\upsilon_f}\right) \end{cases}. \qquad 4\text{-}19$$

Using Equation 4-18 and 4-19 and applying a theoretical line load of $F = {}^{1N}\!/_{mm}$, and taking a Young's modulus of $E_f = 72.4GPa$ [17] and a Poisson's ratio of $\upsilon_f = 0.16$ [9], the stress and strain shifts along the 1'- and 2'-axis, are determined for a 80 µm and a 125 µm optical fibre, see Table 4-7:

Table 4-7: The stress and strain shifts induced in the core of a 125 µm or 80 µm SM fibre due to a diametrically applied load of 1Nmm^{-1}.

	$\frac{\Delta\sigma_{1'}}{F}$ $[\frac{MPa}{N/mm}]$	$\frac{\Delta\sigma_{2'}}{F}$ $[\frac{MPa}{N/mm}]$	$\frac{\Delta\varepsilon_{1'}}{F}$ $[\frac{\mu\varepsilon}{N/mm}]$	$\frac{\Delta\varepsilon_{2'}}{F}$ $[\frac{\mu\varepsilon}{N/mm}]$
$D_f = 80\mu m$	7.96	-23.87	168.3	-341.7
$D_f = 125\mu m$	5.09	-15.28	107.7	-218.7

By assuming a plane strain state ($d\varepsilon_{3'} = 0$), the wavelength shifts of the two polarization modes are written as a function of the transverse strain components ($d\varepsilon_{1'}$ and $d\varepsilon_{2'}$) only (Equation B-15, Appendix B), and are reduced to:

$$\begin{cases} \frac{d\lambda_{B,1'}}{\lambda_{B,0}} = -\frac{1}{2}\bar{n}_{1'}^2\left(p_{11}d\varepsilon_{1'} + p_{12}d\varepsilon_{2'}\right) \\ \frac{d\lambda_{B,2'}}{\lambda_{B,0}} = -\frac{1}{2}\bar{n}_{2'}^2\left(p_{11}d\varepsilon_{2'} + p_{12}d\varepsilon_{1'}\right) \end{cases}. \qquad 4\text{-}20$$

Writing Equation 4-20 in matrix notation, assuming small perturbations and replacing d by Δ, and taking $\bar{n}_1 \overset{SMF}{=} \bar{n}_2 = \bar{n}$, the wavelength shifts are given by:

$$\begin{bmatrix} \frac{\Delta\lambda_{B,1'}}{\lambda_{B,0}} \\ \frac{\Delta\lambda_{B,2'}}{\lambda_{B,0}} \end{bmatrix} = -\frac{1}{2}\bar{n}^2\begin{bmatrix} \Delta\varepsilon_1 & \Delta\varepsilon_2 \\ \Delta\varepsilon_2 & \Delta\varepsilon_1 \end{bmatrix}\begin{bmatrix} p_{11} \\ p_{12} \end{bmatrix}. \qquad 4\text{-}21$$

By substituting the calculated strains from Table 4-5 in Equation 4-21, and filling in the strain optic coefficients of Bertholds and Dändliker ($p_{11} = 0.113$ and $p_{12} = 0.252$), we can determine the theoretical wavelength shifts induced by a diametrical load of $F = 1N/mm$. By taking $\lambda_{B,0} = 1550$ nm , and the in Section 3.2.4 determined refractive index, $\bar{n} = 1.4459$, the theoretical wavelength shifts for a 80 µm and a 125 µm FBG are calculated. The values are given in Table 4-8. We can see that the theoretical wavelength shift per unit load is positive for the Bragg peak polarized along the 1'- axis and that it is negative for the Bragg peak polarized along the 2'- axis. From the spectral response (Figure 4-17) we know that the peak polarized along the S*low* - axis shifts toward the longer wavelengths when the optical fibre is loaded transverse. As such for the diametrical loading case, with the transverse loading along the 2'-axis, the author defines the *Slow*- axis along the 1'-axis and the Fast- axis along the 2'-axis.

Table 4-8: Theoretical wavelength shifts for a 80 µm and 125 µm FBG due to a diametrically applied load of 1Nmm^{-1}.

	$\frac{\Delta\lambda_{B,1'}}{F}$	$\frac{\Delta\lambda_{B,2'}}{F}$
	$[\frac{nm}{N/mm}]$	$[\frac{nm}{N/mm}]$
$D_f = 80\mu m$	0.109	-0.006
$D_f = 125\mu m$	0.070	-0.004

Equation 4-21 can be transformed to determine the strain optical coefficients, p_{11} and p_{12}:

$$\begin{bmatrix} p_{11} \\ p_{12} \end{bmatrix} = -\frac{2}{\bar{n}^2} \begin{bmatrix} \Delta\varepsilon_1 & \Delta\varepsilon_2 \\ \Delta\varepsilon_2 & \Delta\varepsilon_1 \end{bmatrix}^{-1} \begin{bmatrix} \frac{\Delta\lambda_{B,1'}}{\lambda_{B,0}} \\ \frac{\Delta\lambda_{B,2'}}{\lambda_{B,0}} \end{bmatrix} \qquad 4\text{-}22$$

Thus, the coefficients are experimentally determined by measuring the wavelength shift, $\Delta\lambda_{B,1'}$ and $\Delta\lambda_{B,2'}$, during a controlled diametrical loading and substituting in Equation 4-22. The experimental approach used to determine the strain optic coefficients experimentally is explained next.

To apply a diametrical load, a similar setup as the one used by Guemes and Menedez is used in this dissertation [12]. A load stamp is used to simultaneously load two fibre Bragg gratings. The calibration device is shown in Figure 4-19:

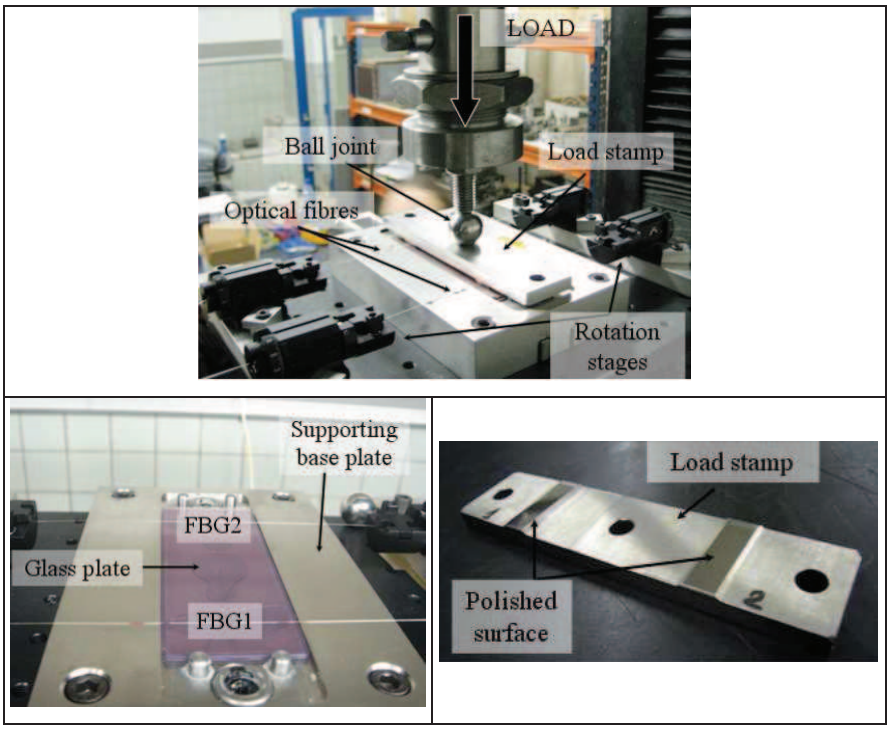

Figure 4-19: Calibration setup designed by Lucykx and Voet, mounted on a mechanical bench, using a load stamp to simultaneously load two fibre Bragg gratings [18].

A mechanical bench is used to transfer the load on to a ball joint which transfers the load further on to the load stamp with polished surfaces (Figure 4-19, bottom-right) which push on two FBGs simultaneously. The fibres are held steady using fibre rotation stages with small fibre clamps (Figure 4-19, top). The two stripped 125 µm DTG®s are used to experimentally determine the p_{11} and p_{12}. The wavelength shifts of the two stripped DTG®s are measured against the applied line load and the mean value of the sensitivity of the two sensors, is used to calculate the strain optic coefficients. The calibration is repeated for four different orientations of the fibres, by sequentially rotating the rotation stages over 90°. An example of a calibration curve at one defined orientation is shown in Figure 4-20. We can clearly see that, the two sensors react differently, pointing out that even though a ball joint is used, the fibres are loaded unbalanced.

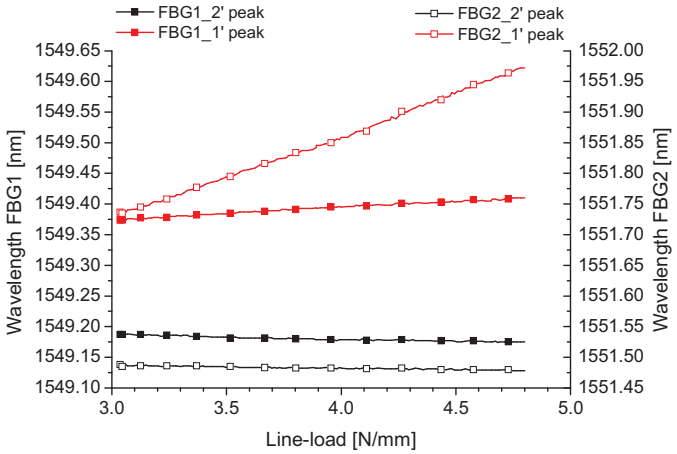

Figure 4-20: Example of a transverse calibration using the diametrical setup, with two stripped DTGs® loaded simultaneously.

By substituting the calculated strains from Table 4-5 in Equation 4-22, and filling in the measured mean wavelength shifts, using the convention defined above, with the Bragg peak shift $\Delta\lambda_{B,1'}$ corresponding to the second peak (i.e. Slow or longer wavelength) and the Bragg peak shift $\Delta\lambda_{B,2'}$ corresponding to the first peak (i.e. Fast or shorter wavelength), the resulting strain optic coefficients are experimentally determined, see Table 4-9 .

Table 4-9: Measured mean wavelength shifts of the 1' peaks and 2' peaks, and the experimentally determined strain optic coefficients for a stripped 125 DTG®.

Orientation	0°	90°	180°	270°	Mean
$\frac{\Delta\lambda_{B,1'}}{F}$ $[\frac{nm}{N/mm}]$	0.07797	0.07314	0.06766	0.06561	0.0711 ± 0.00558
$\frac{\Delta\lambda_{B,2'}}{F}$ $[\frac{nm}{N/mm}]$	-0.00596	-0.00462	-0.00348	-0.00556	-0.00491 ± 0.0011
p_{11} [-]	0.121	0.117	0.111	0.100	0.112 ± 0.008
p_{12} [-]	0.280	0.264	0.246	0.234	0.256 ± 0.017

The mean result obtained for the experimentally determined coefficients, are in good agreement with the coefficients, $p_{11} = 0.113$ and $p_{12} = 0.252$ from Bertholds and Dändliker, however, a large scatter on the coefficients is noticed over the different experiments (i.e. different orientations).

Although a lot of effort was put in optimizing the setup, the device is found inaccurate to be used for calibrating 80 µm DTG®s. Therefore, only 125 µm fibres were envisaged in this section. Because both fibres have identical S_ε-*factors* (Section 0), it is believed that the calibrated strain optic coefficients are also valid for the 80 µm DTG®s.

4. 4. 3. Temperature calibration

The temperature calibrations are performed using a Fluke 9170 metrology well calibrator (Figure 4-21, left). A reference thermometer (Platinum Resistance Thermometer) is used to monitor the temperature. The metrology well has a temperature stability of ± 0.005°C and an accuracy of approximately ± 0.014°C. Therefore, the device is very well suited to perform accurate temperature cycles. In total 6 probes from the PR2007_2 run are prepared: three 80 µm and three 125 µm DTG®s (Table 4-10). Firstly, the gratings are stripped, using a chemical acid dichloremethane (CH_2CL_2), to avoid that the temperature sensitivity will vary due to possible changes in relative humidity. From literature, it is known that polymers tend to absorb water. The same effect is seen with polymer fibre coatings. The absorptive effect of polymers can even be that high that polymer coated FBGs can be used as a humidity sensor [19].
Secondly, the optical fibre is angle cleaved to avoid backscatter of the input light at the end. Finally, it is encapsulated in a small glass capillary of approximately 50 mm long, see Figure 4-21, right. As such, the DTG® is free to expand and is isolated from external strain which could act on the fibre. All samples are immersed in an Aluminium-Bronze bulk alloy insert with small holes. The bulk insert has a depth of approximately 200mm and reduces possible errors which are related to heat conduction. The radial temperature uniformity in such insert is approximately ±0.02°C. To guarantee an axial uniform temperature distribution along the length of the immersion, all the capillaries are lowered to the bottom of the insert.

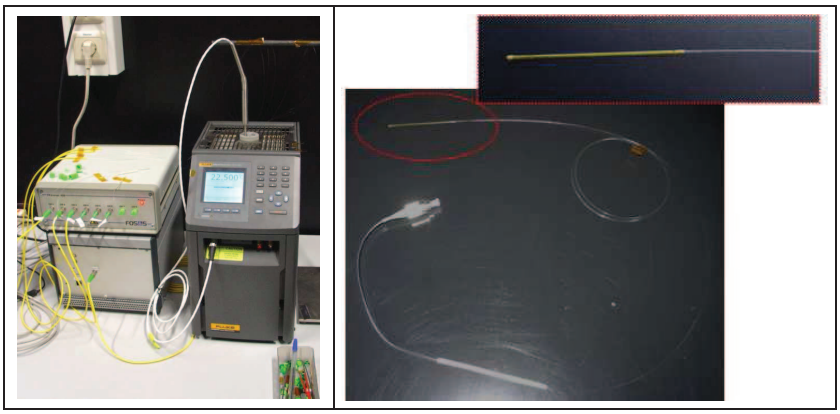

Figure 4-21: Temperature calibration setup (left), probe finalized in glass capillary (right).

4. 4. 3. a. Theoretical background on the thermo-optic relationship

The dependency of the Bragg wavelength to temperature is given by (Appendix B, Equation B-29):

$$\frac{d\lambda_B(dT)}{\lambda_B(dT)} = \left(\alpha_n + \alpha_f\right) dT\,, \qquad 4\text{-}23$$

where $\alpha_n = \frac{1}{\bar{n}} \frac{\partial \bar{n}}{\partial dT}$ is the *thermo-optic coefficient* and $\alpha_f = \frac{1}{\Lambda} \frac{\partial \Lambda}{\partial dT}$ is the *thermal expansion coefficient* of the fibre (typical $0.55 \cdot 10^{-6} K^{-1}$ for silica fibres [20]) For a large temperature range α_n is linear dependent on the temperature and is given by $\alpha_n = aT + b$ [21], hence when considering high temperature ranges, a more accurate equation is necessary.

Pal S. et al. already studied the non-linear temperature dependency of Type I and Type II FBGs written in several co doped silica fibres [22]. The temperature response of the Bragg wavelengths is studied using the best polynomial regression. They reported best fits using a second order and third order polynomial.

In this work Equation 4-23 is elaborated by integrating between a definite interval. The solution for an interval between an initial (reference) temperature, T_{ref} and the temperature T, is given by the following quadratic function (Appendix B, Equation B 34):

$$\ln \frac{\lambda_B}{\lambda_{B,ref}} = S_{T1} \Delta T + S_{T2} \Delta T^2 , \qquad 4\text{-}24$$

With $\Delta T = T - T_{ref}$ the temperature difference between the reference temperature and actual temperature, S_{T1} and S_{T2} the wavelength independent linear and quadratic temperature sensitivities, respectively, $\lambda_{B,ref}$ the Bragg wavelength at the reference temperature, T_{ref}, and λ_B is the measured wavelength at the actual temperature T. The temperature sensitivities, S_{T1} and S_{T2}, are determined by performing a temperature calibration and fitting the calibration using a second order polynomial.

4. 4. 3. b. Calibration of the temperature sensitivities

The temperature is cycled twice from -22.5°C up to 135°C in steps of 22.5°C, see Figure 4-22, left. The first cycle is performed to pre-anneal the DTG®s, and the second cycle is then used to calibrate the sensors. Annealing is in principle necessary to avoid possible drift of the Bragg wavelength due to intrinsic temperature effects (i.e. in-stability) at higher temperatures. Investigations on the temperature stability of DTG®s (Section 4. 5. 1.), however, have shown that the sensors are stable up to temperatures of approximately 150°C. Each temperature level is kept constant for approximately 30 minutes. Simultaneously, the peak wavelength of all samples is continuously monitored. An example of the experimental calibration curve is shown in Figure 4-22, right. A polynomial (Equation 4-24) is fitted to the data points, Figure 4-22, right to determine S_{T1} and $S_{T2.}$

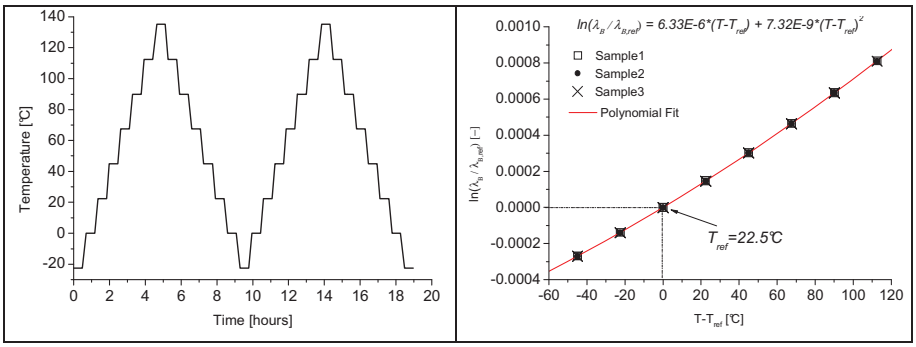

Figure 4-22: Temperature calibration cycles from -22.5°C – 135°C (left), calibration curve for three 80 µm DTG®s fitted polynomial, with $T_0 = 22.5°C$ (right).

The calibration curve shows that the data points of temperature calibration of the three samples overlap and a quadratic fit nicely matches all data points. The resulting S_{T1} and S_{T2} sensitivities are shown in Table 4-10:

Table 4-10: Temperature sensitivities of the 80 µm and 125 µm samples.

	# samples	S_{T1} [10^{-6}]	S_{T2} [10^{-9}]
80 µm (PR2007_2)	3	6.360 ± 0.010	7.6 ± 0.104
125 µm (PR2007_2)	3	6.323 ± 0.008	7.6 ± 0.256
Mean	-	6.342	7.6

The values of both fibres correspond well. Hence, the thermo-optic dependency of the 80 µm and 125 µm fibre can be considered as identical.

4. 5. ABSOLUTE SENSOR PROPERTIES?

An FBG is a passive optical component with absolute defined intrinsic sensor properties. Its reflected Bragg wavelength does not depend on the amount of optical power which is launched into the fibre, but, it is fixed by its effective refractive index and grating period. In practice, this implies that there is no need to re-calibrate or use any electronic compensating techniques once an FBG is installed. However, drift of the centre Bragg wavelength and reflected power can occur in time when an FBG is for instance exposed to elevated temperature or highly ionizing radiation environments.

When Type I FBGs are exposed to high temperatures, typical negative wavelength shifts and a large drop in FBG reflectivity are noticed [22-25]. Masuda et al., for example, reported a negative shift of the central wavelength of more than 0.75 nm and a loss in reflectivity of 6dB for hydrogen loaded fibres annealed for 3 hours at 140°C [23]. This drift is mainly caused by the diffusing of hydrogen due to high temperatures. Pal S. et al. [22] studied the temperature-induced irreversible Bragg wavelength shift and shift in refractive index modulation, Δn_g, on B – Ge co-doped FBGs. A negative wavelength shift of 0.52 nm and $\Delta n_g = 2.18 \cdot 10^{-4}$ was reported for an FBG annealed at 400 °C for 405 minutes. They also estimated the reflectivity

and shift in Bragg wavelength for different working temperatures during the life-time of the FBG. The results of the aging experiment, with a period which is equivalent to a 100 years, show that an FBG with an initial 99 % reflectivity decays to 8 % reflectivity at 300 °C and a wavelength shift of 1.5 nm of the centre wavelength.
Similar wavelength shifts are noticed for FBGs in highly ionizing radiation environments. Gusarov et al. [26-27] reported positive wavelength shifts in the order of a few tens of picometer (pm) when FBGs where exposed to Gamma radiation doses Their results also showed that intrinsic photosensitive fibres, such as highly Ge-doped fibres, show to be more stable to irradiation than hydrogen loaded fibres. However, these effects are beyond the scope of this work and are not further discussed. The interested reader is referred to the work of Gusarov et. Al [26-27] who performed some excellent research on the irradiation properties of FBGs written in different optical fibres and with different coatings.
In principle the effect of drfit can be encountered before usage. Annealing of the FBGs, is a commonly applied technique to stabilize FBGs at elevated temperatures and to limit the (rather small) drift in time. Annealing of the newly developed DTG®s is subject of the next Section, in which both reflected power and centre wavelength shift are studied for temperatures up to 350 °C. Results, show that the DTG®s are very stable up to 150 °C. However, once beyond this temperature, similar effects are found as reported by Pal S. et al.

4. 5. 1. Thermal stability of DTG®s

During the embedding process (curing) of Fibre Bragg sensors in fibre reinforced plastic (subject of Part II), the sensors are exposed to high temperatures (up to 350°C). This raises important questions on the thermal stability of DTG®s. Therefore in this section we thermally cycle the sensors in steps up to a temperature of 350 °C. The experimental method employed here is in analogy with annealing experiments which are employed to study the thermal decay of FBGs in terms of grating reflectivity and Bragg wavelength shifts [22-23, 25, 28]. A commonly used parameter to investigate thermal decay of FBGs is the integrated coupling coefficient (ICC) or normalized ICC (NICC). The NICC is directly proportional to the peak reflectivity, and is given by:

$$\eta_{t,T} = \frac{\tanh^{-1}(\sqrt{R_{t,T}})}{\tanh^{-1}(\sqrt{R_{0,RT}})}, \qquad 4\text{-}25$$

where $R_{t,T}$ is the peak reflectivity after an annealing period, t at a certain temperature level, T and $R_{0,RT}$ is the initial reflectivity at room temperature.

Additionally, Pal S et al. analysed the shift of the Bragg wavelength as function of time for each annealing temperature. An example of the evolution of the NICC (reflectivity) and shift of the Bragg spectrum in time for FBG sensors exposed at different temperatures, is shown in Figure 4-23. We notice a large drop of the NICC within the first few minutes. The effect is much more severe at higher temperatures, and no significant effect is noticed at a temperature of 100 °C. After about 100 minutes the steep slope smoothens and the decrease of the NICC continues slowly.

For the course of the Bragg wavelength similar effects are noticed, however, because the shifts are small compared to the scaling of the abscissa the shifts are not that pronounced. The slope however, is much flatter and no significant decrease is noticed after 100 minutes.

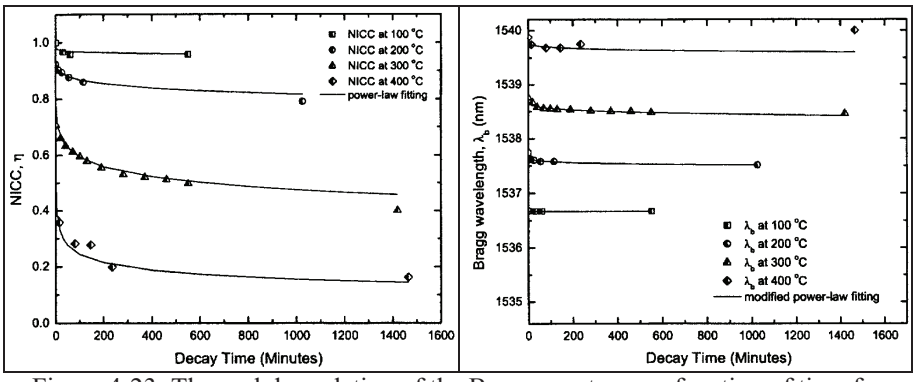

Figure 4-23: Thermal degradation of the Bragg spectrum as function of time for various temperature levels; the NICC (left) and the Bragg wavelength shift (right) [[22]].

In principle, FBG users are interested in establishing a "master ageing curve" which shows the decrease of the NICC of the grating as function of the "demarcation energy" (E_d). This energy is depending on the temperature, T in which the sensor is used and the age, t of the sensor at that specific temperature [22]. An example of such a master ageing curve for an FBG is shown in Figure 4-24:

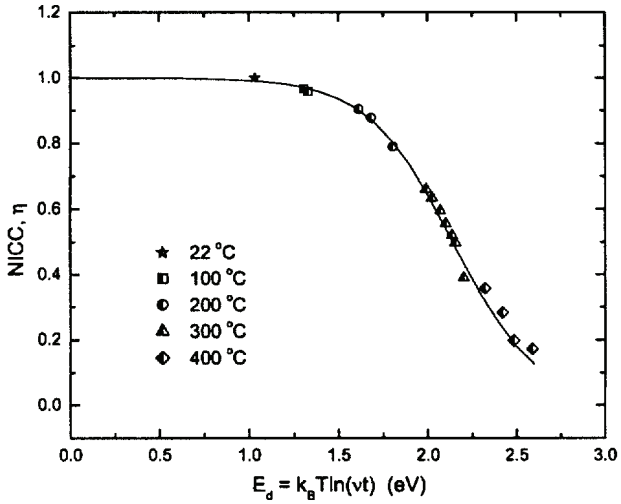

Figure 4-24: Plot of the NICC as a function of the demarcation energy, E_d, for the grating for isothermal testing [22] .

After the establishment of the master ageing curve and best fitting of the shape of the curve with the power-law expression [29-30] the degradation of the grating for any combination of time and temperature can be projected. This helps the user to

estimate the lifetime of the gratings in terms of the decay of the reflectivity and the shift in Bragg wavelength if the appropriate power law is applied. These aging curves can in fact be applied to determine specific annealing regimes for FBGs so their temperature stability can be enhanced for different application.
The curves from Pal et al. shown in Figure 4-23 and Figure 4-24 are drawn according to a isothermal test situation, i.e. the measurements are repeated at different temperatures by each time using a different sample. However, both the isothermal and isochronic approaches can be used to obtain the same results [30]. In fact it was observed by Razafimahatratra et al. [30] that isochronic step decays could be used to predict isothermal decays. The advantage of ischronical steps is that there is no need to use new samples for each temperature level.

Annealing experiment
In this work, it is not the purpose to setup master ageing curves. The real purpose of the annealing experiment here is to investigate the thermal stability of DTG®s at temperatures levels and exposure times which are realistic for the real fabrication cycle of the thermoplastic composite (Chapter 6). During the composite production cycle the embedded DTG®s are exposed for approximately one hour to temperatures up to 320 °C. In order to save time and to limit the number of test-samples, the author has chosen to use a progressive isochronic temperature cycle (Figure 4-25). The temperature is increased in steps of 50 °C up to 350 °C, and is kept constant for approximately 60 min at each temperature level. By using progressive temperature cycling, we imitate the extreme embedding conditions with temperatures larger than 300 °C. In analogy with master ageing curves, information on the thermal stability of the grating is obtained; i.e. the decay of the reflectivity of the Bragg spectrum and the stability of the Bragg wavelength.

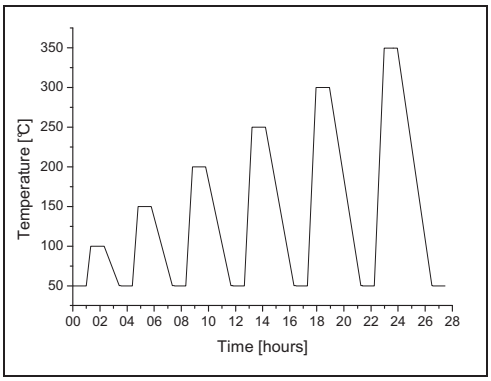

Figure 4-25: Progressive isochrone temperature cycle programmed in the FLUKE 9173.

Similar prepared six sensor probes as being used for the temperature calibration (Table 4-10) are used in the temperature annealing experiment. The setup is similar to the temperature calibration using the Fluke 9170, see Figure 4-21. However, instead of using the Fluke 9170, a high temperature Fluke 9173 metrology well calibrator is used. The Fluke 9173 system has a heating range of 50 °C – 700 °C, uses a built in reference unit by which the temperature accuracy is better than ±0.02 °C, and the stability for temperatures below 350 °C is better than ±0.01 °C.

The temperature from the reference probe, the peak wavelength and the maximum reflected peak power are monitored synchronously. Before and after the test, the spectrum of each sensor is saved at a temperature of 50 °C. An example of the spectral behaviour of an 125 µm FBG is shown in Figure 4-26. We can clearly see a decay of the reflectivity and a negative wavelength shift after annealing.

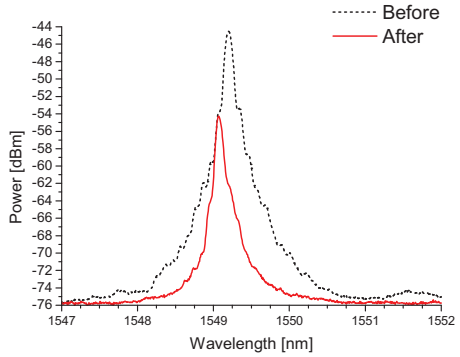

Figure 4-26: Spectra taken at a temperature level of 50°C before and after the temperature cycle (sample 125µm).

In the repetitive progressive temperature cycle (Figure 4-25), the temperature is step-wise increased (i.e. annealing step) and after each annealing step it is returned to 50 °C. By measuring the Bragg spectrum initially at 50 °C and after each annealing step, the decay of the reflectivity and the wavelength shift can be plotted (Figure 4-27).

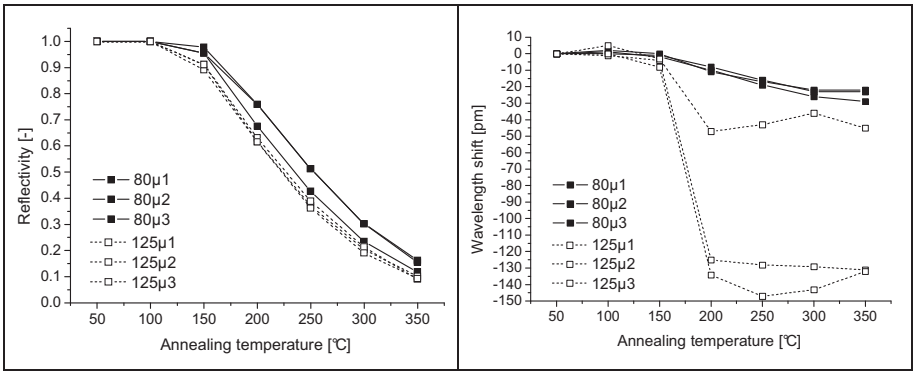

Figure 4-27: Reflectivity decay (left) and wavelength shift (right) as function of the last temperature level.

The temperatures indicated on the x-axis represents the annealing temperature at which the gratings were exposed to. For the decay of the reflectivity we see a continuous decay as function of the temperature, starting at approximately 150 °C. At the end of the annealing cycle, we notice a significant decay of reflection to a level of 10 % of the initial reflected power for all samples. Interesting to note is that both plots, i.e. reflectivity decay and wavelength shift, start changing significantly at temperatures higher than 150 °C. Moreover, no wavelength shift at all was noticed

for temperatures up to 135 °C during the temperature calibration cycle in Section 4. 4. 3. . The results of the temperature calibration and the annealing experiment performed here, show that DTG®s are intrinsically thermally stable up to approximately 150 °C. This effect has been mentioned at the end of Chapter 2, where the application of the ORMOCER® coating is discussed. The reason of the temperature stability up to 150 °C, is that the gratings are already shortly annealed during the production process when they pass the UV curing process of the ORMOCER® coating, see Chapter 2 (Section 2.7). Remarkable is that the DTG®s are in fact only exposed for a few seconds (2-3 seconds) to the UV-lamp.
From Figure 4-27, right, it is noticed that a significant difference in wavelength shift exists for the 80µm- and the 125µm DTG®s at temperatures larger than 150°C. for two out of three 125 µm samples, we notice a large negative shift (>130pm) which is a lot bigger than the maximal shift of approximately 30pm observed for all 80 µm samples. It is believed that this large difference is merely owing to the homogeneous or mean part of the refractive index change of the grating, Δn_d (Chapter 2, Equation 2-9). According Hong Ky. [31] the mean refractive index change in an FBG is given by:

$$\Delta n_d = \frac{\overline{n}\Delta\lambda_B}{\Gamma\lambda_B}, \qquad 4\text{-}26$$

which is in accordance with Equation A-14 derived in Appendix A, with $\overline{n}$ the effective refractive index of the fibre, and Γ the confinement factor. We can see from Equation 4-26 that indeed the wavelength shift of an FBG is proportional to the mean refractive index change. In [24] the refractive index developments are studied experimentally. It is found that the mean refractive index change decreases rapidly during the first minutes at higher temperatures. This confirms that the Bragg wavelength shifts to lower wavelengths. It is believed that the mean refractive index of the 125 µm DTG®s is initially slightly higher than the index change of the 80 µm DTG®s. Suppose that the mean index change decays to zero at temperatures higher than 300 °C, we can assume that the total wavelength shift to lower wavelengths will be higher for the 125 µm. This could be a plausible explanation of the difference in wavelength drifts found for both fibres. However, the actual cause of the initial index difference between the 80 µm and 125 µm is not clear. Probably the drawing conditions and DTG® writing conditions are slightly different for a smaller diameter fibre, however, further research on this phenomena is needed to be able to draw any conclusions on this matter.

4. 5. 2. Temperature dependence effects

It is reported that FBGs, apart from the thermo-optic effects, additionally show an intrinsic temperature dependence of the strain and stress sensitivity [32-33]. The thermal dependence of the strain sensitivity arises from the temperature sensitivity of the strain-optic coefficients, the Poisson's ratio and the refractive index. According to [32-33], the dependency of the strain sensitivity to temperature, was found to be 0.2 fm $\mu\varepsilon^{-1}{}^{\circ}C^{-1}$ for FBGs in the 850 nm range. A similar study was reported by Maier et al. [33] on the dependency of the "stress sensitivity" to

temperature for FBGs in the 1550 nm range. However, the term "stress" is a little deceiving, as the researcher reports values which represent the "sensitivity to force", i.e. the change in Bragg wavelength per unit applied load. Maier R.J.R. et al. performed tensile tests on stripped and Acrylic-coated FBGs between -38 °C and 110 °C. They report values of $-0.1618\ pm\ N^{-1}{}^{\circ}C^{-1}$ or $-0.0020\ pm\ MPa^{-1}{}^{\circ}C^{-1}$ for a 125 µm fibre. They noted that it is predominantly the temperature dependence of the Young's modulus of the silica fibre which induces this effect. In addition, they observed that the (re)coated fibre influences the stress response below 0°C. At lower temperatures the coating becomes much stiffer. Because the volume fraction of the coating is high for the coated fibre the change in stiffness, has a large influence on the composite modulus and stress response of the fibre. Hence, proportionally more force is taken by the coating material at lower temperature and the stress response will decrease.

In this section the aim is to examine the effect of the temperature dependence of the strain (Section 4. 5. 2. a.) and stress response (Section 4. 5. 2. b.) of 80 µm DTG®s in comparison to the 125 µm DTG®s the DTG®s. The experimental setup consists of the same mechanical test-setup with the optical extensometer system, as has been used during the strain calibrations in Section 4. 4. 1. (Figure 4-8). Additionally to the strain calibrations the adapted fibre clamping mechanism is mounted in a small temperature controlled chamber. The chamber can be heated with hot air and it is cooled down using liquid Nitrogen. The experiments are preformed at temperatures from -60°C up to 140°C. Additionally, from the difference in strain between a stripped and coated 125 µm DTG® at different temperatures, the author has attempted to estimate the Young's modulus of the ORMOCER® coating in the same temperature range. The procedure to estimate the Young's modulus of the ORMOCER® coating using two DTG®s is explained in 4. 5. 2. c. .

4. 5. 2. a. Temperature dependence of the strain response of DTG®s

The axial strain calibrations on the DTG®s are similar to the axial strain calibrations with the automated setup, which are presented in Section 4. 4. 1. . The gauge length between the reflection points is set to approximately 0.2 m, and is limited because of the small climate chamber which is surrounding the clamping mechanism. The intention of the experiments is to determine the dependency of the the S_ε*-factor* at temperatures, ranging from -60 °C till 140 °C. The calibrations are performed using a second strain free FBG, to compensate for pure temperature effects. As such we can consider the Bragg wavelength shift of the calibrated FBG as function of the physical elongation only. Before the experimental results are discussed, first a theoretical approach is given.

Theoretical approach:

The theoretical temperature dependence of the axial strain sensitivity of an FBG can be calculated from the Bragg wavelength as function of strain (Appendix B, Equation B-18):

$$\frac{d\lambda(T)}{\lambda} = \left(1 - P(T)\right) d\varepsilon_3 = S_\varepsilon(T) d\varepsilon_3 . \qquad 4\text{-}27$$

In which *P(T)* is the temperature dependent strain optic constant defined by:

$$P(T) = \frac{1}{2}\bar{n}(T)^2\left(p_{12}(T) - \upsilon_f(T)\left(p_{11}(T) + p_{12}(T)\right)\right). \qquad 4\text{-}28$$

As we are interested in determining the temperature dependence of the S_ε*-factor*, Equation 4-27 can then be written out as follows:

$$\frac{d\lambda(T)}{\lambda d\varepsilon_3} = S_\varepsilon = \left(1 - \frac{1}{2}\left(\bar{n}(T)^2 p_{12}(T) - \bar{n}(T)^2 \upsilon_f(T) p_{11}(T) - \bar{n}(T)^2 \upsilon_f(T) p_{12}(T)\right)\right). \qquad 4\text{-}29$$

By deriving Equation 4-29 for temperature and taking together some of the variables, we obtain the following result:

$$\frac{dS_\varepsilon}{dT} = \frac{d\bar{n}}{dT}\left(\nu\left(p_{11} + p_{12}\right) - p_{12}\right) + \frac{1}{2}\bar{n}^2\left(\frac{dp_{11}}{dT}\nu + \frac{dp_{12}}{dT}\left(\nu - 1\right) + \frac{d\nu}{dT}\left(p_{11} + p_{12}\right)\right). \qquad 4\text{-}30$$

Equation 4-30 can be used to simulate the temperature dependence of the S_ε*-factor*. To calculate the temperature dependency of the S_ε*-factor*, the following parameters are used: $\nu = 0.16$ [9][ref] with $d\nu / dT = 1.4 \cdot 10^{-6}$ [34] $p_{11} = 0.112$ and $p_{12} = 0.255$ (Table 4-9) with $dp_{1i} / dT = -0.134 \cdot 10^{-3} K^1$ [32], To obtain the temperature dependence of the refractive index $d\bar{n} / dT$, we will use the calibration factors determined in this work. For more background information on the following calculation, the reader is referred to Appendix B, where a detailed derivation is given of the determination of the calibration coefficients as function of temperature.

Using $\alpha_n = \frac{d\bar{n}}{\bar{n}dT} = aT + b$, with $a = 2S_{T2}$ and $b = b' - aT_{ref} = S_1 - \alpha_f - aT_{ref}$ (typically $T_{ref} = 22.5°C$), with the temperature calibration factors $S_{T1} = 6.342 \cdot 10^6$ and $S_{T2} = 7.6 \cdot 10^{-9}$ (Section 4. 4. 3. , Table 4-10), we find that $\alpha_n = \frac{d\bar{n}}{\bar{n}dT} = 1.52 \cdot 10^{-8} T + 6.13 \cdot 10^{-6}$. With $\bar{n} = 1.4459$ (Chapter 3) we obtain:

$$\frac{d\bar{n}}{dT} = 2.2 \cdot 10^{-8} T + 8.86 \cdot 10^{-6}. \qquad 4\text{-}31$$

In fact the second term of Equation 4-30 preponderates the result of the temperature dependency of the S_ε*-factor*, as such we can neglect the first term of Equation 4-31 and we can use $d\bar{n} / dT = 8.86 \cdot 10^{-6} \cdot °C^{-1}$.

Filling in all determined temperature dependence parameters in Equation 4-30 we find that $dS_\varepsilon / dT = 9.41 \cdot 10^{-5} \cdot °C^{-1}$ and with $\lambda = 1550\ nm$, the theoretically dependence of the strain sensitivity to temperature we find that

$\frac{d\lambda / d\varepsilon_3}{dT} = \frac{\lambda dS_\varepsilon}{dT} = 0.15$ fm $\mu\varepsilon^{-1}{}^\circ C^{-1}$, which is in good agreement with the value of 0.2 fm $\mu\varepsilon^{-1}{}^\circ C^{-1}$ reported by [32] for gratings in the 850 nm range.

Using $S_{\varepsilon,RT} = 0.777$ (determined at room temperature, see Table 4-6), the simulated strain gauge factor of the DTG®s at any given temperature is given by:

$$S_\varepsilon(T) = 0.777 + 9.41 \cdot 10^{-5} \Delta T \,, \qquad 4\text{-}32$$

With ΔT, the temperature difference with regard to room temperature (i.e. 22 °C). Equation 4-32 can thus be used to simulate the S_ε-*factor* at any given temperature. If we have for example, a temperature difference of 100 °C, we obtain a strain gauge factor of 0.786, which is approximately 1.2 % higher than the strain gauge factor at room temperature ($S_{\varepsilon,RT} = 0.777$). Hence, if we do not take into account the temperature dependence, the stain will be approximately 98.8 % of the actual strain in the fibre.

Experimental approach

As mentioned before, the experimental temperature dependence of the 80 µm and 125 µm DTG®s is determined from -60 °C till 140 °C in steps of 40°C. The temperature is monitored using a Pt100 probe and a typical temperature variation measured in the climate chamber during the strain cycle is in the order of 1 °C - 2 °C. The temperature fluctuations of the strain-free grating, used for temperature compensation, are in close agreement with the temperatures recorded by the Pt100 sensor. Therefore, the actual temperature fluctuations are not critical for the accuracy of the strain measurements.

The calibrations are preformed using the Zwick test-frame and adapted clamping setup as depicted in Figure 4-8, with a ramped loading scheme as explained in the section of the automated calibration (Page 102). In total three 80 µm samples and three 125 µm samples are tested. The calibrations were repeated three times at each temperature. Some of the samples are broken during testing, as such it was possible to repeat all calibration three times (see Table 4-11 for the exact number of tests).

The strain rate, ($d\varepsilon_{3'}/dt$), is monitored with the optical extensometer and simultaneously the wavelength shift in time, ($d\lambda/dt$) is monitored with the FBG interrogator. The wavelength shift as function of the applied strain, i.e. the strain sensitivity ($d\lambda/d\varepsilon_{3'}$), is then the ratio of both slopes (Equation 4-13). The strain gauge factor at each temperature is then given by:

$$S_\varepsilon = \frac{1}{\lambda_{B,0}} \frac{d\lambda_B}{d\varepsilon_{3'}} \,, \qquad 4\text{-}33$$

with $\lambda_{B,0}$, the initial nominal wavelength of each calibration. The calculated averages of the S_ε-*factor* for the 80 µm and 125 µm DTG®s at each temperature and their standard deviations are found in Table 4-11 and the data for each fibre is plotted in Figure 4-28.

Table 4-11: Overview of the S_ε-factor at different temperatures of the 80µm and 125µm DTG®s, using the automated test setup using a ramped loading scheme

DTG® Sample	# tests	S_ε - factor					
		-60°C	-20°C	20°C	60°C	100°C	140°C
80 µm (PR2008_1)	7	0.7766 ± 0.0166	0.7857 ± 0.0121	0.7866 ± 0.0153	0.7914 ± 0.0295	0.7778 ± 0.0196	0.7901 ± 0.0228
125 µm (PR2008_1)	8	0.7440 ± 0.0191	0.7460 ± 0.0418	0.8004 ± 0.0211	0.7958 ± 0.0191	0.8054 ± 0.0139	0.7829 ± 0.0163
Mean	15	0.7592 ± 0.0241	0.7645 ± 0.0368	0.7939 ± 0.0193	0.7937 ± 0.0237	0.7925 ± 0.0215	0.7863 ± 0.0192

The variation of the *S_ε-factor* over temperature for the 125 µm fibre is much higher compared to the 80 µm which is likely to be more stable. However, a large scatter is seen in both of the data at different temperatures. To have a better idea on the average response at each temperature, the data of all samples at each temperature is taken together and the mean values are calculated (bottom row in Table 4-11).

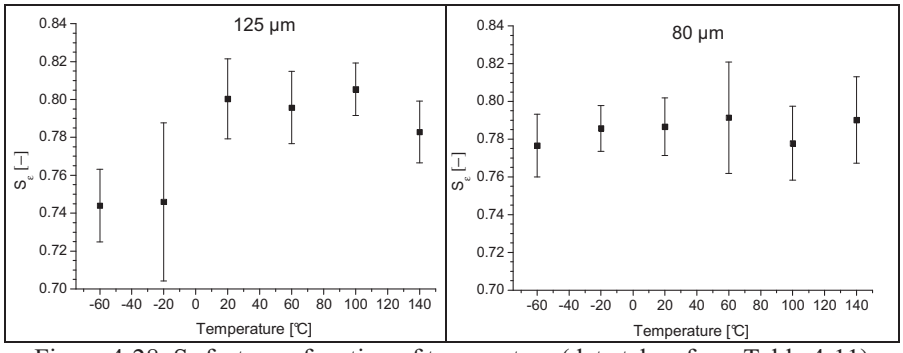

Figure 4-28: S_ε-factor as function of temperature (data taken from Table 4-11)

Qualitatively both fibres show the same behaviour over the complete temperature range. We can see that the strain response decreases at lower temperatures. However, a large scatter is visible from the data and the behaviour at higher temperatures from 20 °C till 140 °C does not show a visible trend, indicating that the dependence of the strain gauge factor on temperature at higher temperatures is not really distinct. It is believed that the large scatter in the *S_ε-factor* is owing to exertion of the fibre in the thread on the spools, which occurs after a certain strain level, as explained in the section of the automated calibration (Page 102) using the ramped loading approach. A such, small fluctuations in the applied strain occur, and large fluctuations in the read-out of the optical extensometer system occur because of the rather simple proportional control. Since the values of the *S_ε-factor* for both the 80 µm and 125 µm DTG®s are in the same order of magnitude the average *S_ε-factor* is calculated and is plotted against the temperature in Figure 4-29.

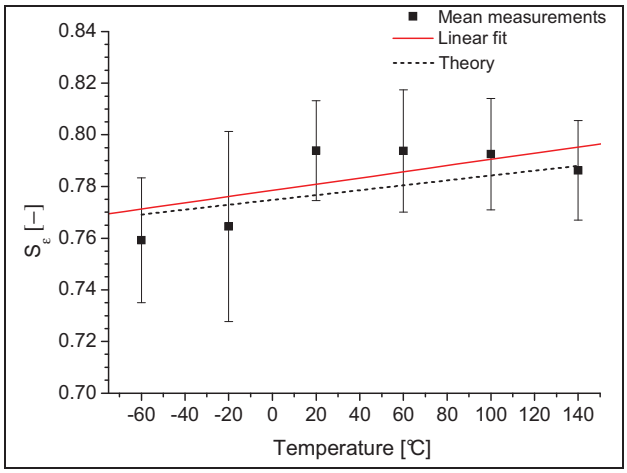

Figure 4-29: Mean values of the S_ε-factor as function of temperature between -60°C and 140°C for the 80µm and 125µm DTG®s.

The linear fit of this data is plotted as well, together with the simulated temperature dependent *S_ε-factor*, calculated using Equation 4-31. From the slope of the linear fit of the experimental data we find that $dS_\varepsilon^{fit}/dT = 1.2 \cdot 10^{-4} \cdot °C^{-1}$, which is slightly higher than the theoretical slope of $dS_\varepsilon/dT = 9.41 \cdot 10^{-5} \cdot °C^{-1}$. Although the data shows a large scatter, the linear slope matches more or less the theoretical slope, which indicates indeed a dependency of the strain gauge factor on temperature of the DTG®s is observed. However, because of the large scatter in all of the strain measurements, and because a discrepancy exists between the 80 µm and 125 µm at lower temperatures, no real quantitative conclusions can be drawn on the dependency of the *S_ε-factor*. Hence, the temperature dependency of the strain gauge factor will not be taken into account in the calculations in the next chapters, but remark that one should keep in mind that these effects exist and could affect the measurements.

4. 5. 2. b. Temperature dependence of the load response of DTG®s

To determine the temperature dependency of the load or stress response of the DTG®s, the exact same setup as explained in the experiments on the temperature dependence of the strain response is used, however, another approach is applied. Instead of using the strain data, which is recorded by the optical extensometer system, we use the applied load measured by the load cell, to calculate the load sensitivity of the DTG®s. One extra 80 µm sample and 125 µm sample are tested using this approach. The calibrations were repeated three times at each temperature, see Table 4-12.

The determination of the load sensitivity is performed similar to the case of the strain sensitivity previously described in Section 4. 5. 2. a. . The rate of the load, (dF/dt), is monitored with the optical load cell and simultaneously the wavelength shift in time, ($d\lambda/dt$) is monitored with the FBG interrogator. An example of the plots is shown in Figure 4-30:

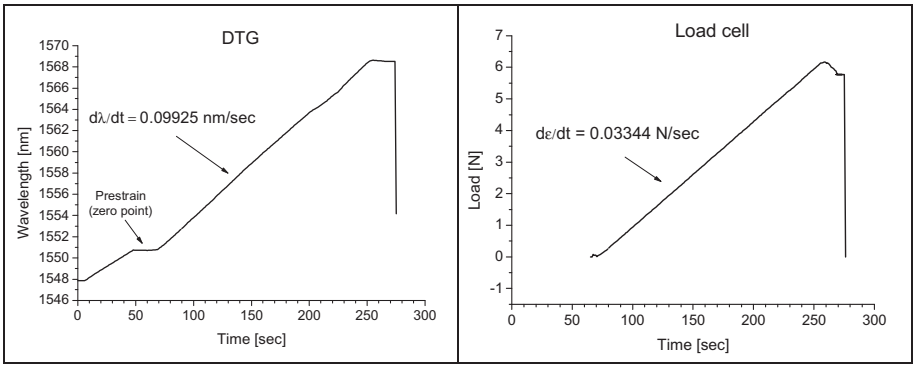

Figure 4-30: Plot of the wavelength versus time (left), plot of the applied load versus time (right).

The wavelength shift as function of the applied load, i.e. the load sensitivity, ($d\lambda/dF$) is then calculated from the ratio of both slopes.

$$\frac{d\lambda}{dF} = \frac{\frac{d\lambda}{dt}}{\frac{dF}{dt}}. \qquad 4\text{-}34$$

The load sensitivity, i.e. wavelength shift per unit applied force, of optical fibres is defined by the cross sectional surface of the fibre. The load sensitivity of the 80 µm DTG®, is higher than the 125 µm DTG®, and is understood by the fact that a thinner optical fibre will elongate more for the same amount of force than a thicker optical fibre, hence more wavelength shift is induced for the same amount of applied force for a thinner fibre Bragg grating. The load sensitivities of both fibres is given in Table 4-12 and plotted in Figure 4-31.

Table 4-12: Overview of the load sensitivity ($d\lambda/dF$) at different temperatures of the 80µm and 125µm DTG®s, using the automated test setup using a ramped loading scheme

DTG® Sample	# tests	$\frac{d\lambda}{dF}$ [nm/N]					
		-60°C	-20°C	20°C	60°C	100°C	140°C
80 µm (PR2008_1)	3	2.859 ± 0.003	2.889 ± 0.007	2.924 ± 0.009	2.943 ± 0.001	2.933 ± 0.001	2.940 ± 0.011
125 µm (PR2008_1)	3	1.238 ± 0.002	1.245 ± 0.002	1.258 ± 0.002	1.268 ± 0.005	1.265 ± 0.004	1.259 ± 0.011
Ratio (80 / 125)	-	2.31	2.32	2.35	2.32	2.32	2.34

The load sensitivity is in fact inversely proportional to the square of the diameter of the optical fibre. The ratio of the cross sectional surface of the two fibres will define the ratio of the load sensitivities of the DTG®s. The ratio of the load sensitivities is given in the bottom row of Table 4-12 and ranges between 2.31 and 2.35. To calculate the surface ratio the actual diameter of the 80 µm fibre and 125 µm fibre of the PR2008_01 is measured using a microscope and is found to be 82.5 µm and 124.7 µm respectively (Chapter 3, Table 3-3). The ratio of the surfaces is then $124.7^2 / 82.5^2 = 2.28$. It is noted the surface ratio does not take into account the coated surface of the DTG®s. As such a small error is made on the calculated surface ratio. However, when comparing the surface ratio with the ratio calculated from the load sensitivities of both fibres (Table 4-12), we can see that the values are in good agreement.
If we look at the graphs in Figure 4-31, we notice that qualitatively over the complete temperature range, the behaviour of the 80 µm and 125 µm DTG®s is more or less the same. A clear decrease is seen at the negative temperatures. In general the scatter of the sensitivities of the 80 µm fibre is higher than seen in the results of the 125 µm fibre, which is owing to the fact the 80 µm DTG®s are more sensitive to (small) load variations.

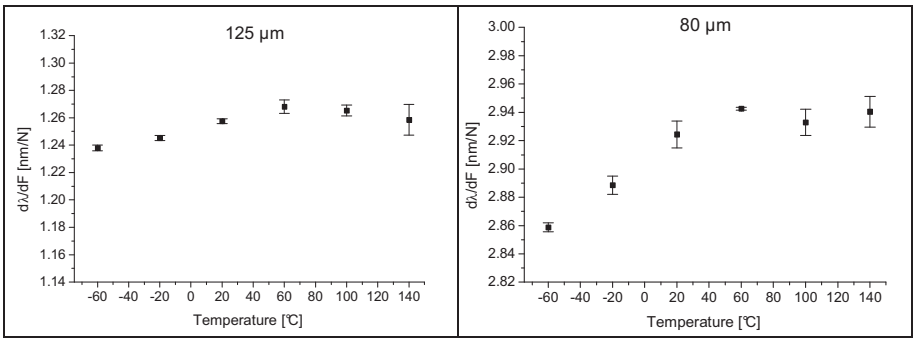

Figure 4-31: Load sensitivities of the 80 µm and 125 µm DTG®s (coated)

Maier R.J.R et al. [33] performed tests in a similar temperature range, i.e. -38 °C till 120 °C, and reported discontinuities in the response of a recoated FBG with acrylic recoating material, particularly at temperatures below room temperature. The glass transition temperature T_g, of the acrylic polymer starts at 26 °C and the coating below T_g becomes much harder. Because the material changes significantly over the tested temperature range and because the volume fraction of the coating is typically >50 %, it has a large impact on the load sensitivity of (re)coated FBGs. Since both the DTG®s have the ORMOCER® coating it is believed the untypical response seen in Figure 4-31 is owing to the change of material properties of the coating.
To investigate the influence of the ORMOCER® coating material, an additional 125µm test-sample consisting of 2 DTG®s (i.e. one stripped and one coated DTG® in series), with a nominal wavelength of 1530 nm and 1532 nm, and a spatial separation of 100 mm, is tested. As such, the two DTG®s are loaded simultaneously and the load sensitivities of both sensors can be compared. The plots are shown in Figure 4-32. The response of the coated DTG®s (Figure 4-32, left) is similar to the results plotted for the 125 µm DTG®s in Figure 4-31 (note that the scale of the y-axis is different), however, we notice a completely opposite response for the stripped

DTG®. This test clearly illustrates that the coating of the optical fibre has a significant influence on the load sensitivity of the fibre Bragg grating. It proves that, when the coating becomes stiffer at lower temperatures, the total stiffness (i.e. composite modulus) of the fibre increases and the load sensitivity decreases at lower temperatures. The stiffness of the ORMOCER® coating at different temperatures is further discussed in the Section 4. 5. 2. c. .

If we look at the response of the stripped fibre (Figure 4-32, right) we notice a negative trend of the curve over the complete temperature range. The linear fit is plotted in the graph as well, and it is found that for the 125 µm DTG® tested here, the temperature dependence of the load sensitivity is $-0.0986\ pm\ N^{-1}{}^{\circ}C^{-1}$ which corresponds to $-0.0012\ pm\ MPa^{-1}{}^{\circ}C^{-1}$ for a 124.7 µm silica cladding. The values are in the same order of magnitude as the values of $-0.1618\ pm\ N^{-1}{}^{\circ}C^{-1}$ or $-0.0020\ pm\ MPa^{-1}{}^{\circ}C^{-1}$ reported by Maier R.J.R. et al. [33]

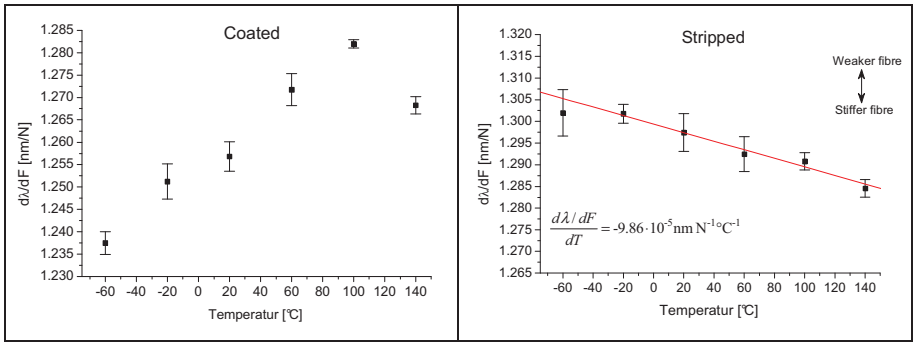

Figure 4-32: Plot of the load sensitivity for a coated 125 µm DTG® (left), and a stripped 125 µm DTG® (right)

The observations indicate that the optical fibre becomes stiffer at higher temperatures. This is in accordance with reports found in literature, where it is found that the temperature dependency of the Young's modulus of pure silica is found $E_{SiO_2} = 72.2 + 0.0093 \cdot \Delta T \ \left[GPa\right]$ [17] with $E_{SiO_2} = 72.2$ GPa at 0 °C. This corresponds to a variation of the Young's modulus of approximately 1.3 % over a temperature difference of 100 °C.

With $d\lambda / dF \big/ dT = S_F$, the temperature dependence of the load sensitivity of the 125 µm DTG®s can then be expressed as follows:

$$S_F(T) = 1.297 - 9.86 \cdot 10^{-5} \cdot \Delta T \ \left[nm\ N^{-1}\right], \qquad 4\text{-}35$$

with ΔT, the temperature difference with regard to T = 20 °C. In terms of the stress sensitivity, $d\lambda / d\sigma \big/ dT = S_\sigma$ with a silica cladding of 124.7 µm we can then write:

$$S_\sigma(T) = 0.016 - 0.12 \cdot 10^{-5} \cdot \Delta T \ \left[nm\ \mathrm{MPa}^{-1}\right]. \qquad 4\text{-}36$$

Remark that Equation 4-36 is independent on the fibre diameter and thus holds for both the 125 µm as well as for the 80 µm DTG®s. From these results it is found that the load –or stress sensitivity varies 0.75 % over a 100 °C temperature difference. It is believed that the dependency is mainly caused by the dependency on temperature of the Young's modulus of the fibre. However, from [17] the variation of Young's modulus of the pure silica over the same temperature difference is 1.3 %, which is much higher compared to the variation observed for the DTG®s. Because of the still large scatter in all of the results shown in Figure 4-32, no exact quantitative analysis can be performed. For a more quantitative comparison, the setup needs to be improved and a larger number of tests need to be carried out. However, even though the response is small, qualitatively these tests have clearly proven that a temperature dependency of the load / stress response of (stripped) DTG®s exist.

4. 5. 2. c. Method for calculating the Young's Modulus of fibre coating as function of temperature

In this section, a more or less straightforward analytical approach is used, to determine the dependency of the Young's modulus of the ORMOCER® coating on temperature in the temperature range of -60 °C till 140 °C. As seen in the previous sections there exists a clear influence of the coating on the strain -and load sensitivity of a DTG®. This property will be exploited to determine the Young's modulus of the ORMOCER®. The method of calculation is based on the difference in wavelength shifts (i.e. strain) of a stripped and coated DTG® during a loading cycle. Two DTG® arrays are tested, similar to the one which is tested in previous section. The sensors have a nominal wavelength of 1530 nm (coated) and 1532 nm (stripped), and they are spatially separated by 100 mm. The principle of the experiment is illustrated in Figure 4-33:

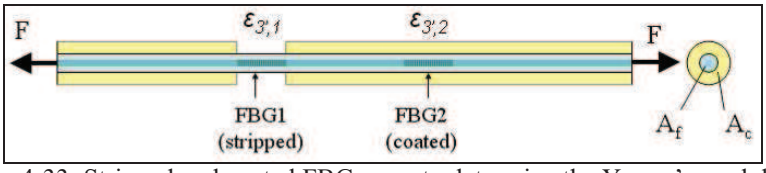

Figure 4-33: Stripped and coated FBG array to determine the Young's modulus of the fibre coating

If the fibre, as illustrated in Figure 4-33, is loaded in axial direction, an axial strain is induced in both FBGs (or DTG®s), with $\varepsilon_{3',1}$ the axial strain induced in the stripped FBG and $\varepsilon_{3',2}$ the axial strain induced in the coated FBG, with $\varepsilon_{3',1} > \varepsilon_{3',2}$. We can then write the following stress equations:

$$\begin{cases} \dfrac{F}{A_f} = \sigma_f = \varepsilon_{3',1} \cdot E_f \\ \dfrac{F}{A_{tot}} = \sigma_{tot} = \varepsilon_{3',2} \cdot E_{tot} \end{cases}, \qquad 4\text{-}37$$

with A_f the cross sectional surface of the silica, $A_{tot} = A_f + A_c$ the total fibre surface with coating and A_c the surface of the coating, E_f the Young's modulus of the fibre and E_{tot} the composite modulus of the coated fibre, calculated using a 'parallel model' in analogy to the classical laminate theory (CLT), given by:

$$E_{tot} = \frac{A_f}{A_{tot}} E_f + \frac{A_c}{A_{tot}} E_c \,. \tag{4-38}$$

with E_c the Young's modulus of the coating material. From the ratio of the stress equations in Equation 4-37 we can determine the composite modulus:

$$E_{tot} = \frac{A_f \cdot \varepsilon_{3',1} \cdot E_f}{A_{tot} \cdot \varepsilon_{3',2}} \,. \tag{4-39}$$

To express the axial strains we will assume small axial strain perturbations. We can write the axial strains in accordance with Equation 4-10:

$$\left.\begin{aligned} \varepsilon_{3',1} &= \frac{1}{S_\varepsilon}\frac{\Delta\lambda_1}{\lambda_{1,0}} \\ \varepsilon_{3',2} &= \frac{1}{S_\varepsilon}\frac{\Delta\lambda_2}{\lambda_{2,0}} \end{aligned}\right\} \Rightarrow \frac{\varepsilon_{3',1}}{\varepsilon_{3',2}} = \frac{\Delta\lambda_1 / \lambda_{1,0}}{\Delta\lambda_2 / \lambda_{2,0}} \,. \tag{4-40}$$

Hence, the ratio of the axial strains can be calculated simply by using the ratio of the measured wavelength shifts. Substituting in Equation 4-39, we obtain the following equation for the composite modulus:

$$E_{tot} = \frac{A_f \cdot E_f}{A_{tot}} \cdot \frac{\Delta\lambda_1 / \lambda_{1,0}}{\Delta\lambda_2 / \lambda_{2,0}} \,. \tag{4-41}$$

Note that, this composite modulus is determined from the wavelength shifts measured for the stripped and the coated DTG®, independent from the applied load. This allows in fact to determine the Young's Modulus for a static loading case as well.

By reorganizing Equation 4-38 and substituting the composite modulus of Equation 4-41, we obtain a generalized formula for the calculation of the Young's modulus of the fibre coating:

$$E_c = \frac{E_{tot} A_{tot} - A_f E_f}{A_c} = \frac{A_f \cdot E_f}{A_c} \cdot \left(\frac{\Delta\lambda_1 / \lambda_{1,0}}{\Delta\lambda_2 / \lambda_{2,0}} - 1 \right) \,. \tag{4-42}$$

Equation 4-42 can then be used at an arbitrary loading case to calculate the Young's modulus of the fibre at any given temperature. By filling in $E_f = 72.4\ GPa$ [17], $A_f = \frac{\pi}{4} d_f^2 = 0.01221\ mm^2$, with $d_f = 0.1247\ mm$, the diameter of the silica fibre (Chapter 3, Table 3-3) and $A_c = \frac{\pi}{4}\left(d_{tot}^2 - d_f^2\right) = 0.01620\ mm^2$, with $d_{tot} = 0.190\ mm$, the total outer diameter of the coated fibre, the stiffness of two DTG®s arrays, as illustrated in Figure 4-33, is determined over the complete temperature range from -60 °C till 140 °C, see Figure 4-34. Sample 1 is tested over the complete range and Sample 2 has been tested from 20 °C till 140 °C to validate the measurements. Because a temperature dependency of the Young's Modulus of silica exists, see Section 4. 5. 2. b. , additionally, the data of Sample 1 is corrected using $E_{SiO_2} = 72.2 + 0.0093 \cdot \Delta T \ \left[GPa\right]$ [17]. However, no large influence on the Young's Modulus of the ORMOCER® is found, see Figure 4-33.

For both samples it is found that the ORMOCER® coating weakens at higher temperatures and that the coating becomes stiffer at lower temperatures. At 20 °C an untypical behaviour is noticed. A sudden increase is found which is not corresponding to the normal 'course' of the curve. This effect is seen in both measurements. It is believed that the effect is caused by humidity which is absorbed by the ORMOCER® at temperatures close to the ambient temperatures. The absorption of water and the sensitivity to relative humidity (RH %) by a polyimide polymer coatings has been studied by Kronenberg [19]. Kronenberg found that the wavelength shift per percentage of relative humidity change is approximately $2.21 \pm 0.10 \cdot pm\%RH^{-1}$ for the specific coating material he has been using. This means that apart from the applied strain, an additional hygroscopic strain is acting on the coated DTG®, which influences the measured wavelength shifts. In case of a polyimide coating a change of 20 %RH at room temperature would add approximately 44 pm to the resulting wavelength shift. Hence the calculation of the E-modulus is strongly dependent on the additional humidity response of the sensor. Papadogiannisa D.Y. et al [35] have investigated the effect of humidity on the Young's modulus of an ORMOCER® composition. They found that stiffness of the wetted ORMOCER® composition decreases 9 % compared to the dry material. Because in this work the tests at each temperature are not performed on the same day, it is believed that the results on the Young's modulus of the ORMOCER® coating are influenced by relative humidity changes, moreover, when considering a closed climate chamber (or oven), depending on the absolute humidity the relative humidity can change significantly between 0 °C and 100 °C [19].

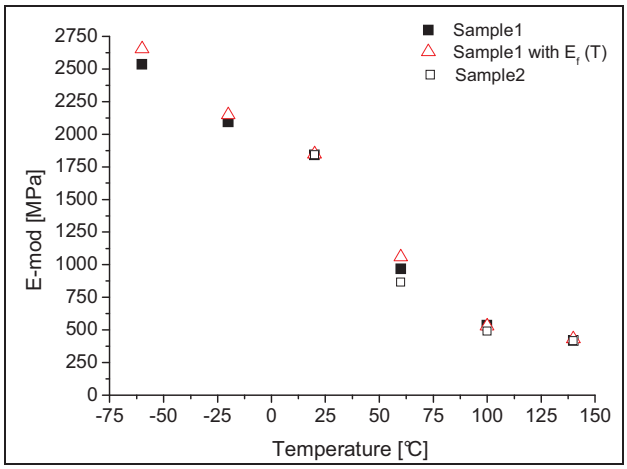

Figure 4-34: Young's modulus of the ORMOCER® against temperature for two samples, from -60 °C till 140°C.

Because of the uncertainty of the effects of the hygroscopic strains no exact determination of the Young's Modulus of the ORMOCER® is possible. To study better the humidity effects and to obtain more accurate results the experiments should be repeated in a climate chamber where the temperature and relative humidity are controllable parameters. However, the method applied here confirms that the Young's Modulus of the ORMOCER® is temperature dependent and that in principle the fibre Bragg grating is a suitable tool to estimate the coating' stiffness. Note that the 'parallel model' of the CLT is used to calculate the composite modulus. In this model the difference between the Poisson' ratio of the silica fibre and fibre coating is neglected. To improve the calculation of the Young's Modulus of the fibre coating a more accurate model to determine the composite modulus needs to be implemented.

4. 6. DTG® SENSOR PROPERTIES_SUMMARY

In Table 4-13 all properties determined for the 80 µm DTG®s in Chapter 3 and this chapter are summarized. It can be seen as a kind of specification sheet of the newly developed 80 µm DTG®s.

Table 4-13: Summary table of all the specifications of the newly developed 80 µm DTG®

Parameter	**Unit**	**Value**
Fibre diameter (cladding)	µm	80
Core diameter	µm	≈ 4.5
Coating type	-	ORMOCER®
Coating fibre diameter	µm	114 (minimum)
Fibre attenuation	dB/km	>15 @1550nm
Fibre Numerical Aperture	-	≈ 0.2
Fibre Relative refractive index (Δ)	10^{-3}	10.48
Fibre effective index	-	≈ 1.446
Grating length	mm	8
Reflectivity	%	>15 @1550nm
FWHM	pm	110 ± 4 @1550nm
Temperature sensitivity	K^{-1} , K^{-2}	$S_{T1} = 6.360 \cdot 10^{-6}$, $S_{T2} = 7.6 \cdot 10^{-9}$
Strain gauge parameter (S_ε)	-	0.777
Operational Temperature range	°C	-180 …+200 (+300)*
Tensile strain (ε_{ULT})	[%]	6
Tensile strength (σ_{ULT})**	[MPa]	4700

4. 7. CONCLUSIONS

In this chapter the author has elaborated in detail the methods and setups to characterize the reflectivity, the opto-mechanical and thermo-optic properties and the thermal behaviour of the 80 µm and 125 µm reference DTG®s. The properties of both types are compared and in general the author can conclude that it is possible to produce 80 µm and 125 µm DTG®s with identical performances. The draw tower process allows thus to produce high quality single pulse smaller diameter FBGs with identical peak reflectivity and peak width (FWHM) as the standard diameter. However, it is shown that the exact sensors characteristics of DTG®s or fibre Bragg gratings in general are not easily determined. There are multiple factors which need to be taken into account, such as the intrinsic (cross-)sensitivity of strain

* short term, annealing effect on reflectivity and Bragg wavelength

** calculated using the 'composite' modulus of a coated DTG® fibre with ORMOCER®

and temperature, the thermal stability, the coating properties and last but not least the calibration setup itself. If one makes errors on the level of calibration parameters (i.e. determination of the FBG' sensitivities), obvious this will have later on consequences on the output of the sensor when being employed. Thus calibrations of FBGs should be carried out with care.

Strain gauge parameter

The author has shown that the calibration of the strain gauge parameter (S_ε), is not straightforward. The fixation of the (smaller diameter) optical fibre and a stable and accurate reference strain measurement system are necessary to obtain accurate results. Large errors on the calculation of the strain gauge parameter can occur if these two factors are not optimal. From the presented results on the strain gauge factors we can conclude that the manual calibration using a long piece of fibre (approximately 0.8 m – 1 m) fixated in small steel capillaries by using (epoxy) glue is the most accurate method to determine the axial strain sensitivity of both the 80 µm and 125 µm DTG®s. A strain gauge factor of $S_\varepsilon \approx 0.777$ is found for both types. This value is found lower than the theoretical determined S_ε-factor of $S_{\varepsilon,theor} \approx 0.798$, however, because of the possible scatter on the theoretical strain gauge factor due to the uncertainty of the exact optical properties (i.e. $\overline{n}$, υ_f) and the strain optic coefficients (p_{11} and p_{12}) the author believes that the experimental and theoretical obtained S_ε-factor are matching within acceptable limits. As such the experimental strain gauge factor will be further applied in this work.

Temperature sensitivity and thermal stability

From the point of view of temperature calibration it is proven that over a large temperature range the linear approximation is not accurate. To determine the temperature sensitivity over a large temperature range, we need to take into account the linear effect of the refractive index as function of temperature. As such the temperature dependence of an FBG is given by a second order polynomial. Matching results are found when fitting the logarithmic calibration curve with a second order polynomial. As such two temperature parameters are found (S_{T1} and S_{T2}) which again are found identical for the 80 µm and 125 µm DTG®s ($S_{T1} = 6.34 \cdot 10^{-6} °C^{-1}$ and $S_{T2} = 7.6 \cdot 10^{-9} °C^{-2}$). These parameters will further in this work become important when considering accurate temperature compensation techniques to determine for example the thermal expansion of composite laminates (Chapter 6 and Chapter 8). Another issue which has been elaborated with regard to exposing the DTG®s to high temperature, is the thermal stability of these gratings. It is found that the DTG®s are shortly annealed during the UV-curing process of the ORMOCER® coating. As such these gratings are thermally stable up to approximately 150 °C. However, when exposed to higher temperatures (T_{max} = 350 °C) the reflectivity of both the 80 µm and 125 µm DTG®s drops to approximately 10 % of their initial power. When comparing the wavelength shift (drift) during annealing, the behaviour is found clearly different. The drop is approximately four times higher in case of the 125 µm DTG®s. A possible explanation is the probably higher homogeneous refractive index of the 125 µm DTG®s, however, further research and more annealing experiments are necessary to prove this statement.

Temperature dependence of the strain and load (stress) sensitivity

In literature is reported that there exists a temperature dependency of the strain and stress sensitivity of FBGs [32-33]. First the author has analytically determined the S_ε-factor as function of temperature from the temperature dependency of the strain-optic coefficients, the Poisson's ratio and the refractive index, and found that $S_\varepsilon(T) = 0.777 + 9.41 \cdot 10^{-5} \Delta T$. For a temperature difference of ±100 °C this results in a relative change of the strain gauge factor of ±1.2 %, which is a significant error if we want to accurately determine strains over a large temperature range. Then the author has attempted to reproduce these results experimentally for temperatures between -60 °C and 140 °C. The experimental results however, showed a large scatter on the $S_\varepsilon(T)$-factor. Although a match is found between the linear fit of the experiments of both the 80 µm -and 125 µm DTG®s and the theory, the author has no confidence in these results because of the uncertainty of the strain readings of the optical extensometer. More experiments are necessary using another strain referencing technique to validate these results, hence this is subject for future work.

More confidence is found in the load -or stress-sensitivity as function of temperature. Now, using the same setup, the load-cell readings are used instead of the strain. It is found that the load sensitivity of a 80 µm is approximately 2.3 times higher than the 125 µm DTG®s, which is in accordance with the ratio of the cross-sectional surface. The results show that the coating has a large influences on the results. Similar testing on a stripped and a coated DTG®s confirms this effect, which proves that the coating stiffness is temperature dependent as well. The author has found a stress sensitivity of $S_\sigma(T) = 0.016 - 0.12 \cdot 10^{-5} \cdot \Delta T \quad \left[nm \text{ MPa}^{-1} {}^\circ C^{-1} \right]$ for the stripped fibre, which is in accordance with the results reported by Maier R.J.R. et al [33]. It is believed that the temperature dependence of the Young's Modulus of the silica fibre is the main cause of this effect. For a temperature difference of 100 °C this results in a relative change of the stress sensitivity of approximately -0.75 %.

Additionally to the analysis of the strain and stress sensitivity as function of temperature, tests are performed to estimate the temperature dependency of the Young's modulus of the ORMOCER® coating. In principle, when the same (axial) force is applied on a coated and stripped FBG, one is able to estimate the Young's Modulus of the fibre coating, based on the difference in strain (i.e. wavelength shift) between both FBGs. Results prove that the Young's modulus of the ORMOCER® coating material is temperature dependent and that the coating becomes stiffer at lower -and weaker at higher temperatures. However, most probably relative humidity changes have influenced the results at ambient temperatures and no accurate determination of the Young's modulus is possible. More experiments in a humidity and temperature controlled environment are necessary to accurately determine the temperature dependency of the coating stiffness.

From these numerous experiments and results the author concludes that the properties and performances of the newly developed 80 µm DTG®s are equal to the standard 125 µm version. Thus there is no fundamental reason why we should not use the new smaller diameter high quality FBGs for strain monitoring in composites. Moreover, they have one major advantage; they are smaller and thus even better suited to be used for the incorporation in FRPs, which is subject of Part II.

4. 8. REFERENCES

1. FOS&S. Available from: http://www.Fos-s.com.
2. Dyer, S.D., Williams, P.A., Espejo, R.J., Kofler, J.D., and Etzel, S.M., *Fundamental limits in fiber Bragg grating peak wavelength measurements*, in *17th International Conference on Optical Fibre Sensors, Pts 1 and 2*, M. Voet, et al., Editors. 2005. p. 88-93.
3. Feynman, P., Richard., *The Feynman lectures on physics mainly electromagnetism and matter*. Vol. 2. 1964.
4. FBGSTechnologies. Available from: http://www.fbgs-technologies.com/.
5. Window, A.L. and Holister, G.S., *Strain Gauge Technology*. 1982, London: Applied Science Publishers LTD.
6. Wan, K.T., Leung, C.K.Y., and Olson, N.G., *Investigation of the strain transfer for surface-attached optical fiber strain sensors.* Smart Materials & Structures, 2008. **17**(3).
7. Li, W.Y., Cheng, C.C., and Lo, Y.L., *Investigation of strain transmission of surface-bonded FBGs used as strain sensors.* Sensors and Actuators a-Physical, 2009. **149**(2): p. 201-207.
8. Bertholds, A. and Dandliker, R., *Determination of the individual strain-optic coefficients in single-mode optical fibers.* Journal of Lightwave Technology, 1988. **6**(1): p. 17-20.
9. Othonos, A. and Kalli, K., *Fiber Bragg gratings: Fundamentals and Applications in Telecommunications and Sensing*. 1999: Artech House.
10. Abdi, A.M., Suzuki, S., Schulzgen, A., and Kost, A.R., *Modeling, design, fabrication, and testing of a fiber Bragg grating strain sensor array.* Applied Optics, 2007. **46**(14): p. 2563-2574.
11. Pinnow, D., *Elastooptical Materials*, in *Handbook of Lasers*, R.J. Pressley, Editor. 1971: Cleveland (OH).
12. Guemes, J.A. and Menendez, J.M., *Response of Bragg grating fiber-optic sensors when embedded in composite laminates.* Composites Science and Technology, 2002. **62**(7-8): p. 959-966.
13. Luyckx, G., *Multi-axial strain monitoring of fibre reinforced thermosetting plastics using embedded highly birefringent optical fibre Bragg sensors*, in *Department of Materials Science & Engineering*. 2010, Ghent University.
14. Johnson, K.L., *Contact Mechanics*. 1987, Cambridge: Cambridge University Press.
15. Wagreich, R.B., Atia, W.A., Singh, H., and Sirkis, J.S., *Effects of diametric load on fibre Bragg gratings fabricated in low birefringent fibre.* Electronics Letters, 1996. **32**(13): p. 1223-1224.
16. Beitz, W. and Küttner, K.-H., *Dubbel: Handbook of mechanical engineering*. 1994: Springer-Verlag.
17. Fukuhara, M., Sanpei, A., and Shibuki, K., *Low temperature elastic moduli, Debye temperature and internal dilational and shear frictions of fused quartz* J. Mater. Sci. , 1997 **32**(1207–11).
18. Luyckx, G. and Voet, E., *MASSFOS: Detailed sensor configuration*. 2009: Gent.
19. KRONENBERG, P., *Construction material monitoring with optical hair hygrometers*. 2003, École polytechnique fédérale de Lausanne (EPFL): Lausanne.

20. Fibercore, *Factnote 4.1.2: The Physical properties of Silica and UV Cure Axrylate Coating Packages*. 2004: Chilworth.
21. Kühn, B. and Schadrack, R., *Thermal expansion of synthetic fused silica as a function of OH content and fictive temperature.* Journal of Non-Crystalline Solids, 2009. **355**(4-5): p. 323-326.
22. Pal, S., Sun, T., Grattan, K.T.V., Wade, S.A., Collins, S.F., Baxter, G.W., Dussardier, B., and Monnom, G., *Non-linear temperature dependence of Bragg gratings written in different fibres, optimised for sensor applications over a wide range of temperatures.* Sensors and Actuators a-Physical, 2004. **112**(2-3): p. 211-219.
23. Masuda, Y., Nakamura, M., Komatsu, C., Fujita, K., Yamauchi, M., Kimura, M., Mizutani, Y., Kimura, S., Suzaki, Y., Yokouchi, T., Nakagawa, K., and Ejima, S., *Wavelength evolution of fiber Bragg gratings fabricated from hydrogen-loaded optical fiber during annealing.* Journal of Lightwave Technology, 2004. **22**(3): p. 934-941.
24. Lindner, E., Chojetzki, C., Bruckner, S., Becker, M., Rothhardt, M., and Bartelt, H., *Thermal regeneration of fiber Bragg gratings in photosensitive fibers.* Optics Express, 2009. **17**(15): p. 12523-12531.
25. Rathje, J., Kristensen, M., and Pedersen, J.E., *Continuous anneal method for characterizing the thermal stability of ultraviolet Bragg gratings.* Journal of Applied Physics, 2000. **88**(2): p. 1050-1055.
26. Gusarov, A., Vasiliev, S., Medvedkov, O., McKenzie, I., and Berghmans, F., *Stabilization of Fiber Bragg Gratings Against Gamma Radiation.* Ieee Transactions on Nuclear Science, 2008. **55**(4): p. 2205-2212.
27. Gusarov, A., Chojetzki, C., McKenzie, I., Thienpont, H., and Berghmans, F., *Effect of the Fiber Coating on the Radiation Sensitivity of Type I FBGs.* Ieee Photonics Technology Letters, 2008. **20**(21-24): p. 1802-1804.
28. Poumellec, B., Riant, I., and Tessier-Lescourret, C., *Precise life-time prediction using demarcation energy approximation for distributed activation energy reaction.* Journal of Physics-Condensed Matter, 2006. **18**(7): p. 2199-2216.
29. Erdogan, T., Mizrahi, V., Lemaire, P.J., and Monroe, D., *Decay of ultraviolet-induced fiber Bragg gratings.* Journal of Applied Physics, 1994. **76**(1): p. 73-80.
30. Razafimahatratra, D., Niay, P., Douay, M., Poumellec, B., and Riant, I., *Comparison of isochronal and isothermal decays of Bragg gratings written through continuous-wave exposure of an unloaded germanosilicate fiber.* Applied Optics, 2000. **39**(12): p. 1924-1933.
31. Hong, K., Nguyen, H.G., Limberger, R.P., Salathe´, F., Cochet, L., and Dong, *UV-irradiation induced stress and index changes during the growth of type-I and type-IIA fiber gratings.* Opt. Commun. , 2003. **216**(225).
32. O'Dwyer, M.J., Ye, C.C., James, S.W., and Tatam, R.P., *Thermal dependence of the strain response of optical fibre Bragg gratings.* Measurement Science & Technology, 2004. **15**(8): p. 1607-1613.
33. Maier, R.R.J., MacPherson, W.N., Barton, J.S., Jones, J.D.C., McCulloch, S., and Burnell, G., *Temperature dependence of the stress response of fibre Bragg gratings.* Measurement Science & Technology, 2004. **15**(8): p. 1601-1606.

34. Scholze, H., *Glass- Nature, Structure and Properties*. 1991, New York: Springer Verlag.
35. Papadogiannisa, D., Y., Lakesb, R., S. , Papadogiannis, Y., Palaghiasd, G., and Helvatjoglu-Antoniades, M., *The effect of temperature on the viscoelastic properties of nano-hybrid composites.* Dental materials, 2008. **24**: p. 257-266.

PART II

DTG®s embedded in Thermoset and Thermoplastic composites

In Part I the manufacturing and the characteristics of non-embedded DTG®s are discussed. In part II, the author embeds the DTG®s in particular types of thermoset and thermoplastic carbon reinforced plastic laminates. In both cases the sensors are used to measure the strain field inside the composite material.

However, the functionality of the embedded sensor is multiple. The author will use the newly developed DTG®s in several stages of the composite lifetime. It starts with the monitoring of the composite manufacturing process and it ends with fatigue testing till failure of the composite laminates. During the different experiments, the sensors will be subjected to high temperatures, high pressures, extreme longitudinal strains and transvere strains and in the mean time they will be used to very accurately measure (multi-axial) strains inside composites at microstrain level (~10^{-6}).

One should bear in mind that, whatever strain field is acting on the DTG®s, the Bragg spectrum of the grating can either shift to higher or lower wavelengths, or becomes a little or heavily distorted, or both. In any case, the trick is to use the right methods and experimental approaches to unravel the correct information. Part II of this work will show that much more information is gathered from embedded FBGs than one might expect.

Chapter 5 MEASURING STRAIN WITH EMBEDDED FIBRE BRAGG GRATINGS_AN INTRODUCTION

The emphasis of this Chapter is to provide a general overview on strain measurements in fibre reinforced plastics by the usage of embedded fibre Bragg gratings. The reader will first be introduced to some technical issues which need to be considered when embedding FBGs in carbon fibre reinforced plastic (CFRP) laminates (Section 5. 1.). In the following sections, some topics are introduced which are relevant for the following Chapters where the focus lies on measurements by usage of the embedded DTG®s. Only a short introduction is aimed for to situate the different topics. For example, in Section 5. 2. the need to monitor residual strains during the manufacturing process is considered. In Section 5. 3. , the author will show that the strains inside the optical fibre, which can be seen as an inclusion in the host material, is not equal to the strains of that structure at the position of the optical fibre. Section 5. 4. teaches us that the response of the reflection spectra of Bragg sensors embedded in different types of composite materials can differ significantly. When the reflection spectrum tends to deform, this is sometimes seen as an additional problematic, however, by using the right measurement principles to determine the peak wavelength of (distorted) Bragg spectra this problem can be overcome. In addition a method is given to distinguish between transverse and longitudinal strain effects. Inevitably, an FBG exhibits a cross-sensitivity of strain and temperature. In practical the use of FBGs as strain sensor, we should compensate for intrinsic temperature effects. In this work in particular two techniques are used to compensate for temperature. The basic principle of both techniques and an overview of other temperature compensating methods used in literature will be given in Section 5. 5. .

5. 1. FBG SENSORS AND FIBRE REINFORCED PLASTICS: A SUCCESSFUL MARRIAGE?

High performance carbon fibre reinforced plastics are today more and more employed as primary structural parts in advanced engineering constructions. Despite the growing popularity of structural composite materials, one has to realize that the mechanical behaviour of anisotropic fibre reinforced plastics (FRPs) is significantly different compared to conventional isotropic construction materials. Unlike steel, aluminium (magnesium) alloys and titanium, no detailed histograms exists of the numerous composite materials which are on the market today or even more important, which are being developed at the time being. To improve knowledge on the (long term) structural response we need to record the feedback from applied loads, deformations and temperatures of (and especially inside) existing composite structures in real conditions. This will lead to highly valuable information for design criteria and composite lifetime predictions. Strain monitoring of an in-service structure should greatly enhance the insight and confidence in the (long-term) behaviour of high performance composite structures.

Therefore, research is being conducted worldwide on monitoring composite materials using embedded FBGs; starting from the occurrence of residual strains during the manufacturing process [1-3], and the measuring of the fatigue life of the composite material [4], up to the initiation of damage in the material [5-6].

However, is the combination of (embedded) Bragg sensors and composite materials a successful marriage? The answer of the author is a clear yes as will be proven in the next chapters, though, some technical issues needs to be considered.

5. 1. 1. Embedding process

Optical fibre sensors have a number of well-known advantages including insensitivity to electromagnetic interference, small dimensions, light weight, multiplexing capabilities and resistance to corrosion which can be used for their benefit of integrating them into a composite structure [7]. By integrating an FBG into a structure, it becomes very robust and it can survive the sometimes harsh environment in which FRPs are used. The compatibility of these sensors with various composite manufacturing processes, has already been proven in literature, and can be seen as an extra advantage. Typical examples found in literature are (Figure 5-1): *pultrusion* [8], where the Bragg grating is embedded in pultruded CFRP rods by feeding in the optical fibre together with the carbon fibres in the pultrusion line, *co-braided* with 3D-braided composites [9-12] where the optical fibre is incorporated in the axial yarn, running straight and parallel to the braiding direction in the specimen, and *lamination*, where the optical fibre is typically embedded parallel with the reinforcement fibres in thermoplastic laminates, consolidated during hot moulding press [13-14] and thermoset *laminates* and *technological specimens* [15] fabricated during autoclave processing. And thanks to their small size (diameter: 40µm-125µm) and particular shape (fibre), they can fairly easily be embedded in different fibre reinforced plastics without compromising the strength of the structure [16].

.

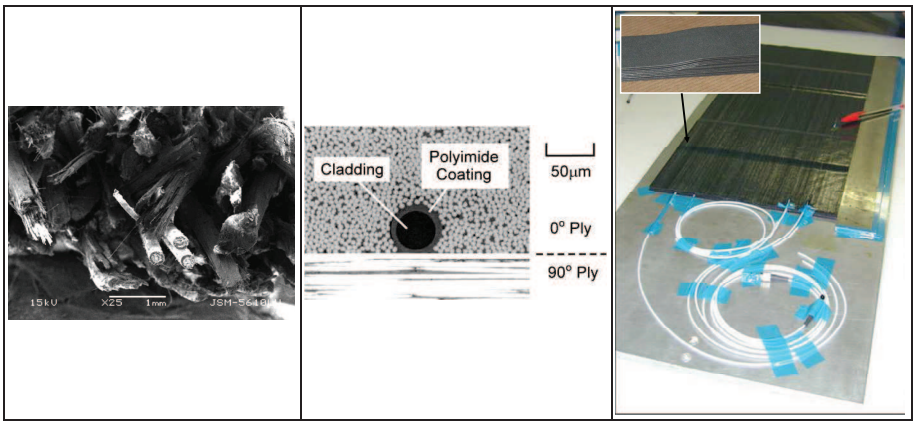

Figure 5-1: Typical examples of optical fibres co-braided [10](left), embedded in the 0°-reinforcement fibres in a laminate [6] (middle), and embedded in a 'technological specimen' with a ply drop-off zone (inset) [15] (right).

5. 1. 2. The optical fibre ingress

Despite the compatibility of these FBGs with the structures in which they are embedded, a major remaining issue is the ingress (or entry point) of the optical fibre lead in the composite material which is prone to breaking. A literature overview to

overcome this problem is given by Green et al [17]. Mainly two options exists to protect the fibre egress point in composite laminates: either integrating a fibre connector at the edge or surface of the laminate [18] or integration of a fibre feed-through mechanism [19], which is often realised in test-coupons by use of a flexible (and thermal resistant) tubing or fibre jacketing (Figure 5-1, right). Both methods enable the optical fibre to be led smoothly out of the stiff laminate (surface or edge) without excessive bending and curvature. However, it should be mentioned that decades of research have not illuminated the community to come up with the ideal entry point in a material which is insensitive to delamination. In the future, perhaps, one should focus on eliminating the entry point entirely by wireless transmission of data from the embedded sensor to a read-out unit. In this matter, Teitelbaum et al. is experimenting with wireless transmission of video data via a multimode fibre in a smart structure [20-21]. And in SMARTFIBER [22], a European FP7-project, the researchers try to miniaturize the read-out unit, so that it can be embedded together with the optical fibre in the composite material, see Figure 5-2 for a schematic principle of two possible applications. The dimensions are not drawn to scale. It is clear that in the last two solutions, edge trimming, which is commonly needed after composite fabrication, will become possible.

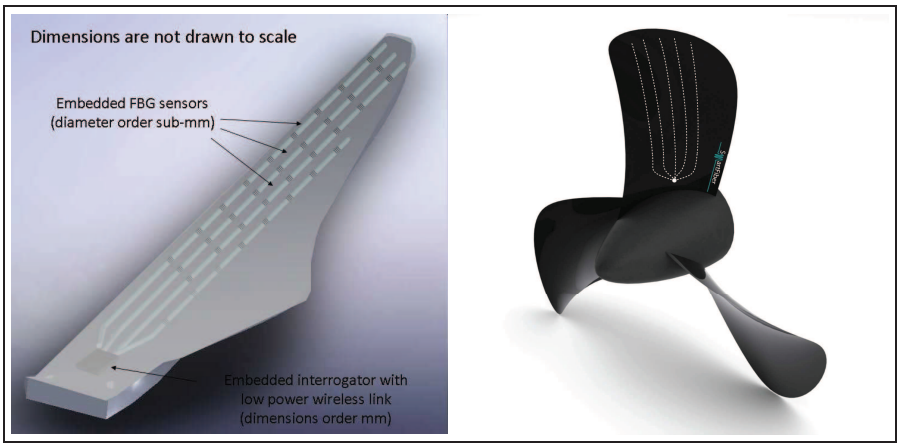

Figure 5-2: SMARTFIBER principle with embedded interrogator and FBG sensors in a wind turbine blade and a propeller [22].

5. 1. 3. Distortion of the composite

Another issue is the distortion of the composite structure at the surroundings of the optical fibre. The size of the FBG sensor ranges from 125 µm (which is a classical telecom fibre) down to 52 µm [23]. This is still one order of magnitude larger than the most commonly used reinforcement fibres (Glass : 5-20 µm, carbon: 5-10 µm). Thus, the embedded optical fibre will cause a local distortion in the host material (Figure 5-3). Minimizing the optical fibres will reduce the composite distortion. However, not only the mismatch in size between the optical fibres and the reinforcement fibres, but also the type of composite material which is used (uni-directional, cross-ply, woven-fabric, stitched, braided …), and the relative alignment of the optical fibre with respect to the reinforcement fibres influences the distortion.

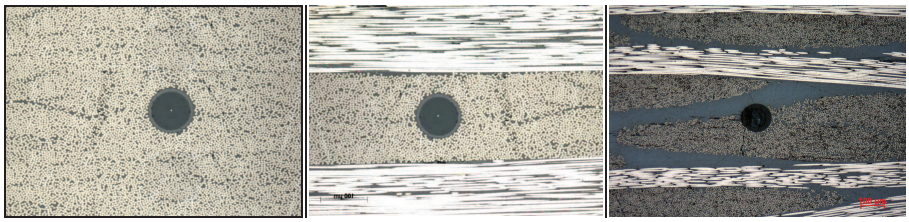

Figure 5-3: Optical fibre embedded in a unidirectional laminate (left), in a cross-ply laminate (middle), in a cross-ply woven-fabric laminate (right).

Research has proven that small diameter optical fibres do not cause any significant reduction in strength of composites and standard 125µm optical fibres have a minimum perturbation of the host material when embedded parallel to the reinforcing fibres in laminates [24-25]. In addition, for small diameter optical fibres, no resin-rich regions (also called resin eyes) are found around the fibre which to the contrary in some cases, can be found for embedded standard telecom optical fibres [26], see Figure 5-4.

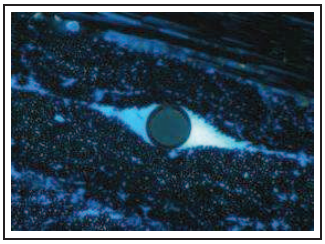

Figure 5-4: Resin eye around a standard telecom fibre [27].

Shivakumar and Emmanwori [28] embedded optical fibres with a relative orientation to the reinforcement fibres and found that the structural properties were not affected when the fibre was embedded parallel to the reinforcement fibres. This is clearly illustrated in Figure 5-3, where the optical fibres are oriented along the 0°-directional reinforcement and integrated well in between the reinforcement fibres. As such it can be assumed that the interaction between the host-material and the integrated sensor is optimal. Throughout the work it is assumed that, because the optical fibre and specifically the FBG is fully embedded, the longitudinal strain transfer from the host material onto the sensor is 100%. Correlation with surface mounted sensors, extensometers and DIC analysis during mechanical testing in this work have proven that this assumption is correct, also in case of the ORMOCER® coated DTG®s (Chapter 7 and Chapter 8).

5. 2. RESIDUAL STRAINS

A very important aspect of the composite manufacturing process is the appearance of residual strains and stresses during the curing and consolidation cycle. Composites exhibit large residual strains after curing (thermoset) or consolidation (thermoplastic) which vary dependent on the type of composite constituents, composite lay-up (Figure 5-3) and manufacturing technology [29]. An example of the effect of non-uniform cooling during the manufacturing cycle on the residual strain formation in a glass fibre reinforced plastic (GFRP) is shown in Figure 5-5.

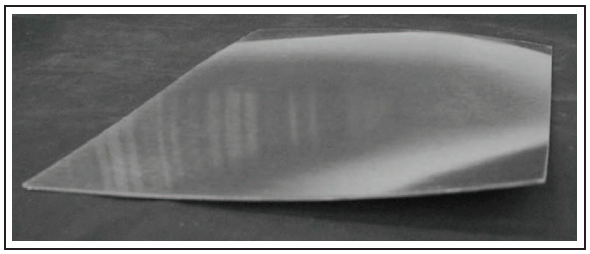

Figure 5-5: Distorted glass fibre fabric reinforced polyetherimide laminate due to non-uniform cooling of the hot platen press [29]

The formation of thermal residual strains arise mainly from the difference in thermal expansion between the reinforcement fibres and the matrix (or resin) material but the origin of strain development is completely different than mechanical induced strains. If an FBG is embedded in a composite laminate, the spectral response will depend on the external perturbations. These perturbations arise not only from externally loading of the structure, but also from residual strains which build up during the manufacturing process of FRP laminates. When the optical fibre is completely sealed within the material during curing (or consolidation) and from the moment forces can be transferred from the matrix onto the embedded sensor, strain measurements during curing and consolidation are in fact possible. Recent research on process monitoring shows that FBGs exhibit large potential on this level as well [1, 15, 30-33]. The use of FBGs during the manufacturing process is further elaborated in detail in Chapter 6.

5. 3. MULTI-AXIAL STRAIN TRANSFER

When embedded in a structure the user should be aware that not only axial strains, but the total strain field around the optical fibre affects the Bragg grating, which makes interpretation of the sensor response not straightforward. In fact, to determine the in-situ composite strain components we need to define a relationship between the strains of the optical fibre ($\Delta\varepsilon_i^s$) and the strains in the laminate ($\Delta\varepsilon_i^h$), see Figure 5-6.

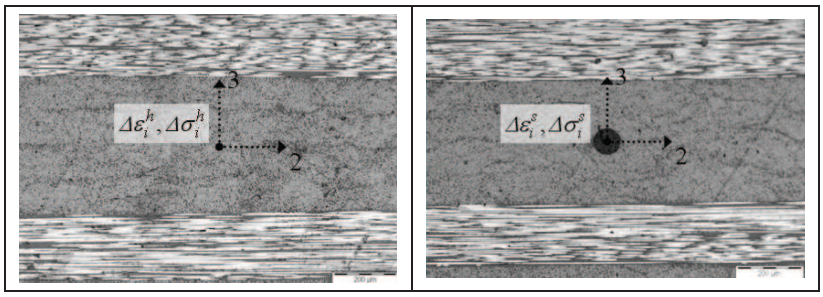

Figure 5-6: The strain in the host material $\Delta\varepsilon_i^h$ (left) differs from the strains in the embedded optical fibre $\Delta\varepsilon_i^s$ (right).

According to Luyckx [34] and as presented in [35], when considering *multi-axial strain monitoring* with embedded FBGs, the general relationship between the response of the embedded sensor and the strains in a (loaded) composite laminate is defined in three steps: (i) sensor calibration, (ii) strain transfer and (iii) multiple sensing points. In analogy to the work of Luyckx, only the first two steps are considered in this work, see Figure 5-7.

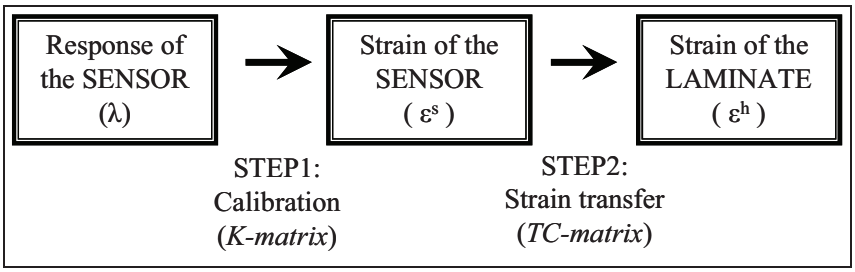

Figure 5-7: Flow chart with the relationship between the (embedded) sensor response and the strain present in the composite laminate.

The *first step* is the creation of an optical fibre sensor which is sensitive to all strain components inside the laminate and relating its wavelength shift (λ) with the strain present in the sensor (ε^s). The first step is then accomplished by calibrating the FBG to determine its strain sensitivities (Chapter 4). To solve the multi-axial wavelength equations, we need to determine the multi-axial strain sensitivity matrix, or K-matrix. This is done by configuring a sensor existing out of two FBGs which each of them measuring different components of the induced strain field (i.e. longitudinal and transverse). A possible solution to this problem is to use a sensor configuration existing out of one encapsulated FBG to measure pure axial strain and one FBG 'normally' embedded in the composite to measure all strains.

The *second step* is the modelling of the relation of the composite strain ($\Delta\varepsilon_i^h$) with the strain of the optical fibre ($\Delta\varepsilon_i^s$) (Figure 5-6). The strain transfer relation is typically written in matrix notation [35], and is called the TC-matrix. Remark that because the optical fibre is embedded along its complete length the strain transfer in the longitudinal direction is ~100 %, as such it is assumed that $\Delta\varepsilon_1^h = \Delta\varepsilon_1^s$. The experimental validation and correlation with extensometer readings in Chapter 7 confirms that this assumption is valid.

5. 4. RESPONSE OF THE EMBEDDED BRAGG GRATING

In the scope of this work, several types of carbon fibre reinforced plastic (CFRP) laminates of thickness 1.5 mm – 2.4 mm are produced with DTG®s embedded in the mid-plane of these laminates. The procedure of embedding will be explained in detail for thermoset carbon-epoxy laminates and thermoplastic carbon-PPS woven-fabrics (Cetex® [36]) in Chapter 6. In Figure 5-8, examples of the spectral response of the Bragg grating embedded in different composite types is shown. We can see that the spectral shape of the embedded sensors is totally different. The shape of the Bragg spectrum of a DTG® embedded in a *carbon-epoxy UD* laminate or in *carbon-PPS cross-ply* laminate is not distorted in comparison to the initial spectrum of a

non-embedded DTG®. in the case of a *carbon-epoxy cross-ply* laminate, however, the peak has completely split in two well-defined subpeaks. This indicates that *high birefringence effects* are present in the core of the optical fibre ($\varepsilon_{1'} \neq \varepsilon_{2'}$), and hence, a *high transverse residual strain* difference exists in the cross-ply laminate, i.e. $\varepsilon_y \neq \varepsilon_z$ with the y-direction in the in-plane direction and the z-direction in out-of-plane (through-the-thickness) direction.

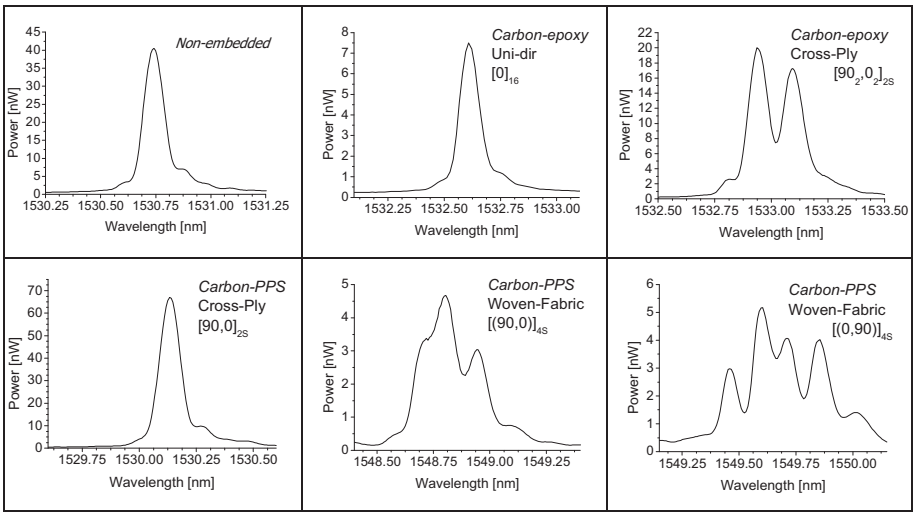

Figure 5-8: Spectral response of embedded DTG®s for different CFRP laminates: carbon-epoxy laminates (top), carbon-PPS laminates (bottom).

If the same DTG® is embedded in *carbon-PPS woven-fabrics* (Figure 5-3, right), we notice a severe distortion of the Bragg spectrum, i.e. the complete Bragg peak becomes wider and the Bragg spectrum splits up in multiple small peaks. The peak-splitting is partly caused by birefringence effects induced by transverse residual strains, but in addition, by non-uniform local strain effects which occur in the carbon weave pattern of the laminate. More details on the residual strain calculations in all types of laminates are found in Chapter 6.

All examples of the reflection spectra given in Figure 5-8 are for coated DTG®s. Okabe et al. [31] performed simulations on an optical fibre with and without coating and found that the strain profiles around the coated optical fibre changes drastically compared to the stripped strain profile. The transverse strains in the core of the coated optical fibre are found much smaller. The same effect is observed in this work (Chapter 6 and 8) and is also seen in the reflection spectra of stripped Bragg gratings, where the peak separation, because of residual transverse strain formation, is more distinct than the spectral splitting for a coated Bragg grating. Moreover, from finite element (FE) simulations in this work (Chapter 7), we can state that the transverse effects on a coated optical fibre during longitudinal loading are very small. This feature of the coated DTG®s enables us to neglect the transverse effects when calculating the longitudinal strains in the thermoplastic woven fabrics during tension tests.

Note that in principle using a uni-axial (i.e. low birefringent) FBG, one can not distinguish the difference between the in-plane and out-of-plane transverse strains.

However, if we embed an FBG in for instance a carbon-epoxy cross-ply laminate (Figure 5-8, top-right), the spectrum splits up in two distinct Bragg peaks which can thus be monitored separately. This residual induced birefringence in the uni-axial fibre allows to work with the grating as if it is a FBG written in a HiBi fibre, with the only difference that the optical polarization axes for this birefringence are perfectly aligned with the mechanical axes of the composite. This feature will be exploited in Chapter 6 to measure the in-plane, out-of-plane and longitudinal residual strains and in chapter 7 to measure the multi-axial strain components of CFRP-elements.

5. 4. 1. Determining the Bragg wavelength from distorted spectra

The interpretation of the spectrum of a non-embedded FBG (Figure 5-8, top-left) is straightforward. During a longitudinal calibration, the shift of the spectrum can directly be linked with the gauge factor of the FBG (Chapter 4). Several methods are reported in literature to analyze the shift of such a spectrum of which the 'Full Width at Half Maximum' (FWHM) algorithm and the 'centre of gravity' (COG), or 'centroid' algorithm are the most popular ones [37-38]. Remark that the measurement of the Bragg-wavelength first of all depends on the stability and reproducibility of the employed interrogators. The measurement algorithm of the interrogator, however, is as important. The determination of the Bragg wavelength using a FWHM algorithm can differ from a Bragg wavelength determined by a centroid calculation algorithm. This is due to the influence of the grating characteristics (mainly uniformity of the spectral shape, amplitude) and the sampling density of the FBG spectrum, as well as on the uncertainty of the curve fit algorithm or peak picking parameters for the determination of the Bragg wavelength. An overview of other demodulation techniques, using for example tuneable filters, are reported in Zhao et al. [39].

Strain gradients

FBGs can be considered as a point sensor. However, when embedded local strain gradients (axial [5, 40] as well as transvere strains [31, 41-42]) can severely distort the Bragg spectrum. The gradients can be related to the embedding process [43-44] of the FBG in the composite material or can originate from a specific loading case (e.g. bending [40, 45]). For example Figure 5-9 represents the spectrum of an FBG embedded in a woven-fabric thermoplastic composite. The axial strain profile of such a material has been numerically determined by Daggumati et al. [46-47]. A clear strain gradient exists over the length of the embedded grating, hence this local strain distribution causes the Bragg spectrum to heavily deform. By using the COG method however, with the right peak picking settings (see further in this paragraph), the individual peaks can be monitored and minimum and maximum strains along the grating can be measured. The evaluation of the local strain distribution along the unit-cell of the weave pattern in the woven-fabric laminate will be further elaborated in this work and is subject of Chapter 8. An important notice is that when measuring strain in woven-fabrics, or textile composites the size of the unit cell has to be considered. It has been stated by Lang and Chou [48] that the sensor should at least be one unit cell long (or width) to measure the complete strain profile.

There is evidence in literature that the local strain distribution and strain concentrations along the gratings are directly proportional to the perturbation of the refractive index in the grating structure which on its turn disturbs the Bragg peak

shape. Black et al. and Wang et al. characterized high birefringent fibres subjected to non-homogeneous transverse loads [41-42]. Under these non-homogeneous loads one of the peaks gets heavily distorted. Ling et al. simulated the reflection spectra of FBGs using the T-matrix formulation for a linear and a quadratic strain gradient [49]. This was done for small as well as for large strain gradients. Peters et al. presented a experimental verification of the response of embedded FBGs in epoxy specimens to applied non-homogeneous strain fields [50]. These strain fields could be controlled by machining the cross section of the specimen. Similar investigations are performed by Colpo et al. [51], who characterized the non-uniform residual strains of epoxy blocks by using FBGs in combination with the Optical Low Coherence Reflectometry (OLCR) –technique [52]. These results confirm that in the case of the distorted Bragg peak of a DTG® embedded in the woven-fabric the origin of distortion is multiple, i.e. transverse -and longitudinal non-uniform strains. The difference between both is often difficult to make. A method to discriminate between both types can be found in the polarization control of the input light which is coupled in the optical fibre [14, 53]. This method is illustrated in the next subsection. First a short notice follows on the COG method which is applied in this work to calculate the wavelength shifts of the embedded DTG®s.

Calculating the Centre Of Gravity wavelength

In this work the COG method is applied on all spectral measurements including heavily distorted spectra. It is a very simple, but powerful tool which can be implemented in any software code (e.g. Labview, C++, C-sharp, etc.) or analytical program (e.g. mathlab, mathcad, origin, etc.) to determine the centroid peak and 'global' wavelength shifts from distorted spectra such as Figure 5-8, bottom-right. The COG wavelength, or centroid wavelength, of the spectrum in Figure 5-9 is calculated according to [37]:

$$\lambda_{COG} = \frac{\sum_i \lambda_i I_i}{\sum_i I_i}, \qquad 5\text{-}1$$

with λ_{COG}, the centroid wavelength of the peak, λ_i and I_i, the wavelength and power at position "i", respectively. Typically, a threshold is chosen with respect to the maximum peak power, and a horizontal secant is drawn. As such the count of "i" starts at the first intersection point of the secant, and stops at the second intersection point (Figure 5-9). The centroid wavelength is then the centre of gravity of the curve above the threshold. The threshold value is defined manually and is typically defined as a ratio of the total peak power, for example 10% to 15 % of the maximal peak power of the Bragg peak. The threshold is best taken as low as possible (but above the noise level), as such the deformation and peak splitting of the complete spectrum is taken into account. Note that, the threshold level should be fixed for al the spectra of one single sensor, not to make relative calculation errors. An example of the result of a centroid wavelength calculation is given in Figure 5-9 for a severe distorted spectrum of a DTG® embedded in a woven-fabric laminate. The result is $\lambda_{COG} = 1540.618$ nm .

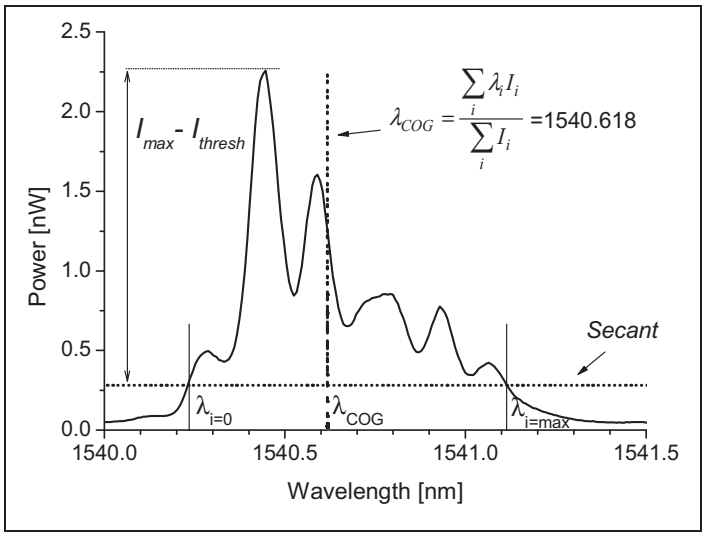

Figure 5-9: Illustration of the centroid peak calculation method for a distorted Bragg peak

5. 4. 2. Measuring the birefringence in the FBG by use of controlled polarized light.

For the spectrum of the embedded sensor in the carbon-epoxy cross-ply laminate, Figure 5-8, top-right, the occurring residual strains during the production process causes the spectrum to split into *two well-separated Bragg peaks* one for each propagation mode. Both Bragg peaks can then be monitored separately (FWHM- or COG-algorithm). By adding one [54-59], or several [60-61] extra FBGs, one can think of making a multi-axial strain sensor. For example, Lawrence et al. [54], and Mawatari and Nelson [57] suggest to inscribe an extra grating at the position of the first grating in a PM-fibre. To obtain a working solution, the wavelength of both Bragg sensors should be chosen sufficiently separated (for example in the 1300 nm and 1550 nm range). Drawback of this solution is the need of two separate light sources. In Luyckx et al. [58] [60] this drawback is overcome by encapsulating the second grating in a capillary. As such, the second grating is isolated from transverse stresses and will react differently to external loading of the composite structure than the first grating. The capillary will, however, locally cause more distortion to the composite. Though, when appropriately prepared this sensor configuration is well suited to measure accurate strains. It is also applied in this work to measure multi-axial strains (Chapter 6 and Chapter 7).

Typically the birefringence in uni-axial (i.e. low birefringent) FBGs is very small and sometimes no peaksplitting, but solely a wider spectra is observed after embedding. This is for instance the case for the coated DTG®s embedded in the uni-directional carbon-epoxy laminate (stacking $[0°]_{16}$) and the cross-ply carbon-PPS laminate ($[90,0]_{2S}$) shown in Figure 5-8. In this work, the reflection spectra are measured using a FBG-interrogator with a depolarized light source (FBG-scan X08 from FOS&S). If the (external induced) birefringence effect in the embedded uni-axial FBG is small, we will not be able to distinct the two peaks using the total

recorded spectrum. However, by using a polarization controller (HP8169A), which is positioned between the light source and the optical path towards the FBG, we can tune the linear polarization state (i.e. angle) of the light which is coupled into the fibre. As such, the light in the optical fibre is travelling according to a fixed linear polarization axis. Because the polarization state inside low birefringent single mode fibres changes randomly, the path between the polarizer and the FBG needs to be unperturbed, i.e. the fibre needs to be fixed not to create errors on the angle of linear polarization. An example of a full polarization sweep and its effect on the detected peak wavelength (COG) is shown in Figure 5-10, left. We clearly see sinusoidal course and the existence of a maximum and minimum wavelength. The magnitude of the peak separation is small, i.e. approximately 120pm. The corresponding spectral peaks of the minimum (peak 1), maximum (peak 2) and mean wavelengths are plotted in Figure 5-10, right. Note that the mean peak, which is illuminated at an angle 45° relative to one of the major polarization axes, looks like a 'non-embedded" Bragg peak.

This controlled polarization technique is used in this work to determine small peak separations in FBGs (Chapter 6 and Chapter 7), but it is also used to determine the birefringence in heavily distorted Bragg spectra (Chapter 6 and Chapter 8). In the latter case the peaksplitting can be caused by both transverse and longitudinal non-uniform strains, hence we are only able to distinguish both effects by using the polarization controlled interrogation technique.

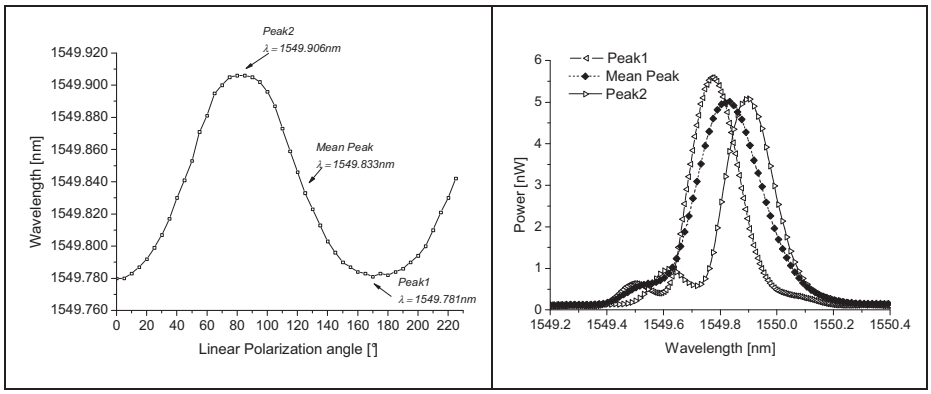

Figure 5-10: Peak separation measured using controlled polarized light, complete linear polarization sweep from 0° to 220° in steps of 10° (left), separate minimum, mean and maximum peak (right)

5. 5. TEMPERATURE COMPENSATION TECHNIQUES

Since for FBGs a *cross-sensitivity for the strain and temperature* exists, one has to find solutions to compensate the strain for temperature effects. Several methods using fibre Bragg technology are studied in literature, a short overview is given below.

5. 5. 1. Extra strain-free reference (FBG) sensor

The most simple method is measuring the temperature with an *external temperature sensor* and use it to compensate the intrinsic temperature effects of the embedded grating. A reference FBG can, for example, be used as an external temperature sensor. An extra *strain free FBG* is added in the measurement system [62-63] and discrimination between strain and temperature can be done by separately evaluating the Bragg wavelength shifts of both FBGs ($\Delta\lambda_{B,1}$, $\Delta\lambda_{B,2}$) with their respective strain and temperature sensitivity (k_ε , $k_{T,i}$):

$$\begin{bmatrix} \Delta\lambda_{B,1} \\ \Delta\lambda_{B,2} \end{bmatrix} = \begin{bmatrix} k_\varepsilon & k_{T,1} \\ 0 & k_{T,2} \end{bmatrix} \begin{bmatrix} \Delta\varepsilon \\ \Delta T \end{bmatrix} \qquad 5\text{-}2$$

Although not necessary for temperature compensation, the use of an identical FBG makes compensation very easy by just subtracting the wavelength shift of the strain free sensor from the total wavelength shift of the strain sensor. If one only wants to compensate for the intrinsic temperature behaviour of the grating, one can think of encapsulating a reference grating and embed this in the material. This reference grating should be isolated from the existing strain field in the material by ending it strain–free inside the capillary (glass, fused silica or metal) (Figure 5-11, top) [58, 64-65]. For embedded strain sensors this method can be expanded by embedding or mounting an extra Bragg sensor in or on top of a strain free compensating plate which has an identical lay-up as the structure in which the strain sensor is embedded (Figure 5-11, bottom) [66]. As such, one can focus only on mechanical induced strain fields caused by external loads. The reference FBG should of course be located in the same thermal environment as the strain sensor.

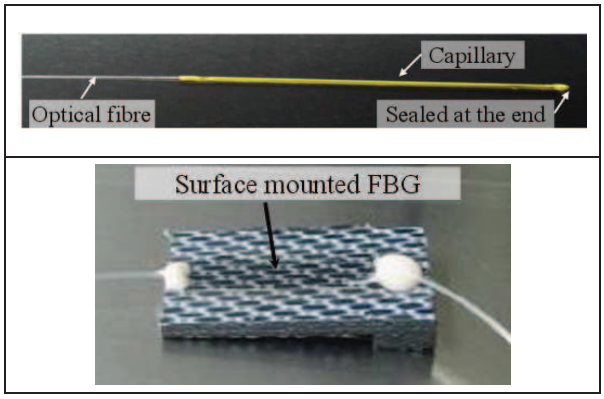

Figure 5-11: Example of an encapsulated FBG (top), and temperature compensating plate with surface mounted FBG (bottom) (Chapter 6 and Chapter 8).

Note that, if a second order polynomial temperature effect is considered (Chapter 4) which is definitely necessary for cure monitoring purposes or large temperature ranges, Equation 5-2 has to be expanded. This is subject of Chapter 6, where the author will compensate for the intrinsic temperature sensitivities during the curing process of the thermoset composite laminates. In Chapter 8 the method of the compensating plate (Figure 5-11) is elaborated for the thermoplastic woven fabrics.

5. 5. 2. Extra FBG which is imposed to a different strain field

Instead of a strain free configuration, one can also think of the use of an extra grating, *imposed to a different strain field* than the first grating. Since both gratings are then sensitive to strain and temperature, the discrimination method of Equation 5-2 should be expanded with extra strain and temperature coefficients:

$$\begin{bmatrix} \Delta\lambda_{B,1} \\ \Delta\lambda_{B,2} \end{bmatrix} = \begin{bmatrix} k_{\varepsilon,1} & k_{T,1} \\ k_{\varepsilon,2} & k_{T,2} \end{bmatrix} \begin{bmatrix} \Delta\varepsilon \\ \Delta T \end{bmatrix} \qquad 5\text{-}3$$

For example, when both gratings are loaded similar but opposite in sign (e.g. like in a bending experiment), temperature is compensated by just subtracting both wavelength shifts and divide the result by two [67-69]. By artificially enlarging the stiffness of the compensating grating, it will sense a different strain (by integrating it in a capillary [70], by bonding it to another dummy fibre [71], or embedding it into another material [72]. Another special configuration is introduced by Silva et al. [73]. A transverseload sensor is created by winding a grating which is written in a polarization maintaining fibre, around a classical single mode fibre with grating. So, both gratings will react differently to transverse load, and temperature can be discriminated. James et al. [74] proposed a sensor configuration with an extra grating written in an optical fibre with a smaller diameter spliced to the first FBG (strain sensor). The same effect can be reached by etching the fibre at the grating position so that it becomes smaller [75]. However, it should be mentioned that, these configurations are prone to breaking during the embedding process and lose all of their efficiency (like any of the extra grating configuration discussed before) when considering the embedded situation.

5. 5. 3. Extra FBG which reacts differently to the same strain field

Another technique is adding an extra grating which *reacts differently on the same strain field*. This can be done by using different FBG types which have different temperature induced wavelength shift [76-79], or by using a second grating which is differently doped than the first one [80-83]. A lot of research is done on the fabrication of hybrid sensors which combines an FBG with another ('similar') type of sensor [84-87]. These last configurations all have in common that the demodulation of the sensor signal becomes a lot more complicated. In the last decade, researchers also focused on discrimination of strain and temperature using Bragg gratings written in polarization maintaining (PM) and micro-structured fibres. Although a small difference exists in temperature sensitivity [88-90] for the Bragg peaks of FBGs written in classical PM-fibres (bow-tie, panda, and elliptical core), discriminating axial strain and temperature remains very difficult [56, 58]. In classical PM-fibre, birefringence is most of the time induced by temperature

dependent stress applying parts while in micro-structured fibre, this mainly originate from the micro-structure inside the fibre. Therefore, almost no difference exists in temperature sensitivity for both polarization axes of the micro-structure fibre. By subtracting both wavelength shifts, one creates a temperature-independent measurement [58, 91].

5. 5. 4. Remarks concerning temperature compensation

In most of the discussed configurations a discrimination is made between temperature and axial strain in the optical fibre. The user should however, be careful when the fibre Bragg grating is embedded in a composite, because transverse strains are acting on the grating too. These transverse strains are sometimes to high to be neglected. To measure pure longitudinal strains an encapsulated FBG, free from transverse strains (not strain-free) can be used. As such the assumption of pure longitudinal induced strain holds and the temperature compensation technique can be applied for the embedded case. In addition, note that if a second order polynomial temperature effect is considered, which is definitely necessary for large temperature ranges, only the reference temperature sensor method is suited (Section 5. 5. 1.).

Usually we are only interested in the mechanical strain or thermal strain of the structure. If we consider only the longitudinal strain, there are actually three contributions to the wavelength shift of an embedded optical fibre:

1. The mechanical strain applied on the composite and fibre,
2. The thermo-optic effect and thermal expansion of the FBG,
3. The thermal expansion of the structure in which the fibre is embedded. This will cause an additional excess strain (or compression if the CTE of the structure is smaller than that of silica).

The third effect, however, has to be included in the strain term $\Delta\varepsilon$ in the above used equations. The method how to do this will be derived in detail in Chapter 6 using a logarithmic approach including the consideration of the second order polynomial effect and will be extended in Chapter 8 for an embedded situation.

5. 6. CONCLUSIONS

From the numerous cited research in this chapter, we can state that the properties of fibre Bragg gratings are matching the requirements of fibre reinforced plastics. So the answer on the question, “if it is a successful marriage?”, is a clear yes! However, as in every marriage, and because of their different 'characters', one needs to work continuously on the (long term) ‘relationship’. Accordingly, depending on the type of composite and manufacturing technology, small adaptations will always be necessary, to have a good match. For example, the interaction between embedded sensor and its composite host-material will depend on the type of composite used. To be successful, the user needs to interpret the sensors' response well. This is definitely the case, when the Bragg spectrum is ‘lacerated’ due to ‘brute stress behaviour’ of the composite material. Moreover, if the composite gets ‘heated’, the resulting response of the embedded sensor is ‘exorbitant’. Therefore, the user will need to carefully compensate for temperature by using an appropriate technique.

In the next following chapters, the author elaborates in detail the practical solutions and methods to measure strains with DTG®s in different types of composite material. For example, in Chapter 6, the focus is on embedding the DTG®s in both thermoset carbon-epoxy and thermoplastic carbon-PPS laminates using two different manufacturing processes. It will be shown that in both cases the embedded Bragg sensors can be used to monitor the residual strains which build up during the manufacturing process. In Chapter 7, the multi-axial strain transfer (the strain interaction between the optical fibre and the composite material) will be tackled for a non-coated and coated DTG® in thermoset cross-ply laminates. It will be proven that the transverse strain effects are much smaller for coated than for non-coated optical fibres. That is why, the influence on the axial strain readings of the embedded Bragg grating can be neglected when a longitudinal load case is envisaged. In Chapter 8, this feature of coated DTG®s will be used to measure the longitudinal strains in thermoplastic carbon-PPS woven-fabrics during fatigue testing at 0.5 % and even up to failure of the specimens (which is approximately 1 % strain). In every experiment done in this research, the sensor outperformed the material under test, i.e. it was still working notwithstanding the fact that the material already failed. This points out that even though the extreme loading conditions, we have not yet driven the DTG®s to its limits.

5. 7. REFERENCES

1. Mulle, M., Collombet, F., Olivier, P., and Grunevald, Y.H., *Assessment of cure residual strains through the thickness of carbon-epoxy laminates using FBGs, Part I: Elementary specimen.* Composites Part a-Applied Science and Manufacturing, 2009. **40**(1): p. 94-104.
2. Kang, H.K., Kang, D.H., Bang, H.J., Hong, C.S., and Kim, C.G., *Cure monitoring of composite laminates using fiber optic sensors.* Smart Materials & Structures, 2002. **11**(2): p. 279-287.
3. Murukeshan, V.M., Chan, P.Y., Ong, L.S., and Seah, L.K., *Cure monitoring of smart composites using Fiber Bragg Grating based embedded sensors.* Sensors and Actuators a-Physical, 2000. **79**(2): p. 153-161.
4. De Baere, I., Voet, E., Van Paepegem, W., Vlekken, J., Cnudde, V., Masschaele, B., and Degrieck, J., *Strain monitoring in thermoplastic composites with optical fiber sensors: Embedding process, visualization with micro-tomography, and fatigue results.* Journal of Thermoplastic Composite Materials, 2007. **20**(5): p. 453-472.
5. Kuang, K.S.C., Kenny, R., Whelan, M.P., Cantwell, W.J., and Chalker, P.R., *Residual strain measurement and impact response of optical fibre Bragg grating sensors in fibre metal laminates.* Smart Materials & Structures, 2001. **10**(2): p. 338-346.
6. Takeda, S., Minakuchi, S., Okabe, Y., and Takeda, N., *Delamination monitoring of laminated composites subjected to low-velocity impact using small-diameter FBG sensors.* Composites Part a-Applied Science and Manufacturing, 2005. **36**(7): p. 903-908.

7. Othonos, A. and Kalli, K., *Fiber Bragg gratings: Fundamentals and Applications in Telecommunications and Sensing*. 1999: Artech House.
8. Kalamkarov, A.L., Fitzgerald, S.B., MacDonald, D.O., and Georgiades, A.V., *The mechanical performance of pultruded composite rods with embedded fiber-optic sensors.* Composites Science and Technology, 2000. **60**(8): p. 1161-1169.
9. Jung, K. and Kang, T.J., *Cure monitoring and internal strain measurement of 3-D hybrid braided composites using fiber Bragg grating sensor.* Journal of Composite Materials, 2007. **41**(12): p. 1499-1519.
10. Li, X.H., Zhao, C.S., Lin, J., and Yuan, S.F., *The internal strain of three-dimensional braided composites with co-braided FBG sensors.* Optics and Lasers in Engineering, 2007. **45**(7): p. 819-826.
11. Yuan, S.F., Huang, R., and Rao, Y.J., *Internal strain measurement in 3D braided composites using co-braided optical fiber sensors.* Journal of Materials Science & Technology, 2004. **20**(2): p. 199-202.
12. Jung, K., Kang, T.J., Lee, B., and Kim, Y., *Estimation of residual strain and stress in interply hybrid composite using fiber bragg grating sensor.* Fibers and Polymers, 2007. **8**(4): p. 438-442.
13. Voet, E.J., Luyckx, G., De Baere, I., Degrieck, J., Vlekken, J., Jacobs, E., and Bartelt, H. *High Strain monitoring during Fatigue Loading of Thermoplastic Composites using imbedded Draw Tower Fibre Bragg Grating Sensors*. in *3rd International Conference on Smart Materials, Structures and Systems*. 2008. Acireale, ITALY.
14. Sorensen, L., Gmur, T., and Botsis, J. *Residual strain development in an AS4/PPS thermoplastic composite measured using fibre Bragg grating sensors*. in *2nd International Conference on Composites Testing and Model Identification (CompTest 200)*. 2004. Bristol, ENGLAND.
15. Mulle, M., Collombet, F., Olivier, P., Zitoune, R., Huchette, C., Laurin, F., and Grunevald, Y.H., *Assessment of cure-residual strains through the thickness of carbon-epoxy laminates using FBGs Part II: Technological specimen.* Composites Part a-Applied Science and Manufacturing, 2009. **40**(10): p. 1534-1544.
16. Shivakumar, K. and Emmanwori, L., *Mechanics of failure of composite laminates with an embedded fiber optic sensor.* Journal of Composite Materials, 2004. **38**(8): p. 669-680.
17. Green, A.K. and Shafir, E., *Termination and connection methods for optical fibres embedded in aerospace composite components.* Smart Materials & Structures, 1999. **8**(2): p. 269-273.
18. Sjogren, B.A., *Static strength of CFRP laminates with embedded fiber-optic edge connectors.* Composites Part a-Applied Science and Manufacturing, 2001. **32**(2): p. 189-196.
19. Green, A.K., Zaidman, M., Shafir, E., Tur, M., and Gali, S., *Infrastructure development for incorporating fibre-optic sensors in composite materials.* Smart Materials & Structures, 2000. **9**(3): p. 316-321.
20. Teitelbaum, M.E., O'Brien, D.J., Wetzel, E.D., and Goossen, K.W. *Passive and active data porting to composite integrated optical fibers via integrated optics - art. no. 69282Q*. in *Conference on Active and Passive Smart Structures and Integrated Systems*. 2008. San Diego, CA.

21. Teitelbaum, M.E., Yarlagadda, S., O'Brien, D.J., Wetzel, E.D., and Goossen, K.W., *Normal incidence free space optical data porting to embedded communication links.* Ieee Transactions on Components and Packaging Technologies, 2008. **31**(1): p. 32-38.
22. *SMARTFIBER- European FP7 project*. 2010 - 2013; Available from: http://www.smartfiber-fp7.eu/.
23. Takeda, N., Okabe, Y., Kuwahara, J., Kojima, S., and Ogisu, T., *Development of smart composite structures with small-diameter fiber Bragg grating sensors for damage detection: Quantitative evaluation of delamination length in CFRP laminates using Lamb wave sensing.* Composites Science and Technology, 2005. **65**(15-16): p. 2575-2587.
24. Saton, K., Fukuchi, K., Kurosawa, Y., Hongo, A., and Takeda, N. *Polyimide-coate small-diameter optical fiber sensors for embedding in composite laminate structures*. in *SPIE*. 2001. Newport Beach, CA USA: SPIE.
25. Jensen, D.W. and Sirkis, J.S., *Integrity of composite structures with embedded optical fibers*, in *Fiber Optic Smart Structures*, E. Udd, Editor. 1995, Wiley: New York. p. 109 -129.
26. Leka, L.G. and Bayo, E., *A close look at the embedment of optical fibers into composite structures.* Journal of Composites Technology & Research, 1989. **11**(3): p. 106-112.
27. De Waele, W., *Structural monitoring of composite elements using optical fibres with Bragg-sensors.*, in *Department of mechanical construction and production*. 2001-2002, PhD dissertation at Ghent University: Ghent.
28. Shivakumar, K. and Bhargava, A., *Stress concentrations caused by embedded optical fiber sensors in composite laminates.* Cmc-Computers Materials & Continua, 2004. **1**(2): p. 173-190.
29. Parlevliet, P., Patricia., *Residual strains in thick thermoplastic composites an experimental approach*. 2010, Delft University of Technology.
30. Guemes, J.A. and Menendez, J.M., *Response of Bragg grating fiber-optic sensors when embedded in composite laminates.* Composites Science and Technology, 2002. **62**(7-8): p. 959-966.
31. Okabe, Y., Yashiro, S., Tsuji, R., Mizutani, T., and Takeda, N., *Effect of thermal residual stress on the reflection spectrum from fiber Bragg grating sensors embedded in CFRP laminates.* Composites Part a-Applied Science and Manufacturing, 2002. **33**(7): p. 991-999.
32. Karalekas, D., Cugnoni, J., and Botsis, J., *Monitoring of process induced strains in a single fibre composite using FBG sensor: A methodological study.* Composites Part a-Applied Science and Manufacturing, 2008. **39**(7): p. 1118-1127.
33. Parlevliet, P.P., Bersee, H.E.N., and Beukers, A., *Measurement of (post-)curing strain development with fibre Bragg gratings.* Polymer Testing. **29**(3): p. 291-301.
34. Luyckx, G., *Multi-Axial Strain Monitoring of Fibre Reinforced Thermosetting Plastics Using Embedded Highly Birefringent Optical Fibre Bragg Sensors*, in *Materials science and engineering*. 2009-2010, PhD dissertation at Ghent University: Ghent.

35. Luyckx, G. and et al., *Multi-axial strain transfer from laminated CFRP composites to embedded Bragg sensor: I. Parametric study.* Smart Materials and Structures. **19**(10): p. 105017.
36. Ten Cate Advanced Composites. Available from: http://www.tencate.com/.
37. Dyer, S.D., Williams, P.A., Espejo, R.J., Kofler, J.D., and Etzel, S.M., *Key metrology considerations for riber Bragg grating sensors*, in *Smart Structures and Materials 2004: Smart Sensor Technology and Measurement Systems*, E. Udd and D. Inaudi, Editors. 2004. p. 181-189.
38. Fernandez, A.F., Gusarov, A., Berghmans, F., Kalli, K., Polo, V., Limberger, H., Beukema, M., and Nellen, P., *Round-robin for fibre Bragg grating metrology during COST270 action*, in *Reliability of Optical Fiber Components, Devices, Systems, and Networks Ii*, H.G. Limberger and M.J. Matthewson, Editors. 2004. p. 210-216.
39. Zhao, Y. and Liao, Y.B., *Discrimination methods and demodulation techniques for fiber Bragg grating sensors.* Optics and Lasers in Engineering, 2004. **41**(1): p. 1-18.
40. Kang, D.H., Park, S.O., Hong, C.S., and Kim, C.G., *The signal characteristics of reflected spectra of fiber Bragg grating sensors with strain gradients and grating lengths.* NDT & E International, 2005. **38**(8): p. 712-718.
41. Black, K., Udd, E., Schulz, W., Kreger, S., Kunzler, M., Taylor, T., and Lumsden, R. *Using Multi-Axis Fiber Grating Strain Sensors to Measure Transverse Strain and Transverse Strain Gradients In Composite Materials with Complex Weave Structures*. in *SPIE*. 2002.
42. Michaille, L., McCall, M.W., Lai, Y.C., and Williams, J.A.R., *Analysis of single and multiple, non-permanent, tunable, birefringent spectral holes in a fibre-Bragg grating stop-band produced via uniaxial pressure.* Optics Communications, 2003. **222**(1-6): p. 1-8.
43. Ivanov, D.S., Lomov, S.V., Ivanov, S.G., and Verpoest, I., *Stress distribution in outer and inner plies of textile laminates and novel boundary conditions for unit cell analysis.* Composites Part a-Applied Science and Manufacturing. **41**(4): p. 571-580.
44. Summerscales, J. and Russell, P.M., *Observations on the fibre distribution and fibre strain in a woven fabric reinforcement.* Advanced Composites Letters, 2004. **13**(3): p. 135-139.
45. Tao, X., Tang, L., Du, W.-c., and Choy, C.-l., *Internal strain measurement by fiber Bragg grating sensors in textile composites.* Composites Science and Technology, 2000. **60**(5): p. 657-669.
46. Daggumati, S., Voet, E., Van Paepegem, W., Degrieck, J., Xu, J., and Lomov, S.V., *Local strain in a 5-harness satin weave composite under static tension: part I - experimental analysis.* Composite Science and Technology, 2010(Under review).
47. Daggumati, S., Voet, E., Van Paepegem, W., Degrieck, J., Xu, J., and Lomov, S.V., *Local strain in a 5-harness satin weave composite under static tension: part II - Meso-FE analysis.* Composite Science and Technology, 2010(Under review).
48. Lang, E.J. and Chou, T.W., *The effect of strain gage size on measurement errors in textile composite materials.* Composites Science and Technology, 1998. **58**(3-4): p. 539-548.

49. Ling, H.Y., Lau, K.T., Jin, W., and Chan, K.C., *Characterization of dynamic strain measurement using reflection spectrum from a fiber Bragg grating.* Optics Communications, 2007. **270**(1): p. 25-30.
50. Peters, K., Pattis, P., Botsis, J., and Giaccari, P., *Experimental verification of response of embedded optical fiber Bragg grating sensors in non-homogeneous strain fields.* Optics and Lasers in Engineering, 2000. **33**(2): p. 107-119.
51. Colpo, F., Humbert, L., Glaccari, P., and Botsis, J., *Characterization of residual strains in an epoxy block using an embedded FBG sensor and the OLCR technique.* Composites Part a-Applied Science and Manufacturing, 2006. **37**(4): p. 652-661.
52. Giaccari, P., Dunkel, G.R., Humbert, L., Botsis, J., Limberger, H.G., and Salathe, R.P., *On a direct determination of non-uniform internal strain fields using fibre Bragg gratings.* Smart Materials & Structures, 2005. **14**(1): p. 127-136.
53. Yamate, T., Schroeder, R.J., Ramos, R.T., and Udd, E., *Seperation method of dual peaks produced by birefringence using polarization control*, in *Proceedings of OFS 16*. 2003: Nara, Japan. p. 64-67.
54. Lawrence, C.M., Nelson, D.V., Udd, E., and Bennett, T., *A fiber optic sensor for transverse strain measurement.* Experimental Mechanics, 1999. **39**(3): p. 202-209.
55. Abe, I., Kalinowski, H.J., Frazao, O., Santos, J.L., Nogueira, R.N., and Pinto, J.L. *Superimposed Bragg gratings in high-birefringence fibre optics: three-parameter simultaneous measurements*. in *Proceedings of 16th International Conference on Optical Fibre Sensor (OFS-16)*. 2003. Nara City, JAPAN.
56. Abe, I., Frazao, O., Schiller, M.W., Nogueira, R.N., Kalinowski, H.J., and Piinto, J.L., *Bragg gratings in normal and reduced diameter high birefringence fibre optics.* Measurement Science & Technology, 2006. **17**(6): p. 1477-1484.
57. Mawatari, T. and Nelson, D., *A multi-parameter Bragg grating fiber optic sensor and triaxial strain measurement.* Smart Materials & Structures, 2008. **17**(3).
58. Luyckx, G., De Waele, W., Degrieck, J., Van Paepegem, W., Vlekken, J., Vandamme, S., and Chah, K., *Three-dimensional strain and temperature monitoring of composite laminates.* Insight, 2007. **49**(1): p. 10-16.
59. Udd, E., Nelson, D., and Lawrence, C. *Three axis strain and temperature fiber optic grating sensor*. in *Proceedings of the Conference on Smart Sensing, Processing, and Instrumentation - Smart Structures and Materials 1996*. 1996. San Diego, Ca.
60. Levin, K. and Matrat, J. *Strain measurements using an interferometrically interrogated embedded fibre optic rosette - art. no. 661945*. in *Proceedings of the 3rd European Workshop on Optical Fibre Sensors*. 2007. Naples, ITALY.
61. Matrat, J., Levin, K., and Jarlas, R. *Implementation of a Bragg grating strain rosette embedded in composites*. in *Proceedings of the Smart Structures and Materials Conference 2001*. 2001. Newport Beach, Ca.
62. Kim, M.J., Kim, Y.H., Mudhana, G., and Lee, B.H., *Simultaneous measurement of temperature and strain based on double cladding fiber*

interferometer assisted by fiber grating pair. Ieee Photonics Technology Letters, 2008. **20**(13-16): p. 1290-1292.

63. Xu, M.G., Archambault, J.L., Reekie, L., and Dakin, J.P., *Thermally-compensated bending gauge using surface mounted fiber gratings.* International Journal of Optoelectronics, 1994. **9**(3): p. 281-283.
64. Montanini, R. and D'Acquisto, L., *Simultaneous measurement of temperature and strain in glass fiber/epoxy composites by embedded fiber optic sensors: I. Cure monitoring.* Smart Materials & Structures, 2007. **16**(5): p. 1718-1726.
65. Montanini, R. and D'Acquisto, L., *Simultaneous measurement of temperature and strain in glass fiber/epoxy composites by embedded fiber optic sensors: II. Post-cure testing.* Smart Materials & Structures, 2007. **16**(5): p. 1727-1735.
66. Tanaka, N., Okabe, Y., and Takeda, N., *Temperature-compensated strain measurement using fiber Bragg grating sensors embedded in composite laminates.* Smart Materials & Structures, 2003. **12**(6): p. 940-946.
67. Zhao, Y., Liao, Y.B., and Lai, S.R., *Simultaneous measurement of down-hole high pressure and temperature with a bulk-modulus and FBG sensor.* Ieee Photonics Technology Letters, 2002. **14**(11): p. 1584-1586.
68. Zhao, Y. and Zhao, M.G., *Novel force sensor based on a couple of fiber Bragg gratings.* Measurement, 2005. **38**(1): p. 30-33.
69. Sheng, H.J., Liu, W.F., Lin, K.R., Bor, S.S., and Fu, M.Y., *High-sensitivity temperature-independent differential pressure sensor using fiber Bragg gratings.* Optics Express, 2008. **16**(20): p. 16013-16018.
70. Song, M.H., Lee, S.B., Choi, S.S., and Lee, B.H., *Simultaneous measurement of temperature and strain using two fiber Bragg gratings embedded in a glass tube.* Optical Fiber Technology, 1997. **3**(2): p. 194-196.
71. Frazao, O., Marques, L., Marques, J.M., Baptista, J.M., and Santos, J.L., *Simple sensing head geometry using fibre Bragg gratings for strain-temperature discrimination.* Optics Communications, 2007. **279**(1): p. 68-71.
72. Jin, L., Zhang, W.G., Zhang, H., Liu, B., Zhao, H., Tu, Q.C., Kai, G.Y., and Dong, X.Y., *An embedded FBG sensor for simultaneous measurement of stress and temperature.* Ieee Photonics Technology Letters, 2006. **18**(1-4): p. 154-156.
73. Silva, S.F.O., Frazao, O., Santos, J.L., Araujo, F.M., and Ferreira, L.A., *Discrimination of temperature, strain, and transverse load by using fiber Bragg gratings in a twisted configuration.* Ieee Sensors Journal, 2006. **6**(6): p. 1609-1613.
74. James, S.W., Dockney, M.L., and Tatam, R.P., *Simultaneous independent temperature and strain measurement using in-fibre Bragg grating sensors.* Electronics Letters, 1996. **32**(12): p. 1133-1134.
75. Yan, J.H., Zhang, A.P., Shao, L.Y., Ding, J.F., and He, S., *Simultaneous measurement of refractive index and temperature by using dual long-period gratings with an etching process.* Ieee Sensors Journal, 2007. **7**(9-10): p. 1360-1361.

76. Frazao, O., Lima, M.J.N., and Santos, J.L., *Simultaneous measurement of strain and temperature using type I and type IIA fibre Bragg gratings.* Journal of Optics a-Pure and Applied Optics, 2003. **5**(3): p. 183-185.
77. Shu, X.W., Liu, Y., Zhao, D.H., Gwandu, B., Floreani, F., Zhang, L., and Bennion, I., *Dependence of temperature and strain coefficients on fiber grating type and its application to simultaneous temperature and strain measurement.* Optics Letters, 2002. **27**(9): p. 701-703.
78. Chehura, E., James, S.W., and Tatam, R.P., *Temperature and strain discrimination using a single tilted fibre Bragg grating.* Optics Communications, 2007. **275**(2): p. 344-347.
79. Kang, S.C., Kim, S.Y., Lee, S.B., Kwon, S.W., Choi, S.S., and Lee, B., *Temperature-independent strain sensor system using a tilted fiber Bragg grating demodulator.* Ieee Photonics Technology Letters, 1998. **10**(10): p. 1461-1463.
80. Yoon, H.J., Costantini, D.M., Limberger, H.G., Salathe, R.P., Kim, C.G., and Michaud, V., *In situ strain and temperature monitoring of adaptive composite materials.* Journal of Intelligent Material Systems and Structures, 2006. **17**(12): p. 1059-1067.
81. Frazao, O. and Santos, J.L., *Simultaneous measurement of strain and temperature using a Bragg grating structure written in germanosilicate fibres.* Journal of Optics a-Pure and Applied Optics, 2004. **6**(6): p. 553-556.
82. Guan, B.O., Tam, H.Y., Ho, S.L., Chung, W.H., and Dong, X.Y., *Simultaneous strain and temperature measurement using a single fibre Bragg grating.* Electronics Letters, 2000. **36**(12): p. 1018-1019.
83. Patrick, H.J., Williams, G.M., Kersey, A.D., Pedrazzani, J.R., and Vengsarkar, A.M., *Hybrid fiber Bragg grating/long period fiber grating sensor for strain/temperature discrimination.* Ieee Photonics Technology Letters, 1996. **8**(9): p. 1223-1225.
84. Rao, Y.J., *In-fibre Bragg grating sensors.* Measurement Science & Technology, 1997. **8**(4): p. 355-375.
85. Kang, H.K., Kang, D.H., Hong, C.S., and Kim, C.G., *Simultaneous monitoring of strain and temperature during and after cure of unsymmetric composite laminate using fibre-optic sensors.* Smart Materials & Structures, 2003. **12**(1): p. 29-35.
86. Singh, H. and Sirkis, J.S., *Temperature and strain measurement by combining ILFE and Bragg grating optical fiber sensors.* Experimental Mechanics, 1997. **37**(4): p. 414-419.
87. Lin, C.M., Liu, Y.C., Liu, W.F., Fu, M.Y., Sheng, H.J., Bor, S.S., and Tien, C.L., *High-sensitivity simultaneous pressure and temperature sensor using a superstructure fiber grating.* Ieee Sensors Journal, 2006. **6**(3): p. 691-696.
88. Chehura, E., Ye, C.C., Staines, S.E., James, S.W., and Tatam, R.P., *Characterization of the response of fibre Bragg gratings fabricated in stress and geometrically induced high birefringence fibres to temperature and transverse load.* Smart Materials & Structures, 2004. **13**(4): p. 888-895.
89. Chen, G.H., Liu, L.Y., Jia, H.Z., Yu, J.M., Xu, L., and Wang, W.C., *Simultaneous pressure and temperature measurement using Hi-Bi fiber Bragg gratings.* Optics Communications, 2003. **228**(1-3): p. 99-105.

90. Chen, G.H., Liu, L.Y., Jia, H.Z., Yu, J.M., Xu, L., and Wang, W.C., *Simultaneous strain and temperature measurements with fiber Bragg grating written in novel Hi-Bi optical fiber.* Ieee Photonics Technology Letters, 2004. **16**(1): p. 221-223.

91. Frazao, O., Carvalho, J.P., Ferreira, L.A., Araujo, F.M., and Santos, J.L., *Discrimination of strain and temperature using Bragg gratings in microstructured and standard optical fibres.* Measurement Science & Technology, 2005. **16**(10): p. 2109-2113.

Chapter 6 CURE AND CONSOLIDATION CYCLE EFFECTS

6. 1. INTRODUCTION

In this chapter, we focus on the *embedding of DTG®s in carbon fibre reinforced plastic* (CFRP) samples and the use of an embedded sensor to measure the strain development during composite manufacturing. An example of a DTG® fibre embedded in a CFRP laminate, with optical fibre aligned along the carbon reinforcement fibres, is shown in Figure 6-1:

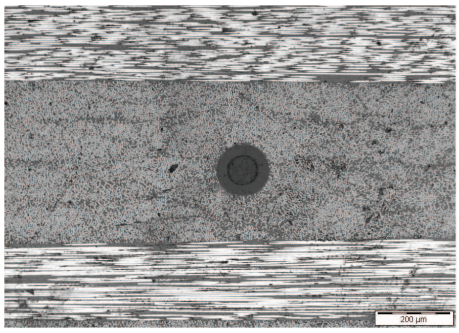

Figure 6-1: Microscopic picture, cross sectional view, of a coated optical fibre embedded in the centre of a carbon – epoxy cross ply laminate.

Two different types of CFRP plates are investigated in detail: cross ply laminates with a *thermoset epoxy resin matrix* and a woven fabric laminates and cross-ply laminate with a *thermoplastic polyphenylene sulphide (PPS)* polymer matrix. Two different composite manufacturing processes are used to produce the composite test-coupons (autoclave vacuum bagging technology and hot moulding press). After manufacturing, residual strains are present in a composite material and because the optical fibre is fully embedded within the carbon-bundles and matrix material (Figure 6-1), it is forced to deform with the composite material. The embedded DTG®s reacts to the applied strain in the optical fibre and hence, it can provide us information on the strain development during manufacturing. However, this sounds easier than it actually is. Because there are complex interactions between the host-material and the sensor, it is important to know, how to interpret the sensor response. If wrong assumptions are made in the calculation model, this could lead to faulty interpretations of the optical fibre strain results.

First, a literature overview is given with research on residual strain monitoring with fibre Bragg gratings (Section 6. 2.). The author will describe in short detail their work and will discuss some of the earlier published results with an indication of some points of attention. The composite nomenclature with respect to the used local and global coordinate systems in this work and the specific stacking notations for the different composite types is explained (Section 6. 3.). Then, the manufacturing of the thermoset (Section 6. 4.) and thermoplastic (Section 6. 5.) test-coupons is discussed and it is explained in detail how the optical fibres are embedded. After that, the author elaborates the monitoring of the residual strain field with DTG®s using different methods and approaches. E.g. the transverse residual strain difference is measured from the birefringence effects and the longitudinal strain is

measured by using encapsulated DTG®s. An attempt is made to disconnect the transversal and longitudinal strain components (Section 6. 6.) and a method with polarization controlled testing is used to determine the birefringence in severe distorted spectra (Section 6. 7.).

6. 2. MONITORING RESIDUAL STRAINS_AN INTRODUCTION

Up till now, no standard monitoring system is employed to follow up the in-situ strains of a composite during manufacturing. Quality control of composites is usually performed after fabrication by using (standard) manual or automated commercial NDT inspection techniques such as, ultrasonic A, C and D-scans, laser ultrasonic testing, shearography, thermography [1]. The same techniques are also used during maintenance for detection of flaws, porosities, debondings, delaminations, and damage after impact. Although they are excellent tools for quality control and crack detection, they do not provide any information on the internal strain state of the laminate (e.g. during laminate production). The latter is a very important given, because the internal residual strains inside a laminate are in fact thermal strains which in some cases can exceed the strains during service. As such damage inside a composite can already be initiated during the manufacturing cycle and will determine heavily the performance of the composite in-service.

Since the last decade, it has been shown that integrating fibre optic sensors in FRPs offers composite manufacturers an opportunity for measuring the in-service strain of composite structures. Moreover, embedded FBG technology can be employed during the curing cycle to monitor residual strain formations. First, a short overview of other common techniques used to measure residual strains is given. Then, a literature review on the monitoring of the curing / consolidation cycle using embedded FBGs is given, with some highlights and recommendations of the author. The author focuses on the autoclave curing cycle and the hot-press manufacturing process.

6. 2. 1. Experimental techniques for measuring residual strains_a short overview

During the curing cycle, residual strains arise in the FRP laminate. They are mainly caused by the mismatch in thermal expansion coefficient (CTE) of the composite constituents (i.e. reinforcement fibres and polymer matrix). The exact thermal behaviour of an FRP is complex and depends on many parameters, such as matrix morphology (i.e. amorphous, semi-crystalline), the kind of reinforcement fibres and the properties of these fibres, such as their surface roughness and surface treatment (i.e. bonding of matrix and reinforcement fibres), the stacking sequence of the composite lay-up and the interaction between the sub-sequent layers, the thickness of the laminate and eventually, the manufacturing process itself. In [2], the authors review a number of destructive and non-destructive experimental techniques to determine the residual strain formation in fibre reinforced thermoplastic composites. These techniques are based on the intrinsic composite constituents' properties, on in-plane and out-of-plane deformations, the relaxation behaviour of FRP laminates, and the embedding of (foreign) extrinsic particles and sensors. Popular techniques to measure the residual strains in the matrix and reinforcement fibre are the photo-elasticity technique and Raman-spectroscopy. They are, however, limited to transparent resins and amorphous materials. Another well known technique based on

interferometry is the Moiré technique or cure reference method (CRM), which enables to measure in-plane and out-of-plane deformations resulting from a changing Moiré (interference) pattern. However, the technique is only suitable to measure deformations on the surface of test-specimens, hence, it is not possible to measure the internal strain field. The most often, and relatively easy technique to measure residual strains, is the curvature method, which is mostly applied in case of non-symmetrical laminates. Measurement of the sample curvature are derived from progressively etching off its surface. A relationship is obtained to correlate curvature data as function of etching depth to the original residual strain profile. Besides destructive techniques such as layer removal and hole drilling, only a few methods are available or suitable, to study residual strains of a laminate in the through-the-thickness direction. One of the techniques which seems capable of providing in-situ strain measurements and even three dimensional strain distribution profiles during the composite manufacturing cycle, is the use of embedded FBGs. A short literature review on residual strain monitoring using embedded FBGs will follow next.

6. 2. 2. Monitoring the process cycle using embedded FBGs_an overview of literature, highlights and points of attention

Several authors have already attempted to study residual strain formations in fibre reinforced composites using embedded FBGs [3-9]. Most of the research is focussed on thermoset composite materials and to a lesser extent on thermoplastics. From these investigations, we can state that embedded FBG sensors are suitable to detect and qualify residual strains in FRPs. Often, it is observed that peak-splitting of the embedded FBG spectrum occurs during the cooling phase of the cure cycle, indicating that large residual transverse strains are acting on the FBG. However, in many cases, researchers try to investigate solely the in-plane longitudinal residual strains, and the variation of them through the thickness, by embedding multiple FBG sensors in between different plies in the composite stacking. They usually tend to neglect the transverse in-plane and out-of-plane strains. Only a few studies will be highlighted here, i.e. the research of Mulle et al., the research of Güemes and Menendez, the research of Okabe et al. and the work of Luyckx. They will serve as an introduction to typical residual strain effects which appear during laminate manufacturing and will form a basis for the reader to understand the effects on the response of embedded FBGs. The author will sometimes put some critical notes and at the end of this section, concluding remarks and recommendations are given. Later in this work, references will be made to these studies, as most of the research in this work is performed similarly to the techniques which will be discussed here.

6. 2. 2. a. Cure monitoring using uni-axial FBGs

Uni-axial FBGs, such as DTG®s, are written in low-birefringent optical fibres (only the single mode is considered in his work), and exhibit initially a single reflecting Bragg peak. However, when embedding these sensors three dimensional strain effects act upon the grating and external birefringence effects can be induced which lead to a (small) splitting of the spectrum because of a (small) difference in refractive index along both polarization axes of the optical fibre.

Longitudinal strains

Mulle et al. [3] assessed the variation of the residual longitudinal strains through the thickness of fibre reinforced laminates during the autoclave cure cycle. They have monitored an eight layer uni-directional stacked ($[0_8]$) carbon-epoxy laminate (Figure 6-2) and a so-called 'technological' carbon-epoxy specimen with a combination of 0°, 45° and 90° oriented reinforcement layers Figure 6-3.

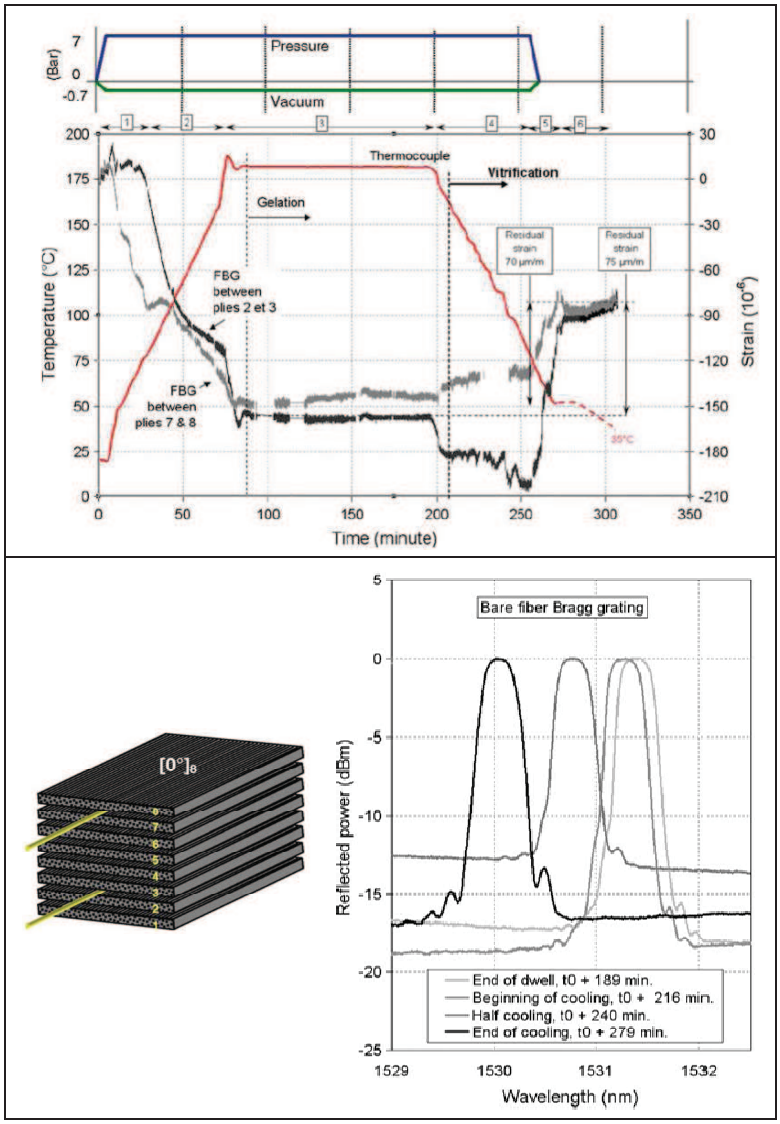

Figure 6-2: Process induced strain changes measured by FBGs through the thickness of a $[0_8]$ stacked laminate during the autoclave curing cycle (top), the ply stacking sequence with position of embedded FBGs (bottom, left), and spectral response of the embedded uni-axial FBG during the cooling down phase [3].

The technological specimen consists of a reinforced area, i.e. a thicker section in the laminate, in which a number of uni-axial 125 µm FBGs are embedded between different layers at several locations through the thickness of the lay-up. The cure cycles of both types of laminates are shown in Figure 6-2, top and Figure 6-3, top, with the individual strain evolution of the FBGs indicated in the graphs.
For the cure monitoring of the $[0_8]$ stacked specimens the authors have used a second FBG ending inside a capillary, free from strain to compensate for intrinsic temperature effects. For the technological specimens, they have used a thermocouple and the intrinsic temperature sensitivity of the optical fibre to perform temperature compensation. Mulle et al. have neglected transverse strain effects and only considered axial strains in the optical fibre. To calculate the axial strains they defined the reference wavelengths for each FBG at 90 min after the start of the isothermal dwell (cure step 3 on top of Figure 6-2, top), which is referred to as the onset of vitrification at which the molecular movement of the whole polymer matrix is restricted and load transfer onto the fibre is made possible. Note that, this is a very important given, because all calculated strain data obtained from the FBGs is referred to the (reference) wavelengths at that specific point. This is a point of attention that will be further elaborated in this work when discussing the calculation of longitudinal strains in Section 6. 6. 2. . At the end of the cooling down phase, they have reported a small splitting of the spectrum for the $[0_8]$ stacked laminate (Figure 6-2, bottom-right). That is why, they assume that the possible error which could be induced by transversal effects in the readings of the axial strain is negligible. Though, we should be careful by assuming that the transverse effects are small, since in a uni-directional lay-up, the strains in the transverse directions (in-plane and out-of-plane) are in theory equal and therefore induces no birefringence effects in the embedded optical fibre. Remark as well that Mulle et al. have explicitly reported that they use a Micronoptics si720 to record the spectra of both embedded FBGs and a Micronoptics si425 read-out system to measure the Bragg peak shifts. The light source of such devices is highly polarized and is in fact not suitable to investigate birefringence effects (or non-uniform strain effects) without the proper use of a polarization controller. No spectra at different polarization angles are presented, so most probably the Bragg peaks are recorded at one specific polarization angle and thus no significant birefringence effects are noticeable.
The same cure monitoring experiment was done for the 'technological' sample using four 125 µm FBGs embedded in between the 0°-directional plies at several places in the reinforcement area of the laminate. The lay-up locations of the individual FBGs of this 'technological' sample is shown in Figure 6-3, left. Note that every FBG are embedded in only one 0°-direction reinforcement ply, and in close contact with the $\pm 45°$ plies, hence the optical fibre will induce distortion in the interface of these plies and it will sense complex strain fields, moreover, the strain transfer from composite to the optical fibre will as well be complex. This can be noticed in the distorted spectra which they have recorded. Note as well that care should be taken when comparing the transverse strain sensitivity of High Birefringent (HiBi) FBGs with those of an uni-axial FBG. The orientation of the HiBi fibre in the laminate is of major importance in this story, a small misalignment can significantly reduce the transversal strain sensitivity [8, 10]. The transversal strain sensitivity of an uni-axial FBG, however, remains the same for all orientations Because of the former statements, the author believes that it is difficult to draw any conclusions out of these uni-axial wavelength readings without further research.

To accurately measure solely the longitudinal strain variation through the thickness of the specimen, the author suggests to use an encapsulated FBG or use a dual sensor configuration with one FBG inside a capillary and one normally embedded to measure multi-axial strains. This latter approach will be elaborated in Chapter 7.

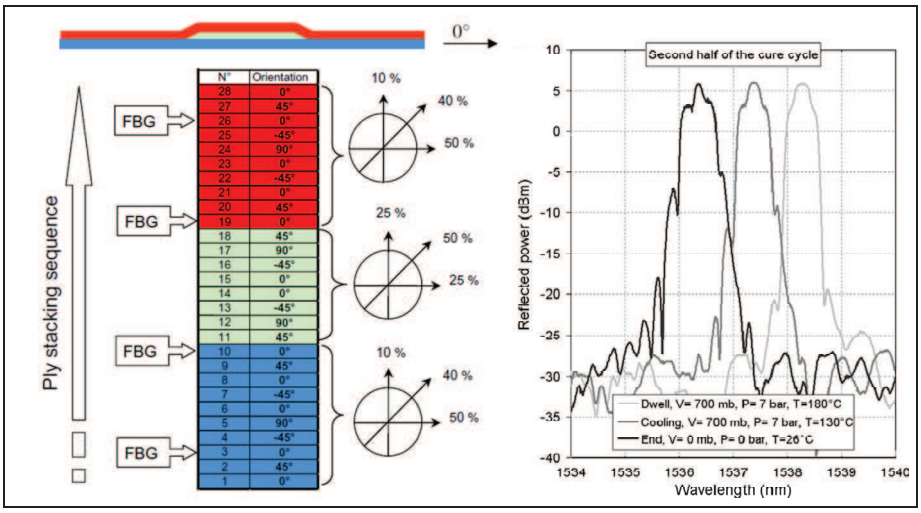

Figure 6-3: The ply stacking sequence with position of embedded FBGs (left), and spectral response of the HiBi FBG during heating and cooling down phase (right) [4].

Spectral response

The influence of the occurring residual curing stress on the spectral response of stripped, polyimide coated normal and polyimide coated small diameter FBG sensors. was studied by Okabe et al. [11]. The optical fibres were embedded in an eight layer cross-ply stacked laminate ($[0_2,90_4,0_2]$) in the 0° ply, in contact with the 90° ply (Figure 6-4).

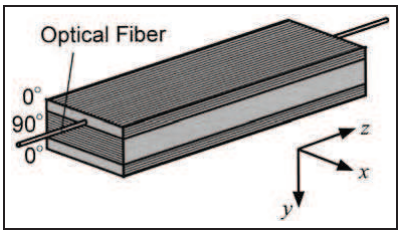

Figure 6-4: Embedding of the optical fibre in a $[0_2,90_4,0_2]$ cross-ply laminate in the 0° ply in contact with the 90° ply [11].

Major goal of their research was the minimization of the effect of non-axisymmetric thermal residual stress on the spectrum of these FBG sensors by coating or minimizing the diameter of the sensor. For the uncoated FBG sensor, birefringence effects occured in the optical fibre which lead to a split of the Bragg peak into two distinct peaks. A clear illustration of the behaviour of the spectral splitting for a stripped FBG during the curing process is given in Figure 6-5 [11]. As mentioned by Mulle et al. [3], this splitting is driven by vitrification of the matrix.

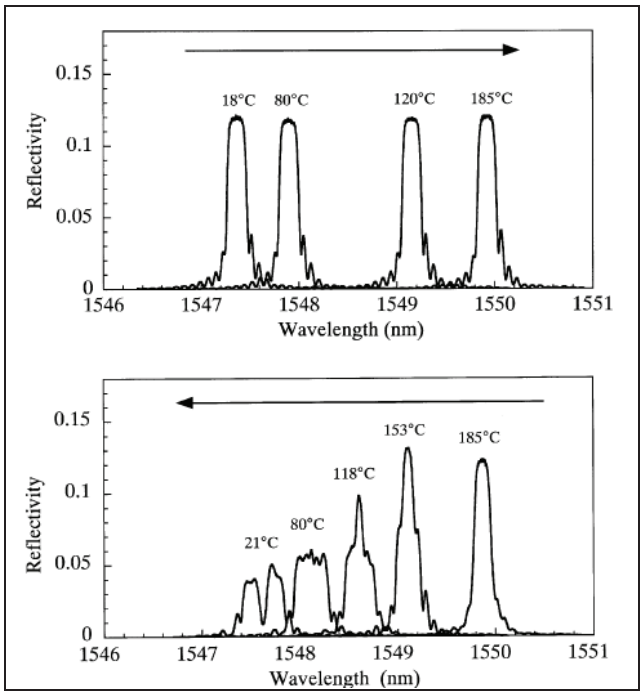

Figure 6-5: Reflection spectra from an uncoated uni-axial FBG sensor, which was embedded into a CFRP laminate, measured during a hot-press manufacturing cycle. During the heating process (top) and during the cooling process (bottom) [11].

This spectral splitting is not observed for the polyimide coated FBGs because the coating acts as a barrier or buffer for the occurring non-axisymmetric residual stresses. In addition, they recorded the spectra of the FBG during thermal cycling of the laminate after manufacturing. The spectra for the stripped FBG shows that the spectral distortion is reversible (Figure 6-6). The spectrum at 185°C gets back to its original shape, moreover, if we further cool down, at -60°C and at -150°C the spectrum is even more distorted than at 20°C. These effects clearly illustrate that the transversal residual strain inside a composite laminate is more or less reversible with increasing temperature. To validate the spectral measurements, Okabe et al. performed 2D FE-simulations by assuming plane strain in their model, to determine the thermal induced (transversal) strains in the optical fibre.

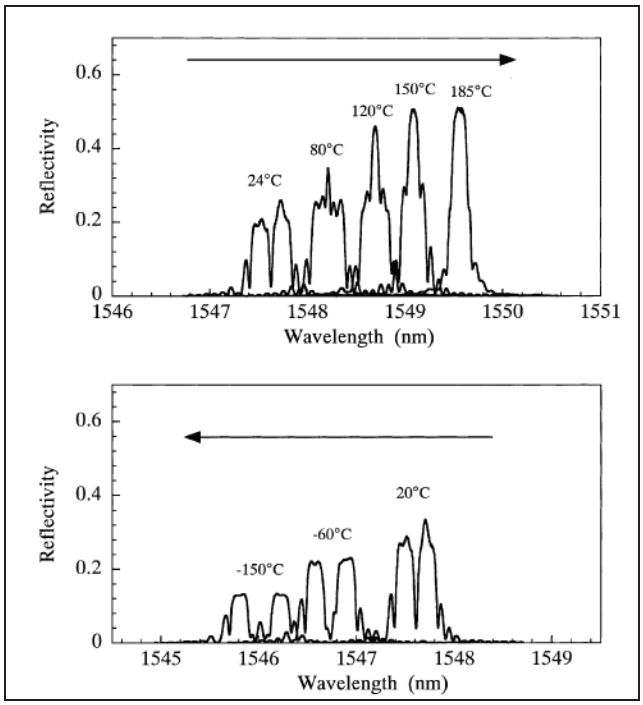

Figure 6-6: Reflection spectra from an uncoated uni-axial FBG sensor, which was embedded into a CFRP laminate, measured during heating (top) and cooling (top) after manufacturing [11].

They performed simulations on a stripped optical fibre as well as on a coated optical fibre and found that the strain profiles around the coated optical fibre changes drastically compared to the stripped strain profile. The transversal strains in the core of the coated optical fibre are much smaller, which confirms the effects that they have seen in the measured spectra. They have then used the numerical strains together with a software program to solve the coupled mode equations, by using the (optical) transfer matrix method [12], to calculate the FBG reflection spectra at different temperatures, see Figure 6-7. If we compare the simulated spectra with the measured spectra of Figure 6-5 and Figure 6-6, the response is matching very well, with a clear peak-splitting after manufacturing. However, if we look closer, we observe that in the measured spectral response there are small additional side-peaks present, which are not present in the 'symmetric' simulated spectra, which illustrates that non-uniform strain fields are present. Okabe et al. deliberately have embedded the optical fibre at the interface of the 0° ply with the 90° ply (Figure 6-4), hence the strain field along the length of the FBG is not uniform and are in reality more complex than the 2D simulated strains (plane-strain). .

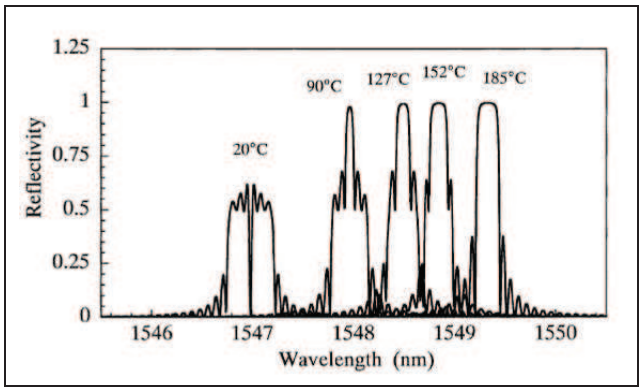

Figure 6-7: Calculated reflection spectra for a stripped FBG affected by thermal residual strain [11].

Transversal strain difference

Güemes and Menendez [5] have estimated the longitudinal and transversal residual strains in a carbon-epoxy laminate with quasi-isotropic (symmetric and balanced) stacking ($[45,-45,0,90,0,-45,45,0,90,45,-45]_{2S}$), using a single 125 µm FBG embedded in the intermediate plies aligned along the reinforcement fibres. The plate was cured at 190°C using a hot press cycle with a maximum pressure of 7 bar. Because it is not possible to distinguish the individual strain components using a single FBG, Güemes and Menendez have assumed a plane stress state in the laminate (i.e. no external stress in the thickness direction). However, the residual (thermal) stress which build-up during curing in the laminate will appear in three directions. As such the assumption of plane stress during curing is not correct. Moreover, because of a difference in material properties between the optical fibre and the composite laminate, the assumption of plane stress in the optical fibre is not valid. Therefore, the author will not go into detail on the calculated strains presented in [5]. Although, the method of strain quantification of Güemes and Menendez is not completely correct, the method to analyse the curing cycle with embedded FBGs is considered very valuable. In Figure 6-8 the curing cycle used to produce a quasi-isotropic carbon-epoxy laminate is plotted. The evolution of the wavelength and the temperature is plotted against the time. We can see that the Bragg peak starts to split during the cooling phase of the process, as is also shown in Figure 6-5,b. After the curing process, the plate is further cooled down to -20°. The spectral response at -20°C is shown in the inset in Figure 6-8, clearly showing the two distinct peaks.

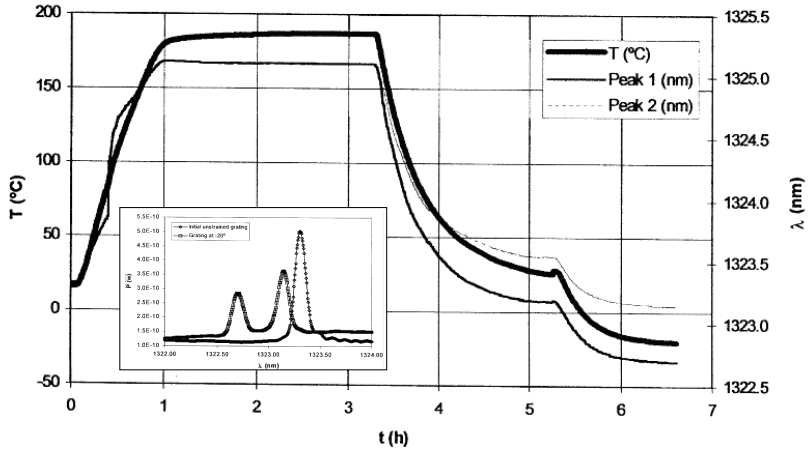

Figure 6-8: Evolution of the temperature and the Bragg wavelength with time along a curing process, inset shows the peak-splitting at -20°C [[5]]

In Figure 6-9, the evolution of the two peak wavelengths is plotted against temperature. Note that, this is the raw wavelength data against temperature. This data includes longitudinal, thermal and transversal strain effects. The wavelength plot gives a very good overview of the different stages and typical behaviour of the embedded FBG during the cure cycle (i.e. heating phase, pressure appliance, cooling phase). The path starts at room temperature and the wavelength increases linear with temperature which is associated with the dependence of the FBG and thermal expansion of the (non-cured) laminate, or tool (i.e. press), see considerations further in this paragraph. At approximately 80°C, pressure is applied and a jump of the wavelength is visible until pressure has reached its maximum (i.e. 7bar). The wavelength evolution after applying pressure is again linear with temperature until 190°C. At the level of 190°C, the epoxy cures for approximately two hours (Figure 6-8), and the optical fibre is "frozen" in the laminate. Note that at this time no wavelength shifts are observed and that no peak-splitting occurs. This indicates clearly that no longitudinal nor transverse load is transferred on the optical fibre during matrix polymerisation. Mulle M. et al. [3] described the same effect and supposed that load transfer to the optical fibre (and reinforcement fibres) only happens from the onset of matrix vitrification, i.e. at the start of the cooling down phase. When cooling the (cured) specimen, shrinkage of the laminate occurs, and because of the mismatch of CTE between the reinforcement fibres and the matrix, the residual strains are building up and transverse strains start to appear which causes the Bragg peak to split.

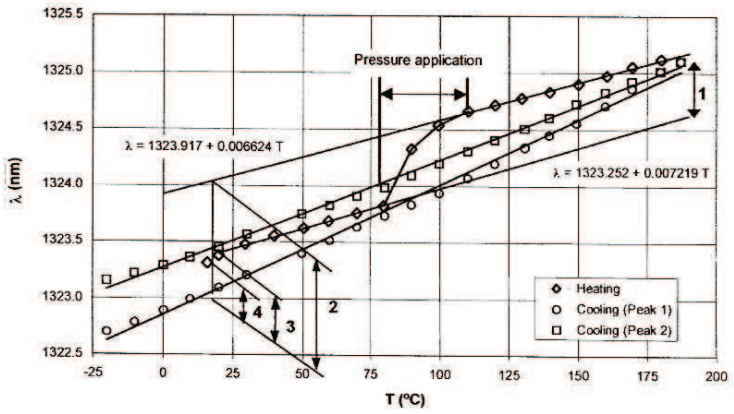

Figure 6-9: Dependency of the Bragg wavelength with temperature during the curing process [5].

At the end of the curing cycle at room temperature, indicated as 3 in Figure 6-9, we end up with a high mechanical induced birefringence in the fibre. The peaks are approximately separated 400 pm at room temperature, which is in the same order of magnitude as the separation of a an FBG in a HiBi fibre (e.g. bow-tie) [13].
The separation of the peaks is a measureable parameter, and because of the fact that residual strain in the host material induces high birefringence effects in the core of the optical fibre, we can use the peak-splitting to estimate the residual strain difference. By using the following equation (Equation B-25, Appendix B):

$$\varepsilon_{1'} - \varepsilon_{2'} = \Delta\varepsilon_{trans} = \frac{2}{\bar{n}^2} \frac{\lambda_{B,1'} - \lambda_{B,2'}}{\left(\lambda_{B,0}\right)\left(p_{12} - p_{11}\right)}, \qquad 6\text{-}1$$

and filling in the peak separation, the corresponding transversal strain difference measured in the core of the optical fibre can be calculated . With a peak separation of $\lambda_{B,1'} - \lambda_{B,2'} = 0.4\ nm$ according to the convention used in this work (Section 4.4.2.b, Chapter 4), with the Fast axis corresponding to the 2'-polarization axis and the Slow axis corresponding to the 1'-polarization axis, a mean wavelength $\lambda_{B,0} = (\lambda_{B,1'} + \lambda_{B,2'})/2 \approx 1323.3\ nm$ determined from Figure 6-9, p_{11}=*0.113*, p_{12}=*0.252*, and $\bar{n} = 1.4496$, we find a $\Delta\varepsilon_{trans} = 0.114\%$. Note that Equation 6-1 does not depend on temperature and that the residual transversal strain difference can be calculated from the separation of the peaks at any temperature (e.g. room temperature). The example of Güemes and Menendez clearly illustrates that by following the wavelength evolution of a uni-axial FBG during the cure cycle, we can gather already valuable information on the internal transversal strain state of a composite laminate.
Sorenson et al. [14] have performed polarization measurements on embedded uni-axial 125µm FBGs during the hot-moulding of a 28 layer uni-directional stacked ($[0_{28}]$) thermoplastic AS4/PPS (polyphenylene sulphide) carbon reinforced laminate. The length of the FBGs is 22 mm and the FBG is embedded in the 3rd and 4th outer 0° plies, i.e. along the longitudinal direction of the laminate. They have used a tunable laser-based system, capable of polarization control, to read-out the FBGs.

Thermocouples embedded close to the FBGs are used for temperature compensation on the monitored Bragg wavelengths. Sorenson et al. estimated the residual strain difference in the FBGs from the wavelength difference between the two Bragg peaks for several samples. An example of the spectral response before and after consolidation with separated Bragg peaks polarized along the two main polarization axes is shown in Figure 6-10. The separation of the Bragg peaks ($\lambda_{B,x} - \lambda_{B,y}$) in the consolidated samples is relatively small compared to the carbon epoxy sample of Güemes and Menendez and varies between 0.030 nm and 0.071 nm, corresponding to a transversal strain difference of 0.012 % and 0.027 %, respectively. The difference is small because of the uni-directional lay-up, however, the results of Sorensen et al. clearly illustrates Bragg peak-splitting even in the presence of small induced birefringence in the optical fibre.

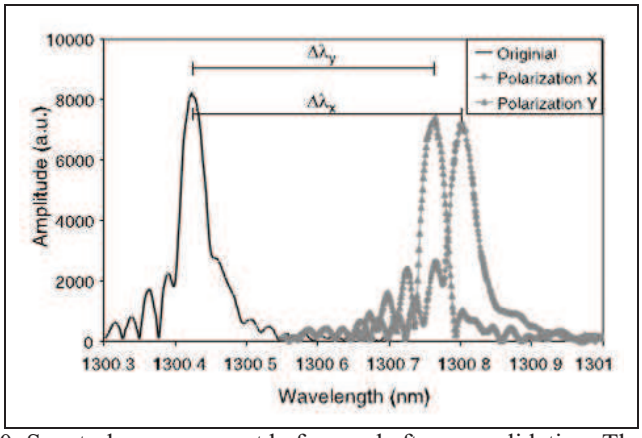

Figure 6-10: Spectral measurement before and after consolidation. The two right-hand peaks represent the two major polarization axes [14].

Additional to the residual strain difference, Sorensen et al. performed plain strain FE-simulations on the consolidation of the laminate during cooling. They have verified the experimental results with the results of an unconstrained and constrained simulated model, where the difference between both models is that in the latter the steel mould is modelled as well and is perfectly attached to the laminate. From the comparison of the FBG response and the modelling, it is indicated that the specimen–tool interaction plays a significant role in the development of residual strains in the unidirectional composite. They stated that the combination of FBG measurement with numerical modelling can serve as a good tool for measuring residual strain accumulation. However, no matching results were found because of in-appropriate boundary conditions, indicating that modelling the specimen-tool interaction and identifying the appropriate contact-conditions is a challenging problem. Sorensen et al. pointed out that one should be very careful considering the type of strain field which is present in the core of the optical fibre, before interpreting its signal, i.e. the Bragg peak. A potential interpretation error on the longitudinal strain calculation was discussed for their specific case and a relative error of 180 % in the longitudinal direction and 110 % in the transversal direction is found, when considering only the Poisson's ratio of the fibre and neglecting the induced birefringence effect in the optical fibre!

6. 2. 2. b. Cure monitoring with HiBi-fibres

FBGs written in high-birefringent (HiBi) fibres exhibit two independent polarization axes, i.e. the "fast" -and "slow"-axis, which is induced geometrically (e.g. elliptical core) or through the use of stress applying parts in the cladding, near the core of the optical fibre (e.g. Panda, Bow-tie), see Figure 6-11:

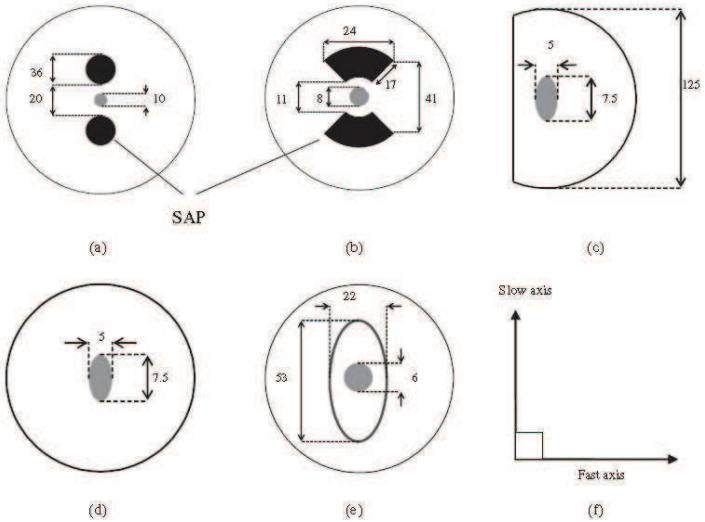

Figure 6-11: HiBi fibre cross-sectional geometry: (a) Panda and true Phase fibres, (b) bow-tie fibre, (c) D cladding and elliptical core fibre, (d) elliptical core fibre, (e) elliptical cladding and (f) polarization axes configuration [13].

The birefringence of these fibres causes the Bragg spectrum to initially consist of two independent Bragg peaks instead of one: one corresponding to the fast axis and one corresponding to the slow axis. With these kind of FBGs, we are in principle able to distinct the three principal strain components of a composite laminate [15]. To distinct the three orthogonal strain components we need in fact a multi-axial approach, which can be applied using two HiBi FBGs with a difference in sensitivities between both sensors to solve the multi-axial Bragg equations [16]. This matter has been investigated by Luyckx for a number of carbon-epoxy laminates under different loading conditions [8]. A multi-axial strain (MAxS) sensor was developed during that research. The MAxS-sensor consists of two FBGs written in a 80 µm bow-tie fibre. One FBG is encapsulated using a small glass capillary, which keeps the FBG free from transversal stresses, hence, it measures only longitudinal, Poisson's induced transverse and thermal strains. The other embedded FBG is stripped and "normally" embedded. This FBG measures all strain components including the thermal strains. The same sensor system is used to monitor the wavelength shifts of the individual HiBi FBGs during a curing cycle. The MaxS sensor is embedded in between the bottom 0° layer of a 12 layer CFRP laminate (stacking $[\pm 45_2, 0_2, 90_2]_S$). An example of the evolution of the wavelength of all four Bragg peaks with temperature is shown in Figure 6-12. We clearly observe that FBG 1 has an absolute negative shift and FBG 2 (inside capillary) an absolute positive shift. Both shifts are in the order of 1 nm. At the start of the cycle, we observe a drop of the wavelength of all four peaks, because of vacuum pressure applied on the

laminate. At approximately 90°C a raise of all four wavelengths is noticed, which is explained by the fact that the viscosity of the epoxy becomes lower and so the optical fibre is free to expand. It is noted that no pressure in the autoclave is applied at this moment.

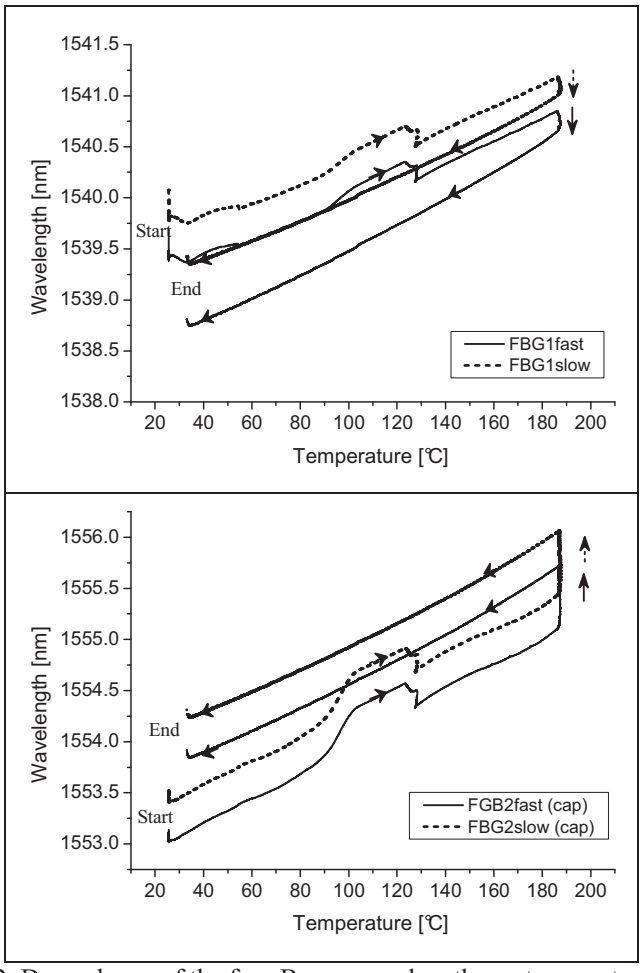

Figure 6-12: Dependency of the four Bragg wavelengths on temperature. FBG 1 is 'normally' embedded in the laminate and FBG 2 is the sensor inside the capillary [8].

Then, during the *dwell step* at 120°C we see that all wavelengths slowly decrease. After the dwell step (at approximately 130°C), a uniform pressure of approximately 7 bars is applied on the laminate. A sudden drop of the wavelengths is noticed, and the magnitude of this decrease is identical for both FBGs, indicating a (uniform) compressive strain of the optical fibre. During the heating from 130°C up to 180°C, both the sensors react more or less linear. At maximum temperature during curing of the epoxy matrix, we notice a significant difference in response. The stripped FBG which is "normally" embedded, shows a decrease in wavelength, while the FBG inside the capillary shows an increase. It is difficult to explain the exact reason of

this behaviour. In order to get a better insight in the curing behaviour and the real strains which are acting on the FBGs, we need to define the multi-axial strain transfer mechanism for this specific laminate during curing. This is not at all a straightforward matter and will be elaborated in Chapter 7 for specific loading conditions on a cured laminate. Moreover, the response of the normally embedded FBG could be misleading, because we do not know the orientation of the bow-tie fibre in the laminate. Orientation of the polarization maintaining optical fibre during the embedding process was found to be very difficult. It should be kept in mind that when the optical axes of the embedded bow-tie fibre are not well aligned with the mechanical axes of the laminate, the resulting errors in calculating the residual strains using the wavelength reading of a HiBi FBG with uncertain orientation could be very high [8].
Although, we do not know the orientation of the bow-tie with respect to the out-of-plane axis of the laminate (i.e. 3-direction), we notice a clear peak separation of the "normally" embedded FBG during the cooling phase, which indicates that transverse strains are building up. The encapsulated FBG, free from transverse strains, is only affected by the negative CTE of the laminate and even though the wavelengths are not temperature compensated a homogeneous positive wavelength shift of both peaks is noticed after cooling, indicating a relative high longitudinal strain. The response of the MaxS sensor clearly indicates that a multi-axial strain field is building up during curing. It is however very difficult to calculate accurate the 3D strains inside the HiBi optical fibre because of the uncertain orientation of the bow-tie fibre. Moreover, no temperature compensation technique is implemented in the multi-axial approach of the MaxS sensor [8], as such large errors on the transversal strains is induced.

6. 2. 2. c. Concluding remarks

Care has to be taken when interpreting the wavelength shifts of embedded FBGs and when relating them to real residual strains. First of all it is very important to use an appropriate FBG interrogation system not to make errors in the wavelength determination, as this is the basis of the measurement. Using a depolarized light source or a polarization controllable system is recommended, to be able to detect birefringence effects. A second matter of importance is that the strains we measure are the strains present in the core of the optical fibre. Hence, a strain transfer method is necessary to relate the strain of the optical fibre with the strain in the host material [17-18]. For a cured laminate, it is possible to define the strain transfer matrix numerically and experimentally, see Chapter 7. However, the defined transfer matrix in Chapter 7 is in principle only valid at room temperature. In reality and also during the curing process, the material properties (e.g. Young's modulus) of the optical fibre, the fibre coating and host material are temperature dependent, which has an influence on the strain transfer. Moreover, polymerisation, crystallization, visco-elasticity of the matrix, coating material of the optical fibre and bonding mechanisms (physical and chemical) make the in-situ strain relation even more complex. It is very difficult to define the reference wavelength of the embedded sensor. Several effects should be taken into consideration: (i) thermal stability of the FBG itself, i.e. pre-annealing is necessary to avoid possible wavelength drifts, which affect the real monitored wavelength shift (Chapter 4) (ii) placement (manual) of the FBG in the pre-preg layer, i.e. it is uncertain how much pre-strain is put on the fibres during placement and how much pre-strain is lost during the process. Finally,

tooling effects and specimen-tool interaction can affect the residual strains. The mould will define the boundary effects of the curing and thermal contractions of the cured laminate, which affects on its turn the residual strains through-the-thickness. All the afore mentioned issues illustrate the difficulty of accurately quantifying the residual strain formation. Though, the examples above clearly illustrated the ability of uni-axial FBGs and HiBi FBGs to qualify residual strain formation in composites. This knowledge is used further in this chapter to monitor the curing of thermoset and thermoplastic CFRP laminates. However, before directly discussing the cure and consolidation cycle effects, first, an overview is given of the used composite nomenclature in the following sections.

6. 3. COMPOSITE NOMENCLATURE

6. 3. 1. Pre-preg and semi-preg

All composite laminates, discussed in this work, are manually stacked using different composite plies.

In the case of the thermoset CFRP test-samples, the laminates are stacked using reinforcing carbon fibre layers, pre-impregnated with epoxy resin. Such uni-directional carbon-epoxy layers are simply called *pre-pregs*. An example of such a pre-preg layer with a protective (white) polyethylene foil, is shown in Figure 6-13, left. A laminate is formed by curing a number of stacked pre-preg layers.

In the case of the thermoplastic CFRP, the laminates are stacked using carbon-PPS woven fabrics, or *semi-pregs*. A pre-fabricated carbon-PPS semi-preg consist of three layers: (i) a PPS film, (ii) a layer of carbon-fabric and (iii) again a PPS film. The thermoplastic PPS is melted on the carbon fabric at two sides using a hot press, so, after cooling down, it becomes consolidated. The brand name of this material is Cetex® [19]. An example of a carbon-PPS semi-preg, or Cetex®-PPS layer, is shown in (Figure 6-13, right). By hot – pressing a number of semi-pregs, a laminate is formed.

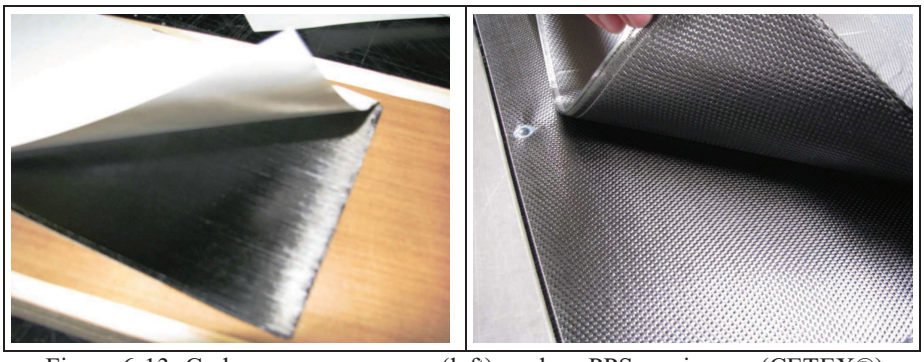

Figure 6-13: Carbon-epoxy pre-preg (left), carbon-PPS semi-preg (CETEX®) (right).

6. 3. 2. Local and global coordinate system - notation of stacking sequence

6. 3. 2. a. Uni-directional lamina

It is common to use two coordinate systems to define the directions of the strains inside composite laminates. One on the level of the plies (i.e. local) and one on the level of the composite laminate (i.e. global).
In Figure 6-14 (left), the local coordinate system used for the individual ply (lamina) is shown. The 1-axis is aligned with the reinforcement fibres while the 2-axis is aligned transversally in-plane, and the 3-axis is aligned transversally out-of-plane. The coordinate system on the optical fibre level is defined in Chapter 4. The notation 1‘, 2’ and 3’ is chosen to avoid confusion with the local coordinate system of the composite laminate. The 3’- axis is taken along the length of the optical fibre. Typically, the optical fibre is embedded along the reinforcement fibres, hence, the 1-axis of a single composite layer and the 3’-axis of the optical fibre are co-linear.

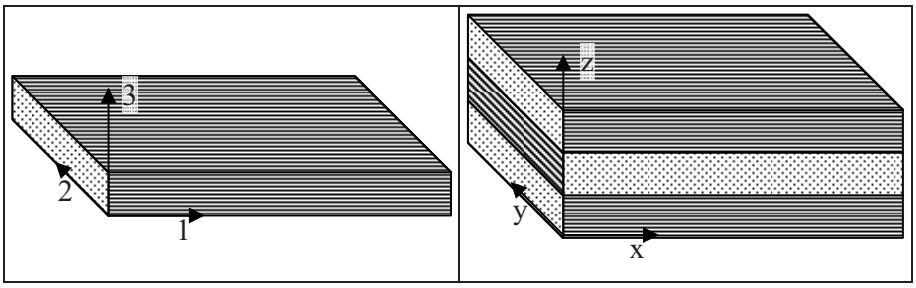

Figure 6-14: Local coordinate system on ply level (left), global coordinate system on laminate level.

A global coordinate system is used to define the strains in the principal geometrical directions of the laminate (x- , y-, and z-direction). In Figure 6-14 (right) a cross-ply laminate consisting of three individual lamina is shown. The x-axis is aligned with the major direction (length) of the plate. The y-axis is the transverse in-plane direction (width) and the z-axis is the transverse out-of-plane direction of the laminate. As such, Figure 6-14 (right) illustrates a cross-ply laminate with [0, 90, 0] stacking, i.e. the 1-axis of the bottom and top lamina are oriented along the x-axis, while the 1-axis of the middle ply is rotated 90° with the x-axis.
A difference exists between the notation of the stacking sequence of the uni-directional lamina and that of the woven fabrics. Typically, for an eight layer stacking of uni-directional lamina, the following notations are applied:

$[0]_8$: All eight reinforcement layers have the same orientation of 0 degrees with respect to the x-axis of the global coordinate system. The complete notation is [0,0,0,0,0,0,0,0].

$[0,90]_{2S}$: This laminate too consists of eight layers in total. The “s” means that the lay-up is symmetrically stacked with respect to the mid-plane. The “2” means that the stacking sequence of the *0 degrees* and *90 degrees* is

repeated two times. The complete notation is [0,90,0,90,90,0,90,0]. Note that the *0 degrees* are the outer layers of the laminate.

6. 3. 2. b. Woven fabric

In the case of woven fabrics or textile composites the same local and global coordinate system is used, however, a different nomenclature is used. Typical for a textile composite the term "warp" and "weft" is used in analogy to the textile industry, with the warp- and weft yarns corresponding to the 1-axis and the 2-axis of the local coordinate system, respectively. A yarn is a carbon bundle, typically containing 3000 to 10000 carbon fibres (i.e. filaments). The semi-preg plies used in this work have a 5-harness satin weave pattern (Section 6. 5.). An example of the warp and weft yarn directions in a 5-harness satin weave pattern is shown in Figure 6-15:

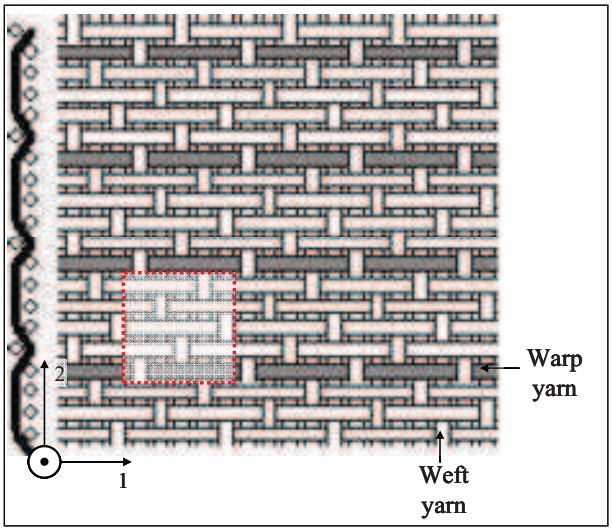

Figure 6-15: Warp and weft direction in a 5-harness satin weave pattern [20].

The 5-harness satin weave is characterized by five or more weft yarns floating over a warp yarn or vice versa, five warp yarns floating over a single weft yarn. The harness weave pattern increases uniformity in strength (in the 1- and 2-direction) in comparison to a plain weave, where each weft yarn passes alternately under and over a warp yarn. The term "5-harness" means that the weft yarns alternately crosses and passes 5 yarns before the pattern repeats. This repetitive pattern is also referred to as the *unit-cell* of the weave. The unit-cell is indicated by the small rectangle inset in Figure 6-15 and the weft and yarn repetitive interlacing pattern along one yarn is shown at the left side of Figure 6-15.

Stacking of these plies is similar to cross-ply laminates. However, to define the stacking sequences of fabric reinforcement, in analogy to the work of Ives De Baere, another type of notation is used [21]. The notation of one semi-preg is (0,90), with the *0 degrees* corresponding to the warp direction of the weave, i.e. the direction along the 1-axis of the local coordinate system, Figure 6-14 (left). Typically a (0,90) semi-preg has the warp-yarns situated more at the bottom side of the semi-preg and the weft yarns situated more at the top side of the semi-preg.

In this work two differently stacked laminates are used to produce test-coupons, i.e. a $[(0,90)]_{4s}$ and $[(90,0)]_{4s}$ stacked laminate, each with a total of 8 semi-pregs, with this difference that the former has a so called *in-phase stacking sequence* at the mid-plane (symmetry-plane) plies and the latter has an *out-of-phase stacking* sequence at the mid-plane plies. The warp yarns are aligned along the length (x-axis) of the test-coupons, Figure 6-26.
The term *in-phase stacking* in this work refers to the fact that the semi-pregs in the mid-plane plies are stacked symmetric with the weft yarns oriented towards each other. If the stacking is called *out-of-phase*, this refers to the fact that the semi-pregs in the mid-plane plies are stacked symmetric with the warp yarns oriented towards each other. Because the warp and weft yarns are both identical carbon bundles with the same amount of carbon filaments, there exists no significant difference in composite properties on macroscopic level. However, microscopically, the local strain fields in the mid-plane differ for both types of stacking. This difference is visible when embedding an optical fibre inside the mid-plane of both lay-ups.
In the woven fabric test-coupons the optical fibre is always embedded in the centre of the laminate and aligned along the x-axis of the test-coupons. Hence, for the *in-phase stacking,* it is crossed by the *weft yarns* and for the *out-of-phase stacking* it is crossed by the *warp yarns*. The difference is shown in Section 6. 5. 2. (Figure 6-26). It is clear that for both type of lay-ups a different microscopic local strain field surrounds the optical fibre. The response of the embedded DTG® in these two types of laminates is further discussed in Section 6. 7. .

6. 4. THERMOSET CFRP TEST-COUPONS

The M55j/M18 material from Hexcel [22], a carbon-epoxy prepreg, is used to manufacture the thermoset CFRP samples. The material is space qualified UD fibre reinforced epoxy [22]. The reinforcement fibres are high modulus carbon fibres with a Young Modulus of 540 GPa [23].

6. 4. 1. Autoclave curing

To manufacture the thermoset CFRP samples a small scale autoclave at Ghent University has been used, see Figure 6-16:

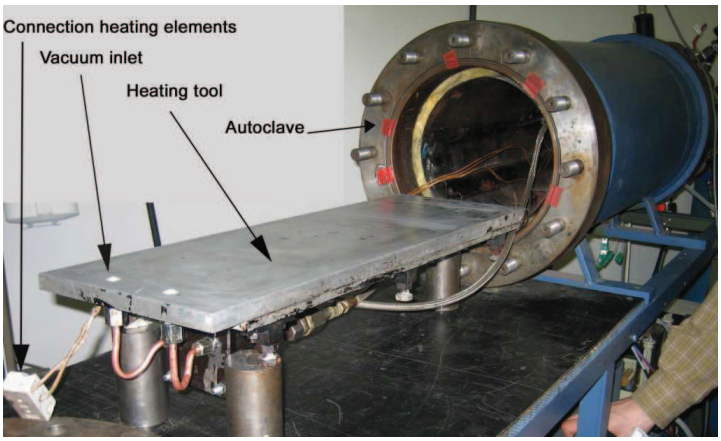

Figure 6-16: The autoclave of Ghent university, department of Materials Sciences and Engineering.

The carbon pre-preg layers (Figure 6-13, left) have a thickness of approximately 0.1 mm. The lay-up is manually stacked in the right sequence, and is pressed together with a roller pin to assure good contact between the pre-preg plies (according to the procedure described by Geert Luyckx) [8]. The pre-preg lay-up is then prepared using standard vacuumbagging technology, see Figure 6-17:

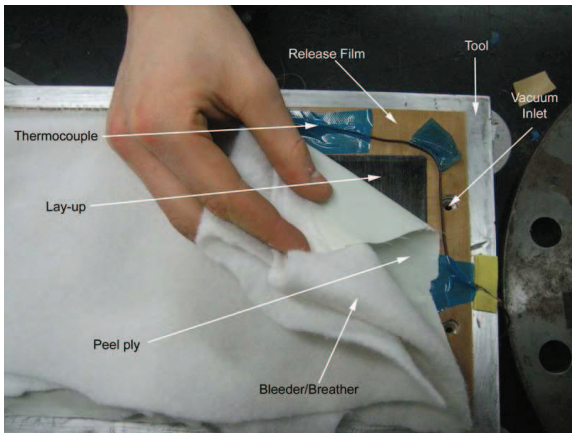

Figure 6-17: Vacuumbagging build-up of the laminate for autoclave curing.

First, a *release film* is placed between the tool and the prepreg lay-up, to avoid sticking of the (cured) laminate to the heating tool. Then a *peel-ply* (with microscopic holes) is placed on top of the prepreg laminate, together with a breather */ bleeder fabric* to outgas the curing resin and to absorb excess resin from the curing laminate. The peel ply is easily removed after curing and provides a smooth surface on the laminate. *Thermocouples* are used at specific spots and in the vicinity of the laminate to monitor the temperature during the curing cycle. The prepared laminate is finally covered by a *vacuumbag* and sealed using elastic *tacky tape*. An example of a prepared sample sealed with a vacuumbag before curing is shown in Figure 6-16, left. The function of the breather / bleeder fabric underneath the vacuumfoil is shown in Figure 6-16, where we see the absorbed excess epoxy resin during curing.

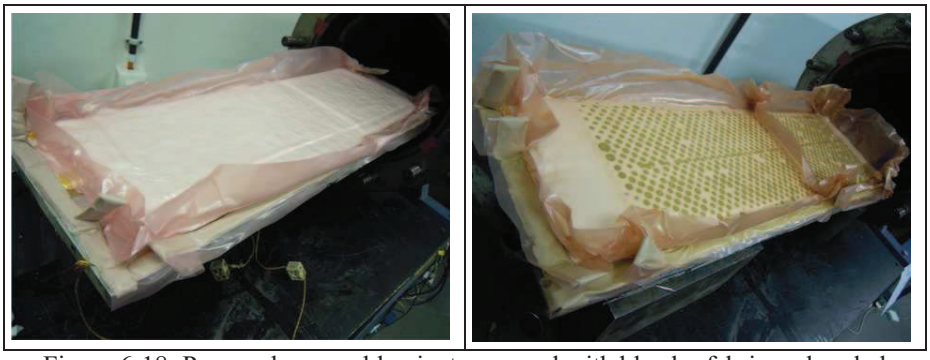

Figure 6-18: Prepared uncured laminate covered with bleeder fabric and sealed vacuumbag (left), laminate with sealed vacuumbag and absorbed excess resin by bleeder fabric after cuing (right).

The curing cycle used to produce the CFRP laminates using the M55j/M18 prepreg material, is deduced from practical experience obtained during a master thesis at Ghent University [24]. The thermal and pressure cycle is shown in Figure 6-19:

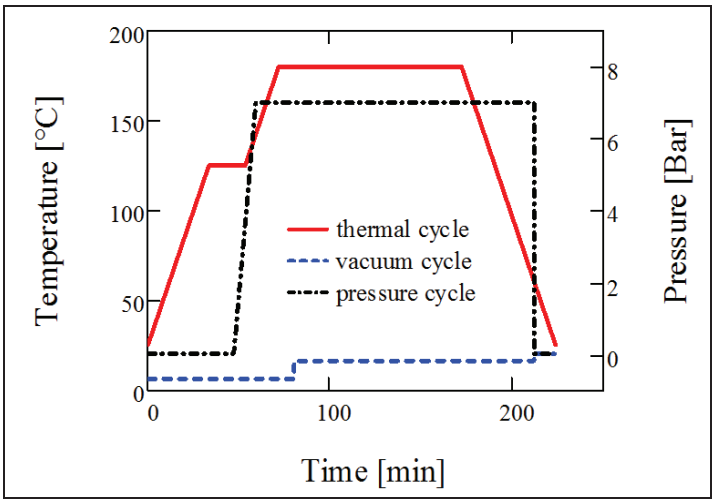

Figure 6-19: Curing cycle used to produce the M55j/M18 CFRP samples.

At start a vacuum pressure of approximately -0.7 bar is build up inside the vacuum bag. If the vacuum is stable, and no leakage is found in the sealant, the temperature is raised at a rate of 3°C/min and kept for approximately 20 minutes at 120°C. This first plateau is called the *dwell step* of the curing cycle. During the dwell step, the epoxy viscosity is optimal [25], allowing the epoxy to flow and the prepreg layers to stick together. A consolidating pressure of 7 bar is applied in the autoclave at the end of the dwell step, and the temperature is raised to a maximum of 180°C. When the temperature in the autoclave has reached 180°C, vacuum pressure is put off, and temperature is kept constant for 100min. During this period the *polymerisation* of the epoxy resin takes place, i.e. the *laminate cures*. Finally, the heating is turned off and the autoclave is cooled down. The pressure of 7 bar is kept during the cool-down phase to prevent deformation of the plate due to thermal stresses. When a temperature of 60°C is reached, the autoclave pressure is put back to atmospheric pressure and the samples are taken out of the autoclave.

6. 4. 2. Embedding optical fibre sensors during the autoclave process

Figure 6-20 shows how the laminate with optical fibres are prepared for an autoclave cycle. A certain amount of prepreg plies is piled in the right sequence and a high temperature *kapton (polyimide) foil* is put at the side of the laminate to provide an elastic *fibre egress*. In the example illustrated below, the DTG®s are encapsulated, using a small glass capillary, and are embedded between the centre plies in alignment with the reinforcement fibres. The fibre is gently pushed in the "soft" prepreg, and because the epoxy is sticky at room temperature, the optical fibres are kept in place. Consequently, the fibre is *fixed* to the kapton foil using a *small kapton tape*. Next, the second half of the prepregs are piled according to the right sequence on top of the embedded fibres and a thermocouple is placed to monitor the temperature in the laminate. Afterwards, the uncured laminate is placed

on the Teflon release film on the *Aluminium heating tool* (support plate) and the optical fibre tails are wound up on the film or, if monitoring during curing is preferred, they are lead towards the optical fibre signal 'feedthrough' in the autoclave cover (Section 6. 2.). Finally, the laminate and optical fibre is covered with a *peel ply* and finalized using the afore mentioned autoclave manufacturing procedure (Figure 6-18).

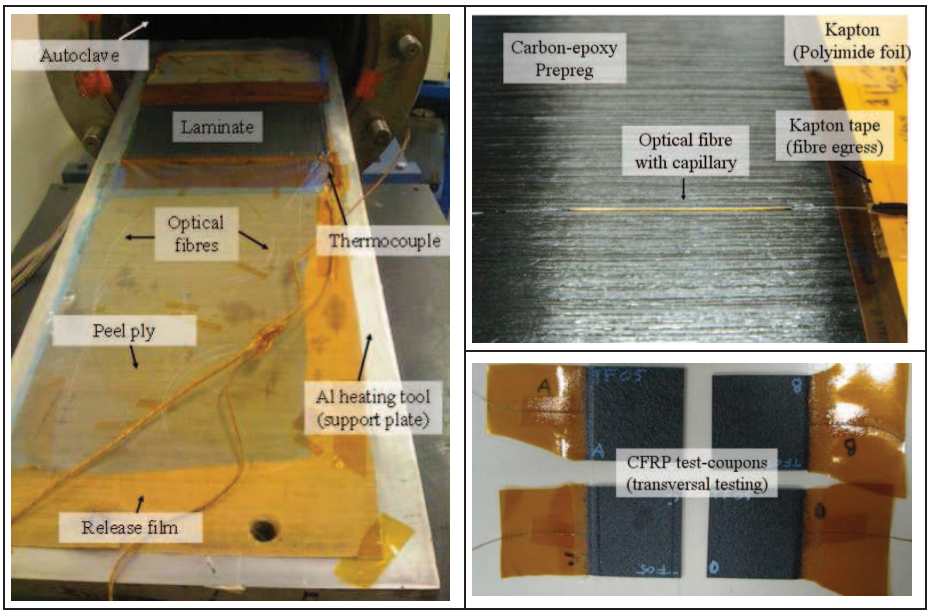

Figure 6-20: Optical fibre preparation (with capillary) for embedding in small rectangular CFRP test-coupons using the autoclave process.

After curing, the laminate is cut into test-coupons using a water-cooled diamond saw. In the example illustrated in Figure 6-20, bottom-right, the laminate is cut into four identical rectangular shaped specimens, used for through-the-thickness transversal compression testing (Chapter 7). See Table 6-3 (Section 6. 4. 4.) for more details regarding the prepared test-coupons and the embedded sensors.
If an optical fibre is embedded in composite laminates, it is preferred to embed it in between two (or more) uni-directional lamina aligned with the reinforcement fibres. The carbon-epoxy cross-ply laminates used in this work have a total of sixteen layers and are stacked symmetrically with a stacking sequence $[90_2, 0_2]_{2S}$ or $[0_2,90_2]_{2s}$ (Section 6. 4.). The optical fibre is embedded in between the zero degree mid-plane layers. An example of the cross-section of a cross-ply laminate with an embedded optical fibre is shown Figure 6-21.
It is noted that, if one embeds fibre Bragg gratings in the outer layers of the lay-up, more to the surface of the laminate, it is possible to measure strain or compression during bending tests.

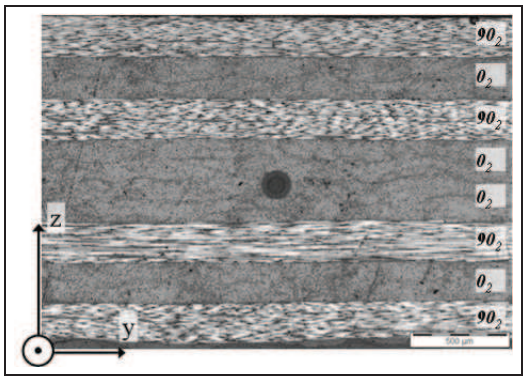

Figure 6-21 Example of a $[90_2, 0_2]_{2S}$ cross-ply laminate with optical fibre, embedded at mid-plane thickness and aligned with the uni-directional reinforcement fibres.

6. 4. 3. Material properties of the thermoset CFRP laminates

The mechanical properties of the M55J/M18 carbon-epoxy were determined in the scope of the PhD-research of Geert Luyckx [8]. A number of standardized test-samples were manufactured and tested according to the D3039 ASTM standard [26]. Because the mechanical properties are dependent on the quality of lay-up and manufacturing parameters, i.e. curing cycle, two additional sets of five 0° UD and five 90° UD samples are manufactured and characterized in [27]. In Table 6-1, the experimental determined properties of all calibration samples are compared with those of the manufacturer [23] and a study of Jose S. [28].

Table 6-1: Elastic and strength properties for the M55J/M18 material, determined from experimental characterizations, compared with those of the manufacturer.

		[24]	[27]	[23]	[28]
Elastic constants	Longitudinal modulus E_{11} [GPa]	298.4	294.8	340.0	329.0
	Transverse modulus E_{22} [GPa]	6.3	5.7	6.3	6
	Poisson's ratio ν_{12} [-]	0.321	0.291		0.346
	Poisson's ratio ν_{21} [-]	0.0017			
	Poisson's ratio ν_{23} [-]			0.38	
	Shear modulus G_{12} [GPa]				4.4
Strength properties	Longitudinal strength [MPa]	2131		2010	1327
	Transverse strength [MPa]	22		34	22

If we compare the results obtained from [27] with those obtained in the work of Luyckx we see that there exist some discrepancies. It is believed that this is caused by a difference in resin content of the new samples (the manufacturing procedure was slightly adapted without continuous vacuum throughout the complete cure cycle). For later use in finite element modelling (Chapter 7), an average is stroke out of the elastic values of Table 6-1. The adopted values are given in Table 6-2.

Table 6-2: Engineering constants for the M55J/M18 carbon/epoxy UD material.

E_{11} [GPa]	$E_{22} = E_{33}$ [GPa]	$G_{12} = G_{13}$ [GPa]	G_{23} [GPa]	$\nu_{12} = \nu_{13}$ [-]	$\nu_{23} = \nu_{32}$ [-]	$\nu_{21} = \nu_{31}$ [-]
300.0	6.3	4.3	2.3	0.320	0.380	0.002

6. 4. 4. Inventory of all thermoset CFRP test-coupons

A complete inventory of all produced thermoset CFRP test-samples with embedded DTG®s, is given in Table 6-3 (see next page). All samples consist of 16 uni-directional layers. The samples 1 – 10 have a thickness of 1.54 mm and the samples 12 – 22 have a thickness of 1.8 mm. The difference in thickness between both sets of samples is again caused by the difference in resin content, due to the slightly adapted manufacturing cycle.

The stacking sequence of each sample is indicated in the first column. The 0 degree direction is always aligned along the x-axis of the global coordinate system (Section 6. 3. 2.). The optical fibre is embedded in the mid-plane (i.e. between the 8^{th} and the 9^{th} layer). Counting of the layers is started from the bottom of the laminate. The sensor alignment, with respect to the global coordinate system, is indicated in the second last column. In the last column extra remarks are implemented, if there is written 80 or 125, it refers to if a 80 µm or 125 µm DTG®s is embedded, respectively. “Stripped” means that the fibre coating is removed at the position of the DTG® and “cap” means the DTG® is coated and encapsulated in a glass capillary. If no extra info written the DTG® is coated. The total outer diameter of the coated DTG®-fibres is approximately 138 µm for the 80 µm sensors and 190 µm for the 125 µm DTG®s.

The rows marked with (*) or with the characters put in *italic*, indicate the samples which were non-useable for testing, because the fibres were broken during autoclave production or after production during handling. In total 13 out of 22 samples survived and were tested. The main reason why a lot of the fibres broke, is due to the labour intensive autoclave procedure. Most of the fibres of the samples broke during the “rough “ un-packing of the cured composite out of the vacuumbag. In addition some of the fragile stripped fibres broke at the grating during the production cycle or were already broken during the prep-preg stacking procedure.

Table 6-3: Inventory of all thermoset CFRP test-coupons with embedded sensors.

	Lay-up	Length	Width	Thickness	Sensor alignment	Remark
n°.		[mm]	[mm]	[mm]	Global	
1	*$[90_2,0_2]_{2S}$*	*50*	*50*	*1.54*	*x-axis*	*125 (stripped)**
2	*$[90_2,0_2]_{2S}$*	*50*	*50*	*1.54*	*x-axis*	*125 (stripped)**
3	*$[90_2,0_2]_{2S}$*	*50*	*50*	*1.54*	*x-axis*	*125**
4	$[90_2,0_2]_{2S}$	50	50	1.54	x-axis	80 (stripped)
5	$[90_2,0_2]_{2S}$	50	50	1.54	x-axis	80 (stripped)
6	$[90_2,0_2]_{2S}$	50	50	1.54	x-axis	80
7	$[90_2,0_2]_{2S}$	50	50	1.54	x-axis	80 (cap)
8	*$[90_2,0_2]_{2S}$*	*50*	*50*	*1.54*	*x-axis*	*80 (cap)**
9	$[90_2,0_2]_{2S}$	50	50	1.54	x-axis	80 (cap)
10	$[90_2,0_2]_{2S}$	50	50	1.54	x-axis	80 (cap)
11	*$[90_2,0_2]_{2S}$*	-	-	-	*x-axis*	*80 (stripped)**
12	$[90_2,0_2]_{2S}$	250	24.17	1.80	x-axis	80 (stripped)
13	$[90_2,0_2]_{2S}$	250	24.17	1.80	x-axis	80 (stripped)
14	*$[90_2,0_2]_{2S}$*	*250*	*24.67*	*1.80*	*x-axis*	*80 (cap)**
15	$[90_2,0_2]_{2S}$	250	24.26	1.80	x-axis	80 (cap)
16	$[90_2,0_2]_{2S}$	250	24.41	1.80	x-axis	80 (cap)
17	$[0_2,90_2]_{2S}$	250	30.19	1.80	y-axis	80 (stripped)
18	*$[0_2,90_2]_{2S}$*	250	*30.52*	*1.80*	*y-axis*	*80 (stripped)**
19	*$[0_2,90_2]_{2S}$*	-	-	-	*y-axis*	*80 (stripped)**
20	$[0_2,90_2]_{2S}$	250	29.90	1.80	y-axis	80 (cap)
21	*$[0_2,90_2]_{2S}$*	-	-	-	*y-axis*	*80 (cap)**
22	$[0_2,90_2]_{2S}$	250	30.77	1.80	y-axis	80 (cap)

* The optical fibre is broken

6. 5. THERMOPLASTIC CFRP TEST-COUPONS

Carbon-pps semi-preg (Figure 6-13, right), Cetex® material from Tencate Advanced Composites, is used to manufacture the thermoplastic woven fabric CFRP laminates. The Cetex® PPS is a semi-crystalline thermoplastic composite offering outstanding toughness and excellent chemical and solvent resistance, and is qualified for commercial aviation for multiple structural applications [19].

6. 5. 1. Hot moulding press

Although it is possible to use an autoclave process, the woven-fabric laminates in this work are consolidated using a hot moulding press at the facilities of Tencate Advanced Composites, see Figure 6-22:

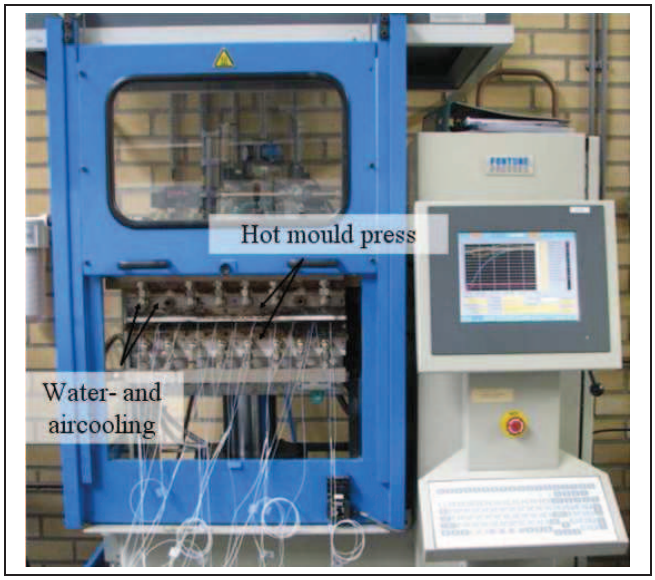

Figure 6-22: The hot mould press system of Tencate Advanced Composites, Nijverdal, the Netherlands.

The semi-preg layers as shown in Figure 6-13, right, have a thickness of approximately 0.32 mm. The stacking procedure is similar to the thermoset pre-preg lay-up. The plies are manually stacked, however, the carbon-PPS layers are not sticky like the soft pre-preg layers with epoxy resin. Therefore, to avoid the plies from shifting in the lay-up, they are spot welded using an ultrasonic gun to melt the PPS, see Figure 6-23:

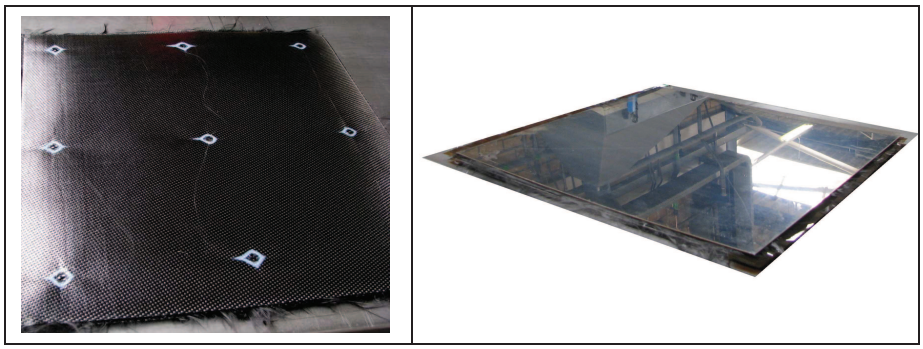

Figure 6-23: Stacked Cetex® layers, spot welded using an ultrasonic gun to melt the PPS local (left), laminate lay-up between two steel molds (right).

Two steel plates are treated with release agent and are used as moulds below and on top of the laminate lay-up (Figure Figure 6-23, right). The complete lay-up with moulds is then put in the hot mould press, as shown in Figure 6-22. To melt and consequently consolidate the carbon-pps laminate a temperature of 320°C and moulding pressure of approximately 10 bar is used. The manufacturing cycle of the Cetex® plates is shown in Figure 6-24:

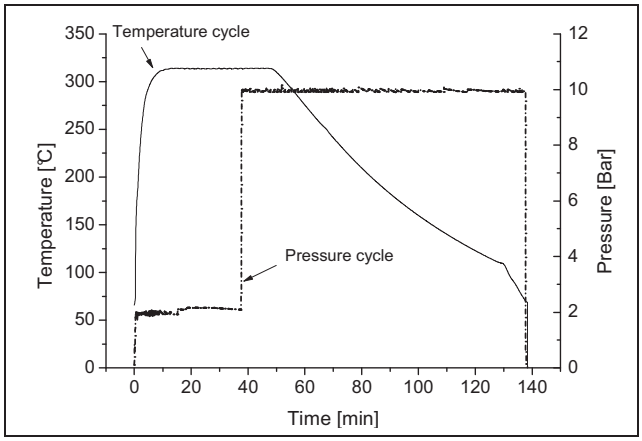

Figure 6-24: Hot moulding curing cycle to produce the Cetex® samples.

During the hot moulding press cycle, two plates can be placed and manufactured simultaneously. This procedure is used to simultaneously produce the in-phase and out-of-phase stacked laminate, used in this work.
The procedure is as follows. First, the moulds are closed and a small *pressure* of approximately *2 bar* is applied. The hot press is rapidly *heated,* and within approximately 10 minutes the moulds reach a maximum *temperature* of *320°C*. Next, the temperature is kept constant for 50 minutes so *melting and crystallization* of the PPS can take place. After 35 minutes a consolidating pressure of 10 bar is applied. Approximately 50 minutes later the moulds are cooled using circulating air. During cooling the thermoplastic PPS matrix partly arranges its polymer chains, which results in a partially crystalline and amorphous structure. The semi-crystalline PPS polymers show a significant shrinkage when solidifying. Therefore, to prevent

deformation of the laminate, the pressure is kept at 10 bars during the complete cooling phase. When a temperature of 130°C is reached, the air-cooled circuit is changed by water-cooling. Finally, at approximately 60°C the moulds are opened and the consolidated laminate is taken out of the hot moulding press.

6. 5. 2. Embedding optical fibre sensors during hot moulding

The procedure of embedding the optical fibres is slightly different compared to the method applied using the thermoset pre-preg layers. The procedure is illustrated in Figure 6-25. The lay-up is symmetric too. First the bottom half of the lay-up is prepared by stacking two times two semi-pregs. Kapton foil is used at the laminate edges, and the optical fibres are manually placed on the laminate. The semi-preg material is not sticky, such as the "soft" epoxy from the thermoset pre-preg material. To hold the optical fibres at their position during lay-up, local spot-welding of small PPS films is used, and the fibre ends are fixed with kapton tapes on the kapton foils at both sides of the laminate. For the test-plates shown in Figure 6-25, a small diameter PTFE tubing (900µm) is used at the fibre egress points. The top part of the lay-up, consisting again of two times two semi-pregs, is then symmetrically stacked on top of the first half of the lay-up now containing the optical fibres.

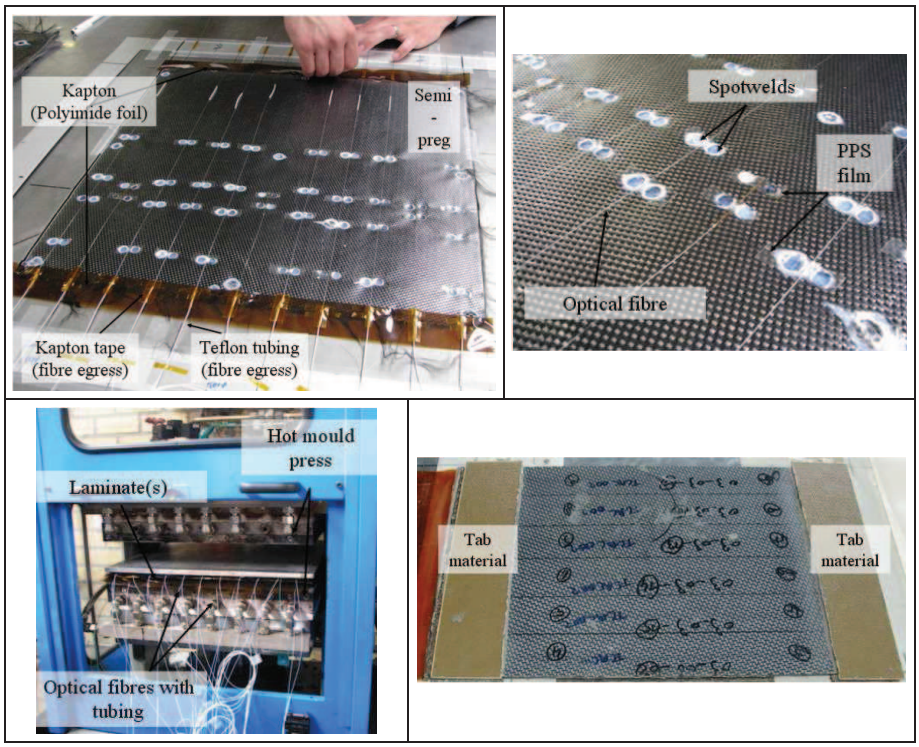

Figure 6-25 Procedure of embedding the optical fibres for the hot moulding process at the facilities of Ten Cate Advanced Composites.

As such the fibres are embedded in the mid-plane of the lay-up. Finally, the total lay-up is placed in the hot mould press to cure. After curing, the plate is prepared with end tabs and cut into test-coupons, using a water-cooled diamond saw. See

Table 6-6 (Section 6. 5. 4.) for more details regarding the prepared test-coupons and the embedded sensors. As mentioned in Section 6. 3. 2. two types of laminates with embedded optical fibres are prepared; one with the mid-plane semi-pregs stacked in-plane and one with the mid-plane semi-pregs stacked out-of-plane. An example of the cross-section of both laminates with an embedded optical fibre is shown in Figure 6-27:

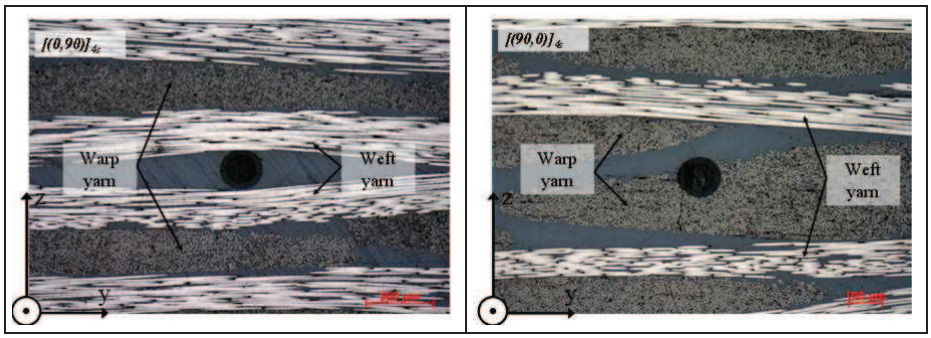

Figure 6-26: Optical fibre embedded in the mid-plane of a symmetrical stacked woven fabric laminate: in-phase stacking (left), and out-of-phase stacking (right).

6. 5. 3. Material properties of the thermoplastic CFRP woven fabric

The exact identification name of the carbon-PPS semi-preg Cetex® material is Carbon 5H CD0286/PPS. The mechanical properties, modulus and strength, were taken from documents of two independent instances: (i) from the mechanical data-sheet of the supplier Ten Cate Advanced Composite (TCAC) and (ii) from the Technical University of Delft (TUDelft), who determined the mechanical properties according to the "MIL 17 Guidelines for Characterization of Structural Materials" [29]. The Poisson's ratio is taken from the research of Ives de Baere [21]. In his research a tensile strength in the warp direction of 734 MPa is given. The elastic properties given in the last column are the simulated values taken from the work of Daggumati R. [30], who performed micro-scale 3D modelling of the woven fabric structure. Unless otherwise noted, the material properties given in Table 6-4 apply for a temperature of 23°C and a relative humidity of 50%.
The engineering constants which are used to perform the finite element modelling in Chapter 8, are given in Table 6-5 [30].

Table 6-4: Elastic and strength properties for the Carbon 5H CD0286 T300J 3K material, determined from experimental characterizations, compared with those of the manufacturer.

		TCAC [19]	TCAC 80°C dry [19]	TUDelft	[21]	[30]
Elastic constants	Tensile modulus Warp E_{11} [GPa]	56.0	57.0	56.00		56.5
	Tensile modulus Weft E_{22} [GPa]	54.0	53.0	57.00		56.5
	Transverse Modulus E_{33} [GPa]					10.5
	Compression modulus Warp [GPa]	51.0	51.0	52.00		
	Compression modulus Weft [GPa]	51.0	51.0	50.00		
	Shear modulus (in-plane) G_{12} [GPa]	4.0	2.7	4.2		4.3
	Shear modulus $G_{13} = G_{23}$ [GPa]					3.1
	Poisson's ratio ν_{12} [-]				0.033	0.08
	Poisson's ratio $\nu_{13} = \nu_{23}$ [-]					0.41
Strength properties	Tensile strength Warp X_T [MPa]	758	730	617	734	
	Tensile strength Weft Y_T [MPa]	755	646	754		
	Compression strength Warp X_C [MPa]	644	558	567		
	Compression strength Weft Y_C [MPa]	637	526	498		
	Shear Strength (in-plane) S_T [MPa]	119	108	110		

Table 6-5: Engineering constants (homogenized) for the Carbon 5H CD0286 T300J 3K woven fabric material

E_{11} [GPa]	E_{22} [GPa]	E_{33} [GPa]	G_{12} [GPa]	$G_{13} = G_{23}$ [GPa]	ν_{12} [-]	$\nu_{13} = \nu_{23}$ [-]
56.5	56.5	10.5	4.3	3.1	0.08	0.41

6. 5. 4. Additional non-woven thermoplastic CFRP plate

A number of complex strain effects act on the embedded FBGs when embedding them in woven-fabrics, see Section 6. 2. . To investigate the matrix shrinkage effects it is chosen to produce an additional non-woven carbon-PPS laminate. Because of a joint collaboration between the company TenCate Advanced Composites, FOS&S and Fokker Aerospace, the author has had the opportunity of

producing a carbon-PPS laminate using the autoclave curing system of Fokker Aerospace (Figure 6-27).

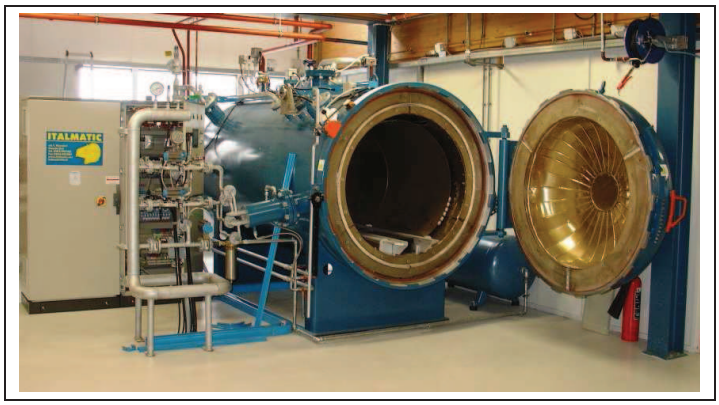

Figure 6-27: The autoclave system at Fokker Aerospace (courtesy of Fokker).

As such, a thermoplastic cross-ply laminate with embedded DTG®s is prepared and manufactured at the facilities of Fokker Aerospace. The laminate has a stacking sequence $[90,0]_{2S}$. It consists of eight UD carbon-PPS layers of approximately 0.1 mm thickness, cut from a spool of UD carbon-PPS tape (i.e. prepreg) obtained from Fokker Aerospace. The vacuum bagging preparation is similar to the thermoset CFRP laminates, but the maximum melting temperature used to produce the carbon-PPS laminate exceeds 310°C, which is much higher compared to the maximum temperature of 180°C for the carbon-epoxy laminates, hence, high temperature vacuum bagging materials are used.

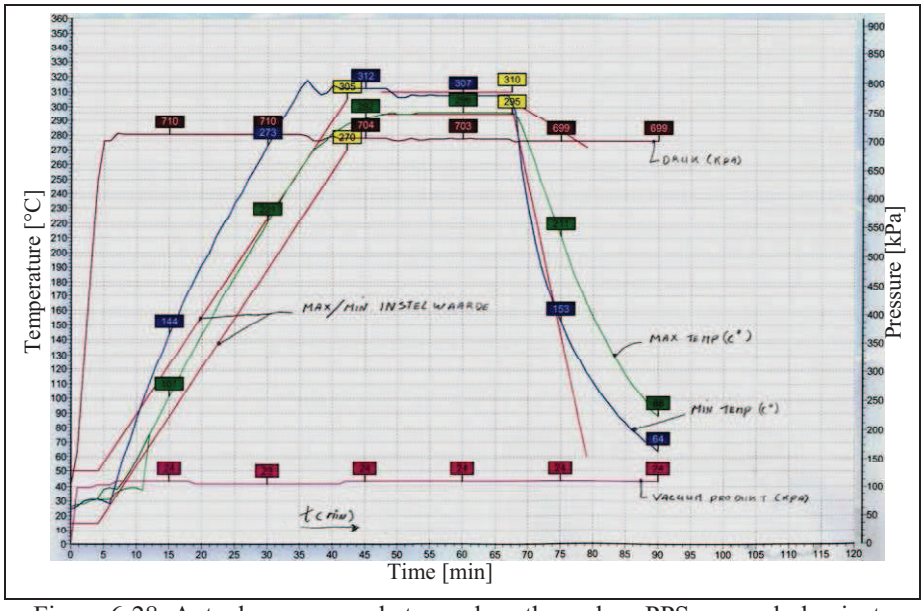

Figure 6-28: Autoclave cure cycle to produce the carbon-PPS cross-ply laminate [31].

The thermoplastic laminates were manufactured using the autoclave cure cycle as depicted in Figure 6-28. At the start of the cycle a vacuum pressure of -0.76 bar (24kPa) is applied and the pressure in the autoclave is put at approximately 7 bars (700kPa). When the pressure of 7 bar is reached, the temperature of the heat tool is raised up to 310°C, at a rate of approximately 7°C/min. A minimum and maximum temperature level is used to regulate the heater, and the temperature is measured using thermocouples at two locations: one in the autoclave (MIN), and one in the laminate near the heating tool (MAX.).
The embedding procedure of the optical fibres in the cross-ply lay-up, is similar to the woven fabrics (Figure 6-29). Again kapton foil and kapton tapes are used at the edges of the laminate (fibre egress points) and the fibres are fixed on the lamina using the spot welding method with small PPS films. Two 80 µm and two 125 µm DTG®s (from PR2008_01) with a length of 8mm and one 80 µm and 125 µm DTG® with a length of 4mm are embedded. All sensors are coated and have a total outer diameter of approximately 138 µm for the 80 µm sensors and 190 µm for the 125 µm DTG®s. The optical fibres are aligned along the 0 degree direction of the UD layers and are embedded in between the (0 degrees) mid-plies. An Aluminium plate with release agent is put on top of the lay-up to get a flat and smooth top surface of the laminate. Finally, the lay-up is finished using the standard vacuum bagging materials, i.e. peel-ply, bleader, vacuum bag and sealing tape, and is put in the autoclave to consolidate.

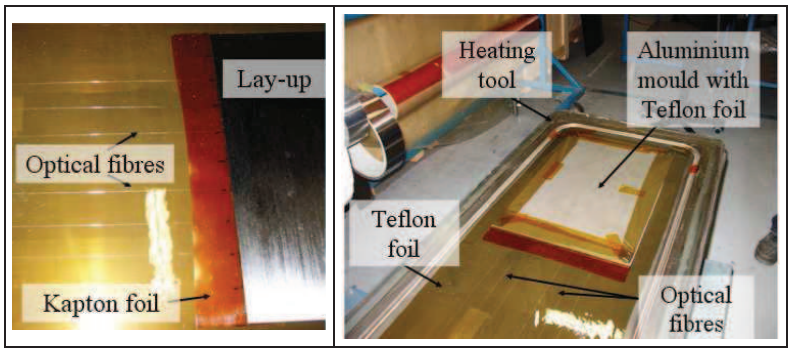

Figure 6-29: Preparation and fabrication of the carbon-PPS cross-ply with embedded optical fibres.

It is noted that no test-coupons are cut from this cross-ply laminate. The plate is solely used to study the transversal strain effects which occur during curing (i.e. shrinkage) of the PPS matrix. This is further elaborated in Section 6. 7. .

6. 5. 5. Inventory of all thermoplastic CFRP test-coupons

A complete inventory of all produced thermoplastic CFRP test-samples with embedded DTG®s, is given in Table 6-6. All samples consist of 8 semi-preg layers stacked according to the lay-up indicated in the first column.

Table 6-6: Inventory of all thermoplastic CFRP test-coupons with embedded sensors

	Lay-up	Length	Width	Thickness	Sensor alignment	Remark
n°		[mm]	[mm]	[mm]	Global	
1	$[(0,90)]_{4S}$	300	28.9	2.4	x-axis	80 (4mm)*
2	$[(0,90)]_{4S}$	300	30.1	2.4	x-axis	125 (4mm)
3	$[(0,90)]_{4S}$	300	30.1	2.4	x-axis	125 (4mm)
4	$[(0,90)]_{4S}$	300	30.9	2.4	x-axis	125*
5	$[(0,90)]_{4S}$	300	30.6	2.4	x-axis	125*
6	$[(0,90)]_{4S}$	300	26.2	2.4	x-axis	125
7	$[(0,90)]_{4S}$	300	26.3	2.4	x-axis	125
8	$[(0,90)]_{4S}$	300	30.1	2.4	x-axis	125*
9	$[(0,90)]_{4S}$	300	30.0	2.4	x-axis	125
10	$[(90,0)]_{4S}$	300	29.6	2.4	x-axis	125
11	$[(90,0)]_{4S}$	300	29.7	2.4	x-axis	125*
12	$[(90,0)]_{4S}$	300	28.8	2.4	x-axis	80*
13	$[(90,0)]_{4S}$	300	28.4	2.4	x-axis	80

The stacking $[(0,90)]_{4S}$ corresponds to the in-phase stacked mid-plane (i.e. standard stacking), and the $[(90,0)]_{4S}$ corresponds to out-of-phase stacked mid-plane. The 0°-direction (warp) is always aligned along the x-axis of the global coordinate system (Section 6. 3. 2.). The optical fibre is always embedded in the mid-plane (i.e. between the 4th and the 5th layer). The sensor alignment, with respect to the global coordinate system, is indicated in the second last column. In the last column extra remarks are implemented. If 80 or 125 is written, it refers to an 80 µm or a 125 µm embedded DTG® with coating which is embedded in the sample. The DTG®s are all from one of the first production runs (PR2007_2). The outer diameter of the coating is approximately 124 µm for the 80 µm DTG®s and 190 µm for the 125 µm DTGs

6. 6. MONITORING THE CURE CYCLE OF AUTOCLAVE PRODUCED THERMOSETS

Because the author uses uni-axial FBGs, it is not possible to tell the difference between the two transversal strain components and the axial strain component in the optical fibre. To estimate the different strain components a more straightforward method is applied using a dual FBG configuration with a normal embedded DTG® and an encapsulated DTG®. This method has already been briefly described in Chapter 5 and allows to disconnect the axial strain from the transversal strains. First

* Additionally surface mounted DTG®s were used

the transversal strain difference is estimated from the Bragg peak separation of the normal embedded DTG®s. To do that, the cure cycle of a carbon-epoxy cross-ply laminate is monitored using a stripped and coated embedded DTG®. During the cure cycle we then measure the "temperature independent" transversal strain difference (Equation 6-1) and additionally, the cure cycle of an identical CFRP coupon is monitored using an encapsulated DTG®. In this case, only axial strains and temperature effects are measured. The effects of axial strain during curing are isolated by using a temperature compensated method. Both the transversal and the longitudinal strain values determined in this section give a qualitative view on the residual strain formations in the composite laminate during curing (see the strain transfer step chapter 5).

6. 6. 1. Transversal residual stain determination

In analogy to response of the FBG shown in Figure 6-8 from Güemes and Menendez, the wavelength evolution of two embedded 125 µm DTG® (one stripped and one coated) is monitored during the autoclave curing cycle of a small cross-ply laminate (100 mm x 150 mm x 1.54 mm, stacking $[90_2,0_2]_2$). The sensors are aligned along the 0 degrees reinforcement layers (Table 6-3, Sample n°1 and n°3). The temperature during curing, is plotted in the same graph (Figure 6-30). An error occurred in the control parameters of the autoclave temperature cycle, which caused the laminate to pass two times through the cure cycle. This is, however, not detrimental to the purpose of the test, which is the monitoring of the curing cycle. The second cycle can in principle be seen as a kind of thermal treatment or post-curing of the laminate. We can see from the wavelength evolution, that the response of the stripped and coated DTG® is similar during the heating phase of the cure cycle. Both curves are in accordance with the temperature curve, however, during cooling, after approximately 10 hours in the cure cycle, we see a sudden drop in the curve of the stripped DTG®. At this stage the residual strains are high enough to influence the total shape of the Bragg peak. The birefringence, however, is not high enough for the FBG-interrogator (FBG-scan X08 from FOS&S [32]) to distinct the two peaks. At approximately 65°C, we can observe that the curve splits because the second peak is detected as well. However, the peak-splitting for the coated DTG® (for the same FBG peak picking settings) occurs a little later. Though, the transversal strain effect for the coated DTG® is not high enough to be detected by the FBG-scan. Herewith, the difference between the response of a coated and stripped DTG® with regard to the transversal strain effect, is already illustrated.

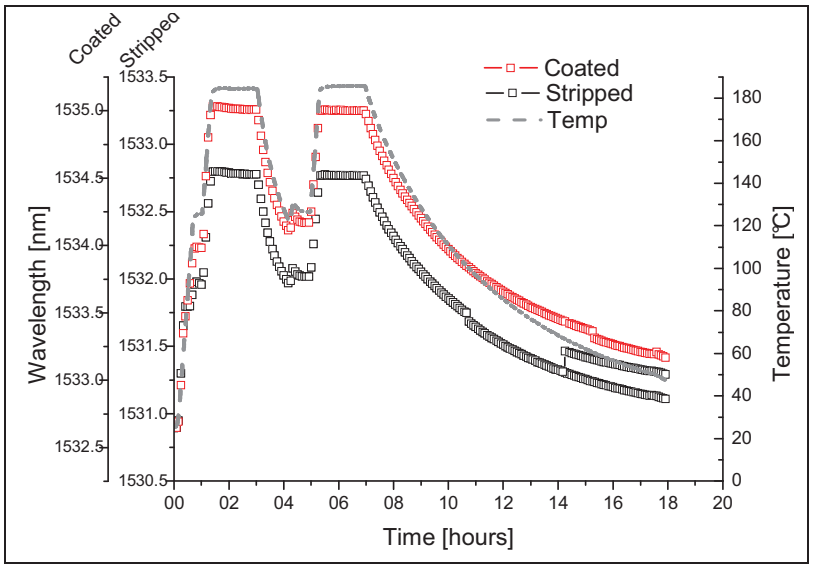

Figure 6-30: The wavelength evolution for a stripped and coated DTG®, during the curing cycle (autoclave) of a $[90_2,0_2]_{2S}$ CFRP laminate

The monitoring of the curing cycle was stopped at 50°. Afterwards, the spectra of both samples are recorded at room temperature and compared with the spectra recorded before vacuum was applied (Figure 6-31). We can clearly see that peak-splitting has occurred in both cases. If we examine more in detail, we observe that the separation of the peaks for the coated sensor is indeed smaller. Additionally we see a higher positive (total) peak shift for the coated DTG®, however, because of the former stated concluding remarks in Section 6. 2. 2. c. such as the fact that it is very difficult to define the reference wavelength (i.e. initial pre-strain of the fibre), no real conclusions can be drawn from this difference in spectral response

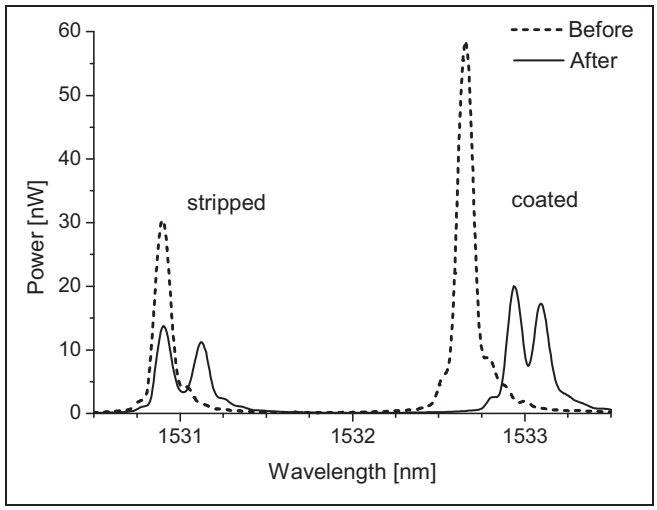

Figure 6-31: Spectra of the stripped and coated DTG® before and after curing.

In Table 6-7, left, the peak separation is determined from the wavelengths of each individual (small) peak. Using the optical properties of the 125 µm DTG®s, determined in Chapter 3 and Chapter 4, with $p_{11} = 0.112$, $p_{12} = 0.256$ and $\overline{n} = 1.4459$, and substituting the values of Table 6-7 in Equation 6-1, with $\lambda_{B,1'strip} = 1531.123\ nm$, $\lambda_{B,2'strip} = 1530.908\ nm$, $\lambda_{B,1'coat} = 1533.095\ nm$ and $\lambda_{B,2'coat} = 1532.943$ nm, the transversal strain difference in the core of both optical fibres is estimated, see Table 6-7, right. Note that the 1' -and 2'-polarization axis of the Bragg peaks are chosen according the convention defined in Chapter 4.4.2.b, with the 1'-polarization axis along the Slow-axis and the 2'-polarization axis along the Fast axis.

Table 6-7: Peak separation and transversal strain difference for the stripped and coated DTG® after manufacturing.

$\Delta\lambda_{stripped}$ [nm]	$\Delta\lambda_{coated}$ [nm]	$\Delta\varepsilon_{trans,\ stripped}$ [%]	$\Delta\varepsilon_{trans,\ coated}$ [%]
0.215	0.152	0.0933	0.0660

The calculated value of the stripped sensor is in accordance with the calculated residual strain difference of $\Delta\varepsilon_{trans} = 0.114\%$, determined from the results of Güemes and Menendez for a quasi-isotropic laminate. We clearly notice that the coating of the DTG® acts as a buffer for the transversal strains, hence the coated DTG® is less sensitive (approximately 30 %) to transversal (residual) strains during curing than the stripped DTG®.

6. 6. 2. Longitudinal residual strain determination

In order to estimate the longitudinal residual strains, we have monitored the cure cycle of an identical cross-ply laminate as before, but this time by using embedded 80 µm DTG®s which are encapsulated in a small glass capillary (length: 30 mm, ID:180 µm, OD:340 µm). The sensors are aligned along the 0 degrees reinforcement fibres (Table 6-3, sample n° 9 and 10). The surrounding capillary is fixed to the optical fibre before and after the sensor. During fixation, a small fibre pre-strain is applied, so the sensor is able to detect compression too. The capillary keeps the sensor free from transversal strain effects, hence, it will sense only longitudinal strains in the composite laminate. The evolution of the wavelength of the encapsulated DTG®s is shown in Figure 6-32. Unfortunately, the thermocouple which was attached to the laminate was not recorded during the cycle. Only the temperature readings of the second thermocouple used for the control loop were noted down, they are indicated in Figure 6-32. It is mentioned in the concluding remarks (Section 6. 2. 2. c.), that it is difficult to define the reference wavelength during curing to calculate the exact wavelength shift. According Mulle et al. and Sorensen the reference is taken at the point at which the laminate is cured, or solidified in case of a thermoplastic. At this point the thermal strains can start building up and the load transfer from composite to the optical fibre can happen. Indeed, from the evolution of the "normal" embedded DTG® (i.e. without capillary, Figure 6-30) we can clearly see that the residual transversal strain builds up during the cooling down phase of the cure cycle. It is believed that the longitudinal residual

strains occur as well from this point. In analogy to Mulle et al. we will assume the cured laminate at the maximum temperature (approximately 176°C, see Figure 6-32), as being the starting point of the measurement. The thermal contraction of the laminate in the longitudinal direction is estimated by calculating the axial strain measured in the encapsulated DTG®s.

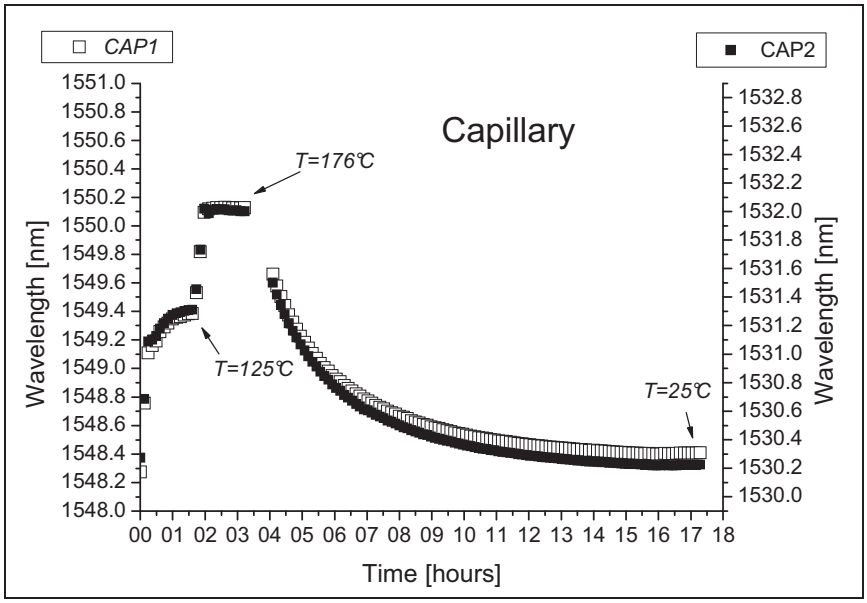

Figure 6-32: The wavelength evolution for two encapsulated DTG®s, during the curing cycle (autoclave) of a $[90_2,0_2]_{2S}$ CFRP laminate

However, due to the cross-sensitivity of an FBG to temperature and axial strain, we are obliged to compensate for intrinsic temperature effects. For this, the author uses the calibrated intrinsic temperature sensitivities (S_{T1} and S_{T2}), which are determined in Chapter 4.

6. 6. 2. a. Temperature compensation method for longitudinal strain

If we consider the case of an encapsulated DTG®, we can start from the simplified axial strain formulation for a non-embedded FBG (Chapter 4, Equation 4-12), given by:

$$\ln\frac{\lambda_B}{\lambda_{B,0}} = S_\varepsilon \Delta\varepsilon_{3'}, \qquad 6\text{-}2$$

with $\Delta\varepsilon_{3'}$ the axial strain in the optical fibre. In principle, if an FBG is embedded in a composite, there are two different contributions of the strain:

- The mechanical strain applied on the composite and fibre.
- The thermal expansion of the structure in which the fibre is embedded. This is referred to as the thermally induced strain or simply *the thermal strain*.

In this case, Equation 6-2 transforms into:

$$\ln\frac{\lambda_B}{\lambda_{B,0}} = S_\varepsilon\left[\Delta\varepsilon_{3'} + f(\Delta T,\Delta T_0)\right] + g\left(S_{T1},S_{T2},\Delta T,\Delta T_0\right), \qquad 6\text{-}3$$

where $f(\Delta T,\Delta T_0)$ is a function that describes the excess thermal strain of the laminate with regard to the thermal expansion of the optical fibre, and $g\left(S_{T1},S_{T2},\Delta T,\Delta T_0\right)$ is the intrinsic temperature dependency and thermal expansion of the optical fibre, with S_{T1}, S_{T2} the calibration coefficients determined in Chapter 4 (Equation 4-24), $\Delta T = T - T_{ref}$, the difference in temperature between the reference temperature during calibration (T_{ref}) and an arbitrary time during the measurement (T), and $\Delta T_0 = T_0 - T_{ref}$, the difference in temperature between the zero point of the measurement (T_0) and the reference temperature during calibration (T_{ref}, typically $T_{ref} = 22.5$ °C). In case the thermal expansion is purely linear and assuming 100 % strain transfer from laminate to the optical fibre in the longitudinal direction, the excess thermal strain which acts on an embedded optical fibre can be written as:

$$f\left(\alpha_s,\Delta T,\Delta T_0\right) = \left(\alpha_s - \alpha_f\right)(\Delta T - \Delta T_0), \qquad 6\text{-}4$$

with α_s the Coefficient of Thermal Expansion (CTE) of the laminate and α_f the CTE of the fibre, typically $0.55\cdot10^{-6}K^{-1}$. Note that, if the CTE of the optical fibre and composite laminate are equal, Equation 6-4 is equal to zero, and no extra thermal strain is induced in the fibre by the laminate. All contributing terms of Equation 6-3 are illustrated in Figure 6-33.

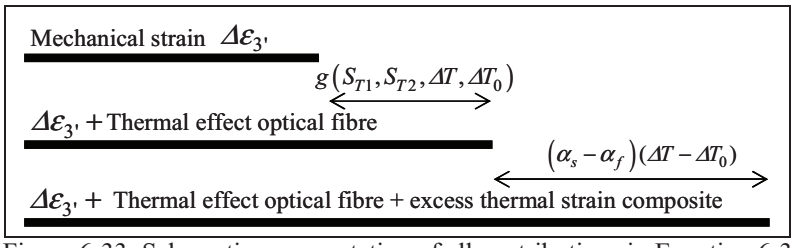

Figure 6-33: Schematic representation of all contributions in Equation 6-3

From the above, the mechanical strain on the laminate can be deduced. Provided that the temperature can be monitored, Equation 6-3 transforms into:

$$\Delta\varepsilon_{3'} = \frac{1}{S_\varepsilon}\left[\ln\frac{\lambda_B}{\lambda_{B,0}} - S_{T1}\left(\Delta T - \Delta T_0\right) - S_{T2}\left(\Delta T^2 - \Delta T_0^2\right)\right] - \left(\alpha_s - \alpha_f\right)(\Delta T - \Delta T_0) \qquad 6\text{-}5$$

Formula 6-5 is the generic formula for calculating the *temperature compensated mechanical (axial) strain* of an embedded DTG® (encapsulated), which is free of transversal stress effects.

When cooling down the cured laminate from maximum temperature to room temperature, no external mechanical strain is applied on the laminate and only thermal strains are acting on the DTG®, hence the term $\Delta\varepsilon_{3'}$ can be omitted. Equation 6-5 can then be written as:

$$\alpha_s(\Delta T-\Delta T_0)=\frac{1}{S_\varepsilon}\left[\ln\frac{\lambda_B}{\lambda_{B,0}}-S_{T1}\left(\Delta T-\Delta T_0\right)-S_{T2}\left(\Delta T^2-\Delta T_0^2\right)\right]+\alpha_f(\Delta T-\Delta T_0)\text{, 6-6}$$

with $\alpha_s(\Delta T-\Delta T_0)$ the thermal strain of the laminate measured in axial direction of the fibre. Equation 6-6 will then be used to calculate the (longitudinal) thermal induced strain from the measurements of the encapsulated DTG®, during the cooling down phase.

6. 6. 2. b. Calculation of the thermal strain during curing

By taking $T_0 = 176°C$ (reference point), $T = 25°C$ (Figure 6-32), and using the calibrated temperature coefficients for the 80 µm DTG® $S_{T1}=6.360\cdot10^{-6}$, $S_{T2}=7.592\cdot10^{-9}$ (Chapter 4, Table 4-10), $S_\varepsilon=0.777$ (Chapter 4, Table 4-13) and $\alpha_f=0.55\cdot10^{-6}$ and filling in all the parameters in Equation 6-6, the thermal strain measured in the core of the optical fibre during cooling down can then be found by filling in the respective Bragg wavelengths of each DTG®. All values are given in Table 6-8. We can see that both thermal strains are much smaller compared to the transversal strain difference given in Table 6-7, and they are both negative.

Table 6-8: Wavelengths at T_0=176°C and T=25°C and calculated thermal (longitudinal) strains for the two encapsulated DTG®

	λ_1 [nm]	$\alpha_s(\Delta T-\Delta T_0)_1$ [%]	λ_2 [nm]	$\alpha_s(\Delta T-\Delta T_0)_2$ [%]
$\lambda_{B,0}$	1550.127	-0.0053	1532.004	-0.0118
λ_B	1548.407		1530.226	

Even though the wavelength evolutions in Figure 6-32 are very similar, there exists a relative large difference in the results of both measurements. The thermal strain measured by the second DTG® is twice that of the first DTG®. Because the cooling down process has elapsed very slowly and both DTG®s are embedded in the same plate, we can assume that the temperature at the positions of both sensors is equal. As such the difference is not explained by the temperature compensation. It is believed that the difference is probably caused because of a small misalignment with the x-direction or z-direction (i.e. through-the-thickness) of the laminate. Because the capillaries are relative large in diameter (~340 µm) and length, the integration between the carbon reinforcement fibres is not optimal. If there is a small misalignment the residual strain acting on the capillary is not 100% longitudinal. As such the local strain development can be slightly different at the two locations.

From the measured thermal strains we can estimate the linear CTE of the composite at both positions. Using the thermal strains from Table 6-8, we find that $\alpha_{s,1} \approx 0.35 \cdot 10^{-6} K^{-1}$ and $\alpha_{s,2} \approx 0.78 \cdot 10^{-6} K^{-1}$. If, in our case, the in-plane CTE's for a UD carbon-epoxy ply are $\alpha_{11} = -0.55 \cdot 10^{-6} K^{-1}$ and $\alpha_{22} = 34.1 \cdot 10^{-6} K^{-1}$ [23, 25], we can calculate the CTE using the classical laminate theory (CLT) [33]. For a balanced and symmetrical cross-ply laminate a CTE of $\alpha_{xx} = \alpha_{yy} = 0.38 \cdot 10^{-6} K^{-1}$ is found. We can see that the measured CTE α_s, of the first encapsulated DTG®s is in good approximation with the theoretical obtained value. The CTE obtained from the second DTG® is twice as high, however, the value is still in the same order of magnitude. It is noted that, because the thermal strains are very small in this cross-ply laminate, the error on the measurements induced by inaccurate temperature readings can be high. If we assume for example a temperature difference of 1°C, the longitudinal strain calculated using Equation 6-6 varies with approximately 20 % and 10% in case of DTG®1 and DTG®2, respectively. This indicates that we have to be very careful when interpreting the measured longitudinal (temperature compensated) strains during curing.

6. 6. 2. c. Estimation of the transversal out-of-plane strain component

From the CLT we know that, for a balanced and symmetrical stacked flat cross-ply laminate, the CTE in the in-plane directions is macroscopically the same. Hence the thermal in-plane strains are identical [33] and thus, the in-plane measured thermal strain ($\alpha_s(\Delta T - \Delta T_0) = \varepsilon_{3',thermal}$), from the encapsulated DTG®s given above (Table 6-8), can be assumed the same as the in-plane transverse strain, i.e. $\varepsilon_{3',thermal} = \varepsilon_{1',thermal}$. Additionally, the transversal strain difference in the laminate is estimated from the transversal strain difference measured in the "normally" embedded optical fibre (Table 6-7), i.e. $\Delta\varepsilon_{trans} = \varepsilon_{1'} - \varepsilon_{2'}$, with $\varepsilon_{1'}$ the in-plane transverse strain component and $\varepsilon_{2'}$, the out-of-plane transverse strain component, with respect to the fibre coordinate system (Chapter 4). By using the measured transversal strain difference of Table 6-7 and the thermal (in-plane) strain of Table 6-8, we can estimate the through-the-thickness strain, $\varepsilon_{2'}$ of the optical fibre for a stripped and coated DTG®. The values are calculated using the strains of both encapsulated DTG®s. The estimated out-of-plane strains for the stripped and DTG®s are given in Table 6-9 together with the mean calculated value.

Table 6-9: Out-of-plane transversal strain $\varepsilon_{2'}$, for the stripped and coated DTG® after manufacturing using the strain of both encapsulated DTG®s.

	$\varepsilon_{2',strip}$ [%]	Mean Stripped [%]	$\varepsilon_{2',coat}$ [%]	Mean Coated [%]
CAP1	-0.0986	-0.1019	-0.0713	-0.0746
CAP2	-0.1051		-0.0778	

Obviously, the transversal out-of-plane strain is smaller in case of the coated sensor, however, both values are large compared to the in-plane strains calculated in Table 6-8, which signifies that in the case of a balanced and symmetric cross-ply laminate, the peak-splitting of the Bragg peak is caused mainly by the through-the-thickness residual (compressive) strain formation. This result shows that the transversal out-of-plane strain $\varepsilon_{2'}$ induced in the optical fibre is approximately a factor 10 to 20 times higher than the transversal in-plane strains $\varepsilon_{1'}$ and $\varepsilon_{3'}$. This illustrates that neglecting the through-the-thickness strains, as has been assumed by Mulle et al. [3-4] and Güemes and Menendez [5], would be in-correct, and can lead to wrong interpretations and faulty conclusion of the strain development in the optical fibre during curing. As indicated by Lorensen et al. [14] large errors occur when neglecting these effects and if one simply calculates with the formula for axial strain. Eventually to estimate this error, one could repeat the same procedure of the longitudinal strain calculation using Equation 6-6 with the measured wavelengths of the stripped and coated DTG® shown in Figure 6-30. However, because the temperature interval is not identical for both curing cycles, hence the thermal induced strain over both intervals in the laminates is not comparable. Moreover, because the peak-picking parameters in the measurements shown in Figure 6-30 are not optimal, these calculations are not performed, not to draw faulty conclusions.

6. 6. 2. d. Concluding remarks

By using a normal embedded uni-axial DTG® and an encapsulated DTG®, we have determined the transverse strain difference (independent on temperature), and the longitudinal thermal strain (temperature compensated) during curing, respectively. Some important (qualitative) information on the curing behaviour of the composite can be gathered from both methods. The measurements using encapsulated sensors are very useful to determine solely the in-plane thermal strains, however, because the in-plane strains in a cross-ply laminate are very small compared to the out-of plane strains, the accuracy of the measurements of these sensors is low and relative large errors occur when the alignment of the capillaries is not 100%. Care should be taken when interpreting the longitudinal measurements, certainly if we refer to the strain at maximal temperature. The temperature compensation on very small longitudinal strains can induce large errors in the measurements if the temperature at the location of the sensors is not accurately measured.

It is found that the embedded DTG® with coating, is less sensitive for transversal strain than the stripped DTG®, which is also reported in the research of Okabe et al. [11]. Based on the measurements in a thermoset cross-ply laminate, the coated sensor measures approximately 70 % of the transversal out-of-plane strains obtained for the stripped sensor.

The combined methods applied in this section are very interesting to give qualitative information on the complex effects which occur during composite manufacturing. In case of a cross-ply laminate the author has found that the out-of-plane strains are 10 to 20 times larger than the in-plane strains. This clearly illustrated that if one would neglect the (large) transversal out-of-plane strains induced in the FBG, the results will be completely different. Moreover, if one would simply calculate the longitudinal strains with the recorded wavelength shifts and neglecting any transversal effect no real conclusions can be drawn. Because composite laminates with different stacking sequence will exhibit different residual strains, interpretation

of the response of embedded FBGs should be done with care, not to draw faulty conclusions on the appearing effects in the laminates during curing.

6. 7. MONITORING THE THERMOPLASTIC CONSOLIDATION CYCLE DURING AUTOCLAVE AND HOT MOULDING

In analogy to the monitoring of the curing cycle of the thermoset carbon-epoxy laminate, the residual strain formation in thermoplastic carbon-PPS laminates is investigated by using several coated DTG® which were embedded in the mid-plane of each laminate. Both the carbon-PPS woven fabrics with the in-phase and out-of-phase stacked mid-plane plies (Section 6. 5. , stacking $[(0,90)]_{4S}$ and $[(90,0)]_{4S}$, respectively), were simultaneously monitored during the hot moulding consolidation cycle. As mentioned in Chapter 5, the Bragg spectrum of the embedded DTG®s in woven fabrics can become heavily distorted. Mainly the cause of such severe peak-splitting are the high strain gradients which are present inside woven fabric composites, i.e. non-uniform strain acting along the grating. Additionally, high (non-uniform) transverse strain components are acting on the grating which broadens the spectrum even more. Controlled polarization measurements are used to measure the average induced birefringence in the embedded sensors. As such, a mean value of the transverse residual strain difference of each sensor is estimated. For comparison, the transverse residual strain difference is measured in a carbon-PPS cross-ply laminate (stacking $[90,0]_{2S}$), as well.

6. 7. 1. Response of the embedded DTG® during consolidation of a woven-fabric

The $[(0,90)]_{4S}$ and $[(90,0)]_{4S}$ woven fabric laminates are similarly prepared, with the sensor configuration as shown in Figure 6-34, left.

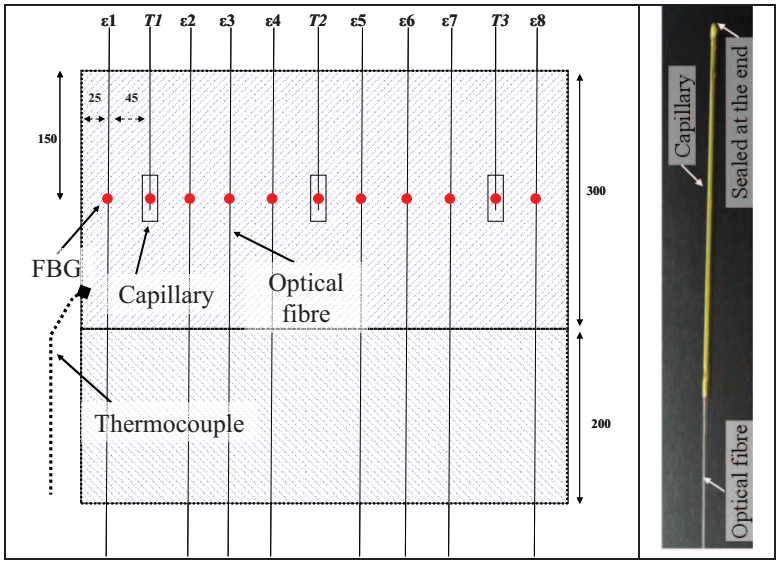

Figure 6-34: Configuration of the embedded sensors in the woven-fabric laminates, "ε1 – ε8" are strain sensing lines and "T1 – T3" are temperature FBGs in capillaries (left), example of a temperature FBG ending in a sealed glass capillary (right).

Each plate contains, three embedded (stripped) 125µm DTG®s with a surrounding capillary (strain free), to measure the temperature during consolidation (*T1, T2, T3*), and eight "normally" embedded 125 µm DTG®s to measure the strain (*ε1 – ε8*).
The purpose is to monitor the wavelength evolution of the temperature sensors (i.e. temperature) at several spots in the laminates, and to investigate the response of the spectra of several strain sensors during the hot press cycle.
The temperature sensors were prepared with a small surrounding capillary of approximately 40 mm long and ID: 252µm and OD:365µm with the fibre ending in the capillary, to keep the FBG free from being strained (Figure 6-34, bottom). Several sensors per plate are connected to a multi-channel optical switch and are sequentially monitored during the complete consolidation cycle. The peak wavelength of the temperature sensors, and the spectra of 8 out of 16 strain sensing lines (i.e. ε2, ε4, ε5 and ε7 for each plate) are recorded using a separate FBG-scan. All data is monitored on the same (absolute) time basis, so data is synchronized during post-calculations.

6. 7. 1. a. Temperature monitoring

The peak wavelengths of the embedded FBG temperature sensors are converted into temperature using the following equation (Appendix B, Equation B-35):

$$T = 22.5 + \frac{-S_{T1}}{2S_{T2}} + \sqrt{\left(\frac{S_{T1}}{2S_{T2}}\right)^2 + \frac{1}{S_{T2}} \ln \frac{\lambda_B}{\lambda_{B,ref}}}\,, \qquad 6\text{-}7$$

with $S_{T1} = 6.323 \cdot 10^{-6}$ and $S_{T2} = 7.605 \cdot 10^{-9}$ the temperature sensitivities for the 125 µm DTG® (from Chapter 4, Table 4-10) and $\lambda_{B,ref}$ the reference wavelength for each sensor at 22.5°C. The temperature values determined from the FBG sensors are compared with two thermocouples which were placed at the left side of each plate, closest to T1 (Figure 6-34, top). Before starting discussing the results, two remarks have to be made with respect to the temperature measurements: (i) 4 out of 6 temperature capillaries were damaged during closure of the hot press, (ii) the temperature readings at maximum temperature were not accurate because the experiment is performed using non-annealed DTG®. As seen in Chapter 4, the sensors show a negative drift at temperatures higher than 180°C. The maximum drift measured during annealing at temperatures higher than 300°C, was approximately -130 pm, which corresponds to a maximum temperature shift of approximately 13 °C.
In Figure 6-35, the temperature development during the production cycle is plotted. The cycle is identical to the temperature and pressure cycle discussed in Section 6. 5. 1. The maximum temperature (approximately 310°C), is reached after 10min (1) and kept constant for approximately 70 min (2). Then the cooling-phase starts and the mould of the press is air-cooled until approximately 100 °C (5) at which water-cooling starts. At approximately 60°C the mould is opened and the plates are taken out of the press, to further cool down until room temperature (6).

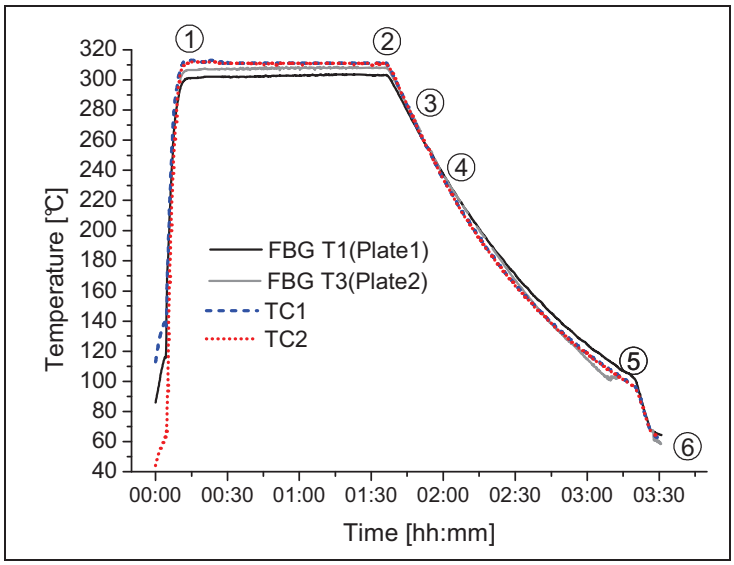

Figure 6-35: Temperature development of T1, plate1 and T3, plate2, compared to two thermocouples (TC1 and TC2)

We can see from Figure 6-35 that the shape of the temperature development of the FBGs measurements from plate 1 and plate2 (T1 and T3, respectively) is matching that of the two thermocouples (TC1 and TC2). Due to the annealing effect, which takes place rapidly at the higher temperature at the start of the cycle, the readings of the maximum temperature level of the FBGs do not reach the maximum temperature measured by the thermocouples. The drift, however, is stabilized at maximum temperature for both the FBGs, and the mismatch is approximately 5 – 10 °C between the time at (1) and (2). As seen from the development from (3) to (5), the slope and the FBG readings at lower temperatures are almost identical to the readings of the thermocouples. T1 ends up a little higher at the end of the cycle (5), which is expected if drift has occurred. T3, which is located at the right side of plate 2, shows a little drop just before time-stamp (5). It is unclear what has caused this sudden drop. However, it is believed that the total reflected power during the annealing effect has dropped as well. So, the FBG-scan could had problems to properly detect the Bragg peak. As shown in Chapter 4, Section 4.5.1., the reflectivity at temperatures above 300 °C can decrease until 10 % of the initial reflection. If the peak detection settings of the FBG-scan are not set optimal, they can cause interruptions during the measurement. On the whole, the readings are satisfying, and it is shown that FBGs are suitable to monitor the temperature during the press cycle. However, the fact that only 2 out of 6 capillaries have survived the hot press moulding, demonstrates that the design of the temperature FBG sensors is not robust for this “harsh environment”. Moreover, if real accurate temperature readings above 300°C are desired, the DTG®s should be annealed prior to the temperature monitoring.

6. 7. 1. b. Spectral response during consolidation

Additional to the temperature readings, the spectral behaviour of the embedded strain sensors (*ε1 – ε8*) has been followed-up during consolidation, see Figure 6-36. The same time-stamps (from (1) to (6)), as indicated on the temperature plot, are indicated in the development of the spectra. Two typical examples of the spectral response during consolidation are shown: (i) a DTG® embedded at the right edge (*ε8*) of the in-phase stacked laminate (Figure 6-36, top), and (ii) a DTG® embedded at the inner left side (*ε2)* of the out-of-phase stacked laminate (Figure 6-36, top).

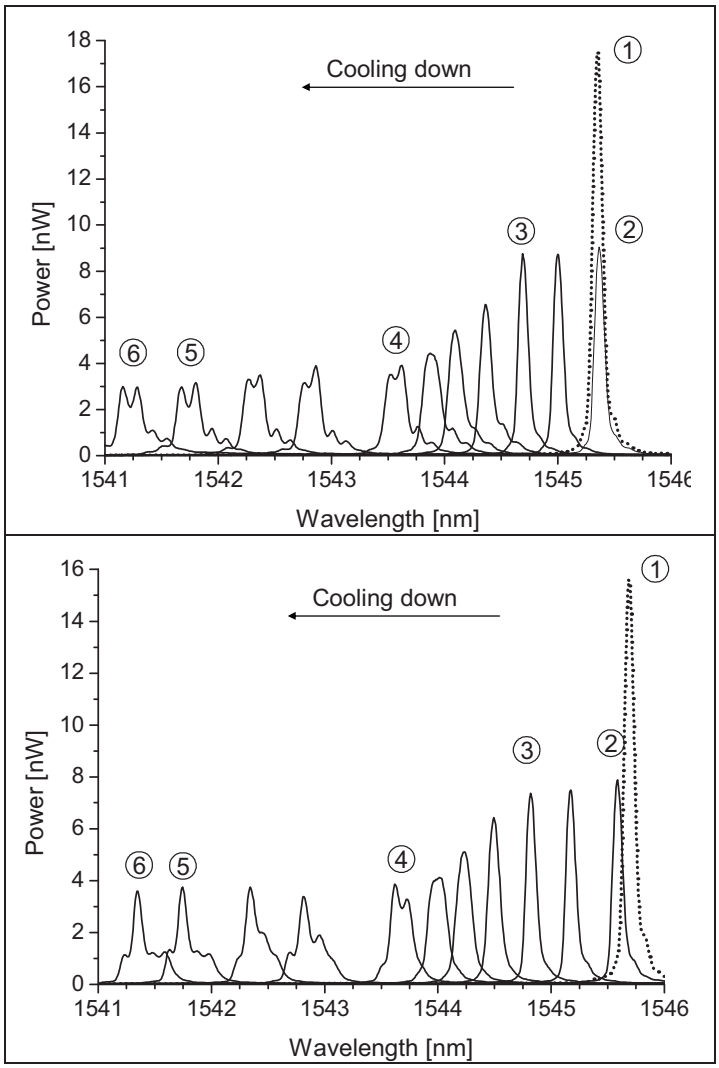

Figure 6-36: Spectral response of the DTG®s during consolidation, for a $[(0,90)]_{4S}$ 'in-phase' stacked (top) and $[(90,0)]_{4S}$ 'out-of-phase' stacked (bottom) laminate.

From step (1) to (2), we clearly see the annealing effect in a reflectivity drop of both DTG®s. The power after heating at approximately 310°C is more or less half of the

initial peak power, but it still has its original non-distorted shape. Then the cool-down phase starts at step (2), and we see that during the first fifteen minutes until (3) the peak keeps its shape and shifts towards the shorter wavelengths. During the time between (3) and (4), we notice in both cases that the peak-power drops because of peak broadening. During this phase the PPS matrix starts to shrink and (large) residual strains, which severely distort the spectra, are build up. Because the melting temperature of PPS is around 290°C [34], we can assume that the start of the distortion of the spectra is an indication of solidification of the matrix. Between the time at (4) and (5) the spectra further deform. We can see that the spectra at (5), i.e. at approximately 100°C, have already a similar shape as the final spectra at (6), which indicates that the matrix is completely solidified at (5). It is noted that during the whole period from (2) until (5) the pressure of the moulding press was approximately 10 bar, which states that the transversal load of the mould does not initiate any significant birefringence effects. Additionally, the spectral response is investigated during the heating phase, i.e. between (1) and (2), at the time the mould pressure changed. An example of a spectrum recorded at 2 bars and 10 bars is shown in Figure 6-37, indeed no significant change (or broadening) of the spectrum is observed. This effect is confirmed by polarization tests at a moulding pressure of 2 bars and 10 bars, which indicated no significant birefringence.

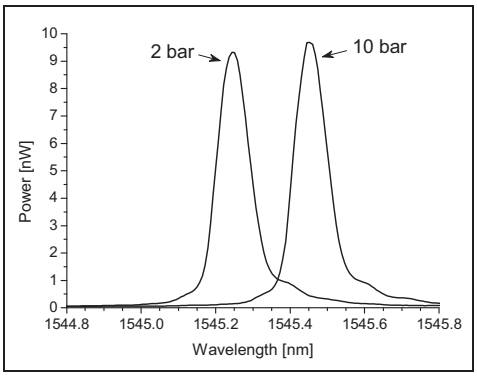

Figure 6-37: Example of the spectral response at 315°C at a mould pressure of 2 bars and 10 bars.

If we compare the spectral response of all the embedded DTG®s of the in-phase and out-of-phase stacked laminates, it is found that more severe distortion of the spectra is present in the DTG®s embedded in the in-phase stacked laminate. The examples shown in Figure 6-36 more or less confirm this behaviour. We see that the spectrum at (6) for the in-phase stacked laminate is split into two distinct peaks, and that the spectrum of the out-of-phase stacked laminate shows one main peak with a wide abdomen.

By simply looking at the depolarized spectra as shown in Figure 6-36, it is very difficult to distinguish both residual strain effects. To get more insight in the origin of the peak distortion, controlled polarization sweeps are performed. This topic is discussed in the next section.

6. 7. 2. Transversal residual strain in thermoplastic woven fabrics

In analogy to the thermoset cross-ply laminates, the birefringence of the embedded DTG®s is used to estimate the residual transversal strain difference in the woven fabrics. Due to the severe distortion of the spectrum, the author uses controlled polarization testing to better analyse the individual spectra with regard to the induced birefringence. The spectrum at each polarization angle is recorded, and the centroid wavelength is determined using the COG procedure, as described in Chapter 5 (Equation 5-1). An example of the development of the COG wavelength against the linear polarization angle for one DTG® of the in-phase stacked plate, is shown in Figure 6-38, left. We can clearly see the sinusoidal shape with a maximum wavelength at 40° (peak2) and a minimum wavelength at 130°. The corresponding minimum and maximum Bragg peaks are shown in Figure 6-38, right. From the difference in height between Peak1 and Peak2, we can conclude that a bigger part of the DTG® is polarized along the polarization axis of peak1. This illustrates that non-uniform strain fields are acting on the grating, which is understandable because the the DTG® is surrounded by a weave pattern. However, because we use uni-axial DTG®s, we can not distinguish along which mechanical axis Peak1 or Peak2 is polarized, neither at which part of the grating the highest strain is appearing.
The wavelength difference between the centroid wavelengths of both peaks is a measure for the mean birefringence effect which is present in the core of the DTG®. Note that, if we take the superposition of Peak1 and Peak2 we get the exact same shape as the (depolarized) peak shown in Figure 5-9, Section 5.4.1. Indeed, if we would take the mean of the centroid wavelength of Peak1 and Peak2, we get the centroid wavelength of the depolarized Bragg peak of Figure 5-9.

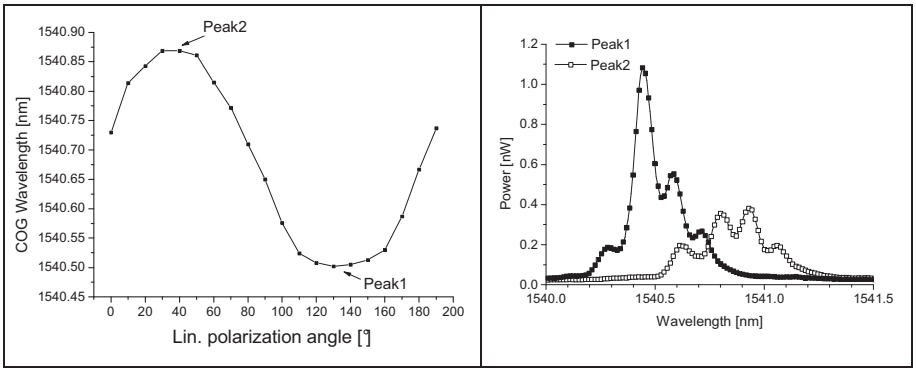

Figure 6-38: Development of the centroid wavelength against the linear polarization angle (Left), Polarized spectra according 1' and 2' axis (right)

Using Equation 6-1 with the optical properties of the 125 μm DTG®s, determined in Chapter 3, and with $p_{11} = 0.112$, $p_{12} = 0.256$ and $\overline{n} = 1.4459$, the transversal strain difference is calculated for all the embedded DTG®s (ε1 – ε8) of both plates. The results of the plates after fabrication at room temperature are shown in Figure 6-39. The residual strain difference in the $[(0,90)]_{4S}$ stacked woven fabric laminate shows a larger scatter. Values range from approximately 0.05% up to more than 0.15%. We can notice that the DTG®s embedded near the edge (i.e. ε1 and ε8) show higher values. If we compare the values of the $[(90,0)]_{4S}$ stacked laminates, we can see that they are much lower and the average of these values is below the minimum

residual strain difference measured in the $[(0,90)]_{4S}$ stacked laminate. This illustrates that even though macroscopically both laminates are identical, there clearly exists a difference between the local residual strain formation in the mid-plane of both plates. Note that, the transversal residual strain differences measured in the $[(0,90)]_{4S}$ stacked laminate (0.01 % - 0.06 %) are comparable to the value of the carbon-epoxy cross-ply laminate (i.e. 0.066%), measured with the coated DTG® (Table 6-7).

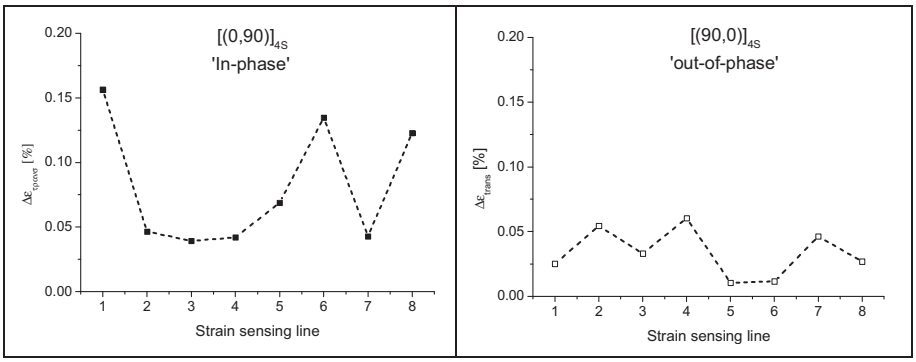

Figure 6-39: Transversal strain difference ($\Delta\varepsilon_{trans}$) of all channels ($\varepsilon1 - \varepsilon8$), for the $[(0,90)]_{4S}$ stacked (left) and $[(90,0)]_{4S}$ stacked (right) carbon-PPS woven fabrics.

6. 7. 3. Transversal residual strain in a thermoplastic cross-ply laminate

As mentioned in Section 6. 5. 4. an additional carbon-PPS cross-ply laminate (stacking $[90,0]_{2S}$) is manufactured using an autoclave consolidation cycle. In total three 80 µm DTG®s and three 125 µm DTG®s are embedded (Figure 6-40). No monitoring of the sensors during the consolidation cycle has been performed, though the spectral response of all channels after consolidation is examined. In contrary to the carbon-epoxy cross-ply laminate (Section 6. 6. 1.), non of the embedded DTG®s showed peaksplitting after embedding (Figure 6-41), which already indicates that the induced birefringence in the fibres during consolidation is small.

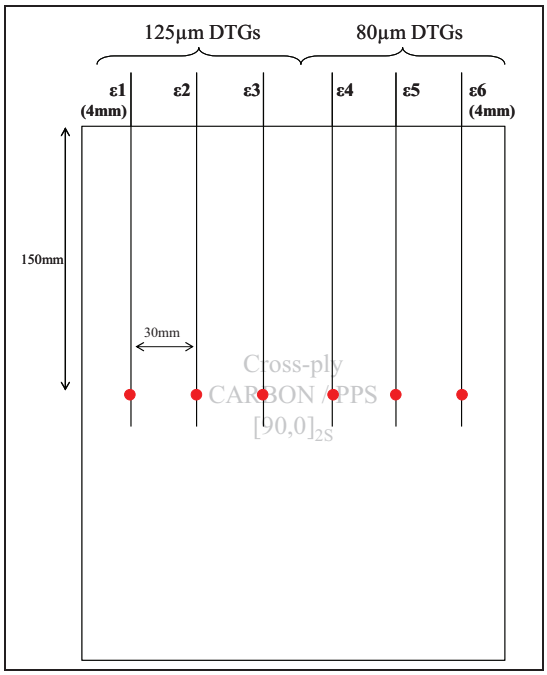

Figure 6-40: Configuration of the embedded sensors in the carbon-PPS cross-ply laminate, with "ε1 and ε6" the 4mm DTG®s and "ε2- ε5" the 8mm DTG®

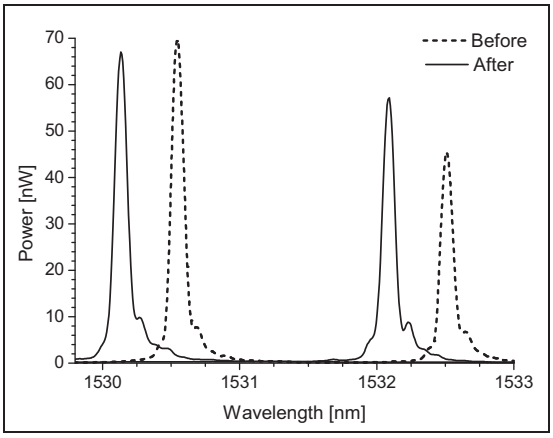

Figure 6-41: Spectra of line ε2 and ε3 before and after embedding (spectra after are measured using a more powerful light source)

Using the polarization controller to examine the birefringence, the residual strain difference of all channels is calculated using Equation 6-1. The resulting profile is shown in Figure 6-42. The y-axis is scaled identical with regard to the profiles of the woven fabric laminates (shown in Figure 6-39).

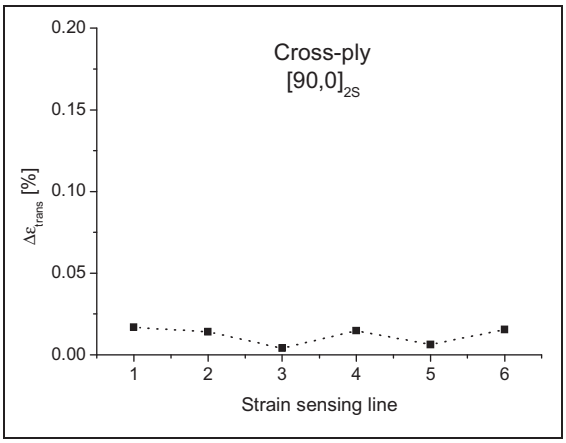

Figure 6-42: Profile of the residual strain difference in the carbon-PPS cross-ply laminate measured using 6 embedded coated DTG®

The measurements of the 80 µm and 125 µm DTG®s are identical. There is found no difference between the 4 mm and 8 mm DTG®s, which is expected for sensors embedded in UD layers. The residual transversal strain ranges from almost zero to approximately 0.017 % which is much lower than the residual strains measured in the carbon-epoxy cross-ply laminate and the carbon-PPS woven fabrics.

6. 7. 4. Concluding remarks

The values found for the carbon-PPS (thermoplastic) cross-ply are much lower compared to the residual strain difference of 0.066 %, found for the coated DTG® in the carbon-epoxy (thermoset) cross-ply laminate (Table 6-7). The origin of this difference is difficult to explain. However, the carbon-epoxy cross-ply laminate has a stacking sequence $[90_2,0_2]_{2S}$ with sixteen layers in total, which is approximately two times thicker than the carbon-PPS cross-ply laminate $[90,0]_{2S}$, with eight layers in total. Hence, it is believed that, the residual strains through the thickness are higher because of the thicker carbon-epoxy laminate. If we compare the profile of the transverse residual strain difference of the carbon-PPS cross-ply, shown in Figure 6-42, with the profiles of the carbon-PPS woven fabric laminates, shown in Figure 6-39, we see that in both the woven-fabric laminates the values of the transversal residual strain differences are higher. However, the values found for the thin cross-ply laminate are close to the values measured in the 'out-of-phase' stacked woven fabric. The carbon-PPS cross-ply laminate $[90,0]_{2S}$ and the carbon-PPS $[(90,0)]_{4S}$ 'out-of-phase' stacked laminate have a similar stacking sequence. It is noted that, in the case of the 'out-of-phase' stacked laminate, the mid-plane warp yarns in the semi-preg below and on top of the optical fibre are turned towards the optical fibre. Therefore, it is believed that the environs for the embedded optical fibres in the cross-ply and out-of-phase stacking is comparable. This indicates that the optical fibres are mainly influenced by the local residual strain field in the adjacent layers of the mid-plane. If the complete residual strain profile needs to be measured, more sensors are necessary through the thickness of the laminate.

6. 8. CONCLUSIONS

The manufacturing of thermoset and thermoplastic CFRP laminates and test-coupons is discussed. The autoclave and the hot moulding press to manufacture the CFRP laminates is discussed and the author has elaborated the embedding procedures of the DTG®s. The formation and measurements of residual strains in composite laminates is discussed in detail. The focus is on embedded FBGs and their response during the composite curing and consolidation process. The relevant methods and results of other researchers are quoted and compared with own results. Different approaches are possible to obtain information of the response of embedded FBGs. One can measure the temperature inside a composite by keeping the FBG free from strains and encapsulating it. From the induced birefringence in normally embedded DTG® the residual transverse strain differences can be measured independent from temperature. By encapsulating a sensor and keeping it free from transverse strains, it is possible to measure the purely (temperature compensated) longitudinal strains. An attempt is made to disconnect the transversal strains from the longitudinal strain in thermoset cross-ply laminates and the CTE of the composite is determined. It is shown that the through-the-thickness strain is the largest component in cross-ply laminates and that this strain is the main cause of peaksplitting in the FBG spectra. The coated DTG® shows less peak separation after composite manufacturing and is found less sensitive to transverse strain than the stripped DTG®. The method of polarization testing has been applied to decode the birefringence in severe distorted spectra and to calculate transversal strain differences in the thermoplastic woven-fabrics. The transversal strains are found highest in the thermoset cross-ply laminates and lowest in the thermoplastic laminates. The mid-plane strain of an 'in-phase' and 'out-of-phase' stacked woven-fabric are compared. It is found that the transverse strain difference is highest in the standard 'in-phase' stacking ($[(0,90)]_{4S}$, where the fibre is squeezed between the weft yarns of the adjacent semi-pregs instead of in between the warp yarns in case of the 'out-of-phase' stacking ($[(90,0)]_{4S}$).

In this chapter it is shown that the embedded DTG®s are suitable to provide valuable information on the strain development during composite manufacturing, however, we have only been looking at the strain in the optical fibre. Because there exists a difference in material properties between the embedded sensor and the composite material, the strain inside the optical fibre is not necessarily equal to the strain present in the composite. As such we have to define a strain transfer method which relates the strains in both materials. A method to do that will be elaborated in the next chapter. Then we will use embedded DTG®s to measure the composite strains in thermoset CFRP during different kinds of loading conditions. In the final chapter embedded DTG®s in thermoplastic woven-fabric test-coupons are subjected tension testing and to high strain levels to measure long term deformation.

6. 9. REFERENCES

1. Schnars, U. and Henrich, R.; Available from: http://www.ndt.net/article/cdcm2006/papers/schnars.pdf.
2. Parlevliet, P.P., Bersee, H.E.N., and Beukers, A., *Residual stresses in thermoplastic composites - A study of the literature - Part I: Formation of*

residual stresses. Composites Part a-Applied Science and Manufacturing, 2006. **37**(11): p. 1847-1857.

3. Mulle, M., Collombet, F., Olivier, P., and Grunevald, Y.H., *Assessment of cure residual strains through the thickness of carbon-epoxy laminates using FBGs, Part I: Elementary specimen.* Composites Part a-Applied Science and Manufacturing, 2009. **40**(1): p. 94-104.
4. Mulle, M., Collombet, F., Olivier, P., Zitoune, R., Huchette, C., Laurin, F., and Grunevald, Y.H., *Assessment of cure-residual strains through the thickness of carbon-epoxy laminates using FBGs Part II: Technological specimen.* Composites Part a-Applied Science and Manufacturing, 2009. **40**(10): p. 1534-1544.
5. Guemes, J.A. and Menendez, J.M., *Response of Bragg grating fiber-optic sensors when embedded in composite laminates.* Composites Science and Technology, 2002. **62**(7-8): p. 959-966.
6. Sorensen, L., Gmur, T., and Botsis, J. *Residual strain development in an AS4/PPS thermoplastic composite measured using fibre Bragg grating sensors*. in *2nd International Conference on Composites Testing and Model Identification (CompTest 200)*. 2004. Bristol, ENGLAND.
7. Chehura, E., Skordos, A.A., Ye, C.C., James, S.W., Partridge, I.K., and Tatam, R.P., *Strain development in curing epoxy resin and glass fibre/epoxy composites monitored by fibre Bragg grating sensors in birefringent optical fibre.* Smart Materials & Structures, 2005. **14**(2): p. 354-362.
8. Luyckx, G., *Multi-Axial Strain Monitoring of Fibre Reinforced Thermosetting Plastics Using Embedded Highly Birefringent Optical Fibre Bragg Sensors*, in *Materials science and engineering*. 2009-2010, PhD dissertation at Ghent University: Ghent.
9. Lee, Y.W., Yoon, Y., and Lee, B., *A simple fiber-optic current sensor using a long-period fiber grating inscribed on a polarization-maintaining fiber as a sensor demodulator.* Sensors and Actuators a-Physical, 2004. **112**(2-3): p. 308-312.
10. Bosia, F., Giaccari, P., Botsis, J., Facchini, M., Limberger, H.G., and Salathe, R.P., *Characterization of the response of fibre Bragg grating sensors subjected to a two-dimensional strain field.* Smart Materials & Structures, 2003. **12**(6): p. 925-934.
11. Okabe, Y., Tanaka, N., and Takeda, N., *Effect of fiber coating on crack detection in carbon fiber reinforced plastic composites using fiber Bragg grating sensors.* Smart Materials & Structures, 2002. **11**(6): p. 892-898.
12. Yamada, M. and Sakuda, K., *Analysis of almost-periodic distributed feedback slab wave-guides via a fundamental matrix approach.* Applied optics, 1987. **26**(16): p. 3474-3478.
13. Chehura, E., Ye, C.C., Staines, S.E., James, S.W., and Tatam, R.P., *Characterization of the response of fibre Bragg gratings fabricated in stress and geometrically induced high birefringence fibres to temperature and transverse load.* Smart Materials & Structures, 2004. **13**(4): p. 888-895.
14. Sorensen, L., Gmur, T., and Botsis, J., *Residual strain development in an AS4/PPS thermoplastic composite measured using fibre Bragg grating*

sensors. Composites Part a-Applied Science and Manufacturing, 2006. **37**(2): p. 270-281.
15. Lawrence, C.M., Nelson, D.V., Udd, E., and Bennett, T., *A fiber optic sensor for transverse strain measurement.* Experimental Mechanics, 1999. **39**(3): p. 202-209.
16. Luyckx, G., De Waele, W., Degrieck, J., Van Paepegem, W., Vlekken, J., Vandamme, S., and Chah, K., *Three-dimensional strain and temperature monitoring of composite laminates.* Insight, 2007. **49**(1): p. 10-16.
17. Luyckx, G. and et al., *Multi-axial strain transfer from laminated CFRP composites to embedded Bragg sensor: I. Parametric study.* Smart Materials and Structures. **19**(10): p. 105017.
18. Voet, E. and et al., *Multi-axial strain transfer from laminated CFRP composites to embedded Bragg sensor: II. Experimental validation.* Smart Materials and Structures. **19**(10): p. 105018.
19. Ten Cate. Available from: http://www.tencate.com/smartsite.dws?id=9483.
20. Plymouth_University. Available from: http://www.tech.plym.ac.uk/sme/MATS324/MATS324C2%20fabrics.htm.
21. De Baere, I., *Experimental and Numerical Study of Different Setups for Conducting and Monitoring Fatigue Experiments of Fibre-Reinforced Thermoplastics*, in *Materials science and engineering*. 2008, PhD dissertation at Ghent University: Ghent.
22. Hexcel. 2007; Available from: http://www.hexcel.com/.
23. Toray. Available from: http://www.toraycfa.com/pdfs/M55JDataSheet.pdf.
24. Tavernier, B. and Verbeke, T., *Health Monitoring of Carbon-Epoxy Laminates Used in Space Applications by Means of Embedded Optical Fibres*, in *Faculty of Engineering*. 2005-2006: Gent.
25. Hexcel. Available from: http://www.hexcel.com/NR/rdonlyres/7E68292D-4EDE-4CA7-A73D-AFA4C8CE0248/0/HexPly_M18_eu.pdf.
26. ASTM, *D3039: Standard Test Method for Tensile Properties of Polymer Matrix Composite Materials*. 2002: USA.
27. Lammens, N., *Advanced strain sensing in carbon fibre reinforced thermoset laminates, using normal and specialty Bragg sensors*, in *Faculty of Engineering*. 2009-2010: Gent.
28. Jose, S., Kumar, R.R., Jana, M.K., and Rao, G.V., *Intralaminar fracture toughness of a cross-ply laminate and its constituent sub-laminates.* Composites Science and Technology, 2001. **61**(8): p. 1115-1122.
29. Department of defense USA, *Composite Materials Handbook, Volume 1: Polymer Matrix Composites: Guidelines for Characterization of Structural Materials*. 2002.
30. Daggumati, S., Voet, E., Van Paepegem, W., Degrieck, J., Xu, J., and Lomov, S.V., *Local strain in a 5-harness satin weave composite under static tension: part II - Meso-FE analysis.* Composite Science and Technology, 2010(Under review).
31. Fokker, *personal communications*.
32. FOS&S. Available from: http://www.Fos-s.com.
33. Herakovitch, C.T., *Mechanics of fibrous composites*. 1998, New York: John Wiley and Sons inc.
34. Dai, K.H. and Scobbo, J.J., *The effect of curing on the crystallization of poly(phenylene sulfide).* Polymer Bulletin, 1996. **36**(4): p. 489-493.

Chapter 7 MECHANICAL TESTING OF THERMOSET CFRPS

7. 1. INTRODUCTION

This chapter focuses on the usage of the newly developed 80 µm DTG®s to measure multi-axial strains in thermoset CFRP cross-ply laminates. The strain relationship of an integrated sensor and the host material is simple when the elastic properties of both materials are the same. However, in reality, a difference in properties (e.g. Young's Modulus, Poisson's ratio) exists between the host material and the embedded sensor, hence, a different strain state in both materials exists. With regard to measuring strains of composite materials using an embedded fibre Bragg grating, we need to define the exact strain transfer from the composite laminate to the embedded sensor.

In the work of Luyckx G. [1-2], a general structural health monitoring scheme, which gives a clear view on the different steps necessary to relate the embedded sensor response to the far field strain in a structure, is defined. The three necessary steps are, i.e. (i) sensor calibration, (ii) strain transfer and (iii) multiple sensing points. In analogy to the work of Luyckx, only the first two steps are considered in this work, see Figure 7-1.

The flow chart illustrates the general relationship between the response of the embedded sensor and the strains in a (loaded) composite laminate.

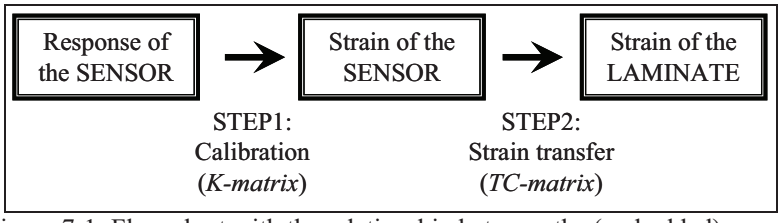

Figure 7-1: Flow chart with the relationship between the (embedded) sensor response and the strain present in the composite laminate.

The response of the FBG sensor to multi-axial strain (Step1) is elaborated in Section 7. 2. . A matrix formalism is developed which relates the sensor response of a specific FBG-configuration with the strains in the core of the optical fibre by using the fibre's intrinsic strain-optic coefficients. This matrix formalism is also referred to as the *K-matrix*. In the *strain transfer step* (Step 2), a relation has to be found between the measured strain in the optical fibre and the one in the composite material. This step will be elaborated in Section 7. 3. . The mechanism of the strain transfer from host material to sensor will be analysed in detail using finite element simulations.

Both procedures (Step 1 and Step 2) have been presented in detail in [2-3], and is validated experimentally for one loading condition, i.e. out-of-plane loading. In this work the author will go a step further; the strain transfer matrix is experimentally validated by loading CFRP laminates with embedded DTG®s along three independent loading directions and both non-coated and coated 80 µm DTG®s are tested. In the continuation of Luyckx' research [1], a parametrical study is

performed by varying the coating material properties, to investigate the interaction of a coated optical fibre with the composite laminate. It will be shown that for the coated DTG® the strain field disturbance in the host material is completely different, but not definite negative for the structural integrity of the composite. The response of the embedded coated DTG® is validated for a transverse out-of-plane loading condition, for a number of varied TC-matrices. It will be shown that the response is optimal for a specific combination of coating material properties, and that it is feasible to use both the stripped and coated embedded DTG®s to measure (multi-axial) composite strains.

7. 2. MULTI-AXIAL STRAIN SENSING USING BRAGG GRATINGS

To relate the response of an FBG with a multi-axial strain field present in the core of the optical fibre, we have to define multi-axial gauge parameters, or a *K*-matrix using the strain-optic coefficients which are calibrated in Chapter 4 (Section 4.4.2).
In this section, first, the sensor response of an FBG to multi-axial strain is discussed and a method is shown how to isolate the FBG from transverse stress components. Secondly, with this knowledge, the K-matrix is derived for a specific embedded sensor configuration using two FBGs; one 'normally' embedded in a composite laminate and one embedded but surrounded with a capillary. The term 'normally' stands for a non-encapsulated sensor.

7. 2. 1. The sensor response

When a differential transverse strain ($d\varepsilon_{1'} \neq d\varepsilon_{2'}$) is applied on a uni-axial FBG, birefringence is induced in the core of the optical fibre and as a result, two orthogonal polarization axes will exist. As already shown in Chapter 4, during transverse strain calibrations, if the birefringence effect in the core of the optical fibre is high enough, the Bragg peak splits into two distinct Bragg peaks. Each Bragg peak wavelength (corresponding to the 1'- and 2'-axis, Figure 7-2) is dependent on the total strain field present in the core of the optical fibre sensor.

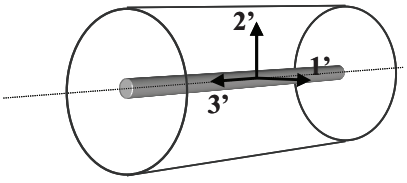

Figure 7-2: The used coordinate system of the optical fibre.

For small variations of the Bragg peak wavelengths (typically in the nm-range which is small compared to an optical Bragg peak wavelength of 1550 nm) we can consider $d\lambda = \Delta\lambda$ and $d\varepsilon = \Delta\varepsilon$.

Under the assumption of an isothermal condition ($\Delta T = 0$), the wavelength shifts corresponding to the 1'- and 2'-axis can then be written as (Appendix B, Equation B-15):

$$\begin{cases} \dfrac{\Delta\lambda_{B,1'}}{\lambda_{B,1'}} = \Delta\varepsilon_{3'} - \dfrac{1}{2}\bar{n}_{1'}^2\left(p_{11}\Delta\varepsilon_{1'} + p_{12}\left(\Delta\varepsilon_{2'} + \Delta\varepsilon_{3'}\right)\right) \\ \dfrac{\Delta\lambda_{B,2'}}{\lambda_{B,2'}} = \Delta\varepsilon_{3'} - \dfrac{1}{2}\bar{n}_{2'}^2\left(p_{11}\Delta\varepsilon_{2'} + p_{12}\left(\Delta\varepsilon_{1'} + \Delta\varepsilon_{3'}\right)\right) \end{cases} \quad 7\text{-}1$$

where $\Delta\varepsilon_{1'}$, $\Delta\varepsilon_{2'}$, $\Delta\varepsilon_{3'}$ are the strain perturbations along the axes of the fibre's coordinate system (Figure 7-2). The $'$ is used to avoid confusion with the coordinate system corresponding to a single layer of a composite laminate. The relation between the coordinate axes of the optical fibre and the single composite ply will be further elaborated The strain components $\Delta\varepsilon_{4'}$, $\Delta\varepsilon_{5'}$, $\Delta\varepsilon_{6'}$ are usually neglected in terms of the sensor response [4-5]. Further in Equation 7-1, $\Delta\lambda_B$ is the Bragg peak wavelength shift, λ_B is the initial mean Bragg peak wavelength, and p_{11} and p_{12} are the strain-optic coefficients (as already defined in Chapter 4). It is clear from Equation 7-1 that axial elongation ($\Delta\varepsilon_{3'} > 0$, $\Delta\varepsilon_{1'} = \Delta\varepsilon_{2'} = -\nu_f\Delta\varepsilon_{3'}$) or uniform compression ($\Delta\varepsilon_{1'} = \Delta\varepsilon_{2'} < 0$) will cause the Bragg peak(s) to shift to higher or lower wavelengths, respectively. However, due to a different change of the strain field in the core of the optical fibre (i.e. $\Delta\varepsilon_{1'} \neq \Delta\varepsilon_{2'}$), the refractive index change will differ along the optical eigenaxes (*1'* and *2'*), hence the wavelength shifts along the *1'* and 2'-axes will differ and the Bragg peaks can separate further or they can unite again if the differentiated strain-field is removed.
This birefringence effect occurs, for example, when embedding a uni-axial FBG in a cross-ply laminate because of the appearance of large residual strains after manufacturing. In Chapter 6, it is, for instance, shown that during the composite curing cycle, the Bragg peak of a stripped and a coated 125 µm DTG® splits into two well-separated Bragg peaks, one for each propagation mode, i.e. along the fast – and the slow-axis (Figure 7-4, left). This enables us to record both wavelength shifts in a simple manner and to use Equation 7-1 without the need of a HiBi FBG. Remark that the indication 1' and 2' does not represent the 'first' peak and 'second' peak of the Bragg spectrum. In this work the author uses a fixed coordinate system for the optical fibre (Figure 7-2), which will be related further in Section 7. 2. 3. to the local coordinate system of the composite laminate. The relation between the optical polarization axes (i.e. fast and slow) and the 'mechanical' coordinate system will then be fixed when defining this relation, see Equation 7-14 (page 238).

Further, an embedded FBG can be shielded from transverse stress by integrating it in a capillary and close/fix both ends (Figure 7-3), enabling to establish a situation of pure axial stress, in analogy to a non-embedded FBG.

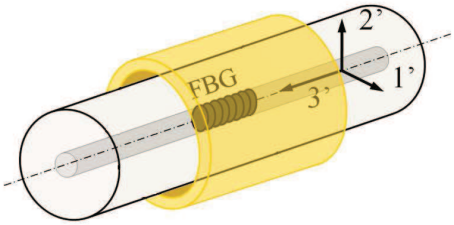

Figure 7-3: Representation of an FBG integrated in a capillary, shielded from transverse stress [3].

In this case the transverse strain components are directly related to the axial strain component via the Poisson's coefficient of the optical fibre ($\Delta\varepsilon_{1'} = \Delta\varepsilon_{2'} = -\nu_f \Delta\varepsilon_{3'}$). By substituting this relation in Equation 7-1, the equation simplifies and wavelength shifts in function of the axial strain are given by Equation 7-2:

$$\frac{\Delta\lambda_{B,1'}}{\lambda_{B,1'}} = \frac{\Delta\lambda_{B,2'}}{\lambda_{B,2'}} = \left((1 - \frac{1}{2}\bar{n}^2 p_{12}) + \frac{1}{2}\bar{n}^2 \upsilon_f (p_{11} + p_{12}) \right) \Delta\varepsilon_{3'} \qquad 7\text{-}2$$

Note that Equation 7-2 is the general formula often applied in literature to calculate axial strain from the measured wavelength. As mentioned in Chapter 4 for the axial strain calibrations, where the logarithmic approach is elaborated, errors on the strain calculation larger than 0.5 % occur if this equation is used at strain levels above 1.25 %. However, if the applied strain is kept below 0.5 %, the error on the strain calculation using Equation 7-2 is kept below 0.2 %. Because the applied strain in most of the experiments performed on the thermoset CFPR laminates is below 0.1 % the error on the strain caluclation is neglectable and the usage of Equation 7-2 is accurate enough.
Before sealing the capillary, the optical fibre is pre-strained inside the capillary (Figure 7-4, right).

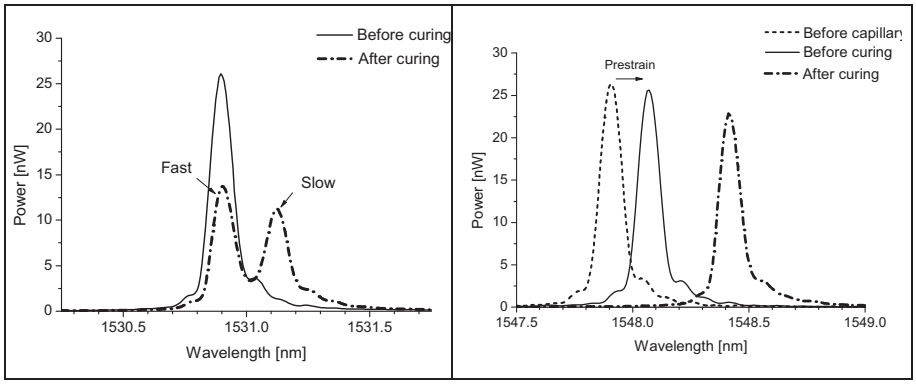

Figure 7-4: Example of a spectrum of the FBG sensor without (left) and with capillary (right) before and after the manufacturing process of a cross-ply laminate.

This enables the shielded FBG to measure (small) axial compression as well. As shown in Figure 7-4, right, the shielding of the FBG in the capillary from transverse strains, ensures that the spectrum, after curing, still consists of a single peak without distortion. The assumption of the full longitudinal strain transfer from laminate onto the shielded FBG will be elaborated in the next section.

7. 2. 2. Longitudinal strain transfer of an encapsulated DTG®

Further in Section 7. 3. , the strain transfer of the laminate to an encapsulated DTG® is stated to be 100%. However, one can have doubts about this statement. To validate this, a tensile standard test is performed on two samples with an encapsulated DTG® embedded within (Table 7-4, n° 15 and 16). The axial strain readings of the embedded DTG®s shielded with a capillary are compared with the strain readings of a surface mounted extensometer. The measurements were repeated three times for each sample. Equation 7-2 is used to calculate the axial strains in the optical fibre from the measured wavelength shifts. The measurements are plotted in Figure 7-5 against the applied longitudinal stress.

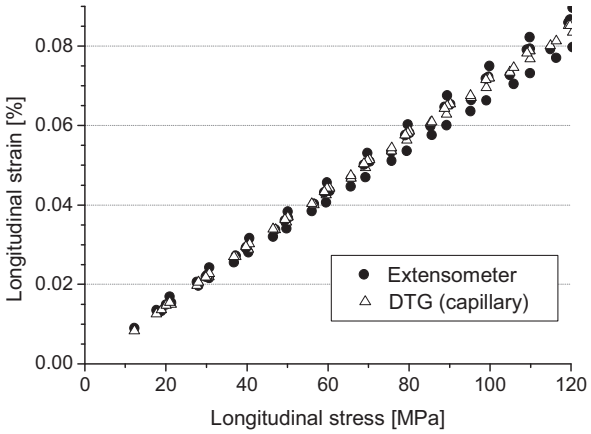

Figure 7-5: Longitudinal strain readings during a tensile test from the encapsulated DTG® (triangles) compared to the reference strain measured using an extensometer (circles), and the simulated strain using finite element modelling (solid line).

The maximal applied longitudinal stress is approximately 120 MPa, which equals approximately 800 µstrain (10^{-6}). The simulated longitudinal strain of the optical fibre is plotted as well. We notice that the measured strain readings of the embedded encapsulated DTG®s and extensometer match very well, however a large scatter is visible for the extensometer readings. Typically, an external mounted extensometer has small sharp blades to grip on the test-specimen. Because the extensometer is mounted on the composite surface layers, i.e. the 90° oriented layers in the case of the $[90_2,0_2]_{2s}$ laminate, small errors can occur in the strain readings due to misalignments of the extensometer' blades. It is also noted that the composite laminates are manually prepared, and that most probably no perfect stacking of the pre-preg layers is achieved using hand lay-up. Hence, small misalignments between the extensometer and the embedded Bragg sensor is possible. Though, a good

similarity is found, which is a strong indication that a 100% longitudinal strain transfer is obtained for an encapsulated DTG® embedded in the composite material.

7. 2. 3. A multi-axial strain sensor_the K-matrix

The system in Equation 7-1 has three independent variables. It is clear that the use of only one FBG does not yield enough information to determine the total strain field ($\Delta\varepsilon_{1'}$, $\Delta\varepsilon_{2'}$, $\Delta\varepsilon_{3'}$) at the core of the (embedded) optical fibre sensor. Therefore, a second FBG should be used, which is positioned in the close vicinity of the first FBG, but which responds differently to external perturbations like axial and transverse strain components. As shown in Section 7. 2. 1. , an FBG integrated in a capillary can be used for this purpose. The combination of the wavelength shifts of the sensor in a capillary (Equation 7-2) with the wavelength shifts of another FBG (Equation 7-1) are sufficient to determine the multi-axial strain field at the core of the optical fibre. By combining Equation 7-1 and 7-2, the following relationship can be written [6-7]:

$$\begin{bmatrix} \Delta\varepsilon_{1'} \\ \Delta\varepsilon_{2'} \\ \Delta\varepsilon_{3'} \end{bmatrix} = K^{-1} \begin{bmatrix} \Delta\lambda_{B1,1'} \\ \Delta\lambda_{B1,2'} \\ \Delta\lambda_{B2,1'} \end{bmatrix}. \qquad 7\text{-}3$$

Where $\Delta\lambda_{B1,1'}$ and $\Delta\lambda_{B1,2'}$ are the wavelength shifts of the first FBG along its respective 1'- and 2'-axis and $\Delta\lambda_{B2,1'}$ is the wavelength shift of the second FBG along its 1'-axis. The same convention as defined in Chapter 4 will be used to relate the Bragg peaks with the polarization axis. Again, we remark that the Bragg peak shift $\Delta\lambda_{B,1'}$ corresponds to the second peak (i.e. Slow or longer wavelength) and that the Bragg peak shift $\Delta\lambda_{B,2'}$ corresponds to the first peak (i.e. Fast or shorter wavelength), see Figure 7-4.
Since the second FBG is integrated in a capillary, both wavelength shifts $\Delta\lambda_{B2,1'}$ and $\Delta\lambda_{B2,2'}$ are equal. K represents the multi-axial strain sensitivity matrix of the sensor. The matrix K equals

$$K = \begin{bmatrix} \lambda_{B1,1'} & 0 & 0 \\ 0 & \lambda_{B1,2'} & 0 \\ 0 & 0 & \lambda_{B2,1'} \end{bmatrix} \begin{bmatrix} -\frac{\overline{n}^2}{2}p_{11} & -\frac{\overline{n}^2}{2}p_{12} & 1-\frac{\overline{n}^2}{2}p_{12} \\ -\frac{\overline{n}^2}{2}p_{12} & -\frac{\overline{n}^2}{2}p_{11} & 1-\frac{\overline{n}^2}{2}p_{12} \\ 0 & 0 & (1-\frac{\overline{n}^2}{2}p_{12})+\upsilon_f\frac{\overline{n}^2}{2}(p_{11}+p_{12}) \end{bmatrix} \qquad 7\text{-}4$$

Equation 7-4 represents the general K-matrix for a multi-axial sensor system consisting of two independent FBGs. The right term in the K-matrix is defined by the Poisson's ratio and the intrinsic strain optic coefficients of the optical fibre. By using $\overline{n} = 1.4459$, $\upsilon_f = 0.16$ and the calibrated strain optic coefficients,

$p_{11} = 0.112$ and $p_{12} = 0.256$ (Chapter 4), the K-matrix for the DTG® fibre is then given by

$$K = \begin{bmatrix} \lambda_{B1,1'} & 0 & 0 \\ 0 & \lambda_{B1,2'} & 0 \\ 0 & 0 & \lambda_{B2,1'} \end{bmatrix} \begin{bmatrix} -0.12 & -0.27 & 0.73 \\ -0.27 & -0.12 & 0.73 \\ 0 & 0 & 0.79 \end{bmatrix} \qquad 7\text{-}5$$

Equation 7-5 will further be applied to convert the measured Bragg wavelength shifts into strain in the core of the optical fibre.

7. 2. 4. Resolution of the multi-axial fibre strains

By substituting Equation 7-5 in Equation 7-3, we can calculate the multi-axial strain field present in the optical fibre. The sensitivity or resolution of the sensor configuration is determined by the K-matrix of the system and the wavelength resolution of the read-out system. By presuming a certain peak measurement resolution (e.g. 1 pm), we can estimate the error for the measured multi-axial strains in the fibre, $\Delta\varepsilon_{1'}$, $\Delta\varepsilon_{2'}$, $\Delta\varepsilon_{3'}$. In analogy to the 'resolving power' calculated by Luyckx for the MAxS sensor [1], a simple statistical error calculation is employed to calculate the variance ($Var([\Delta\varepsilon])$) and the standard deviation $\sigma_{\Delta\varepsilon}$, on the calculated strain ($[\Delta\varepsilon]$), by assuming a certain variance on the wavelength shifts ($Var([\Delta\lambda])$):

$$Var(\Delta\varepsilon_i) = \left(\left(K_{i,1}^{-1}\right)^2 + \left(K_{i,2}^{-1}\right)^2 + \left(K_{i,3}^{-1}\right)^2 \right) Var([\Delta\lambda]) \quad i = 1,2,3. \qquad 7\text{-}6$$

The standard deviation (i.e. error) on the calculated strain ($[\Delta\varepsilon]$) is then given by

$$\sigma_{\Delta\varepsilon,i} = \sqrt{Var(\Delta\varepsilon_i)}. \qquad 7\text{-}7$$

The error on each strain component determines the minimal possible strain fluctuation or resolution of the system and is dependent on the variance of the wavelength shifts. The variance on the wavelength shift is determined by the wavelength resolution of the used FBG interrogator (FBG-scan X08 from FOS&S, [8]) and is equal for all wavelength shifts, $\Delta\lambda_{1,1'}$, $\Delta\lambda_{1,2'}$, $\Delta\lambda_{2,1'}$. The variance on the wavelength, $Var([\Delta\lambda]) = 1pm$, and the estimated error, $\delta\Delta\varepsilon_i$ on the multi-axial fibre strains is given in Table 7-1.

Table 7-1: Error analysis for the multi-axial fibre strains for the dual FBG sensor configuration.

	Standard deviation
Longitudinal $\delta\Delta\varepsilon_{3'}$ [$\mu\varepsilon$]	0.8
Transverse in-plane $\delta\Delta\varepsilon_{1'}$ [$\mu\varepsilon$]	3.7
Transverse out-of-plane $\delta\Delta\varepsilon_{2'}$ [$\mu\varepsilon$]	3.7

The errors calculated in Table 7-1 is directly related to the sensor configuration and respective K-matrix, and thus to the intrinsic fibre strain-optic coefficients. We can see that the resolution on the transverse fibre strains is approximately five times higher than the axial fibre strain, which indicates that the transverse strain resolution of this sensor configuration is poor compared to the longitudinal strain resolution. This error estimation is only valid for the strains measured in the optical fibre. In the next section the author will show that a difference exists between the strain field measured in the optical fibre and the strain field in the composite laminate, hence the resolution of the composite strains will change too dependent on the strain transfer.

7. 3. MULTI-AXIAL STRAIN TRANSFER

7. 3. 1. Strain transfer coefficient matrix_the principle

When an optical fibre is embedded in a material, one can consider it as a circular inclusion in the material. It is known that at the position of the inclusion, the stress ($\Delta\sigma_i$) and strain ($\Delta\varepsilon_i$) fields are altered. The strain of the far field ($\Delta\varepsilon_i^{h,\infty}$) differs from the strain near the inclusion $\Delta\varepsilon_i$, for example at point P (Figure 7-6), where a certain gradient of strain and stress exists. The strain in the core of the optical fibre sensor $\Delta\varepsilon_i^s$ will not be equal to the strain at the same point of the host material without inclusion $\Delta\varepsilon_i^h$. This gradient is different for a non-coated optical fibre than for a fibre which is coated.

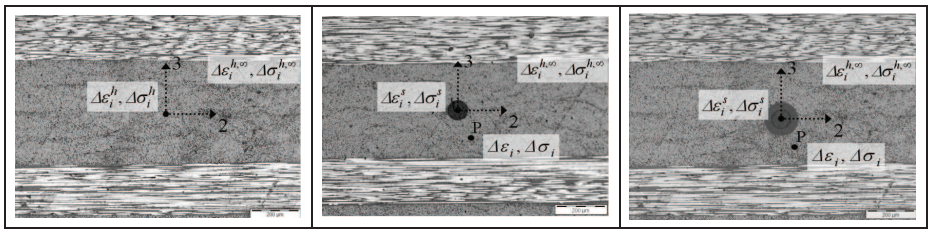

Figure 7-6: An inclusion (e.g. an optical fibre sensor) alters the stress and strain fields in a material, stripped fibre (centre), coated fibre (right).

Lekhnitskii [9] prooved that for the hypothetical case that a certain load is applied at infinity, the strain and stress in the material at a distance far from the sensor (3 or 4 sensor diameters) approximates the far-field strain and stress in the host material ($\Delta\varepsilon_i^{h,\infty}, \Delta\sigma_i^{h,\infty}$). In the forthcoming analysis, it is assumed that $\Delta\varepsilon_i^h = \Delta\varepsilon_i^{h,\infty}$ and $\Delta\sigma_i^h = \Delta\sigma_i^{h,\infty}$, and that the stresses and strains in the sensor are constant over its entire cross-section and length. Kim et al. [10] have shown analytically that this condition is valid for uncoated sensors embedded in an anisotropic material. For coated fibres this condition is valid as well for the cross-section of the fibre, but, due to the lower coating stifness, a large gradient of strain and stress can exist in the coating region. In the determination of the total strain transfer from host material to the optical fibre (with or without coating), only the strains in the optical fibre are

considered, hence the deformation of the coating is not detrimental for the forthcoming analysis. The altering of the strain field due to the coating material is subject of Secion 7. 5. , where the strain disturbance is simulated using a FE model.

Due to the complex interaction between the host material and the embedded optical fibre sensor, the relationship between the strains present in the core of the sensor and in the host material, is not straightforward. A number of other researchers have measured strain inside or on the surface of composite materials and have studied the strain transfer relationship between the optical fibre sensor and the substrate or host material.
Research on measuring strain using optical fibres can be mainly divided in *uni-axial strain sensing* and *multi-axial strain sensing.*

7. 3. 1. a. Uni-axial strain sensing

For *uni-axial strain sensing* applications, the optical fibre is usually provided with a protective coating. If one considers an embedded optical fibre, the coating will act as the interface between the optical fibre and the host material. It is clear that this can have a definite impact on the transfer of strains from the matrix to the fibre. By choosing the right coating, the strain transfer can be improved in certain principal directions. For example, it is possible to choose a coating for which stress concentrations around the fibre can be avoided and composite distortion minimizes [11-12]. A lot of research on strain transfer mechanisms are related to surface mounted FBGs. One should, however, remark that the relation of the strain of the sensor to that of the substrate for surface mounted FBG strain sensors, embedded in a thin layer of adhesive, and bonded to the surface of a structure is substantially different from that of embedded strain sensors. In the first case, the adhesive layer thickness and mechanical properties of this layer have a certain influence on the strain transferred from the structure to the bonded FBG [13] Moreover, when bonded on a thin and low-modulus substrate, the FBG could change the original strain of the substrate [14]. Wan et al. [15] found that for a surface bonded fibre, the strain transfer is dominated by (i) adhesive thickness between the bottom of the fibre and the substrate and (ii) the bond length of the fibre. Since embedded fibres are completely surrounded by the host material, one cannot speak of bond thickness and bond length in the second case. In this matter, apparent strain gradients only exist over ~2 mm (depending on the material properties) starting at the entry point of the embedded fibre[16].
Several authors have embedded FBG sensors in composite specimens to measure solely strain along the axial direction of the optical fibre. In these researches, the relationship between the axial strain of the sensor and the host material is discussed. Cox [17] analytically determined the uni-axial strain transfer for the case of a finite length cylindrical inclusion, embedded into an isotropic material subjected to an axially constant strain field. This theory is often referred to as the *shear-lag analysis*, because the longitudinal strain of the host material is transferred through the shear strain in the interface coating/optical fibre. However, this theory does not consider the mechanical properties of the host material. Afterwards, several authors improved the shear-lag theory. For example, Jiang et al. [18] developed formulas to predict the strain field distributions of fibre and host material by combining the shear-lag theory and the theory of elasticity. In 2009, Li et al. [19] gave an overview of the parameters (mechanical properties of the coating and host material,

and the gauge length of the FBG) which can affect the strain transfer. Anyhow, the above referred literature proves the necessity of in-situ calibration of the strain sensitivity of embedded optical fibre sensors.
In some cases *no coating* at the location of the FBG is chosen in axial strain sensing applications. As such, the strain acts directly onto the cladding's surface of the optical fibre sensor. Fan et al. [20] experimentally determined the influence of the additionally induced radial strain in optical fibres when embedding them in a host material. The authors tried to quantify this mismatch by producing two $[0_8,90_4]_s$ composite specimens in which two FBGs were embedded; one along the the 0 degree direction and one along the 90 degree direction. Measurement errors up to 8% were found when using the bare FBGs gauge factor for axial strain. To correct this gauge factor, the authors suggested to use a coefficient which is dependent on the type of load, + 3% for tensile loads and -8% for compressive loads. Care should, however, be taken by introducing correction coefficients which are dependent on the type or direction of the load.

7. 3. 1. b. Multi-axial strain sensing

Nevertheless, direct strain transfer of the host material to the optical fibre sensor can be interesting in terms of *multi-axial strain measurements* of composite laminates. Former research activities by other authors [21-22] pointed out the need to determine the total strain field response of an embedded FBG in a host material. Bosia et al. [23] studied the response of a sensor without coating embedded in an epoxy specimen experiencing biaxial loading. Finite elements showed the stress distribution in the vicinity of the embedded fibre. The difference in transverse strain of the host material and embedded sensor was evaluated for transversely applied loads. It proves the necessity of a multi-axial strain transfer approach in such situations. Prabhugoud and Peters [24] predicted the spectral response of an (embedded) FBG under a multi-axial strain field through a combined opto-mechanical study. Even the FBG spectral response for non-uniform strain and stress in the laminate could be predicted. The reverse problem, however, was not tackled. Kollar and Vansteenkiste [25] developed an analytical model of the multi-axial strain transfer between an embedded optical fibre and an infinite anisotropic host material. The stress and strain relationships where derived for loading and boundary conditions applied at infinity. However, composites can be relatively thin and the lay-up of the laminate and the position of the sensor in a certain layer should be taken into account to improve multi-axial measurements with optical fibres [2-3].

At the moment, a standard experimental approach is still non existing, however, the author believes that multi-axial strain measurements with FBG sensors can be of added value in monitoring the structural integrity of composites. Therefore a more elabortated method, based on a multi-axial strain principle is dicussed next.

7. 3. 1. c. General strain relationship

In general form the strain relationship between the host material and the optical fibre sensor can be written as:

$$\begin{bmatrix} \Delta\varepsilon_1^h \\ \Delta\varepsilon_2^h \\ \vdots \\ \Delta\varepsilon_6^h \end{bmatrix} = \begin{bmatrix} TC_{11} & TC_{12} & \cdots & TC_{16} \\ TC_{21} & TC_{22} & \cdots & TC_{26} \\ \vdots & \vdots & \ddots & \vdots \\ TC_{61} & TC_{62} & \cdots & TC_{66} \end{bmatrix} \begin{bmatrix} \Delta\varepsilon_1^s \\ \Delta\varepsilon_2^s \\ \vdots \\ \Delta\varepsilon_6^s \end{bmatrix}. \qquad 7\text{-}8$$

In which $\Delta\varepsilon_i^h$ ($i = 1, 2..., 6$) are the strain components in the composite material (at the location of the sensor) as if no optical fibre sensor was present, and $\Delta\varepsilon_i^s$ ($i = 1, 2..., 6$) are the strain components present at the core of the optical fibre sensor (Figure 7-6). The coordinate axes are taken according the local coordinate system on composite ply level (Chapter 6, Section 6.3.2). In both cases the subscript $i = 1, 2..., 6$ refers to the components of stresses and strains in contracted notation [26]. The strain relationship (Equation 7-8) is thus based on 36 independent strain transfer coefficients (TC_{ij} ($i, j = 1, 2..., 6$). Considering the small dimensions of the optical fibre sensor, one can assume that the temperature of the sensor equals that of the host material, and as such, it will be neglected in the analysis.

It should be noted that, when measuring with optical FBG sensors, the shear deformations ($\Delta\varepsilon_4^s$, $\Delta\varepsilon_5^s$ and $\Delta\varepsilon_6^s$), have no effect on the refractive indices of the optical fibre and thus on Bragg wavelength shifts [5, 27]. In addition, the results of an analytical model of Kollar and Vansteenkiste [25] showed a one-on-one relationship for the shear components of host and embedded optical fibre (only TC_{44}, TC_{55}, TC_{66} are not equal to zero). Therefore, shear deformations will not affect the measurements and Equation 7-8 can be reduced to

$$\begin{bmatrix} \Delta\varepsilon_1^h \\ \Delta\varepsilon_2^h \\ \Delta\varepsilon_3^h \end{bmatrix} = \begin{bmatrix} TC_{11} & TC_{12} & TC_{13} \\ TC_{21} & TC_{22} & TC_{23} \\ TC_{31} & TC_{32} & TC_{33} \end{bmatrix} \begin{bmatrix} \Delta\varepsilon_1^s \\ \Delta\varepsilon_2^s \\ \Delta\varepsilon_3^s \end{bmatrix}. \qquad 7\text{-}9$$

This strain transfer coefficient matrix is further also called the *TC*-matrix, and can be derived from finite element modelling. The method applied to determine the TC-matrix by using FE-simulation is discussed in detail in the next section.

7. 3. 2. The TC-matrix for a cross-ply laminate: finite element analysis

Finite element modelling is a powerfull tool to examine the multi-axial strain transfer effects of an embedded optical fibre. In this section the strain transfer matrix (TC-matrix) for a cross-ply laminate with embedded optical fibre ($[0_2,90_2]_{2s}$), determined using finite element modelling, will be elaborated. The resulting TC-

matrix can then be used to relate the strains in the optical fibre with the strains in the cross-ply laminate, to perform multi-axial strain measurements inside the composite.

The FE-model

It is a challenge to develop suitable and accurate finite element models which relate the (multi-axial) strain in the anisotropic host material to the strain in the optical fibre sensor. In [2], Luyckx G. et al presented a method to establish a TC-matrix by use of finite element analysis on a composite model with an embedded (stripped) optical fibre. In analogy to this research, FE analysis is performed on a cross-ply laminate, once with a stripped embedded optical fibre and once with a coated embedded optical fibre.

Several assumptions have been made in developing the FE-model using Abaqus^{TM}:

1. The optical fibre is aligned with the reinforcement fibres of the adjacent plies of the host material. This is done to avoid the occurence of a resin eye and associated complexity of strain transfer [28].
2. Perfect bonding between the optical fibre, coating and the host material is assumed.
3. Deformations are assumed to be small (~1%).
4. Both materials (sensor and host) are considered to behave in a linear elastic manner.
5. The boundary conditions are chosen as such that symmetry is applied in the *xy*-, *xz*-, and *yz*-plane, hence, only 1/8 of a specimen with embedded optical fibre is modelled (Figure 7-7).

The composite laminate model (10 mm x 0.8 mm x 10 mm, for a 16 layer laminate) is illustrated in Figure 7-7. Each layer has a thickness of 0.1mm and the stacking sequence of the complete laminate is $[(90_2,0_2)]_{2S}$. Only 8 layers in thickness are modelled because of symmetry (left inset in Figure 7-7). The mesh is chosen edge biased, with the finest meshing towards the vicinity of the fibre, to enhance accuracy of the results near the optical fibre. In total the model consists of 74700 linear hexahedral elements of type C3D8R[29]. The mesh of the optical fibre is refined as well (right inset in Figure 7-7). The embedded optical fibre (diameter 80 µm, coating diameter 140 µm and length 10 mm) consists of 5750 and 2500 linear hexahedral elements of type C3D8R for the fibre and coating, respectively. The (anisotropic) material properties of the uni-directional (cured) lamina, used in the finite element simulations are given in Table 7-2. The material properties are defined according to the local coordinate axes.

Table 7-2: Engineering constants for the M55J/M18 carbon/epoxy UD material.

E_{11}	$E_{22} = E_{33}$	$G_{12} = G_{13}$	G_{23}	$\nu_{12} = \nu_{13}$	$\nu_{23} = \nu_{32}$	$\nu_{21} = \nu_{31}$
[GPa]	[GPa]	[GPa]	[GPa]	[-]	[-]	[-]
300.0	6.3	4.3	2.3	0.320	0.380	0.002

To obtain the stacking sequence of the $[(90_2,0_2)]_{2S}$ cross-ply laminate, the material properties of the individual layers in the modelled laminate are oriented according to the global coordinate system of the composite, see Figure 7-7 and top-left inset. The (isotropic) material of the optical fibre is fused silica (E_s = 72.4GPa, ν_s = 0.16), and the material of the coating is ORMOCER®, if used. The material properties of the coating material will be varied in the forthcoming parametric study (Section 7. 5.), on the determination of the *TC*-matrix of the coated DTG®. To determine the TC-matrix of a stripped DTG® the material properties and material orientations of the coating are simply replaced with those of the adjacent composite layer to keep identical meshing in the surrounding of the optical fibre.

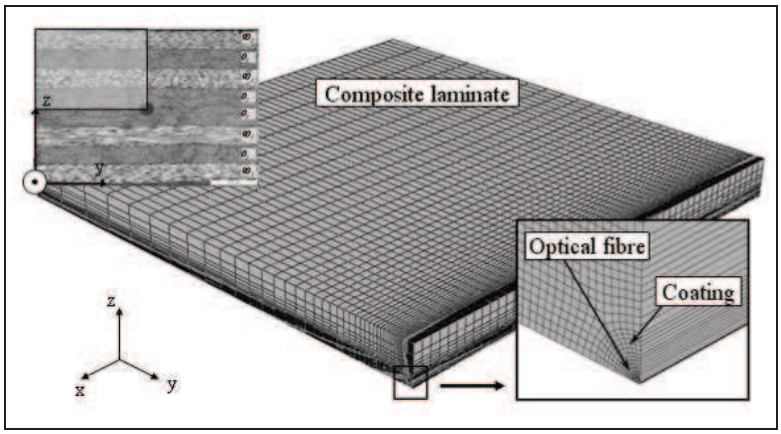

Figure 7-7: Finite element model used for simulation of the strain transfer between embedded optical fibre and CFRP laminate.

To determine the 9 independent parameters of the *TC*-matrix, we need to perform finite element simulations of three independent loading conditions (Figure 7-8). In this work the author applies load on the model along the three principal axes. The laminate is loaded longitudinal along the optical fibre axis ('LONG', transversely in-plane ('SIDE'), and transversely out-of-plane ('TOP').

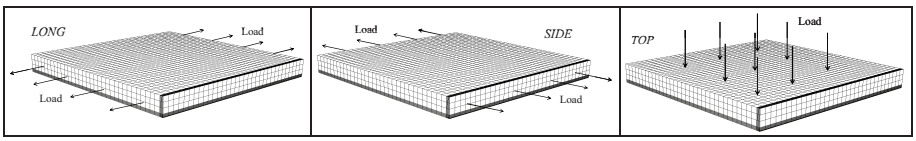

Figure 7-8: (a) Longitudinally applied load ('LONG'), (b) Transversely applied load in-plane ('SIDE'), (c) Transversely applied load out-of-plane ('TOP').

The direct strain transfer coefficients

The individual strain transfer coefficients for each loading condition are derived from the simulations by considering the three principal strains in the core of the optical fibre ($\Delta\varepsilon_1^s$, $\Delta\varepsilon_2^s$, $\Delta\varepsilon_3^s$) and comparing them with the composite strains ($\Delta\varepsilon_1^h$, $\Delta\varepsilon_2^h$, $\Delta\varepsilon_3^h$) in an identical FE model without embedded optical fibre (Figure 7-6).

The ratio of the individual numerical strain components of the composite laminate, $\Delta\varepsilon_i^h$ and the optical fibre, $\Delta\varepsilon_i^s$ represent the direct strain transfer coefficients for each loading case. The direct strain ratios provide a clear view of the strain transfer effect which is not always as straightforward as one might think. The ratios for a stripped optical fibre for all loading conditions are given in Table 7-3. The ratios are similar to the results presented in [3], however, small differences are present because the material properties used for the optical fibre in the FE modelling in this work are slightly changed.

Table 7-3: Strain ratios for three loading conditions applied to a $[90_2,0_2]_{2s}$ laminate with a stripped optical fibre.

Loading direction	$\varepsilon_1^s / \varepsilon_1^h$	$\varepsilon_2^s / \varepsilon_2^h$	$\varepsilon_3^s / \varepsilon_3^h$
Longitudinal (LONG)	100.0%	986.6%	40.3%
Transverse in-plane (SIDE)	100.0%	12.4%	6.7%
Transverse out-of-plane (TOP)	100.0%	-116.6%	13.4%

By looking at the different load directions in Table 7-3, we observe that the strain transfer of the longitudinal strain is 100% in all cases. For the transverse directions the transfer of strain is completely different and it is strongly dependent on the loading direction. For instance in the case of the transverse out-of-plane loading we see that the strain transfer coefficient for the in-plane strains ($\varepsilon_2^s / \varepsilon_2^h$) has a negative sign. This means the measured strain in the optical fibre has the opposite sign of the strain in the composite laminate. This clearly illustrates that the fibre strains measured in the core of the optical fibre do not represent the real near field strain of the composite material. In the case of the longitudinal applied loading we see for instance that the in-plane strain in the optical fibre is almost 10 times the real composite strain.

The total TC-matrix

The 9 direct strain transfer coefficients of Table 7-3 are not to be mixed up with the 9 independent *TC*-coefficients of Equation 7-9. To determine the 9 unknown *TC*-coefficients of Equation 7-9 we need to solve 9 equations. The system of 9 equations can be written as follows

$$TC_{ij} = \sum_k \Delta\varepsilon_{ik}^h \left(\Delta\varepsilon_{kj}^s\right)^{-1} \quad i,j,k = 1,2,3\,, \tag{7-10}$$

With *k* representing the loading case (i.e. 1 = LONG, 2 = SIDE and 3 = TOP). The loading case 'LONG', 'SIDE' and 'TOP' are typically chosen according the global x-, y-, and z-axis of the composite laminate, respectively (Figure 7-8). Equation 7-10 can be written in matrix form and is given by

$$[TC] = [E_h] \cdot [E_s]^{-1}\,, \tag{7-11}$$

where $[E_h]$ represents a 3x3 matrix with the composite strains and $[E_s]$ a 3x3 matrix with the strains of the optical fibre. With $[E_h] = \Delta\varepsilon_{ij}^{h}$ and $[E_s] = \Delta\varepsilon_{ij}^{s}$, with *i,j = 1,2,3* , the matrix multiplication of Equation 7-11 is written fully as follows

$$\begin{bmatrix} TC_{11} & TC_{12} & TC_{13} \\ TC_{21} & TC_{22} & TC_{23} \\ TC_{31} & TC_{32} & TC_{33} \end{bmatrix} = \begin{bmatrix} \Delta\varepsilon_{11}^{h} & \Delta\varepsilon_{12}^{h} & \Delta\varepsilon_{13}^{h} \\ \Delta\varepsilon_{21}^{h} & \Delta\varepsilon_{22}^{h} & \Delta\varepsilon_{23}^{h} \\ \Delta\varepsilon_{31}^{h} & \Delta\varepsilon_{32}^{h} & \Delta\varepsilon_{33}^{h} \end{bmatrix} \begin{bmatrix} \Delta\varepsilon_{11}^{s} & \Delta\varepsilon_{12}^{s} & \Delta\varepsilon_{13}^{s} \\ \Delta\varepsilon_{21}^{s} & \Delta\varepsilon_{22}^{s} & \Delta\varepsilon_{23}^{s} \\ \Delta\varepsilon_{31}^{s} & \Delta\varepsilon_{32}^{s} & \Delta\varepsilon_{33}^{s} \end{bmatrix}^{-1} \qquad 7\text{-}12$$

The columns indicated in Equation 7-12 represent the numerical strains of the laminate and the sensor in the 1,2 and 3 direction of the global coordinate system, i.e. in the x-, y- and z-direction. The column numbers of each matrix represent the loading cases, i.e. 1 = LONG, 2 = SIDE and 3 = TOP. As an example, the two columns indicated with a solid circle represent the longitudinal loading case, with $\Delta\varepsilon_{11}^{h}$, $\Delta\varepsilon_{21}^{h}$, $\Delta\varepsilon_{31}^{h}$ the three principal strains in the composite and $\Delta\varepsilon_{11}^{s}$, $\Delta\varepsilon_{21}^{s}$, $\Delta\varepsilon_{31}^{s}$ the three principal strains in the sensor along the 1-, 2- and 3-axis.

Using Equation 7-12, the numerically determined *TC*-matrix for an embedded optical fibre without coating is then given by

$$TC_{Stripped} = \begin{bmatrix} 1 & 0 & 0 \\ 0.77 & 7.85 & -1.36 \\ 0.76 & -1.37 & 7.83 \end{bmatrix}. \qquad 7\text{-}13$$

Again, it is noted that the TC-matrix Equation 7-13 is slightly different than the TC-matrix presented in [3], because of the difference in material properties of the optical fibre used in the FE models.
The full *TC*-matrix of Equation 7-13 can then be substituted in Equation 7-9, to determine the experimental composite strains from the measured strains of the embedded optical fibre sensor for any given loading case. The experimental validation of the numerical strain transfer matrix is shown in the following section.

General strain-relationship between the composite laminate and optical fibre

During the composition of the *TC*-matrix in Section 7. 3. , the notation $\Delta\varepsilon_{i}^{s}$ is used to avoid confusion between the coordinate system of the optical fibre sensor and the composite laminate. As such, the relationship between the strain of the sensor and that of the laminate is more clear. The sensor strain, $\Delta\varepsilon_{i}^{s}$ is defined along the local composite layer' coordinate system and the strains in the optical fibre core, $\Delta\varepsilon_{i'}$ is defined along the coordinate system of the optical fibre (Figure 7-2). They are related to each other according to the following one-on-one equation

$$\begin{bmatrix} \Delta\varepsilon_1^s \\ \Delta\varepsilon_2^s \\ \Delta\varepsilon_3^s \end{bmatrix} = \begin{bmatrix} \Delta\varepsilon_{3'} \\ \Delta\varepsilon_{1'} \\ \Delta\varepsilon_{2'} \end{bmatrix}. \qquad 7\text{-}14$$

Using the *TC*-matrix, the strain relationship (Equation 7-9) between the strains measured in the optical fibre ($\Delta\varepsilon_{1'}$, $\Delta\varepsilon_{2'}$, $\Delta\varepsilon_{3'}$) and the three principal strains in the composite laminate ($\Delta\varepsilon_1^h$, $\Delta\varepsilon_2^h$, $\Delta\varepsilon_3^h$), is then given by

$$\begin{bmatrix} \Delta\varepsilon_1^h \\ \Delta\varepsilon_2^h \\ \Delta\varepsilon_3^h \end{bmatrix} = \begin{bmatrix} TC_{11} & TC_{12} & TC_{13} \\ TC_{21} & TC_{22} & TC_{23} \\ TC_{31} & TC_{32} & TC_{33} \end{bmatrix} \begin{bmatrix} \Delta\varepsilon_{3'} \\ \Delta\varepsilon_{1'} \\ \Delta\varepsilon_{2'} \end{bmatrix} \qquad 7\text{-}15$$

Equation 7-15 is applied in the next sections to calculate the experimental composite strains from the embedded optical fibre sensors.

7. 4. EXPERIMENTAL VALIDATION OF THE TC-MATRIX OF A STRIPPED DTG® EMBEDDED IN A CROSS-PLY LAMINATE

Based on the response of an embedded sensor, two subsequent steps as illustrated in Figure 7-1 are necessary to determine the total strain field in a composite laminate. In Section 7. 2. the multi-axial gauge factors, or the *K*-matrix, of the optical fibre is determined (Step1). The K-matrix relates the measured Bragg wavelength shifts with the induced strain in the optical fibre. In Section 7. 3. the TC-matrix is developed (Step2). By then combining the *K*-matrix (Step1) and the *TC*-matrix (Step2), we are able to convert the measured wavelength shifts, and the strains in the embedded optical fibre, into the real strains of the composite laminate for different in-plane and out-of-plane loading cases.
By substituting the K-matrix for the DTG®-fibres used in this work (Equation 7-5), and writing it according the coordinates of the fibre strains (Equation 7-14) and using Equation 7-3, we can write the following equation

$$\begin{bmatrix} \Delta\varepsilon_{1'} \\ \Delta\varepsilon_{2'} \\ \Delta\varepsilon_{3'} \end{bmatrix} = \begin{bmatrix} -0.12 & -0.27 & 0.73 \\ -0.27 & -0.12 & 0.73 \\ 0 & 0 & 0.79 \end{bmatrix} \begin{bmatrix} \Delta\lambda_{B1,1'} / \lambda_{B1,1'} \\ \Delta\lambda_{B1,2'} / \lambda_{B1,2'} \\ \Delta\lambda_{B2,1'} / \lambda_{B2,1'} \end{bmatrix}. \qquad 7\text{-}16$$

Note, that the initial wavelengths are extracted from the K-matrix to obtain a wavelength independent equation. Equation 7-16 defines the intrinsic strain sensitivity of the dual sensor configuration, and is used to calculate the strains in the optical fibre core from the measured wavelength shifts for any applied loading case.

To obtain the general strain transfer relationship for a stripped 80 µm DTG®, the TC-matrix of a stripped 80 µm optical fibre (Equation 7-13) is substituted in the general strain relationship between the composite and the embedded optical fibre (Equation 7-15). The general strain transfer relationship for a stripped 80 µm DTG® is then given by

$$\begin{bmatrix} \Delta\varepsilon_1^h \\ \Delta\varepsilon_2^h \\ \Delta\varepsilon_3^h \end{bmatrix} = \begin{bmatrix} 1 & 0 & 0 \\ 0.77 & 7.85 & -1.36 \\ 0.76 & -1.37 & 7.83 \end{bmatrix} \begin{bmatrix} \Delta\varepsilon_{3'} \\ \Delta\varepsilon_{1'} \\ \Delta\varepsilon_{2'} \end{bmatrix}. \qquad 7\text{-}17$$

The numerical TC-matrix shown in Equation 7-17, is validated experimentally by filling in the measured optical fibre strains for three different applied loading conditions, which are chosen identical to the simulated load cases, as shown in Figure 7-8:

1. longitudinal along the optical fibre axis ('LONG'),
2. transversely in-plane ('SIDE'),
3. transversely out-of-plane ('TOP').

For each loading case, different CFRP cross-ply laminates with embedded optical fibres were prepared. The laminates have a balanced and symmetric lay-up ($[90_2,0_2]_{2s}$ or $[0_2,90_2]_{2s}$) with a total of 16 layers. Such cross-ply laminates provide a maximal in-plane stiffness (x- and y-direction) and the lowest out-of-plane stiffness (z-direction). In case of transverse compressive loading, for instance, these laminates are expected to have equal strains in x –and y-direction. This makes them well suited to experimentally validate the TC-matrix. Details on the used test-samples and the embedded DTG® sensors is given in the next sub-sections for each respective loading case (Table 7-4 and Table 7-5). To determine the multi-axial strain field in the embedded optical fibre for each of the above mentioned loading cases, the dual sensor configuration, as described in Section 7. 2. 3. , is imitated using two sets of identical test-samples. One set with an embedded encapsulated DTG®s to shield the transverse strains and to measure pure axial strain, and one set with an embedded stripped DTG®s without capillary to measure the total strain field acting on the grating. Both sets are subjected to the same longitudinal or transverse loading case and the wavelength shift of both DTG®s as function of the applied stress is then used to determine the multi-axial strains. In all test-samples the newly developed 80 µm DTG®s are used (from PR2008_1). The optical fibres are always embedded in the mid-plane of each composite laminate. In the case of the stripped, DTG®s the coating has been chemically removed along a few centimetres at the position of the grating. The capillary is a fused silica tubing coated with polyimide; its inner diameter is 180 µm and the outer diameter is 340 µm.
An example of the cross-sections for a $[90_2,0_2]_{2s}$ cross-ply laminate with a stripped optical fibre and a capillary embedded in between the mid-plane layers, is shown in Figure 7-9. Here, the optical fibres are aligned along the 0° - oriented reinforcement fibres, i.e. along the x-axis of the composite laminate.

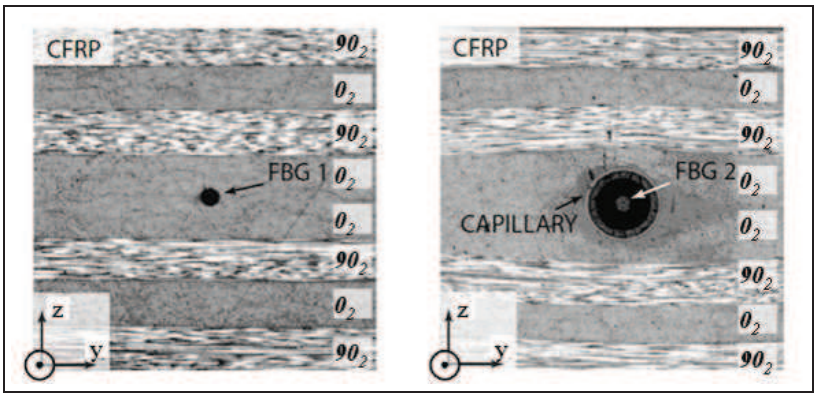

Figure 7-9: The cross-sections of the dual FBG configuration inside a cross-ply laminate with stacking $[90_2,0_2]_{2s}$, stripped 80 µm DTG® (left), 80 µm DTG® inside a glass capillary (right).

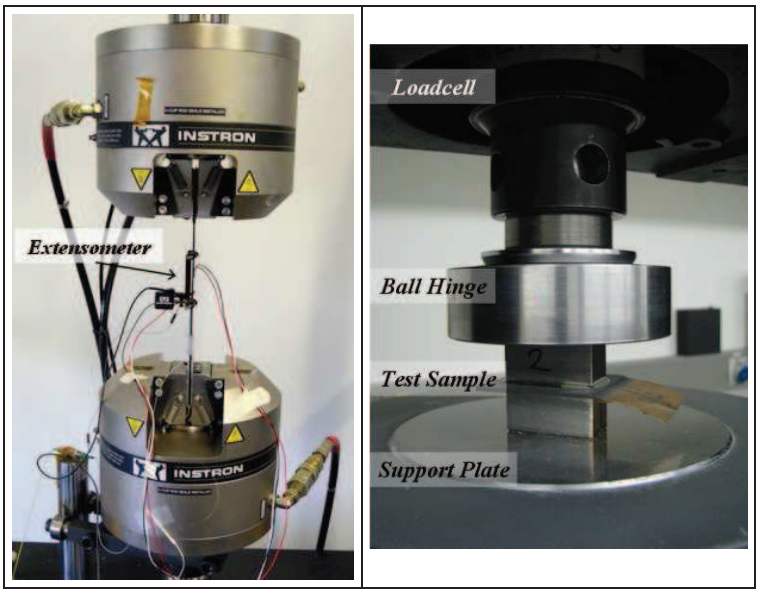

Figure 7-10: Test setup to load longitudinal and transversely in-plane (left), setup to perform controlled transverse compression testing to load transversely out-of-plane (right).

To induce three different strain states inside the CFRP cross-ply laminates, two different setups are used. A standard hydraulic test-bench (INSTRON 8801) with wedge shaped clamps is used to perform the longitudinal and transverse in-plane tension testing (Figure 7-10, left), and a mechanical test-frame (INSTRON 8500) with an adapted compression loading setup, is used to perform the out-of-plane transverse loading (Figure 7-10, right). In both setups the load cell and the wavelength readings (and spectral response) are monitored during loading and additional during longitudinal and in-plane transverse testing an extensometer is mounted on top of the specimen to serve as reference strain measurement.

7. 4. 1. Longitudinal loading

Test-samples

To validate the TC-matrix for the longitudinal tensile loading case, several standardized ([30]) cross-ply laminates with stacking $[90_2,0_2]_{2s}$ are manufactured, see Figure 7-11. The laminates are foreseen with aluminium end-tabs with 1 mm thickness, fixed on the composite surface with cyanoacrylate glue (i.e. superglue). The laminates are loaded in the x-direction of the global composite coordinate system, using the standard hydraulic test-bench as shown in Figure 7-10, left. The optical fibres are embedded in the mid-plane of the composite laminate. The optical fibres are aligned parallel to the 0°-oriented reinforcement layers (Figure 7-11).

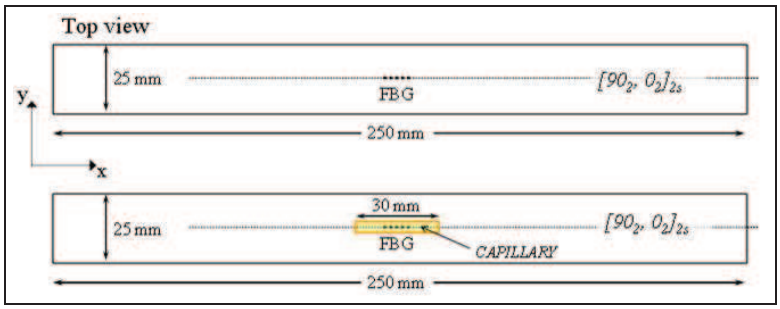

Figure 7-11: Schematic drawing of the composite laminates used for the longitudinal loading case.

The number of samples, their stacking sequence, the laminates' dimensions and the applied loading case are listed in Table 7-4. It is noted that fragile stripped sensors are used which easily break during composite lay-up. Therefore, two out of six test-samples could not be tested.

Table 7-4: Inventory of the CFRP test-coupons for longitudinal loading

	Lay-up	Length	Width	Thickness	Sensor alignment	Loading case**
n°*		[mm]	[mm]	[mm]	Global	
12	$[90_2,0_2]_{2S}$	250	24.17	1.80	x-axis	LONG
13	$[90_2,0_2]_{2S}$	250	24.17	1.80	x-axis	LONG
15	$[90_2,0_2]_{2S}$	250	24.26	1.80	x-axis (cap)	LONG
16	$[90_2,0_2]_{2S}$	250	24.41	1.80	x-axis (cap)	LONG

* The numbering of the samples is conform to Table 6-3 (Chapter 6), all 80 µm DTG®s are from PR2008_1 (Table 3-3, Chapter 3)

** The loading case is similar to the simulated loading case (Figure 7-8)

Multi-axial strain measurements

During loading, the wavelength shifts of the two DTG®s are monitored. In case of the stripped DTG® embedded in a CRFP cross-ply laminate, two peaks are present after curing because of birefringence effects (Figure 7-4, left). In analogy to FBGs written in HiBi-fibres [23], the first peak (i.e. shorter wavelength) represents the Bragg wavelength polarized along the 'fast' axis, and the second peak (i.e. longer wavelength) represents the Bragg wavelength polarized along the 'slow' axis. The evolution of the wavelength shifts for each DTG® is shown in Figure 7-12, left, and the spectral response of the stripped DTG® (DTG1) at zero load and maximum load is shown in Figure 7-12, right.

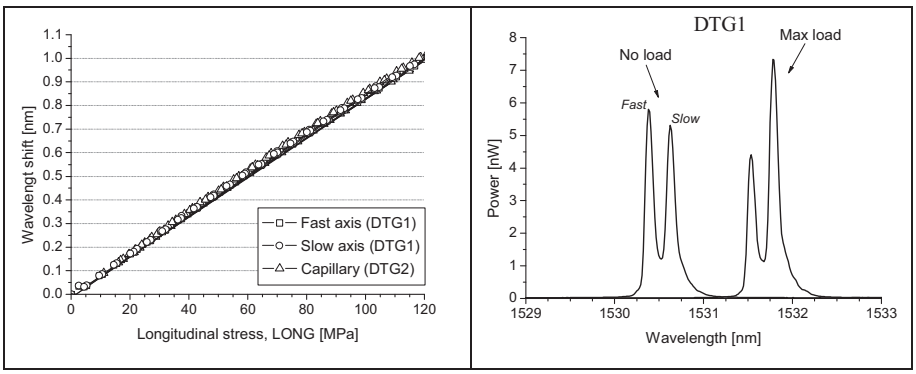

Figure 7-12: Wavelength shifts as function of the applied longitudinal stress (left), spectral response of DTG1at zero load and maximal load (right).

From the evolution of the wavelengths of both DTG®s, no big difference is found between the fast-axis or the slow-axis of DTG1, and DTG2 which is shielded by a capillary. As such, we can state that the effect of transverse strains of the host material on the embedded optical fibre are small. However, by looking at the slopes, we find that the encapsulated DTG®s (DTG2) has a sensitivity of 8.30 pm/MPa, whereas the Fast peak and Slow peak of DTG1 have a sensitivity of 8.36 pm/MPa and 8.41 pm/MPa, respectively. The peak separation between the fast and slow peak increases with approximately 5 pm / 100MPa, which illustrates that there is a differential transverse effect acting on the embedded sensor, though the transverse sensitivity is found small. The longitudinal sensitivity of the slow peak is approximately 1.3 % higher than the sensitivity of the encapsulated DTG®. The error for the fast is much lower (0.7%). This means that if we would calculate the longitudinal strain during this experiment using the slow peak shift or fast peak shift instead of using the wavelength shift of the encapsulated DTG®, we would estimate the strain at 98.7% or 99.3 % of the real induced strain, respectively. The author notices that this error is largely dependent on the lay-up of the composite laminate and the position of the optical fibre in the stacking. The latter numbers are specifically for a $[90_2,0_2]_{2S}$ with the optical fibre embedded in the mid-plane.

From the spectral response of DTG1 (Figure 7-12, right), we notice that merely a positive shift of the Bragg peaks is present. The peak separation of 5 - 6 pm at maximum loading is not evident from the spectral shapes. At maximum loading, we see that the Bragg peak polarized along the slow-axis possesses a larger portion of

the peak power, which could indicate that the strain field surrounding the grating becomes non-uniform at higher load levels.
By using Equation 7-16 we are able to calculate the three principal strains present in the optical fibre from the measured wavelength shifts. The calculated strains as function of the applied longitudinal stress are shown in Figure 7-13, top.

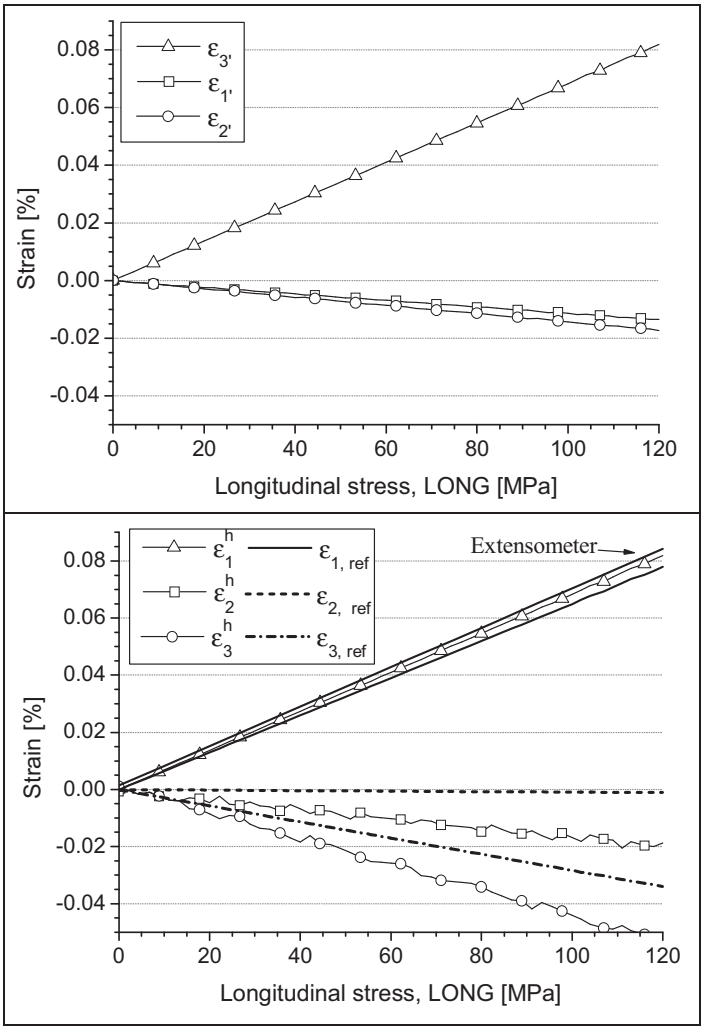

Figure 7-13: Calculated strains in the core of the optical fibre (top), and composite strains (bottom) for a $[90_2,0_2]_{2s}$ laminate and longitudinal applied stress.

Even though the transverse effects in a longitudinal loading case are small, we can clearly see that during longitudinal loading transverse strains are induced in the optical fibre. It is noticed that the transverse strains in the fibre are almost equal, indicating that the transverse contraction of the fibre in the material is more or less isotropic. The axial strain is found approximately four times greater than the transverse strains.

By using the general strain relationship of Equation 7-17 and filling in the calculated fibre strains ($\Delta\varepsilon_{3'}$, $\Delta\varepsilon_{1'}$, $\Delta\varepsilon_{2'}$), we are able to determine the three near field principal strains in the composite laminate ($\Delta\varepsilon_1^h$, $\Delta\varepsilon_2^h$, $\Delta\varepsilon_3^h$). The result of this calculation together with the simulated reference strains ($\Delta\varepsilon_{1,ref}$, $\Delta\varepsilon_{2,ref}$, $\Delta\varepsilon_{3,ref}$), is shown in the bottom plot of Figure 7-13. The linear fit of the strain readings of the extensometer are plotted as well.

The measured composite strain in the 1-direction is directly proportional to the axial strain measured with the sensor, see Equation 7-17, hence, we see the same result as already shown in Figure 7-5; the measured longitudinal strain is matching very well the linear fit of the reference strain measured using the extensometer. We can observe that the slopes of the measured strain curves are slightly higher than that of the simulated strain. Because the composite is manually stacked, the stiffness in longitudinal direction of the laminate can differ slightly from the engineering constants used in the finite element model. If the specimen is not put 100 % straight in the loading clamps, a small misalignment of the loading direction with the stacked reinforcement fibres and the embedded sensor occurs. As such, small differences occur between the axial strain readings of the DTG® during the experiment and the simulated longitudinal strain in the laminate layer. We additionally see in the plot that both the calculated in-plane and out-of-plane transverse composite strains are overestimated. We see a much larger scatter in the data of the calculated transverse strains, which is caused by the scatter in the measured wavelength shifts. Because the difference between the slow -and fast peak wavelength shift is very small ~10 pm, the scatter is defined by the resolution of the FBG-scan system, which is ±1 pm. However, even though the scatter is relative high, a clear linear trend is visible in all strain calculations.

With regard to the overestimation of the transverse strains, there are a number of factors which have influence on the total strain calculation, such as: the engineering constants (and the laminate geometry) used in the model, any misalignment of the composite layers with the global coordinate axis, or the intrinsic 'theoretical' FBG strain sensitivities. It is believed that the deviation of the transverse strains is mainly caused by small errors in the latter mentioned factor. Namely, to calculate the multi-axial strain we make use of the coefficients of the K^{-1}-matrix defined by:

$$\begin{bmatrix} \Delta\varepsilon_{1'} \\ \Delta\varepsilon_{2'} \\ \Delta\varepsilon_{3'} \end{bmatrix} = \begin{bmatrix} -0.12 & -0.27 & 0.73 \\ -0.27 & -0.12 & 0.73 \\ 0 & 0 & 0.79 \end{bmatrix} \begin{bmatrix} \Delta\lambda_{B1,1'} / \lambda_{B1,1'} \\ \Delta\lambda_{B1,2'} / \lambda_{B1,2'} \\ \Delta\lambda_{B2,1'} / \lambda_{B2,1'} \end{bmatrix} \qquad 7\text{-}18$$

If we take a closer look at the individual coefficients of the K^{-1}-matrix in Equation 7-18, the numbers of the first and the second column define the sensitivity of the optical fibre to transverse strains. They are much smaller compared to the coefficients in the third column, which define the 'axial strain sensitivity' of the sensor system. Remark that the purely axial strain sensitivity of 0.79 is equal to the theoretical gauge factor of an FBG (Chapter 4, Table 4-2). Because of the poor transverse strain sensitivity of the system, the transverse strains in the optical sensor

are strongly influenced by the axial wavelength shifts of the encapsulated DTG®. In the case of longitudinal loading of the composite laminate, the axial strain shifts are highest, hence, large errors in the transverse composite strain calculation can occur because of small errors in the axial directions. If in Equation 7-18 the axial wavelength shift increases ~1%, the error for the transverse strains will increase with approximately ~13%. It is noted that the K^{-1}-matrix is theoretically determined using optical constants, see Equation 7-4. Small errors in these (strain) optical coefficients can induce relative large errors in the transverse strain calculations. This underlines the fact that, from the point of view of the fibre sensor, it is very difficult to very accurately determine the transverse strains inside the composite certainly for a longitudinal loading case.

7. 4. 2. Transverse in-plane loading case

Test - samples

The sensor system is validated for the transverse in-plane loading too. Now $[0_2,90_2]_{2s}$ laminates are used, with the optical fibres embedded in the 90° reinforcement layers (Figure 7-14) and again they are subjected to a load in the x-direction.

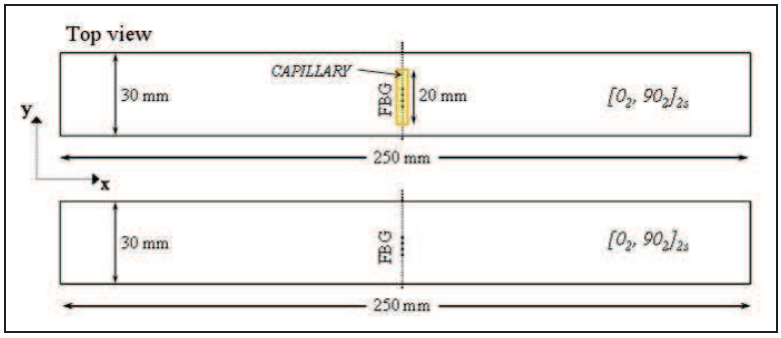

Figure 7-14: Schematic drawing of the composite laminates used for the transverse in-plane loading case.

The number of samples, their stacking sequence, the laminates' dimensions and the applied loading case are listed in Table 7-5.

Table 7-5: Inventory of the CFRP test-coupons for transverse in-plane loading

	Lay-up	Length	Width	Thickness	Sensor alignment	Loading case**
n°*		[mm]	[mm]	[mm]	Global	
17	$[0_2,90_2]_{2S}$	250	30.19	1.80	y-axis	SIDE
20	$[0_2,90_2]_{2S}$	250	29.90	1.80	y-axis (cap)	SIDE
22	$[0_2,90_2]_{2S}$	250	30.77	1.80	y-axis (cap)	SIDE

* The numbering of the samples is conform to Table 6-3 (Chapter 6), all 80 µm DTG®s are from PR2008_1 (Table 3-3, Chapter 3)

** The loading case is similar to the simulated loading case (Figure 7-8)

Again it is noted that fragile stripped sensors are used which happened to break easily during the composite lay-up, and that because of fibre fractures three out of six test-samples could not be tested. During the validation process, fragile stripped sensors are used which happened to break easily during the composite lay-up. Furthermore, in the case of the $[0_2,90_2]_{2s}$ laminates, the fibre egress points are very fragile. In principle, the author uses small pieces of kapton foil to smoothly lead out the optical fibre out of the laminate (Section 6.4.2, Chapter 6), however, in the $[0_2,90_2]_{2s}$ laminates, the risk of inducing composite delamination is high for these specific laminates because of the limited space before and after the sensor zone. As such, no kapton foils are used at the fibre egress point and fibres could break more easily during the dismantling of the vacuum bag after composite laminate manufacturing.

Multi-axial strain measurements

The mid-plane layers of these laminates are oriented 90° with the x-axis, hence, if the composite laminate is loaded in the x-direction, they are subjected to an in-plane transverse loading (Figure 7-14). Due to the high in-plane stiffness in the 1-direction of the mid-plane composite lamina, the embedded DTG® in this loading case will be mainly subjected to in-plane transverse strains and to a much lesser extent to longitudinal strain. The result of the wavelength shifts of the dual sensor configuration for all tests is shown in Figure 7-15, left, and an example of the spectral response of the stripped DTG® (DTG1) at zero load and maximum load is shown in Figure 7-15, right.

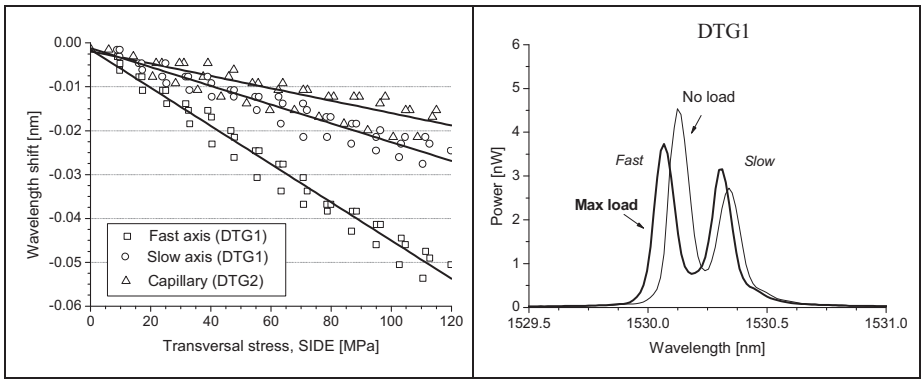

Figure 7-15: Wavelength shifts as function of the applied transverse in-plane stress (left), spectral response of DTG1at zero load and maximum load (right).

From the wavelength evolutions, we notice that all shifts are negative. The shifts are in the order of tens of picometer, which is approximately twenty times smaller than in the longitudinal loading case, see Figure 7-12. We can notice a larger scatter in all the results, which is owing to the fact that the measured wavelength shifts are very small. At maximal loading the encapsulated DTG® (DTG2) shows the lowest shift (~0.02 nm) and the Bragg peak polarized along the fast-axis shows the highest shift (~0.05nm), indicating that indeed mainly transverse strain is induced in the core of the optical fibre. The same effect is visible from the spectral response of DTG1. We indeed see that the complete spectrum shifts slightly to lower wavelengths and that the Bragg peak separation increases. We also notice that the 'fast' peak is shifted

more to the lower wavelengths and the 'slow' peak more towards the high wavelengths, indicating that the differential transverse strain around the optical fibre is changing.
By using again Equation 7-16 (or Equation 7-18) and filling in the measured wavelength shifts of the dual sensor configuration, we are able to calculate the three principal strains present in the optical fibre. The calculated strains as function of the applied transverse stress are shown in Figure 7-16, top.

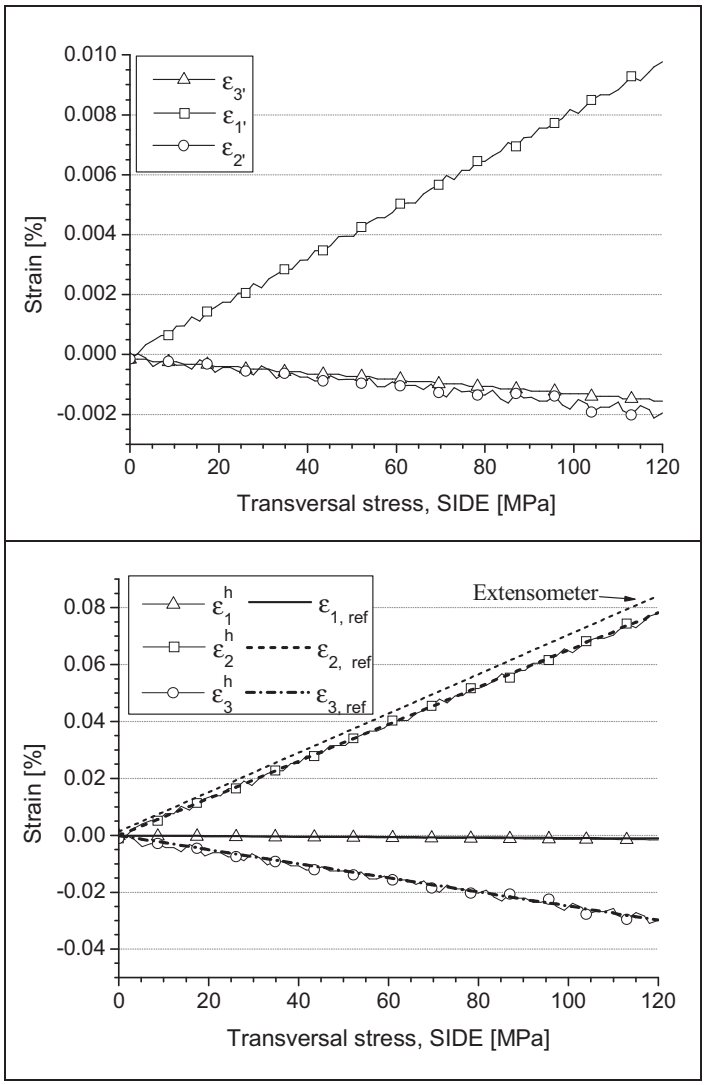

Figure 7-16: Calculated strains in the core of the optical fibre (top), and composite strains (bottom) for a $[0_2,90_2]_{2s}$ laminate and transverse in-plane applied stress.

As illustrated in Equation 7-18, the transverse strain coefficients are negative in sign. We see that by loading the $[0_2,90_2]_{2s}$ sample in the x-direction, i.e. transverse to the optical fibre axis, the in-plane transverse strain field in the optical fibre, $\Delta\varepsilon_{1'}$ is

positive and the other two components are negative and almost equal. We also notice that the magnitude of $\Delta\varepsilon_{1'}$ is much higher than the axial and out-of-plane strain components and because of the resolution of ±1 pm of the FBG-scan system and the very small wavelength shifts (Figure 7-15), the scatter on the results is clearly higher for the transverse in-plane loading than for the longitudinal load case .
By using the general strain relationship of Equation 7-17 and filling in the calculated fibre strains ($\Delta\varepsilon_{3'}$, $\Delta\varepsilon_{1'}$, $\Delta\varepsilon_{2'}$), we can again determine the three near field principal strains in the composite laminate ($\Delta\varepsilon_1^h$, $\Delta\varepsilon_2^h$, $\Delta\varepsilon_3^h$). The result of this calculation together with the simulated reference strains ($\Delta\varepsilon_{1,ref}$, $\Delta\varepsilon_{2,ref}$, $\Delta\varepsilon_{3,ref}$) is shown in the bottom plot of Figure 7-16.
The extensometer is mounted along the x-direction of the sample, as such it measures in the transverse in-plane (2-direction) of the mid-plane 90° composite layers (Figure 7-14). As expected from the strains in the optical fibre, the in-plane transverse strain in the laminate is positive and as one would expect for a cross-ply laminate, loaded transversely, the out-of-plane strain (i.e. through the thickness) of the laminate is negative and the longitudinal strain (in the 1-direction of the lamina) is almost zero and slightly negative. The extensometer reading is slightly higher than the calculated composite strain in the 2-direction. We can see that the calculated composite strains match very well the simulated reference strains, which illustrates that the numerical determined TC-matrix is well-defined. The reason that the multi-axial transverse strains match better the simulated strains, is because for the in-plane transverse loading, the longitudinal strains are very small. As such only small errors are induced in the calculation (Equation 7-18) of the transverse strains of the optical fibre.
Remark that, in both the case of the longitudinal loading as well as the transverse in-plane loading, the samples are subjected to a tensile test in the x-direction. From the bottom plots in Figure 7-13 and Figure 7-16, we can see that for both loading cases the maximum composite strains measured in the loading direction (x) are approximately 800 µstrain, corresponding to $\Delta\varepsilon_1^h$ in the case of longitudinal loading and $\Delta\varepsilon_2^h$ in the case of transverse in-plane loading, This illustrates clearly that by applying the general strain transfer relationship, given by Equation 7-17, it is possible to measure multi-axial strains inside a composite laminate using embedded optical fibre sensors in different directions.

7. 4. 3. Transverse out-of-plane testing

Test - samples

To validate the TC-matrix for a transversely out-of-plane loading condition, a different approach is used. Five rectangular shaped 1.54 mm thick $[90_2,0_2]_{2s}$ cross-ply laminates (50 mm x 50 mm x 1.54 mm) are produced with 80 µm DTG®s (and capillaries) embedded in the mid-plane (Table 7-6). A similar dual sensor configuration is used as discussed in the previous sections, with stripped DTG®s and encapsulated DTG®s, to measure the multi-axial strain field. Again, two sets of laminates are manufactured, see Figure 7-17, top. In total two laminates with a stripped DTG® and three laminates with a capillary are tested (Table 7-6). The sensors are embedded in the 0°-oriented reinforcement layers.

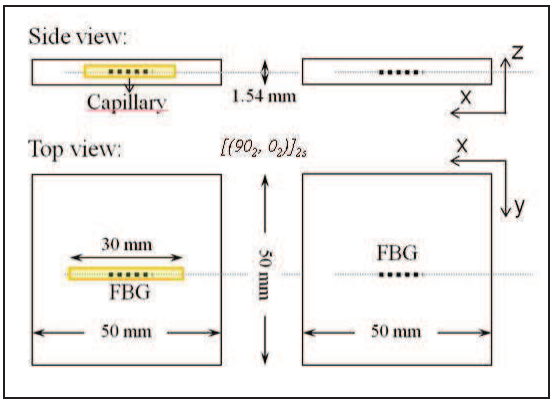

Figure 7-17: Schematic drawing of the composite laminates (top).

Table 7-6: Inventory of the CFRP test-coupons for transverse out-of-plane loading

	Lay-up	Length	Width	Thickness	Sensor alignment	Loading case**
n°*		[mm]	[mm]	[mm]	Global	
4	$[90_2,0_2]_{2S}$	50	50	1.54	x-axis	TOP
5	$[90_2,0_2]_{2S}$	50	50	1.54	x-axis	TOP
7	$[90_2,0_2]_{2S}$	50	50	1.54	x-axis (cap)	TOP
9	$[90_2,0_2]_{2S}$	50	50	1.54	x-axis (cap)	TOP
10	$[90_2,0_2]_{2S}$	50	50	1.54	x-axis (cap)	TOP

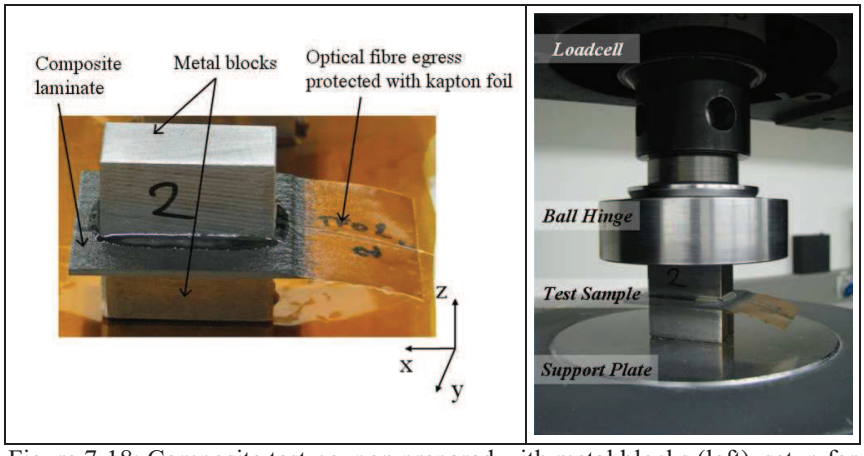

Figure 7-18: Composite test-coupon prepared with metal blocks (left), setup for transverse (out-of-plane) compression testing.

* The numbering of the samples is conform to Table 6-3 (Chapter 6), all 80 µm DTG®s are from PR2008_1 (Table 3-3, Chapter 3)
** The loading cases are similar to the simulated load cases (Figure 7-8)

To validate the TC-matrix a test procedure is developed to introduce a well-defined homogeneous transverse out-of-plane strain field inside a composite laminate. Two metal blocks (20 mm x 40 mm x 20 mm) are glued to the specimen surfaces, using a thin epoxy layer with a uniform thickness (Figure 7-18, left). The test-samples are then positioned on a support plate and loaded via a pressure plate, which is connected to a 100kN load cell. In addition, a ball hinge and a piece of stiff rubber are used on top of the metal blocks during testing, to ensure a uniform stress distribution on the surface of the sample (Figure 7-18, right). The sample is loaded in compression in the z-direction up to a maximum contact pressure of 33 MPa. Each test sample is subjected to an equal transverse stress and each experiment is repeated three times.

Multi-axial strain measurements

The wavelength shifts of all embedded DTG®s as function of the compression loading are shown in Figure 7-19, left. The spectral response at zero load and at maximum load is shown in Figure 7-19, right. During compression loading the applied strain on the composite is negative in z-direction. The wavelength shifts of the sensors are all positive, with the lowest shift found for the encapsulated DTG®s (~0.1 nm) and the highest shift for the 'slow' Bragg peak (~0.25 nm). The same effect is seen in the spectral response of the grating. The total Bragg spectrum shifts to longer wavelengths and the peak separation is increasing with applied pressure.

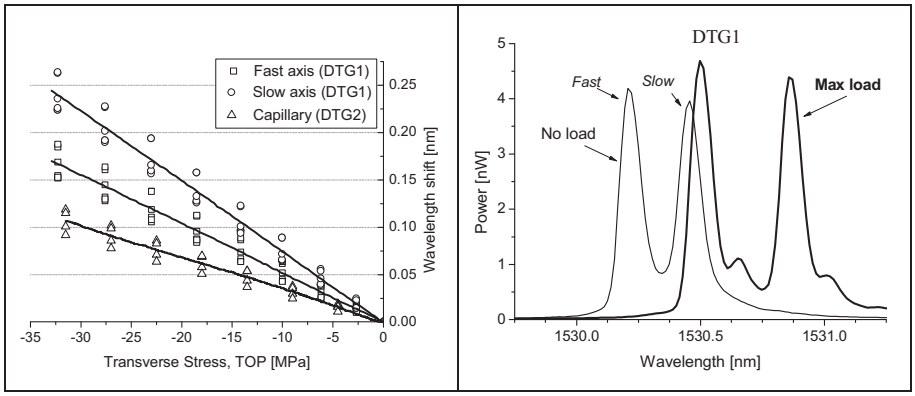

Figure 7-19: Wavelength shifts as function of the transverse stress applied on top of the sample (left), spectral response of DTG1 (stripped) at zero load and maximum load (right).

Substituting the measured wavelength shifts of the dual sensor configuration into Equation 7-16 (or Equation 7-18), the three principal strains present in the optical fibre are calculated and plotted in Figure 7-20, top, as function of the applied transverse stress on top of the laminate. By applying a homogeneous transverse stress the laminate tends to be compressed in the transverse out-of-plane direction (2') and stretched in the two orthogonal directions (1' and 3'). One would expect that the fibre will deform in a similar way. Indeed, the applied stress results in a positive axial strain in the core of the optical fibre, $\Delta\varepsilon_{3'}$. This axial strain component is directly related to the wavelength shift of the encapsulated DTG® (DTG2) and is thus directly related to the positive strain of the composite in that

direction. Besides, the out-of-plane strain, $\Delta\varepsilon_{2'}$ shows a negative shift with applied stress. Since the stiffness of the laminate in this direction is the lowest (Table 7-2), and the load is applied accordingly, the resulting strain in the fibre, $\Delta\varepsilon_{2'}$ is the highest. However, the in-plane strain, $\Delta\varepsilon_{1'}$ in the optical fibre shows a slightly negative shift while the laminate strain is expected to be positive. At first sight, this could seem rather odd. Though, if we take a look at the direct strain ratios determined in Table 7-3, we can see that for the transverse out-of-plane loading, the simulated in-plane fibre strain and composite strain are opposite in sign. This effect is pure caused by the difference in material properties between the optical fibre and the composite laminate.

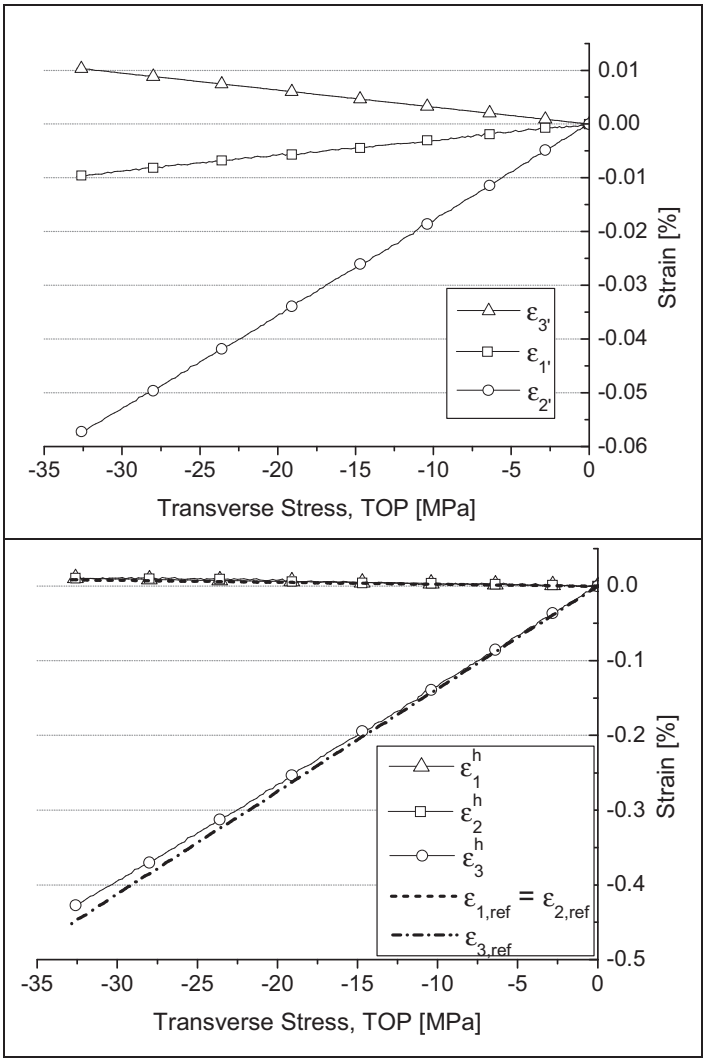

Figure 7-20: Calculated strains in the core of the optical fibre (top), and composite strains (bottom) for a $[90_2,0_2]_{2s}$ laminate and transverse stress through-the-thickness.

By using the general strain relationship of Equation 7-17 and filling in the calculated fibre strains ($\Delta\varepsilon_{3'}$, $\Delta\varepsilon_{1'}$, $\Delta\varepsilon_{2'}$) the three near field principal strains in the composite laminate ($\Delta\varepsilon_1^h$, $\Delta\varepsilon_2^h$, $\Delta\varepsilon_3^h$) are determined. The result of this calculation together with the simulated reference strains ($\Delta\varepsilon_{1,ref}$, $\Delta\varepsilon_{2,ref}$, $\Delta\varepsilon_{3,ref}$) are shown in the bottom plot of Figure 7-16. As expected for the cross-ply laminate, the out-of-plane transverse strain in the laminate is negative and the transverse in-plane and longitudinal strains in the laminate are small and positive. We can see that for this loading case the calculated composite strains match very well the simulated reference strains, which illustrates that the numerical determined TC-matrix is well-defined. Again, the reason that the multi-axial strains match better the simulated strains than in the case of the longitudinal loading, is because that for the out-of-plane transverse loading, the longitudinal strains in the laminate are very small. As such the errors in the calculation of the transverse strains of the optical fibre are kept small.

7. 4. 4. Resolution of the embedded sensor configuration using a stripped DTG®

The resolution of the embedded sensor configuration determines the minimal possible measurable composite strain shift. It is depending on the resolution of the FBG interrogator, the K-matrix of the optical fibre and the strain relationship between the sensor and the host material. To estimate the resolution on the multi-axial composite strains, $\Delta\varepsilon_1^h$, $\Delta\varepsilon_2^h$, $\Delta\varepsilon_3^h$, the following general formulation is used:

$$\left[\Delta\varepsilon^h\right] = TC \cdot K^{-1}\left[\Delta\lambda\right]. \qquad 7\text{-}19$$

When filling in the TC-matrix of the stripped optical fibre (Equation 7-13) and transposing the K-matrix coefficients of Equation 7-16, we obtain the following general formulation for an embedded sensor configuration with a stripped DTG®:

$$\begin{bmatrix}\Delta\varepsilon_1^h\\ \Delta\varepsilon_2^h\\ \Delta\varepsilon_3^h\end{bmatrix} = \begin{bmatrix}1 & 0 & 0\\ 0.77 & 7.85 & -1.36\\ 0.76 & -1.37 & 7.83\end{bmatrix}\begin{bmatrix}0.79 & 0 & 0\\ 0.73 & -0.12 & -0.27\\ 0.73 & -0.27 & -0.12\end{bmatrix}\begin{bmatrix}\Delta\lambda_{B2,1'}/\lambda_{B2,1'}\\ \Delta\lambda_{B1,1'}/\lambda_{B1,1'}\\ \Delta\lambda_{B1,2'}/\lambda_{B1,2'}\end{bmatrix} \qquad 7\text{-}20$$

Again a simple statistical error calculation is employed in analogy to the error estimation on the fibre strains (Section 7. 2. 4.) to calculate the variance ($Var(\left[\Delta\varepsilon^h\right])$), Equation 7-21, and the standard deviation $\sigma_{\Delta\varepsilon}$, on the calculated strain ($\left[\Delta\varepsilon^h\right]$), by assuming a certain variance on the wavelength shifts ($Var(\left[\Delta\lambda\right])$).

$$Var\left(\Delta\varepsilon_i^h\right)=\left(\left(TC\cdot K^{-1}\right)_{i,1}^2+\left(TC\cdot K^{-1}\right)_{i,2}^2+\left(TC\cdot K^{-1}\right)_{i,3}^2\right)Var\left(\left[\Delta\lambda\right]\right)\quad i=1,2,3 \quad 7\text{-}21$$

The standard deviation (i.e. error) on the calculated composite strains ($\left[\Delta\varepsilon^h\right]$) is then given by

$$\sigma_{\Delta\varepsilon,i}=\sqrt{Var(\Delta\varepsilon_i)}\,. \quad 7\text{-}22$$

The variance on the wavelength shift is determined by the wavelength resolution of the used FBG interrogator (FBG-scan X08 from FOS&S, [8]) and is equal for all wavelength shifts, $\Delta\lambda_{1,1'}$, $\Delta\lambda_{1,2'}$, $\Delta\lambda_{2,1'}$. The variance on the wavelength, $Var(\left[\Delta\lambda\right])=1\,pm$, and the estimated resolution, $\delta\Delta\varepsilon_i$ on the multi-axial fibre strains is given in Table 7-7.

Table 7-7: Resolution of the sensor configuration with a stripped DTG®.

	Standard deviation
Longitudinal $\delta\Delta\varepsilon_1$ [$\mu\varepsilon$]	0.8
Transverse in-plane $\delta\Delta\varepsilon_2$ [$\mu\varepsilon$]	9.0
Transverse out-of-plane $\delta\Delta\varepsilon_3$ [$\mu\varepsilon$]	9.0

The embedding of the optical fibre in the cross-ply laminate has no influence on the longitudinal resolution, but the error on the transverse strain readings increases significantly. The worse resolution in the transverse directions is caused by the mismatch between the relative low stiffness of the matrix (i.e. 6.3 GPa, Table 7-2) in the reinforcement layer in the 2 –and 3-direction, and the Young's modulus of the optical fibre (i.e. 72.4 GPa), hence the transverse strains in the composite are determined less accurate.

7. 5. TC-MATRIX OF A COATED DTG® EMBEDDED IN A CROSS-PLY LAMINATE: FE-ANALYSIS AND EXPERIMENTS

In this section, the material parameters of the coating material are varied and different TC-matrices are derived for a coated 80 μm DTG®. The influence of the variation of the coating parameters on the sensitivity of the *TC*-matrix is studied and discussed in detail for a transverse compression test, i.e. out-of-plane loading.

7. 5. 1. ORMOCER® coating properties

If we want to determine the strain relationship of the composite strain with the strains inside a coated optical fibre, we need to import in the FE-model the right material properties of the coating material. However, the exact properties of the coating material are unknown. According to the manufacturer the Young's modulus of bulk ORMOCER® cured on a flat plate is typical around 200 MPa. However, the UV curing conditions and the boundary conditions for bulk material and a thin coating layer on a fibre are difficult to compare. As such in Chapter 4 the author has already made an attempt to determine the Young's modulus of the ORMOCER® coating at different temperatures. From these experiments a clear trend is found in the temperature behaviour of the stiffness of the ORMOCER®; i.e. at higher temperatures the coating becomes weaker and at low temperatures it becomes stiffer. At room temperature, it is estimated that the coating has a stiffness of approximately 1.8GPa. This is 9 times stiffer than the value obtained from the manufacturer. It is believed that the real stiffness will lie somewhere in between these values. To be able to simulate the coating material in the used 3D model properly, we need to estimate the Poisson's ratio of the ORMOCER®. Unfortunately no exact data on these properties is available. In literature no identical ORMOCER® material is found, however, Papadogiannisa D.Y. et al. [31] examined the effect of temperature on the visco-elastic properties of an ORMOCER® dental composite, with trade name Admira®. The material is a hybrid composition of SiO_2, Barium Aluminium Silicate glass particles and an ORMOCER® adhesive/matrix [32]. Although, this composite material differs from the material used in this work, the investigations of Papadogiannisa D.Y are relevant to note, because similar effects of the material are noticed in this work. Their investigations show a much higher Young's modulus of the material (~12GPa at 21 °C), which is logical for a composition of silica particles and ORMOCER®, but the temperature dependency of the stiffness is similar as has been shown in this work. A decrease of the Young's modulus of approximately 40 % was reported for a temperature increase of 30 °C. In addition, they have investigated the Poisson's ratio of this ORMOCER® composite and found that the Poisson's ratio increases from 0.36 at 21 °C till 0.42 at 50 °C, which corresponds to an increase of more than 16 %. Additionally, the effect of humidity is investigated. Their results show that the stiffness decreases with more than 9 %, and that the Poisson's ratio increases with approximately 6 % when the ORMOCER® composite is wetted for 24h. These results clearly illustrate the sensitivity to temperature and humidity of the ORMOCER® material. It is believed that these effects are also present in the coated fibre in this work.

Because the exact ORMOCER® material parameters are unknown and a large scatter on the properties exists, including a large temperature and humidity dependency, the author has performed a small parametric study of the TC-matrix by changing the Young's modulus and Poisson's ratio of the coating material used in

the simulations. It is started from a high stiffness of 1.84 GPa which is estimated in Chapter 4 at room temperature and a high Poisson's ratio of 0.44. The combinations of the material properties which are used in the model to perform simulations are given in Table 7-8.

Table 7-8: Combinations of Young's modulus and Poisson's ratio for the coating used in the simulations

Young's modulus [GPa]	Poisson's ratios [-]			
1.84	0.44	0.32	-	0.1
1.5	-	0.32	0.15	0.08
0.8	-	0.32	0.15	0.08
0.2	-	0.32	-	0.08

The effects of the variation of the coating parameters on the strain transfer relationship between composite laminate and optical fibre is discussed in Section 7. 5. 2. . The study of the effect of the varied TC-matrix on the experimental results is discussed in Section 7. 5. 3. .

7. 5. 2. Effect of coating properties on the TC-matrix_a parametric study

The exact same procedure as discussed in Section 7. 3. is applied here to determine the 9 independent TC-coefficients. In order to study the effect of the coating of the embedded optical fibre on the strain transfer coefficients of the TC-matrix, the FE simulation on the three loading conditions as shown in Figure 7-21, is repeated for every combination of the Young's modulus and Poisson's ratio given in Table 7-8.

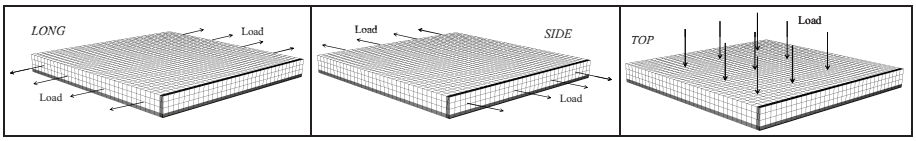

Figure 7-21: (a) Longitudinally applied load ('LONG'), (b) Transversely applied load in-plane ('SIDE'), (c) Transversely applied load out-of-plane ('TOP').

Before discussing the influence of the coating parameters on the complete TC-matrix, first, a comparison is given of the direct strain ratios of an embedded stripped optical fibre with the embedded coated optical fibre for several combinations of the coating properties.

7. 5. 2. a. Strain field disturbance of the fibre coating

When discussing the strain transfer principle (Section 7. 3. 1.), the optical fibre is compared with an inclusion in the material. A certain disturbance exists in the near strain field around the optical fibre which is influenced by the polymer (weak) coating material. To illustrate the effect of a fibre coating the simulated near strain field is analysed for both a non-coated and coated optical fibre. A coating with stiffness $E_c = 0.8$ GPa, and $\nu_c = 0.32$ is taken as an example. The FE-model

illustrating the strain disturbance inside the $[90_2,0_2]_{2s}$ laminate for the coated fibre, is shown in Figure 7-22:

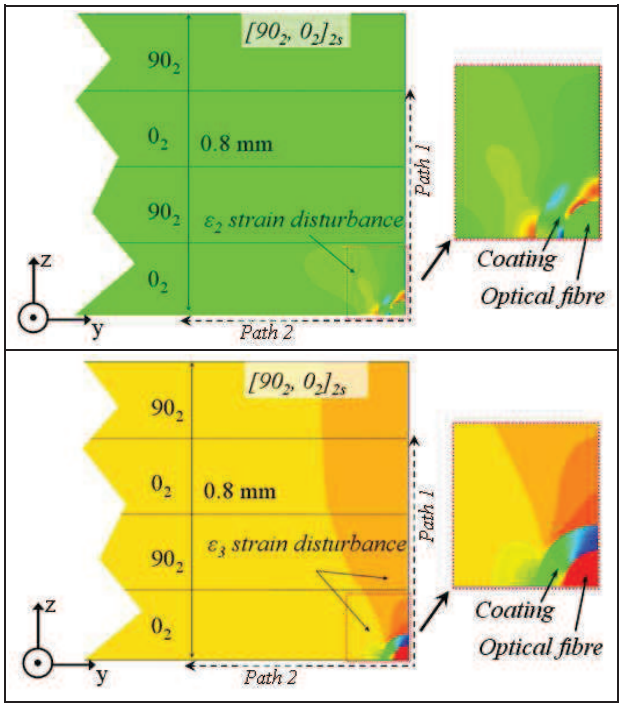

Figure 7-22: Transverse strain disturbance in the 2- direction (top) and 3-direction (bottom) for a cross ply laminate with a $[90_2,0_2]_{2s}$ stacking sequence, loaded in the transverse out-of-plane direction, with the coated optical fibre sensor embedded in the symmetry-planes of the laminate.

A transverse out-of-plane displacement is applied on the laminate, which induces a through-the-thickness strain of 0.1 %. The top and bottom image in Figure 7-22 show the strain disturbance in the 2-direction and 3-direction of the mid-plane composite layers, respectively. We notice that in both cases, there exists a “flower” shaped coloured pattern, which indicates that the strain field near the (coated) optical fibre is disturbed. We also notice that the coloured pattern inside the coating layer is changing as well, indicating that strain gradients exist in the coating. However, no such gradients are visible in the optical fibre area, which indicates that the strain along the cross-section of the optical fibre is constant. This confirms the statement of Kim et al. [10], see Section 7. 3. 1. , and prooves that the condition of a constant strain along the optical fibre cross-section is valid too for a coated fibre. From the colour contrasts in Figure 7-22, we can state that for a transverse out-of-plane loading the distortion in the in-plane strain (2-direction) is concentrated in the composite - coating interface and the coating – fibre interface at the side and on top of the optical fibre, respectively, and that the distortion in the through-the-thickness strain (3-direction) shows a ‘cloud-shaped’ colour pattern which starts at the optical fibre and moves towards the top-surface of the laminate. In the area towards the surface there is no gradient visible, but near the coating small bulges are present which arises in the coating.

The FE-software (Abaqus^{TM}) alows to draw paths along specific nodes (i.e. integration points) in the model. The strain values of the strain disturbance are obtained at these integration points. The two paths are indicated in Figure 7-22; Path 1 is drawn along the z-direction, i.e. through the thickness, and Path 2 is drawn along the y-direction of the symmetry-planes. The recorded strain values are presented in Figure 7-23 for a stripped and coated optical fibre. The distance in the y–and z-direction is plotted on the abscissa; the origin of the curves is put in the centre of the optical fibre. Note that the optical fibre has a radius of 40 µm and that the coating has an outer radius of 70 µm. Bullet number '1' represents the interface optical fibre/composite laminate for the stripped optical fibre, and the interface optical fibre/coating for the coated optical fibre. Bullet number '2' represents the interface coating/composite laminate.

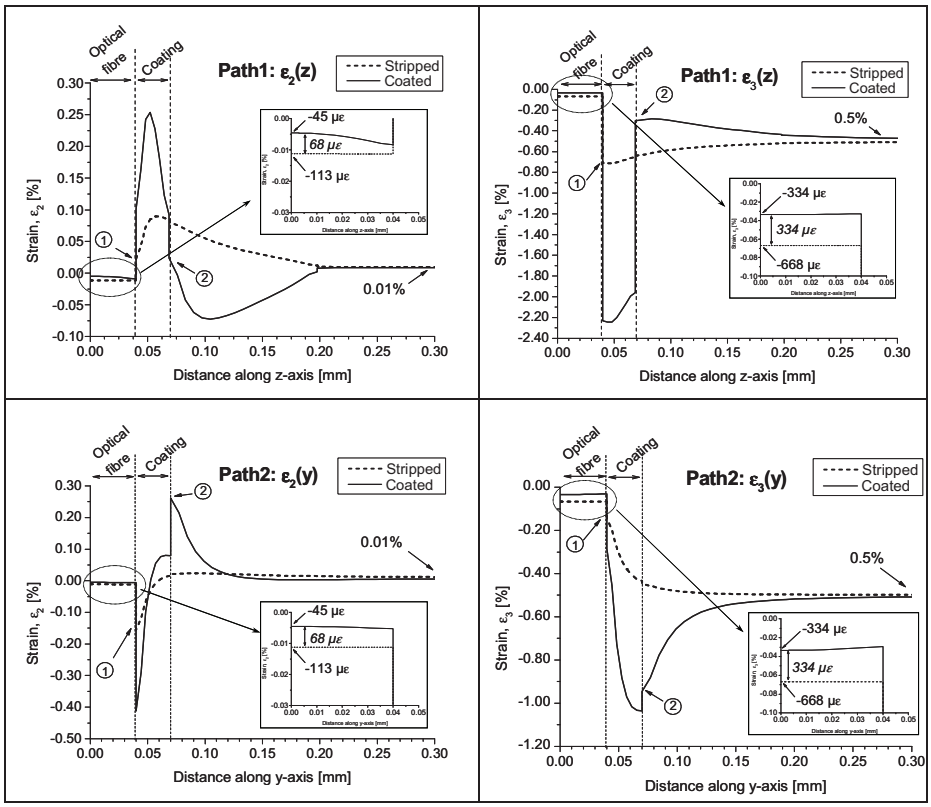

Figure 7-23: Strain values in the 2-direction (left) and 3-direction (right) along Path 1 (top) and Path 2 (bottom) for a stripped and coated optical fibre ($E_c = 0.8$ GPa, and $\nu_c = 0.32$), with the laminate loaded in the transverse out-of-plane direction.

We can see that at a distance larger than 0.25 mm, the through-the-thickness strains, ($\varepsilon_3(y,z)$) of the laminate is matching the applied compressive strain of 0.5 %, hence it confirms the results of Lekhnitskii [9], who prooved that at a distance of 3 to 4 diameters the strain approximates the far field strain (Section 7. 3. 1.). The in-

plane transverse strain $\varepsilon_2(y,z)$ in the composite is very small (~0.01 %) and is understood by the relative high stiffness in the in-plane directions of the a cross-ply lay-up.
From the curves of Path 1, we notice that the strain disturbance in the composite is opposite in sign. If we follow the path of Figure 7-23 (top-left) from right to left, for a stripped optical fibre the in-plane strain in the composite, $\varepsilon_2(z)$ increases first and then suddenly decreases near the interface '1', however, for a coated optical fibre it first decreases and then increases at the interface '2'. For the out-of-plane strain, $\varepsilon_3(z)$ (Figure 7-23, top-right) we notice the opposite effect; the compressive strain decreases for the stripped optical fibre and increases, i.e. the compressive strain becomes smaller, near the coated optical fibre. The latter effect is understood by the fact that the weaker coating deforms much more in the out-of-plane loading direction than the matrix and composite layers stacked on top of the optical fibre. This effect is clearly visible from the strains inside the coating layer, see Figure 7-23 (top-right), where the coating is compressed nearly -2.2 %, which is more than 4 times the applied compressive strain (-0.5 %) in the composite laminate.

Hence, from the results of Path 1, we can state that the coated optical fibre induces less composite distortion along the z-axis than the stripped optical fibre, however high compressive strain levels are reached in the coating layer.
If we take a look at Path2, again the opposite effect is noticed at the interfaces (number '1' & '2'), now the 'strain peaks" are higher at the coating / composite interface. This effect is clearly visible in Figure 7-23 (bottom-right), where the composite strain at the '2' interface is almost twice the applied strain. Hence, the optical fibre with coating induces higher distortion along the y-axis than the stripped optical fibre.
The induced out-of-plane, $\varepsilon_3(y,z)$ and in-plane, $\varepsilon_2(y,z)$ strain in the optical fibre, is shown in the insets in each graph. The values through-the-thickness in the fibre are a magnitudes smaller (~0.05 %) than the composite strain, and the in-plane strains in the optical fibre are opposite in sign (~-0.01 %). We observe that the strain in the coated optical fibre is smaller in magnitude than the strain in the non-coated fibre. The out-of-plane strain for the non-coated optical fibre is -668 με, which is 334 με lower than the strain in the coated optical fibre, and which is approximately 13 % of the applied strain in the laminate. For the coated optical fibre the strain transfer goes down to approximately 7 %. This shows that the coating will take most of the strain for its part and that the transfer of strain from the laminate onto the optical fibre is blocked by the coating. A similar behaviour is seen in the in-plane transverse direction $\varepsilon_2(y,z)$, where the compressive strain of the coated fibre is lower than the non-coated fibre, -45 με compared to -113 με, respectively.
The strains along Path 1 as well as along Path 2 clearly illustrate the "buffering" effect of the coating, i.e. large strain gradients are present in the coating layer and the induced transverse strains in the coated optical fibre are always smaller than the strains in the stripped optical fibre. Additionally, we see from the insets that the strain development in the in-plane transverse direction $\varepsilon_2(y,z)$, in the optical fibre with coating is not 100 % constant over the fibre radius. The effect is highest along Path 1, where the strain in the core of the optical fibre is -45 με and -84 με at the optical fibre – coating interface. The cause of the effect is not clear, most probably the large deformation and strain gradient in the coating layer is inducing a non-

homogeneous strain field on top of the optical fibre. This behaviour is, however, not detrimental for the further calculations in this work, and will further not be discussed.

The author has shown that the strain developments in the FE-model can learn us to understand better the interaction of an optical fibre with the composite material. Strain-concentrations are appearing near the optical fibre, which could be critical if concerning damage effects. In case of the out-of-plane strains along the y-direction, Figure 7-23 (bottom-right), where the strain at the interface of the composite and coating surface exceeds twice that of the applied strain, it is clear that care should be taken not to damage the composite. This information cannot be obtained from the transfer coefficients solely, hence, the investigation on the strain disturbance using FE-simulations is a must when considering damage initiations. However, this is not in the scope of the work and is a provender for further research.

By calculating the ratio between the strain in the optical fibre and the (far field) strain in the composite layer, it is possible to define the direct strain ratios or direct strain transfer coefficient. The calculated strain ratios of different combinations of coating material properties are given in Table 7-9, in the next sub-section.

7. 5. 2. b. The direct strain transfer coefficients

The direct strain transfer for each loading case is determined by measuring the three principal strains in the model in the optical fibre centre, and in the laminate without optical fibre. As shown in Figure 7-22, the strain values at a distance of 0.25 mm in the laminate layer, are equal to the applied strain in the laminate. Both methods provide the same strain ratios. In Table 7-9, the results of all loading cases are given for the coated optical fibre with a coating-stiffness of 1.84 GPa, 0.8 GPa and 0.2 GPa. For each stiffness, the Poisson's ratio is varied according to the values given in Table 7-8. The direct strain ratios of the fibre without coating (Table 7-3) are used as a reference.
From the values in Table 7-9, we see that the coating has no significant effect on the direct strain transfers in the 1-direction. In all cases the strain ratio between the sensor and host in the 1-direction is nearly 100 %, except in the case of the very weak coating with $E_c = 0.2$ GPa, $\nu_c = 0.32$ / $\nu_c = 0.08$ we notice a small decrease of the strain transfer when the laminate is loaded in the transverse directions. This is exactly the effect one would expect from the shear lag theory for a weak coating [19]. If the optical fibre is coated with a material with very low stiffness, less shear is transferred to the optical fibre and hence the longitudinal strain transfer is influenced. Additional to the strain ratios it is interesting to compare the strain values in the optical fibre. These values are not indicated in Table 7-9, however they are used to determine the strain transfer for each loading case. If we strain the laminate for instance with one percent in the longitudinal direction, the transverse strain in the non-coated fibre in the 2 –and 3-direction will be -0.0013 and -0.0018, respectively. For the coated fibre the values for the 2 –and 3-direction vary from -0.0013 to -0.0016 and -0.0017 to -0.0016, respectively, for a stiff coating versus a weak coating. These results confirm the statement before, that the embedded coated optical fibre in a cross-ply laminate behaves more in its natural

way (i.e. pure isotropic Poisson's effect) for a longitudinal loading condition than a non-coated fibre. Hence the induced birefringence effect during an axial strain measurement with a coated DTG®s is small.

Table 7-9: Comparison of the strain ratios for three loading conditions applied to a $[90_2,0_2]_{2s}$ laminate with embedded stripped optical fibre and embedded coated optical fibre, for different coating properties.

No coating. Loading direction	$\varepsilon_1^s / \varepsilon_1^h$	$\varepsilon_2^s / \varepsilon_2^h$	$\varepsilon_3^s / \varepsilon_3^h$
Longitudinal (LONG)	100.0%	986.6%	40.3%
Transverse in-plane (SIDE)	100.0%	12.4%	6.7%
Transverse out-of-plane (TOP)	100.0%	-116.6%	13.4%

$E_c = 1.84$ GPa, $\nu = 0.32$ / $\nu = 0.1$ Loading direction	$\varepsilon_1^s / \varepsilon_1^h$	$\varepsilon_2^s / \varepsilon_2^h$	$\varepsilon_3^s / \varepsilon_3^h$
Longitudinal (LONG)	100.0% / 100.0%	1023% / 1058%	39.2% / 39.44%
Transverse in-plane (SIDE)	100.1% / 100.0%	9.6% / 8.7%	6.1% / 5.3%
Transverse out-of-plane (TOP)	100.1% / 99.9%	-68.0% / -67.4%	10.1% / 9.2%

$E_c = 0.8$ GPa, $\nu = 0.32$ / $\nu = 0.08$ Loading direction	$\varepsilon_1^s / \varepsilon_1^h$	$\varepsilon_2^s / \varepsilon_2^h$	$\varepsilon_3^s / \varepsilon_3^h$
Longitudinal (LONG)	100.0% / 100.0%	1086% / 1116%	38.3% / 38.5%
Transverse in-plane (SIDE)	99.9% / 99.8%	6.4% / 5.5%	3.99% / 3.8%
Transverse out-of-plane (TOP)	99.9% / 99.7%	-47.1% / -34.2%	6.7% / 5.8%

$E_c = 0.2$ GPa, $\nu_c = 0.32$ / $\nu_c = 0.08$ Loading direction	$\varepsilon_1^s / \varepsilon_1^h$	$\varepsilon_2^s / \varepsilon_2^h$	$\varepsilon_3^s / \varepsilon_3^h$
Longitudinal (LONG)	100.0% / 100.0%	1169% / 1181%	37.2% / 37.3%
Transverse in-plane (SIDE)	99.6% / 99.6 %	2.4% / 2.0%	1.0% / 1.1%
Transverse out-of-plane (TOP)	99.6% / 99.5 %	-26.8% / -17.7%	2.5% / 2.1%

Compared to the stripped fibre, the strain transfers of the coated fibre in the 2 –and 3-directions are reduced when the laminate is transversely loaded. For the out-of-plane loading direction the change is most significant for the transverse in-plane ratio, $\varepsilon_2^s / \varepsilon_2^h$. When the stiffness of the coating is relatively high $E_c = 1.84$ GPa, the ratio is half the ratio of a stripped optical fibre. This indicates that the coating indeed acts as a buffer for transverse loads; which is obvious, because the coating

material is weaker than the optical fibre, and thus the coating material will deform more than the optical fibre when load is applied on the laminate.
The "buffering" effect of the coating for transverse strains has already been observed during curing of the composite laminates. As shown in Chapter 6, residual strains build up during the composite shrinkage process; the highest strains can be found in the transverse out-of-plane direction because the laminate exhibits the lowest stiffness in that direction. Comparing the spectra of the stripped and coated DTG® shown in Figure 7-24, the "buffering" effect is indeed visible. The peak separation for the coated sensor after curing is clearly smaller, hence, the induced birefringence in the core of the optical fibre is much lower. The same effect is noticed when the different embedded DTG®s are loaded in the out-of-plane direction of the laminate. The separation of the peaks at maximum loading is much more distinct in the case of the non-coated DTG®.

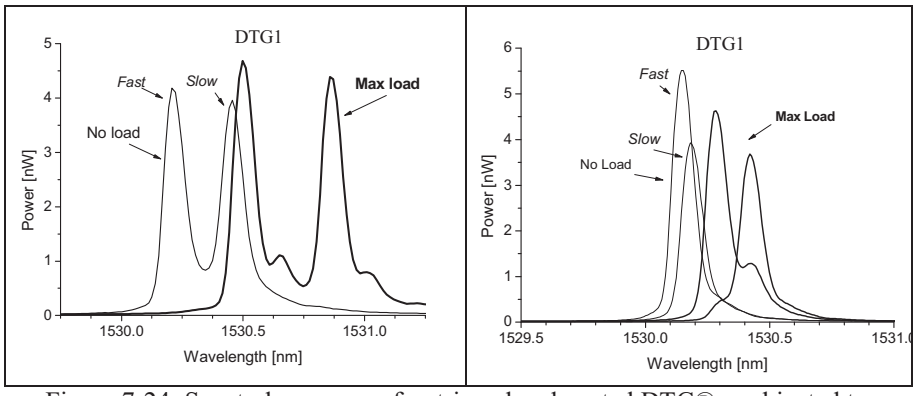

Figure 7-24: Spectral response of a stripped and coated DTG®s, subjected to a residual strain field after manufacturing (dashed line), and at maximum loading of a laminate in the through-the-thickness direction (solid line).

Note that if the coating material would have been weaker, the "buffering" effect would even have been more pronounced. To visualize this effect, the finite element calculations were executed using an embedded optical fibre with a weaker coating. By observing the values in Table 7-9 at the bottom for an embedded optical fibre with a weak coating, $E_c = 0.2$ GPa , we see that the strain ratios decrease for loads in the out-of-plane direction. The strain ratios even decrease further when the Poisson's ratio becomes smaller.
As for uncoated embedded optical fibres, coated embedded optical fibres show a transverse in-plane strain ratio $\varepsilon_2^s / \varepsilon_2^h$, if the laminate is loaded in the longitudinal direction, which is extremely high (>1000%). This means that the fibre in-plane transverse strain during axial loading will be 10 times that of the composite. If we apply for instance 1 % strain in the longitudinal direction of the laminate, the composite strain in the transverse in-plane direction will be $\sim -130 \cdot 10^{-6}$ and the fibre strain $\sim -1.3 \cdot 10^{-3}$. During axial loading, the low stiffness of the coating, allows the fibre to deform in a "free" manner (according to its Poisson's ratio, $\upsilon_f = 0.16$) in the transverse directions. If the stiffness of the coating would even go

to zero, the fibre is completely free to contract and the induced strains in the transverse direction would be $\sim -1.6 \cdot 10^{-3}$.
Remark that if the laminate is loaded in longitudinal direction, and the coated fibre can more or less behave in its natural way (i.e. extra induced transverse strains are blocked), the error in the axial strain calculated from the wavelength shift will be small for a coated DTG®. This advantageous property will be further elaborated in Chapter 8, in which coated DTG®s are used to measure longitudinal strains in thermoplastic woven fabrics during tension testing.

7. 5. 2. c. The total TC-matrix for the coated optical fibre

The TC-matrix of the composite material with coated optical fibre is examined by using Equation 7-23:

$$\begin{bmatrix} \Delta\varepsilon_1^h \\ \Delta\varepsilon_2^h \\ \Delta\varepsilon_3^h \end{bmatrix} = \begin{bmatrix} TC_{11} & TC_{12} & TC_{13} \\ TC_{21} & TC_{22} & TC_{23} \\ TC_{31} & TC_{32} & TC_{33} \end{bmatrix} \begin{bmatrix} \Delta\varepsilon_1^s \\ \Delta\varepsilon_2^s \\ \Delta\varepsilon_3^s \end{bmatrix}. \qquad 7\text{-}23$$

The different TC-matrices, shown in Table 7-10, are calculated using the combinations given in Table 7-8. In case the material properties of the optical fibre and the carbon composite are identical, the TC-matrix is given by the unity matrix, see the first TC-matrix in Table 7-10. Note that in the table, rows 2 till 5 are organized as such, that the coating stiffness decreases from top to bottom, and that the Poisson's ratio decreases from left to right.
If the foreign material in the composite has the same material properties, then the TC-matrix is given by the unity matrix. If the foreign material has different properties, the strain field is distorted (Figure 7-22) by the foreign inclusion. This is clearly seen in the TC-matrix of the stripped fibre. The diagonal TC_{ii} elements are 7.8 times greater than the elements of the unity matrix. We also notice from the other elements in row 2 and 3, that an interaction between the transverse and longitudinal strains of the host material and the "foreign" sensor exists. The individual elements change even more if a coating is added to the fibre. We see that for a stiff coating the TC-matrix does not significantly changes, however, we notice that there is a large difference between the TC-matrices of the stiff and the weak coating, with the clearest effect the strong increase of the diagonal TC_{ii} elements for the coating with lower stiffness. Higher numbers indicate that there is a stronger disturbance in the strain transfer between the host material and the sensor. Obvious, since the coating acts as a kind of barrier to transfer the strains (Figure 7-23), this effect will be higher for weaker coatings.

Table 7-10: All TC-matrices for the combination of Young's modulus and Poisson's ratio according Table 7-8

Identical properties $\begin{bmatrix} 1 & 0 & 0 \\ 0 & 1 & 0 \\ 0 & 0 & 1 \end{bmatrix}$	No coating $\begin{bmatrix} 1 & 0 & 0 \\ 0.77 & 7.85 & -1.36 \\ 0.76 & -1.37 & 7.83 \end{bmatrix}$	$E_c = 1.84$ GPa, $\nu_c = 0.44$ $\begin{bmatrix} 1 & 0 & 0 \\ 0.89 & 8.56 & -1.06 \\ 0.89 & -1.05 & 8.55 \end{bmatrix}$
$E_c = 1.84$ GPa, $\nu_c = 0.32$ $\begin{bmatrix} 1 & 0 & 0 \\ 1.15 & 10.27 & -1.31 \\ 1.16 & -1.29 & 10.31 \end{bmatrix}$		$E_c = 1.84$ GPa, $\nu_c = 0.1$ $\begin{bmatrix} 1 & 0 & 0 \\ 1.3 & 11.28 & -1.54 \\ 1.31 & -1.51 & 11.34 \end{bmatrix}$
$E_c = 1.5$ GPa, $\nu_c = 0.32$ $\begin{bmatrix} 1 & 0 & 0 \\ 1.28 & 11.19 & -1.39 \\ 1.29 & -1.36 & 11.24 \end{bmatrix}$	$E_c = 1.5$ GPa, $\nu_c = 0.15$ $\begin{bmatrix} 1 & 0 & 0 \\ 1.47 & 12.36 & -1.51 \\ 1.49 & -1.48 & 12.44 \end{bmatrix}$	$E_c = 1.5$ GPa, $\nu_c = 0.08$ $\begin{bmatrix} 1 & 0 & 0 \\ 1.49 & 12.48 & -1.55 \\ 1.51 & -1.51 & 12.56 \end{bmatrix}$
$E_c = 0.8$ GPa, $\nu_c = 0.32$ $\begin{bmatrix} 1 & 0 & 0 \\ 1.91 & 15.65 & -1.87 \\ 1.95 & -1.79 & 15.79 \end{bmatrix}$	$E_c = 0.8$ GPa, $\nu_c = 0.15$ $\begin{bmatrix} 1 & 0 & 0 \\ 2.33 & 17.95 & -1.69 \\ 2.38 & -1.59 & 18.12 \end{bmatrix}$	$E_c = 0.8$ GPa, $\nu_c = 0.08$ $\begin{bmatrix} 1 & 0 & 0 \\ 2.39 & 18.19 & -1.63 \\ 2.43 & -1.53 & 18.37 \end{bmatrix}$
$E_c = 0.2$ GPa, $\nu_c = 0.32$ $\begin{bmatrix} 1 & 0 & 0 \\ 6.03 & 44.9 & -5.41 \\ 6.19 & -5.05 & 45.54 \end{bmatrix}$		$E_c = 0.2$ GPa, $\nu_c = 0.08$ $\begin{bmatrix} 1 & 0 & 0 \\ 8.2 & 55.32 & -2.44 \\ 8.42 & -1.95 & 56.16 \end{bmatrix}$

7. 5. 3. Experimental results

Test sample and method

The exact same compressive loading experiment as discussed in Section 7. 4. 3. is repeated for a third composite laminate, but now an 80 µm DTG® with coating is tested. The composite laminate is identical to the laminates shown in Figure 7-17 and the test-coupons is prepared with metal blocks to apply compressive loading (Figure 7-18). The ORMOCER® coating has an outer diameter of approximately 140 µm. Similar to the laminates with stripped embedded DTG®s, the test-coupon is loaded in compression in the z-direction up to a maximum contact pressure of approximately 33 MPa. The longitudinal wavelength readings are obtained from the same test-samples with encapsulated DTG®s as used before.

Multi-axial strain measurements

The wavelength shifts of all embedded DTG®s as function of the compression loading are shown in Figure 7-25, left. Because the grating is coated, the birefringence effects induced in the core of the optical fibre are smaller compared to a stripped DTG®, i.e. the coated DTG® is less sensitive to transverse strains.

Because the peak separation after curing is not as pronounced as in the case of the stripped DTG®, a different approach using a polarization controller (Chapter 5) is used to record the individual wavelength shifts (fast and slow) during loading. The spectral response at zero load and at maximum load is shown in Figure 7-25 right. During compression loading the applied strain on the composite is negative in the z-direction. The wavelength shifts of the sensors are all positive, with the lowest shift found for the encapsulated DTG®s (~0.1nm) and the highest shift for the 'slow' Bragg peak (~0.22nm). The same effect is seen in the spectral response of the grating. The total Bragg spectrum shifts to longer wavelengths and the peak separation is increasing with applied pressure.

If we compare the response of the 'fast' and 'slow' peaks of the coated DTG® (Figure 7-25) with the stripped DTG® (Figure 7-19), at first sight the wavelength evolution of both sensors during the out-of-plane loading looks similar. However, a small difference exists, which is clearly visible if we apply Equation 7-16 (or Equation 7-18) to calculate the three principal strains in the core of the optical fibre. The result is plotted in Figure 7-26. The strains in the core of the coated DTG® react similar to the stripped DTG® (Figure 7-20, top), and the in-plane strain, $\Delta\varepsilon_{1'}$ and out-of-plane strain, $\Delta\varepsilon_{2'}$ shows a negative shift with applied stress. However, the magnitude of the transverse strains measured in the coated sensor is almost halved, which indicates that the transverse sensitivity for a grating coated with ORMOCER® is less than the transverse sensitivity of a stripped grating. This effect confirms the simulated strain developments in Figure 7-23.

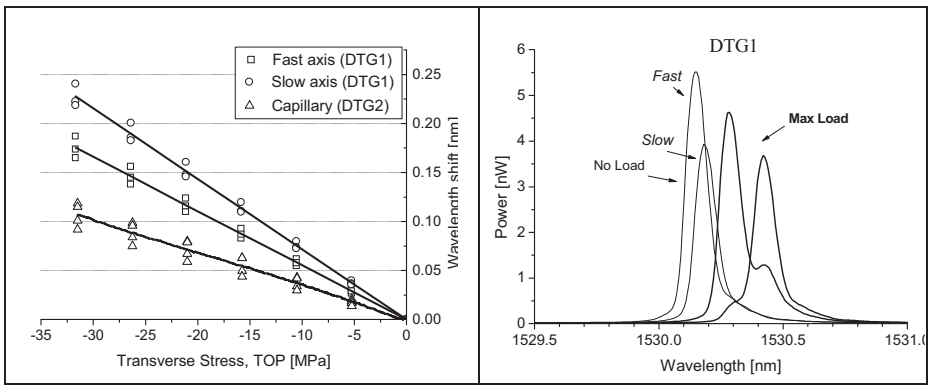

Figure 7-25: Wavelength shifts as function of the transverse stress applied on top of the sample (left), spectral response of DTG1 (coated) at zero load and maximum load, recorded using a polarization controller (right).

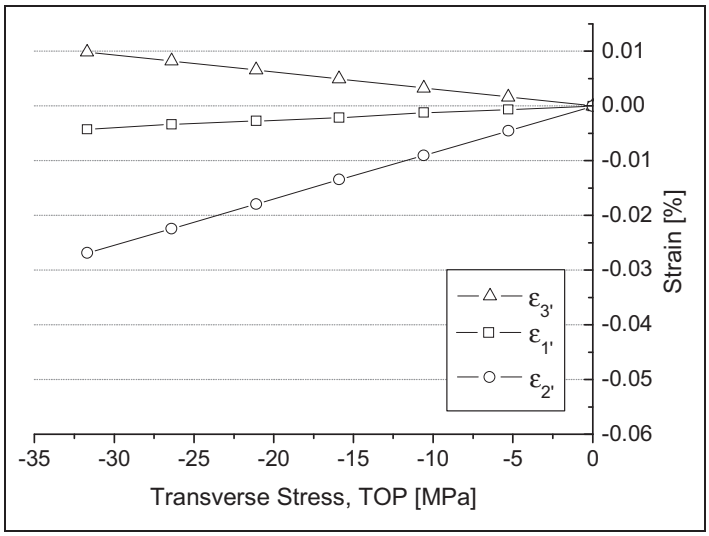

Figure 7-26: Calculated strains in the core of the coated optical fibre, for a $[90_2,0_2]_{2s}$ laminate and transverse stress through-the-thickness.

To calculate the composite strains from the measured wavelength shifts of the two DTG®s, the same procedure is used as shown in Section 7. 4. 3. . The relationship, to directly relate the wavelength shifts of the dual sensor configuration with the laminate strains, is derived from Equation 7-16 and Equation 7-15, and is given by

$$\begin{bmatrix} \Delta\varepsilon_1^h \\ \Delta\varepsilon_2^h \\ \Delta\varepsilon_3^h \end{bmatrix} = \begin{bmatrix} TC_{11} & TC_{12} & TC_{13} \\ TC_{21} & TC_{22} & TC_{23} \\ TC_{31} & TC_{32} & TC_{33} \end{bmatrix} \begin{bmatrix} 0 & 0 & 0.79 \\ -0.12 & -0.27 & 0.73 \\ -0.27 & -0.12 & 0.73 \end{bmatrix} \begin{bmatrix} \Delta\lambda_{B2,1'} / \lambda_{B2,1'} \\ \Delta\lambda_{B1,1'} / \lambda_{B1,1'} \\ \Delta\lambda_{B1,2'} / \lambda_{B1,2'} \end{bmatrix} \quad 7\text{-}24$$

Three times two different combinations of Young's modulus and Poisson's ratio are simulated, with the coating stiffness taken as $E_c = 1.84$ GPa , $E_c = 0.8$ GPa and $E_c = 0.2$ GPa . The results are shown in Figure 7-27. From these plots we observe that by using the TC-matrix of the stiffer coating $E_c = 1.84$ GPa , the calculated composite strain in the transverse out-of-plane direction, $\Delta\varepsilon_3^h$ is underestimated compared to the reference strain, however, good results are obtained for the in-plane transverse strain, $\Delta\varepsilon_2^h$. No significant effect is found for the stiff coating with a lower Poisson's ratio. If we lower the Young's modulus from $E_c = 1.84$ GPa till $E_c = 0.2$ GPa , we see that the effect is opposite. The transverse out-of-plane strain, $\Delta\varepsilon_3^h$ is now overestimated and additionally the in-plane transverse strain, $\Delta\varepsilon_2^h$ does not match anymore the reference strain. If we then lower the Poisson's ratio, the deviation is amplified and the in-plane transverse strain even changes sign.

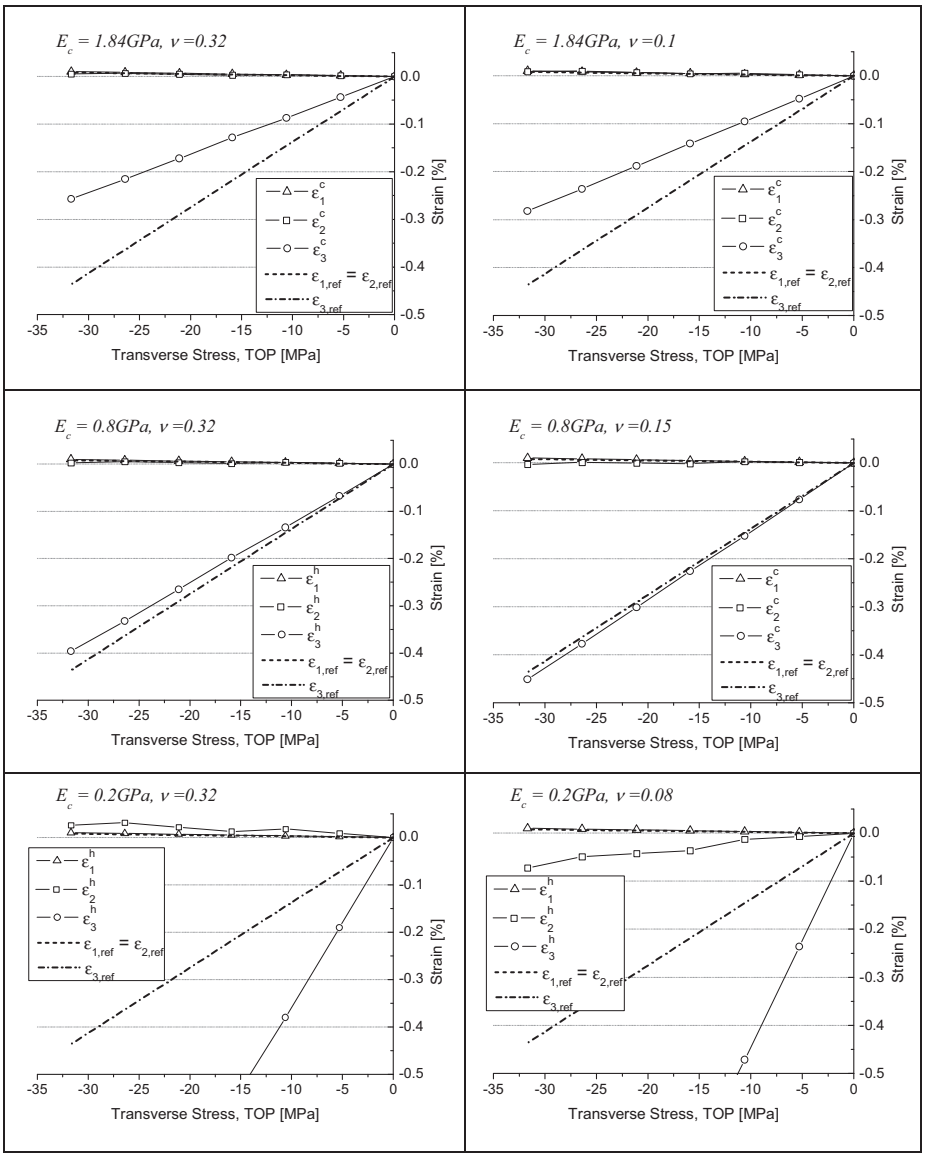

Figure 7-27: Composite strains for a $[90_2,0_2]_{2s}$ laminate and transverse stress through-the-thickness for a number of combinations of the coating material properties.

It is observed that by using the TC-matrix of the softer coating, large errors occur in the calculation of the transverse strain (Figure 7-27, bottom). However, if we apply the TC-matrix of the coating with stiffness $E_c = 0.8$ GPa , the results match much better (Figure 7-27, centre). The combination of $E_c = 0.8$ GPa, $\nu_c = 0.15$ induces a deviation of the in-plane transverse strain, $\Delta\varepsilon_2^h$ at higher stress levels. It is found that the combination of $E_c = 0.8$ GPa, $\nu_c = 0.32$ gives the optimal results. This plot is nearly identical to the plot shown in Figure 7-20, calculated by using a stripped

optical fibre. These results indicate that whenever the correct coating parameters are used, indeed the same experimental composite strains can be obtained from a stripped and coated DTG®. It is believed that the real material properties of the ORMOCER® coating are close to the optimal combination shown here. As such the material properties of the coating are found to be $E_c = 0.8$ GPa, $\nu_c = 0.32$. If we compare the optimal Young's modulus with the experimental determined Young's modulus of Chapter 4, we see that a large difference exists between both values. As discussed in Section 4.5.2.c., there is an uncertainty on the measured Young's modulus because of relative humidity changes, moreover the surrounding condition of the coating for an embedded optical fibre are different compared to an non-embedded optical fibre in free air. Therefore, the optimal material properties given above are believed to be more accurate than the measurements presented in Section 4.5.2.c. The optimal properties found here will further be used in the FE simulations in Chapter 8, when considering the thermoplastic CFRP laminates.

7. 5. 4. Resolution of the embedded sensor configuration using a coated DTG®

The exact same procedure as explained in Section 7. 4. 4. is applied to determine the resolution in case of the coated DTG®. Instead of using the TC-matrix of the stripped optical fibre, the optimal TC-matrix of the coating with $E_c = 0.8$ GPa, $\nu_c = 0.32$ (Table 7-10) is substituted in Equation 7-19. The following general formulation is obtained for an embedded sensor configuration consisting of a coated DTG®:

$$\begin{bmatrix} \Delta\varepsilon_1^h \\ \Delta\varepsilon_2^h \\ \Delta\varepsilon_3^h \end{bmatrix} = \begin{bmatrix} 1 & 0 & 0 \\ 1.91 & 15.65 & -1.87 \\ 1.95 & -1.79 & 15.79 \end{bmatrix} \begin{bmatrix} 0.79 & 0 & 0 \\ 0.73 & -0.12 & -0.27 \\ 0.73 & -0.27 & -0.12 \end{bmatrix} \begin{bmatrix} \Delta\lambda_{B2,1'} / \lambda_{B2,1'} \\ \Delta\lambda_{B1,1'} / \lambda_{B1,1'} \\ \Delta\lambda_{B1,2'} / \lambda_{B1,2'} \end{bmatrix} \quad 7\text{-}25$$

Once again a simple statistical error calculation is employed in analogy to the error estimation on the fibre strains (Section 7. 2. 4.) to calculate the variance ($Var(\left[\Delta\varepsilon^h\right])$) and the standard deviation $\sigma_{\Delta\varepsilon}$, on the calculated strain ($\left[\Delta\varepsilon^h\right]$), by assuming a certain variance on the wavelength shifts ($Var([\Delta\lambda])$).

$$Var\left(\Delta\varepsilon_i^h\right) = \left(\left(TC \cdot K^{-1}\right)_{i,1}^2 + \left(TC \cdot K^{-1}\right)_{i,2}^2 + \left(TC \cdot K^{-1}\right)_{i,3}^2\right) Var\left(\left[\Delta\lambda\right]\right) \quad i = 1,2,3 \quad 7\text{-}26$$

The standard deviation (i.e. error) on the calculated composite strains ($\left[\Delta\varepsilon^h\right]$) is then given by

$$\sigma_{\Delta\varepsilon,i} = \sqrt{Var(\Delta\varepsilon_i)} \,. \quad 7\text{-}27$$

The variance on the wavelength shift is determined by the wavelength resolution of the used FBG interrogator (FBG-scan X08 from FOS&S, [8]) and is equal for all wavelength shifts, $\Delta\lambda_{1,1'}$, $\Delta\lambda_{1,2'}$, $\Delta\lambda_{2,1'}$. The variance on the wavelength, $Var([\Delta\lambda]) = 1$ pm , and the estimated resolution , $\delta\Delta\varepsilon_i$ on the multi-axial fibre strains is given in Table 7-11.

Table 7-11: Resolution of the sensor configuration with a coated DTG® with $E_c = 0.8$ GPa, $\nu_c = 0.32$.

	Standard deviation
Longitudinal $\delta\Delta\varepsilon_1$ [$\mu\varepsilon$]	0.8
Transverse in-plane $\delta\Delta\varepsilon_2$ [$\mu\varepsilon$]	17.1
Transverse out-of-plane $\delta\Delta\varepsilon_3$ [$\mu\varepsilon$]	17.1

The transverse resolution for an embedded fibre with coating is very bad compared to the longitudinal strain resolution. The combination of a 'weak' coating and cross-ply laminate, with a low in-plane and low out-of-plane stiffness in the reinforcement layer because of the matrix material is causing this effect. The transverse strain transfer for a coated DTG®s is worse than for the stripped DTG® (Table 7-7), the error has approximately doubled, therefore the sensor configuration with the ORMOCER® coating is not suited to measure accurately transverse in-plane composite strains.

7. 6. CONCLUSIONS

In this chapter the focus has been on the multi-axial strain transfer from host material to the embedded optical fibre sensor. The author has shown that because of different material properties between the optical fibre and the (anisotropic) composite laminate, the strains measured in the embedded optical fibre differ from the strains present in the composite laminate. A dual sensor configuration, with one DTG® embedded normal in the laminate, and one embedded encapsulated DTG® which is free from external transverse strains is used to develop a multi-axial strain relationship between the optical fibre sensors and CFRP cross-ply laminates. It is shown that by performing FE simulations on a composite laminate model with embedded optical fibre, we can numerically determine the individual strain transfer coefficients. As such a strain transfer matrix, i.e. TC-matrix is determined for a stripped optical fibre, which is validated experimentally by subjecting different composite test-coupons to a well defined loading case. It is found that for a stripped optical fibre the error on the transverse strain measurements is the largest when loading the composite in the longitudinal direction. It is illustrated that the K-matrix, which defines the intrinsic multi-axial strain-optic relationship of an FBG, is strongly dependent on the axial strain component, hence, the strain resolution in transverse direction (~3.7 με) in these optical fibres is relatively low compared to the resolution in longitudinal direction (~0.8 με). As such, the errors on the calculated composite transverse strains are higher when the axial strain of the fibre

during loading is high. The transverse strain resolutions for an embedded DTG® without coating (~9 με) are worse compared to the non-embedded case. However, when the cross-ply laminates with stripped embedded DTG® are loaded transversely in-plane and out-of-plane, matching results are found for the measured composite strains and the numerical reference strains.
For the coated embedded DTG® a slightly different approach is used. By performing a parametric study on the material properties of the fibre coating in the model, it is illustrated that the strain transfer is influenced significantly. It is shown that when using less stiff coatings the elements in the TC-matrix tend to increase drastically, indicating that for such a coating material the transverse strain transfer is poor and that the disturbance of the near surrounding strain field is more severe in the transverse in-plane direction when the laminate is loaded out-of-plane. Several TC-matrices, defined using different combinations of the Young's modulus and Poisson's ratio of the coating material, are validated experimentally using the controlled out-of-plane compressive loading case. It is shown that for a specific combination of coating properties, the results of the compression test are optimal and the measured strains in the composite match the numerical strains. It is believed that these optimal coating properties represent the real material properties of the ORMOCER® coating. The strain resolution is determined for the embedded optical fibre with 'optimal' coating properties and obvious the transverse strain resolution (~17 με) is worse than for the stripped sensor. Therefore the sensor configuration with the ORMOCER® coating is not suited to measure accurately transverse in-plane composite strains.

The presented results clearly illustrate that by using embedded fibre Bragg gratings we are able to measure multi-axial strain fields in composites. However, because the numerical determined TC-matrix is very sensitive to the used material properties in the model, care has to be taken that the used material properties are accurate, not to induce large errors in the simulations. Certainly in the case of coated optical fibres, where the transverse strain transfers are poor. However, the embedded optical fibre with coating will be able to behave more or less natural when the laminate is loaded longitudinal. As such, only small external transverse effects appear on the grating and thus the errors in the longitudinal strain calculations are kept small. This advantageous property of the coated DTG®s will be used in Chapter 8, where the focus is on tensile testing experiments of thermoplastic test-coupons.

7. 7. REFERENCES

1. Luyckx, G., *Multi-Axial Strain Monitoring of Fibre Reinforced Thermosetting Plastics Using Embedded Highly Birefringent Optical Fibre Bragg Sensors.*, in *Materials science and engineering*. 2009-2010, PhD dissertation at Ghent University: Ghent.
2. Luyckx, G. and et al., *Multi-axial strain transfer from laminated CFRP composites to embedded Bragg sensor: I. Parametric study.* Smart Materials and Structures. **19**(10): p. 105017.
3. Voet, E. and et al., *Multi-axial strain transfer from laminated CFRP composites to embedded Bragg sensor: II. Experimental validation.* Smart Materials and Structures. **19**(10): p. 105018.

4. De Waele, W., *Structural monitoring of composite elements using optical fibres with Bragg-sensors.*, in *Department of mechanical construction and production*. 2001-2002, PhD dissertation at Ghent University: Ghent.
5. Guemes, J.A. and J.M. Menendez, *Response of Bragg grating fiber-optic sensors when embedded in composite laminates.* Composites Science and Technology, 2002. **62**(7-8): p. 959-966.
6. Luyckx, G., J. Degrieck, W. De Waele, W. Van Paepegem, J. Vlekken, and K. Chah. *Multi-axial fiber Bragg sensors for monitoring purposes*. in *ECCM 12 12 th European Conference on Composite Materials*. 2006.
7. Luyckx, G., W. De Waele, J. Degrieck, W. Van Paepegem, J. Vlekken, S. Vandamme, and K. Chah, *Three-dimensional strain and temperature monitoring of composite laminates.* Insight, 2007. **49**(1): p. 10-16.
8. FOS&S. Available from: http://www.Fos-s.com.
9. Lekhnitskii, S., *Theory of elasticity of an anisotropic body*. 1977, Moscow: MIR Publishers.
10. Kim, K.S., L. Kollar, and G.S. Springer, *A model of embedded fiber optic Fabry-perot temperature and strain sensors.* Journal of Composite Materials, 1993. **27**(17): p. 1618-1662.
11. Dasgupta, A. and J.S. Sirkis, *Importance of coatings to optical fiber sensors embedded in smart structures.* Aiaa Journal, 1992. **30**(5): p. 1337-1343.
12. Sirkis, J.S. and A. Dasgupta. *Optimal coating for intelligent structure fiber optical sensors*. in *Conf on Fiber Optic Smart Structures and Skins 3*. 1990. San Jose, Ca.
13. Cheng, C.C., Y.L. Lo, B.S. Pun, Y.M. Chang, and W.Y. Li, *An investigation of bonding-layer characteristics of substrate-bonded fiber Bragg grating.* Journal of Lightwave Technology, 2005. **23**(11): p. 3907-3915.
14. Li, W.Y., C.C. Cheng, and Y.L. Lo, *Investigation of strain transmission of surface-bonded FBGs used as strain sensors.* Sensors and Actuators a-Physical, 2009. **149**(2): p. 201-207.
15. Wan, K.T., C.K.Y. Leung, and N.G. Olson, *Investigation of the strain transfer for surface-attached optical fiber strain sensors.* Smart Materials & Structures, 2008. **17**(3).
16. Chang, C.C., M. LeBlanc, and S. Vohra. *Investigation of transverse stress measurements by using embedded fiber Bragg grating sensors subjected to host Poisson's effect*. in *Smart Structures and Materials 2000 Conference*. 2000. Newport Beach, Ca.
17. Cox, H.L., *The elasticity and strength of paper and other fibrous materials.* British Journal of Applied Physics, 1952. **3**(3): p. 72-79.
18. Jiang, Z.G., J.S. Lian, D.Z. Yang, and S.G. Dong, *An analytical study of the influence of thermal residual stresses on the elastic and yield behaviors of short fiber-reinforced metal matrix composites.* Materials Science and Engineering a-Structural Materials Properties Microstructure and Processing, 1998. **248**(1-2): p. 256-275.
19. Li, H.N., G.D. Zhou, L. Ren, and D.S. Li, *Strain Transfer Coefficient Analyses for Embedded Fiber Bragg Grating Sensors in Different Host Materials.* Journal of Engineering Mechanics-Asce, 2009. **135**(12): p. 1343-1353.

20. Fan, Y. and M. Kahrizi, *Characterization of a FBG strain gage array embedded in composite structure.* Sensors and Actuators a-Physical, 2005. **121**(2): p. 297-305.
21. Luyckx, G., E. Voet, W. De Waele, W. Van Paepegem, J. Degrieck, and J. Vlekken. *Strain monitoring of FRP elements using an embedded fibre optic sensor*. in *Advances in Science and Techology*. 2008.
22. Voet, E., G. Luyckx, and J. Degrieck. *Response of embedded fibre Bragg gratings: strain transfer effects*. in *Proceedings of OFS 20*. 2009. Edinbrugh, UK.
23. Bosia, F., P. Giaccari, J. Botsis, M. Facchini, H.G. Limberger, and R.P. Salathe, *Characterization of the response of fibre Bragg grating sensors subjected to a two-dimensional strain field.* Smart Materials & Structures, 2003. **12**(6): p. 925-934.
24. Prabhugoud, M. and K. Peters, *Finite element model for embedded fiber Bragg grating sensor.* Smart Materials & Structures, 2006. **15**(2): p. 550-562.
25. Kollar, L.P. and R.J. Van Steenkiste, *Calculation of the stresses and strains in embedded fiber optic sensors.* Journal of Composite Materials, 1998. **32**(18): p. 1647-1679.
26. Beitz, W. and K.-H. Küttner, *Dubbel: Handbook of mechanical engineering*. 1994: Springer-Verlag.
27. Pinnow, D., *Elastooptical Materials*, in *Handbook of Lasers*, R.J. Pressley, Editor. 1971: Cleveland (OH).
28. Eaton, N.C., R.C. Brew, and H. Geiger, *Finite-element stress and strain analysis in composites with embedded optical fiber sensors.* Smart Materials & Structures, 1995. **4**(2): p. 113-117.
29. ABAQUS, *ABAQUS: User's Manual*. 2002, New York: Hibbit, Karlsson & Sörensen inc.
30. ASTM, *D3039: Standard Test Method for Tensile Properties of Polymer Matrix Composite Materials* 2002: USA.
31. Papadogiannisa, D., Y., R. Lakesb, S. , Y. Papadogiannis, G. Palaghiasd, and M. Helvatjoglu-Antoniades, *The effect of temperature on the viscoelastic properties of nano-hybrid composites.* Dental materials, 2008. **24**: p. 257-266.
32. ISODENT. Available from: http://www.dentaltroef.nl/nasl_voco_admira.htm.

Chapter 8 MECHANICAL AND THERMAL TESTING OF THERMOPLASTIC CFRPS

8. 1. INTRODUCTION

In the previous chapters and from the mechanical testing on the thermoset CFRP, it is shown that we are capable of accurately measuring (multi-axial) strain with embedded DTG®s. As discussed in Chapter 6, the thermoplastic woven fabric or Cetex®, is a high performing composite which exhibits a complex (residual) internal strain field due to the woven structure. The complex residual strain field induces non-uniform strains in the optical fibre and causes the Bragg peak to distort. Moreover, because of the warp and weft yarn interlacing pattern (Figure 8-1), and PPS matrix pockets, a complex strain distribution arises in the material if the composite is loaded.

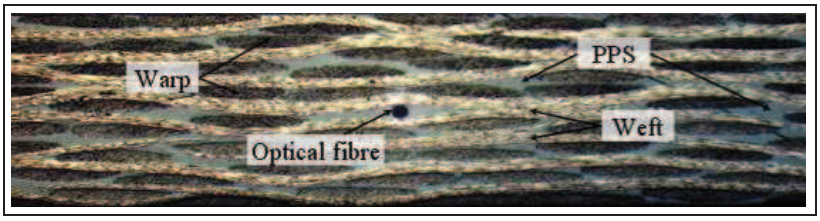

Figure 8-1: Cross-section of a $[(0,90)]_{4S}$ stacked Cetex® laminate with warp and weft yarn interlacing pattern and embedded optical fibre in the centre.

This chapter will not focus on the (complex) multi-axial strain field, but it is the purpose to investigate the longitudinal (in-situ) strain distribution, and to study the (permanent) deformation of the thermoplastic carbon-PPS woven fabrics by using embedded DTG®s during tension-tension fatigue testing at strain levels up to 0.5 % and tensile testing up to failure (approximately 1 % strain). As mentioned in Chapter 6, care has to be taken when interpreting the sensor (spectral) response, faulty conclusions on the strain results are easily drawn. The local internal composite strain field is evaluated, therefore, the spectral response of the embedded DTG®s is examined in detail during and after loading (Section 8. 2.). Other researchers have already used similar approaches; mostly the experimental spectral response to non-uniform strain fields is validated using simulated Bragg spectra where the grating is considered as an initially non-uniform grating subjected to a uniform strain field [1-2], or to simulate the response of the Bragg grating to damage effects and different crack lengths [3]. In [4] the spectral and local Bragg wavelength evolutions are examined for an FBG partially embedded in cylindrical epoxy specimens. An Optical Low Coherence Reflectometry (OLCR) – based technique [5] is used to interrogate the FBG to obtain measurements of the local Bragg wavelength distribution due to non-uniform strain effects. The OLCR based technique is, however, not applied in this work. These researches confirm that we can determine local (microscopic) strain distributions along the length of the grating from the full distorted Bragg spectrum.

In this work the author will use digital image correlation (DIC) and meso-FE simulations to validate the minimum and maximum strain readings determined from the distorted peaks.
The mechanical loading methodology used in this chapter is the key to gather the necessary sensor output from the embedded DTG®. It consists of repetitive progressive (quasi-static) loading cycles, alternated with fatigue loading cycles (Section 8. 2.). Such a loading scheme allows to perform measurements at specific intervals, i.e. after a certain amount of loading cycles, or even to perform testing at specific load levels, during which the linear polarization angle of the light coupled in the fibre is controlled (Chapter 5). It is found that this method is well suited to characterize the long term behaviour of composite CFRP laminates in lab conditions. Additional to the mechanical testing, a detailed temperature test is performed on a number of test-coupons to investigate the residual strain release and annealing effects during thermal cycling (Section 8. 3.). Moreover, the CTE of the laminates is determined using surface mounted and embedded DTG®s.

8. 2. MECHANICAL TESTING

In this section, the local strain distribution (Section 8. 2. 4.) and the global (macroscopic) strain measurements (Section 8. 2. 5.), obtained from the spectral response of the DTG®s will be elaborated. For the local (microscopic) strain measurements, the results of embedded and surface mounted DTG®s are compared with the surface strain profile experimentally obtained using digital image correlation (DIC) and numerical (inner and outer) strain distributions computed using meso-scale FE simulations. Additionally, the fatigue characteristics, such as stiffness degradation (Section 8. 2. 5.) and permanent strain measurements (Section 8. 2. 6.) of the $[(0,90)]_{4S}$ -and $[(90,0)]_{4S}$ stacked laminates are mapped. Finally, in analogy to the measurements of the (residual) transverse strain difference in Chapter 6, detailed polarization testing is performed during loading to investigate the transverse differential strains (Section 8. 2. 7.).

8. 2. 1. Preparation of test-coupons

To investigate the strain response of the thermoplastic CFRP, test-coupons according to the ASTM D3039 standard [6] are cut from larger Cetex® plates, see Section 6.5 and Table 6-6 for a complete inventory of all produced test-samples. Before cutting of the test-coupons small PEI glass fibre reinforced (GFRP) composite end-tabs, with thickness 1.5 mm, are fixed according to a prescribed procedure of TenCate advanced composites [7], see Figure 8-2, top. Not many adhesives are suited to stick to the PPS material and last during fatigue testing. To properly fix the GFRP end-tabs on the carbon-PPS a two-component epoxy adhesive (Hysol 9394, from Henkel-Loctite) is used. A small mass fraction of glass pearls (Ø100 µm - 200 µm) is added to the mixture, to obtain a uniform layer thickness of epoxy between the GFPR end-tab and the composite surface (Figure 8-2, bottom). After curing of the epoxy adhesive, the composite plate is cut into test-coupons (Figure 8-3). In this way, both the $[(0,90)]_{4S}$ ('in-phase') as well as the $[(90,0)]_{4S}$ ('out-of-phase') test-coupons, consisting each of eight semi-pregs in total (thickness 2.4mm), are prepared. The optical fibres are always embedded in the mid-plane and are aligned along the x-axis of the test-coupons.

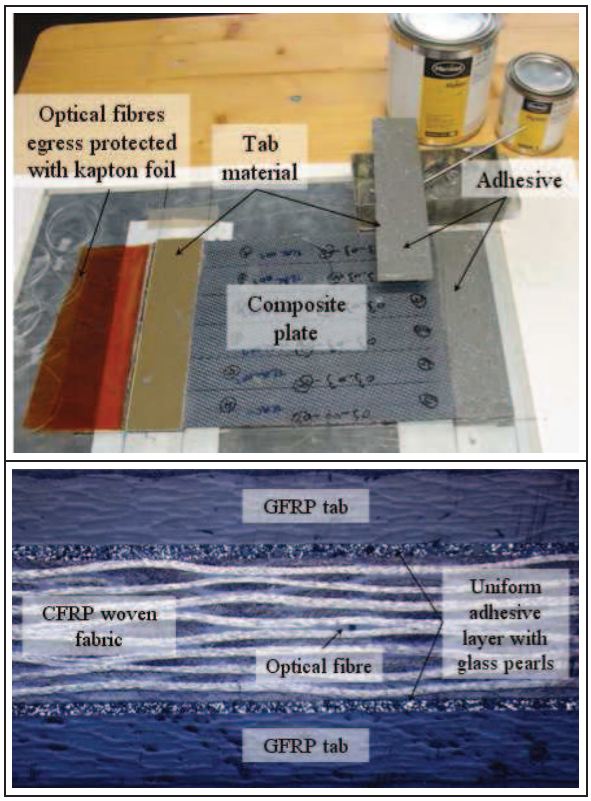

Figure 8-2: Preparation of the GFRP end-tabs on the thermoplastic CFRP plate (top), cross-section of a test-coupon with end-tabs and uniform adhesive layer (bottom).

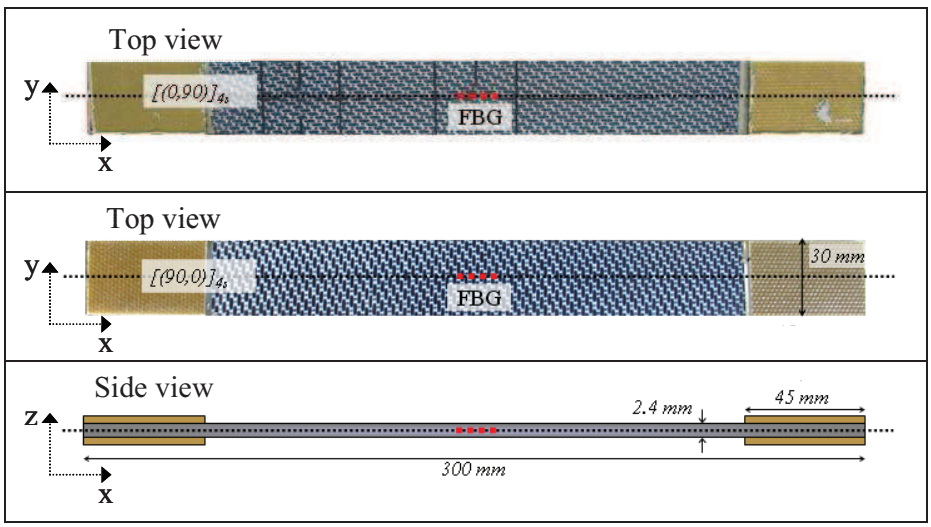

Figure 8-3: Example of an in-phase (top) -and out-of-phase stacked (middle) test-coupons with embedded fibre Bragg gratings in the mid-plane (bottom).

In Figure 8-3, a picture of the two differently stacked test-coupons is shown. The different stacking sequences are recognized by their typical surface texture. If we look at the black grains on the surface of the specimens we see that, in the case of a $[(0,90)]_{4S}$ stacked test-coupons (top picture) the warp yarns are visible on the composite surface and in the case of the $[(90,0)]_{4S}$ stacking (bottom picture) the weft yarns are visible, with the warp and weft yarns aligned along the 0°-direction (x-axis) and 90° axis, respectively.

Macroscopically, both types of plates should have identical mechanical properties (Table 6-4 and 6-5). However, as already mentioned in Chapter 6, the local strain distribution in the mid-plane area around the embedded DTG® is different, see Figure 8-4 and Figure 8-5.

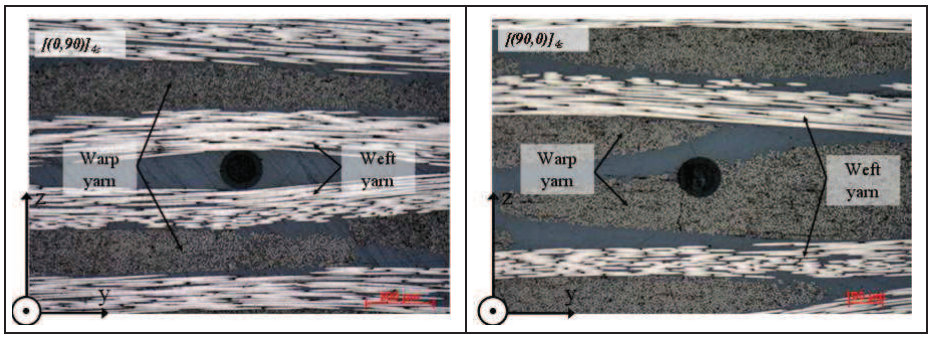

Figure 8-4: Optical fibre embedded in a symmetrical stacked woven fabric laminate: $[(0,90)]_{4S}$ 'in-phase' stacking (left), and $[(90,0)]_{4S}$ 'out-of-phase' stacking (right).

In the mid-plane (i.e. symmetry plane) the semi-pregs in the $[(0,90)]_{4S}$ stacking will touch the optical fibre mainly with the 90° oriented carbon bundles, i.e. weft yarns (Figure 8-4, left) and in the $[(90,0)]_{4S}$ stacking the optical fibre will be integrated in the 0° oriented carbon bundles, i.e. warp yarns (Figure 8-4, right). In Figure 8-5 a schematic representation is given of the side view of the optical fibre and FBG embedded in between the two mid-plane semi-preg layers of each lay-up. The length of the unit-cell is indicated as well. The difference between the two lay-ups is clear; in Figure 8-5, top, the fibre is mainly embedded between the weft yarns and in Figure 8-5, top the optical fibre is mainly embedded between the warp yarns. Although macroscopically the laminates have identical properties, it is obvious that the local mid-plane strain distribution along the length of the unit-cell and the embedded FBG is different in both lay-ups. Note that the schematic drawing in Figure 8-5 depicts a perfect stacking. Such a perfect stack, however, is never realised in practise but it demonstrates the difference in the mid-plane area.

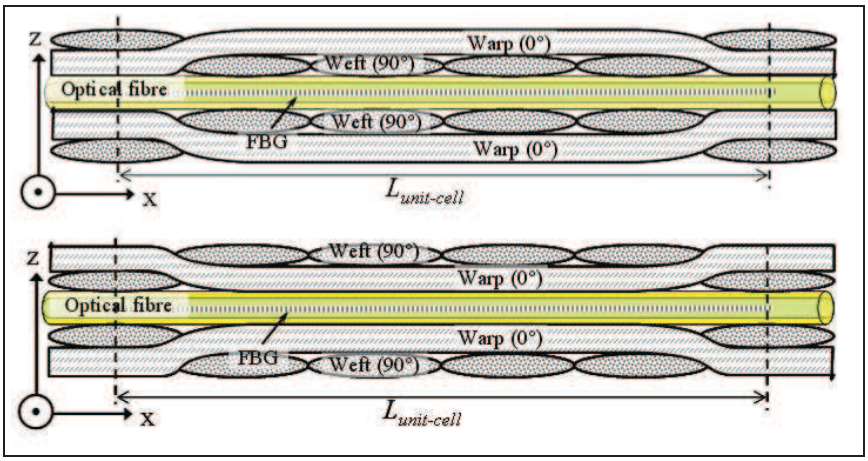

Figure 8-5: Side view of the optical fibre embedded in a symmetrical stacked woven fabric laminate: $[(0,90)]_{4S}$ 'in-phase' stacking (top), and $[(90,0)]_{4S}$ 'out-of-phase' stacking (bottom).

In some of the experiments additional surface mounted DTG®s are used to measure the longitudinal applied strain. To fixate the surface mounted DTG®s, the author has used a methodology developed by FOS&S [8]. With regard to the specimen preparation, the method is similar to the fixation of electrical strain gauges. Grinding paper and alcohol are used to prepare the specimen and degrease the specimen and sensor, respectively. Next, a fixation method is applied based on a *UV-curable glue* and a *sensor pad* (Figure 8-6, left), to position the optical fibre (i.e. sensor). First, the UV curable glue is spread along the sensor zone (approximately 30 mm x 8mm) and the sensor is positioned manually using the UV transparent sensor pad. Then, the optical fibre is gently pushed against the specimen by using the glass plate and in the same time a first UV pre-cure is applied, by illuminating the location of the sensor zone, through the UV transparent pad, for approximately 30 seconds. After the pre-cure, the glue has become stiff, and the sensor pad can be removed to apply a post-cure by illuminating the sensor zone for approximately 5 minutes. The sensor is now fixed to the specimen. Finally, to protect the optical fibre from being ripped off, it can be finished at both sides of the sensor zone using an instant adhesive (e.g. X60 from HBM, see Figure 8-9) or simply an adhesive tape (Figure 8-6, right).

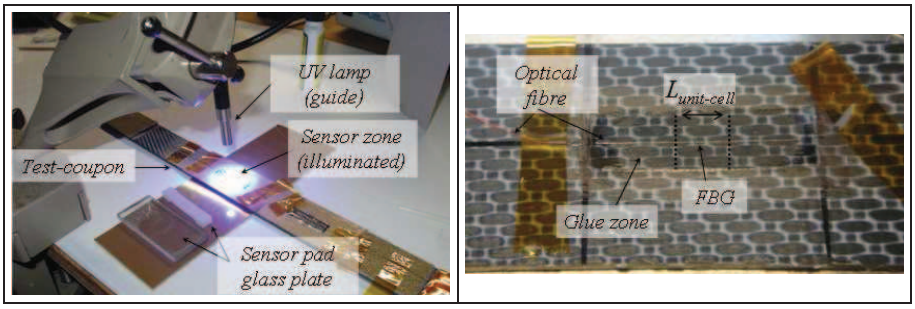

Figure 8-6: Preparation of surface mounted DTG® on the Cetex® test-coupons, applying the methodology of FOS&S [8] with a UV-curing system and sensor pad (left), result of a fixated DTG® (right).

Note that, to ensure accurate surface strain measurements, it is important that the position of the FBG in the optical fibre is well known, to ensure that the glue zone covers the whole sensor length. The position of the DTG®s used in this work are marked in the draw tower process with two black dots on the coating surface, with the DTG®s positioned in the centre of the marking. To check this, the author has used a heat-wire to detect the exact position. The DTG®s have a grating length of 8 mm and they are positioned exactly in the middle of the sensor zone. Remark that when measuring the strain distribution of a textile composite, the size of the unit cell has to be considered. It has been stated by Lang and Chou [9] that the sensor should at least be one unit cell long (or width). The DTG®s (embedded and surface mounted) used here are typical 8 mm long, which is slightly longer than the unit-cell size (i.e. 7.4 mm [10]), hence, the strain envelope along the length of the unit-cell is completely covered by the sensor (Figure 8-10, right).

Different methods are used to investigate the strain fields in both types of laminates. First an introduction of the test setup and the applied experimental method is explained.

8. 2. 2. Mechanical test setup

The specimens are loaded in longitudinal direction by using an INSTRON hydraulic test-bench 8801 (Figure 8-7). The applied experimental method to investigate the deformation of the composite laminates uses repetitive *progressive loading cycles* (quasi-static), which are *alternated* with *dynamic (fatigue) cycling* at 5Hz (tension – tension) in between the successive progressive quasi-static tests (Figure 8-7-right). The loading scheme typically followed during testing is shown in Figure 8-8. The first and second cycle are quasi-static followed by fatigue tension-tension cycling at 5 Hz. Intermediate quasi-static cycles are performed to monitor the permanent strain as function of the amount of cycles. Typically at the end of the fatigue cycling a final quasi-static cycle is performed.
During the quasi-static progressive loading cycle, the load level is hold for a period of time to perform full spectral analysis using the (static) FBG-scan X08 (typical 90 seconds are used when more than one sensor is recorded). Each time after a certain load level, the sample is unloaded and a measurement is performed at zero loading before going to higher wavelengths. This procedure is repeated for gradually increasing load levels, therefore, it is referred to as ‘repeated progressive loading’. In analogy to standard quasi-static loading, where a slow but continuous increasing load is applied, we are able to evaluate the local strain distribution or global strain as function of the applied stress (e.g. stress-strain analysis), which provides similar results as standard tensile stress-strain plots. But more important, the unloading sequences allow comparing the measurements after each applied loading level, also referred to as the ‘subsequent zero loading’. These reveal possible permanent deformations (longitudinal and transverse) with respect to the initial readings, i.e. before any loading has been applied. The results of these measurements provide very useful information on the load level at which permanent deformation is initiated in the composite.

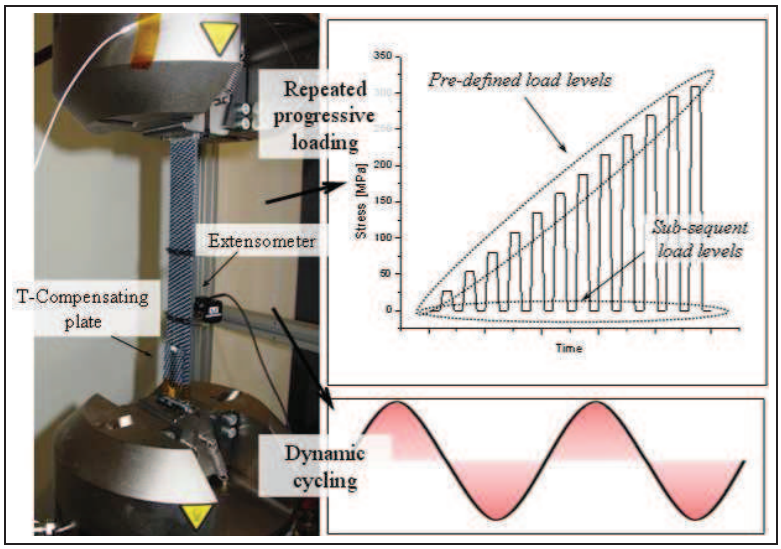

Figure 8-7: Clamped test-specimen (top-left), schematic progressive load cycles and dynamic sinusoidal loading actuation (top-right).

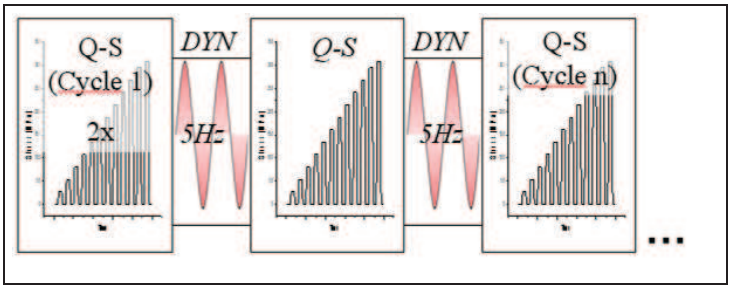

Figure 8-8: Loading scheme with Quasi-Static (QS) and Dynamic (DYN) tension-tension loading cycles (bottom).

In most of the applied loading schemes, the samples are loaded until maximum 300MPa, corresponding to approximately 0.5% longitudinal strain, except in Section 8. 2. 4. , where the laminates are strained up to more than 1 % to initiate damage. A surface mounted electrical *extensometer* is used in all experiments to serve as a *reference* for the global applied longitudinal strain. To compensate for thermal induced strains during testing, the author has used a temperature compensating plate with a surface mounted DTG®, see Section 8. 2. 3. . The tensile testing scheme is automated and during testing the optical recorded data, the load from the load-cell, and the strain from the extensometer is synchronized.

8. 2. 3. Temperature compensation

To calculate the longitudinal strain of the embedded DTG®s the logarithmic approach elaborated in Chapter 4 (Equation 4-12, Section 4.4.1a), is used. To measure the strain independent of environmental temperature fluctuations, the author has used a temperature compensating plate (T-compensating plate) with a cantilever design (Figure 8-9, left). A DTG®s is fixated on the surface of the T-

compensating plate by using the former described method (Section 8. 2. 3.). The plate is then fixed on the test-coupon by use of some adhesive tape (Figure 8-9, right). The cantilever design ensures that no strain is applied on the T-compensating plate, hence only thermal strain fluctuations are measured by the surface mounted DTG®. Note that the T-compensating plate will measure mainly environmental temperature fluctuations. Because the author applies quasi-static testing cycles the heat induced because of cycling is neglectable. Therefore, we can state that the method is applicable and accurate enough, without further need of accurately measuring the generated heat inside the sample.

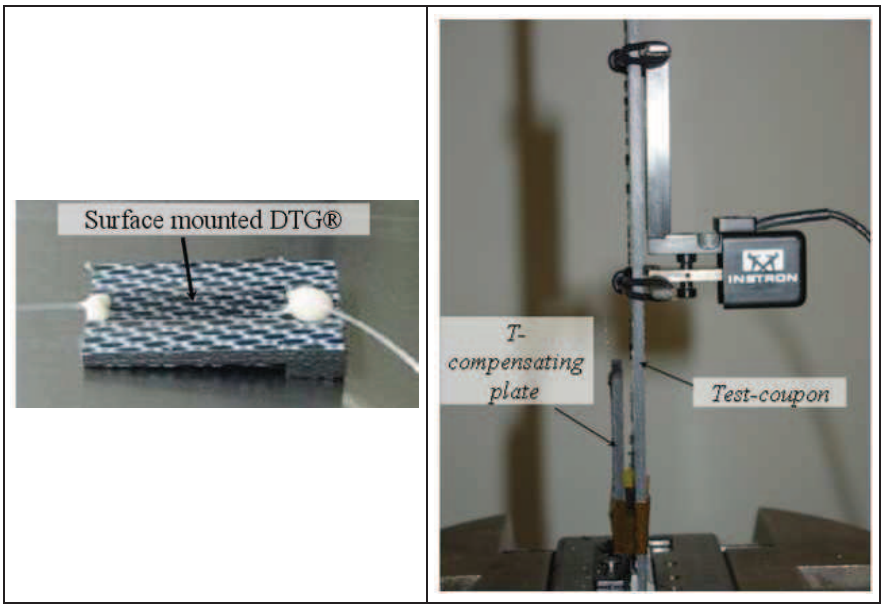

Figure 8-9: Temperature-compensating plate (cantilever-design) with surface mounted DTG® (left), mounted T-compensated plated on top of specimen (right).

The standard strain calculation formalism of Chapter 4 (Equation 4-10) is modified and a temperature compensating term is added. The equation used to calculate the T-compensated strain is given by

$$\Delta\varepsilon_{3'} = \frac{\left(\ln\frac{\lambda_\varepsilon}{\lambda_{\varepsilon,0}} - \ln\frac{\lambda_T}{\lambda_{T,0}}\right)}{S_\varepsilon} = \frac{\left(\ln\frac{\lambda_\varepsilon}{\lambda_{\varepsilon,0}} - \ln\frac{\lambda_T}{\lambda_{T,0}}\right)}{0.777}, \qquad 8\text{-}1$$

with $\lambda_{\varepsilon,0}$ and $\lambda_{T,0}$ the wavelength at the start of the measurement of the strain sensor and the temperature compensating sensor, respectively, λ_ε and λ_T the respective measured wavelengths during testing, and $S_\varepsilon = 0.777$ the calibrated strain gauge factor determined in Chapter 4.

It should be noted that there are residual and transverse strains acting onto the embedded sensor. However, as discussed in Chapter 7, the ORMOCER® coating acts as a 'buffer' and so the influence of transverse effect on the longitudinal strain

is very small during longitudinal testing. The FE- simulations support this assumption as during loading the transverse strains in the composite are about one order of magnitude smaller (and opposite in sign) than the longitudinal composite strains [10]. In Section 8. 2. 7. , the author will further investigate the transverse strain differences in the optical fibre during tension loading of the test-coupons. It will be shown that the transverse strain state change during longitudinal loading is small, therefore, the error on the (relative) longitudinal strain calculation is neglected in further calculations .

8. 2. 4. Evaluation of the local strain distribution inside Cetex®

Satin woven composites have a regular weave pattern and can be seen as a series of connected unit cells (i.e. repetitive pattern, see Section 6.3.2, Figure 6-15) with a definite length and width. Over the length and width of one unit cell, local strain fields can vary significantly due to the yarn interlacing pattern [9-11]. As shown in Chapter 5 and 6 the spectra of the embedded DTG®s is sometimes severely distorted, because of the local (residual) strain distribution. By using FBGs (surface or embedded) one is in principle able to measure the local composite strain variations. If a fibre Bragg grating is strained uniform, the period and refractive index perturbation in the grating will deform uniformly, which is translated in a simple Bragg peak shift, i.e. a positive shift in case of applied axial strain and a negative shift in case of applied axial compression. However, if a non-uniform (uni-axial) strain (e.g. chirp) is acting on a fibre Bragg grating, the period and refractive index perturbation will deform non-uniformly. In case of a simple chirp the spectrum will become wider. If strain concentrations are present along the grating the FBG spectrum will become wider, and if the local strain concentrations are high enough the FBG spectrum will split into one or more individual Bragg peaks [1]. By following the individual Bragg peak shifts in a distorted spectrum, it is possible to determine minimal and maximal strain concentrations.
An example of the deformation of a Bragg spectrum of an embedded DTG® during longitudinal loading because of the internal (non-uniform) strain envelopes is shown in Figure 8-10.

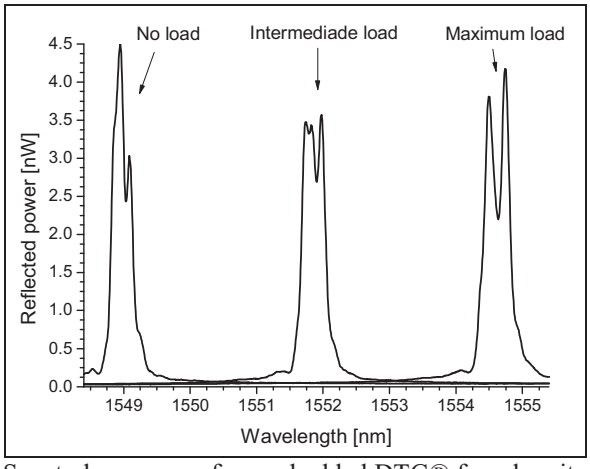

Figure 8-10: Spectral response of an embedded DTG® for a longitudinal loading case.

We notice that at maximum loading (approximately 300 MPa) the Bragg peak splits up into two distinct peaks. If we assume that the peak separation during loading is mainly caused by a non-uniform longitudinal strain field along the length of the unit-cell, we can state that a maximum and minimum strain field is present. The spectral measurements are performed using the FBG-scan X08 (FOS&S [12]) which uses a Fabry-Perot tunable filter (FPTF). The FPTF sweeps over the complete wavelength bandwidth (~40nm) within a specific time (~ms) and high spectral resolution (~7pm). Although the spectral resolution of this FBG interrogation system is high, and one is able to ravel out small Bragg peak distortions, it is not possible to directly specify the exact spatial position of the minimum and maximum strain over the gauge length of the Bragg grating. As such with this interrogation technique, solely from the peak separation, one is not able to say at which location along the grating the strains concentrations are acting.
To gather more insight in the local strain field along one unit-cell, the strain concentrations are located with the help of an experimental DIC (Digital Image Correlation) technique and meso-FE simulations. From the DIC we are able to obtain the full-field strain of the surface of the test-coupons and the meso-FE simulations allow to predict both the surface and internal strain fields. The test coupons are stretched quasi statically till 0.5% and maximum and minimum strain envelopes from the DIC strain readings and FE-modelling are discussed and compared with the spectral analysis of the DTG® sensors (surface mounted as well as embedded DTG®)

8. 2. 4. a. DIC and meso-FE simulations

Digital image correlation (DIC) is a non-contact method for measuring the full-field displacements in 2D and 3D. DIC allows to capture severe strain gradients and large strain differences at a close location, with a high spatial resolution [13]. The DIC in this work is used to measure the surface strain (2D) during tensile testing. The working principle of DIC as well as the theoretical background for the calculation of strains is explained by many researches [14-16] . Typical, the test-specimens have a speckle pattern on the surface, which allows to capture relative speckle displacements on the surface using a CCD camera by correlating between the initial image of the virgin specimen recorded before any loading and the consequent images during loading of the test-specimen. A series of three composite test specimens (Cetex®), with stacking $[(0,90)]_{4S}$, are prepared according to the ASTM standard [6] and strained up to 0.5 % strain. Each test-specimen has an area on the surface (approximately 40 mm x 25 mm) which is painted with a white spray followed by the black speckle pattern. The experimental setup used for the DIC measurements is shown in Figure 8-11. The area covers about 40mm x 25mm which comes down to approximately 5 unit cells and 3 unit cells in the loading direction and the in-plane transverse direction, respectively (Figure 8-11., top-left). The correlation between the initial image of the virgin specimen recorded before any loading, is used to compute the local strains at different locations on the composite surface using 'Vic 2D' (LIMESS) software [17]. By taking the entire window of the speckle pattern for full-field strain registration, the average strain is computed over 5 unit cells. This technique allows giving qualitative as well as quantitative information of the local displacements.

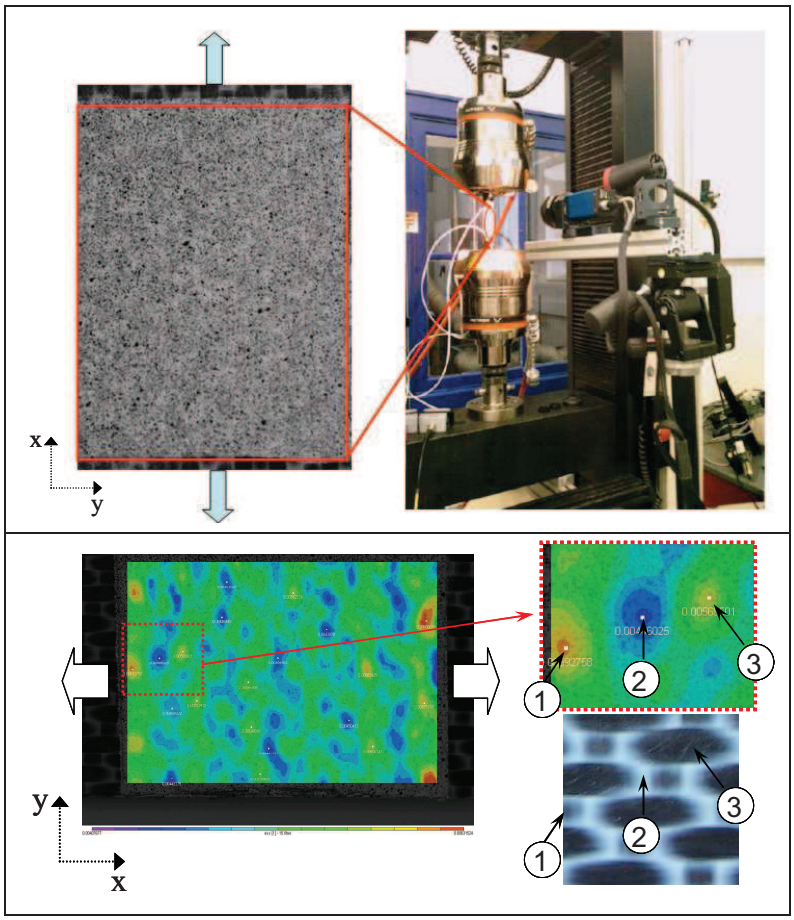

Figure 8-11: Experimental setup for the DIC measurement (top-right), test-specimen with speckle pattern (top-left), and Maximum (1), minumum (2), and average longitudinal strain $\Delta\varepsilon_1$, measured using DIC (bottom).

Even though the contours depicted in Figure 8-11, bottom, are not very clear, the strain values obtained for the strains in the x-direction (longitudinal) are showing a clear strain pattern with 3 main areas: (1) Maximum strain occurring at the centre of the weft yarn cross-over, (2) Minimum strain occurring in the matrix pockets, (3) Average strain along the flat portion of the load carrying yarn (warp). The applied average strain is approximately 0.5 %, the measured strains along 5 unit-cells for the former mentioned strain areas are given in Table 8-1:

Table 8-1: Measured strain values in zone 1 till 3, for a (global) applied strain of 0.50 ± 0.01 %.

Method	Maximum strain (%)	Average strain (%)	Minimum strain (%)
DIC (surface)	0.58 - 0.62	0.48 – 0.52	0.43 - 0.46

Additional to the experimental DIC surface strain measurements, meso-FE simulations using 3D periodic boundary conditions are performed by Daggumati et al. [18-19] to determine surface as well as internal strain fields for an $[(0,90)]_{4S}$ laminate, with a unit cell of 7.4 mm and 'in-phase' unit cell stacking (Figure 8-12). Choosing four unit cells in the stack from the laminate of eight layers, the meso-FE analysis of the unit cell stack is accomplished with the in-plane periodic boundary conditions [20]. In addition to that, symmetry boundary conditions are applied at the bottom xy-surface (Figure 8-12) and the top xy-surface is allowed to deform in the out-of-plane direction. The step stacking unit cell model is developed using the 'MeshTex' software [21]. From the meso-FE simulations we are able to compute local strain profiles of the inner and outer plies separately. It is noted that strain is applied on the model using 'hard displacement'. At the xy-symmetry plane this constraints the yarn crimp in the z-direction. As such, the internal strain measurements in the model are conducted along a path at the interface between the first and second ply counted from the bottom layer at the symmetry plane (inner dashed line in Figure 8-12, bottom). The strain measurement path on the outer ply is conducted at the outer surface of the laminate (dashed line Figure 8-12, top), hence, the values are representative for the experimental obtained strain values from the DIC and surface mounted DTG®s.

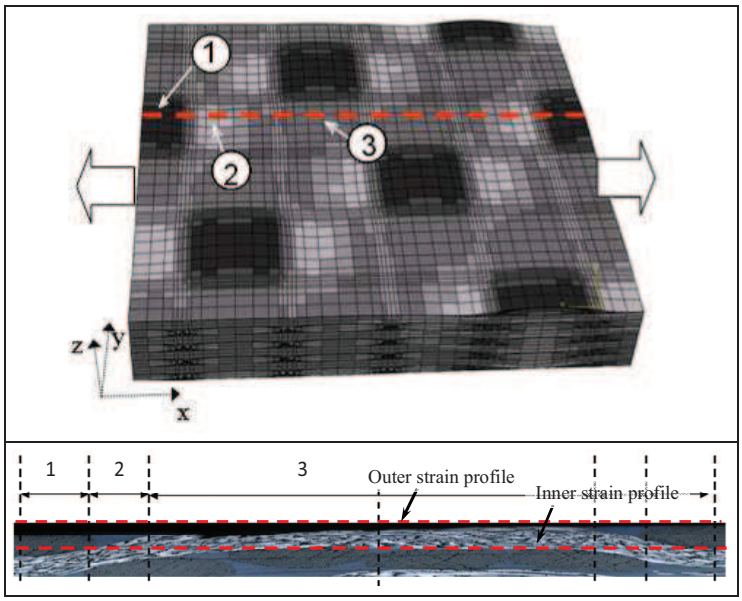

Figure 8-12: Maximum (1), minimum (2), and average (3) longitudinal strain ($\Delta\varepsilon_1$) at the outer surface (top), illustration of the strain path inside and outside along the length of the unit cell (bottom), measured from meso-FE simulations for an in-phase unit-cell stack [19].

Because the path along the inner ply is different, the computed longitudinal strain profile at the inner ply of the laminate has another pattern than the strain profile computed at the surface (Figure 8-13). At the outer ply the local longitudinal computed strain values are maximal at the surface of the weft yarn and minimal in the matrix pockets (Table 8-2), which corresponds well to the surface strain profile

measured with the DIC, however, the maximal simulated values are clearly overestimated (0.72 % against 0.62 %). According to Daggumati S. [19]the effect of internal yarn nesting affects strongly the local strain behaviour of satin weave composites. To predict the surface strains quantitatively comparable to experimental results, a unit-cell geometery with maximum ply shift should be developed, however it is a tedious process to develop a full scale model of a unit cell stack with the detailed internal yarn nesting. This is however, not within the scope of the research in this work. The interested reader is referred to [10].

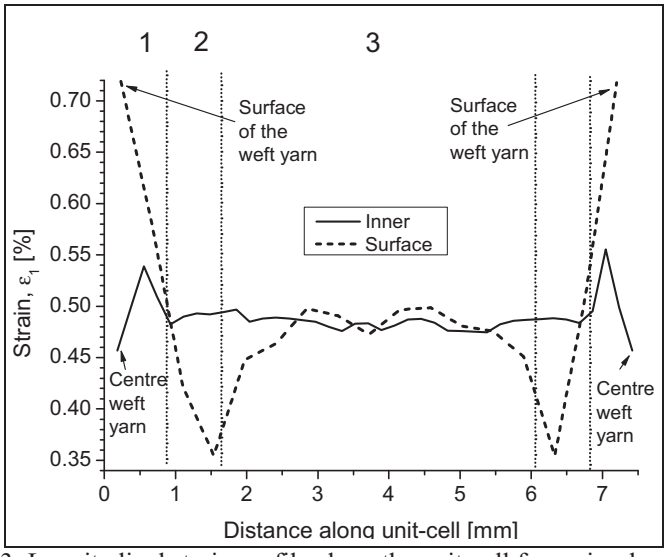

Figure 8-13: Longitudinal strain profile along the unit-cell for an in-phase stacking, surface strain (dashed) and inner strain (solid).

For the inner ply the path starts at the centre of the weft yarn, instead of at the surface of the weft yarn which contributes to a different strain profile. The most significant effect is that the overall strain variation is much less than computed at the surface. A maximal value and minimal value of 0.55 % and 0.46 % is measured, respectively (Table 8-2). It is noted that the inner strain path in area 2 (Figure 8-12) does not go through a matrix pocket, however, the strain at the underside of the yarn in area 3, is measured in the matrix – yarn interface, and stays more or less constant. This indicates that the inner plies are subjected to a more homogeneous strain field than the outer plies, however, the strain variation with respect to the global applied strain of 0.5 % is still approximately ± 8 % (i.e. 0.50 ± 0.04 %).

Table 8-2: Simulated strain values from the meso-FE model in zone 1 till 3, at the surface and inner ply, for a (global) applied strain of 0.50 %.

Method	**Maximum strain (%)**	**Average strain (%)**	**Minimum strain (%)**
Meso-FE (surface)	0.72	0.48	0.36
Meso-FE (inner)	0.55	0.49	0.46

8. 2. 4. b. Surface mounted and embedded DTG®

From the DIC and meso-FE simulations it is found that a strain profile exists at the outer and inner composite plies. Now the goal is to calculate the local longitudinal minimum and maximum strain in the grating (along one unit cell) from the distorted spectra at 0.5 % applied strain, and to compare the strain readings with the DIC measurements and the meso-FE simulations. To determine the local maximum and minimum strain envelopes using the DTG®s, three test-coupons with stacking sequence $[(0,90)]_{4S}$ (in-phase stacking) are prepared (Table 8-3) with each specimen having an embedded and a surface mounted DTG®. The embedded sensors are positioned in the mid-plane and the centre of the laminate along the load carrying warp yarns (Figure 8-3). The surface mounted sensors are positioned on top of the embedded sensors, so the location of strain measurement is the same. Additional, an extensometer is mounted at the opposite location of the surface mounted DTG®. The strain readings of this extensometer are used as reference measurement for the global applied strain. The 80 µm and 125 µm sensors have a total diameter with ORMOCER® coating of approximately 140 µm and 190 µm, respectively. The specimens are subjected to one quasi-static loading cycle till maximum 300 MPa (approximately 0.5 % stain), and the spectral response of both embedded and surface mounted DTG® is followed during loading.

Table 8-3: : Inventory of the CFRP test-coupons used for the strain distribution tests.

	Lay-up	Length	Width	Thickness	Sensor alignment	Remark**
n°*		[mm]	[mm]	[mm]	Global	
4	$[(0,90)]_{4S}$	300	30.9	2.4	x-axis	80 surface
5	$[(0,90)]_{4S}$	300	30.6	2.4	x-axis	80 surface
8	$[(0,90)]_{4S}$	300	30.7	2.4	x-axis	80 surface

An example of the spectral response of a surface mounted and embedded DTG® during longitudinal testing at zero loading, at an intermediate load level and at maximal loading (300 MPa ≈ 0.5 %) is shown in Figure 8-14. Both sensors show increasing peak distortion with increasing load. At the intermediate strain level of approximately 0.2 % the shape of the peak is more or less similar to the initial spectrum, however at maximum strain level the shape has completely changed and both the surface mounted as well as the embedded DTG® show clearly additional small side peaks in the spectra.

* The numbering of the samples is conform to Table 6.6 (Chapter 6), all embedded DTG®s are from PR2007_2

** The surface mounted 80 µm DTG®s are from PR2008_1.

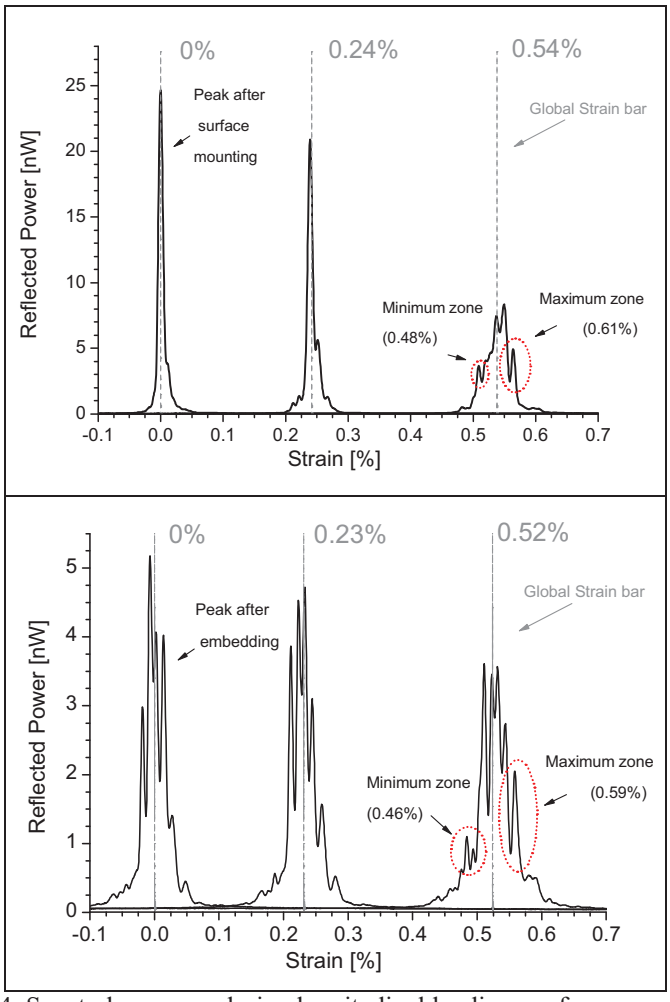

Figure 8-14: Spectral response during longitudinal loading, surface mounted DTG® (top), embedded DTG® (bottom)

Two different approaches are used to calculate the strain from the Bragg peak shifts. First the COG method (Chapter 5) is applied on the complete (distorted) spectrum to calculate the global Bragg wavelength. This COG wavelength at nominal load is taken as $\lambda_{\varepsilon,0}$ and the determined COG during loading, λ_{ε} is then substituted in Equation 8-1 to calculate the longitudinal strain at each load level. The strain calculation of the complete spectrum is further referred to as *global strain*. The global strain bars are indicated in each plot of Figure 8-14. We see that the global applied strain measured with the surface and embedded DTG® match well, moreover, the strain values match very well the strain readings of the extensometer. This is subject of the next sections where the (global) stress-strain calibrations will be further elaborated.

To determine the minimum and maximum strains from the distorted spectra at maximum loading (i.e. ~0.5 %), the COG of the individual peaks is determined and substituted in Equation 8-1. It is noticed that the loading of the test-coupons is

performed using load control. Because the same load sequence is used for all test-coupons the applied strain differs slightly from coupon to coupon, because of different dimensions, i.e. widths. To allow comparison of the strain results from the response of the DTG®s, with the strains obtained from the DIC and the meso-FE simulations, a correction factor is used to scale the minimum and maximum strains for a global strain of 0.5 %. For example the global strain of the surface mounted DTG® in Figure 8-14, top, is approximately 0.54 % and the minimum and maximum strains are 0.48 % and 0.61 %, respectively. As such, the scaled minimum and maximum values in this example are $0.5 / 0.54 = 92.6\%$ of the measured values, hence we find 0.44 % and 0.56 %, respectively. This correction factor is calculated for all DTG®s individually. The scaled calculated minimum and maximum strains are given in Table 8-4. The comparison of the results of all measured and computed strain values is found in Table 8-5 in the next sub-section.

Table 8-4: Calculated strain values from the surface and embedded DTG®s, for a (global) applied strain of 0.50 %.

Method	**Maximum strain (%)**	**Minimum strain (%)**
DTG® (surface)	0.56 – 0.59	0.44 – 0.45
DTG® (embedded)	0.55 – 0.57	0.43 – 0.45

The results show that the surface and embedded DTG®s measure identical minimum, global, and maximum strains. This indicates that the influence of transverse effects during longitudinal loading on the longitudinal strain calculations of the embedded DTG®s are small.

8. 2. 4. c. Local strain distribution results

The results of the DIC measurements, the meso-FE simulations and the measurements using the surface and embedded DTG®s are summarized in Table 8-5. The average strain is not calculated for the DTG®s, as it is not possible to define exactly which individual peaks of the distorted spectra are associated to the average strain along the warp yarns.

Table 8-5: Strain results for the DIC, Meso-FE and DTG® (surface mounted and embedded)

Global strain (0.5 ±0.01%)	***Maximum strain (%)***	***Average strain (%)***	***Minimum strain (%)***
DIC (surface)	0.58 - 0.62	0.48 – 0.52	0.43 - 0.46
Meso-FE (surface)	0.72	0.48	0.36
Meso-FE (inner)	0.55	0.49	0.46
DTG® (surface)	0.56 – 0.59	/	0.44 – 0.45
DTG® (embedded)	0.55 – 0.57	/	0.43 – 0.45

We can see that the resulting strain profiles of all methods match well. As mentioned before the maximal simulated surface strains are approximately 50 % overestimated, which is most probably caused by the internal yarn nesting effect which in a real manually stacked laminate is less distinct then in the (perfect stacked) in-phase model with 3D periodic boundary conditions. The strain profile is

similar to the experimentally obtained results and the minimum and average strains are matching better the DIC.
Remark that the surface readings of the DIC and the DTG®s match very well. With the help of DIC and meso-FE simulations we are in principle capable of allocating the minimum and maximum strain concentrations in the grating along the length of a unit-cell. From the inner strain profile simulated with the meso-FE model we see that the inner strain distribution is less distinct. Although that in a real laminate the unit-cell stack is not perfect, we find a very good correlation between the computed inner strain distribution and the strain values measured using the embedded DTG®s. These results show that we are capable of measuring strain (longitudinal) distributions with embedded DTG®s, also even though the Bragg spectra are severely distorted at high strain levels, the COG method allows to accurately determine the induced global strains. This allows to investigate the long term behaviour, i.e. deformation, of the composite using embedded DTG®s. The effect of load cycling on the internal global strain state is elaborated in the following sections.

8. 2. 5. Global stress – strain analysis: stiffness degradation?

As shown in Figure 8-14 it is possible to accurately calculate the global strain at each applied strain (stress) level from the COG wavelength of the full spectrum. The global strain values obtained from both DTG®s can be used to plot stress-strain curves and to investigate the stiffness of the material. The goal is to study the long term behaviour of the material using the approach as explained in Section 8. 2. 2. . The full spectrum of the embedded DTG®s will be recorded and the longitudinal strain is calculated using the COG of the total Bragg peak at each stress level, during the quasi-static progressive loading cycle up to 300 Mpa (Figure 8-7, top-right). The measurements are repeated at different cycling intervals, i.e. during the first loading cycle (Cycle1), the second loading cycle (Cycle2), and after 1.3 million (dynamic) load cycles at 5Hz (CycleFinal). A typical stress-strain plot of the first, second and final cycle, is shown in Figure 8-15 and Figure 8-16 for a $[(0,90)]_{4S}$ and $[(90,0)]_{4S}$ stacked laminate, respectively.

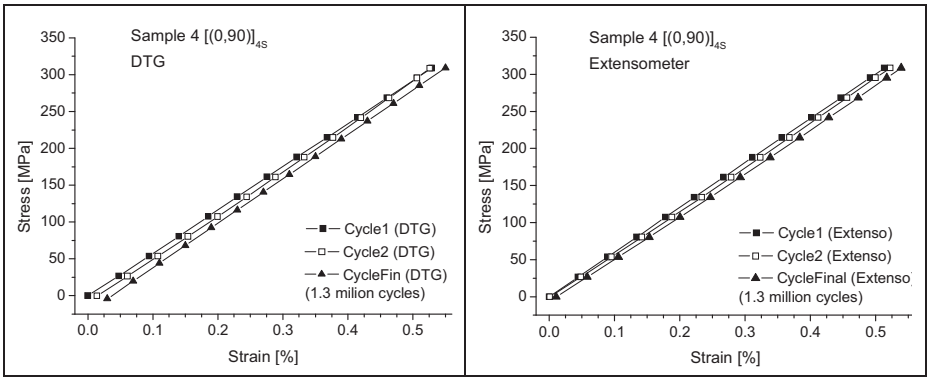

Figure 8-15: Stress – strain curves for the $[(0,90)]_{4S}$ lay-up of Cycle 1, Cycle 2 and after 1.3 million cycles for the embedded DTG® (left), and extensometer (right).

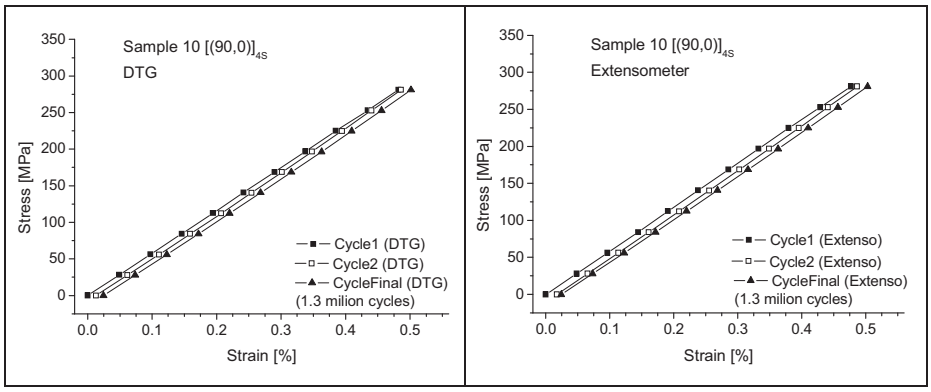

Figure 8-16: Stress – strain curves for the $[(90,0)]_{4S}$ lay-up of Cycle 1, Cycle 2 and after 1.3 million cycles for the embedded DTG® (left), and extensometer (right).

The strain is plotted against the applied stress for an embedded DTG® and an externally mounted extensometer. The correlation between the extensometer and embedded DTG®s is very good. The slope of the curves represents the stiffness (GPa) of the composite and are given in Table 8-6. The values are a little higher than the tensile moduli (E_{11}) given in Table 6-4 (Chapter 6), however, this is most probably caused by the difference in testing method. In a classical quasi-static tensile test, the samples are loaded using a ramped loading scheme until failure. This is not the case in the experimental method applied here.

Table 8-6: Slopes of the stress – strain curves of all tested samples, of Cycle 1, Cycle 2 and after 1.3 milion cycles.

n°*			*Slopes [GPa]*	
		Maximum applied stress (MPa)	*DTG® Cycle1 / Cycle2 / CycleFin*	*Extensometer Cycle1 / Cycle2 / CycleFin*
4	$[(0,90)]_{4S}$	309	58.6 / 60.4 / 60.3	60.2 / 59.5 / 58.5
5	$[(0,90)]_{4S}$	305	60.1 / 61.7 / 60.6	58.6 / 59.8 / 58.2
8	$[(0,90)]_{4S}$	290	58.2 / 60.9 / -	- / 59.1 / -
10	$[(90,0)]_{4S}$**	281	58.4 / 59.5 / 58.9	59.2 / 59.9 / 58.7
11	$[(90,0)]_{4S}$**	281	59.0 / 60.0 / 59.3	58.2 / 59.7 / 59.0
12	$[(90,0)]_{4S}$***	290	58.4 / 59.9 / 59.1	59.1 / 60.2 / 59.5
13	$[(90,0)]_{4S}$***	294	60.3 / 60.8 / 61.0	59.1 / 60.6 / 60.0

	DTG	*Extensometer*
Mean_Cycle 1	*59.0 ± 0.9*	*59.1 ± 0.7*
Mean_Cycle 2	*60.5± 0.7*	*59.8 ± 0.5*
Mean_Cycle Final	*60.0 ± 0.8*	*59.0 ± 0.7*

* The numbering of the samples is conform to Table 6.6 (Chapter 6), all embedded DTG®s are from PR2007_2

** sample n°10 and n°11 are annealed during a temperature cycle (Section 8. 3.)

*** 80 µm DTG® embedded, coating diameter approximately 125µm

The results show that even after more than 1.3 million load cycles at 300MPa no stiffness degradation occurs. In the research of De Baere I. [22] the same behaviour for stress levels up to 550 MPa has been presented for identical test-coupons and similar intermediate quasi-static tests up to 1.2 million cycles. No difference is found between the $[(0,90)]_{4S}$ and $[(90,0)]_{4S}$ stacked laminates and the two samples with a 80 µm DTG® (sample 12 and 13) show identical results. The deviation in the results for both the embedded DTG®s and the extensometer is within acceptable limits for composite materials. If we look at the mean calculated stiffness for each loading cycle (bottom values in Table 8-6), we notice a small increase in stiffness in cycle 2 compared to the initial cycle, and after 1.3 million cycles the stiffness tends to decrease slightly. This indicates that even after 1.3 million loading cycles at 0.5 % strain, the embedded sensors still follow the internal deformation of the composite. From these results we can state that the bonding of sensor to the host structure stays intact, moreover, if we look closer to the curves of the embedded DTG®s in Figure 8-15 and Figure 8-16, we notice a shift of the curves to the right (~0.025 %), which indicates that permanent deformation of the composite laminate occurs. The same effect is noticed by De Baere I. [22], who indicated that the permanent deformation in these laminates tends to develop in the first sixty loading cycles.
Most probably the slight change in stiffness between cycle 1 and 2 is caused by crack initiation and residual strain relief of the woven structure, however, no immediate conclusion on the level of material properties can be drawn at this time. The best way to investigate this permanent strain effect is by looking at the full Bragg spectra after a certain load level at zero loading. The shift of the Bragg peak after loading can provide information on the permanent strain shift, and the shape of the individual Bragg peaks can provide useful information on a possible change in strain state along the grating. The permanent deformation during cycling is investigated in the following section.

8. 2. 6. Permanent deformation measurements

Apart from the global stress-strain curves, the repeated progressive loading cycle (Figure 8-7, top-right), allows to perform full spectrum measurements at each ‘subsequent zero loading’ level. As such, the spectral response of the embedded DTG®s at zero load level can be compared with the initial spectrum, before loading has been applied. The global shift of the spectrum is then a measure for the permanent deformation. Because of the repeated progressive load cycling, the global peak shifts can be determined at several load intervals. An example of the spectral response at zero loading during the first quasi-static loading cycle is shown in Figure 8-17, where we see three recorded Bragg spectra: one measured before load has been applied (grey line), i.e. initial spectrum after embedding, one measured at zero load after having the sample tensioned up to 160 MPa (black line), and one measured at zero load after having the sample tensioned up to 309 MPa (red line). Note that the indicated stress level in the graph is the previous stress level to which the sample has been applied before the measurement at zero loading. The dots in the graph represent the COG wavelengths of each peak. We observe a small increase of the COG wavelength (approximately 215 pm), which indicates a positive permanent deformation of the sample under test.

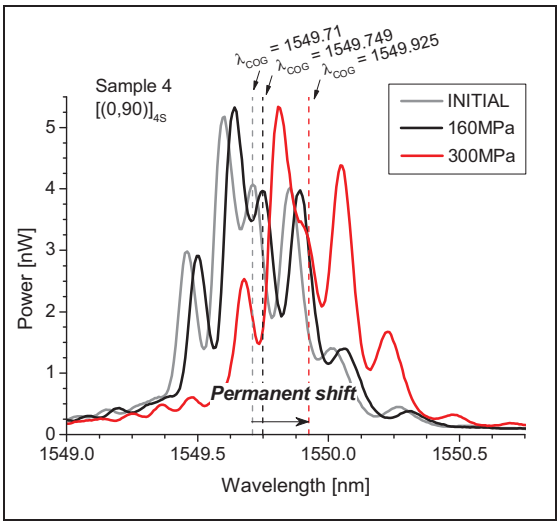

Figure 8-17: Spectra recorded at zero loading after different (previous) load levels during cycle 1, initial (grey), 160 MPa (black), and 309 MPa (red), the COG wavelength of each peak is indicated as well (dashed lines).

To determine the permanent strain as function of the number of loading cycles, the same procedure is repeated at intermediate quasi-static cycles during fatigue testing. An example of the zero load spectra is shown in Figure 8-18, where the permanent peak shift is illustrated for a spectrum after 1 loading cycle, and after 1.3 million loading cycles at a stress level of 300 MPa.

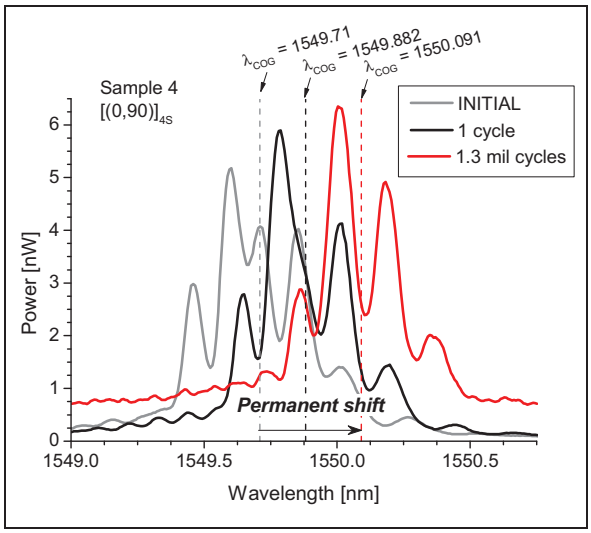

Figure 8-18: Spectra recorded at zero loading after certain cycles illustrating the permanent (wavelength) shift, initial (grey), 1 cycle (black), and after 1.3 million cycles (red), the COG wavelength of each peak is indicated as well (dashed lines).

The dashed lines represent the COG wavelength of each peak. We clearly see a positive permanent wavelength shift (~120pm) as function of the applied cycles. A correlation can thus be found between the permanent elongation of the composite and the number of applied loading cycles.
The loading scheme followed to investigate the permanent strain is shown in Figure 8-8, bottom. First, full spectral measurements are performed during two quasi-static progressive loading cycles until approximately 300 MPa, then the measurements are repeated after 8, 54000, 169000 and 1.3 million fatigue cycles. The COG wavelength shifts are converted into longitudinal (i.e. permanent) strain using Equation 8-1. The results are shown in Figure 8-19. We observe a clear increase in permanent strain during the first loading cycle. A non-linear shift of approximately 0.015 % is noticed, indicating a gradual increase of the permanent strain. This is in accordance with the results shown in [10-11], where initial damage (i.e. cracks) is detected at around the 100 MPa stress level at the edges of the weft yarn inside the laminate. By increasing the stress level from 100 to 400 MPa, the damage is observed at the nested yarn configurations at various locations in the laminate. The gradually increasing permanent strain measured by the embedded DTG®s is thus related with the damage initiation in the composite.

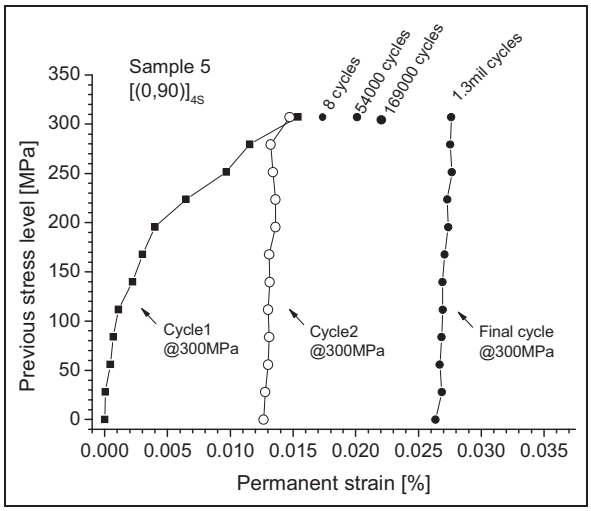

Figure 8-19: Example of the permanent strain shift measured at zero loading (0 MPa) during the first cycle, second cycle, and final cycle after 1.3 million cycles. The stress level is indicative, see text for explanation.

At the start of the second cycle, which is performed within a few minutes after cycle 1, the strain has decreased slightly, indicating a small elastic 'contraction' of the sample. The effect is explained by the fact that the cracks in the laminate are being compressed during relaxation. At the end of cycle 2, the permanent strain is equal to the strain at the end of cycle 1. If the applied cycles increase, the permanent strain increases too. After 54000 cycles, for example, the strain is approximately 0.020%, and after 1.3 million cycles the permanent strain is approximately 0.028%. Permanent strain does however not continu to increase as we can see that the relative shift in permanent strain between the different amount of load cycles decreases. We clearly see that in the second and final full quasi-static cycle the permanent strain

stays more or less constant. The exact same behaviour is noticed for nearly all tested samples. The permanent strains for all tested samples after cycle 1 and after 1.3 million cycles are shown in Table 8-7. Except for sample n°13 all samples show a similar behaviour. Note that the applied stress is not equal for all samples. Because no linear behaviour is found between the permanent strain and the applied load, no scaling is applied on the values of Table 8-7. As such the scatter on the results is relatively high. The mean permanent strain is approximately 0.02 % after one loading cycle, and approximately 0.03% after 1.3 million cycles. This indicates that although cracks occur in the laminate below 400 MPa [10-11], the permanent strain stays low, even after more than 1 million cycles.

Table 8-7: Permanent strains of all tested samples, of Cycle 1 and after 1.3 million cycles.

n°[*]		*Max. applied stress (MPa)*	*Permanent strain Cycle1 [%]*	*Permanent strain 1.3 mil. cycles [%]*
4	$[(0,90)]_{4S}$	309	0.017	0.030
5	$[(0,90)]_{4S}$	305	0.016	0.028
8	$[(0,90)]_{4S}$	290	0.023	*NA*
10	$[(90,0)]_{4S}$[**]	281	0.015	0.026
11	$[(90,0)]_{4S}$[**]	281	0.012	0.024
12	$[(90,0)]_{4S}$[***]	290	0.019	0.029
13	$[(90,0)]_{4S}$[***]	294	*0.006*	*0.018*

	Cycle1	*Cycle final*
Mean[****]	*0.017 ± 0.004*	*0.027 ± 0.002*

Interesting to note is that the increase in permanent deformation of the sample is largely dependent on the applied load and less dependent on the amount of samples. Sample n°8 is loaded two times; the first cycle up to 290 MPa and the second cycle until failure of the tabs (514 MPa). The spectra at zero load after these two cycles is shown in Figure 8-20, left.

[*] The numbering of the samples is conform to Table 6.6 (Chapter 6), all embedded DTG®s are from PR2007_2

[**] sample n°10 and n°11 are annealed during a temperature cycle (Section 8. 3.)

[***] 80 µm DTG® embedded, coating diameter approximately 125µm

[****] the mean value is determined without sample n°13

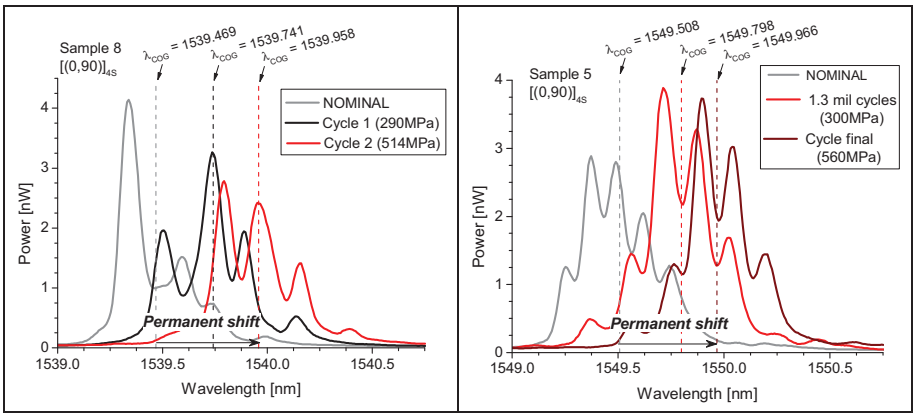

Figure 8-20: Example of the permanent peak shift measured at zero loading during the first cycle at 290 MPa and second cycle at 514 MPa for sample n°8 (left), and during the first cycle at 300MPa, after 1.3 million cycles at 300 MPa, and final cycle at 560 MPa for sample n°5 (right).

The COG wavelength shift of sample n°8 after 514 MPa is approximately 490 pm which correspond to a permanent strain of approximately 0.041% which is almost twice the permanent strain measured after cycle 1 (0.023 %). To compare the effect of load against the applied amount of fatigue cycles, sample n°4 and n°5 are subjected to a tensile test up to failure after the 1.3 million fatigue cycles. A longitudinal stress of 430 MPa and 560 MPa is applied on sample n°4 and n°5, respectively. Both specimens failed in the tabs, however, measurements of the DTG®s are again performed until failure and similar to the tensile test on Sample n°8, an additional gradual increase in permanent strain is found, indicating that damage in the material is increasing. The values for the permanent strains at these higher stress levels are given in Table 8-8. An example of the spectral response and permanent Bragg peak shift for sample n°5 till 560 MPa is shown in Figure 8-20, right.

To look for cracks in the sample after failure, the author has performed a post-mortem visual inspection using a microscope. An example of the microscopic cross-sections is given in Figure 8-21. In the left picture we clearly observe (vertical) cracks in the weft yarns, as was also presented by Dagummati in [10-11]. No damage is seen in the warp yarns (i.e. loading direction), neither around the optical fibre (right inset), indicating that the bonding of the ORMOCER® coating with the matrix material at these high stress levels stays intact. It confirms also that damage is not caused because of the inclusion (i.e. optical fibre) in the host material.

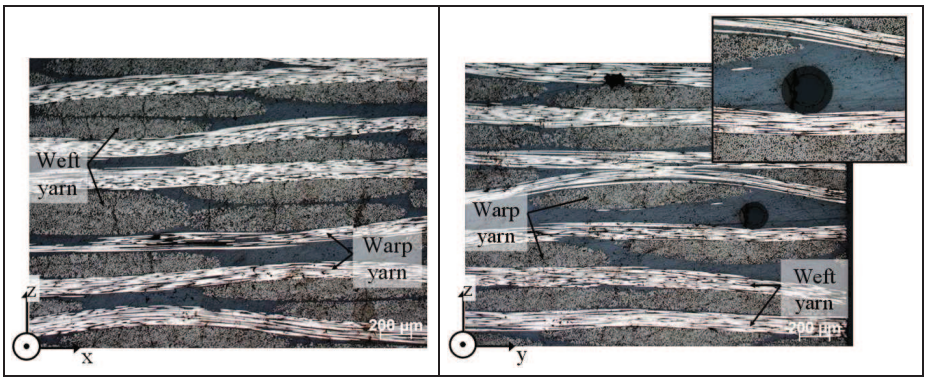

Figure 8-21: Post-mortem cross-sections of sample n°8 indicating cracks in the weft yarns (left) after 514 MPa, but no damage is visible in the warp yarns or around the optical fibre (right).

An example of the permanent strain curve for sample n°5 is shown in Figure 8-22. We observe a clear increase up to approximately 0.04 % (Table 8-8), which is 40 % higher than the permanent strain at 300 MPa after 1.3 million cycles, but remark that the permanent strain is more than twice the permanent strain after cycle 1.

Table 8-8: Permanent strain at higher stress levels

n°[*]		*Maximum applied stress (MPa)*	*Permanent strain Cycle Failure [%]*
4	$[(0,90)]_{4S}$	430	0.032
5	$[(0,90)]_{4S}$	560	0.039
8	$[(0,90)]_{4S}$	514	0.041[**]

This illustrates that the load is the driving factor for the damage initiation in these woven fabric composites, and that even though cracks are present in the material, the fatigue resistance is very high. In Figure 8-22 we observe an equal and linear trend of cycle 1 starting from a 'previous stressed' level of 200 MPa and the two final cycles with a maximum 'previous stressed' level of 300 MPa and 560 MPa, respectively, see dashed-dotted line.

[*] The numbering of the samples is conform to Table 6.6 (Chapter 6), all embedded DTG®s are from PR2007_2

[**] Measured after cycle 2

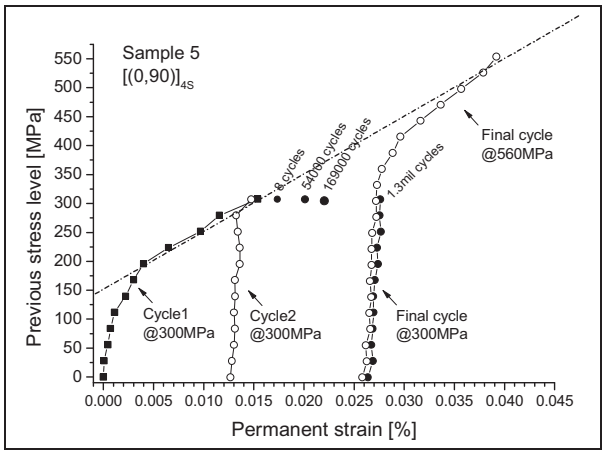

Figure 8-22: Example of the permanent strain shift measured at zero loading during the first cycle, second cycle, final cycle after 1.3 million cycles till 300 MPa, and final cycle at 560 MPa.

This trend line is solely dependent on the applied stress, and shows the maximum permanent strain against the applied stress. The inverse of the slope of this plateau gives an idea on the amount of permanent strain as function of the applied stress. The slope is found to be approximately $\approx 0.008\ \%/100\ MPa$. Note that we would end on the same straight fitted line if we plot the permanent strain of one repeated progressive quasi-static cycle until failure. However, for sample n°8 only permanent strain measurements are performed without cyclic loading, as such no full quasi-static cycle until failure is plotted. To really validate the assumption of above more samples need to be tested until failure using the exact same method. This is subject of further research.

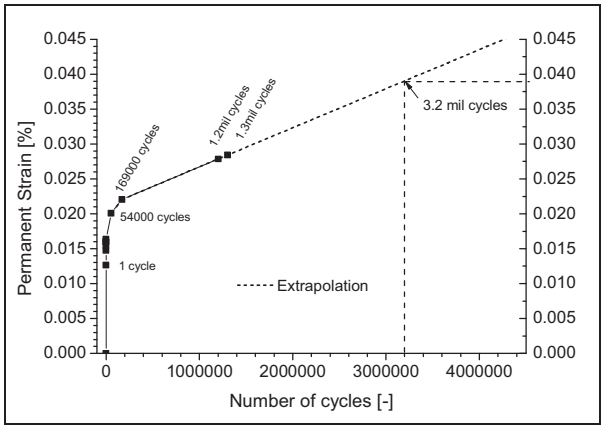

Figure 8-23: Extrapolated permanent strain for 300 MPa against the number of cycles.

To estimate the permanent strain as function of applied fatigue cycles the data of the permanent strain at 300 MPa is extrapolated starting at 54000 cycles, see Figure

8-22, right. We see that, to obtain the same amount of permanent strain of 0.039 %, the number of loading cycles at 300 MPa exceeds 3.2 million. The linear slope of the function starting at 169000 cycles is found $\approx 0.0056\ \% \big/ 10^6\ cycles$, which corresponds to approximately 60 µstrain permanent strain increase per million applied load cycles, which indicates that the woven fabric composite has a very high fatigue resistance at 300 MPa ($\approx 0.5\%$ strain). Note that this slope is at rough estimate and more data points are necessary to accurately predict the fatigue life. The slope is therefore most probably overestimated, however, it can be applied to form a general idea on the expected permanent strain increase during fatigue cycling.

8. 2. 7. Transverse strains

Additional to the global stress-strain and longitudinal permanent strain analysis, the transverse strain difference is investigated in Sample n° 10 – n°13 ($[(90,0)]_{4S}$ stacking) during the longitudinal tests. Polarization testing during the experiments provides information on the birefringence effects in the optical fibre during loading. As such, the transverse strain difference in the DTG®s is experimentally determined. The author has performed a small numerical study using a homogenized FE composite model with embedded optical fibre, which is loaded in the longitudinal direction. The FE-analysis helps estimating the strains in the optical fibre during loading. The numerical results of the transverse strain difference will then be compared with the measurements.

8. 2. 7. a. Numerical results

In analogy to the FE-simulations performed in Chapter 7, the direct strain transfer of the optical fibre with coating is determined for the thermoplastic CFRP laminate. Because of the complexity of the woven-fabric structure the simulations with embedded optical fibre are simplified by using the homogenized engineering constants determined in Chapter 6 (Table 6-5). The engineering constants are given in Table 8-9:

Table 8-9: Engineering constants (homogenized) for the Carbon 5H CD0286 T300J 3K woven fabric material [10].

E_{11} [GPa]	E_{22} [GPa]	E_{33} [GPa]	G_{12} [GPa]	$G_{13} = G_{23}$ [GPa]	ν_{12} [-]	$\nu_{13} = \nu_{23}$ [-]
56.5	56.5	10.5	4.28	3.05	0.08	0.41

The FE simulation is only performed for the longitudinal loading case, but for both the embedded 125 µm and 80 µm coated DTG®s. The coating outer diameter is 190 µm and 125 µm, respectively (PR2007_2). The coating material properties are chosen from the optimal combination of Young's modulus and Poisson's ratio found in Chapter 7, with $E_c = 0.8$ GPa, $\nu_c = 0.32$. It is not the purpose to validate the numerical strain transfers. The FE model is used to estimate the transverse strains in the optical fibre and laminate during tensile loading, to compare the values further in

this section, with the transverse strain difference measured in the DTG®s during tensile loading.
The numerical strain values of the optical fibre with coating and composite laminate for a longitudinal applied strain of 0.5 %, are given in Table 8-10. The results of the simulations show that no difference exists between the coated 80 µm and 125 µm optical fibre. The direct strain ratio's between the optical fibre and composite are given as well.

Table 8-10: Numerical strains and strain ratio's for the 125 µm and 80 µm coated fibres embedded in a thermoplastic CFRP for a loading of 1 % strain

Longitudinal loading direction (0.5 % applied strain)	
Optical fibre strains	$\varepsilon_1^s = 0.5000\%$ $\varepsilon_2^s = -0.0783\%$ $\varepsilon_3^s = -0.0807\%$
Composite strains	$\varepsilon_1^h = 0.5000\%$ $\varepsilon_2^h = -0.0400\%$ $\varepsilon_3^h = -0.2084\%$
Strain ratio	$\varepsilon_1^s / \varepsilon_1^h = 100\%$ $\varepsilon_2^s / \varepsilon_2^h = 196\%$ $\varepsilon_3^s / \varepsilon_3^h = 39\%$

The transverse strain difference in the optical fibre at 0.5 % longitudinal applied strain is $\Delta\varepsilon_{trans} = \varepsilon_2^s - \varepsilon_3^s = 0.0024\%$. In the following section the transverse strain difference is experimentally determined during longitudinal loading by investigating the spectral response of the DTG®s

8. 2. 7. b. Experimental results

The transverse strain difference in the optical fibre during longitudinal loading of four $[(90,0)]_{4S}$ laminates is determined by measuring the birefringence effect in the embedded DTG®s. Important to note is that in analogy to the transverse residual strain difference measurements in Chapter 6, a polarization controller (HP8169A) has been used to rotate the linear polarization angle of the input light with 190° in steps of 10°, to determine the maximal peak separation of the Bragg peaks. The full Bragg spectra are recorded at each step and the polarization sweeps are performed at three load levels: at the start of the test (unloaded), at half of the load level and at the maximum load level (≈ 300MPa). An example of the recorded spectra polarized along the principal polarization axes is shown in Figure 8-12, top, for cycle 2 at 140 MPa. The COG wavelengths are indicated in the graph. The birefringence is small ($1551.912 - 1551.866 = 0.046\ nm$), hence the transverse strain difference is small too (~0.021 %). An example of the polarization sweeps at zero loading, at 140 MPa and at 300 MPa is shown in Figure 8-12, bottom. We clearly see a sinusoidal shape of the COG wavelengths as function of the linear polarization angle. Note that the vertical axis which correspond to different load levels, are scaled one to one, however, because during longitudinal loading of the sample the axial wavelength shift is much higher than the wavelength shifts presented in the polarization plots, the author has given each axis an offset to fit all plots into one graph. Identical polarization tests are carried out at three different time periods, i.e. during the first cycle, during the second cycle and after 1.2 million of dynamic load cycles.

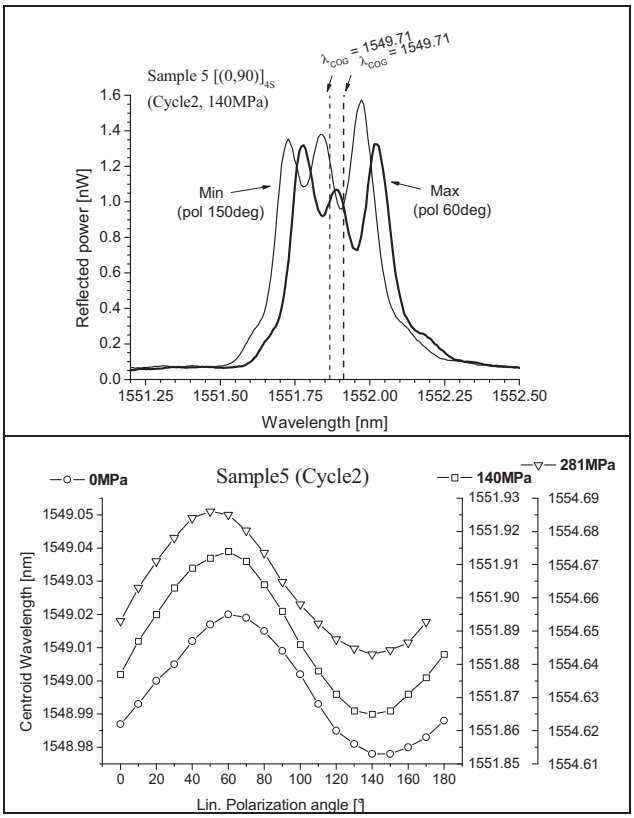

Figure 8-24: Example of the minimum and maximum spectra (top), polarization sweep with centroid wavelength calculated from the spectra for Cycle 2 at 0MPa, 140MPa and 281MPa (bottom).

The difference in transverse strain, $\Delta\varepsilon_{trans}$, is given by (Equation B-25, Appendix B):

$$\varepsilon_{1'} - \varepsilon_{2'} = \Delta\varepsilon_{trans} = \frac{2}{\overline{n}^2} \frac{\lambda_{B,1'} - \lambda_{B,2'}}{\left(\lambda_{B,0}\right)\left(p_{12} - p_{11}\right)}. \qquad 8\text{-}2$$

Substituting $p_{11} = 0.112$, $p_{12} = 0.256$, $\overline{n} = 1.4459$, the minimal and maximal COG wavelengths, as depicted in Figure 8-12, and $\lambda_{B,0} = \frac{\lambda_{B,1'} + \lambda_{B,2'}}{2}$, for each load level at the different cycle intervals in Equation 8-2, we can determine the evolution of the transverse strain state during the load cycling. The transverse strain difference for all tested samples is shown in Figure 8-25 for Cycle1, Cycle2 and the final cycle after 1.3 million cycles. The individual linear slopes of all curves are given in Table 8-11. We observe from the first graph in Figure 8-25, that the initial (residual) transverse strain differences of all samples range between 0.018% and 0.035%. The magnitude of these values is conform with the transverse residual strain measurement performed on the $[(90,0)]_{4S}$ plate after consolidation in Chapter 6 (Section 6.7.2).

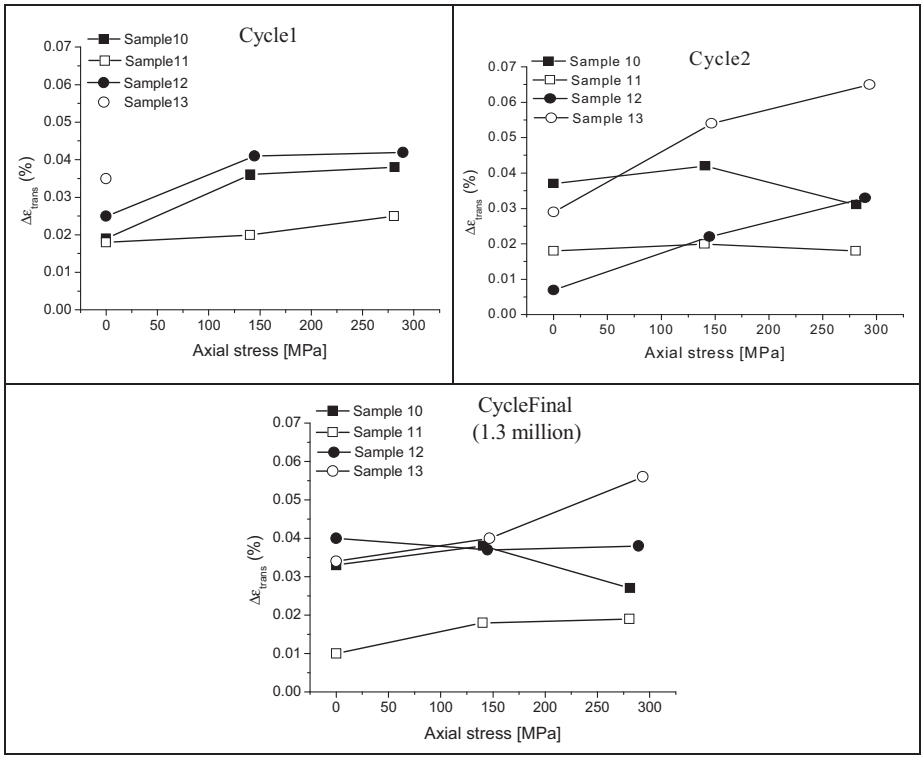

Figure 8-25 Evolution of the transverse strain difference during Cycle 1, Cycle2 and the final cycle, for all samples. Sample number are according Table 8-11.

Table 8-11: Individual and Mean slopes of the transverse strain for Cycle 1, Cycle 2 and final cycle. Mean slopes are indicated in the plots in Figure 8-25.

n°*		*Maximum applied stress (MPa)*	*Slope Cycle1 [% / 100 MPa]*	*Slope Cycle2 [% /100 MPa]*	*Slope 1.3 mil.cycles [% /100 MPa]*
10	$[(90,0)]_{4S}$**	281	0.0059	-0.0021	-0.0021
11	$[(90,0)]_{4S}$**	281	0.0029	0	0.0032
12	$[(90,0)]_{4S}$***	290	0.0068	0.0090	-0.0007
13	$[(90,0)]_{4S}$***	294	-	0.0123	0.0074

The behaviour of all samples during the first load cycle is similar and a positive slope is found for all samples. The course of the curve of sample n°11 is slightly different (no values are recorded for sample n°13 during Cycle 1. From the slopes the increase of transverse strain at maximal load is estimated. At 300 MPa (~0.5 % strain) the transverse strain has increased with approximately 0.018 %, 0.009 % and

* The numbering of the samples is conform to Table 6.6 (Chapter 6), all embedded DTG®s are from PR2007_2

** sample n°10 and n°11 are annealed during a temperature cycle (Section 8. 3.)

*** 80 µm DTG® embedded, coating diameter approximately 125µm.

0.020 % for sample n°10, n°11, and n°12, respectively. Note that the highest increase is more than eight times higher than the simulated transverse strains using the homogenized material properties (~0.0024 %, Table 8-10). Because of the complexity of the strain distribution in the woven composite, the quantity of the computed strain values using the homogenized FE-model is not representative for the local strain measurements in the weave pattern. This is confirmed by the large scatter in the measurements.

8. 3. THERMAL TESTING

In this section, the DTG®s are used to investigate the internal strain effects when the composite is subjected to a temperature cycle. If composite laminates are subjected to temperatures above the glass-transition temperature of the matrix (T_g), relaxation or crystallisation take place which is, in analogy to the annealing of isotropic material, referred to as annealing effects [23]. Composite annealing is often carried out on thermoplastic FRPs to relax the residual stress, to minimize the residual strain gradient through the thickness or to obtain optimal levels of crystallinity [24-26]. By performing an annealing cycle, the stress-free temperature of a composite may effectively be [24]. The glass transition temperature of the PPS matrix of the composite laminates used in this work is T_g = 90 °C (ref MATWEB). In this section a temperature test is carried out from -20 °C till 160 °C (Figure 8-27, top). Because the maximum temperature in this cycle is exceeding the T_g of the PPS-matrix, annealing effects take place in the composite laminates. The maximum temperature during testing (160 °C) is kept far below the melting temperature of the PPS (~280 °C - 290 °C,[7])

To investigate these annealing effects, two specimens of each lay-up (i.e. $[(0,90)]_{4S}$ and $[(0,90)]_{4S}$) are put in a climate chamber (Figure 8-27) and all four samples are connected to the FBG-scan X08 interrogator to analyse the spectral response of the embedded DTG®s during temperature cycling. Temperature readings of a Pt100-probe and measurements with the FBG-scan are synchronized using a Labview based software program.

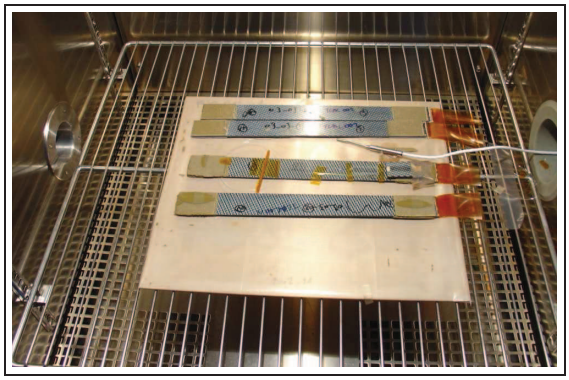

Figure 8-26: Test-coupons placed in a climate chamber to perform temperature tests. A Pt-100 probe is placed next to the samples to register the temperature.

Two approaches are used: First a temperature cycle (Cycle I) is executed in two steps using the following temperature sequences:

- 20 °C (initial measurement 'before'),
- Cycle Ia: -20 °C till 60 °C (Figure 8-27, bottom),
- Cycle Ib: 40 °C till 160 °C (Figure 8-27, bottom).

At each temperature level the Bragg spectrum of all samples is recorded and a full polarization sweep (0° – 190°) is performed to analyse the birefringence effects and transverse residual strain release (Section 8. 3. 1.).

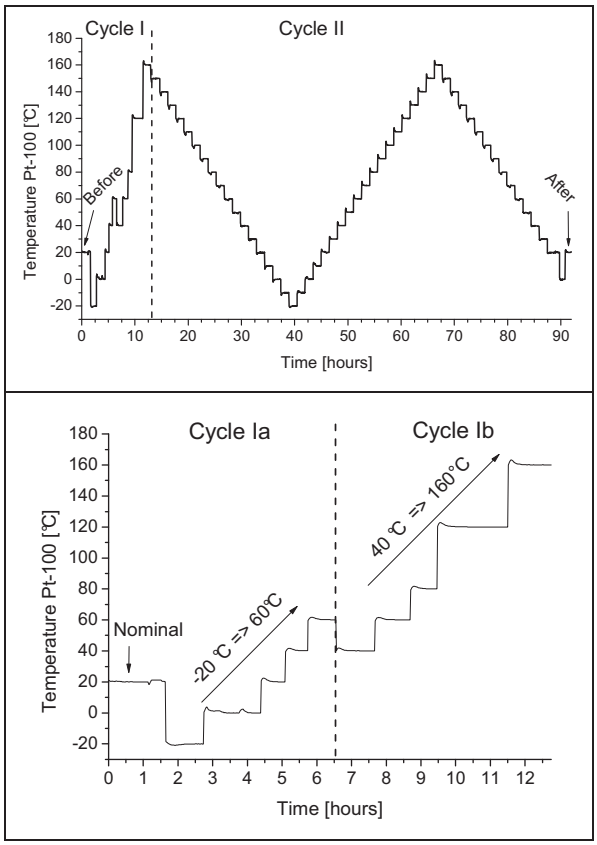

Figure 8-27: Complete temperature profiles from -20 °C till 160 °C divided in two cycles (top), detail of Cycle 1 (bottom).

After the first temperature cycle the COG wavelength of the full de-polarized spectra of all DTG®s is followed during a second temperature cycle (Cycle II) which is executed in three steps:

- Cycle IIa: 160 °C till -20°C
- Cycle IIb: -20 °C till 160 °C
- Cycle IIc: 160 °C till 0°
- 20°C (measurement 'after')

This cycle is used to compare (i.e. characterize) the macroscopic thermal behaviour of both types of laminates by measuring the global peak shift as function of temperature. This will be further discussed in Section 0.

8. 3. 1. Thermal transverse residual strain release_annealing effects

8. 3. 1. a. Total Bragg peak response

To illustrate the influence of the thermal strains in the composite at different temperatures, the Bragg response from room temperature up to 160 °C is shown in Figure 8-28 for a $[(0,90)]_{4S}$ laminate (sample n°7) and for a $[(90,0)]_{4S}$ laminate (sample n°11). As mentioned in Chapter 6 the Bragg peak is typically more heavily distorted in the $[(0,90)]_{4S}$ laminate. This same behaviour is also seen for the samples of the two lay-ups investigated here. We observe from the spectra in Figure 8-28 that the 'initial' distortion at 20 °C of the Bragg peak in the $[(0,90)]_{4S}$ sample is much wider than the Bragg peak in the $[(90,0)]_{4S}$ sample.

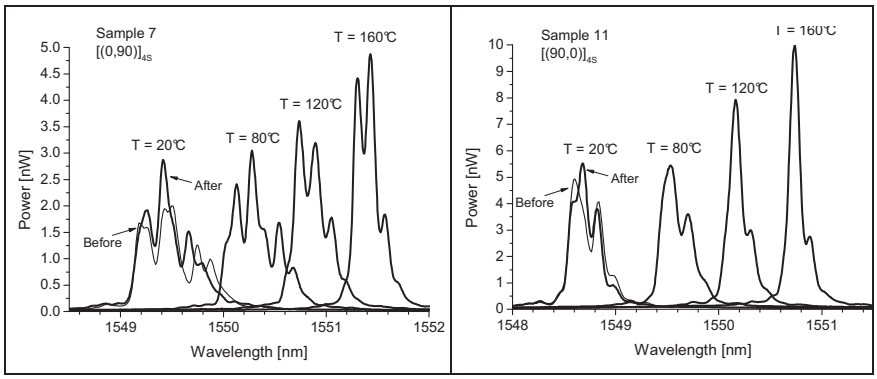

Figure 8-28: Spectral response for sample n°7 ($[(0,90)]_{4S}$) (left), and sample n°11 ($[(90,0)]_{4S}$) (right) at different temperatures. The spectrum at 20°C before and after the test is indicated in each graph.

However, for both samples we notice that the peak distortion decreases at higher temperatures, and as a consequence the width of the spectra is reduced. Moreover, for sample n°11 we even see that the Bragg peak at 160 °C becomes almost non-distorted. This illustrates that the effect of heating reverses the thermal induced strains in the composite. Obviously, the transverse strain difference changes as well. A permanent change of the spectra at 20 °C is observed as well; if we compare the spectrum recorded at 20 °C before and after the temperature cycling, the Bragg spectra of both samples changed indicating a residual strain release. This effect is further explored in the following subsection.

8. 3. 1. b. Transverse residual strain release

In analogy to the monitoring of the transverse strain difference during longitudinal loading in previous section, the procedure of polarization testing is applied here to study the birefringence in the embedded DTG®s during thermal testing. An example

of the spectral response of the 'fast' and 'slow' peak of the DTG embedded in sample n° 7 at the two extreme temperatures (-20 °C and 160 °C) is shown in Figure 8-29, left, with the de-polarized spectra plotted as well (dashed lines). As expected from the narrowing of the peaks seen in Figure 8-28, left and Figure 8-29, left, the transverse strain difference in the $[(0,90)]_{4S}$ is high at lower temperatures and it decreases at higher temperatures. The evolution of the calculated transverse strain difference against temperature for all samples is shown in Figure 8-29, right.

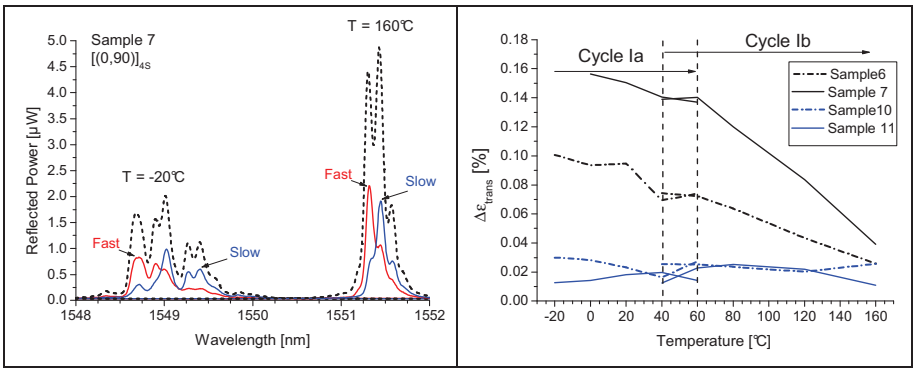

Figure 8-29: Spectral response of the 'fast' and 'slow' peak for sample n°7 at -20 °C and 160 °C (left), evolution of the transverse strain difference $\Delta\varepsilon_{trans}$, against temperature for all samples during Cycle Ia and Cycle Ib (right).

Although the transverse strain difference changes clearly for the $[(0,90)]_{4S}$ samples, the effect is not manifesting in the $[(90,0)]_{4S}$ samples; only a very small decrease is found for sample n°10, and no clear course is found in the strain evolution of sample n°11. As such we can conclude that the transverse thermal strains in the mid-plane layers of the $[(90,0)]_{4S}$ lay-up are much lower compared to the $[(0,90)]_{4S}$ lay-up, which confirms that the residual transverse strain formation in the mid-planes of the $[(90,0)]_{4S}$ laminate during consolidation is much lower too.

To investigate the annealing effect or residual strain release, the author compares the transverse strain difference of all samples measured at 20 °C before and after the complete temperature test. The de-polarized spectra of all four samples before and after the test are shown in Figure 8-30. We observe that all Bragg spectra have changed shape, however, the effect is most significant in the $[(90,0)]_{4S}$ stacked laminates. The individual peaks are shifted and the peak width after the test is narrower, which proves that the strain state around the optical fibre has changed.

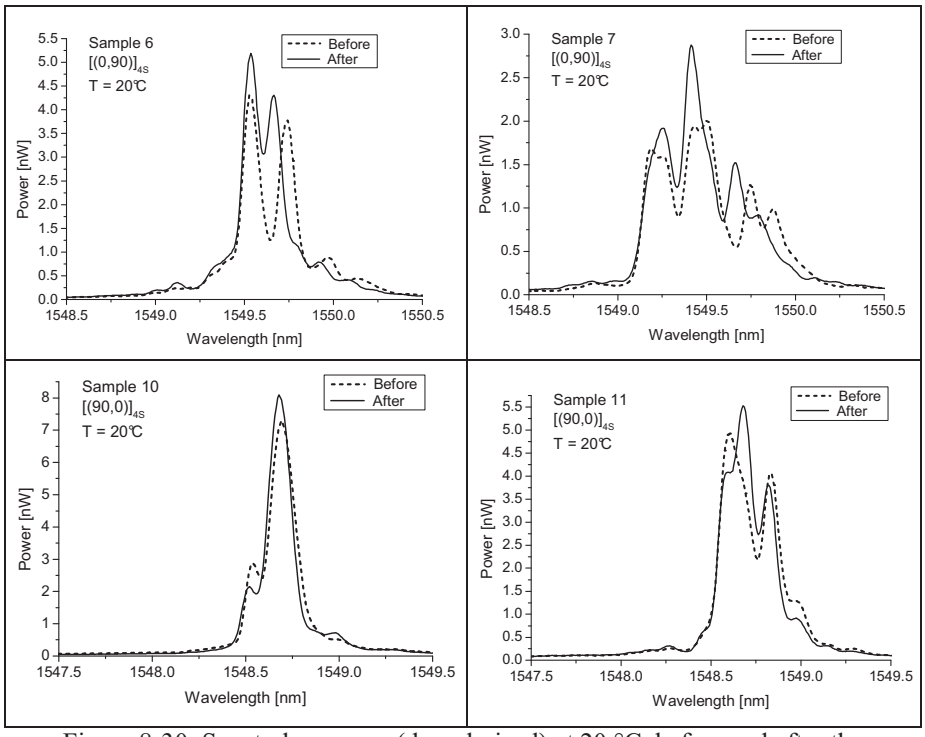

Figure 8-30: Spectral response (de-polarized) at 20 °C, before and after the temperature test, for all samples.

The transverse strain difference before and after testing is calculated from the change in birefringence effects for all samples, using the polarization controller to analyse the spectra, and values are given in Table 8-12.

Table 8-12: Transverse strain, $\Delta\varepsilon_{trans}$ at 20°C, before and after the temperature test.

		$\Delta\varepsilon_{trans}$ [%]	
n°*		Before	After
6	$[(0,90)]_{4S}$	0.0812	0.0283
7	$[(0,90)]_{4S}$	0.1450	0.1099
10	$[(90,0)]_{4S}$	0.0233	0.0173
11	$[(90,0)]_{4S}$	0.0212	0.0241

As expected, no significant transverse residual strain release is found in case of the $[(90,0)]_{4S}$ lay-up, however, in case of the $[(0,90)]_{4S}$ stacked laminates, the value of $\Delta\varepsilon_{trans}$ for sample n°6 and sample n°7 has decreased with approximately 300 % and 30 %, respectively. Again the distribution of the results is large which proves that the local residual strain in the woven fabric composite is complex and varies significantly along the length of the unit cell.

*The numbering of the samples is conform to Table 6.6 (Chapter 6), all embedded DTG®s are from PR2007_2

8. 3. 2. Temperature characterization

In analogy to the temperature calibration of a non-embedded DTG® (Chapter 4), the wavelength independent linear and quadratic temperature coefficients (S_{T1} and S_{T2}) of the embedded DTG®s in all samples are determined during the second cycle (Cycle II, Figure 8-27). The purpose is to use these coefficients to compare the 'global' thermal behaviour of the $[(0,90)]_{4S}$ and $[(90,0)]_{4S}$ laminates, and to investigate the influence of thermal cycling on the individual coefficients. As an example, the COG wavelength shift of sample n°7 during Cycle IIa (160 °C till -20 °C), Cycle IIb (-20 °C till 160 °C), and Cycle IIc (160 °C till 20 °C) is plotted in Figure 8-31 against the applied temperature. From this plot no significant changes are visible. To demonstrate the influence of the temperature cycling the author has determined the linear and quadratic temperature coefficients, $S_{T1'}$ and $S_{T2'}$, of the individual curves.

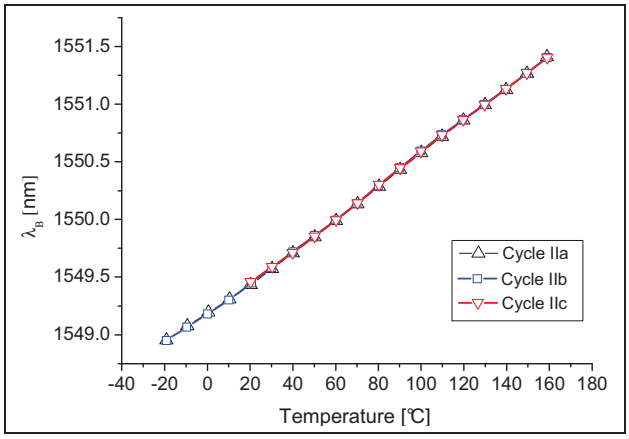

Figure 8-31: Example of the COG wavelength evolution of sample n°7 during Cycle IIa, Cycle IIb and Cycle IIc.

To calculate the $S_{T1'}$ and $S_{T2'}$ coefficients, the logarithmic calibration approach (Equation 4-23, Section 4.3.3) is applied similar to the temperature calibrations performed in Chapter 4. To determine the $S_{T1'}$ and $S_{T2'}$ coefficients the curves of $\ln \lambda_B / \lambda_{B,0}$ are fitted against the temperature difference ($T - T_{ref}$) using a second order polynomial. The individual coefficients of all samples are given in Table 8-13.

Table 8-13: Linear ($S_{T1'}$) and quadratic ($S_{T2'}$) temperature coefficients of all samples for Cycle IIa, Cycle IIb and Cycle IIc.

		Cycle IIa		Cycle IIb		Cycle IIc	
n°*		S_{T1} [10^{-6}]	S_{T2} [10^{-9}]	S_{T1} [10^{-6}]	S_{T2} [10^{-9}]	S_{T1} [10^{-6}]	S_{T2} [10^{-9}]
6	$[(0,90)]_{4S}$	9.005	3.3	9.029	2.7	9.382	0.2
7	$[(0,90)]_{4S}$	8.651	3.7	8.833	2.1	9.296	-1.0
10	$[(90,0)]_{4S}$	9 .177	4.1	9.285	3.1	9.625	0.8
11	$[(90,0)]_{4S}$	9.003	4.8	9.133	3.7	9.438	1.7

From the values of Cycle IIa, we observe that the coefficients of all samples are in the same order of magnitude. Compared to a non-embedded DTG® with $S_{T1} = 6.342 \cdot 10^{-6}$ and $S_{T2} = 7.6 \cdot 10^{-9}$ (Table 4-10) we notice that the linear term for the embedded DTG®s is approximately 40 % higher, indicating that the thermal expansion of the laminate is dominating the total wavelength shift. The CTE of the composite will be determined in the next section.

If we compare the values of the individual cycles, we notice an increase of the linear term ($S_{T1'}$) and a decrease of the quadratic term ($S_{T2'}$) for all samples. For the $[(0,90)]_{4S}$ test-coupons, we see that initially (Cycle IIa) the $S_{T1'}$ of sample n°7 is lower than the $S_{T1'}$ of sample n°6, however in Cycle IIc, the coefficients become nearly identical. This indicates that the residual strain state in the longitudinal direction changes and more or less neutralizes during thermal cycling. This is confirmed by the fact that in Cycle IIc, all linear coefficients are matching. As such we can conclude that after annealing the global temperature behaviour of both types of lay-up is found identical. Remark that in Cycle IIc the $S_{T2'}$ of all samples are very small compared to Cycle IIa. No clear explanation is found for this effect, however, this effect that the linear term, i.e. the thermal strain or CTE of the composite is dominating the wavelength shifts of the embedded sensors. The calculations of the thermal strains and CTEs for all samples are elaborated next.

8. 3. 3. Calculation of the thermal strain during the temperature cycle

In principle, as discussed in Chapter 6 on the calculation of the thermal strains during curing of the carbon-epoxy laminate, one can use the coated DTG®s to calculate the thermal strains of the composite by means of a temperature compensation technique. The temperature compensated thermal strain is given by (Equation 6-6, Section 6.6.2):

$$\alpha_s(\Delta T - \Delta T_0) = \frac{1}{S_\varepsilon}\left[\ln\frac{\lambda_B}{\lambda_{B,0}} - S_{T1}\left(\Delta T - \Delta T_0\right) - S_{T2}\left(\Delta T^2 - \Delta T_0^2\right)\right] + \alpha_f(\Delta T - \Delta T_0)\,, \quad 8\text{-}3$$

with α_f the CTE of silica, α_s the CTE of the composite material, $\Delta T = T - T_{ref}$, the difference in temperature between the reference temperature during calibration (T_{ref}) and an arbitrary time during the measurement (T), and $\Delta T_0 = T_0 - T_{ref}$, the

* The numbering of the samples is conform to Table 6.6 (Chapter 6), all embedded DTG®s are from PR2007_2

difference in temperature between the zero point of the measurement (T_0) and the reference temperature during calibration. Because in this calibration the zero point is the same as the reference temperature ($T_0 = T_{ref} = 20.3\ °C$ the term $\Delta T_0 = 0$ and can be omitted in Equation 8-3. During the complete temperature cycle, additionally, the author has placed two temperature compensating plates next to the test-coupons, each having a surface mounted DTG® (Figure 8-9) and a stripped DTG® in a capillary (identical to the specimens used during temperature calibration of a non-embedded DTG®, Chapter 4). By assuming that the thin layer of UV cured glue of the surface mounted DTG®s has no significant influence on the thermal strain, these items are used to calculate the thermal strain in the composite during the last cycle (Cycle IIc). In fact, because we use a second (identical) DTG® in a capillary which is kept strain free, we can use these sensor readings to compensate for the intrinsic temperature sensitivity of the surface mounted DTG®s on the T-compensating plates. The second term in Equation 8-3 can then be replaced by $\ln \lambda_{B,T} / \lambda_{B,T,0}$. Equation 8-3 can then be reduced to

$$\alpha_s \cdot \Delta T = \frac{1}{S_\varepsilon}\left[\ln\frac{\lambda_B}{\lambda_{B,0}} - \ln\frac{\lambda_{B,T}}{\lambda_{B,T,0}}\right] + \alpha_f \cdot \Delta T\,. \qquad 8\text{-}4$$

As an example the thermal strain ($\alpha_s \cdot \Delta T$) is calculated using Equation 8-4 at three different temperatures, $T = 80\ °C, 100\ °C, 160\ °C$, i.e. just below the T_g, just above T_g and at maximum temperature. By using $\alpha_f = 0.55 \cdot 10^{-6}\ °C^{-1}$, the CTE of the composite can be determined. The values of the thermal strain and CTE calculated using both temperature compensating plates are given in Table 8-14.

Table 8-14: Thermal strain at $T = 80\ °C, 100\ °C, 160\ °C$ calculated using Equation 8-4 for two compensating plates.

	T-compensating plate 1		T-compensating plate 2	
$T_0 = 20.3\ °C$	$\alpha_s \cdot \Delta T$ [%]	α_s [10^{-6} °C^{-1}]	$\alpha_s \cdot \Delta T$ [%]	α_s [10^{-6} °C^{-1}]
T = 80 °C	0.025	4.1	0.026	4.3
T = 100 °C	0.033	4.1	0.034	4.2
T = 160 °C	0.049	3.6	0.050	3.6

Both compensating plates provide similar results. No literature or similar research on the CTE of the Cetex® material is found. However, according the manufacturer' (TenCate Advanced Composites) internal information the values measured using thermomechanical analysis (TMA) are found in the same range, thus the CTE calculated from the DTG®s can be assumed as being correct within acceptable limits. Note that the CTE of the composite material ($\alpha_s \approx 4 \cdot 10^{-6}\ °C^{-1}$) is approximately seven times higher than the CTE of silica ($\alpha_f = 0.55 \cdot 10^{-6}\ °C^{-1}$)

which proves that the linear term ($S_{T1'}$) is dominated by the thermal expansion of the laminate.
In addition to the calculations using the temperature compensating plates the same calculations using Equation 8-4 are repeated for a temperature of T = 160 °C, for the embedded DTG®s of all samples in Table 8-13. The results are given in Table 8-15. We can state that both the surface mounted DTG®s as well as the embedded DTG®s are suited to calculate the thermal expansion of the composite within acceptable limits. Note that in Table 8-13 the values found for the linear temperature coefficients of the $[(90,0)]_{4S}$ laminates are highest, which already indicates that the thermal expansion must be higher. This effect is confirmed by the calculated thermal strain and CTE given in Table 8-15.

Table 8-15: Thermal strain at $T = 160\ °C$ calculated using Equation 8-4 for all test-coupons with embedded DTG®s.

n°*	$T_0 = 20.3\ °C$ $T = 160\ °C$	$\alpha_s \cdot \Delta T$ [%]	α_s [10^{-6} °C^{-1}]
6	$[(0,90)]_{4S}$	0.045	3.3
7	$[(0,90)]_{4S}$	0.040	2.9
10	$[(90,0)]_{4S}$	0.051	3.7
11	$[(90,0)]_{4S}$	0.049	3.5

The CTE calculated for the $[(90,0)]_{4S}$ match very well the CTEs found from the compensating plates. The CTE of the $[(0,90)]_{4S}$ are lower. No exact explanation is found for this different behaviour. However, because of the different stacking sequence, the local thermal strain distribution the mid-plane area, is different when the warp yarns are oriented towards each other ($[(0,90)]_{4S}$) then if the weft yarns are oriented towards each other ($[(90,0)]_{4S}$). Moreover, although the transverse influences are small, there is found a correlation between the magnitude of the transverse strain difference (Table 8-12) and the local longitudinal thermal expansion or CTE. The highest $\Delta\varepsilon_{trans}$ after temperature cycling at 20 ° are found for sample n°6 and sample n°7 ($[(0,90)]_{4S}$) and both these samples have the lowest thermal expansion and α_s during the last cycle (Cycle IIc).

8. 4. CONCLUSIONS

Two types of lay-up of the carbon-PPS woven fabric are investigated using the embedded DTG®s. It is shown that the material exhibits a complex local longitudinal strain distribution because of its weave pattern. The combination of internal yarn nesting of the weft and warp reinforcement bundles and the though thermoplastic PPS matrix are causing high strain gradients along the length of one unit-cell which on their turn are causing the Bragg spectra of the embedded DTG®s to be heavily distorted. This effect is seen immediately after manufacturing, and is more distinct in the mid-plane layers of the $[0,90)]_{4S}$ lay-up because of the contact between the weft yarns and the optical fibre. The effect of Bragg peak distortion is even more severe when the composite is being loaded. Even though the reflected

* The numbering of the samples is conform to Table 6.6 (Chapter 6), all embedded DTG®s are from PR2007_2

Bragg spectrum is severely distorted after manufacturing, the embedded DTG®s are well suited to be used as strain sensor in woven-fabrics for multiple purposes during mechanical testing and thermal testing.

Local strain distribution
The occurrence of the multiple peaks in the distorted spectrum are used to measure local strain concentrations along the length of a unit-cell. The DIC measurements, the meso-FE simulations and the minimum and maximum strain measurements of the DTG®s show matching results. However, the maximum simulated values on the surface are overestimated compared to the experimental results. The meso-FE model needs still to be improved and is provender of the research of Dagummati S. These results underlines the fact that a combination of accurate experimental (strain) measurement systems and simulation tools is a necessity when investigating complex composite materials such as woven fabrics. It is proven that the embedding of fibre Bragg gratings is a perfect tool to better investigate the inner complex strain fields, however, the interpretation of the Bragg spectrum should be done with care. Several authors have presented the simulation of the Bragg spectrum by using the optical transfer matrix formalism for different purposes. This method is based on the electrical field distributions inside the grating structure and allows to implement refractive index perturbations and thus local strain distributions. Hence, the shape of the reflection spectrum can be simulated for any microscopic perturbation, longitudinal and transverse [27]. This technique has certainly potential for (complex) non-uniform strain field measurements and is provender of future research.

Global strain measurements
The global strain determined using the complete spectral shift of the embedded DTG®s match very well the extensometer readings. These results confirm that the transverse effects on the longitudinal strain reading of the coated DTG®s are small. The DTG®s are well suited to measure high strains. Even after more than 1.3 million tension-tension cycles at 0.5 %, the DTG®s showed a perfect response to the applied strain, indicating that the bonding with the composite material is excellent. The DTG®s are used to investigate the stiffness during fatigue cycling, moreover the methodology of mechanical testing with the repeated progressive loading cycles allowed to measure the gradual increase of the permanent deformation during loading and even up to failure of the composite. Even though cracks are initiated at strain levels below 0.5 % applied strain, there is found almost no stiffness degradation.

Permanent strains
The permanent strain in the woven-fabric is strongly dependent on the applied stress and less dependent on the amount of loading cycles. Identical behaviour is found for the two stacking sequences. For load levels up to approximately 500 MPa, the permanent strains are maximal 0.04 %. No matching results are found between the results from the FE-model using the homogenized engineering constants and the transverse strain measurements of the embedded DTG®s. Because of the fact that large strain gradients exist in the woven-fabric composite, the homogenized model underestimates the local effects acting on the embedded sensors. Therefore, the homogenized model can thus not be used to formulate an accurate strain transfer

matrix. Most probably more detailed simulations on the meso-scale level with embedded optical fibre will be necessary to reveal the complex multi-axial strain interaction. Moreover, the tests carried out in this work are limited to tension-tension testing, hence more experiments in the three loading directions are necessary to validate the model. This is provender for further research.

Transverse strain state
From the investigations on the transverse strain difference during fatigue cycling, no real conclusions can be drawn. The maximum transverse strain difference measured during the first loading cycle is small (approximately 0.007 % / 100MPa). Moreover, after 1.3 million cycles the transverse strain difference is still in the same order of magnitude of the fist cycle. These measurements confirm that the influence on the longitudinal strain measurements during the tension-tension testing is small over the complete lifetime of the material. Hence, the assumption that the induced axial strain in the optical fibre is equal to the longitudinal composite strain holds.

Thermal strain effects
Results from the spectral response during heating of the thermoplastic carbon-PPS woven fabrics reverses more or less the thermal residual strains. The shape of the spectrum at 160 °C is close to the undistorted spectral shape. If the material is cooled down again the spectral shape has changed compared to the initial spectrum before heating. This proves that annealing effects take place. The measured transverse strain difference in the DTG®s decreases significantly in case of the $[(0,90)]_{4S}$ stacked laminates (~300 %), however, no significant effects are noticed for the samples with $[(0,90)]_{4S}$ lay-up.
If we characterize the laminates as function of temperature, the temperature calibration coefficients change during thermal cycling. The linear coefficient (S_{T1},) is found higher than the coefficient of a non-embedded DTG®, which proves that the thermal expansion of the laminate is dominating. The calculations of the (longitudinal) thermal strains is performed using the temperature compensation technique. The CTE of the Cetex® is determined and it is found that $\alpha_s \approx 3.6 \cdot 10^{-6}$ °C^{-1}. The values of the $[(90,0)]_{4S}$ laminates match very well the CTE determined using surface mounted DTG®s. For the $[(0,90)]_{4S}$ a correlation is found between the transverse strain states and the lower values found for the thermal strain and CTE ($\alpha_s \approx 3 \cdot 10^{-6}$ °C^{-1}). A maximal difference of approximately 25 % is found between the two lay-ups. This effect confirms that although macroscopically both laminates the identical the thermal strain in the symmetry plane is significantly influenced by the stacking sequence. However, to draw any conclusions on the thermal behaviour of both laminates, additional measurements are necessary with sensors embedded in between different layers through the thickness of the laminate.

Although the Cetex® material has a complex material behaviour, the results in this chapter have certainly shown that the (embedded) DTG® is a valuable and multifunctional tool to study the internal mechanical and thermal strain states in thermoplastic (woven-fabric) fibre reinforced plastics.

8. 5. REFERENCES

1. Peters, K., Studer, M., Botsis, J., Iocco, A., Limberger, H., and Salathe, R., *Embedded optical fiber Bragg grating sensor in a nonuniform strain field: Measurements and simulations.* Experimental Mechanics, 2001. **41**(1): p. 19-28.
2. Ling, H.Y., Lau, K.T., Jin, W., and Chan, K.C., *Characterization of dynamic strain measurement using reflection spectrum from a fiber Bragg grating.* Optics Communications, 2007. **270**(1): p. 25-30.
3. Prabhugoud, M. and Peters, K., *Efficient simulation of Bragg grating sensors for implementation to damage identification in composites.* Smart Materials & Structures, 2003. **12**(6): p. 914-924.
4. Karalekas, D., Cugnoni, J., and Botsis, J., *Monitoring of process induced strains in a single fibre composite using FBG sensor: A methodological study.* Composites Part a-Applied Science and Manufacturing, 2008. **39**(7): p. 1118-1127.
5. Giaccari, P., Dunkel, G.R., Humbert, L., Botsis, J., Limberger, H.G., and Salathe, R.P., *On a direct determination of non-uniform internal strain fields using fibre Bragg gratings.* Smart Materials & Structures, 2005. **14**(1): p. 127-136.
6. ASTM, *D3039: Standard Test Method for Tensile Properties of Polymer Matrix Composite Materials*. 2002: USA.
7. Ten Cate Advanced Composites. Available from: http://www.tencate.com/.
8. Vlekken, J., VAN ROOSBROECK, J., and VOET, M., *Method and means for monitoring a bragg grating fibre on a surface*, F.S. bvba, Editor. 2009: Belgium.
9. Lang, E.J. and Chou, T.W., *The effect of strain gage size on measurement errors in textile composite materials.* Composites Science and Technology, 1998. **58**(3-4): p. 539-548.
10. Daggumati, S., Voet, E., Van Paepegem, W., Degrieck, J., Xu, J., and Lomov, S.V., *Local strain in a 5-harness satin weave composite under static tension: part II - Meso-FE analysis.* Composite Science and Technology, 2010(Under review).
11. Daggumati, S., Voet, E., Van Paepegem, W., Degrieck, J., Xu, J., and Lomov, S.V., *Local strain in a 5-harness satin weave composite under static tension: part I - experimental analysis.* Composite Science and Technology, 2010(Under review).
12. FOS&S. Available from: http://www.Fos-s.com.
13. Ivanov, D.S., Lomov, S.V., Ivanov, S.G., and Verpoest, I., *Stress distribution in outer and inner plies of textile laminates and novel boundary conditions for unit cell analysis.* Composites Part a-Applied Science and Manufacturing. **41**(4): p. 571-580.
14. Anzelotti, G., Nicoletto, G., and Riva, E., *Mesomechanic strain analysis of twill-weave composite lamina under unidirectional in-plane tension.* Composites Part a-Applied Science and Manufacturing, 2008. **39**(8): p. 1294-1301.
15. Takano, N., Zako, M., Fujitsu, R., and Nishiyabu, K., *Study on large deformation characteristics of knitted fabric reinforced thermoplastic composites at forming temperature by digital image-based strain*

measurement technique. Composites Science and Technology, 2004. **64**(13-14): p. 2153-2163.
16. Grediac, M., *The use of full-field measurement methods in composite material characterization: interest and limitations.* Composites Part a-Applied Science and Manufacturing, 2004. **35**(7-8): p. 751-761.
17. Limess. Available from: http://www.Limess.com.
18. Daggumati, S., Van Paepegem, W., Degrieck, J., Xu, J., Lomov, S.V., and Verpoest, I., *Local damage in a 5-harness satin weave composite under static tension: Part II - Meso-FE modelling.* Composites Science and Technology, 2010. **70**(13): p. 1934-1941.
19. Daggumati, S., Voet, E., Van Paepegem, W., Degrieck, J., Praet, T., Verhegghe, B., Xu, J., Ivanov, D.S., Lomov, S.V., and Verpoest, I., *Local strain in a 5 - harness satin weave composite under static tension: Part II – Meso-FE analysis.* Composites Science and Technology, 2010_in review.
20. Zako, M., Uetsuji, Y., and Kurashiki, T., *Finite element analysis of damaged woven fabric composite materials.* Composites Science and Technology, 2003. **63**(3-4): p. 507-516.
21. KULeuven, M.; Available from: http://www.mtm.kuleuven.be/Onderzoek/Composites/software/meshtex.
22. De Baere, I., *Experimental and Numerical Study of Different Setups for Conducting and Monitoring Fatigue Experiments of Fibre-Reinforced Thermoplastics*, in *Materials science and engineering*. 2008, PhD dissertation at Ghent University: Ghent.
23. Barnes, J.A., *Thermal-expansion behavior of thermoplastiv composites.2.* Journal of Materials Science, 1993. **28**(18): p. 4974-4982.
24. Barnes, J.A. and Byerly, G.E., *The formation of residual-stresses in laminated thermoplastic composites.* Composites Science and Technology, 1994. **51**(4): p. 479-494.
25. Manson, J.A.E. and Seferis, J.C., *Process simulated laminate (PSL)- a methodology to internal-stress characterization in advanced composite materials.* Journal of Composite Materials, 1992. **26**(3): p. 405-431.
26. Unger, W.J. and Hansen, J.S., *The effect of cooling rate and annealing on residual-stress development in graphite fiber reinforced PEEK laminates.* Journal of Composite Materials, 1993. **27**(2): p. 108-137.
27. Okabe, Y., Yashiro, S., Tsuji, R., Mizutani, T., and Takeda, N., *Effect of thermal residual stress on the reflection spectrum from fiber Bragg grating sensors embedded in CFRP laminates.* Composites Part a-Applied Science and Manufacturing, 2002. **33**(7): p. 991-999.

Chapter 9 CONCLUSIONS AND FUTURE PERSPECTIVES

To conclude this dissertation the author summarizes the main conclusions and realisations of the work presented in each chapter. Finally, the author will give his recommendations with regard to future work and he will put forward which realisations of this work are relevant with regard to the industrial application. The author will close his work with an abstract of a new European research project which has started in September 2010, where a continuation of his work on the further improvement on smaller diameter Bragg sensors specially, is assured.

9. 1. THIS DISSERTATION

PARTI: The improved draw tower fibre Bragg grating: Manufacturing and characterization

9. 1. 1. Draw tower fibre Bragg grating technology

In this chapter the author has introduced the features of the state of the art draw tower grating technology which will be used in this work and compared it with conventional FBG writing methods. The draw tower technology allows to manufacture high quality coated draw tower fibre Bragg gratings (DTG®s), which are less fragile compared to conventional FBGs. This type of FBG is written in highly GeO_2 doped (photosensitive) silica fibre using one single laser shot during the drawing of the optical fibre. Because of the high dopant concentration, these fibres exhibit a high fibre attenuation compared to standard SMF, however, from bending tests using mandrels of different diameters, the author has found that the bending loss of the DTG®-fibre is extremely low. This result is a very interesting feature with regard to embedding the optical fibres and sensors later on in the woven-fabric laminates. A Talbot interferometer is used to write FBGs with a (uniform) periodic refractive index pattern. A liquid UV curable ORMOCER® coating is applied on the fibre using a coating cup operating at atmospheric pressure and a tapered coating nozzle with a very narrow nose. An important effect on the DTG®-reflectivity is noticed during the UV-curing of the ORMOCER® coating. Tests are carried out on standard DTG®s to investigate the reflectivity drop as function of UV curing time. It is found that the reflectivity drop after exposure is as high as 50 % and that thermal annealing occurs due to the heat generated during the UV-curing process.

9. 1. 2. Developing & manufacturing the 80µm DTG®s

Here the author has elaborated in detail the manufacturing of the 80 µm DTG®s starting from the production of a highly GeO_2 - doped fibre, up to the application of the ORMOCER® coating using three newly developed DTG®-nozzles. The optical properties of the two fibres are investigated in detail. The Equivalent Step Index (ESI) of the single mode fibre is determined from the original preform with $\Delta n = 15.3 \cdot 10^{-3}$. Other important results from this chapter are that the total fibre loss for both fibres is very high: 11.3 dB/km for the 125 µm fibre and 17.6 dB/km for the

80 µm fibre, measured at $\lambda = 1.55\mu m$. The extreme high loss in the fibres originates from inhomogeneities in distribution of the GeO_2 and the germanium oxygen-deficient centres (GODC). The higher transmission losses of the 80 µm compared to the 125 µm fibre are most probably explained by the difference in drawing conditions. The diameter of the core of both fibres is determined and is nearly identical with $d \approx 4.5\mu m$, which is half of the core diameter of standard single mode fibres. From the ESI (Δn), the V-parameter and the normalized propagation constant, the effective refractive index of the optical fibre is determined with $\overline{n} = 1.4459$. This value of the effective refractive index is then used in all further calculations in this work.

New coating-nozzles with smaller exit holes are developed using the state of the art wire spark erosion technology. An optimization procedure resulted in three different coating nozzles. The final design delivered very good results with a total coating diameter of approximately 114 µm and an excellent coating concentricity (<1 µm). These dimensions are very close to the thickness of a typical composite reinforcement layer (~0.1 mm), hence the dimension of the new 80 µm coated DTG®s has improved significantly compared to the standard 190 µm outer diameter of the 125 µm DTG®.

The tensile strain of both the 80 µm and 125 µm fibres is higher than 6 % and the Weibull parameter of both fibres is found $\sigma_0 \approx 4700 MPa$, with a Weibull size parameter for the 80 µm fibre of $m_{82\mu m} \approx 37$, which is a much higher value compared to stripped optical fibres with typical m-values of m = 4 – 5. Which proves that the surface defects are less distinct for the coated optical fibre.

The tensile strength (and strain) of both DTG®-fibres is outstanding. Compared to the mechanical performance of the aerospace qualified composites used in this dissertation, the optical fibre has an ultimate strain which is more than five times higher and an ultimate stress that is approximately three times higher. These results prove that from mechanical point of view the newly developed DTG®s are very well suited to be used for composite testing.

With regard to the splicing of the new 80 µm fibres to standard SMF one should remark that the core radius (and thus mode field diameter) of the highly doped optical fibre is half of the core of the (typical 9 – 10 µm). To avoid excessive splice losses, the author recommends to use a splicing device with core-alignment instead of a cladding-alignment.

9. 1. 3. DTG® characteristics_80µm versus 125µm

In this chapter the author has elaborated in detail the methods and setups to characterize the maximum reflectivity, the opto-mechanical and thermo-optic properties and the thermal behaviour of the 80 µm DTG®s compared to the 125 µm reference DTG®s. It is shown that the exact sensors characteristics of DTG®s or fibre Bragg gratings in general are not easily determined. There are multiple factors which need to be taken into account, such as the intrinsic (cross-)sensitivity of strain and temperature, the thermal stability, the coating properties and last but not least the calibration setup itself. If one makes errors on the level of calibration parameters (i.e. determination of the FBG' sensitivities), obvious this will have later on

consequences on the output of the sensor in service. Thus calibrations of FBGs should be carried out with care.

First of all it is found that both sensors have identical peak reflectivity and peak width (FWHM). The author has shown that the calibration of the strain gauge parameter (S_ε), is not straightforward. From the presented results on the strain gauge factors we can conclude that the manual calibration using a long piece of fibre (approximately 0.8 m – 1 m) fixated in small steel capillaries is the most accurate method to determine the axial strain sensitivity of both the 80 µm and 125 µm DTG®s. A strain gauge factor of $S_\varepsilon \approx 0.777$ is found for both types. This value is found lower than the theoretical determined S_ε-factor of $S_{\varepsilon,theor} \approx 0.798$, however, because of the possible scatter on the theoretical strain gauge factor due to the uncertainty of the exact optical properties (i.e. $\overline{n}$, υ_f) and the strain optic coefficients (p_{11} and p_{12}) the author believes that the experimental and theoretical obtained S_ε-factor are matching within acceptable limits. The experimental strain gauge factor will be further applied in this work.

From the point of view of temperature calibration the author has proven that the temperature dependence of a FBG is given by a second order polynomial. As such two temperature parameters are found (S_{T1} and S_{T2}) which again are found identical for the 80 µm and 125 µm DTG®s ($S_{T1} = 6.34 \cdot 10^{-6} °C^{-1}$ and $S_{T2} = 7.6 \cdot 10^{-9} °C^{-2}$). These parameters will further in this work become important when considering accurate temperature compensation techniques to determine for example the thermal expansion of composite laminates. Another issue which is studied is the thermal stability of these gratings. It is found that the DTG®s are shortly annealed during the UV-curing process of the ORMOCER® coating. As such these gratings are thermally stable up to approximately 150 °C. However, when exposed to higher temperatures (T_{max} = 350 °C) the reflectivity of both the 80 µm and 125 µm DTG®s drops to approximately 10 % of their initial power. When comparing the wavelength shift (drift) during annealing, the drop is approximately four times higher in case of the 125 µm DTG®s. A possible explanation is the probably higher homogeneous refractive index of the 125 µm DTG®s, however, further research and more annealing experiments are necessary to prove this statement.

With regard to the temperature dependency of the strain and stress sensitivity of FBGs the author has analytically determined the S_ε-factor as function of temperature and found that $S_\varepsilon(T) = 0.777 + 9.41 \cdot 10^{-5} \Delta T$. Then the author has attempted to reproduce these results experimentally for temperatures between -60 °C and 140 °C. The experimental results however, showed a large scatter on the $S_\varepsilon(T)$-factor. The author has no confidence in these results because of the uncertainty of the strain readings of the optical extensometer. More confidence is found in the load -or stress- sensitivity as function of temperature. It is found that the load sensitivity of a 80 µm is approximately 2.3 times higher than the 125 µm DTG®s, which is in accordance with the ratio of the cross-sectional surface. The results show that the coating has a large influences on the results. Similar testing on a stripped and a coated DTG®s confirms this effect, which proves that the coating stiffness is temperature dependent as well. The author has found a stress sensitivity of $S_\sigma(T) = 0.016 - 0.12 \cdot 10^{-5} \cdot \Delta T \left[nm \text{ MPa}^{-1} °C^{-1} \right]$ for the stripped fibre, which is in accordance with the results reported in literature. Additionally to the analysis of the

strain and stress sensitivity as function of temperature, tests are performed to estimate the temperature dependency of the Young's modulus of the ORMOCER® coating. In principle, when the same (axial) force is applied on a coated and stripped FBG, one is able to estimate the Young's Modulus of the fibre coating, based on the difference in strain (i.e. wavelength shift) between both FBGs. Results prove that the Young's modulus of the ORMOCER® coating material is temperature dependent and that the coating becomes stiffer at lower -and weaker at higher temperatures. However, most probably relative humidity changes have influenced the results at ambient temperatures and no accurate determination of the Young's modulus is possible. More experiments in a humidity and temperature controlled environment are necessary to accurately determine the temperature dependency of the coating stiffness.

From these numerous experiments and results the author concludes that the properties and performances of the new 80 µm DTG®s are identical to the standard 125 µm version. Thus there is no fundamental reason why we should not use the new smaller diameter high quality FBGs for strain monitoring in composites. Moreover, they have one major advantage; they are smaller and thus even better suited to be used for the incorporation in FRPs, which is subject of Part II.

PART II: DTG®s embedded in Thermoset and Thermoplastic composites

9. 1. 4. Measuring strain with embedded Fibre Bragg Gratings_an introduction

The emphasis of this Chapter has been to provide a general overview on strain measurements in fibre reinforced plastics by the usage of embedded fibre Bragg gratings and to give a concise overview of the work ongoing in the composite research community. The following theorem is posed at the beginning of the chapter: "FBG sensors and fibre reinforced plastics: a successful marriage?"
From the numerous cited research in this chapter, we can state that the properties of fibre Bragg gratings are matching the requirements of fibre reinforced plastics. So the answer on the question, "if it is a successful marriage?", is a clear yes!
The prove of this statement is given in the three following chapters.

9. 1. 5. Cure and consolidation cycle effects

In this chapter the focus is on embedded FBGs and their response during the composite curing and consolidation process. The formation and measurements of residual strains in composite laminates is discussed in detail. The relevant methods and results of other researchers are quoted and compared with own results.
Different approaches are possible to obtain information of the response of embedded FBGs. One can measure the temperature inside a composite by keeping the FBG free from strains and encapsulating it. From the induced birefringence in normally embedded DTG® the residual transverse strain differences can be measured independent from temperature. By encapsulating a sensor and keeping it free from

transverse strains, it is possible to measure the purely (temperature compensated) longitudinal strains.
An attempt is made to disconnect the transversal strains from the longitudinal strain in thermoset cross-ply laminates and the (very low) CTE of the composite is estimated using two encapsulated DTG®s. However, a relative large difference is found for both sensors because of the very small thermal strains. The author remarks that the error on the measurements induced by inaccurate temperature readings can be high. If we assume for example a temperature difference of 1°C, the longitudinal strain can vary up to approximately 20 %, which indicates that one has to be very careful when interpreting the measured longitudinal (temperature compensated) strains during curing.
Based on the measurements in the thermoset cross-ply laminate, the coated sensor measures approximately 70 % of the transversal out-of-plane strains obtained for the stripped sensor. In case of a cross-ply laminate the author has found that the out-of-plane strains are 10 to 20 times larger than the in-plane strains. This clearly illustrated that if one would neglect the (large) transversal out-of-plane strains induced in the FBG, the results will be completely different. Moreover, if one would simply calculate the longitudinal strains with the recorded wavelength shifts and neglecting any transversal effect no real conclusions can be drawn. Because composite laminates with different stacking sequence will exhibit different residual strains, interpretation of the response of embedded FBGs should be done with care, not to draw faulty conclusions on the appearing effects in the laminates during curing.
The method of polarization testing has been applied to decode the birefringence in the (severe) distorted spectra and to calculate transversal strain differences in the thermoplastic woven-fabrics. The transversal strains are found highest in the thermoset cross-ply laminates (~0.066 %) and lowest in the thermoplastic laminates (~0.01 % – 0.06 %), both measured with the coated DTG®s).

In this chapter it is shown that the embedded DTG®s are suitable to provide valuable information on the strain development during composite manufacturing, however, we have only been looking at the strain in the optical fibre. Because there exists a difference in material properties between the embedded sensor and the composite material, the strain inside the optical fibre is not necessarily equal to the strain present in the composite. As such we have to define a strain transfer method which relates the strains in both materials. A method to do that is elaborated in the next chapter.

9. 1. 6. Mechanical testing of thermoset CFRPs

In this chapter the author focusses on the multi-axial strain transfer from host material to the embedded optical fibre sensor. Because of different material properties between the optical fibre and the (anisotropic) composite laminate, the strains measured in the embedded optical fibre differ from the strains present in the composite laminate. A dual sensor configuration, with one DTG® embedded normal in the laminate, and one embedded encapsulated DTG® which is free from external transversal strains is used to develop a multi-axial strain relationship between the optical fibre sensors and CFRP cross-ply laminates. It is shown that by performing

FE simulations on a composite laminate model with embedded optical fibre, we can numerically determine the individual strain transfer coefficients.
For a stripped optical fibre the error on the transversal strain measurements is the largest when loading the composite in the longitudinal direction. It is illustrated that the K-matrix, which defines the intrinsic multi-axial strain-optic relationship of an FBG, is strongly dependent on the axial strain component, hence, the strain resolution in transverse direction (~3.7 με) in these optical fibres is relatively low compared to the resolution in longitudinal direction (~0.8 με). The transverse strain resolutions for an embedded DTG® without coating (~9 με) are worse compared to the non-embedded case. However, when the cross-ply laminates with stripped embedded DTG® are loaded transversally in-plane and out-of-plane, matching results are found for the measured composite strains and the numerical reference strains.
For the coated embedded DTG® a slightly different approach has been used. By performing a parametric study on the material properties of the fibre coating in the model, it is illustrated that the strain transfer is influenced significantly. It is shown that for a specific combination of coating properties, the results of the compression test are optimal and the measured strains in the composite match the numerical strains. The strain resolution is determined for the embedded optical fibre with 'optimal' coating properties and obvious the transverse strain resolution (~17 με) is worse than for the stripped sensor. Therefore the sensor configuration with the ORMOCER® coating is not suited to measure accurately transverse in-plane composite strains.
The presented results clearly illustrate that by using embedded fibre Bragg gratings we are able to measure multi-axial strain fields in composites. However, because the numerical determined TC-matrix is very sensitive to the used material properties in the model, care has to be taken that the used material properties are accurate, not to induce large errors in the simulations. Certainly in the case of coated optical fibres, where the transversal strain transfers are poor. However, the embedded optical fibre with coating will be able to behave more or less natural when the laminate is loaded longitudinal. As such, only small external transversal effects appear on the grating and thus the errors in the longitudinal strain calculations are kept small. This advantageous property of the coated DTG®s will be used in the final chapter, where the focus is on tensile testing experiments of thermoplastic test-coupons.

9. 1. 7. Mechanical and thermal testing of thermoplastic CFRPs

It is shown that the material exhibits a complex local longitudinal strain distribution because of its weave pattern. The combination of internal yarn nesting of the weft and warp reinforcement bundles and the though thermoplastic PPS matrix are causing high strain gradients along the length of one unit-cell which on their turn are causing the Bragg spectra of the embedded DTG®s to be heavily distorted. This effect is seen immediately after manufacturing, and is more distinct in the mid-plane layers of the $[0,90)]_{4S}$ lay-up because of the contact between the weft yarns and the optical fibre. The effect of Bragg peak distortion is even more severe when the composite is being loaded. Even though the reflected Bragg spectrum is severely distorted after manufacturing, the embedded DTG®s are well suited to be used as

strain sensor in woven-fabrics for multiple purposes during mechanical testing and thermal testing.
The occurrence of the multiple peaks in the distorted spectrum are used to measure local strain concentrations along the length of a unit-cell. The DIC measurements, the meso-FE simulations and the minimum and maximum strain measurements of the DTG®s show matching results. The meso-FE model needs still to be improved and is provender of the research of Dagummati. These results underlines the fact that a combination of accurate experimental (strain) measurement systems and simulation tools is a necessity when investigating complex composite materials such as woven fabrics. It is proven that the embedding of fibre Bragg gratings is a perfect tool to better investigate the inner complex strain fields, however, the interpretation of the Bragg spectrum should be done with care.
The global strain determined using the complete spectral shift of the embedded DTG®s match very well the extensometer readings. These results confirm that the transversal effects on the longitudinal strain reading of the coated DTG®s are small. Even after more than 1.3 million tension-tension cycles at 0.5 %, the DTG®s showed a perfect response to the applied strain, indicating that the bonding with the composite material is excellent. The DTG®s are used to investigate the stiffness during fatigue cycling, moreover the methodology of mechanical testing with the repeated progressive loading cycles allowed to measure the gradual increase of the permanent deformation during loading and even up to failure of the composite. Even though cracks are initiated at strain levels below 0.5 % applied strain, there is found almost no stiffness degradation.
The permanent strain in the woven-fabric is strongly dependent on the applied stress and less dependent on the amount of loading cycles. No matching results are found between the results from the FE-model using the homogenized engineering constants and the transverse strain measurements of the embedded DTG®s. Because of the fact that large strain gradients exist in the woven-fabric composite, the homogenized model underestimates the local effects acting on the embedded sensors.
From the investigations on the transversal strain difference during fatigue cycling, no real conclusions can be drawn. The maximum transversal strain difference measured during the first loading cycle is small (approximately 0.007 % / 100MPa). Moreover, after 1.3 million cycles the transversal strain difference is still in the same order of magnitude of the fist cycle. These measurements confirm that the influence on the longitudinal strain measurements during the tension-tension testing is small over the complete lifetime of the material.
Results from the spectral response during heating of the thermoplastic carbon-PPS woven fabrics reverses more or less the thermal residual strains. If the material is cooled down again the spectral shape has changed compared to the initial spectrum before heating. This proves that annealing effects take place. If we characterize the laminates as function of temperature, the temperature calibration coefficients change during thermal cycling. The linear coefficient ($S_{T1'}$) is found higher than the coefficient of a non-embedded DTG®, which proves that the thermal expansion of the laminate is dominating. The CTE of the Cetex® is determined and it is found that $\alpha_s \approx 3.6 \cdot 10^{-6}$ °C^{-1}. The values of the $[(90,0)]_{4S}$ laminates match very well the CTE determined using additional surface mounted DTG®s. For the $[(0,90)]_{4S}$ a correlation is found between the transverse strain states and the lower values found

for the thermal strain and CTE ($\alpha_s \approx 3 \cdot 10^{-6}$ °C^{-1}). A maximal difference of approximately 25 % is found between the two lay-ups. This effect confirms that although macroscopically both laminates the identical the thermal strain in the symmetry plane is significantly influenced by the stacking sequence. However, to draw any conclusions on the thermal behaviour of both laminates, additional measurements are necessary with sensors embedded in between different layers through the thickness of the laminate.

Although the Cetex® material has a complex material behaviour, the results in this chapter have certainly shown that the (embedded) DTG® is a valuable and multifunctional tool to study the internal mechanical and thermal strain states in thermoplastic (woven-fabric) fibre reinforced plastics.

9. 2. FUTURE PERSPECTIVES

9. 2. 1. Recommendations for future work

Like in any PhD research, where the scientist or engineer takes one step or sometimes several steps beyond the state of the art, there are still some unsolved problems or indistinct effects which are not fully explainable. From experience of his own work, the author can state that mostly such issues stay unsolved because there has not been time enough to dig into (extra) detail or simply because there has not been time to repeat some of the measurements.
Therefore the author would like to give his recommendations for future scientists how to improve the experimental results achieved in this work, such as the calibration of the non-embedded FBG and the knowledge of the embedded (coated) FBG sensors and the interpretation of the strain response to external loading.

- Improving the knowledge of the Young's Modulus and Poisson' ratio of the fibre coating
  - note that bulk material properties (typically obtained from the manufacturer) not necessarily represent the fibre coating properties because of other curing environments and material behaviour and that other experimental techniques are necessary to define the material properties of 'thin' coating layers,
  - in analogy to the classical laminate theory (CLT), the method illustrated in Section 4.5.2.c to determine the Young's Modulus of the ORMOCER®, uses a 'parallel model' to calculate the composite modulus. In such a model the difference in Poisson's ratio between the silica fibre and coating material is neglected. To improve the calculations this difference needs to be taken into account.

- Determination of the theoretical strain gauge factor (i.e. strain sensitivity and K-matrix)
  - We need to define the exact strain optic coefficients (p_{11}, p_{12}) of the highly doped (GeO_2) silica core using a precise (transversal) calibration setup (see Section 4.4.2), which is also applicable for smaller diameter fibres. Improvement of the used calibration setup is possible, care should be taken with fibre alignment and material (hardness) of the loading stamp.

- Improving the axial strain calibrations (Section 4.4.1.b) with regard to smaller diameter optical fibres
  - Exact knowledge of the material properties of the fibre coating and adhesive which is being used during the axial calibrations will improve the knowledge on the boundary conditions of the setup,
  - Calculation of the shear lag coefficient can contribute to a better understanding of the strain transfer effects during calibration, hence a variable factor can be taken into account for specific fibres and coatings,

- Considering a better reference measurement of the strain in the optical fibre, a longer fibre basis (hence strain transfer error becomes smaller) or an intrinsic/extrinsic measurement based on the interferometric principle could be a solution.

- Improving the finite element modelling (FEM)
  - Exact knowledge of the (homogenized) engineering constants of the composite material. In principle this data is provided by the material supplier or composite manufacturer, however, a relative large scatter is possible because of different samples or size of the component, sample-thickness, manufacturing technology, etc.. To improve the accuracy on this data and thus the model, 'batch control' specimens, which represent the real (local) structural lay-up or segments, need to be manufactured (using the same manufacturing technology) and then they need to be characterized. Determination of the material properties can be accomplished by using 'classical' experimental techniques according to well know norms and standards. These mechanical tests need to be carried out with much care in order to be useful for the FE models. The author emphasizes that the combination of surface mounted and embedded FBG sensors is sometimes better suited and reliable to perform composite material characterization than surface mounted resistive electrical strain gauges, which measure only surface strains,
  - Textile composites like woven fabrics are very complex materials. The yarn interlacing pattern in the real Cetex® plates is never perfectly regular, as such the real unit-cell is never exactly the same as in the 'perfect' model. This random unit-cell geometry needs to be taken into account in the 'meso-scale' modelling to improve the unit-cell stacking to develop a full scale model and to calculate the homogeneous engineering constants.

- Residual strain monitoring
  - Although the residual measurements cited from literature and also performed in this work show a big potential of the FBGs to be used during the manufacturing cycle of composite laminates, the results are still far from satisfying. To improve the confidence in these results, more samples need to be monitored during manufacturing,
  - Care should be taken by performing accurate temperature measurements. The author emphasises that temperature readings should be performed by using both Pt-100 probes combined with (embedded) FBG temperature probes, this to ensure that accurate temperature compensation techniques can be applied. Care should be taken with annealing effects of the FBG (i.e. wavelength drift due to extreme temperatures). To ensure that no such effects occur, the FBG sensors should be pre-annealed slightly above the 'service' temperature before use,

- Because it is very difficult to define a strain transfer matrix which is applicable during the curing or consolidation process, the focus in Chapter 6 has been to measure solely the strains in the optical fibre and not the strains in the composite layer. However, by back calculating from the raw data, i.e. the wavelength shifts of the slow and the fast peak shifts measured during the out-of-plane loading after manufacturing, it is possible to determine the (initial) out-of-plane residual stress. By then using the slopes of the multi-axial composite strains calculated from these wavelength shifts (e.g. Figure 7-20) it is possible to determine the multi-axial residual strains. The author emphasises that this same procedure can be used for any composite sample, on the condition that birefringence effects are present in the core of the embedded FBG after composite manufacturing.

- Interpretation of the (embedded) sensor response
  - Besides the Centre Of Gravity (COG) method, the author believes that there is another peak calculation method suitable to determine averaged Bragg peak shifts, which is based on the cross-correlation principle and which allows to calculate accurate relative (averaged) peak wavelength shifts from distorted Bragg spectra with regard to its initial state,
  - Simulation of the complex spectral response for different variable strain distributions and loading conditions, which are acting along the length of the grating can help analysing the internal (local) strain state of the optical fibre. This can be done by implementing variable refractive index profiles in the 'optical transfer matrix formalism' which changes the field distributions inside the FBG and which then represents the variation of the strain field inside the FBG.

- A general recommendation with regard to composite testing, strain error calculation
  - Inevitable in any research there exists a scatter on the material properties used in calculations and analytical models or finite element analyses. In this research errors can be made on the opto-mechanical and thermo-optic constants of the optical fibre, which are also intrinsic temperature dependent, on the mechanical properties and dimensions of the optical fibre, fibre coating, and last but not least on the mechanical and thermal properties and dimensions of the composite laminates. Apart from the strain resolution of the (embedded) FBG, which has been calculated in this work, it is interesting to estimate the magnitude of the total error occurring during strain measurements and results as being performed in typical mechanical composite testing or testing as has been presented in this work. Such a total error estimation would be very helpful to gain insight in the (strain) accuracy which one can expect for SHM systems based on FBGs in composite elements and structures.

9. 2. 2. Industrial application

The author believes that the main realisations presented in this work are highly relevant for the material science in general and specific for the composite research community. They show that the embedded FBG sensor technology is capable of providing very useful information on the FRP material' residual strains during manufacturing and the structural integrity of FRP components during service. As mentioned in the introduction of this work, big aircraft manufacturers such as Airbus and Boeing are looking at incorporating SHM systems into their new generation (composite) airplanes. They have also stated that the fibre optic sensor, specially the FBG, is a potential SHM technology. However, one has to realise that seen the complexity of fibre reinforced plastics, there are still some very important problems to be solved with regard to the industrial application of incorporated FBG sensor systems in composite structures in general. Of course this does not only count for aerospace related composite components, but also for wind turbine blades, oil and gas pipelines, boat hulls, etc.. Because it is not possible to assess all problems related, the author will limit this discussion to three issues which are for him the most fundamental ones which need be tackled with regard to the sensor - composite interaction.

One of the main issues is the fact that we are talking about FRPs, which are very complex materials with highly variable material properties. This is even more pronounced if we are dealing with large structural components with stiffeners and reinforcement areas along the structures' length, where the composite properties and thus the (local) mechanical properties are different depending on the location in the structure. As shown in this work, the relation between the strain of the embedded sensor and its host material is not one on one, and needs to be defined using a strain transfer matrix if one wants to measure accurately (in-situ) multi-axial strains. Moreover, apart from the relatively large residual strains after manufacturing, there exists a complex multi-axial strain field when FRPs are being loaded, hence the multi-axial relationship between sensor and host material will become even more complex and thus very difficult to define if the composite properties in the structure are changing. This in fact complicates the interpretation of the sensor readings, certainly if for example one embeds more sensors in series along a structure. Nevertheless, if we are only interested in the longitudinal strains along the structure, the author recommends to use coated FBGs, such as the DTG®s being used in this work, which are less sensitive to transversal effects, hence the errors on the longitudinal strain calculations are smaller and the optical fibre can behave more 'natural' which in the end simplifies the longitudinal strain relationship. In any case, if we want to deal with larger FRP structures it will be more difficult to interpret the difference (i.e. variation) of the sensors' response. The author believes that for such purposes, extended mechanical test programs need to be carried out, which not only deal with testing on test-coupon level and single embedded sensors, but also focuses on large scale demonstrators and 'full scale' mechanical load testing (also fatigue testing), with multiple embedded sensors (in series) covering larger parts of the structure. As such one can map the possible variation and have more insight on the outcome of the sensor system on macroscopic level.

Another issue which should be taken into account is the large scatter on the material properties of composites in general. These properties are of course highly dependent

on the composite constituents, and even more important, on the composite manufacturing technology, e.g. autoclave, hot press (moulding), resin transfer injection and moulding (i.e. RTI and RTM), etc.. By using the same type of FRP material, with a different manufacturing technology, this will result in different material properties of the same test-coupon. Today, in research and industry, more often the material science relies on finite element simulations, i.e. FEM, combined with a 'classical' experimental validation program. This same approach has been used in the work presented here, however only on test-coupon level and for specific loading cases. Note that, to be able to create reliable models on larger components one needs to have more accurate material properties of the complete component, otherwise a match between FEM and the experimental results will never be reached. Because local material properties can change along (large) FRPs whether or not with a complex structure, for example when more (or less) resin content is present, it is a real challenge to get matching results. To gather more information on the variation of the (local) material properties, the behaviour of each new material (or lay-up) should be monitored during the composite curing and consolidation process. Additionally this material should be (mechanically) tested and characterized after manufacturing to define the exact material properties (i.e. engineering constants). As such, one can map the variance in mechanical properties for specific components and manufacturing technologies. In fact this information can be used to set or improve the input engineering data for finite element models for larger structures. Given the fact that today no monitoring system exists to measure the residual strains (stress') in composites during manufacturing, there is certainly some improvement possible on that level. Note that the same embedded FBG sensor can be used both during the manufacturing cycle as well as during mechanical testing, hence the author believes that the FBG is certainly a valuable tool to improve the knowledge on (local) material properties of large FRP components, but important to note is that the integration, i.e. embedding of these sensors, needs to be done already during the composite manufacturing phase and thought about during the design phase, so the sensors or sensor arrays can be placed at specially defined locations.

Third of all, we need to connect the embedded FBG sensor(s) to a read-out system. Hence, to have a reliable sensor system we need to ensure that we have a robust fibre egress point. On test-coupon level there is no need to have a aesthetic, nice and compatible composite fibre optic feed through mechanisms or embedded fibre connectors (edge or surface mounted), however, if we talk about larger composite panels or real composite constructions this can become an issue which needs to be discussed with the composite manufacturer. As such it is important, certainly on industrial level, that this problematic is dealt with already in the design phase of the composite structural component. This is of course another approach than classical being tackled using surface mounted sensors, which can put extra restrictions (e.g. avoidance of cutting edges), to the design of the composite component, however, it is not impossible, but it simply needs to be discussed properly together with the composite manufacturer. Another (elegant) approach is by avoiding fibre egress points and embedding the (miniaturized) FBG interrogator together with the optical fibre. As such the complete system is integrated in the composite and no surface or edge connectors are necessary. The development of such a system is tackled in the SMARTFIBER project (FP7), which is further highlighted in Section 9. 2. 3. .

With regard to industrial application of FBG technology the author believes that one should encourage further the industry, specially the composite industry or composite processing industry, together with the composite research community to follow a more collaborative approach within future research programs. In this way we can solve the industrial relevant problematic with regard to variety of composite properties and accurate monitoring of the structural integrity of large scale FRP structures.

9. 2. 3. The SMARTFIBER project

The author is excited to see a continuation of his established work in the SMARTFIBER FP7 European project (http://www.smartfiber-fp7.eu/), where the know-how and results of this dissertation can directly be applied. The SMARTFIBER project will develop a 'Miniturized monitoring system with autonomous readout micro-technology and fibre sensor', with a group of seven European partners including Airborne technology centre (The Netherlands), FBGS-Technologies (Germany), the Fraunhofer-Institute für Integrierte Schaltungen (Germany), the Universiteit Gent - Mechanics of Materials and Structures (MMS) and Imec, which will handle the project management for SMARTFIBER.

The smart system will enable for the first time fully embedded structural health monitoring of composites used as structural parts in e.g. wind turbine blades, satellites, airplanes, civil constructions, oil and gas wells, boat hulls. Within three years time (start date September 2010), SMARTFIBER will demonstrate a smart system so small that it can be incorporated as a whole in real fibre reinforced plastic structural components. This fully embedded approach will enable direct connection of the FBG interrogator to the FBG sensor array, and thus will eliminate the need for fibre egress points in composite structures.

Interesting to note is that one of the work packages in this research project involves a similar dual approach as has been used in this dissertation, namely, the optical fibre part of the project will be tackled by FBGS-technologies. The goal is to downsize the DTG® sensors even more (< 60 μm), and to couple it directly to the photonic-chip circuit. And the embedding part and experimental and numerical analysis of the embedded system and optical fibre will be tackled by Ghent University, Department of Material Science and Engineering.

The SMARTFIBER project illustrates well the evolution towards the near future composites and incorporation of monitoring systems which in the end is the ultimate tool to provide the user continuous record of the structural integrity.

Appendix A. Wave propagation in Single-Mode Step-Index fibres

If we consider optical fibres as waveguides, we have to solve Maxwell's equations for electromagnetic waves in order to understand the physics of wave propagation. As silica fibres are nonconducting media without free charges, these equations take the form:

$$\nabla \times \vec{E} = -\partial \vec{B} / \partial t \quad \text{A-1}$$

$$\nabla \times \vec{H} = -\partial \vec{D} / \partial t \quad \text{A-2}$$

$$\nabla \cdot \vec{E} = 0 \quad \text{A-3}$$

$$\nabla \cdot \vec{B} = 0 \quad \text{A-4}$$

Where $\vec{E}$ and $\vec{H}$ are the electric and magnetic field vectors, respectively, and $\vec{D}$ and $\vec{B}$ are the corresponding flux densities.

From these equations we can derive wave equations for $\vec{E}$ and $\vec{H}$, which describe wave propagation in dielectric media. After simplification we obtain the wave equation for the $\vec{E}$-field, and is defined as [1]

$$\nabla^2 \vec{E} + n^2(\omega) k_0^2 \vec{E} = 0, \quad \text{A-5}$$

where *n(ω)* is the frequency dependent refractive index and $k_0 = \omega / c = 2\pi / \lambda$ is the free- space wave number and λ the vacuum wavelength of the optical field oscillating at frequency ω.

To solve Equation A-5 we have to consider cylindrical symmetry and we only take into account the axial component of the electric field vector and after considerable algebraic details, we obtain the Eigenvalue equation. It can be solved numerically to determine the propagation constant of the guided mode. Each solution of Equation A-5 corresponds to a guided mode and is uniquely determined by its propagation constant β. For more detailed information regarding the theory on guided modes the reader is referred to [1].

The quantity $\overline{n} = \beta / k_0$, i.e. mode index of the fibre has the physical significance that each fibre mode propagates with an effective refractive index $\overline{n}$ whose value lies in the range $n_1 > \overline{n} > n_2$, with n_1 and n_2 the refractive index of fibre core and cladding, respectively. A mode ceases to be guided when $\overline{n} \leq n_2$ and is said to reach cut-off if $\overline{n} = n_2$. A parameter that plays an important role in determining the cutoff condition of an optical fibre is defined as [1]

$$V = k_0 a\sqrt{\left(n_1^2 - n_2^2\right)} \approx \frac{2\pi}{\lambda} a n_1 \sqrt{2\Delta}\,, \qquad \text{A-6}$$

Where Δ is the fractional refractive index change (defined by equation 3.2) and a is the core-radius. The parameter V is called the *normalized frequency* or simply the V parameter which is common used to estimate the desired core radii of optical fibres. A fibre with a large value of V supports many modes. If a fibre is designed such that $V<2.405$, it will only support the fundamental mode. This is called the *single-mode condition*. The fundamental mode has no cutoff wavelength and is always supported by a fibre. The reason for designing optical fibres with $V<2.405$ is simply because of the fact intermodal dispersion in multi-mode fibres leads to considerable broadening of short pulses.

We now understand how single mode fibres with a proper step index can be designed to guide only one mode with its *mode index* $\overline{\mathrm{n}}$, which is determined by its specific propagation constant β. A fibre Bragg grating acts as a reflection filter and its centre wavelength is called the Bragg wavelength $\lambda_B = 2\overline{\mathrm{n}}\Lambda$ (see Section 1.3.2) Due to index variations with period Λ the forward- and backward-propagating waves are coupled at a given frequency ω. In the next this coupled mode theory (CMT) is explained for a uniform type of FBG

Uniform FBG theory

For simplicity we consider a uniform type of grating (Section 2.6.1) in which the modulation of the refractive index changes periodically as $n(z) = n_1 + \Delta n_d(z) + \Delta n_g(z)\cos\left(\frac{2\pi}{\Lambda(z)}z + \Phi(z)\right)$, where n_1 is the refractive index of the core, Δn_g is the *modulation depth* or *amplitude* (typically ~10^{-4}) and Δn_d the average or homogeneous refractive index modulation. For a uniform FBG $\Delta n_g(z)$, $\Delta n_d(z)$ and $\Lambda(z)$ are constants. The grating index change depends on the amount of UV-radiation during inscription and the amount of dopant (e.g GeO_2) in the core [2]. It is the refractive-index disturbance which is responsible for coupling the forward- and backward-propagating waves in the grating. The coupled mode equations are given by

$$\partial a / \partial z = ia\kappa_d + ib\kappa e^{-i(2\Delta\beta - \phi')z} \qquad \text{A-7}$$

$$\partial b / \partial z = -ib\kappa_d - ia\kappa e^{i(2\Delta\beta - \phi')z}\,, \qquad \text{A-8}$$

where a and b are the *spectral amplitudes* of the forward and backward propagating waves, respectively, the phase change $d\phi/dz = \phi' = const$ for a homogeneous FBG and

$$\Delta\beta = \beta - \pi / \Lambda_{FBG} = 2\pi\bar{n}\left(\frac{1}{\lambda} - \frac{1}{\lambda_B}\right). \qquad \text{A-9}$$

Here $\Delta\beta$ describes the detuning from the Bragg wavelength with $\beta = 2\pi\bar{n}/\lambda$ the propagation constant, $\kappa_d = \frac{2\pi\Delta n_d \Gamma}{\lambda_D} = const$ and $\kappa = \frac{\pi\Delta n_g \Gamma}{\lambda_D}$ the *coupling coefficients* with λ_D the *design-wavelength* of the FBG, which is not necessarily exactly the same as the *Bragg wavelength* λ_B, see Equation A-14. The parameter Γ is called the *confinement factor*; which defines the fraction of the power contained in the core with radius *r* and is given by

$$\Gamma = \frac{P_{core}}{P_{total}} = \frac{\int_0^a |E_x|^2 \rho d\rho}{\int_0^\infty |E_x|^2 \rho d\rho} = 1 - \exp\left(-2r^2/\omega^2\right), \qquad \text{A-10}$$

with ω the *field radius* or *spot size.*

The design-wavelength of the FBG, λ_D, is found by posing the detuning $\Delta\beta=0$, in Equation A-9

$$\lambda_D = 2\bar{n}\Lambda_{FBG}. \qquad \text{A-11}$$

Because of their linear nature the coupled mode equations in Equation A-7 and A-8 can be solved analytically to calculate the complex *reflection-coefficient,* ρ, for a grating with length L_g, and is found to be [1]

$$\rho = |\rho| e^{i\phi} = \frac{b(0)}{a(0)} = \frac{\kappa \sinh\left(sL_g\right)}{q\sinh\left(sL_g\right) - is\cosh\left(sL_g\right)}, \qquad \text{A-12}$$

with $s^2 = \left|\kappa^2\right| - q^2$ and $q = \Delta\beta + \kappa_d$, the coefficient which describes the coupling of the modes with oneself.

The reflectivity, also known as the reflected Bragg spectrum is then given by

$$R = |\rho|^2 = \frac{|\kappa|^2 \sinh^2\left(sL_g\right)}{|\kappa|^2 \cosh^2\left(sL_g\right) - q^2}. \qquad \text{A-13}$$

The maximum of Equation A-13 occurs at $q=0$, when coupling of the modes is maximized. This condition defines the Bragg wavelength, λ_B of the grating. Posing $q=0$ and using Equation A-9 we find $\Delta\beta = -\kappa_d$ and

$$\frac{\lambda_B - \lambda_D}{\lambda_B} = \frac{\Gamma \Delta n_d}{\bar{n}}. \qquad \text{A-14}$$

Equation A-14 describes the grating spectrum shift to higher wavelengths when the homogenous part, Δn_d, of the refractive index change appears during grating inscription. Appearance of a homogeneous refractive index modulation is typically achieved by post UV radiation. The real Bragg wavelength or resonance wavelength of such gratings is then the design wavelength plus a small portion of the initial Bragg wavelength induced by the homogeneous modulation. In principle $\Delta n_d \approx 0$, in the case of uniform FBGs, hence from Equation A-14 we find $\lambda_D = \lambda_B = 2\bar{n}\Lambda_{FBG}$. It is this equalizing which is being used throughout the work for the definition of the Bragg wavelength.

The wavelength window for which the *s*- parameter is real is defined as the stop band of the grating. Outside the stop band *s* is imaginary and the reflectivity is than given by:

$$R = |\rho|^2 = \frac{|\kappa|^2 \sinh^2(sL_g)}{|\kappa|^2 \cosh^2(sL_g) - q^2} \quad \text{for } s^2 > 0, \qquad \text{A-15}$$

$$R = |\rho|^2 = \frac{|\kappa|^2 \sinh^2(sL_g)}{q^2 - |\kappa|^2 \cosh^2(sL_g)} \quad \text{for } s^2 < 0. \qquad \text{A-16}$$

When the Bragg condition is fulfilled the maximum reflectivity is found to be

$$R_{\max} = \tanh^2(\kappa L_g). \qquad \text{A-17}$$

As seen in Equation A-17 in the maximum reflectivity depends on the product κL_g and is called the *grating strength*. The grating strength is depending on the modulation depth, Δn_g, and the length of the grating.

Weak gratings

If low reflective gratings are considered such as the draw tower gratings used in this work, the grating strength $\kappa L_g \ll 1$. For weak FBGs Equation A-7 and A-8 can then be simplified by

$$\partial a / \partial z = ib\kappa e^{-i(2\Delta\beta - \phi')z} \qquad \text{A-18}$$

$$\partial b / \partial z = -ia\kappa e^{i(2\Delta\beta - \phi')z}, \qquad \text{A-19}$$

Integration of Equation A-19 is also known as the *non depleted pump approximation* which is a satisfying approximation to calculate the reflection coefficients of weak gratings. For a weak grating without any chirp ($\phi = 0$) the Reflectivity is then given by

$$R(\Delta\beta) = \left| \int \kappa(z) e^{i2\Delta\beta z} \right|^2 , \qquad \text{A-20}$$

Which is also known as a Fourier integral. The spectrum of weak gratings with length L is then given by

$$R(\Delta\beta) = (\kappa L)^2 \operatorname{sinc}^2(\Delta\beta L) , \qquad \text{A-21}$$

with the maximum reflectivity given by:

$$R_{\max} = (\kappa L)^2 = \left(\frac{\pi \Delta n_g \Gamma L}{\lambda_D} \right)^2 \qquad \text{A-22}$$

From Equation A-17 and A-22 we see the maximum reflection of an FBG depends strongly on the modulation depth, i.e. the coupling coefficient, κ, and the length of the grating, L. Figure A. 1 shows the reflectivity for different values of the grating strength, κL . The reflection is calculated using Equation A-15 , and Equation A-21 for the weaker grating, and plotted against the unit less detuning, $\Delta\beta L$ (Equation A-9).

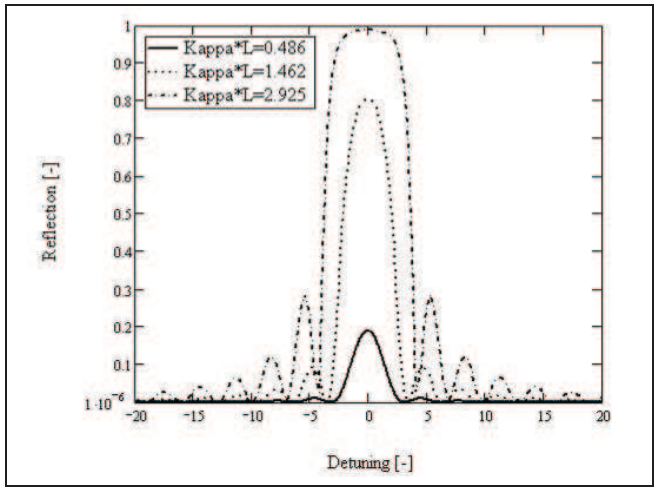

Figure A. 1 Magnitude of the reflectivity plotted as a function of the detuning $\Delta\beta L$

Full width at half maximum

The $\Delta\lambda_{FWHM}$ (Full Width at Half Maximum) of a grating can be numerically calculated and it follows that for strong gratings ($\kappa L>1$), the $\Delta\lambda_{FWHM} \approx \Delta\lambda_{FM}$ (Full Width at First Minima). For weak gratings ($\kappa L«1$) the FWHM is found to be approximately half the width at first minima [2]. This results in the following relation:

$$0.44 \cdot \Delta\lambda_{FM} \leq \Delta\lambda_{FWHM} \leq \Delta\lambda_{FM} \qquad \text{A-23}$$

For calculating $\Delta\lambda_{FM}$, we have to set Equation A-22 equal to zero and after finding the positions of the minima this results in:

$$\frac{\Delta\lambda_{FM}}{\lambda_D} = \sqrt{\left(\frac{\eta\Delta n_g}{\bar{n}}\right)^2 + \left(\frac{2}{N}\right)^2} \,. \qquad \text{A-24}$$

According Equation A-24, the spectral width of the grating is determined by the *modulation depth*, Δn_g, and by the *number of grating periods N*, which is directly related to the length of the FBG with $N = L/\Lambda$

Typically in draw tower runs (Chapter 2) the pulse energy of the laser beam is set maximal when writing the DTG®. As such the modulation depth Δn_g, is maximized independent of the grating length L. The length of the grating is defined by a fixed slit which cuts the beam. If the width of the slit is changed, the grating length, hence the number of grating periods is changed. Figure A. 2 shows the maximal reflection and FWHM for different grating lengths. For a typical length of 8mm $\Delta\lambda_{FM}$

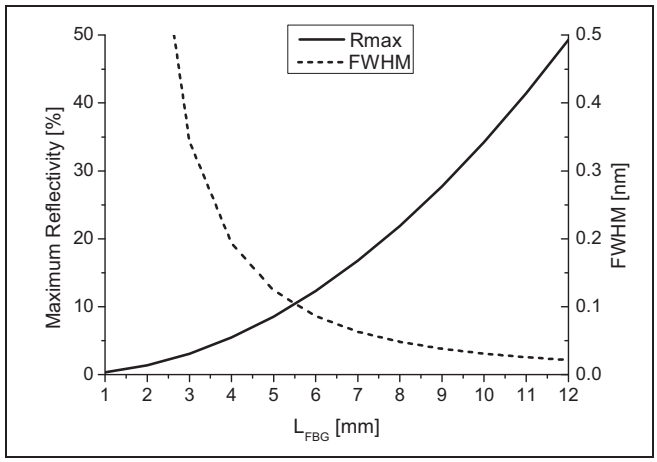

Figure A. 2 Maximum reflectivity and FWHM as function of FBG length at 1550nm

References

1. Agrawal, P., Govind., *Fiber-optic communication systems*. third ed. 2003: Wiley interscience.
2. Hagemann, V.J., *Untersuchungen zum dynamischen Einzelpuls-Einschreiben von Faser-Bragg-Gittern un zu deren Anwendung*. 2001, Friedrich-Schiller University: Jena.

Appendix B. FUNDAMENTALS OF FBG SENSING _MEASURING STRAIN & TEMPERATURE

The calibrations in Section 4.4.3 make use of the formulations which are derived in this appendix. The formulas can be used to calculate the axial and transversal strains in a non-embedded FBG. The non-linear temperature dependence in this appendix describes the quadratic temperature calibration parameters of a non-embedded FBG.

A fibre Bragg grating is sensitive to strain and temperature. The *general Bragg wavelength* for a free fibre grating is given by:

$$\lambda_B(\varepsilon,T) = 2\overline{n}(\varepsilon,T)\Lambda(\varepsilon,T)\,, \qquad \text{B-1}$$

with both the *effective refractive index* $\overline{n}(\varepsilon,T)$ and the *grating period* $\Lambda(\varepsilon,T)$ strain and temperature dependent. If small perturbations of strain, $d\varepsilon_i$, along the principal axis of the optical fibre, and temperature, dT, occur, with

$$\varepsilon_i = \varepsilon_{i,0} + d\varepsilon_i \qquad i = 1,2,3\,, \qquad \text{B-2}$$

and

$$T = T_0 + dT\,, \qquad \text{B-3}$$

the *total shift* of the Bragg wavelength as function of these small strain and temperature perturbation is then given by:

$$\begin{aligned} d\lambda_B(d\varepsilon_i, dT) = {} & 2\left(\Lambda(d\varepsilon_i)\frac{\partial\overline{n}(d\varepsilon_i)}{\partial d\varepsilon_i} + \overline{n}(d\varepsilon_i)\frac{\partial\Lambda(d\varepsilon_i)}{\partial d\varepsilon_i}\right)d\varepsilon_i \\ & +2\left(\Lambda(dT)\frac{\partial\overline{n}(dT)}{\partial dT} + \overline{n}(dT)\frac{\partial\Lambda(dT)}{\partial dT}\right)dT \end{aligned}\,, \qquad \text{B-4}$$

Response to pure strain (*dT=0*):

In the case of an isothermal condition (dT=0) the *Bragg condition* is simplified to pure strain and can then be written as:

$$\lambda_B(d\varepsilon_i) = 2\overline{n}(d\varepsilon_i)\Lambda(d\varepsilon_i)\,. \qquad \text{B-5}$$

By substitution of $2\overline{n}(d\varepsilon_i) = \dfrac{\lambda_B(d\varepsilon_i)}{\Lambda(d\varepsilon_i)}$ and $2\Lambda(d\varepsilon_i) = \dfrac{\lambda_B(d\varepsilon_i)}{\overline{n}(d\varepsilon_i)}$, Equation B-4 can be rewritten as:

$$\frac{d\lambda_B(d\varepsilon_i)}{\lambda_B(d\varepsilon_i)} = \left(\frac{1}{\overline{n}(d\varepsilon_i)}\frac{\partial\overline{n}(d\varepsilon_i)}{\partial d\varepsilon_i} + \frac{1}{\Lambda(d\varepsilon_i)}\frac{\partial\Lambda(d\varepsilon_i)}{\partial d\varepsilon_i}\right)d\varepsilon_i\,. \qquad \text{B-6}$$

Noting that $\frac{\partial \Lambda(d\varepsilon_i)}{\Lambda(d\varepsilon_i)} = \partial d\varepsilon_i$ the second term in this derivation equals 1, the *Bragg wavelength as function of the strain* is written as:

$$\frac{d\lambda_B(d\varepsilon_i)}{\lambda_B(d\varepsilon_i)} = \left(\frac{1}{\overline{n}(d\varepsilon_i)} \frac{\partial \overline{n}(d\varepsilon_i)}{\partial d\varepsilon_i} + 1 \right) d\varepsilon_i . \qquad \text{B-7}$$

The first term of Equation B-7 is understood by working out the linear relationship between the *impermeability tensor* and the *strain tensor*:

$$\Delta\eta_{ij} = \Delta\left(\frac{1}{n^2}\right)_{ij} = p_{ijkl}\varepsilon_{kl} \qquad \text{B-8}$$

with $\Delta\eta_{ij}$ the *change in the optical impermeability tensor*, ε_{kl} the *strain tensor* and the coefficients p_{ijkl} form the *strain-optic tensor*. Since both η_{ij} and ε_{kl} are symmetric tensors, the indices *i* and *j* as well as *k* and *l* in the strain optic tensor can be permuted. In analogy to the symmetry properties of the Kerr's tensor (i.e. quadratic electro-optic effect) Equation B-8 can be simplified using the contracted indices. The *impermeability tensor* becomes then:

$$\frac{1}{n_i^2} = \frac{1}{n_0^2} + p_{ij}\varepsilon_j \quad i,j = 1,2,...,6 \qquad \text{B-9}$$

$$\Leftrightarrow \left(\frac{1}{n_i^2}\right)^{-\frac{1}{2}} = n_i = \left(\frac{1}{n_0^2} + p_{ij}\varepsilon_j\right)^{-\frac{1}{2}} \approx n_0 - \frac{1}{2}n_0^3 p_{ij}\varepsilon_j \qquad \text{B-10}$$

$$\Rightarrow \Delta n_i = -\frac{1}{2}n_0^3 p_{ij}\varepsilon_j \quad i,j = 1,2,...,6 \qquad \text{B-11}$$

Here, Equation B-11 represents the *change of the refractive index* as function of the *applied strain* with n_0 the unperturbed refractive index. For an isotropic medium (i.e. fused silica) the *strain optic tensor*, p_{ij}, will contain only two independent strain optic coefficients p_{11} and p_{12}, and is given by:

$$p_{ij} = \begin{pmatrix} p_{11} & p_{12} & p_{12} & 0 & 0 & 0 \\ p_{12} & p_{11} & p_{12} & 0 & 0 & 0 \\ p_{12} & p_{12} & p_{11} & 0 & 0 & 0 \\ 0 & 0 & 0 & \frac{1}{2}(p_{11}-p_{12}) & 0 & 0 \\ 0 & 0 & 0 & 0 & \frac{1}{2}(p_{11}-p_{12}) & 0 \\ 0 & 0 & 0 & 0 & 0 & \frac{1}{2}(p_{11}-p_{12}) \end{pmatrix} \quad \text{B-12}$$

To derive the *total strain formulation* of a non embedded fibre Bragg grating we use an orthogonal coordinate system as defined in Figure B-1:

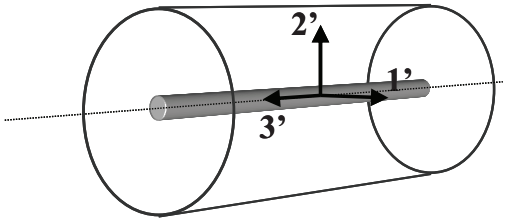

Figure B-1: The coordinate system used for the optical fibre

The indication ' is used in this coordinate system to avoid confusion with the coordinate system of the single composite layers (Chapter 6 & 7). The 3'-axis is taken the longitudinal axis of the fibre, the 1'- and 2'-axis are taken the transversal directions of the fibre.

Response to multi-axial strain

We define now $d\varepsilon = \left[d\varepsilon_{1'}, d\varepsilon_{2'}, d\varepsilon_{3'}\right]^T$ as the three main strain perturbation components along the axes of the coordinate system, as shown in Figure B-1. The strain components $d\varepsilon_{4'}$,$d\varepsilon_{5'}$ and $d\varepsilon_{6'}$ can be left out of consideration because they have no influence neither on the refractive index nor on the spacing of the grating [1]. By using Equation B-11 the following relationships are found between the change in refractive indices and the three principle strain components:

$$\begin{cases} \Delta n_{1'} = -\frac{1}{2} n_0^3 \left(p_{11}\varepsilon_{1'} + p_{12}\left(\varepsilon_{2'} + \varepsilon_{3'}\right)\right) \\ \Delta n_{2'} = -\frac{1}{2} n_0^3 \left(p_{11}\varepsilon_{2'} + p_{12}\left(\varepsilon_{1'} + \varepsilon_{3'}\right)\right) \end{cases} \quad \text{B-13}$$

It is common to use the *effective refractive index*, $\bar{n}$ in stead of the *unperturbed index*, n_0. By substituting $\bar{n}$ in Equation B-13, the first term in Equation B-7 is then written as:

$$\begin{cases} \dfrac{1}{\overline{n}_{1'}(d\varepsilon_i)}\dfrac{\partial \Delta\overline{n}_{1'}(d\varepsilon_i)}{\partial d\varepsilon_i}d\varepsilon_i = -\dfrac{1}{2}\overline{n}_{1'}^2\left(p_{11}d\varepsilon_{2'} + p_{12}\left(d\varepsilon_{1'} + d\varepsilon_{3'}\right)\right) \\ \dfrac{1}{\overline{n}_{2'}(d\varepsilon_i)}\dfrac{\partial \Delta\overline{n}_{2'}(d\varepsilon_i)}{\partial d\varepsilon_i}d\varepsilon_i = -\dfrac{1}{2}\overline{n}_{2'}^2\left(p_{11}d\varepsilon_{2'} + p_{12}\left(d\varepsilon_{1'} + d\varepsilon_{3'}\right)\right) \end{cases}, \qquad \text{B-14}$$

The solution of Equation B-7 *for both polarization axes* in the fibre is then given by:

$$\begin{cases} \left.\dfrac{d\lambda_B(d\varepsilon_i)}{\lambda_B(d\varepsilon_i)}\right|_{1'} = \dfrac{d\lambda_{B,1'}}{\lambda_{B,1'}} = d\varepsilon_{3'} - \dfrac{1}{2}\overline{n}_{1'}^2\left(p_{11}d\varepsilon_{1'} + p_{12}\left(d\varepsilon_{2'} + d\varepsilon_{3'}\right)\right) \\ \left.\dfrac{d\lambda_B(d\varepsilon_i)}{\lambda_B(d\varepsilon_i)}\right|_{2'} = \dfrac{d\lambda_{B,2'}}{\lambda_{B,2'}} = d\varepsilon_{3'} - \dfrac{1}{2}\overline{n}_{2'}^2\left(p_{11}d\varepsilon_{2'} + p_{12}\left(d\varepsilon_{1'} + d\varepsilon_{3'}\right)\right) \end{cases}, \qquad \text{B-15}$$

Equation B-15 is also know as the *total strain response* of a non-embedded FBG to a *multi-axial strain field*.

Pure axial strain

In the case that only a pure axial strain shift is present (i.e. in the 3' direction), we can write the transversal strain perturbations ($d\varepsilon_{1'}, d\varepsilon_{2'}$) as a fraction of the axial strain perturbation ($d\varepsilon_{2'}$):

$$d\varepsilon_{1'} = d\varepsilon_{2'} = -\upsilon_f d\varepsilon_{3'}, \qquad \text{B-16}$$

with υ_f the Poisson ratio of the optical fibre (typical $\upsilon_f = 0.16$) and for a single mode fibre we can assume:

$$\overline{n}_{1'} \overset{SMF}{=} \overline{n}_{2'} = \overline{n} \qquad \text{B-17}$$

Filling in these relations in Equation B-15, we obtain the well known response of an non-embedded FBG subjected to an *axial strain* field:

$$\frac{d\lambda_{B,1'}}{\lambda_{B,1'}} = \frac{d\lambda_{B,2'}}{\lambda_{B,2'}} = \frac{d\lambda_B}{\lambda_B} = (1-P)d\varepsilon_{3'} \qquad \text{B-18}$$

In which P is the *strain optic constant* defined by:

$$P = \frac{1}{2}\overline{n}^2\left(p_{12} - \upsilon_f\left(p_{11} + p_{12}\right)\right) \qquad \text{B-19}$$

Equation B-18 can be integrated, and by defining $(1-P) = S_\varepsilon$, the longitudinal *strain gauge factor*, one gets:

$$\ln\lambda_B = S_\varepsilon\varepsilon_{3'} + C, \qquad \text{B-20}$$

with C being a constant of integration. The constant can be determined by filling in an arbitrary wavelength $\lambda_{B,0}$ and the corresponding axial strain $\varepsilon_{3',0}$. Accordingly, one gets:

$$C = \ln \lambda_{B,0} - S_\varepsilon \varepsilon_{3',0}, \tag{B-21}$$

which yields:

$$\ln \frac{\lambda_B}{\lambda_{B,0}} = S_\varepsilon \Delta\varepsilon_{3'}, \tag{B-22}$$

$$\Rightarrow \Delta\varepsilon_{3'} = \frac{\ln \dfrac{\lambda_B}{\lambda_{B,0}}}{S_\varepsilon} \tag{B-23}$$

where $\Delta\varepsilon_{3'} = \varepsilon_{3'} - \varepsilon_{3',0}$. Equation B-23 represents a practical formula which allows easy calculation of the *longitudinal strain* of a non-embedded FBG by using the *strain gage factor*, S_ε, the *reference wavelength*, $\lambda_{B,0}$ and the *measured wavelength*, λ_B. It is noted the *strain gage factor* is a *calibration parameter* which is *wavelength independent*, and hence can be applied for large strain ranges without inducing calculation errors. In the axial calibrations in Section 4.4.1, on the 80µm and 125µm DTG®s we find a typical value of $S_\varepsilon = 0.777$ (or 7.77E-7/µε).

Response to transversal strain difference

From Equation B-15 we can calculate the difference in Bragg wavelength shift between both polarization modes. The difference in wavelength is calculated with respect to the initial Bragg wavelength, with $\lambda_{B,0,1'} = \lambda_{B,0,2'} = \lambda_{B,0}$, hence without any birefringence in the core of the fibre. By using the relation of the refractive indices for an SMF from Equation B-17, and starting from the initial Bragg wavelength $\lambda_{B,0}$, and substituting in Equation B-15, we can write:

$$\frac{d\lambda_{B,1'} - d\lambda_{B,2'}}{\lambda_{B,0}} = \frac{\overline{n}^2}{2}\left(p_{12} - p_{11}\right)\left(d\varepsilon_{1'} - d\varepsilon_{2'}\right). \tag{B-24}$$

Because the variations of the wavelengths are typically small (~10^2pm) compared to the optical wavelength (1550nm), such that $d\lambda = \Delta\lambda$ and $d\varepsilon = \Delta\varepsilon$, the *difference in transversal strain,* $\Delta\varepsilon_{trans}$, can be expressed as:

$$\Delta\varepsilon_{1'} - \Delta\varepsilon_{2'} = \Delta\varepsilon_{trans} = \frac{2}{\overline{n}^2}\frac{\lambda_{B,1'} - \lambda_{B,2'}}{\lambda_{B,0}\left(p_{12} - p_{11}\right)}, \tag{B-25}$$

with

$$\Delta\lambda_{B,2'} - \Delta\lambda_{B,1'} = \lambda_{B,2'} - \lambda_{B,1'} . \qquad \text{B-26}$$

Equation B-25 is useful to estimate the difference in strain existing in the core of an (embedded) optical fibre. In Section 4.4.2 we make use of this equation to estimate the strain optic coefficients from diametrical compression testing on a non-embedded fibre. In Chapter 6 Equation B-25 is used to determine transversal residual strains in the core of embedded optical fibres.

Response to pure temperature ($d\varepsilon=0$):

In analogy to the case of pure strain, for a tension free FBG ($d\varepsilon_i=0$) the *Bragg condition* is simplified to pure temperature and can then be written as:

$$\lambda_B(dT) = 2\bar{n}(dT)\Lambda(dT) . \qquad \text{B-27}$$

By substitution of $2\bar{n}(dT) = \frac{\lambda_B(dT)}{\Lambda(dT)}$ and $2\Lambda(dT) = \frac{\lambda_B(dT)}{\bar{n}(dT)}$, Equation B-4 can be rewritten as:

$$\frac{d\lambda_B(dT)}{\lambda_B(dT)} = \left(\frac{1}{\bar{n}(dT)} \frac{\partial \bar{n}(dT)}{\partial dT} + \frac{1}{\Lambda(dT)} \frac{\partial \Lambda(dT)}{\partial dT} \right) dT , \qquad \text{B-28}$$

or written in the typical format:

$$\frac{d\lambda_B(dT)}{\lambda_B(dT)} = \left(\alpha_n + \alpha_f \right) dT \qquad \text{B-29}$$

where $\alpha_n(dT) = \frac{1}{\bar{n}(dT)} \frac{\partial \bar{n}(dT)}{\partial dT}$ is the *thermo-optic coefficient* and $\alpha_f(dT) = \frac{1}{\Lambda(dT)} \frac{\partial \Lambda(dT)}{\partial dT}$ is the *thermal expansion coefficient* of the fibre (typical $0.55 \cdot 10^{-6} K^{-1}$ for silica fibres [2]. For large temperature ranges the thermal expansion coefficient, α_f, of silica is found constant [3], however the thermo-optic effect, α_n, is temperature dependent and is given by $\alpha_n = aT + b$ [4].

Substituting in Equation B-29, and considering a definite integration, we can write:

$$\int \frac{d\lambda_B(dT)}{\lambda_B(dT)} = \int \left(aT + b + \alpha_f \right) dT . \qquad \text{B-30}$$

The temperature T in Equation B-30 , however, can be substituted by a *difference in temperature* $\Delta T = T - T_{ref}$, in which the temperature is then given with respect to a reference temperature, T_{ref}. The reference temperature is defined during calibration. The definite integral can then be written as:

$$\int \frac{d\lambda_B(d\Delta T)}{\lambda_B(d\Delta T)} = \int \left(a\Delta T + b' + \alpha_f\right) d\Delta T \,, \qquad \text{B-31}$$

with $b' = b - aT_{ref}$. By using a wavelength interval from $\lambda_{B,0}$ to λ_B, and a temperature range, T_0 to T (with respect to T_{ref}), we can integrate the left and right term of Equation B-31. Its solution is given by:

$$\ln \frac{\lambda_B}{\lambda_{B,0}} = \left[\left(\alpha_f + b\right)\Delta T + \frac{a}{2}\Delta T^2 \right]_{T_0}^{T} . \qquad \text{B-32}$$

If we further elaborate Equation B-32, the solution yields:

$$\ln \frac{\lambda_B}{\lambda_{B,0}} = S_{T1}\left(\Delta T - \Delta T_0\right) + S_{T2}\left(\Delta T^2 - \Delta T_0^2\right), \qquad \text{B-33}$$

in which the *linear coefficient* S_{T1} is the sum of α_f and *b'* and the *quadratic coefficient* S_{T2} is equal to $a/2$, and the temperature difference $\Delta T = T - T_{ref}$ and $\Delta T_0 = T_0 - T_{ref}$ represent the actual and initial temperature shifts with respect to the reference temperature during calibration. It is noted that, once S_{T1} and S_{T2} are determined, Equation B-33 can be used at any arbitrary starting temperature T_0, independent of the reference temperature T_{ref}, defined during calibration.
To calibrate the linear and quadratic coefficients we take $T_0 = T_{ref}$ and $\lambda_{B,0} = \lambda_{B,ref}$, as such the terms $\Delta T_0 = 0$ and Equation B-33 yields:

$$\ln \frac{\lambda_B}{\lambda_{B,0}} = S_{T1}\Delta T + S_{T2}\Delta T^2 . \qquad \text{B-34}$$

Equation B-34 represents the non-linear temperature calibration formula used in Section 4.4.3 in which the coefficients S_{T1} and S_{T2} are found experimentally by fitting Equation B-34 against a second order polynomial. An example of the non-linear calibration curve and its polynomial fit is given in Figure B-2:

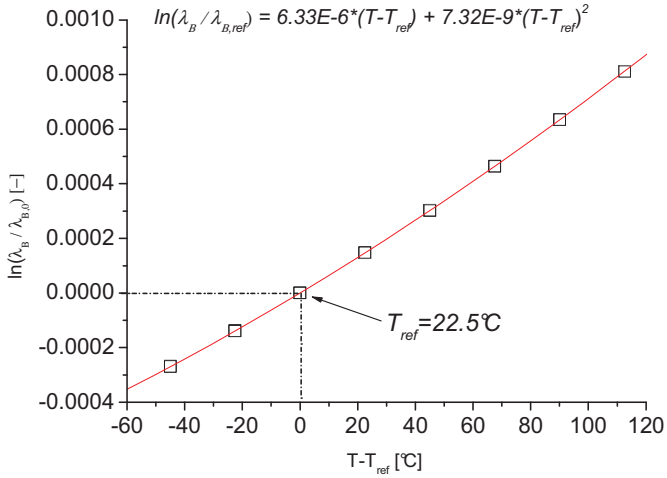

Figure B-2: Calibration curve plotted against $\Delta T = T - T_{ref}$, fitted with a second order polynomial

Inversely, by using the roots of Equation B-34, and filling in the reference wavelength, $\lambda_{B,0} = \lambda_{B,ref}$, at the reference temperature T_{ref}, and using the calibrated values for S_{T1} and S_{T2}, we can calculate the absolute (or relative) temperature, T at any arbitrary wavelength λ_B. The positive root of Equation B-34 is given by:

$$T = T_{ref} + \frac{-S_{T1}}{2S_{T2}} + \sqrt{\left(\frac{S_{T1}}{2S_{T2}}\right)^2 + \frac{1}{S_{T2}} \ln \frac{\lambda_B}{\lambda_{B,ref}}} \quad . \qquad \text{B-35}$$

References

1. De Waele, W., *Structural monitoring of composite elements using optical fibres with Bragg-sensors.*, in *Department of mechanical construction and production*. 2001-2002, PhD dissertation at Ghent University: Ghent.
2. http://www.fibercore.com.
3. Kühn, B. and R. Schadrack, *Thermal expansion of synthetic fused silica as a function of OH content and fictive temperature.* Journal of Non-Crystalline Solids, 2009. **355**(4-5): p. 323-326.
4. Leviton, D.B. and B.J. Frey. *Temperature-dependent absolute refractive index measurements of synthetic fused silica.* 2007; Available from: http://ntrs.nasa.gov/archive/nasa/casi.ntrs.nasa.gov/20070018851_2007019043.pdf.